Wrocław University of Technology
Centre of Advanced Materials and Nanotechnology

Materials Science
Poland

Vol. 25 • No. 2 • 2007

Oficyna Wydawnicza Politechniki Wrocławskiej

From the Coordinator of the national Scientific Network MAG-EL-MAT

The scientific network "New Materials for Magnetoelectronics – MAG-EL-MAT", which was founded at the beginning of 2003, currently gathers over 50 very active research groups, which means about 300 scientists from the Polish universities and other scientific institutions (mostly from the Polish Academy of Sciences). The general theoretical and experimental goal of the network is to investigate electronic and magnetic properties of new materials exhibiting properties useful for the creation of new magnetoelectronic devices.

The first MAG-EL-MAT Meeting, held in Będlewo between 26 and 28 October 2003, and the second Meeting held on 13–16 April 2004, ended without collecting papers summarising the presentations given by their participants.

After the third Meeting on 2–6 May 2005, the organizers and the MAG-EL-MAT Coordinating Committee decided to publish in a regular journal the papers presented at the meeting. Fifty papers, after a regular refereeing procedure, were published on 336 pages of a special issue of of *Materials Science-Poland*[*], edited by Tadeusz Luciński and Stanisław Lipiński.

The fourth Meeting took place on 3–6 May 2006, in the form of a series of small seminars (four special sessions) and a plenary session with lectures delivered by J. Kossut and J. Dubowik. The topics selected for the fourth MAG-EL-MAT Meeting were: biomagnetics and medical physics, strongly correlated electrons in spintronics, modern electronics and nanotechnology. There were 104 participants, who delivered 32 oral contributions and presented 58 posters.

I asked again S. Lipiński and T. Luciński to act as Guest Editors of this special issue of Materials Science-Poland. I express my gratitude to both of them and to all participants and referees for the energy and effort they have put into making these proceedings successful.

Bogdan Idzikowski

---

[*]Mater. Sci.-Poland, 24 (2006), 539–874.

Participants of the Meeting of the Members of Scientific Network New Materials for Magnetoelectronics, MAG-EL-MAT, Będlewo, 3–6 May 2006

Contents

Materials Science-Poland, Vol. 25, No. 2, 2007

Magnetic properties of Dy_5Pd_2 single crystal

M. KLIMCZAK[1], E. TALIK[1*], J. KUSZ[1], W. HOFMEISTER[3], A. WINIARSKI[1], R. TROĆ[2]

[1]Institute of Physics, University of Silesia, Uniwersytecka 4, 40-007 Katowice, Poland

[2]Institute of Low Temperature and Structure Research, Polish Academy of Sciences, Okólna 2, 50-422 Wrocław, Poland

[3]Institut für Geowissenschaften, Universität Mainz, 55099 Mainz, Germany

Thermal variation of the lattice parameters, magnetic susceptibility and magnetization of a Dy_5Pd_2 single crystal has been measured. The single crystal obtained by the Czochralski method crystallized in the cubic Dy_5Pd_2 type structure. The compound exhibits two characteristic temperatures. The former equals about 40 K, and the latter about 20 K, being connected with the complex ordering of the rare earth sublattice and the reorientation process of the magnetic moments, respectively.

Key words: *rare earth–transition metal compound; single crystal; lattice parameters; magnetic susceptibility*

1. Introduction

The R_5Pd_2 intermetallic compounds were investigated by Berkowitz et al. [1]. They reported the existence of four new R_5Pd_2-type (R = Gd, Tb, Dy, Ho) compounds. All these compounds crystallize in the cubic Dy_5Pd_2-type crystal structure belonging to the space group *Fd*3*m* [2]. Recently, magnetic properties of R_5Pd_2 (R = Tb, Dy, Ho, Er) intermetallic compounds were examined [3]. The samples were obtained in a polycrystalline form by induction melting. The electrical resistivity as well as ac and dc magnetic susceptibility measurements show a complex transport and magnetic behaviour of these compounds. The aim of this work was to grow a good quality single crystal of Dy_5Pd_2 and to examine the thermal variations of its lattice parameter as well as its magnetic properties.

*Corresponding author, e-mail: talik@us.edu.pl

2. Experimental

The single crystal was obtained by the Czochralski method from a levitated melt using high purity starting materials. The structure of the "as-grown" crystal was examined by the X-ray Berg–Barrett topography using FeK_α radiation. The lattice parameter of the Dy_5Pd_2 single crystal was studied in the temperature range from 10 K up to 300 K using a multilayer OSMIC monochromator with CuK_α radiation from a Schneider rotating anode and four-circle Huber diffractometer with χ-circle [4]. The diffractometer was controlled by a STADI4 program system and equipped with a two-stage closed-cycle helium-cooling device (CTI-Cryogenics). The temperature was controlled within the accuracy of 0.1 K.

DC magnetic susceptibility and magnetization were measured parallel to the [111] direction in the temperature range 1.9-400 K and in applied magnetic fields up to 5 T using a Quantum Design MPMS (Magnetic Property Measurement System) SQUID magnetometer.

3. Results and discussion

The Berg–Barrett X-ray topography of Dy_5Pd_2 shows that the investigated crystal grew without mosaic structure (Fig. 1). The room temperature lattice constant a is 13.53 Å being in good agreement with the value reported in Ref. [2].

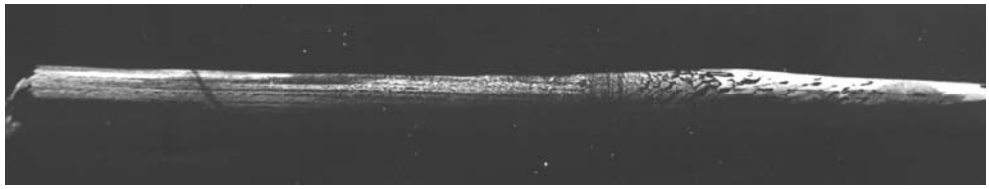

Fig. 1. Berg–Barrett topography of the Dy_5Pd_2 single crystal

Precise measurements of thermal variation of the lattice parameter were carried out for the produced single crystal. The temperature dependence of the unit cell volume V is presented in Fig. 2. The unit cell volume V decreases in agreement with the Grüneisen–Debye theory on decreasing temperature from 300 down to 50 K. Below the latter temperature, which is close to the magnetic ordering temperature, the contraction of the unit cell volume was observed. The obtained thermal dependence of the unit cell volume was fitted according to the Grüneisen–Debye theory assuming the Debye temperature Θ_D = 180 K (Fig. 2). The linear thermal and volume expansion coefficients α_a and α_V in the temperature range from 150 K to 300 K equal $3.99(14)\times10^{-5}$ K^{-1} and $1.34(4)\times10^{-5}$ K^{-1}, respectively.

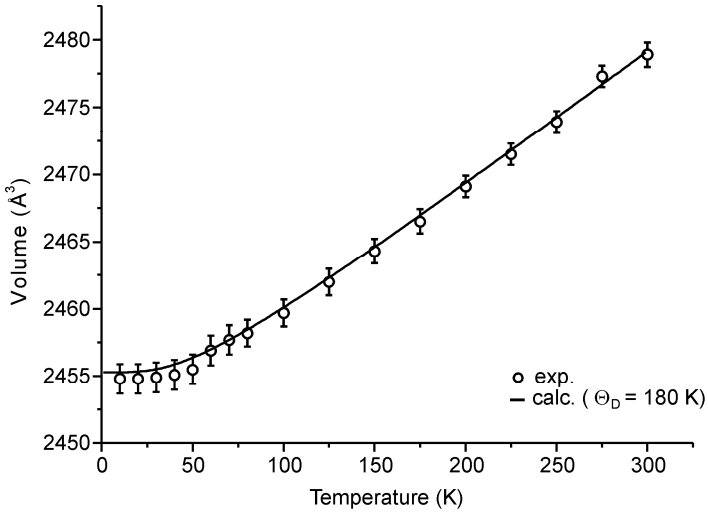

Fig. 2. Thermal variation of the unit cell volume of the Dy_5Pd_2 single crystal

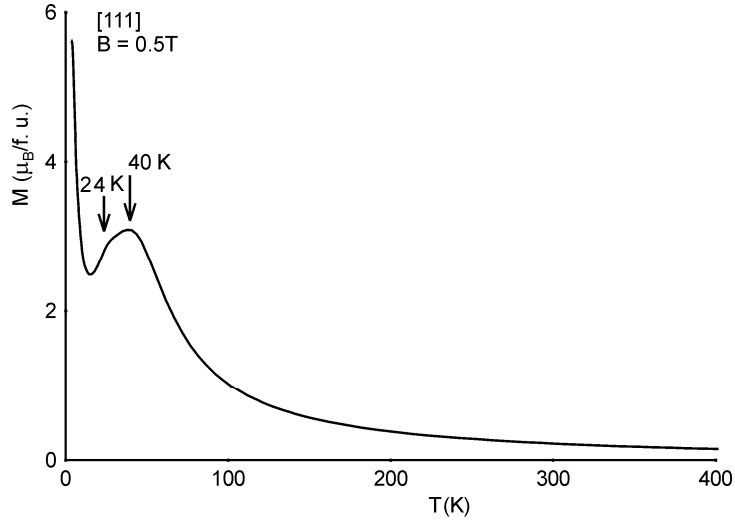

Fig. 3. Temperature dependence of the magnetization for Dy_5Pd_2 single crystal

The temperature dependence of the magnetization susceptibility, measured at the magnetic field of 0.5 T parallel to the [111] direction in the temperature range 1.9–400 K, is shown in Fig. 3. The characteristic feature of this dependence is a wide peak with two contributions: the first one at 40 K is connected with complex ordering of the rare earth sublattice and the second one occurring at 24 K may be attributed to the reorientation process to the magnetic structure with antiferromagnetic contribution. Earlier, similar effects were observed for a polycrystalline sample [3]. Below 14 K a strong increase of the magnetization due to a ferromagnetic arrangement is observed.

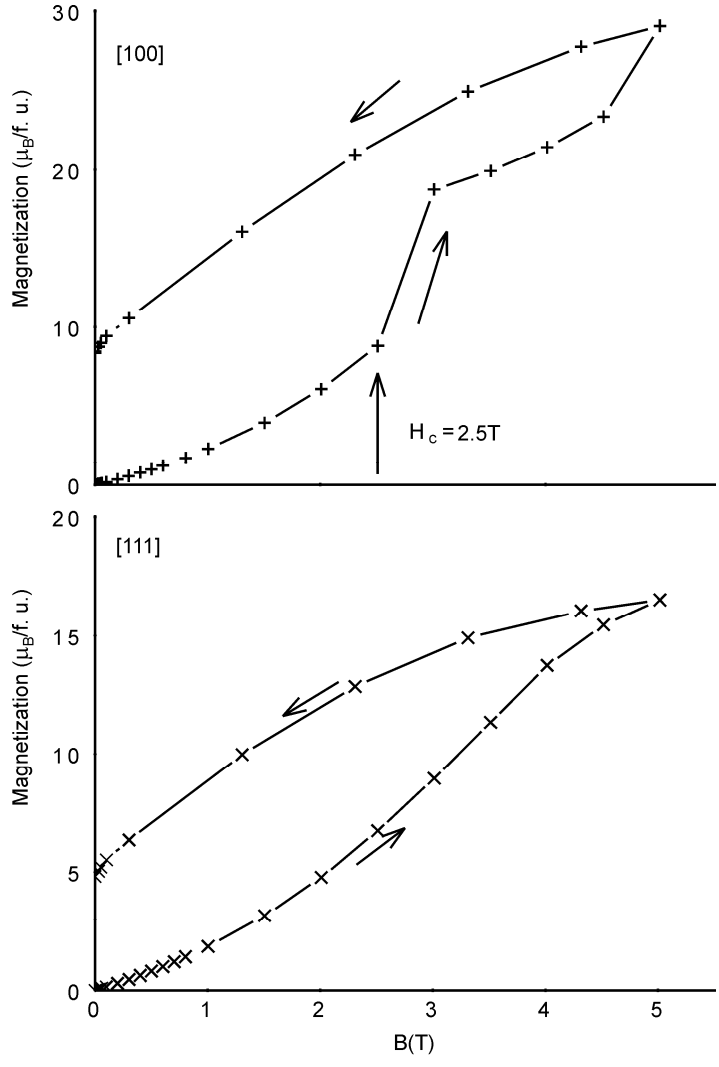

Fig. 4. Magnetization field dependence of Dy_5Pd_2 single crystal measured in different crystallographic directions indicated in the figures

Figure 4 shows the magnetization curve measured at 1.9 K in the magnetic fields up to 5 T. The values of the magnetic moment at 5 T are far from saturation and reach $5.8\mu_B$ for the [100] direction and $3.3\mu_B$ for the [111] direction. The widest hysteresis loops are observed for [111] direction and the value of magnetic remanence is $9\mu_B$/f.u. For [100] direction we observed narrower hysteresis loops with the value of magnetic remanence of $5\mu_B$/f.u. (Fig. 4). The hysteresis measured for [100] direction shows the metamagnetic transition at the critical field H_c = 2.5 kOe, while for the [111] direction such a transition has not been observed.

4. Conclusions

A single crystal of Dy_5Pd_2, obtained by the Czochralski method, crystallizes in a cubic crystal structure. This structure is characterized by the large unit cell volume and three non-equivalent dysprosium sites. The dysprosium ions are arranged into triangle configurations. This might lead to frustration effects that may be modified by the palladium contribution to the conduction band.

References

[1] BERKOWITZ A.E., HOLTZBERG F., METHFESSEL S., J. Appl. Phys., 35 (1964), 1030.
[2] FORNASINI M.L., PALENZONA A., J. Less Common Metals, 38 (1974), 77.
[3] KLIMCZAK M., TALIK E., WINIARSKI A., TROĆ R., J. Alloys Comp., 423 (2006), 62.
[4] KUSZ J., BÖHM H., J. Appl. Crystall., 35 (1002), 8.

Received 7 May 2006
Revised 1 September 2006

Materials Science-Poland, Vol. 25, No. 2, 2007

Electronic structure of $CeRh_2Sn_4$

M. GAMŻA[1*], W. SCHNELLE[1], A. ŚLEBARSKI[1], H. ROSNER[1]

[1]Institute of Physics, University of Silesia, ul. Uniwersytecka 4, 40-007 Katowice, Poland

[2]Max-Planck Institute for Chemical Physics of Solids, Nöthnitzer Str. 40, 01187 Dresden, Germany

We performed a study of the compound $CeRh_2Sn_4$, not investigated so far. Our samples were carefully characterized by X-ray powder diffraction analysis and by locally resolved, energy dispersive X-ray spectroscopy (EDXS). We present a combined experimental and theoretical study based on X-ray photoelectron spectroscopy (XPS) data together with *ab initio* band structure calculations. The Ce 3d XPS spectrum indicates a small mixed valence of Ce. Analysis of the $3d^9 4f^2$ weight using the Gunnarsson–Schönhammer theory suggests a hybridization between Ce 4f states and the conduction band of about 85 meV. The valence band spectrum, dominated by Rh 4d states, is in a very good agreement with the calculated one.

Key words: *electronic structure; XPS; FPLO*

1. Introduction

Many cerium based ternary compounds of Ce-T-X-type, where T is a transition metal and X is a p-element, exhibit unusual physical phenomena such as heavy-Fermi (HF) liquid or non-Fermi-liquid types of behaviour in a metallic state or a Kondo-lattice/valence-fluctuation type of state. The stability of paramagnetic or magnetically ordered ground state in such compounds strongly depends on the on-site hybridization energy among conduction and f electrons, the bare f-level position in the conduction band, the magnitude of intrasite Coulomb interaction and the number of electrons occupying the f-shell.

CeRhSn has attracted great interest during the last years due to its non-Fermi liquid character of low-temperature physical properties [1–6], having been explained in terms of the Griffiths phase. Moreover, in this system, Ce is in a mixed valence state and the Ce 4f states strongly hybridize with the conduction band. It is interesting to examine in detail the effect of stoichiometry and crystal structure on the formation of different ground states of the compound in the system Ce–Rh–Sn. Here, we present a study of a new compound $CeRh_2Sn_4$ which has not been investigated so far.

[*]Corresponding author, e-mail: monika@.xps2.zfcst.us.edu.pl

2. Experimental

A polycrystalline sample of $CeRh_2Sn_4$ was prepared by arc melting of the elemental metals (Ce 99.99%, Rh 99.95% and Sn 99.99% in purity) in stoichiometric amounts on a water cooled hearth in an ultra-high purity Ar atmosphere with an Al getter. Our sample was remelted several times to promote homogeneity and annealed at 800 °C for 7 days. The sample was characterized by X-ray powder diffraction (XRD) analysis performed on a Siemens D-5000 diffractometer using CuK_α radiation. The lattice parameters obtained from the XRD patterns analysis using the POWDER-CELL program are in agreement with those previously reported [7]. The composition of the sample was examined by energy dispersive X-ray spectroscopy (EDXS) microanalysis. The quantitative measurements were performed at many points on the polished surface.

The electronic structure was studied by the Full Potential Local Orbital (FPLO) Minimum Basis method [8] within the local density approximation (LDA) using the experimental lattice parameters. In the scalar-relativistic calculations, the exchange and correlation potential of Perdew and Wang [9] was used. As the basis set, Ce (4f, 5s, 5p, 5d, 6s, 6p), Rh (4s, 4p, 4d, 5s, 5p) and Sn (4s, 4p, 4d, 5s, 5p, 5d) states were employed. The lower-lying states were treated fully relativistically as core states. The Sn 5d states were taken into account as polarization states to increase the completeness of the basis set. The treatment of the Ce (4f, 5s, 5p), Rh (4s, 4p) and Sn (4s, 4p, 4d) semicorelike states as valence states was necessary to account for non-negligible core–core overlaps. The spatial extension of the basis orbitals, controlled by a confining potential $(r/r_0)^4$, was optimized to minimize the total energy. A *k*-mesh of 90 points in the irreducible part of the Brillouin zone (400 in the full zone) was used.

The X-ray photoelectron spectroscopy (XPS) data were obtained with monochromatized AlK_α radiation at room temperature using a PHI 5700 ESCA spectrometer. The spectra were recorded immediately after breaking the sample in a ultra-high vacuum of 10^{-10} Torr. Calibration of the spectra was performed according to [10]. Binding energies were referenced to the Fermi level ($\varepsilon_F = 0$).

3. Results and discussion

Figure 1 shows a part of a polished surface of the sample. The composition of the main phase (phase 1) was examined at a few points and was found not to be in agreement with stoichiometric $CeRh_2Sn_4$. Rather, under the used conditions, the phase $Ce_{1.2}Rh_2Sn_{3.8}$ (see Table 1) forms with the content of ~85 %. There are pieces of an additional phase, marked as phase 2, between the larger grains of the main phase. We found also few grains of a third phase. Based on the combined EDXS and XRD analysis we obtained a fraction of ~9% of $RhSn_2$ (phase 3) and ~6% of $Ce_3Rh_4Sn_{13}$ (phase 2) in the bulk $CeRh_2Sn_4$ sample.

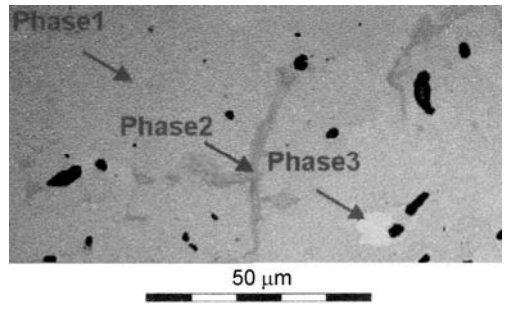

Fig. 1. A part of the polished surface of the sample

Table 1. Average atomic concentrations of Ce, Rh and Sn in phases detected in the sample, estimated on the basis of the EDX patterns analysis

Phase	Ce	Rh	Sn
	at. %		
1	17.34	28.61	54.06
2	16.84	20.14	63.02
3	1.96	32.82	65.21

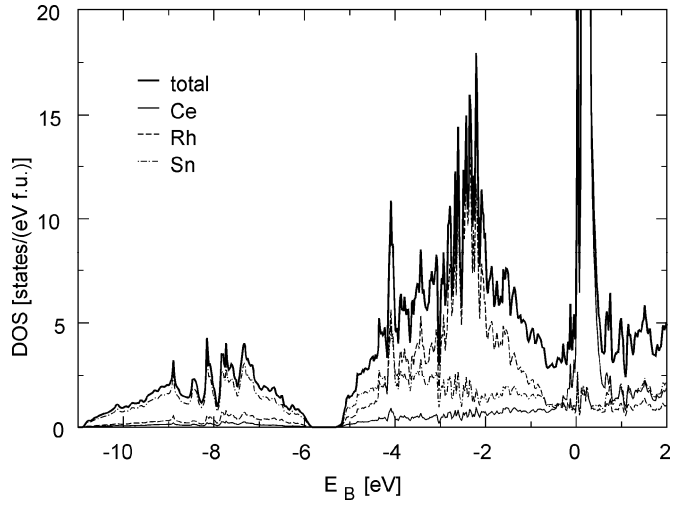

Fig. 2. The total and partial DOS on Ce, Rh and Sn for $CeRh_2Sn_4$

Figure 2 shows the results of the numerical calculations of the total and partial densities of states (DOS) for paramagnetic $CeRh_2Sn_4$ within LDA. The partial l-resolved DOSs were multiplied by the corresponding cross sections [10]. The results were convoluted by a Fermi function for 300 K and by pseudoVoigt function with a full-width-half-maximum (FWHM) of 0.4 eV and 0.4 eV for Lorentzian and Gaussian, respectively, to take into account the live-time broadening of the hole states, the

instrumental resolution and phonon broadening. A background, calculated by means of the Tougaard algorithm [12], was subtracted from the XPS data.

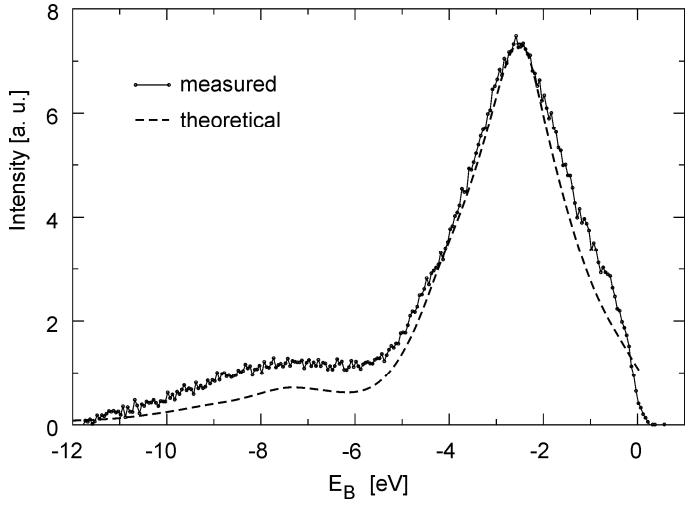

Fig. 3. Measured XPS valence band spectrum and the spectrum calculated by the FPLO method within LDA approximation for paramagnetic $CeRh_2Sn_4$

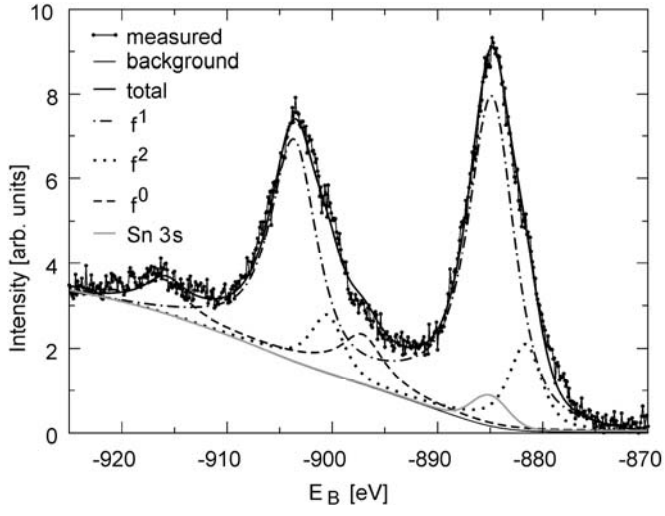

Fig. 4. The Ce 3d XPS spectrum deconvoluted based on the Gunnarsson–Schönhammer theory [15, 16]

The agreement between the calculated and measured XPS valence band spectra is good (Fig. 3). The spectrum reveals that the valence band of $CeRh_2Sn_4$ has a major peak mainly due to the d states of Rh located at about 2.5eV and Sn 5p states. The second peak centered at about 8 eV is mainly due to the Sn 5s states. The Ce 4f states

give only a negligible contribution to the total XPS spectra of $CeRh_2Sn_4$. The Ce 3d core-level XPS spectrum for $CeRh_2Sn_4$ is presented in Fig. 4.

Three final-state contributions f^0, f^1 and f^2 are clearly observed, which exhibit a spin-orbit splitting $\Delta_{SO} \approx 18.8$ eV. This value is in agreement with the one calculated by the FPLO method (18.83 eV). There is also an overlap of the Ce 3d photoemission lines with the Sn 3s peak at the binding energy of 885 eV. he separation of the overlapping peaks in the Ce 3d XPS spectrum was done on the basis of the Doniach-Šunjić theory [13]. The appearance of the f^0 components suggests a mixed valence behaviour of Ce, while the f^2 peaks located at the low-binding energy side of the f^1 components appear when the core hole becomes screened by an extra 4f electron. Such a situation may occur due to a hybridization of the 4f shell with the conduction band. Consequently, the intensity of the f^2 peak with respect to the sum of the intensities of the f^1 and f^2 peaks could reflect the degree of the hybridization. The hybridization energy Δ, which describes the hybridization part of the Anderson impurity Hamiltonian [14], is defined as

$$\Delta = \pi V_{fs}^2 N(E)_{\max}$$

where V is the hybridization matrix element and $N(E)_{max}$ is the maximum value of DOS. We estimated Δ from the ratio $r = I(f^2)/[I(f^1) + I(f^2)]$, in accordance with the procedure given by Gunnarsson and Schönhammer [15, 16]. For $CeRh_2Sn_4$, we obtained $\Delta \approx 85$ meV, which is significantly smaller than that for CeRhSn (~120 meV) suggesting that the Ce 4f states of $CeRh_2Sn_4$ are more localized than those of CeRhSn.

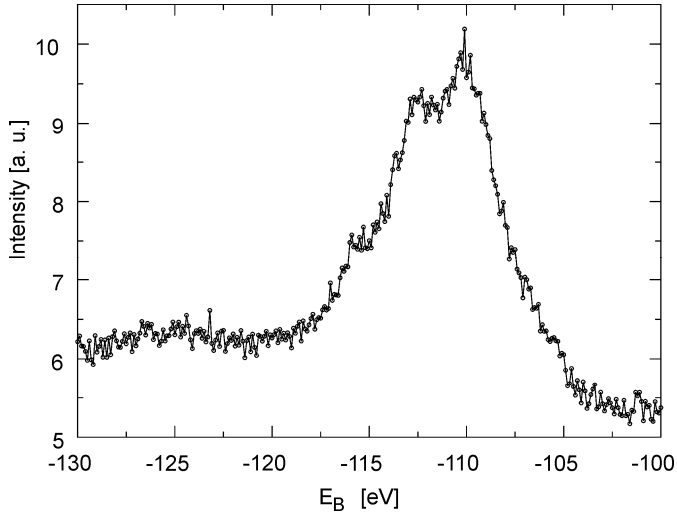

Fig. 5. The Ce 4d XPS spectrum for $CeRh_2Sn_4$

Based on the Gunnarsson-Schönhammer theory we also estimated the Ce 4f occupation number n_f from the intensity ratio: $I(f^0)/[I(f^0) + I(f^1) + I(f^2)]$. We obtained $n_f \approx 0.92$ which

suggests that the valence of Ce in $CeRh_2Sn_4$ is close to 3+. This is consistent with the Ce 4d XPS spectrum (Fig. 5) where one can observe a multiplet structure between the binding energies 104 eV and 119 eV. These lines have been assigned to the $3d^9f^1$ final state. There is no evidence for additional peaks which could be attributed to the Ce $3d^9f^0$ states.

4. Conclusion

A sample of nominal composition $CeRh_2Sn_4$ was characterized by the XRD analysis and by EDXS. It was found that the main phase corresponds to the composition $Ce_{1.2}RhSn_{3.8}$. The core-level XPS spectra exhibited that Ce in $Ce_{1.2}Rh_2Sn_{3.8}$ is nearly trivalent and the hybridization between Ce 4f states and conduction band is of about 85 meV which suggests that in $Ce_{1.2}Rh_2Sn_{3.8}$ Ce 4f states are rather well localized. The valence band spectrum calculated on the basis of FPLO results within the LDA is dominated by Rh 4d states and is in a very good agreement with the measured one. Specific heat, magnetic susceptibility and resistivity measurements are in progress.

Acknowledgements

The authors thank for financial support from the Project No. 1 PO3B 052 28, for the Grant No. N202 010 32/0487 of Ministry of Education and Science and for the DFG, Emmy Noether program.

References

[1] ŚLEBARSKI A., SZOT K., GAMŻA M., PENKALLA H. J., BREUER U., Phys. Rev. B, 72 (2005), 085443.
[2] TOU H., KIM M. S., TAKABATAKE T., SERA M., Phys. Rev. B, 70 (2004), 100407.
[3] ŚLEBARSKI A., JEZIERSKI A., Phys. Stat. Sol. (b), 236 (2003), 340.
[4] KIM M. S., ECHIZEN Y., UMEO K., KOBAYASHI S., SERA M., SALAMAKHA P. S., SOLOGUB O., L., TAKABATAKE T., CHEN X., TAYAMA T., SAKAKIBARA T., JUNG M. H., MAPLE M. B., Phys. Rev. B, 68 (2003), 054416.
[5] ŚLEBARSKI A., MAPLE M. B., FREEMAN E. J., SIRVENT C., RADLOWSKA M., JEZIERSKI A., GRANADO E., HUANG Q., LYNN J. W., Philos. Mag. B, 82 (2002), 943.
[6] ŚLEBARSKI A., SPAŁEK J., GAMŻA M., HACKEMER A., Phys. Rev. B, 73 (2006), 205115.
[7] MÉOT-MEYER M., VENTURINI G., MALAMAN B., ROQUES B., Mat. Res. Bull., 20 (1985), 913.
[8] KOEPERNIK K., ESCHRIG H., Phys. Rev. B, 59 (1999), 1743.
[9] PERDEW J. P., WANG Y., Phys. Rev. B, 45 (1992), 1324413249.
[10] BAER Y., BUSH G., COHN P., Rev. Sci. Instrum., 46 (1975), 466.
[11] YEH J. J., LINDAU I., At. Data Nucl. Data Tables, 32 (1985), 1.
[12] TOUGAARD S., SIGMUND P., Phys. Rev. B, 25 (1982), 4452.
[13] DONIACH S., ŠUNJIĆ M., J. Phys. C 3 (1970), 286.
[14] ANDERSON P. W., Phys. Rev. 124 (1961), 41.
[15] GUNNARSSON O., SCHŐNHAMMER K., Phys. Rev. B, 28 (1983), 4315.
[16] FUGGLE J. C., HILLEBRECHT F. U., ŻOŁNIEREK Z., LÄSSER R., FREIBURG CH., GUNNARSSON O., SCHŐNHAMMER K., Phys. Rev. B, 27 (1983), 7330.

Received 7 May 2006
Revised 1 September 2006

Materials Science-Poland, Vol. 25, No. 2, 2007

Layered alloys for effective magnetic flux concentration in induction heating

V. LESCHYNSKY[1], H. WEINERT[2], A. SZLAFEREK[3*]

[1]Consulting Co. Pittsburgh, PA, USA

[2]Metal Forming Institute, Jana Pawła II 14, 61-139 Poznań, Poland

[3]Institute of Molecular Physics, Polish Academy of Sciences, Smoluchowskiego 17, 60-179 Poznań, Poland

Fundamental requirements for an efficient transformer core material are that it should have a high saturation magnetic polarization and high magnetic permeability as well as low coercivity to minimize hysteresis losses, preferably in combination with high electrical resistivity, so as to minimize eddy current losses. We report on the magnetic and electrical properties of new soft magnetic materials with respect to their application in the induction heating process. The investigation focuses on a composite layered material. The offered materials properties such as saturation of magnetization, remanence, coercive field and coefficients of efficiency of transformation in the flux controllers were defined. These materials are anticipated as magnetic flux concentration materials for very severe induction heating processes because they possess high permeability and saturation flux density, and stable mechanical properties at elevated temperatures.

Key words: *soft magnetic material; composite layered material; saturation magnetic polarization; high magnetic permeability*

1. Introduction

Future power conversion technologies will require high frequency operation of electrical and magnetic components for specialized applications operating at elevated temperatures such as application of magnetic flux field intensifiers (concentrators) in induction heating systems. Magnetic components are widely used in electrical power conversion and management systems, both as energy-storage and energy-transfer elements. The continuing development of better materials for magnetic flux controllers provides the user with benefits such as improvements in heat treatment quality, production rate increase, cost reduction due to energy saving, etc. [1]. Magnetic flux intensifi-

*Corresponding author, e-mail: szlafer@ifmpan.poznan.pl

er enable effective concentration of magnetic field at the work piece, creating consistently reproducible heating patterns. Magnetic flux intensifier materials are characterized by high stability to magnetic shock, low magnetic loss, wide frequency range (50–100 kHz), magnetically non-saturating high heat resistance (up to 500–600 °C), high power loadings (greater than 40–80 kW), easy machining, etc.

Soft magnetic materials such as laminations, composites based on amorphous or nanocrystalline ribbons as well as metal powder and polymer binder (insulator) are applied for magnetic flux field intensifiers. The amorphous and nanocrystalline ribbons were the objects of extensive research in the last three decades of the last century [2]. The reason for broad studies of these materials are their very good soft magnetic properties, to which, first of all, belong high magnetic saturation B_S, low coercion value H_C, high magnetic permeability μ, very low, close to zero magnetostriction λ_S, and finally, low remagnetising losses. Some of these alloys are characterized by relatively high resistivity [2].

Due to melt spinning manufacturing method, these materials are available only in the form of very thin ribbons, and their commercial use is limited. The composite with the polymer matrix reinforced with the amorphous or nanocrystalline particles obtained in the process of the high-energy milling of the amorphous ribbons or mechanical synthesis constitutes an alternative for those materials. Investigation of composite materials obtained by solidification of the metallic powder using various methods has been carried out in many research centres [1, 2].

The best soft magnetic properties are still found around the originally proposed compositions, i.e. $Fe_4Cu_1Nb_3Si_{13–16}B_{6–9}$ [3]. They are comparable with the excellent properties possessed by established materials such as Permalloys or Co-based amorphous alloys. The advantages, however, are a higher saturation induction of 1.2–1.3 T and a significantly better thermal stability of the soft magnetic properties. The combination of high saturation magnetization and high permeability together with good high frequency behaviour, low losses and the good thermal stability allows reductions in the size and weight of magnetic components used in, e.g., switched mode power supplies or telecommunication [3]. Apart from its technical performance, the material is based on inexpensive iron and silicon raw materials. Furthermore, the amorphous precursor material for the Fe–Cu–Nb–Si–B alloys, , is easily accessible by rapid solidification from the melt spinning technique for large-scale production of amorphous metals.

The combination of the above factors has rendered the nanocrystalline solution competitive, not only with amorphous Co-based alloys, but also with classical crystalline alloys and ferrites.

Inhomogeneous layered magnetic materials that may be used in devices operating in medium- and high-frequency range are largely diffused and composed of grains with variable size bounded by a layer whose electrical and magnetic characteristics are sensibly different. Cross-sections of such materials can be approximated by succession of identical elementary cells. This structure influences the macroscopic eddy current circulation, affecting the Joule losses, under an imposed magnetic flux [4].

The schematic cross-section of such structures is shown in Fig. 1. Two parameters of layered structure have to be controlled: thickness of grain and its resistivity. An inherent feature of layered structures is that they work well only in plane-parallel fields, when magnetic field passes along the sheets [1]. This feature has to be taken into account when designing the flux concentrators.

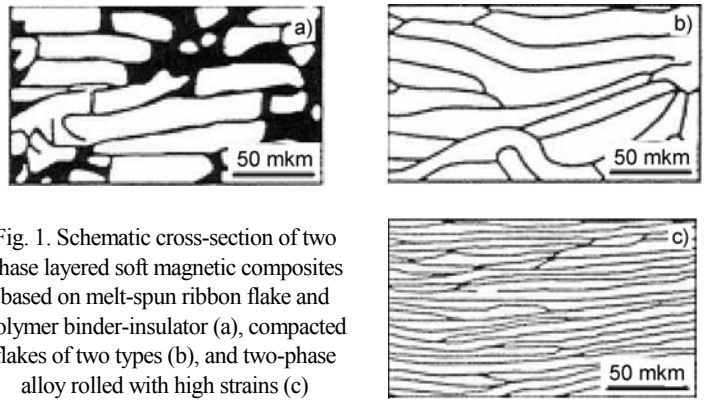

Fig. 1. Schematic cross-section of two phase layered soft magnetic composites based on melt-spun ribbon flake and polymer binder-insulator (a), compacted flakes of two types (b), and two-phase alloy rolled with high strains (c)

However, little work has been done yet in the direction of development of two-phase layered composites. The aim of this work is to examine the magnetic properties of new ferrous-based, two-phase layered composites as candidate materials for flux concentrators.

2. Experimental procedure

A ferrous alloy was melted in alumina crucible at 1700 °C for 10 min (in resistance furnace with heating of coal resistor), and then was cast and rolled into plates 5 mm thick. The samples were cut and subsequently annealed at 800 °C for 3 h. The resistivity of the samples amounted to 83 μΩ·cm. Static hysteresis loops were recorded at room temperature with various magnetic fields using an ADE model 4HF vibrating-sample magnetometer with short samples, 5–8 mm long. The samples were oriented with the long axis in the direction of the applied magnetic field. A Walker AHM-401 automatic hysteresigraph was used to measure the core losses of the samples between 0.1 and 1000 kHz. All measurements were in accordance with AST Standard [5]. The evaluation of the magnetic flux concentrator effectiveness was made for rod (diameter of 30 mm) heated by two wind coils with frequency of 3 kHz. The heating pattern was evaluated visually.

3. Results and discussion

A typical static hysteresis loop of layered alloy is shown in Fig. 2. Its main parameters are following: coercivity $H_C \approx 1.6$ Oe, remanence Br 0.015 T and magnetiza-

tion of saturation B_S = 2 T. The data reveal that the selected technology parameters allow us to achieve the advantageous soft magnetic properties because of getting grain lamellas with the thickness of about 5–10 μm and separation of grains by high resistivity phase, as shown in Fig. 1c.

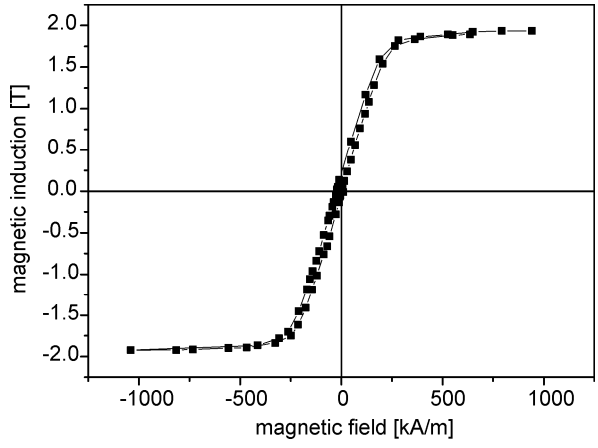

Fig. 2. Static hysteresis loop of two phase ferrous alloy after rolling and heat treatment

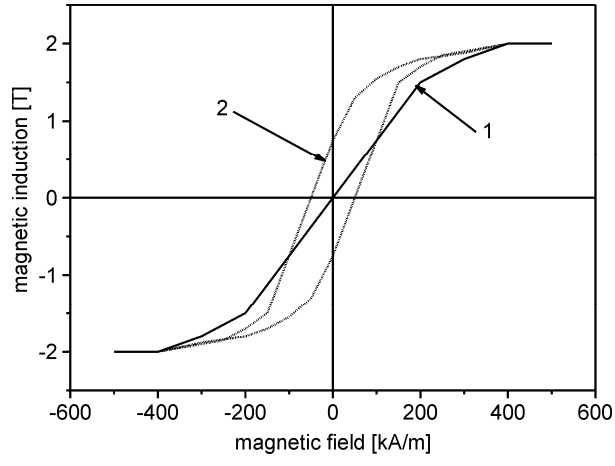

Fig. 3. Static hysteresis loops: 1 – layered two-phase alloy, 2 – polymer composite reinforced with $Co_{68}Fe_4Mo_1Si_{13.5}B_{13.5}$ ribbons [2]

A comparison of static hysteresis loops for the studied layered alloy and a composite with the polymer matrix reinforced with an amorphous or nanocrystalline particles [2] (Fig. 3), clearly demonstrates that the alloy possess lower both the coercivity and remanence. A segment of a static hysteresis loop in low magnetic fields for the studied alloy is presented in Fig. 4 pointing to low losses in the material.

Core loss analysis is of great importance for materials for magnetic flux intensifiers in processes of heat induction. Magnetic material core losses are a direct consequence of Joule heating from electric currents induced in the material by fluctuating magnetization.

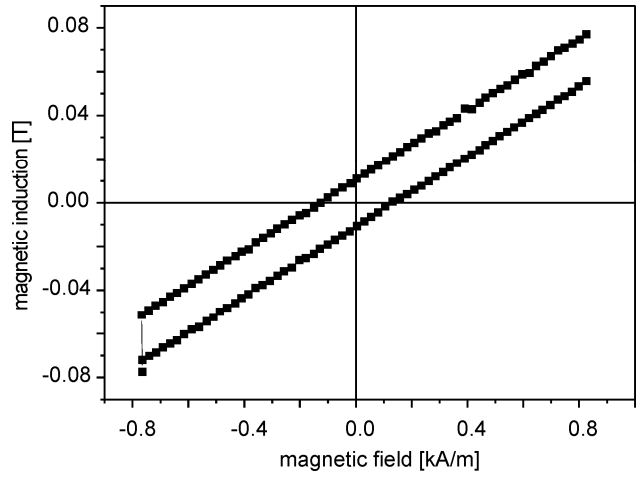

Fig. 4. A segment of a static hysteresis loop in low magnetic fields for the studied alloy

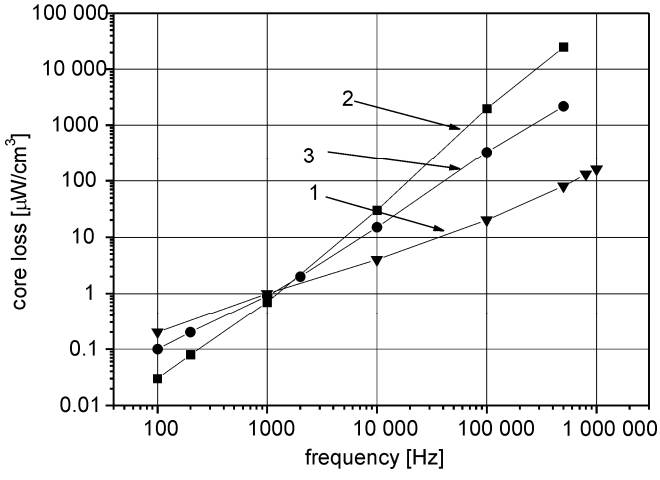

Fig. 5. Core losses of soft magnetic materials: 1– layered two-phase alloy, 2 – classical laminated steel [7], 3 – soft magnetic powder material [7]

Usually, total core losses are divided into three components: static hysteretic losses, classical eddy current losses, and excess eddy current losses (referred to as anomalous or dynamic losses) [6]. Static hysteretic losses are determined by quasi-static loop measurements. Classical eddy current losses are calculated from measurements in a sinusoidal applied field. Excess eddy current losses have contribution from

magnetic domain-wall dynamics with scales on the order of microstructure features [6]. The results of eddy current loss measurement compared with the results obtained for classical laminated steels and soft magnetic powder materials are shown in Fig. 5 as dependences of core losses on frequency.

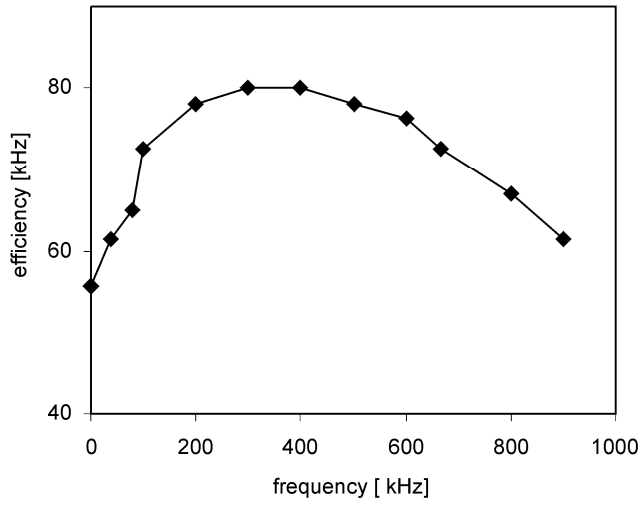

Fig. 6. The efficiency coefficient of transforming for toroidal transformer with core made of the layered two-phase alloy

The effect of decrease of core losses for layered two-phase alloy is greater for higher frequencies. The data demonstrate that core losses may be diminished by 2–10 times in the frequency range of 2–50 kHz. This effect has to be deeper studied in future.

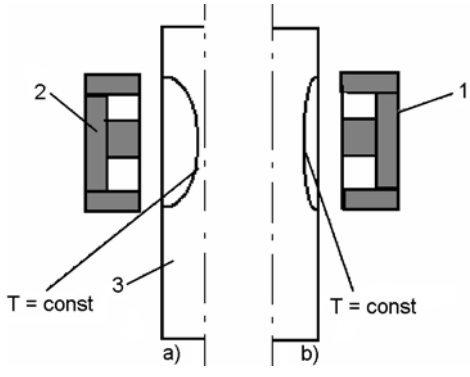

Fig. 7. A scheme of induction heating test: 1 – coil with laminated steel concentrator; 2 – coil with layered alloy concentrator; 3 – bar; induction heating with layered alloy (a) and laminated steel (b) concentrators

The effectiveness of the layered alloy was estimated as a ratio of power in secondary circuit to power brought to primary circuit. The results (Fig. 6) reveal the optimum of frequency depending on the alloy structure parameters. The exploitation tests were performed by comparing of uniformity of induction heating bars by coil with

classical laminated steel concentrator (Fig. 7) and concentrator made of the alloy under study. The depth of heating zone for the former case was twice higher than for standard case (heating time – 7 s, T = 950 °C). The comparison of the main magnetic flux concentrator materials is given in Table 1.

Table 1. Main parameters of magnetic flux concentrator materials

Parameter	FLUXTROL B	FERROTRON 559H	Layered alloy
Density, g/cm^3	5.5–5.7	5.8–6.0	7.68–7.8
Maximum permeability	40	20	
Saturation, B_s, T	1.4	1.2	1.8
Exploitation temperature, T, °C	500		1000
Major range of application frequency, kHz	10–100	15–50	50–500

4. Conclusion

The investigated layered two phase Fe- based alloy is characterized by good magnetically soft properties. Improvement of its magnetic properties may be attained by a strict control of structure parameters such as grain lamellas size and resistivity of both phases. The offered alloy may be effective as the material for magnetic flux concentrators for induction heating.

References

[1] RUFFINI R.S., NEMKOV V.S., , *Technical Paper Society of Manufacturing Engineers*, *CM*, 1998, 5; Industrial Heating, November, 1996.
[2] DOBRZAŃSKI L.A., NOWOSIELSKI R., PRZYBYŁ A., KONIECZNY J., J. Mat. Proc. Techn., 162–163 (2005), 20.
[3] HERZER G., VAZQUEZ M., KNOBEL M., ZHUKOV A., REININGER T., DAVIES H.A., GROSSINGER R., SANCHEZJ.L., J. Magn. Magn. Mat., 294 (2005), 252.
[4] BOTTAUSCIO O., PIAT V.C., CHIAMPI M., CODEGONE M., MANZIN A., J. Magn. Magn. Mat., 290–291 (2005), 1450.
[5] ASTM Standard A 773/A-96, *Standard Test Method for the Magnetic Properties of Materials Using ring and Permeameter Procedures with dc Electronic Hysteresisgraphs*."
[6] WILLARD M.A., FRANCAVILLA T., HARRIS V.G., J. Appl. Phys., 97 (2005), 10F502.
[7] NARASEMHAN K.S., Int. J. Powder Metall., 40 (2004), 25.

Received 7 May 2006
Revised 1 September 2006

Materials Science-Poland, Vol. 25, No. 2, 2007

Nanotechnology. Science or fiction?

Z. KLUSEK*

Division of Physics and Technology of Nanometer Structures,
Department of Solid State Physics, University of Łódź, 90-236 Łódź, Pomorska 149/153, Poland

The paper can be treated as a short introduction to nanotechnology and nanoscience bearing in mind evolution of these terms over years. We will introduce basic ideas of nanotechnology like bottom-up versus top-down philosophy, assemblers and nanomachines. Finally, critics of nanotechnology from physical and chemical points of view will be presented leading to hardcore and pragmatic definitions of nanotechnology and nanoscience. The second part of the paper stands on the pragmatic definition of nanotechnology. The basic obstacles to a further miniaturization of conventional semiconductor devices and application of 0D, 1D and 2D semiconductor quantum devices in electronics will be addressed. Basic principles of operation of molecular electronic devices based on self-assembled molecules will be addressed. The author's scanning tunnelling microscopy and spectroscopy results on self-assembled molecules and derivative adducts to C_{60} molecules will be presented and discussed.

Key words: *nanotechnology, nanoscience, molecular electronics*

1. Brief introduction to nanotechnology

The term "nanotechnology" was for the first time used in 1974 by Prof. Norio Taniguchi in his paper: *On the Basic Concept of Nanotechnology* [1]. Nanotechnology was defined as follows: "Nanotechnology mainly consists of the processing of, separation, consolidation, and deformation of materials by one atom or one molecule" [1].

However, it is commonly recognized that the origins of nanotechnology date from 1959 when at an American Physical Society meeting Prof. Richard Feynman gave his special lecture entitled: *There is plenty of room at the bottom* [2]. In this lecture, he noted that the fundamental principles of physics do not speak against possibility of building things "from the bottom up" using atoms as the building blocks. This revolutionary idea (bottom-up) was treated by majority of physicists as a "next Feynman's joke" and it has been forgotten until eighties last century when Dr. Eric Drexler wrote his book *Engines of Creation – The Coming Era of Nanotechnology* [3]. In this, and

*E-mail: zbklusek@mvii.uni.lodz.pl

especially in his next book [4] he described his own understanding of nanotechnology that is the way of building small and large structures atom by atom or molecule by molecule using nanorobots (nanobot's), particularly assemblers and replicators.

The Drexler's way building of things was (and still is) in contradiction to the traditional building paradigm in which we take away material until what is left is the product. In the new bottom-up philosophy (Feynman, Taniguchi, Drexler – FTD) we add atoms or molecules until the product is created. This philosophy seems very simple and obvious, however it could not appear before quantum mechanics had been developed and understood. It is worth to note that the bottom-up philosophy has been discovered by Nature millions and millions years ago, and is commonly utilized in biological systems.

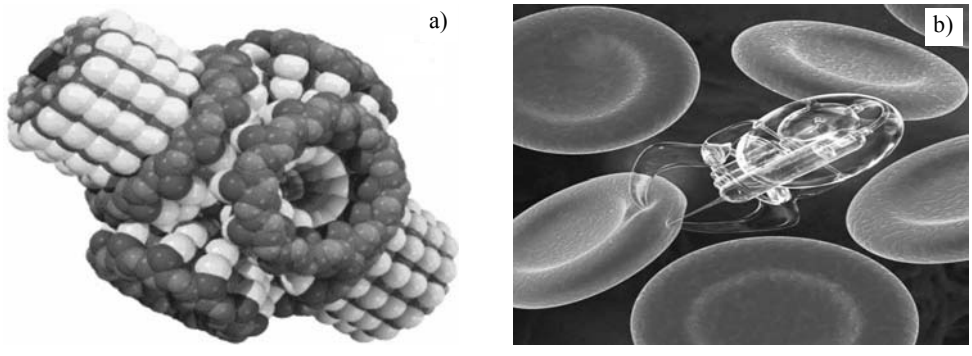

Fig. 1. Visions for the future: a) molecular gear [5], b) microscopic machine travelling through the bloodstream, injecting or taking samples for tests [6]

The essential part of the Drexler idea was to build molecular counterparts of a classical devices like gears, pumps, pipes, gear-wheels, bearings, clamps and so on (see Fig.1a, for example [5]). Using these molecular components creation of nanomachines like: nano-spy, nano-doctor (see Fig. 1b [6]) or, for instance, mechanical nanocomputers would be possible. What is more, these nanometer scale technologies can probably enable mechanical, electronic, chemical and quantum mechanical integration between silicon and carbon systems leading to creation of cybernetics organisms (Cyborgs) [7]. It is commonly believed that the appearance of the nanotechnology/nanotechnologies ideas can directly lead to the next revolution in our human life, just after information technology (IT) and biotechnology (Biotech) revolutions [8]:

1800–1900: First industrial revolution (automation age);
1900–1950: Quantum revolution (atomic age);
1950–2000: IT revolution (electronic age);
2000–2050: Biotech revolution (genomic age);
2050–2100: Second industrial revolution (nano age).

Since the beginning, Drexler's idea has attracted much criticism coming mainly from physicist and chemist communities [9]. It has been argued that Drexler's molecular counterparts of classical devices are unstable form the chemical point of view

or should be even explosive. Furthermore, organic and quantum chemists claimed that chemical synthesis of such huge and big molecules is not possible at all. Physicists pointed out the problems with communication and energy supply to nanomachines. The problems with molecular fluctuations and scalability were also considered. Of particular importance is the latter problem because physical properties of condensed matter dramatically change below 100 nm. It was also proved that the tip of scanning tunnelling microscope (STM) could not be easily used as a manufacturing device due to extremely small speed and low reliability [7]. In particular, it is difficult to imagine that STM can be applied to build three-dimensional structures from isolated atoms [7, 10].

These obstacles and problems related to nanotechnology led to much more pragmatic definition of nanotechnology which can be acceptable for physicists and chemists:

The hardcore definition: Atom or molecular scale assembling or self-organization.

The Pragmatic definition: Novel effects due to controlled structuring in the size range from 1 nm to few 100 nm.

The appearance of the pragmatic definition of nanotechnology stimulated lots of theoretical and experimental studies related to phenomena and processes, which take place in nanoscale. A new scientific discipline called nanoscience has been established. However it should be remembered that the all current technologies containing magic term 'nano' are little related to ambitious nanotechnology program/philosophy predicted by FTD. What is more, the term "nano" opens lots of "doors" and is commonly abused by scientists who are not interesting in ambitious nanotechnology goals – it seems that they are interested in funding only [7].

In conclusion, it seems that nanotechnology considered in terms of their hardcore definition should be still treated as a fiction rather than science. However, it is worth to remember that the fundamental principles of physics do not speak against the bottom-up philosophy as Feynman said about 45 years ago.

2. The pragmatic definition of nanotechnology. The case of molecular electronic devices

2.1. Introduction

As we noted, the pragmatic definition of nanotechnology stimulated lots of theoretical and experimental studies related to phenomena and processes which take place in nanoscale. These studies were mainly focused on designing and building new molecule-based electronic devices called molecular electronic devices (MEDs), applications of carbon nanotubes (CNs) and nanowires in electronics, stamping techniques for micro- and nanofabrication, microfluids and nanoelectromechanical systems [11].

Particularly, studies in MED/CN areas were stimulated by the fact that in IT we still need smaller transistors, because smaller transistors switch faster and allow a greater number of processors to be built within the same space. However, there were

some obstacles to further miniaturization of the conventional metal-oxide-semiconductor-field-effect-transistors (MOSFETs) like: appearance of high electric fields, problems with heat dissipation, shrinkage of the oxide layers caused by heat and electric fields, and vanishing of bulk properties ([12] and references therein). In order to overcome these problems, physicists focused on low-dimensional systems of electrons namely: two-dimensional systems of electrons (2D) called quantum wells (QWs), one-dimensional systems of electrons (1D) called quantum wires (QWRs) and zero-dimensional systems of electrons (0D) called quantum dots (QDs) [12–15]. Particularly, in the case of 0D system, the electron density of state function (DOS) consists of several peaks and this system can be directly used to build a quantum dot transistor (QDT) as presented in Fig. 2.

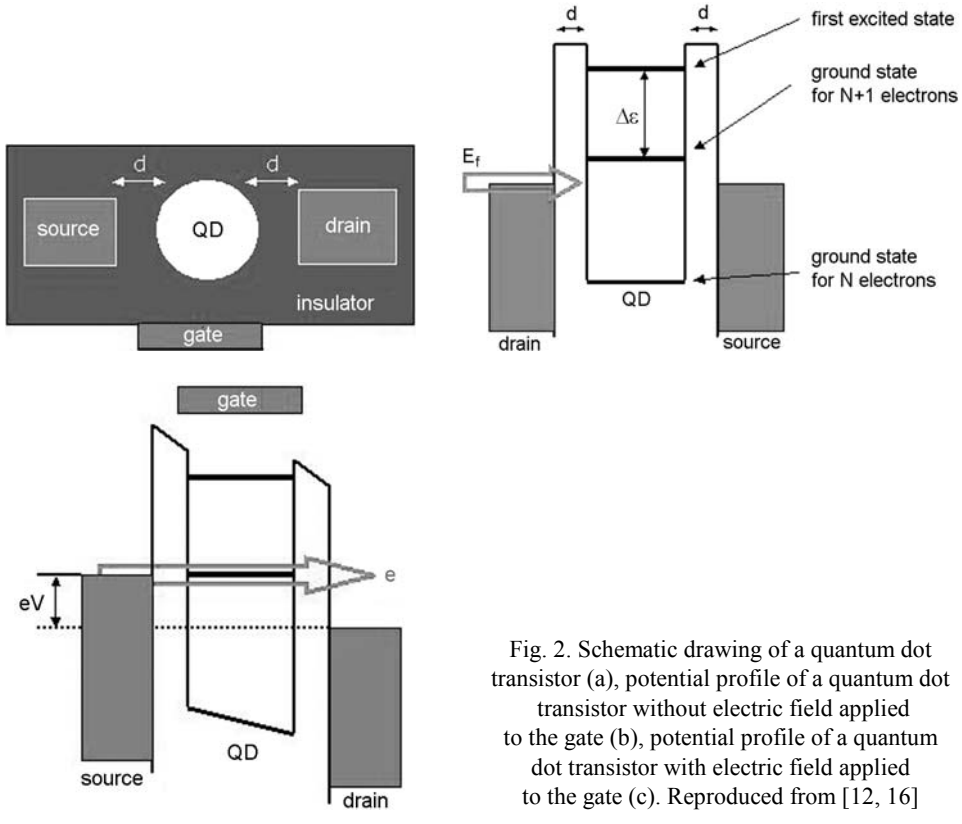

Fig. 2. Schematic drawing of a quantum dot transistor (a), potential profile of a quantum dot transistor without electric field applied to the gate (b), potential profile of a quantum dot transistor with electric field applied to the gate (c). Reproduced from [12, 16]

The central part of the QDT is QD containing discrete energy levels, and two electrodes called source (S) and drain (D). The principle of operation of the QDT is based on the fact that flow of electrons from the source to the quantum dot and after that from the quantum dot to the drain is completely controlled by the bias voltage applied to the gate – the resonant tunnelling. However, there were also some obstacles to manufacture quantum devices based on low-dimensional systems of electrons,

namely: cryogenic operation, extreme sensitivity of the tunnelling current to width of the potential barriers, and extreme difficulty of making islands and tunnelling barriers precisely and uniformly [12].

As a result at the beginning of nineties of the last century, the attention has been turned towards marriage of electronics with chemistry – a new paradigm called molecular electronic devices (MEDs) has been established [11, 12]. This new paradigm was based on the fact that there exist a variety of molecules conducting electric current via resonant tunnelling process or the Coulomb blockade effect occurring in structures with small molecular feature sizes. Briefly, the goal of molecular electronics is to find individual molecules (or carbon nanotubes) to perform functions in electronic circuits commonly performed by semiconductor devices [11].

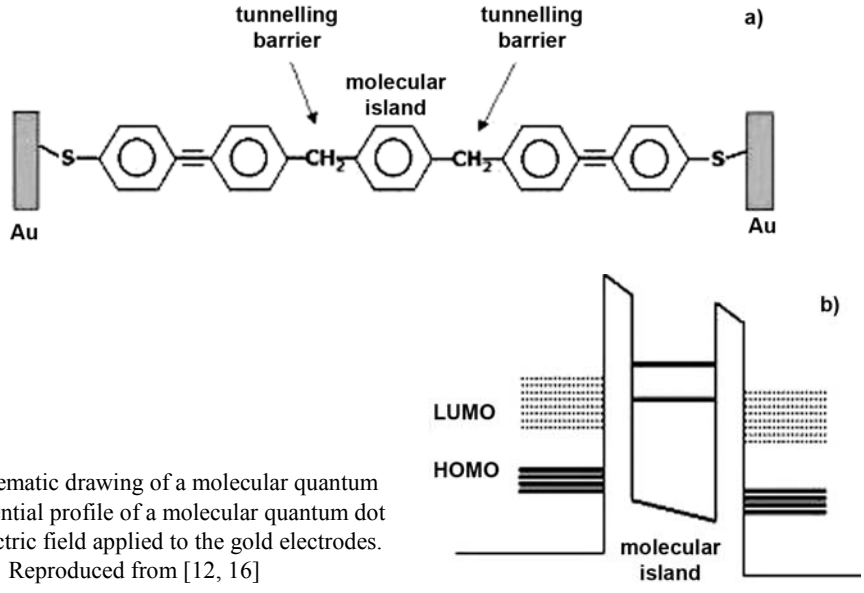

Fig. 3. Schematic drawing of a molecular quantum dot (a), potential profile of a molecular quantum dot without electric field applied to the gold electrodes. Reproduced from [12, 16]

The simplest possible molecular QD is presented in Fig. 3a ([12] and references therein). In this system two $–CH_2–$ groups play a role of tunnelling barriers, while the isolated phenyl group is treated as a molecular quantum dot with discrete energy levels (molecular island). The whole molecular QD structure is connected to the gold electrodes by polyphenylene chains and sulphur atoms. The presented potential profile (Fig. 3b) of molecular QD system shows that we could expect appearance of resonant tunnelling process when we apply bias voltage between gold electrodes. As a result, it is possible to build a molecular resonant tunnelling diode and then molecular resonant tunnelling transistor ([12] and references therein).

There are two types of molecules that have been proposed as the potential basis for molecular electronic devices: polyphenylene based chains and carbon nanotubes [11, 12, 16]. However, the question was open whether a molecule taken individually had appreciable conductance, and whether a molecule taken individually could act as

an electrical switch. Most of the experiments related to measurements of electrical conductance of a molecules and carbon nanotubes have been done using scanning tunnelling microscopy and spectroscopy (STM/STS) techniques [13, 16, 17]. This is because STM/STS configuration can be treated as a natural double barrier system with a molecule located between the surface and the tunnelling tip.

The next part of this paper is devoted to presentation of some results related to studies of electrical conductance of a molecules using STM/STS techniques.

2.2. Resonant tunnelling effects on molecules

Recently, we studied processes leading to formation of one-dimensional (1D), two-dimensional (2D), and three-dimensional (3D) molecular crystals on surfaces by STM technique [18,19]. Furthermore, we were interested in a detailed understanding of the tunnelling spectra recorded by STS, which can be used to determine whether the resonant tunnelling effect via molecular energy levels takes place. In this case, the adsorbed molecule is treated as a quantum well with electronic states between tunnelling barriers. The first barrier is formed between the tunnelling tip and molecule, the second one is formed between a molecule and surface. The surface modulates the molecule states into resonances, which spread throughout the molecule gap. When the voltage bias is sufficient to adjust the quantum state inside the well to be within the range of energies for the tip conduction band, the well is in resonance and the current can flow onto the molecule and out to the substrate. Otherwise, the current is blocked indicating that the system is out of resonance. As a result, current–voltage characteristic with nearly flat regions (NFR) or negative differential resistance regions (NDR) can be observed. The operation effectiveness of molecular devices strongly depends on the peak to valley ratio on tunnelling current characteristic. To enhance this ratio, low temperature or eventually very small quantum well (molecule) are required.

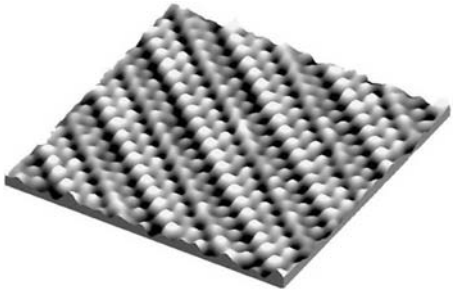

Fig. 4. The STM images of the 8OCB liquid crystal molecules deposited on graphite. Field of view: 23 nm×23 nm

In Figure 4, we present self-assembled monolayer (SAM) of *n*-octylyoxy -4-cyanobiphenyl (8OCB liquid crystal) molecules deposited on the (0001) basal plane of highly oriented pyrolitic graphite (HOPG).

The tunnelling *I–V* curve recorded over pure graphite is presented in Fig. 5a and is typical of this material [18–20]. The *I–V* curve recorded over 8OCB SAM structure

retains an asymmetric shape typical of pure graphite, however additional effects are also visible, including nearly flat regions of the tunnelling current (Fig. 5b) and negative differential resistance on the *I–V* characteristics (Fig. 6).

In our interpretation, at low bias voltages electrons are transported via non-resonant tunnelling through the tails of the molecular levels (mainly HOMO and LUMO) which are Lorentzian enlarged by the molecule-surface interactions. These tails give rise to the LDOS near the Fermi level and lead to non-zero tunnelling current for bias voltages within the HOMO-LUMO energy gap. More precisely, the non-resonant tunnelling regime results in linear *I–V* characteristic at low voltages.

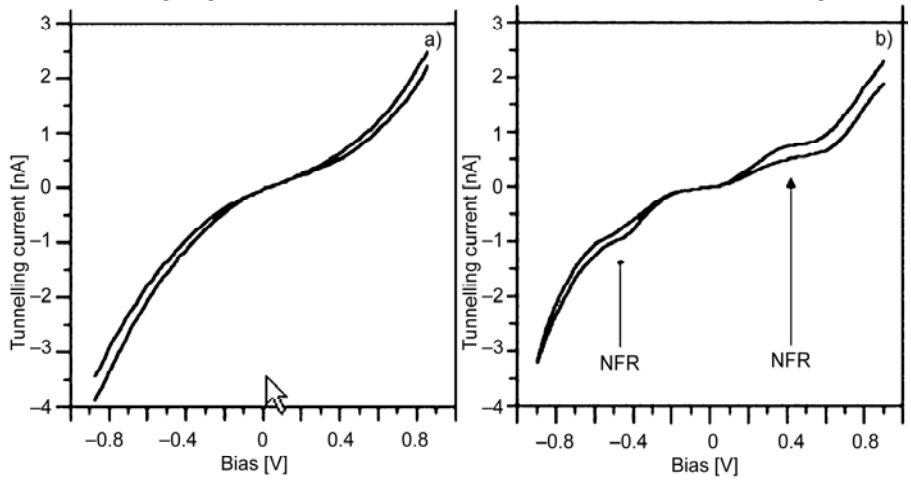

Fig. 5. Typical current–voltage curve recorded over the pure graphite (a), current–voltage curves recorded over the 8OCB SAM structure (b). Reproduced from [18, 19]

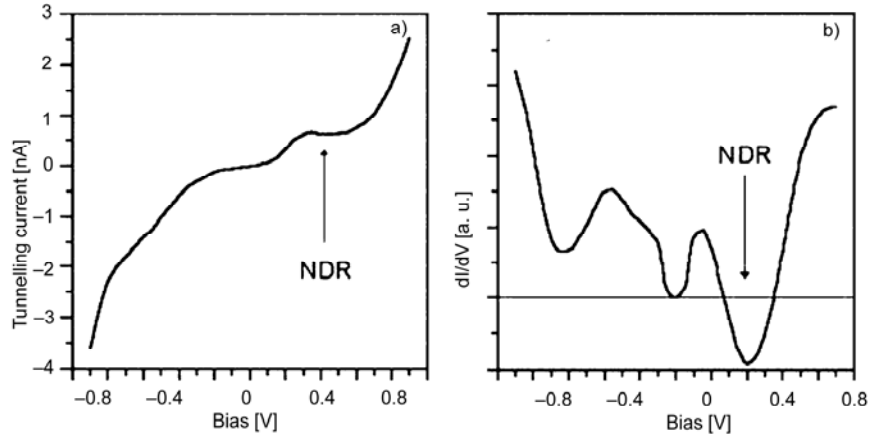

Fig. 6. Current–voltage curves where a distinct negative differential resistance occurs (a), and the normalized first derivative of the *I–V* curve presented in Fig. 6a (b). The NDR dip intersecting the zero level of the normalized conductance. The NDR is marked by an arrow. Reproduced from [18, 19]

This is presented in Figs. 5b and 6a, especially for the occupied electronic states. However, when the voltage bias is sufficient to adjust the discrete energy levels inside the well (8OCB molecule) to be within the range of energies for the tip conduction band, as explained before, the well is in resonance and the current can flow onto the molecule and out to the substrate. Otherwise, the current is blocked, i.e. the system is out of resonance. As a result, *I–V* characteristic with NFR or NDR regions can be observed (Figs. 5b and 6a). On the *dI*/*dV* and (*dI*/*dV*)/(*I–V*) curves the resonant states appear as a pronounced peak. When the system is out of resonance the pronounced dips on the *dI*/*dV* and (*dI*/*dV*)/(*I–V*) characteristics are observed (Fig. 6b).

The *I–V* curves presented in Figs. 5b and 6 clearly show that we deal with resonant tunnelling which takes place on molecules.

2.3. Charging effects on molecules

One of the fundamental problems was the question whether a molecule can be treated as a Coulomb blockade structure or not. In order to answer this question, the STM configuration was used. In the STM configuration, the tunnelling tip is placed above a molecule deposited on an insulating layer. The latter is grown on a conductive material. The vacuum gap between a tip and a molecule and an insulating layer form a well-defined double junction system. Furthermore, a configuration without any insulating layer is also considered as a Coulomb blockade structure. In this system, one barrier is formed between an STM tip and a molecule and the other one is a space interval at a molecule/substrate interface. A double junction system can be described by the orthodox theory which considers the electron transport as a sequence of instantaneous tunnelling events and results in the suppression of the tunnelling current near zero bias voltage – the Coulomb gap ([21, 22] and references therein). The gap has the voltage width $\Delta E = e/2C_{\Sigma}$, where $C_{\Sigma} = C_1 + C_2$ is the total capacitance of the junction, C_1 is the capacitance of the tip/ molecule junction and C_2 is the capacitance of the molecule/substrate interface. In addition to the Coulomb gap, a strongly asymmetric junction system ($R_1 >> R_2$, $C_1 >> C_2$, $R_{\Sigma} \approx R_1$, $C_{\Sigma} \approx C_1$, where $R_{\Sigma} = R_1 + R_2$ denotes the total junction resistance, R_1 is the resistance of the tip/molecule junction and R_2 is the resistance of the molecule/substrate interface) exhibits a series of steps on the current–voltage characteristic – the Coulomb staircase. The steps have the voltage width $\Delta V = e/C_{\Sigma}$ and the current rise $\Delta I = e/R_{\Sigma}C_{\Sigma}$. The only exception is the first current step, where $\Delta I = e/2R_{\Sigma}C_{\Sigma}$. The steps are observed for the temperatures $kT < e^2/2C_{\Sigma}$.

In our experiments, we investigated the sodium dioctyldithiophosphate (NaDDP) molecules deposited from solution on the (0001) graphite substrate as presented in Fig. 7 [21, 22]. However, it is difficult to suggest a model which arranges molecules on the graphite substrate since the obtained topographical results are strongly affected by the electronic states of the molecule/graphite system.

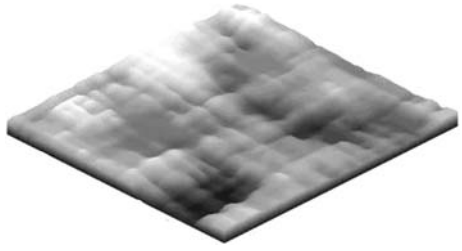

Fig. 7. The 28.8 nm×28.8 nm STM image of the NaDDP molecules deposited onto graphite substrate. Reproduced from [21, 22]

In Figure 8a the *I–V* curves recorded at the same tunnelling conditions over various points on the topography presented in Fig. 7 are shown. In Figure 8b, the theoretical *I–V* curve calculated using the orthodox SET model with the fitting parameters C_1= 1.6×10^{-19} F, C_2= 5×10^{-20} F, R_1=1.6×10^{9} Ω, R_2= 1×10^{5} Ω, T = 300 K is shown [22]. We found that a reasonable fit can be made at low bias voltages but at higher bias the tunnelling current is larger than the orthodox theory predicts. This is caused by non-linear conductance of the tunnel junction, i.e. suppression of the tunnel barrier at high bias voltages.

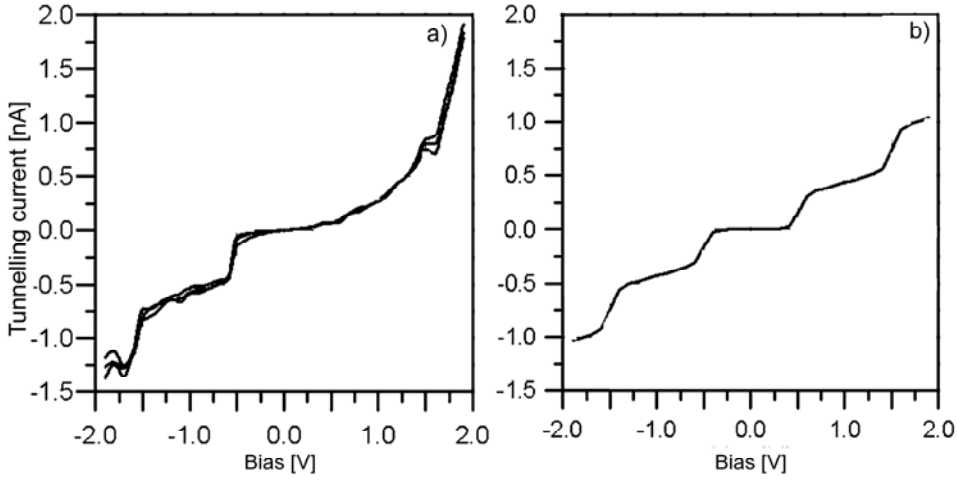

Fig. 8. The *I–V* curves recorded at three different points over NaDDP molecules presented in Fig. 7 (a) and the theoretical *I–V* curve calculated using the orthodox SET model. Reproduced from [21, 22]

Another discrepancy to be observed easily is the asymmetry of current flow for negative and positive voltage bias. The gap and the steps are pronounced at the negative part of the spectra, i.e. for occupied states. The presence of the asymmetry of tunnelling current can be explained considering the effects of the discreteness of the energy spectrum in a molecule. The *I–V* curves presented in Fig. 8a clearly shows that we deal with the Coulomb blockade which takes place on molecules.

2.4. Changes of conformation of a molecule caused by the tunnelling tip

Nano-fabrications of materials realized by scanning tunnelling microscopy tip seems to bee very important in creation of electronic devices in a nanometre scale. Particularly, external electric field generated by the tunnelling tip can be used to change molecule conformation, i.e., it is possible to rotate an active part of the molecule (Fig. 9a) [23, 24]. The STM experiments presented here were performed on the C_{60}ONCFn complexes consisting of the ferrocene (Fn, $C_5H_5FeC_5H_5$) bound to C_{60} at the 6–6 bond by a heterocyclic ring [23, 24]. The cyclopentadienyl ring (cp, C_5H_5) and heterocyclic ring may be either parallel or perpendicular to each other.

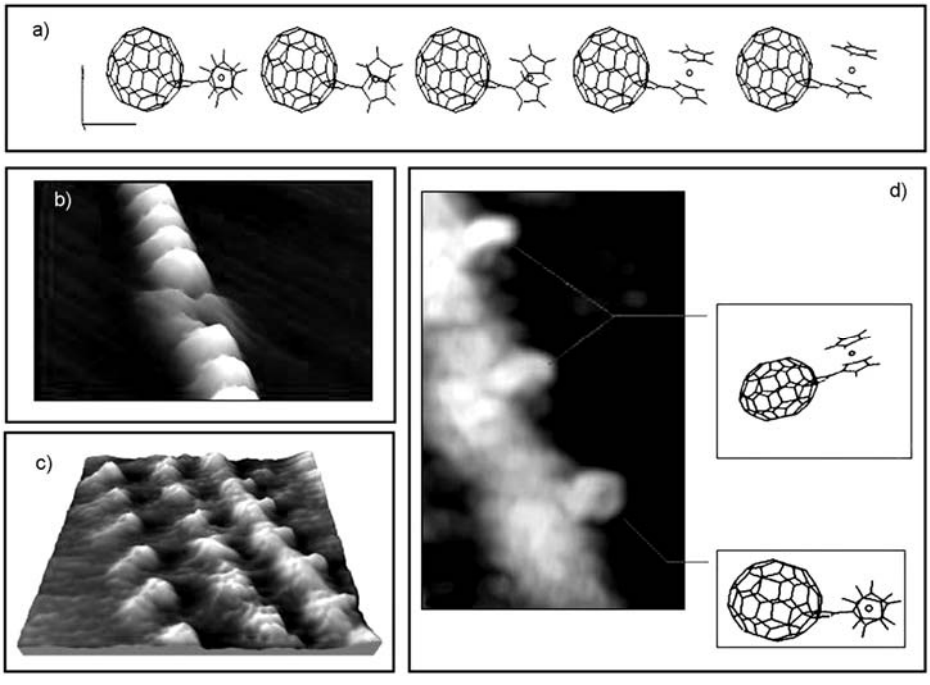

Fig. 9. The snapshot of the C_{60}ONCFn molecule during rotation caused by electric field generated by the tunnelling tip (a), the example showing that the tunnelling tip can be used to change position of the C_{60} molecule in the C_{60} molecular chain (b), 23 nm×23 nm STM image showing well separated four chains built of the C_{60}ONCFn complexes (c), STM topography showing changes of conformations of the C_{60}ONCFn molecules caused by electric field of the tunnelling tip (d)

In our experiments, it was possible to show that the C_{60}ONCFn complexes form a well ordered, self-assembled monolayer (SAM) on the HOPG(0001) surface as presented in Fig. 9c. Because this molecular matrix was formed spontaneously on the graphite substrate we did not need to use the STM tip in order to form such a structure though the STM tip can be easily used as a nanofabrication device (Fig. 9b). Furthermore, we believe that it was possible to change conformation of molecules caused by the electric field of the tip as shown in Fig. 9d.

3. Conclusions

A brief introduction to nanotechnology/nanoscience and molecular electronic devices is presented. Our STM/STS experiments performed on molecules showed both occurrence of the resonant tunnelling and the Coulomb blockade effects. The results presented lead to the conclusion that the external electrode can control flow of the electric current across the molecule. The observed phenomena can be directly applied in construction of molecular transistors.

Studies performed on fullerene adducts were intended to find molecules whose structure may be changed by external electric field leading to storing information in molecular structure. These experiments can lead to future design and construction of molecular memory.

Acknowledgements

The work is partially supported by the 2005 UL grant 505/695. Author is pleased to gratefully acknowledge people who have collaborated with the author in the work reviewed here, mainly at the University of Łódź and Northumbria University at Newcastle upon Tyne: P.K. Datta, W. Kozlowski, P. Kowalczyk, W. Olejniczak, H. Du, S. Pierzgalski and A. Busiakiewicz.

References

[1] TANIGUCHI N., Proc. Int. Conf. Prod. Eng. (1974), Part II, Japan Society of Precision Engineering, Tokyo.

[2] FEYNMAN R., Eng. Sci., 2 (1960), 22.

[3] DREXLER K.E., *Engines of Creation. The Coming Era of Nanotechnology*, Doubleday, New York, 1986.

[4] DREXLER K.E., *Nanosystems, Molecular Machinery, Manufacturing, and Computation*, Wiley, New York, 1992.

[5] DREXLER K.E., MERKLE R. C., *Differential Gear*, http://nanoengineer-1.com/content/index.php.

[6] JAY C., *Nanoinjector with Red Cells*, http://www.sciencephoto.com..

[7] KLUSEK Z., *Introduction to Nanotechnology, Lectures for Computer Science Students*. Faculty of Physics and Chemistry, University of Łódź, (2006).

[8] KERDCHAROEN T., OSOTCHAM T., SIRKHIRIN T., ROBKOB U., Capacity Building Center for Nanoscience and Nanotechnology, Department of Physics, Faculty of Science, Mahidol University, private communication.

[9] REGIS E., *NANO – the Emerging Science of Nanotechnology: Remaking the World – Molecule by Molecule*, Little Brown, Boston, 1995.

[10] EIGLER D., *From the Bottom Up: Building Things with Atoms*, [in:] *Nanotechnology*, G. Timp (Ed.), Springer, 1999, p. 425.

[11] *Springer Handbook of Nanotechnology*, B. Bushan (Ed.), Springer, Berlin, 2004.

[12] ELLENBOGEN J.C, LOVE J.C., *Architectures for molecular electronics computers: I: Logic structures and an adder built from molecular electronic diodes*, Proceedings of the IEEE, 88 (2000), 386.

[13] *Nanotechnology*, G. Timp (Ed.), Springer, New York, 1999.

[14] *Localization and Confinement of Electrons in Semiconductors*, Proceedings of the Sixth International Winter School, F. Kuchar, H. Heinrich, G. Bauer, (Eds.), Springer Series in Solid-State Sciences, 97, 1990.

[15] *Low Dimensional Electronic Systems. New Concepts*, Proceedings of the Seventh International Winter School, F. Kuchar, H. Heinrich, G. Bauer (Eds.), Springer Series in Solid-State Sciences 111, Springer, Berlin, 1992.
[16] KLUSEK Z., KOZLOWSKI W., KOWALCZYK P., BUSIAKIEWICZ A., OLEJNICZAK W., BYSZEWSKI P., KOWALSKA E., POPLAWSKA M., DATTA P.K., BURNELL-GRAY J.S., Acta Phys. Super., 6 (2004), 33.
[17] SAITO R., DRESSELHAUS G, DRESSELHAUS M.S., *Physical Properties of Carbon Nanotubes*, Imperial College Press, London, 1998.
[18] KLUSEK Z., KOZLOWSKI W., J. Electron Spectr. Relat. Phenom. 107 (2000), 63.
[19] KLUSEK Z., KOZLOWSKI W., Electron Technol., 33 (2000), 350.
[20] KLUSEK Z., Appl. Surf. Sci., 151 (1999), 251.
[21] KLUSEK Z., LUCZAK M., OLEJNICZAK W., Appl. Surf. Sci., 151 (1999), 262.
[22] KLUSEK Z., Electron Technol., 33 (2000), 344.
[23] BYSZEWSKI P., KLUSEK Z., [in:] *Low Dimensional Systems; Theory, Preparation, and Some Applications*, L. M. Liz-Marzan, M. Giersig (Eds.), NATO Science Series, II. Mathematics, Physics and Chemistry, Vol. 91, Kluwer, Dordrecht, 2003, p. 293.
[24] BYSZEWSKI P., KLUSEK Z., PIERZGALSKI P., DATTA S., KOWALSKA E., POPLAWSKA M., J. Electron Spect. Relat. Phenom. 130 (2003), 25.

Received 7 May 2006
Revised 1 September 2006

Materials Science-Poland, Vol. 25, No. 2, 2007

Ferromagnetic transition in $Ge_{1-x}Mn_xTe$ semiconductor layers

W. KNOFF*, P. DZIAWA, V. OSINNIY, B. TALIASHVILI, V. DOMUCHOWSKI, E. ŁUSAKOWSKA, K. ŚWIĄTEK, T. STORY

Institute of Physics, Polish Academy of Sciences, al. Lotników 32/46, 02-668 Warsaw, Poland

Magnetic properties of thin layers of p-$Ge_{1-x}Mn_xTe$ ($x < 0.2$) semimagnetic (diluted magnetic) semiconductor exhibiting carrier induced ferromagnetism were experimentally studied. The layers were grown on BaF_2 (111) substrates by molecular beam epitaxy technique. X-ray diffraction analysis performed at room temperature revealed monocrystalline (111)-oriented rhombohedral (exhibiting ferroelectric properties) crystal structure of $Ge_{1-x}Mn_xTe$ layers in the entire range of Mn content studied. The examination of the magnetic properties of the layers carried out by superconducting SQUID magnetometry and ferromagnetic resonance technique showed the ferromagnetic transition with the Curie temperature in the range 10–100 K depending on the Mn content and the hole concentration. Contrary to polycrystalline GeMnTe layers, it was experimentally found that in monocrystalline layers of GeMnTe an easy magnetization axis is directed along a normal to the layer plane. This effect is discussed in terms of strain present in these layers due to thermal expansion coefficients mismatch between the substrate and the GeMnTe layer.

Key words: *ferromagnetic transition; thin layer; semimagnetic semiconductor*

1. Introduction

$Ge_{1-x}Mn_xTe$ mixed crystals are substitutional solid solutions from the family of IV–VI semimagnetic (diluted magnetic) semiconductors [1, 2]. These materials exhibit ferromagnetic transition induced by a very high conducting hole concentration ($p = 10^{19}$–10^{21} cm^{-3}) [1–6]. Very high carrier concentration and the metallic type of electrical conductivity observed in GeMnTe crystals is related to non-stoichiometric crystal composition and high concentration of electrically active native defects (cation vacancies) [1, 2]. Ferromagnetism of GeMnTe is driven by the Ruderman–Kittel–Kasuya–Yosida (RKKY) indirect exchange interaction between well localized $S = 5/2$ magnetic moments of Mn^{2+} ions (electronic configuration $3d^5$) and conducting carriers with the p–d exchange constant $J_{pd} = 0.6$–0.8 eV [4, 5]. In this material,

*Corresponding author, e-mail: knoff@ifpan.edu.pl

a ferroelectric structural transition from the rock salt (high temperature) to the rhombohedral (low temperature, ferroelectric) phase takes place [2, 4]. Upon increasing the Mn content in $Ge_{1-x}Mn_xTe$ crystals, the ferromagnetic transition temperature increases (up to 150 K for $x = 0.5$) while the ferroelectric transition temperature decreases (670 K for GeTe while 300 K for $x = 0.2$) [4]. It offers a unique possibility to realize various temperature scenarios for both transitions.

So far, $Ge_{1-x}Mn_xTe$ alloys have been mostly studied in the form of quenched bulk polycrystals [3, 4] and thin layers grown by either sputtering [5] or ionized cluster beam deposition method [6] of crystal quality not sufficient for the experimental investigations of the interplay of structural (ferroelectric) and ferromagnetic transitions. In this work, we experimentally study the magnetic properties of thin monocrystalline layers of $Ge_{1-x}Mn_xTe$ grown by molecular beam epitaxy (MBE) as well as analyze the relation between the structural and magnetic properties of the layers.

2. Growth, structural and electrical characterization of layers

$Ge_{1-x}Mn_xTe$ layers were grown by home-built MBE facility on freshly cleaved (111) surface of BaF_2 single crystals using effusion cells for GeTe (material purity 5N), Mn (5N), and Te (5N). The growth of $Ge_{1-x}Mn_xTe$ layers was performed under various technological conditions with substrate temperature of about 400-450 °C and pressure during deposition of about 10^{-8} mbar. The thickness of $Ge_{1-x}Mn_xTe$ layers was typically about 0.25 μm. The maximum content of Mn in $Ge_{1-x}Mn_xTe$ was 20 at. % as checked by energy dispersive X-ray fluorescence analysis, while the typical content of Mn in a set of about 30 samples grown for this study was approximately 5–10 at. %. The growth of the $Ge_{1-x}Mn_xTe$ layers was monitored *in situ* by the reflection high energy electron diffraction (RHEED) technique revealing well defined, streaky pattern characteristic of two-dimensional mode of growth. Oscillations of the intensity of specular spot of RHEED diffraction pattern were not observed.

Post-growth, the layers were characterized by X-ray diffraction (XRD) analysis at room temperature revealing the monocrystaline (111)-oriented rhombohedral (ferroelectric) crystal structure of $Ge_{1-x}Mn_xTe$ in the entire range of Mn content studied. The relatively small width of the X-ray rocking curve (100–600 arcsec) observed in $Ge_{1-x}Mn_xTe$ layers proves their good crystalline quality. XRD measurements showed a linear decrease of GeMnTe lattice parameter with an increase of Mn content, in a good agreement with the Vegard law reported in literature for bulk polycrystals [4] and thin layers [5]. Chemical homogeneity of the alloy was examined by secondary ion mass spectroscopy (SIMS), while surface morphology analysis performed by AFM microscopy revealed RMS roughness parameter of 1–10 nm over 10×10 micron area. For electrical characterization of p-type $Ge_{1-x}Mn_xTe$, the standard four-probe dc Hall effect measurements were carried out at room temperature and liquid nitrogen temperature revealing, as expected, very high ($p = 10^{19}$–10^{21} cm^{-3}) hole concentration in $Ge_{1-x}Mn_xTe$ layers.

3. Magnetic properties

The examination of the magnetic properties of $Ge_{1-x}Mn_xTe$ layers was carried out in a broad temperature range of T = 1.9–200 K by superconducting SQUID magnetometry and ferromagnetic resonance (FMR) measurements. Figure 1 shows the temperature dependence of magnetization of $Ge_{1-x}Mn_xTe$ (x = 0.15) layer, exhibiting ferromagnetic transition with the Curie temperature of about 16 K. Magnetic hysteresis loops for the same layer are presented in Fig. 2 and are characterized by coercive field and saturation field (at T = 5 K) of about 100 Oe and 1 kOe, respectively. Both measurements clearly indicate that an easy magnetization axis in GeMnTe layers is directed along normal to the layer plane. This experimental finding is also confirmed by ferromagnetic resonance analysis of magnetic anisotropy in GeMnTe layers. The FMR spectra shown in Fig. 3 reveal that the resonance field is lower for external magnetic field applied along normal to the layer (as compared to the field in-plane case). For regular thin ferromagnetic layer with in-plane easy axis (determined by shape anisotropy), the opposite effect is typically observed (i.e., the FMR resonance field is higher for out-of-plane configuration of external magnetic field due to large demagnetization effects).

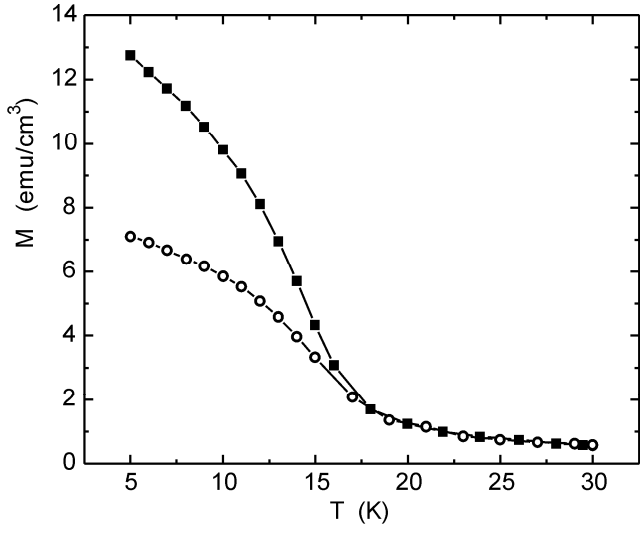

Fig. 1. Temperature dependence of magnetization of $Ge_{1-x}Mn_xTe$ (x = 0.15) layer. External magnetic field of 100 Oe applied perpendicular (full squares) and parallel (open circles) to the plane of the layer

In a set of about 30 $Ge_{1-x}Mn_xTe$ (x<0.2) layers studied so far, ferromagnetic transition was found in the temperature range of T = 10–100 K depending on Mn content and hole concentration. However, for the layers with the highest Curie temperatures a very broad transition region is observed with quasi-linear temperature dependence of magnetization below the transition point. This indicates an insufficient electrical or

chemical homogeneity of these layers. This is also confirmed by a large (up tp 1 kOe) line width of the FMR in GeMnTe layers. To solve this problem, additional technological steps (annealing in MBE vacuum chamber or post-growth isothermal annealing in Te atmosphere) can be applied.

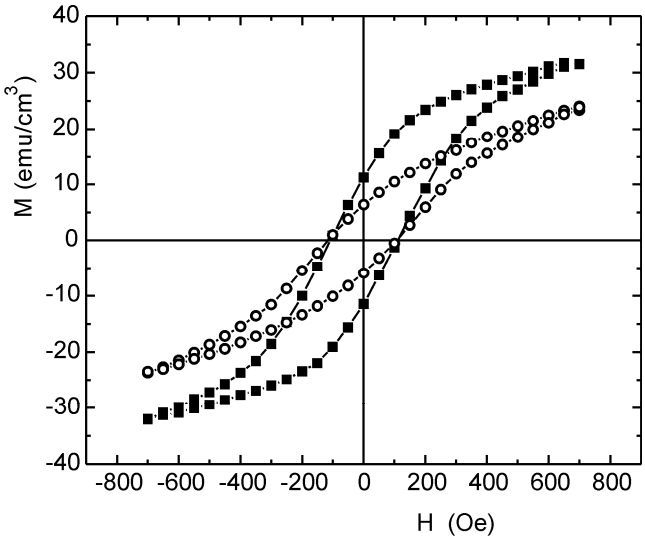

Fig. 2. Magnetic hysteresis loops of $Ge_{1-x}Mn_xTe$ ($x = 0.15$) layer at 5 K. External magnetic field applied perpendicular (full squares) and parallel (open circles) to the plane of the layer

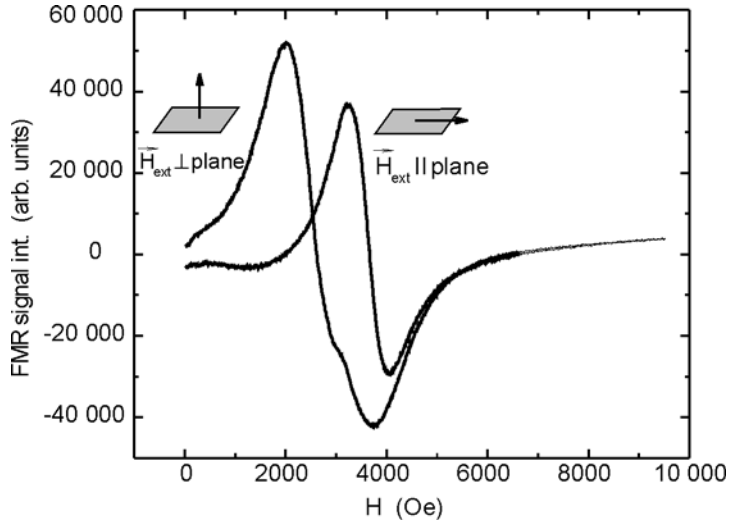

Fig. 3. X-band ferromagnetic resonance spectrum of $Ge_{1-x}Mn_xTe$ ($x = 0.1$) layer for two configurations of the external magnetic field with respect to the layer plane (shown in the figure)

4. Discussion and conclusions

The experimentally observed larger magnetization for the out-of-plane configuration of external magnetic field (as compared to the in-plane case), as well as the results of the FMR anisotropy study, provide evidence that in GeMnTe epitaxial layers grown on BaF_2 substrates the shape (dipolar) contribution to magnetic anisotropy is dominated by other mechanism minimizing the total magnetic energy of the layer for the magnetization vector directed normally to the plane of the layer (i.e., along [111] crystal growth direction). Although in GeMnTe crystal lattice all four [111] crystal directions are equivalent, the effect of thermal strain is expected to remove this degeneracy in epitaxial layers grown on BaF_2 (111) and preferentially select [111] direction normal to the layer. The effect of thermal strain is well known in the studies of optical, magnetic and transport properties of IV–VI semiconductors grown on BaF_2 (111) substrate [1, 2]. It originates from the difference of thermal expansion coefficients of the substrate and the layer (the expansion in the layer is larger than that in the substrate) and is expected to generate tensile strain in the plane of the layer (accompanied by compressive strain normal to the layer as given by Poisson coefficient) [1, 2]. One may also expect that the rhombohedral ferroelectric distortion along [111] directions taking place in these layers above room temperature will result in a single [111] ferroelectric domain structure. The experimental identification of the actual mechanism of this effect as well as the development of the microscopic model of the coupling between local distortion of the crystal lattice and magnetic moment of Mn ions will be the subject of further research in this field.

In conclusion, the magnetic properties of monocrystalline layers of semimagnetic (diluted magnetic) $Ge_{1-x}Mn_xTe$ ($x < 0.2$) semiconductors grown by molecular beam epitaxy on BaF_2 (111) substrates were studied by SQUID magnetometry and ferromagnetic resonance technique revealing ferromagnetic transition related to very high concentration of conducting holes. Magnetic hysteresis loops and ferromagnetic resonance analysis showed in these layers an easy magnetization axis directed along normal to the layer plane. This experimental finding was analyzed in relation to lattice distortions brought about in GeMnTe epitaxial layers by the strain induced by thermal expansion coefficients mismatch between the GeMnTe layer and the BaF_2 (111) substrate as well structural (ferroelectric) rhombohedral distortion of the rock salt lattice.

Acknowledgements

This work was supported by MEiN research project.

References

[1] DOBROWOLSKI W., KOSSUT J., STORY T., [in:] *Handbook on Magnetic Materials*, K.H.J. Buschow (Ed.), Vol. 15, Elsevier North Holland, Amsterdam, 2003, p. 289.

[2] STORY T., in *Lead Chalcogenides-Physics and Applications*, D.R. Khokhlov (Ed.), Taylor and Francis, New York, 2003.

[3] RODOT M., LEWIS J., DODOT H., VILLERS G., COHEN J., MOLLARD P., J. Phys. Soc. Jpn. Suppl., 21 (1966), 627.
[4] COCHRANE R.W., PLISCHKE M., STROM-OLSEN J.O., Phys. Rev. B, 9 (1974), 3013.
[5] FUKUMA Y., ASADA H., NISHIMURA N., KOYANAGI T., J. Appl. Phys., 93 (2003), 4034.
[6] FUKUMA Y., ARIFUKU M., ASADA H., KOYANAGI T., J. Appl. Phys., 97 (2005) 073910.

Received 7 May 2006
Revised 1 September 2006

Materials Science-Poland, Vol. 25, No. 2, 2007

Electronic band structure and X-ray photoemission studies of ternaries APdGe (A = Th,U) in the paramagnetic state

M. SAMSEL-CZEKAŁA[1*], R. TROĆ[1], E. TALIK[2]

[1]Institute of Low Temperature and Structure Research, Polish Academy of Sciences, Okólna 2, P.O. Box 1410, 50-950 Wrocław 2, Poland

[2]Institute of Physics, University of Silesia, Uniwersytecka 4, 40-007 Katowice, Poland

Among uranium transition metal germanides, UPdGe reveals fascinating magnetic and electrical properties. We have recently performed electronic band-structure calculations of this compound and its non-5f electron counterpart ThPdGe in the paramagnetic state. The obtained theoretical electron densities of states (DOS) were compared with newly measured X-ray photoemission spectra (XPS). For UPdGe some disagreement was observed probably due to the predominant localized character of 5f electron states observed in the XPS spectra.

Key words: *electronic structure; photoemission; intermetallic compounds*

1. Introduction

It has been known for some time that UPdGe, crystallizing in the orthorhombic TiNiSi-type crystal structure (*Pnma*), exhibits an interesting complex magnetic behavior and very specific electrical properties [1]. This system undergoes two magnetic transitions at 28 and 50 K, into ferro- and antiferromagnetic state, respectively. At the lowest temperatures, a simple canted ferromagnetic arrangement of the moments within the orthorhombic *ac* plane was first proposed [2] but based on magnetic space group analysis and neutron diffraction studies [1, 3] it has been recently suggested to form a collinear ordering of uranium moments along the orthorhombic *b* axis. It is worth underlining that the collinear ferromagnetic state exists rather at temperatures 20–30 K but below 20 K a conical structure with the net magnetic moment along the *c* axis was reported [4]. This finding agrees well with the recent study of thermopower

[*]Corresponding author, e-mail: m.samsel@int.pan.wroc.pl

and magnetoresistivity. In the temperature range from 28 to 50 K, a sinusoidally modulated antiferromagnetic structure was proposed [2]. As concerns electrical properties of UPdGe, the most interesting fact is that it reveals a giant value (73%) of magnetoresistivity at the transition temperature from ferro- to antiferromagnetic state [1].

This paper is considered to be the first step in understanding the magnetic and electrical properties based on the electronic structure studies of UPdGe and its non-5f electron counterpart ThPdGe in the paramagnetic state. With this aim fully relativistic (4-component) band-structure calculations were performed, using the full-potential local-orbital (FPLO) minimum-basis code [5] with the local density approximation (LDA) of the exchange-correlation potential. The 5f electrons were assumed to be itinerant. We used experimental lattice parameters $a = 7.054$ Å, $b = 4.357$ Å, $c = 7.617$ Å for UPdGe [6] and $a = 7.7006$ Å, $b = 4.3753$, $c = 7.5994$ Å just found for ThPdGe. For both compounds the atom positions were taken as those published in Ref. [3] for UPdGe. We obtained theoretical band energies $E_n(\mathbf{k})$ and total DOS as well as for particular atomic sites and for all the atoms in the unit cell separately. To verify these computations, the partial DOSs for the constituent atoms in each system were multiplied by the respective weight factors proportional to atomic cross-sections on photon scattering [7]. The results were summed and convoluted with a Gaussian to simulate the energy resolution δ of the analyser used in the XPS experiment.

Theoretical XPS obtained in this way were compared with the experimental ones, collected with monochromatised AlK_α (1486.6 eV) radiation on the polycrystalline samples of UPdGe and ThPdGe at room temperature. The energy spectra of emitted electrons with an energy resolution of ~ 0.3 eV were analysed theoretically assuming $\delta = 0.3$ eV. The XPS spectra in a broad range of binding energies (0–1300 eV) were recorded under ultrahigh vacuum of 10^{-10} Torr at room temperature using a PHI 5700/660 Physical Electronics photoelectron spectrometer. Each spectrum was recorded immediately after braking the sample in vacuum. The oxidation of the samples was checked by inspecting the O 1s spectra before and after each measurement. Except for a small contribution of uranium dioxide, in the measured samples also some contamination from carbon was found.

2. Results and discussion

The behaviour of calculated band energies $E_n(\mathbf{k})$ in UPdGe is strongly anisotropic. Narrow band gaps open along a number of main symmetry directions **k**. For other **k** mostly semimetallic character of bands is predicted by the theory. The spin-orbit coupling of U 5f states is of the order of 1 eV. Although the Fermi level E_F cuts the U $5f_{5/2}$ peak yielding a relatively high value of DOS at E_F, a pseudogap opens in the vicinity of E_F. In the region of valence band the contributions from Pd and Ge to the total DOS are very similar to each other for UPdGe and ThPdGe. As we expected, the non-occupied Th 5f states in ThPdGe are shifted far above E_F. Nevertheless, a very

small part of these electronic states may exist also at E_F. For UPdGe, a distinct hybridisation of the U 5f states with the U 6d and Pd 4d as well as Ge 4sp states around E_F is apparent. Analogously, a hybridisation between the Th 5f with Th 6d and Pd 4d and Ge 4sp states is highly probable.

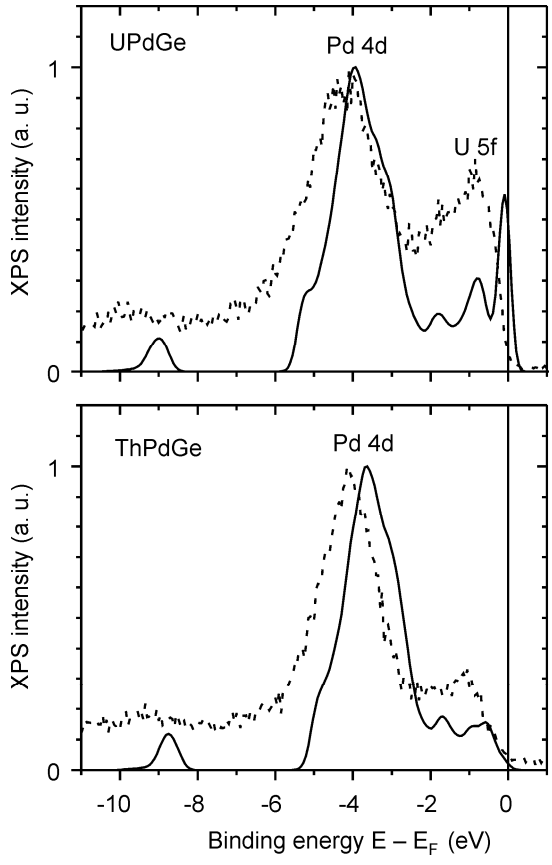

Fig. 1. The theoretical (solid line) and experimental (dashed line) XPS intensity determined for UPdGe and ThPdGe

In this paper, we limit our presentation to comparison of the theoretical and experimental XPS data for UPdGe and ThPdGe in the binding energy region of valence electrons. The obtained results are shown in Fig. 1. The analysis of the calculated XPSs for both compounds reveals that in this range of energy (for AlK_α radiation) we can observe mainly large and very similar contributions originating from the Pd 4d states having a wide peak centred at about 4 eV. This feature is well reproduced by the experimental XPS. Additionally, for UPdGe there is a pronounced contribution of the U $5f_{5/2}$ states located just below E_F. However, in our experiment the maximum of this contribution is shifted from E_F by about 1 eV towards lower energies. This distinct discrepancy is probably connected with a more localised character of U 5f states

in UPdGe, which is well visible in the experimental XPS. Moreover, this contribution is spread in the energy region more than 3 eV, which supports the idea of distinct localisation of 5f electrons in UPdGe due to the formation of the final multiplet. This aspect will require more detailed studies with the UPS technique.

3. Conclusions

To understand the magnetic and electrical properties of UPdGe we studied its electronic structure as well as the structure of its non-magnetic counterpart ThPdGe in the paramagnetic state. We performed fully relativistic and full-potential band-structure calculations using modern FPLO code. The obtained theoretical band energies and electron DOSs were compared with the experimental XPS data. We believe that we achieved a satisfying agreement between the theoretical and experimental data as to the conduction bands, but an apparent disagreement was observed for the U 5f band in UPdGe probably due to its more localised character in this compound being well marked in the experimental XPS spectra.

Acknowledgements

We are very grateful to the network MAG-EL-MAT in Poznań (Poland) for the financial support.

References

[1] TROC R., J. Alloys. Compds., J. Alloys Comp., 423 (2006), 21.
[2] KAWAMATA S., ISHIMOTO K., YAMAGUCHI Y., KOMATSUBARA T., J. Magn. Magn. Mater., 104 (1992), 51.
[3] EL-KHATIB S., CHANG S., NAKOTTE H., BROWN D., BRÜCK E., SCHULTZ A.J., CHRISTIANSON A., LACERDA A., J. Appl. Phys., 93 (2003), 8352.
[4] TRAN V.H., TROC R., BOUREE F., ROISNEL T., ANDRE G., J. Magn. Magn. Mater., 140/144 (1995), 1377.
[5] FPLO-5.00-18 (improved version of the original FPLO code by Koepernik K. and Eschrig H., Phys. Rev. B, 59 (1999), 1743); http://www.FPLO.de.
[6] TROC R., TRAN V.H., J. Magn. Magn. Mater., 73 (1988), 389.
[7] YEH J.J., LINDAU I., At. Data Nucl. Data Tables, 32 (1985), 1.

Received 7 May 2006
Revised 1 September 2006

Materials Science-Poland, Vol. 25, No. 2, 2007

Conductance quantization in magnetic and nonmagnetic metallic nanowires

B. SUSŁA[1*], M. WAWRZYNIAK[2], J. BARNAŚ[3, 4], W. NAWROCKI[2]

[1]Institute of Physics, Poznań University of Technology, ul. Nieszawska 13A, 60-965 Poznań, Poland

[2]Institute of Electronics and Telecommunications, Poznań University of Technology, Piotrowo 3, 60-965 Poznań, Poland

[3]Department of Physics, Adam Mickiewicz University, ul. Umultowska 85, 61-614 Poznań, Poland

[4]Institute of Molecular Physics, Polish Academy of Sciences, ul. Smoluchowskiego17, 60-179 Poznań, Poland

Transport properties of ferromagnetic quantum wires at room temperature are not yet fully understood, and the role of electronic structure of magnetic atoms in the conductance quantization is still under discussion. We present experimental results on the conductance quantization in point contacts between ferromagnetic (Co) or nonmagnetic (Au) wires and semiconductor (Ge) samples. The main features of the conductance histograms for the nonmagnetic wires are consistent with the conductance quantization in the units of quantum conductance $G_0 = 2e^2/h$. For the ferromagnetic Co nanowires, the conductance shows plateaus at nG_0, generally with non-integer n. Such behaviour is a consequence of the complex electronic structure of magnetic 3d transition-metal atoms. A description of the quantization phenomena is presented in terms of the Landauer formalism for the current flowing through a small nanoconstriction.

Key words: *quantized conductance, magnetic nanowire, ballistic transport, quantum point contact*

1. Introduction

Crystalline nanostructures, such as magnetic nanowires, offer unique access to low dimensional condensed-matter physics. Because of the low power consumption, nanowires are very attractive and promising candidates for the next generation electronic and photonic devices. Understanding electron conduction through magnetic (Co, Ni) and semiconductor nanowires connecting two macroscopic electrodes is particularly attractive from the point of view of the fundamental physical properties of such structures, as well as from the point of view of potential applications in spintronic devices.

[*]Corresponding author, e-mail: susla@phys.put.poznan.pl

Since 1988, when the conductance quantization was measured in a two-dimensional electron gas quantum point contact [1, 2], charge transport has been the object of revived scientific interest. In 1993, electrical conductance quantization was found in gold nanowires made with the scanning tunnelling microscope technique at room temperatures [3] as well as at low temperatures [4]. Further studies showed that nanowires could form also in less sophisticated setups; for instance between two vibrating wires [5], or between relay contacts [6]. However, fabrication of stable nanowires of the width comparable with the corresponding Fermi wavelength turned out to be a very difficult task [7–9].

In noble (Ag, Au) and alkali (Li, Na) metals, the last conductance step before wire breaking, most likely corresponding to a monoatomic nanocontact, corresponds to the conductance quantum (per double spin) $G_0 = 2e^2/h$, which can be associated with free propagation of the valence s electrons in two quantum channels (one per each spin orientation). For magnetic transition metals such as Co and Ni, the experimental data are less consistent. Oshima et al. [10] found the conductance steps in Ni nanocontacts near G_0 and $2G_0$ at room temperatures and zero magnetic field, near $2G_0$ at 770K and zero field, and near $1.5G_0$ (occasionally near $0.5G_0$) at room temperatures in a magnetic field. Ono et al. [11] reported again G_0 for Ni at zero field and $0.5G_0$ for Ni in a field. Recently Rodrigues et al. [12] observed one conductance quantum in a Co atomic chain at room temperature and zero magnetic field. Apart from this, Untiedt et al. [13] obtained low temperature zero-field data for several magnetic (Fe, Co and Ni) and nonmagnetic (Pt) quantum wires, and reported a dominance of the conductance steps between G_0 and $1.5G_0$ in Co and Ni.

Although the conductance quantization has been analyzed theoretically within more or less rigorous methods, some features of the electronic transport through point contacts are not well understood yet. For instance, the influence of electron–electron interactions, spin dependent electronic structure of the materials forming the nanocontacts, and magnetic domain walls at the constrictions is still unexplored and is of current interest [14–17].

In this paper, we report on the investigation of the conductance of atomic sized contacts in air and at room temperature which are formed between magnetic (Co) or nonmagnetic (Au) metals and a semiconductor (Ge) samples. We present a clear evidence of the conductance quantization in ferromagnetic Co nanowires.

2. Experimental

Figure 1 shows a schematic diagram of the experimental setup used for measurements of the conductance quantization. The nanowires are formed between the electrodes A and B of the studied material. Measured during the electrode separation, i.e., during the nanowire stretching, the electrical conductance G corresponds to the conductance of the nanowire under investigation. The digital storage oscilloscope, used for signal sampling and recording, must be triggered at a right moment for the meas-

urements to cover the process of stretching and breaking of the last remaining nanowire. The arbitrary waveform generator is used to control movement of the A electrode. The digital storage oscilloscope and arbitrary waveform generator is controlled by a PC through the IEEE-488 interface.

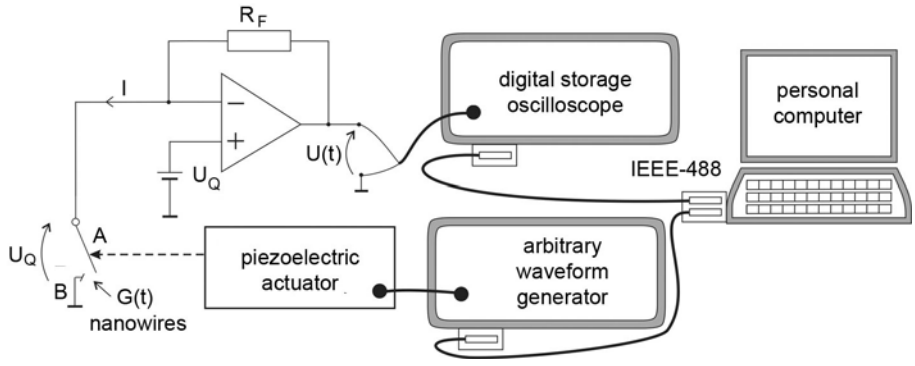

Fig. 1. Schematic diagram of the experimental setup

With an appropriate measurement software, a required number of the conductance curves can be obtained to provide the basis for building the conductance histograms. The nanowire current I is converted into voltage by an operational amplifier in the current amplifier circuit.

3. Results and discussion

The conductance histograms were built up using all consecutive conductance curves at room temperature. In all cases, the individual conductance traces clearly showed more or less pronounced conductance plateaus. In the case of Au–Ge and Co–Ge brake junctions, the corresponding conductance histograms obtained at room temperature and in air showed clear peaks corresponding to the conductance steps. We found no clear peaks in the conductance histograms of Co–Co nanocontacts.

Figure 2 shows one of the individual conductance traces for Au, and clearly demonstrates the conductance quantization, $G = nG_0$ with n roughly integer ($n = 1, 2, 3$). This behaviour corresponds to an almost ideal case of ballistic (scattering-free) electron transport through a nanowire with spin degenerate s-like transport channels. If, however, electron scattering occurs in the nanowire, the conductance steps may occur at lower positions (non-integer n). Therefore, the conductance histograms [1, 6] are built up from a large number of conductance traces. Our data have been statistically analyzed by plotting histograms for more than thousand measured conductance values Such a histogram for Au nanowires is shown in Fig. 3. The positions of peaks (local maxima) in the histogram provide information on the quantization phenomena. In the case of Au, these maxima occur exactly at nG_0 with integer n.

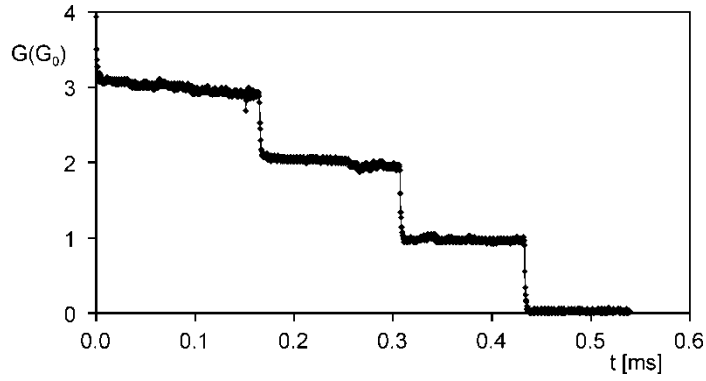

Fig. 2. Electrical conductance in an Au nanowire during elongation

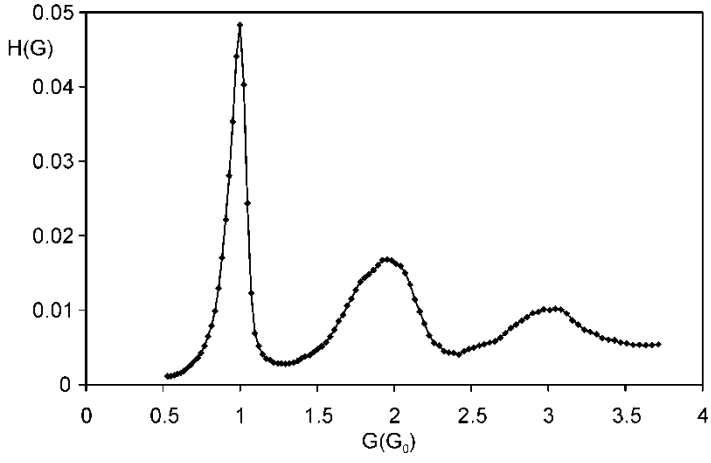

Fig. 3. Conductance histograms for gold nanowires built from 6000 curves

The situation in nanocontacts involving one or two magnetic transition metals becomes much more complex. The conductance then depends on the exact atomic and crystallographic structure of the apexes on both sides of a nanocontact, as well as on the exact electronic structure of the whole nanocontact. Moreover, even assuming the nanocontact is of single-atomic size, one still can have more transport channels as both 4s and 3d electrons can contribute to transport (2s and 7d electrons in Co). All this makes the available experimental data for Co nanowires inconsistent which additionally indicates that the Co nanocontacts in different experiments have different atomic as well as crystallographic structure. To get a qualitative interpretation of the experimental results one would need to investigate the exact atomic structures of the point contacts (including also the effects of contamination, oxidation, etc.) which is not an easy task. Then, a quantitative interpretation could be reached by ab-initio numerical calculations.

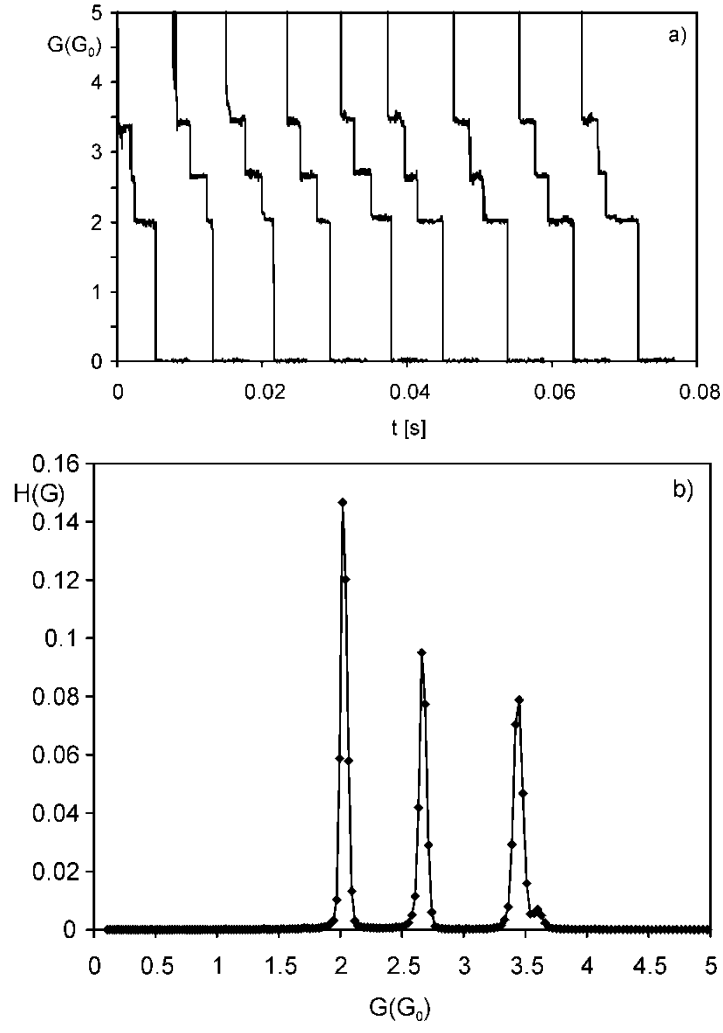

Fig. 4. Room-temperature conductance of Co nanowires and a Ge sample: a) typical electronic transport curves showing the conductance plateaus, b) global histogram exhibiting the statistical conductance for Co. Note that the lowest plateau in (a) and the lowest -conductance peak in (b) are located at $2.01G_0$, which corresponds to the thinnest Co wire

In our case we found the conductance plateaus at $G = 2.01G_0$, $G = 2.66G_0$, and $G = 3.45G_0$ in the room-temperature conductance traces of the Co–Ge break-junctions. The corresponding experimental data are shown in Fig. 4a. The relevant conductance histogram also has pronounced peaks at these conductance values, as shown in Fig.4b. We found no signature of the $0.5G_0$ conductance plateau, observed by others [10, 11]. The lowest plateau in our case occurs at $2.1G_0$ which may indicate that either the corresponding apex is not of one-atomic shape or the atomic structure of the apex is such that it allows contribution from both s and d electrons. One may expect that

s electrons would contribute to plateaus at nG_0 with roughly integer n, whereas d electrons may give contributions differing from that corresponding to perfect transmission as the d electrons of Co atoms must couple to Ge atoms which have different electronic structure. In turn, the higher conductance plateaus, $G = 2.66G_0$ and $G = 3.45G_0$, may indicate the role of d electrons and the presence of spin polarized conductance channels. However, as we have already mentioned above, a detailed investigation of the apex structure and stability would be necessary for a unique interpretation of the quantization plateaus.

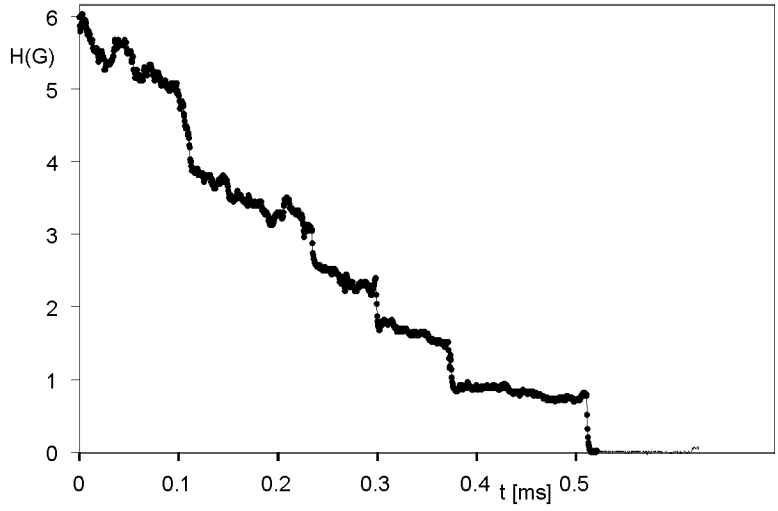

Fig. 5. Conductance traces for a cobalt nanowire during elongation at RT in air

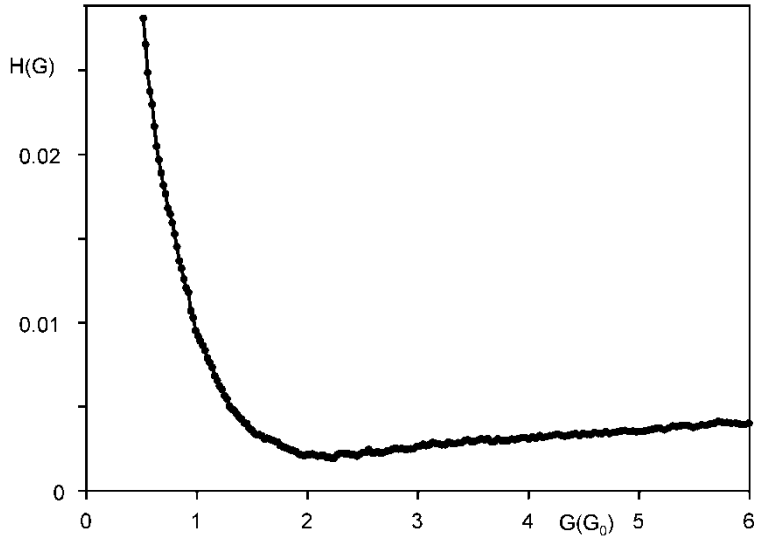

Fig. 6. Conductance histogram for cobalt nanowires built with 5000 consecutive traces

Finally, we would like to mention that the obtained conductance curves in Co–Co nanojunctions at room temperature show conductance quantization plateaus, as presented in Fig. 5, but the corresponding conductance histogram (Fig. 6) does not show clear quantized peaks. In Figure 5, the first plateau occurs roughly at G_0, most likely originating from s-like (spin degenerate) channel. The next plateau occurs roughly at $1.5G_0$ and may originate from the above mentioned s channel and one (spin polarized) d channel. Stretching the wire may then break bounds via the d states and remove the contribution from the d channel. The origin of the absence of distinct peaks in the conductance histogram is not clear. A reason for this may be a strong variation of the apexes' shape in consecutive runs. The difference in conductance traces and conductance histograms for Co–Ge and Co–Co point contacts also indicates that the apex shape strongly depends on the materials and atomic bonds in the nanocontacts.

4. Summary

We have investigated conductance quantization in Au–Ge, Co–Ge and Co–Co nanocontacts. The corresponding conductance traces clearly show the conductance quantization in all investigated nanocontacts. The data have been statistically analyzed by plotting histograms built from a large number of conductance curves. Our measurements show that the lowest conductance plateau in the room-temperature conductance of the Co–Ge break-junctions occurs at $2.1G_0$. We found no signature of the conductance plateau at $0.5G_0$. The higher conductance plateaus indicate the role of spin polarized d channels. However, to interpret properly the results, both qualitatively and quantitatively, a detailed information on the atomic structure of the nanocontacts and their electronic properties would be necessary. The results create new opportunities for a deeper understanding of the spin dependent electronic structure and electronic transport in ferromagnetic quantum wires.

Acknowledgements

This work is partly supported by the project PB 62-208/06.

References

[1] VAN WEES B.J., VAN HOUTEN H., BEENAKKER C.W.J., WILLIAMSON J.G., KOUWENHOVEN L.P., VAN DER MAREL D., FOXON C.T., Phys. Rev. Lett., 60 (1988), 848.
[2] WHARAM D.A., THORTON T.J., NEWBURY R., PEPPER M., AHMED H., FROST J.E.F., HASKO D.G., PEACOCK D.C., RITCHIE D.A., JONES G.A.C., J. Phys. C, 21 (1988), L209.
[3] PASCUAL J.I., MENDEZ J., GOMEZ-HERRERO J., BARO A.M., GARCIA N., THIEN BINH V., Phys. Rev. Lett., 71 (1993), 1852.
[4] AGRAIT N., RODRIGO J.G., VIEIRA S., Phys. Rev. B, 47 (1993), 12345.
[5] COSTA-KRÄMER J.L., GARCIA N., GARCIA-MOCHALES P., SERENA P.A., Surf. Sci., 342 (1995), L1144.
[6] HANSEN K., LAEGSGAARD E., STENSGAARD I., BESENBACHER F., Phys. Rev. B, 56 (1997), 2208.
[7] RODRIGUES V., UGARTE D., Phys. Rev. B, 63 (2001), 73405.

[8] CORREIA A., GARCIA N., Phys. Rev. B, 55 (1997), 6689.
[9] MARTINEK J., NAWROCKI W., WAWRZYNIAK M., STANKOWSKI J., Mol. Phys. Rep., 20 (1997), 157.
[10] OSHIMA H., MIYANO K., Appl. Phys. Lett., 73 (1998), 2203.
[11] ONO T., OOKA YU., MIYAJIMA H., Appl. Phys. Lett., 75 (1999), 1622.
[12] RODRIGUES V., BETTINI J., SILVA P.C., UGRATE D., Phys. Rev. Lett., 91(2003), 96801.
[13] UNTIEDT C., DEKKER D.M.T., DJUKIC D., VAN RUITENBEEK J.M., Phys. Rev. B, 69 (2004), 81401.
[14] LANDAUER R., IBM J. Rev. Dev., 1 (1957) 223; 44 (2000), 251.
[15] COSTA-CRAMER J.L., Phys. Rev. B, 55 (1997), R4875.
[16] DUGAEV V.K., BERAKDAR J., BARNAŚ J., Phys. Rev. Lett., 94 (2006), 47208.
[17] ARAUJO M.A.N., DUGAEV V.K, VIEIRA V.R., BERAKDAR J., BARNAŚ J., http://arxiv.org/abs/cond-mat/0602399.

Received 7 May 2006
Revised 1 September 2006

Materials Science-Poland, Vol. 25, No. 2, 2007

Magnetic phase transitions from the point of view of macroscopic and microscopic methods

A. SZYTUŁA*

M. Smoluchowski Institute of Physics, Jagiellonian University, Reymonta 4, 30-059 Kraków, Poland

Magnetic phase transitions in some rare earth compounds are discussed from the point of view of different experimental methods. The discussion concentrates on the determination of phase transitions in magnetically ordered states. The data presented in this work suggest that the "classical" method, namely the specific heat method, does not yield information on phase transitions between commensurate and incommensurate magnetic structures.

Key words: *magnetic phase transition; rare earth intermetallics; specific heat; electrical resistivity; neutron diffraction*

1. Introduction

One of the important problems of solid state physics are investigations of phase transitions in crystals. The methods used to investigate the magnetic phase transitions could be divided into macroscopic and microscopic ones. Temperature dependences of magnetization, magnetic susceptibility and specific heat measurements belong to the former group while neutron diffraction and the Mössbauer effect to the latter one.

Below characteristic temperatures of magnetic materials, i.e. the Curie temperature (T_C) for ferromagnets and the Néel temperature (T_N) for antiferromagnets, the magnetic moments of atoms order. The transition from the paramagnetic to the magnetically ordered phase is the second order phase transition and a characteristic maximum in the temperature dependence of specific heat is observed [1]. Neutron diffraction methods provide information on the symmetry of the magnetic structure from the intensities of the magnetic peaks. Thermal dependence of the intensities of magnetic peaks gives us information on the critical temperature of the magnetic ordering (T_C or T_N), as well as of the magnetic phase transitions (i.e., changes in the magnetic structure) [2]. Very quick development of these methods in recent years, in particular the

*E-mail: szytula@if.uj.edu.pl

neutron diffraction measurements with multidetectors, allows us to obtain new interesting information on phase transitions. However, information from different experimental data does not always give similar results.

In this work, results for some rare earth intermetallic compounds are discussed. The data presented concern the RT_2X_2 compounds (R is a rare earth element, T is a transition nd-element and X is Si or Ge). These compounds crystallize in a simple tetragonal structure of $ThCr_2Si_2$ type (space group $I4/mmm$). R atoms with localized magnetic moment occupy only one sublattice ($2a$ positions). The information on the magnetic phase transitions in the ternary rare earth compounds is summarized in two papers [3, 4]. The paper focuses on some examples chosen to illustrate the large variety of behaviours in magnetic phase transition regions but its aim is not to give a complete review of these phenomena.

2. Results

2.1. $NdCo_2Ge_2$ compound

In Figure 1, the temperature dependences of magnetization, specific heat, electrical resistivity and plots of neutron diffraction data (the dependence of integrated intensities of some magnetic peaks and the k_z-component of the propagation vector) of $NdCo_2Ge_2$ are presented. The magnetization shows a peak at about 10 K and a small maximum at about 26.5 K [5], while the specific heat and resistivity show only anomalies at 26.5 K [6]. Neutron diffraction data give the explanation of these differences. At 1.5 K two magnetic ordering modes coexist: a simple collinear antiferromagnetic AFI type, in which the Nd magnetic moment at the position (0, 0, 0) is antiparallel to the one at the position (1/2, 1/2, 1/2) and a sine-modulated magnetic structure with the propagation vector $\mathbf{k} = (0, 0, 1 - k_z)$, where $k_z = 0.261$ in the reduced unit cell. With increasing temperature, the intensities of the peaks corresponding to the simple collinear magnetic structure diminish and vanish at 12 K while the intensities of the peaks corresponding to the modulated structure increase up to 12 K and then decrease up to the Néel temperature equal to 26 K. The peak in the k_z value is connected with the transition at T_t (Fig. 1) [7].

2.2. $PrFe_2Ge_2$ and $NdFe_2Ge_2$ compounds

The results of the investigations concerning magnetic phase transitions in $PrFe_2Ge_2$ are summarized in Fig. 2. The temperature dependences of the dc magnetization and ac magnetic susceptibility have the maxima at $T_N = 13$ K and an additional maximum in the ac magnetic susceptibility at 8 K. The resistivity shows anomalies at 8.2 and 14.6 K [8] while the specific heat only at $T_N = 14.2$ K [8, 9]. The neutron diffraction data show the phase transition from simple collinear antiferromagnetic struc-

ture described by the propagation vector **k** = (0, 0, 1/2) to the sinusoidally-modulated structure with the propagation vector **k** = (0, 0, 0.476) at 9 K [10].

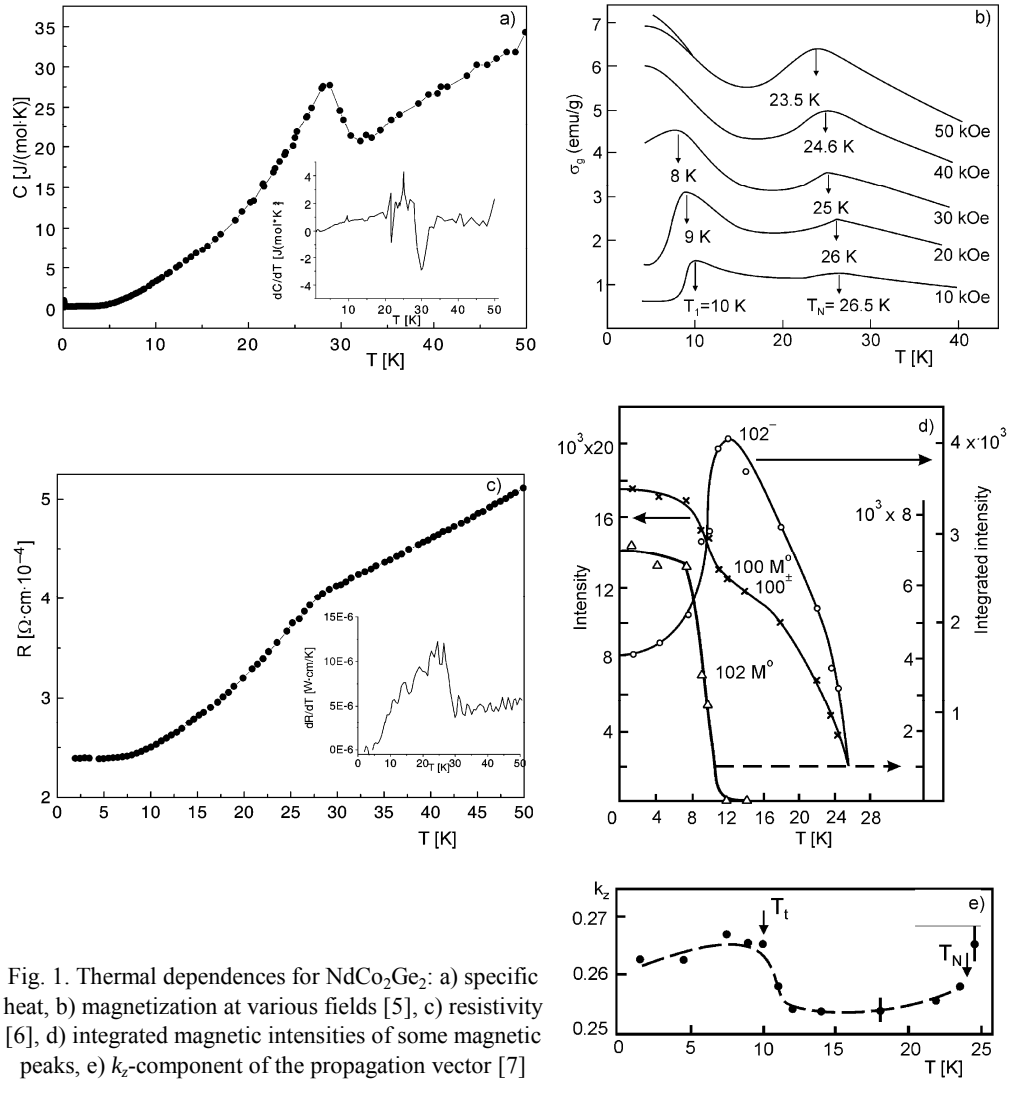

Fig. 1. Thermal dependences for $NdCo_2Ge_2$: a) specific heat, b) magnetization at various fields [5], c) resistivity [6], d) integrated magnetic intensities of some magnetic peaks, e) k_z-component of the propagation vector [7]

Temperature dependence of the ac magnetic susceptibility χ of $NdFe_2Ge_2$ exhibits a maximum at 16.7 K. Below the Néel temperature the maximum at T_t = 13.5 K in the temperature dependence of d χ'/dT indicates an additional phase transition [11]. These anomalies are visible also in the specific heat and resistivity measurements [8]. Neutron diffraction data indicate the phase transition between the collinear antiferromagnetic structure with the **k** = (0, 0, 1/2) below T_t and **k** = (0, 0, 0.46(1)) above T_t [11].

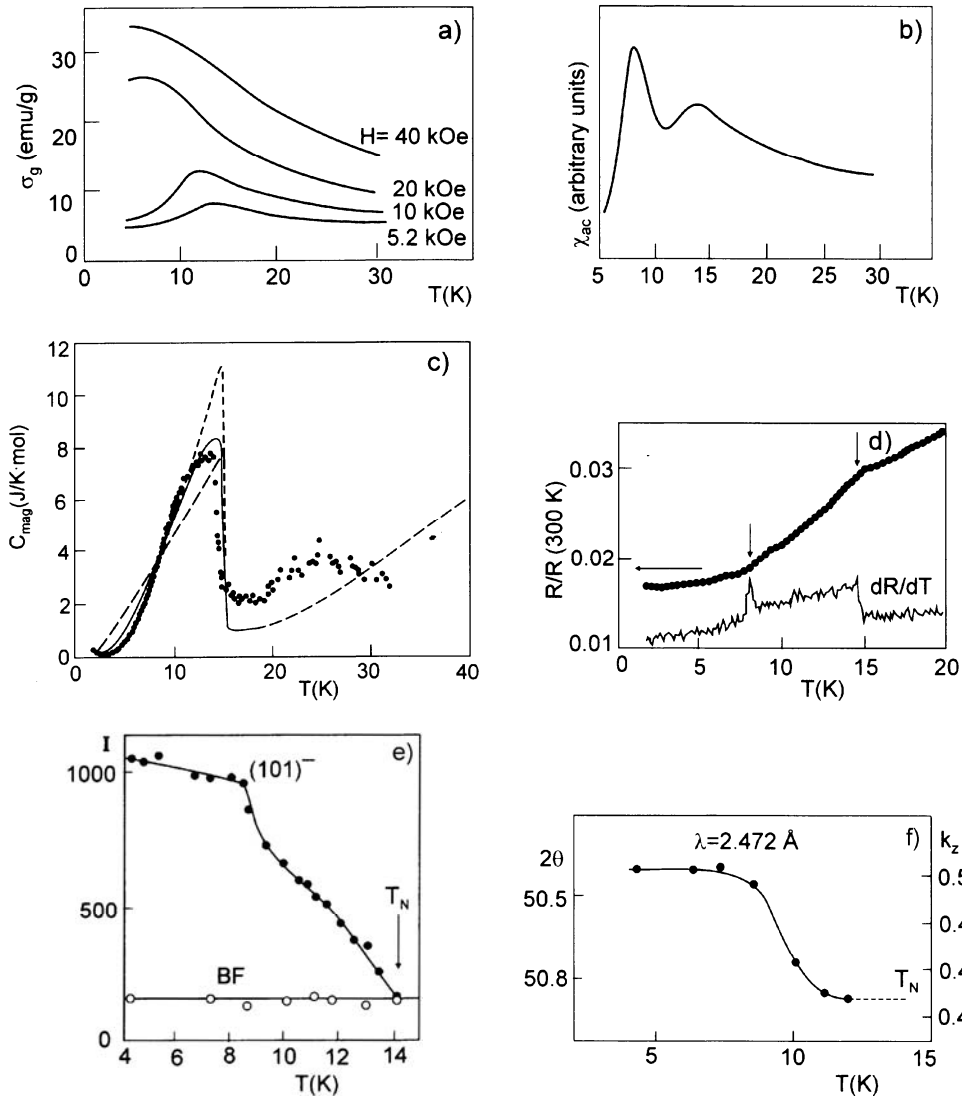

Fig. 2. Thermal dependences of: dc magnetization at various magnetic fields (a), ac magnetic susceptibility (b), specific heat [8] (c), resistivity R and its temperature derivative dR/dT [9] (d) as well as integrated intensity of the magnetic 101, reflection (e) and 2θ position of the $110^{\pm}$ reflection and propagation vector $\mathbf{k}_z$ for $PrFe_2Ge_2$ [10] (f). The dashed and the dotted lines represent the specific heat curves calculated for a simple antiferromagnet and for a modulated magnetic structure below T_N, respectively

2.3. $NdRu_2X_2$ (X = Si, Ge)

The magnetic data indicate that both $NdRu_2X_2$ compounds are ferromagnets at low temperatures [12, 13]. With increasing temperature the change in the magnetic structure from the ferromagnetic ordering to the sinusoidally modulated one for both com-

pounds is observed at T_t = 10 K. Above T_t, sine-wave modulated structure develops with the propagation vector **k**= (k_x, k_x, 0), where k_x = 0.13 for $NdRu_2Si_2$ [12] and 0.12 for $NdRu_2Ge_2$ [14].

For $NdRu_2Si_2$ both phase transitions (at T_t and T_N = 23 K) are clearly visible in the thermal dependence of specific heat and electrical resistivity [15].

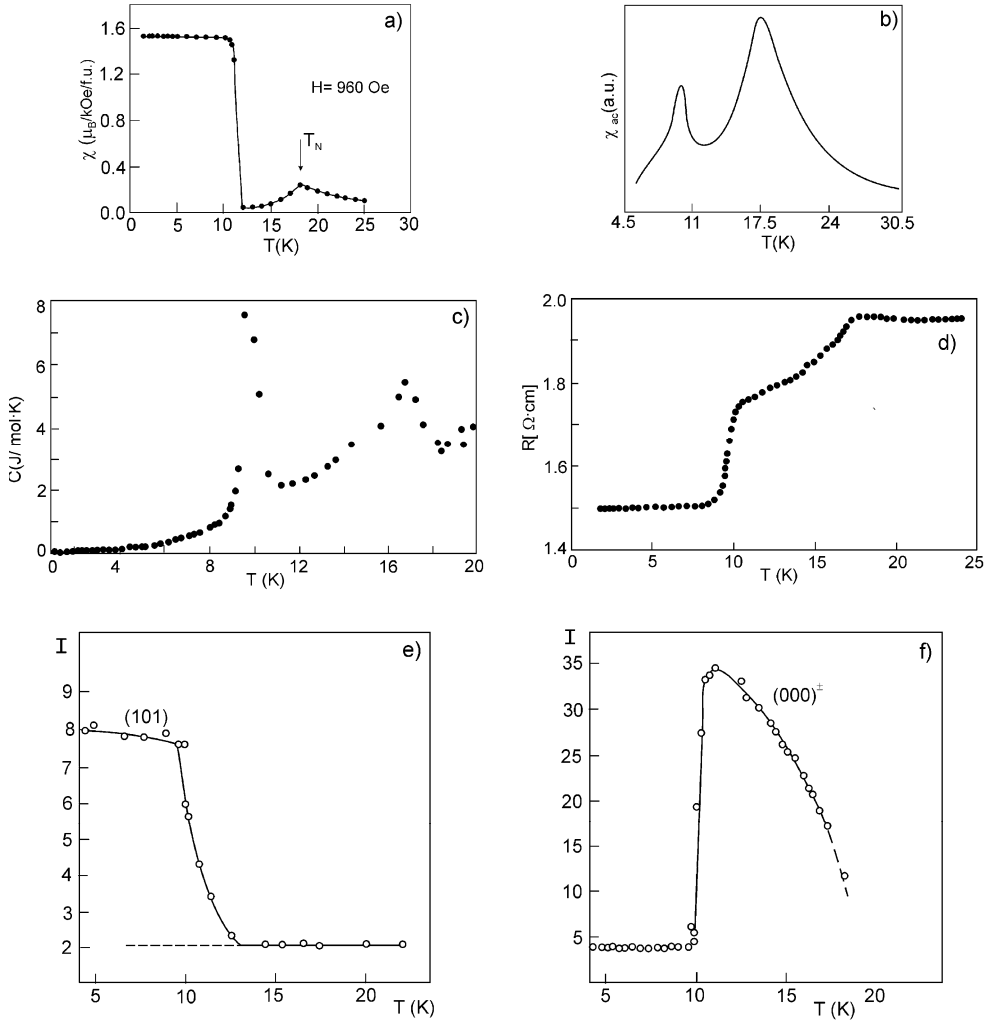

Fig. 3. Temperature dependence of the dc magnetization (a), ac magnetic susceptibility (b), specific heat (c), resistivity (d) and integrated intensities of the 101 (e) and $000^{\pm}$ (f) peaks for $NdRu_2Ge_2$ [14]

In Figure 3, the data concerning the phase transitions in $NdRu_2Ge_2$ are shown. The low temperature thermal variation of the dc susceptibility confirms the first order transition between the ferro- and antiferromagnetic phases at 10 K and the Néel temperature at 18 K. These transitions are confirmed by the ac data which exhibit the

maxima at 9.6 and 17.5 K [16]. At these temperatures, anomalies in the thermal dependences of specific heat and electric resistivity are observed. At T_t = 10 K, the neutron diffraction data show a decrease in the intensity of the 101 magnetic peak corresponding to the ferromagnetic phase and an increase in the intensity of the $000^{\pm}$ reflection corresponding to the modulated phase.

3. Discussion

The results presented in this work clearly show that it is possible to obtain complete information on magnetic phase transitions in rare earth intermetallic compounds only from investigations carried out by means of complementary macro- and microscopic methods. The data presented here show that information obtained from various methods depicts these transitions in different ways. Especially interesting are the results concerning phase transitions in the ordered phase. Also, the results obtained for $NdCo_2Ge_2$ and $PrFe_2Ge_2$ are worth to notice. For these compounds, no anomaly connected with the change in the magnetic structure from a commensurate to an incommensurate one was observed in the temperature dependence of specific heat, while other macroscopic methods, as well as the neutron diffraction method, show an anomaly at T_t. A similar situation is observed in $TbNi_2Si_2$ where at T_t = 8.5 K the neutron diffraction experiment shows a change in the magnetic structure from a commensurate one with **k** = (1/2, 1/2, 0) to an incommensurate one with **k** = (0.604, 0.396, 0), while the thermal dependence of specific heat shows only a λ-type anomaly at T_N = 13.7 K [17]. The data on the magnetic phase transitions in some RT_2X_2 compounds with R = Pr and Nd [18–24] are summarized in Table 1.

Table 1. Magnetic phase transitions in RT_2X_2 (R = Pr, Nd; T – d-electron element; X = Si, Ge) determined from the specific heat measurements

Compound	T_N [K]	T_t [K]	$\Delta C(T_N)$ [J/(mol·K)]	$\Delta C(T_t)$ [J/(mol·K)]	$S(T_N)$ [J/(mol·K)]	$S(T_t)$ [J/mol·K]	ΔS(50 K) /Rln2	Ref.
$PrFe_2Si_2$	7.7	–	0.1		0.6		0.885	[9]
$PrFe_2Ge_2$	14.2		5.7		4.7		1.128	[9]
$PrCo_2Si_2$	29.7	16.4, 9.6	4.7	12.2, 4.7				[18]
$PrNi_2Si_2$	20.0		0.3					[19]
$PrNi_2Ge_2$	20.4	–	8.0		10.3		1.79	[20]
$PrCu_2Ge_2$	15	5.5	9.6	3.25				[21]
$PrRu_2Si_2$	16	14	~0.1	14.0	4.5		1.3	[22]
$NdFe_2Ge_2$	16.4	13.5	7.6	4.9	6.7		1.17	[8]
$NdCo_2Ge_2$	28	–	9.4		9.78		2.47	(this work)
$NdNi_2Ge_2$	16.6	2.6	4.4	0.5	11.5		2.386	[7]
$NdRu_2Si_2$	23.5	10	2.46		4.6	1.5	1.16	(this work)
$NdRu_2Ge_2$	17	10	2.62	6.3	1.84	0.8	0.55	[6]
	18	10	12.0	0.5	2.8	0.47	0.694	[24]

In the mean field description of magnetic phase transitions at T_N, the dependence of the $\Delta C_{\mathrm{mag}}(T_N)$ value on the momentum J is described by the equation:

$$\Delta C_{\mathrm{mag}}\left(T_N\right) = 2.5R\frac{\left(2J+1\right)^2-1}{\left(2J+1\right)^2+1}$$

with the related entropy given by $\Delta S_m = R\ln(2J + 1)$. For the reported Pr and Nd compounds J is equal 4 and 9/2, respectively, and the respective values of $\Delta C_{\mathrm{mag}}(T_N)$ are 20.28 J/(mol·K) for Pr and 20.37 J/(mol·K) for Nd, and $\Delta S(T_N)$ should be equal to 18.27 J/(mol·K) for Pr and 19.14 J/(mol·K) for Nd compounds. In all the discussed compounds, the discontinuity of the specific heat at T_N is reduced. This is in good agreement with the experimental [25] and theoretical [26] results for the compounds with the phase transition from an amplitude modulated magnetic structure to the paramagnetic phase. For some compounds, the magnetic entropy near the Néel temperature is close to the value $R\ln2$ = 5.76 J/(mol·K), the theoretical entropy of a two level system.

Acknowledgements

The author wishes to express special thanks to Dr. T. Jaworska-Gołąb for careful reading of the manuscript and discussions, and Ł. Gondek for interest in this work, in particularl the specific heat data.

References

[1] SERENI J.G., [in:] *Encyclopedia of Materials: Science and Technology*, K.H.J. Buschow,E. Gratz (Eds.), Elsevier Science Ltd., Oxford, 2001, p. 4986.
[2] BACON G.E., *Neutron Diffraction*, Clarendon Press, Clarendon, 1975.
[3] SZYTUŁA A., J. Alloys Comp., 178 (1992), 1.
[4] GIGNOUX D., SCHMITT D., Phys. Rev. B, 48 (1993), 12682.
[5] LECIEJEWICZ J., SZYTUŁA A., ZYGMUNT A., Solid State Commun., 45 (1982), 149.
[6] ŚLASKI M., KURZYK J., SZYTUŁA A., DUNLAP B., SUNGAILA Z., UMEZAWA A., J. Physique, 49 (1988), C8-427.
[7] ANDRÉ G., BOURÉE -VIGNERON F., OLEŚ A., SZYTUŁA A., J. Magn. Magn. Mater., 86 (1990), 387.
[8] AVILA M.A., BUD'KO S.L., CANFIELD P.C., J. Magn. Magn. Mater., 270 (2004), 51.
[9] BLAISE A., FÅK B., SANCHEZ J.P., AMORETTI G., SANTINI P., CACIUFFO R., SCHMITT D., MALAMAN B., VENTIRINI G., J. Phys.: Cond. Matter, 7 (1995), 8317.
[10] SZYTUŁA A., OLEŚ A., PERRIN M., J. Magn. Magn. Mater., 86 (1990), 377.
[11] WAWRZYŃSKA E., BAŁANDA M., BARAN S., LECIEJEWICZ J., PENC B., STÜSSER N., SZYTUŁA A., J. Phys.: Cond. Matter., 17 (2005), 1037.
[12] CHEVALIER B., ETOURNEAU J., HAGENMULLER P., QUEZEL S., ROSSAT-MIGNOD J., J. Less-Common Met., 111 (1985), 161.
[13] FELNER I., NOWIK I., J. Phys. Chem. Solids, 46 (1985), 691.
[14] SZYTUŁA A., OLEŚ A., PERRIN M., ŚLASKI M., KWOK W., SUNGAILA Z., DUNLAP B.D., J. Magn. Magn. Mater., 69 (1987), 305.
[15] SOUSA J.B., AMADO M.A., PINTO R.P., SALGUEIRO SILVA M., BRAGG M.E., CHEVALIER B., ETOURNEAU J., J. Magn. Magn. Mater., 111 (1992), 239.
[16] IVANOV V., VINOKUROVA L., SZYTUŁA A., J. Magn. Magn. Mater., 110 (1992), L250.

[17] BLANCO J.A., GIGNOUX D., SCHMITT D., Z. Phys. B Cond. Mater., 89 (1992), 343.
[18] SHIGEOKA T., IWATA N., HASHIMOTO Y., ANDOH Y., FUJII H., Physica B, 156–157 (1989), 74.
[19] GIGNOUX D., SCHMITT D., J. Alloys Comp., 326 (2001), 143.
[20] BUD'KO S.L., ISLAM Z., WIENER T.A., FISHER I.R., LACERDA A.H., CANFIELD P.C., J. Magn. Magn. Mater., 205 (1999), 53.
[21] SAMPATHKUMARAN E.V., DAS I., VIJAYARANGHAVAN R., YAMAMOTO H., ISHIDA M., Solid State Commun., 83 (1992), 609.
[22] MULDERS A.M., YAOUANC A., DALMAS DE RÉOTIER P., GUBBENS P.C.M., MOOLENAAR A.A., FÅK B., RESSOUCHE E., PROKEŠ K., MENOVSKY A.A., BUSCHOW K.H.J., Phys. Rev. B, 56 (1997), 8752.
[23] VEJPRAVOVA J., SVOBODA P., SECHOVSKY V., JANEČEK M., KOMATSUBARA T., Physica B, 328 (2003), 173.
[24] GARNIER, A., Thesis, Université J. Fourier, Grenoble, 1988.
[25] BOUVIER M., GIGNOUX D., SCHMITT D., Physica B, 43 (1991), 13137.
[26] BLANCO J.A., GIGNOUX D., SCHMITT D., Phys. Rev. B, 43 (1991), 13145.

Received 7 May 2006
Revised 1 September 2006

Materials Science-Poland, Vol. 25, No. 2, 2007

Electronic properties of $CeNi_4Si$ compound

M. FALKOWSKI[1*], A. KOWALCZYK[1], T. TOLIŃSKI[1], G. CHEŁKOWSKA[2]

[1]Institute of Molecular Physics, Polish Academy of Sciences,
Smoluchowskiego 17, 60-179 Poznań, Poland

[2]Institute of Physics, Silesian University, Uniwersytecka 4, 40-007 Katowice, Poland

Temperature dependence of the specific heat for $CeNi_4Si$ was analyzed. These studies were supported by magnetic susceptibility, electrical resistivity and X-ray photoemission spectroscopy measurements. $CeNi_4Si$ is paramagnetic and follows the Curie–Weiss law with $\mu_{eff} = 0.52\ \mu_B$/f.u. and $\theta_P = -2$ K. This effective paramagnetic moment is lower than that for the free Ce^{3+}. The f-occupancy n_f and coupling Δ between the f level and the conduction state are derived to be about 0.91 and 36 meV, respectively. Both the susceptibility data and the XPS spectra have shown that Ce ions are in intermediate valence state. The specific heat has been analyzed considering the electronic contribution, the Schottky anomaly, and the lattice contributions within the Debye model. The scheme of the energy levels created by the crystal electric field split is determined from the Schottky contribution to the specific heat.

Key words: *XPS; specific heat of solids; mixed valence*

1. Introduction

The cerium based ternary compounds demonstrate various phenomena depending on the valence of the Ce ion. It is believed that the hybridization between the conduction electrons and 4f Ce electrons should be responsible for the valence state of Ce. A strong hybridization will decrease the localization of the 4f Ce electrons and result in a non-magnetic intermediate valence state. On the other hand, under a weak hybridization, the Ce 4f electrons become more localized, the localization resulting in a deeper position of the 4f levels.

In this paper, investigations of the specific heat of $CeNi_4Si$ are presented and supported by the magnetic susceptibility and X-ray photoemission spectroscopy (XPS).

* Corresponding author, e-mail: falkowski@ifmpan.poznan.pl

2. Experimental

The sample preparation was described in details in Refs. [1, 2]. The room temperature powder X-ray diffraction pattern revealed $CeNi_4Si$ to be a single phase [1]. Heat capacity measurements were performed by PPMS commercial device (Quantum Design) in the temperature range 2–300 K by relaxation method using the 2τ model.

3. Results and discussion

Our previous studies on $CeNi_4Si$ have revealed its paramagnetic properties with $\theta = -2$ K and $\mu_{eff} = 0.52\ \mu_B$/f.u [1]. However, the derived magnetic effective moment is much lower in comparison with free Ce^{3+} ions value equal to 2.54 μ_B. Since magnetic moment of tetravalent cerium is zero, the observed reduction of magnetic moment can be explained in a natural way by a fractional occupation of $4f^0$ (Ce^{4+}) and $4f^1$ (Ce^{3+}) configurations.

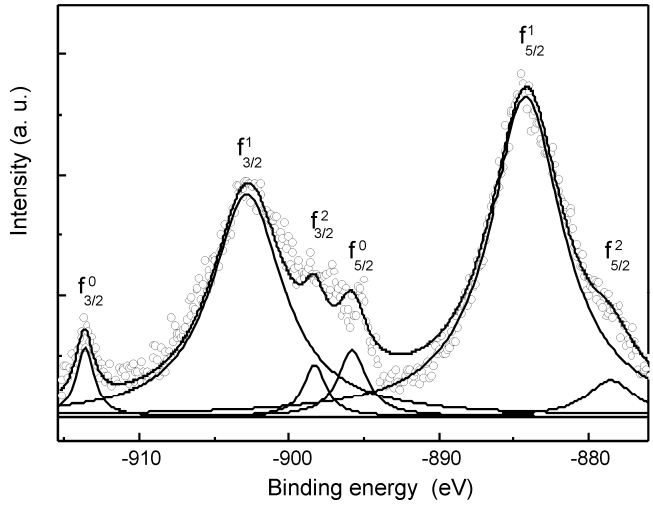

Fig. 1. Experimental XPS spectrum of the Ce($3d_{5/2,3/2}$) doublet for $CeNi_4Si$. A decomposition into main peaks and satellites is also displayed. The notation f^n corresponds to various XPS final states $3d^94f^n$

Figure 1 shows the Ce 3d core-level photoemission spectrum of $CeNi_4Si$. The spectrum exhibits two strong peaks at the binding energies –884.5 and –903.1 eV. These peaks are assigned to $3d_{5/2}$ and $3d_{3/2}$ spin-orbit components of the $3d^94f^1$ final states. It should be mentioned that numerous Ce-based intermetallics show three final states, f^0, f^1 and f^2. Since the ground state of Ce^{3+} ions has electronic configuration $4f^1$, the presence of both $4f^1$ and $4f^0$ states can indicate an intermediate valence character of the Ce ions. The analysis of the Ce (3d) peaks in the framework of the Gunnarsson

–Schönhammer model [3] provides information on the localization degree. The f occupancy n_f and coupling Δ between the f level and the conduction states are derived to be about 0.91 and 36 meV, respectively [1]. Hence, both the susceptibility and XPS spectra show that Ce ions in $CeNi_4Si$ are in an intermediate valence state.

Electrical resistivity of this compound is metallic [1]. Below 15 K, a shallow minimum in $\rho(T)$ is observed, typical of Kondo impurity systems. The increased ρ_0 (≈300 μΩ·cm) is mainly due to a random distribution of Ni(2) and Si on the 3g site. The total specific heat consists of electronic, phonon and magnetic contributions. The magnetic part includes both the contribution originating from the CEF excitations and the contributions due to the magnetic ordering.

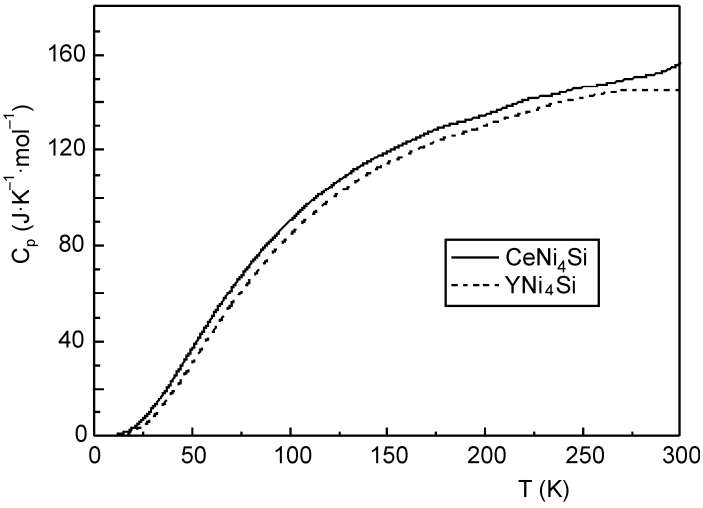

Fig. 2. Temperature dependence of the specific heat of $CeNi_4Si$ and YNi_4Si

Figure 2 shows the temperature dependence of the of the specific heat for YNi_4Si and $CeNi_4Si$ compounds. YNi_4Si is nonmagnetic; therefore, $C_p(T)$ can be described by the standard formula:

$$C_p(T) = \gamma T + 9NR\left(\frac{T}{\Theta_D}\right)^3 \int_0^{\Theta_D/T} \frac{x^4 e^x dx}{\left(e^x - 1\right)^2} \tag{1}$$

where the first and second term correspond to the electronic and the phonon contribution, respectively. $N = 6$ is the number of atoms in the formula unit and $x = h\omega/k_BT$. From the fit to the experimental points (Fig. 2) we get the Debye temperature $\theta_D = 365$ K and the electronic specific heat coefficient $\gamma = 13$ mJ·mol^{-1}·K^{-2}. A similar analysis has been carried out for $CeNi_4Si$ yielding $\theta_D = 335$ K, $\gamma = 16$ mJ·mol^{-1}·K^{-2}.

To analyze the magnetic part of the specific heat of $CeNi_4Si$ we used the specific heat of the nonmagnetic isostructural analogue to get detailed information about the

electronic and phonon contributions. Figure 3 presents C_P/T vs. T for $CeNi_4Si$ after subtracting the specific heat of the YNi_4Si. The formula for the Schottky contribution is as follows [4, 5]:

$$C_{\mathrm{Sch}}(T) = \frac{R}{T^2}\left[\frac{\sum_{i=0}^{n-1}\Delta_i^2 \mathrm{e}^{-\Delta_i/T}}{\sum_{i=0}^{n-1}\mathrm{e}^{-\Delta_i/T}} - \left(\frac{\sum_{i=0}^{n-1}\Delta_i \mathrm{e}^{-\Delta_i/T}}{\sum_{i=0}^{n-1}\mathrm{e}^{-\Delta_i/T}}\right)^2\right] \tag{2}$$

where n denotes the number of the energy levels and $\Delta_0 = 0$. For Ce^{3+} ions, the 4f levels split into three doublets ($n = 3$).

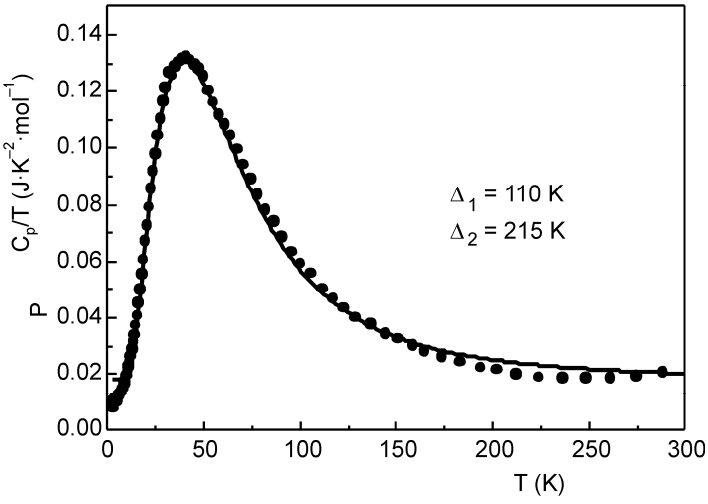

Fig. 3. Magnetic contribution to the specific heat obtained by subtracting the phonon and electronic contributions

The fit presented in Fig. 3 provides an estimate of the energy gaps: $\Delta_1 = 110$ K and $\Delta_2 = 215$ K.

The magnetic entropy

$$S_M = \int_0^T \frac{C_M(T)}{T}\, dT \tag{3}$$

is related to the degrees of freedom using the expression $S_{\mathrm{mag}} = R\ln(2J+1)$. For the Ce ion, the total angular momentum J is equal to 5/2 and consequently the expected value is $(2J + 1) = 6$. The entropy reaches the 100% value of $R\ln 2$ at $T = 62$ K. At room temperature, the entropy reaches 90% of $R\ln 6$.

The low temperature properties of many Ce- and Yb-based intermetallic compounds are well described within the Fermi liquid state. The specific heat C and the electrical resistivity ρ vary as a function of temperature as $C \propto \gamma T$ and $\rho \propto AT^2$. The coefficient γ and A are related to the electron effective mass m^* as $\gamma \propto m^*$ and $A \propto (m^*)^2$. Therefore, the ratio A/γ^2 does not depend on m^*. In fact, Kadowaki and Woods [6] showed that many Ce-based compounds (Fig. 4) show a universal relation $A/\gamma^2 = 1.0\times10^{-5}$ μΩ·cm·mol^2·K^2·mJ^{-2}. The value of the coefficient $A = 4\times10^{-3}$ μΩ·cm·K^{-2} has been obtained for $CeNi_4Si$ by fitting the resistivity data at low temperatures. The resulting A/γ^2 ratio for this compound is 1.5×10^{-5} μΩ·cm·mol^2·K^2·mJ^{-2}.

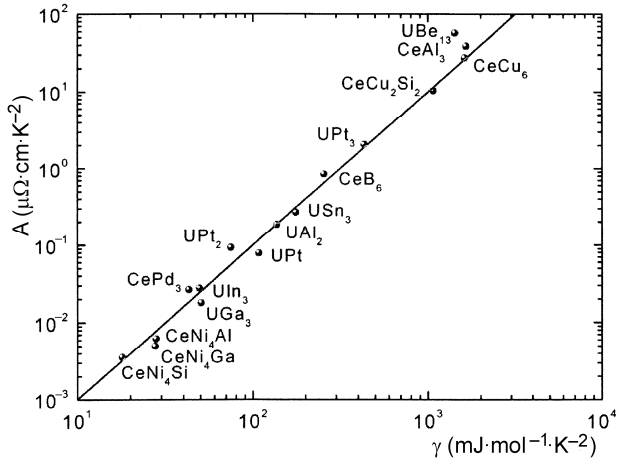

Fig. 4. Plot of the T^2 coefficient of the electrical resistivity, A vs. the T-linear specific heat coefficient γ. The results for $CeNi_4Si$, $CeNi_4Al$ and $CeNi_4Ga$ are added to the original plot of Kadowaki–Woods [6]

For a comparison, we show in Fig. 4 the values of the Kadowaki-Woods ratio, which we obtained for $CeNi_4Al$ ($A = 5\times10^{-3}$ μΩ·cm·K^{-2}, $\gamma = 29$ mJ·mol^{-1}·K^{-2}, and $A/\gamma^2 = 0.6\times10^{-5}$ μΩ·cm·mol^2·K^2·mJ^{-2}) and $CeNi_4Ga$ ($A = 4\times10^{-3}$ μΩ·cm·K^{-2}, $\gamma = 28.7$ mJ·mol^{-1}·K^{-2}, and $A/\gamma^2 = 0.5\times10^{-5}$ μΩ·cm·mol^2·K^2·mJ^{-2}). For the latter compound, the value of γ obtained from the ab initio TB LMTO calculations has been used [7]. It is visible from Fig. 4 that the values of A and γ do not classify the studied Ce-based compounds to the group of heavy fermions which occupy the upper part of the figure. Instead, they are located in the neighbourhood of the compounds known to show mixed valence behaviour (lower part of the figure).

4. Conclusions

$CeNi_4Si$ is paramagnetic and follows the Curie–Weiss law with $\mu_{eff} = 0.52$ μ_B/f.u. and $\theta_P = -2$ K. This effective paramagnetic moment is lower than that for free Ce^{3+}. The f-occupancy n_f and coupling Δ between the f level and the conduction states are

derived to be about 0.91 and 36 meV, respectively. Both the susceptibility data and the XPS spectra have shown that Ce ions are in intermediate valence state. The analysis of the Schottky peak appearing in the magnetic part of the specific heat has provided the scheme of the energy levels being a result of the splitting by the crystal electric field. For Ce, three Kramers doublets with $\Delta_0 = 0$, $\Delta_1 = 110$ K and $\Delta_2 = 215$ K have been obtained. The paramagnetic $CeNi_4Si$ was characterized by the $\gamma = 16$ $mJ \cdot mol^{-1}K^{-2}$ and $\theta_D = 335$ K.

References

[1] KOWALCZYK A., FALKOWSKI M., TOLIŃSKI T., CHEŁKOWSKA G., Solid State Commun., Solid State Commun., 139 (2006), 5.
[2] KOWALCZYK A., SZAJEK A., FALKOWSKI M., CHEŁKOWSKA G., J. Magn. Magn. Mat., 305 (2006), 348.
[3] GUNNARSSON O., SCHÖNHAMMER K., Phys. Rev., B 28 (1983), 4315.
[4] SVOBODA P., VEJPRAVOVA J., KIM-NGAN N-T.H., KAYSEL F., J. Magn. Magn., 272 (2004), 595.
[5] TOLIŃSKI T., KOWALCZYK A., SZEWCZYK A., GUTOWSKA M., J. Phys. Cond. Matter., 18 (2006), 3435.
[6] KADOWAKI K., WOODS S.B., Solid State Commun., 58 (1986), 507.
[7] KOWALCZYK A., PUGACZOWA-MICHALSKA M., TOLIŃSKI T., phys. stat. sol. (b), 242 (2005), 433.

Received 7 May 2006
Revised 1 September 2006

Materials Science-Poland, Vol. 25, No. 2, 2007

Magnetism and electronic transport properties of Ce_5CuPb_3

V. H. TRAN[1*], J. JARMULSKA[2], W. MIILLER[1]

[1]W. Trzebiatowski Institute of Low Temperature and Structure Research, Polish Academy of Sciences, P. O. Box 1410, 50-950 Wrocław 2, Poland

[2]Graduate Student of Wrocław University of Technology, Wrocław, Poland

Polycrystalline sample of the ternary Ce-based compound Ce_5CuPb_3 was prepared and characterized using room temperature powder X-ray, EDX analysis as well as by magnetic susceptibility, electrical resistivity, and thermoelectric power measurements. The compound crystallizes in the Ti_5Ga_4-type structure (space group $P6_3/mcm$) with two different cerium sites: one at the 4d and the other at 6g position. The susceptibility shows two successive magnetic phase transitions at $T_{C1} = 46.0 \pm 0.5$ K and $T_{C2} = 5.0 \pm 0.5$ K. The double magnetic phase transition may be explained by two inequivalent magnetic sublattices of Ce^{3+} ions. The analysis of the magnetic data suggests that the transition at T_{C1} is of ferromagnetic origin and at T_{C2} is of ferrimagnetic one. Both the magnetic susceptibility, and electrical resistivity data imply the localized character of the Ce 4f electron. Above 150 K the $\chi(T)$ data follow the Curie–Weiss law with the effective moment $\mu_{eff} = 2.69$ μ_B/Ce and the paramagnetic Curie temperature θ_p equal to –21.8 K. The electrical resistivity exhibits a clear anomaly at T_{C1}, below which the resistivity sharply decreases due to the reduction in the spin–disorder scattering. The thermoelectric power (TEP, S) of Ce_5CuPb_3 is negative over the temperature range studied, reaching the value of –14 μV/K at room temperature, and weakly varying with decreasing temperature down to T_{C1}. A rapid change in TEP occurs below 25 K with the slope S/T as large as –0.27 μV/K^2.

Key words: successive magnetic phase transitions; magnetic properties; electron transport properties; Ce_5CuPb_3

1. Introduction

Ternary rare earth (R) plumbites R_5CuPb_3 were reported to crystallize in a hexagonal Ti_5Ga_4-type structure (space group $P6_3/mcm$) [1]. These intermetallics, with the chemical 5:1:3 stoichiometry, are characterized by two different sites for the R ions located at 4d and 6g, respectively. Amongst these compounds, only Dy_5CuPb_3 has been studied so far with respect to its magnetic and electron transport properties [2]. It has been argued that in this alloy there are complex magnetic phase transitions, ferromagnetic below 45 K and ferrimagnetic below 6.5 K. The magnetism is believed

* Corresponding author, V.H.Tran@int.pan.wroc.pl

to result from the localized Dy^{3+} ions. In this contribution, we report on the results of experimental investigation of an other member of the R_5CuPb_3 family, namely Ce_5CuPb_3. From magnetic and electron transport measurements, we show that the behaviour of Ce_5CuPb_3 is similar to that of Dy_5CuPb_3, e.g., Ce ions behave as localized ones. Therefore, the character of the Ce 4f electrons in Ce_5CuPb_3 seems to be different from that in other previously studied 513 Ce-based compounds, Ce_5CuSn_3 [3], Ce_5CuSb_3 [4] and Ce_5CuBi_3 [5]. These latter compounds exhibit heavy fermion behaviour, reflected by a large Sommerfeld ratio C_p/T at low temperatures. We also argue that the magnetic properties of the Ce_5CuM_3 (M = Sn, Bi and Pb) series of compounds depend both on the Ce–Ce exchange interaction and strength of the hybridization between the 4f and conduction electrons.

2. Experimental details

Several specimens of Ce_5CuPb_3 were prepared by arc-melting of stoichiometric amounts of high-purity elements (Ce 99.9 wt. %, Cu 99.999 wt. % and Pb 99.999 wt. %) in a Ti-gettered pure argon atmosphere. The specimens were remelted several times to ensure homogeneity. After annealing at 800 °C for one week, the specimens were examined by X-ray powder diffraction at room temperature. The observed Bragg peaks can be indexed to the hexagonal structure with the space group $P6_3/mcm$. The refined lattice parameters are: a = 9.551(2) Å and c = 6.776(2) Å being comparable to those previously reported [1]. The composition of the obtained samples was established using an energy dispersive X-ray analysis. It turns out that in addition to the major 513 phase, there exists a small quantity of free Pb. The data reported in this work were done on the sample containing the Pb contamination lower than 2%.

Dc magnetization measurements were carried out with a Quantum Design SQUID magnetometer in fields up to 5.5 T and in the temperature range 2–400 K. The electrical resistivity was measured by the standard dc four-probe technique in the temperature range 2–300 K. The sample was rectangular with typical dimensions 0.5×0.5×5 mm^3. The voltage and current leads were attached with a silver paste. Thermoelectric power was measured using a differential method in the temperature range 4–220 K. The temperature gradient of about 2 K was applied across the sample length, using an Au–Fe (7%) chromel thermocouple. The relative resolution of the experimental setup reached 10 nV and the absolute accuracy of the presented data was as low as 5% over the studied temperature range.

3. Experimental results and discussion

The temperature dependence of the magnetic susceptibility of Ce_5CuPb_3 measured at the field of 0.5 T and in the temperature range 150–400 K (not shown here) can be described by the Curie-Weiss law:

$$\chi(T) = \chi(T) = \frac{N\mu_{\text{eff}}^2}{3k_B\left(T - \Theta_p\right)}$$

with an effective moment μ_{eff} = 2.69 μ_B/Ce and a paramagnetic Curie temperature θ_p equal to –21.8 K. The experimental value of μ_{eff} is close to the Russell–Saunders value for a free Ce^{3+} ion (2.54 μ_B), designating the localized character of the Ce 4f-electron. A negative value of θ_p may indicate the existence of antiferromagnetic exchange interaction in the studied compound. At low temperatures, the $\chi(T)$ curve shows a step-like increase (Fig. 1a), giving clear evidence of the occurrence of magnetic phase transitions. In Figure 1 b, we display the temperature derivative of the susceptibility, where we observe two anomalies at T_{C1} = 46.0 ± 0.5 K and T_{C2} = 5.0 ± 0.5 K (indicated by arrows). Tentatively, we attribute these anomalies to ferromagnetic-like transitions. In the same manner as in the case of Dy_5CuPb_3 [2], the double magnetic phase transition may be explained by existence of two inequivalent magnetic sublattices of the magnetic ions.

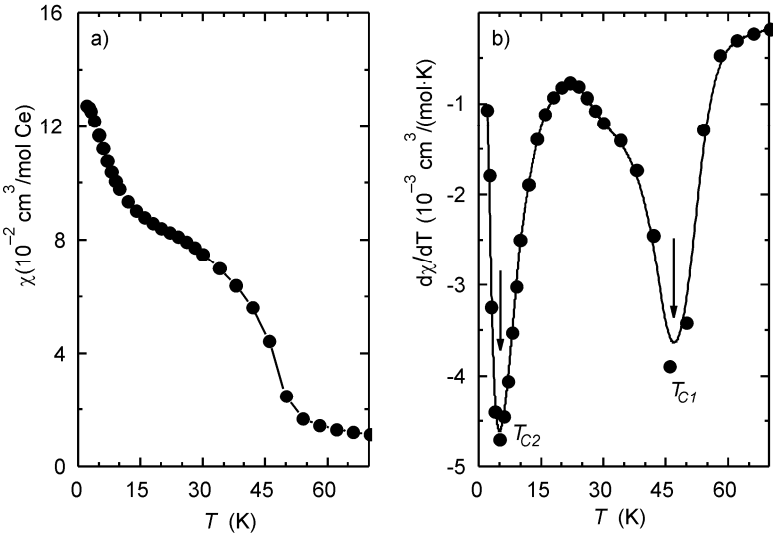

Fig. 1. Temperature dependence of the magnetic susceptibility of Ce_5CuPb_3 (a), and the derivative $d\chi/dT$ as a function of temperature (b). The arrows indicate the magnetic phase transitions

In the upper panel of Fig. 2 we show the magnetization data collected at temperatures 2 K and 5 K, i.e., below T_{C2}. For a clarity of the presentation, the data are vertically shifted. One can see that the initial magnetization is linear and is fitted with the solid line. The linear dependence M vs. H is observed up to 0.5 T for T = 2 K and 0.15 T or T = 5 K. Moreover, these low-temperature data distinguish themselves by a hysteresis, which appears below 1 T. These features imply a ferri- or antiferromagnetic character of the transition at T_{C2}.

The lower panel of Fig. 2 presents magnetization data taken between 10 K and 75 K. As can be seen, the data collected between T_{C2} and T_{C1} (at 10, 25 and 40 K) show spontaneous magnetization. Such a behaviour is consistent with the magnetic phase transition of the ferromagnetic origin at T_{C1}. However, it is noted that the magnetization does not saturate even at the highest applied magnetic field strength of 5 T. This observation hints that only a part of the Ce ions undergo a transition into the ferromagnetic state.

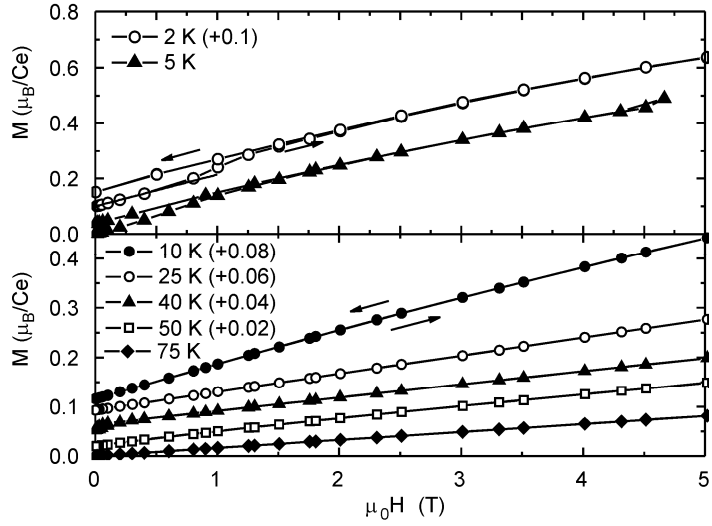

Fig. 2. Magnetization of Ce_5CuPb_3 measured below 75 K. For clarity of presentation, the data collected at 2, 10, 25, 40 and 50 K are shifted upwards by values given in the figure. The arrows indicate increasing or decreasing magnetic field strength

The temperature dependence of the electrical resistivity of Ce_5CuPb_3 shown in Fig. 3a displays a sharp decrease around T_{C1}. Such a decrease is usually attributed to the reduction of spin-disorder scattering. However, it is hard to detect the anomaly associated with the transition at T_{C2}, since the resistivity measurements performed on several synthesized samples of Ce_5CuPb_3 have shown systematic presence of a severe drop in the resistivity at 6.5 K, due to the superconductivity of free lead in the samples. Further investigations, notably the measurements of the specific heat and Hall effect, should provide additional information on the anomalous resistivity behaviour of Ce_5CuPb_3. It should be added that the superconductivity appearing in our samples can be eliminated by measurements in a magnetic field of about 0.05 T. Because of micro-cracks and the oxidation problem, the geometric dimension cannot be exactly determined, thus the absolute values of the measured resistivity should be taken with great caution.

The thermoelectric power of Ce_5CuPb_3 (Fig. 3 b) is negative in the whole temperature range under investigation. As can be seen, the thermopower displays a minimum around T_{C1} followed by a linear temperature dependence, representing the diffusion

thermopower. It is interesting to note that the slope S/T in the temperature range 6–22 K reaches the value as large as –0.27 μV/K^2. From the close relationship between the ratio S/T and C_p/T observed for a number of intermetallics [10], one may expect an enhancement in the electronic specific heat of Ce_5CuPb_3. However, an alternative interpretation may be provided, related to a change in the electronic structure due to a magnetic phase transition below T_{C1}.

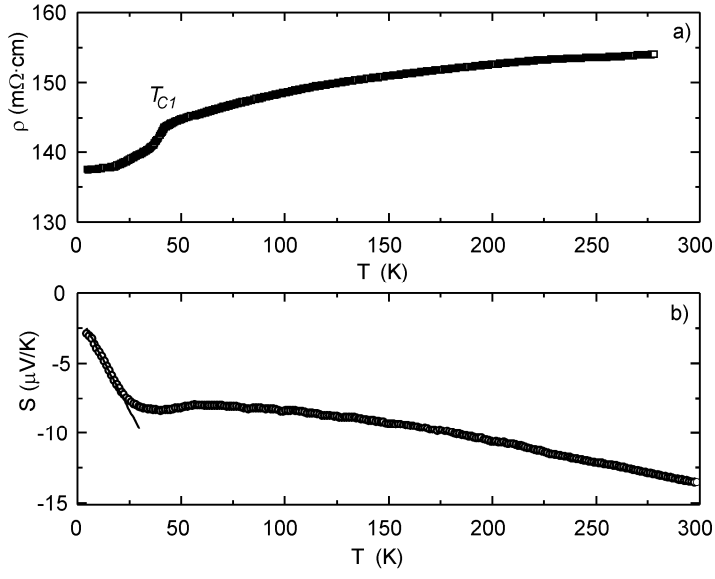

Fig. 3. Temperature dependence of the electrical resistivity (a), and thermoelectric power (b) of Ce_5CuPb_3 as a function of temperature. The solid line (below 25 K) illustrates a high slope S/T

4. Concluding remarks

We measured magnetization, electrical resistivity and thermoelectric power of polycrystalline samples of the Ce-based intermetallic compound Ce_5CuPb_3. The experimental data indicate two successive magnetic phase transitions at T_{C1} = 46.0 ± 0.5 K and T_{C2} = 5.0 ± 0.5 K, caused by Ce–Ce exchange interactions in two different Ce sites. Combined with the previously reported data [3–5], the present results point to a clear influence of the ligands on the magnetic properties of investigated compounds. The fact that the compounds with M = Sn and Bi are found to order at lower temperatures and with a lower effective moment compared to those of Ce_5CuPb_3, may indicate a more localized character of the Ce 4f electrons in the latter compound. This behaviour can be anticipated from the change in the unit cell volume, systematically increasing across the series with M = Sn, Bi and Pb. The increase of the distance between the magnetic central and nonmagnetic ligand ions certainly weakens the hybridization

between 4f and conduction electrons, and in consequence strengthens the localized electron magnetism.

Acknowledgements

This work was supported by theMinistry of Science and Higher Education in Poland, Grant No. N202 082 31/0449.

References

[1] GULAY L.D., STĘPIEŃ -DAMM J., WOŁCYRZ M., J. Alloys Comp., 319 (2001), 148.
[2] TRAN V.H., GULAY L.D., J. Solid State Chem., 179 (2006), 646.
[3] TRAN V.H., J. Alloys Comp., 383 (2004), 281; Czech. J. Phys. 54 (2004), D411.
[4] TRAN V.H., Phys. Rev. B, 70 (2004), 094424.
[5] TRAN V.H., GAMŻA M., ŚLEBARSKI A., JARMULSKA J., Doi: 10.1016/j.jallcom.20.07.04.227.
[6] KONDO J., Prog. Theor. Phys., 32 (1964), 37.
[7] MOTT N.F., Adv. Phys., 16 (1967), 49.
[8] ANDERSON P.W., Phys. Rev., 124 (1961), 41.
[9] LEE P.A., RAMAKRISHNAN T.V., Rev. Mod. Phys., 57 (1985), 276.
[10] BEHANIA K., JACCARD D., FLOUQUET J., J. Phys.: Cond. Matter, 16 (2004), 5187.

Received 7 May 2006
Revised 1 September 2006

Materials Science-Poland, Vol. 25, No. 2, 2007

About negative magnetization in non-superconducting intermetallics

W. SUSKI*

W. Trzebiatowski Institute of Low Temperature and Structure Research,
Polish Academy of Sciences, P.O. Box 1410, 50-950 Wrocław 2, Poland
International Laboratory of High Magnetic Fields and Low Temperatures,
P.O. Box 4714, 50-985 Wrocław 47, Poland

The negative magnetization for ternary and pseudoternary compounds with the tetragonal $ThMn_{12}$ and rhombohedral Th_2Zn_{17} type structure is presented considering various magnetic ordering types. This phenomenon has been observed in compounds of rare earth and uranium. Comparing pecularities of the temperature dependence of the magnetization/magnetic susceptibility we try to find a common reason for this behaviour. The most attractive seems to be the difference in the anisotropy magnitude and direction of the individual magnetic sublattices as well as the crystallographic imperfections.

Key words: *rare-earth intermetallics; magnetic properties; negative magnetization*

1. Introduction

Recently, a few papers appeared describing the negative magnetization in $YbFe_4Al_8$ [1–3]. However, a similar behaviour has been presented for other compounds with the same $ThMn_{12}$ tetragonal type of structure with an f electron element being heavy rare earth [4] as well as the uranium [5] atoms. Also, one representative of the Th_2Zn_{17} rhombohedral type of structure, $Tb_{2.1}Co_{14.9}Si_3$, has been reported to exhibit a negative magnetization [6]. No convincing explanation of this behaviour has been proposed up to now. In the present paper, we review reported properties of the investigated compounds, establishing similarities and differences between them. We also provide preliminary results of magnetic investigations of imperfect single crystal of $YbFe_4Al_8$.

*E-mail: w.suski@int.pan.wroc.pl

2. Results and discussion

Let us inspect similarities between the discussed compounds. All of them are ternary or, more exactly, pseudoternary alloys. Moreover, it seems that at least in the compounds of the heavy rare earth one deals with two or more magnetic sublattices. Therefore, these compounds could be treated as ferrimagnetic ones. This statement is not so obvious in the case of alloys of U.

The earliest report concerns the alloys of magnetic heavy rare earths [4] and perhaps the authors were not very convinced about the physical reality of their observation because the results have never been published in regular journals. In Figure 1, magnetization versus temperature for $SmFe_5Al_7$ in a low field (30 Oe) is shown [4].

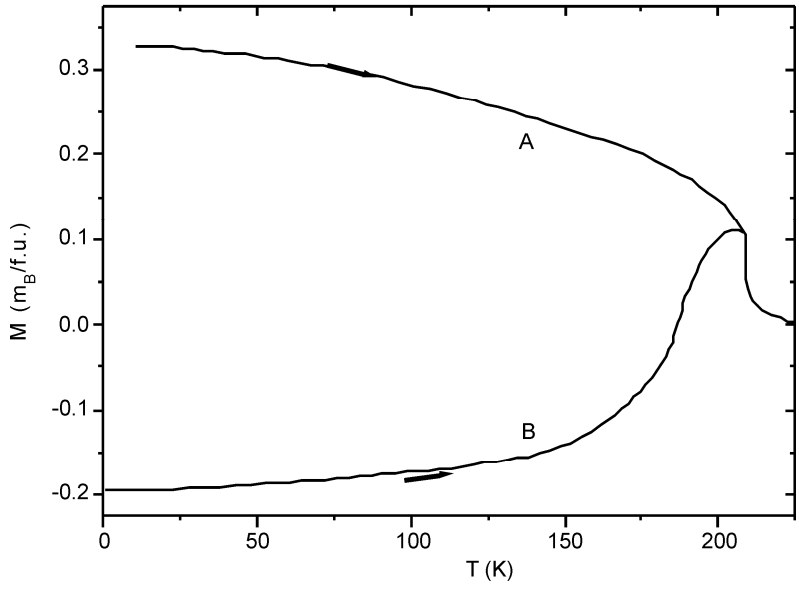

Fig. 1. Magnetization vs. temperature for $SmFe_5Al_7$ [4]

Curve A was obtained on increasing the temperature after slowly cooling the sample, whereas curve B was obtained after cooling the sample to 4.1 K within a few seconds. This pronounced difference between these two curves indicates a strong thermal hysteresis, different anisotropy in various magnetic sublattices and time dependent magnetization. In turn, an unusual behaviour of $TbFe_5Al_7$ and its derivative is presented in Fig. 2. Curve A was obtained when the sample was cooled in zero field, curve B was obtained when the sample was cooled in 100 Oe and then the measurement was carried out upon increasing temperature. Finally, curve C presents the results obtained on decreasing temperature. The quaternary alloy $TbFe_5Al_5Ge_2$ demonstrates different temperature dependence of magnetization with minimum and negative values between ca. 70 K and 120 K. The latter result is particularly peculiar

but at the same time strongly suggests that crystallographic disorder has a substantial influence on magnetic behaviour. Both materials discussed above are ferro /ferrimagnetic without distinct difference in the Curie points of rare earth and iron sublattices.

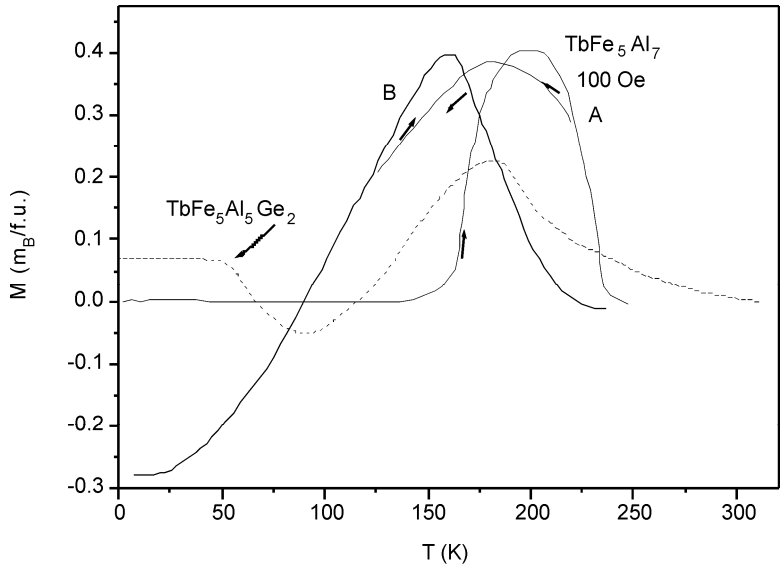

Fig. 2. Magnetization vs. temperature for $TbFe_5Al_7$ and $TbFe_5Al_5Ge_2$ [4]

A qualitatively similar behaviour is exhibited by $YbFe_4Al_8$ (Fig. 3 [1]) examined up to now in two different laboratories (in Wrocław [1] and Poznań [2, 3]) on polycrystalline alloys. As follows from Fig. 3, the zero field cooled (ZFC) sample behaves "normally" with a smooth decrease of the magnetic susceptibility, χ, on increasing temperature without any trace of anomaly at low temperature which could be an indication of the magnetic ordering in the Yb sublattice. Such a transition has been reported by Felner and Nowik [7] at 8 K. Our results demonstrate the maximum on the $\chi(T)$ plot at T ~140 K, corresponding to the Néel point of the Fe antiferromagnetic sublattice, which confirms the earlier results [7]. The $\chi(T)$ dependence for field cooled (FC) sample shows a different character with negative magnetic susceptibility below about 70 K and the maximum at about 140 K. Under slightly higher magnetic field, there is a fine anomaly (minimum) at about 15 K. Also, the anomaly has been detected in the $\chi(T)$ plot measured at 500 Oe and higher magnetic field but it is a maximum related to some paramagnetic impurities (ZFC) [3]. $YbFe_4Al_8$ has a perfect crystallographic structure (superstructure of $ThMn_{12}$ type), however, according to Drulis* a careful examination of the magnetic behaviour for samples with various

*Private communication.

stoichiometry revealed negative susceptibility only for some compositions close to the exact stoichiometry.

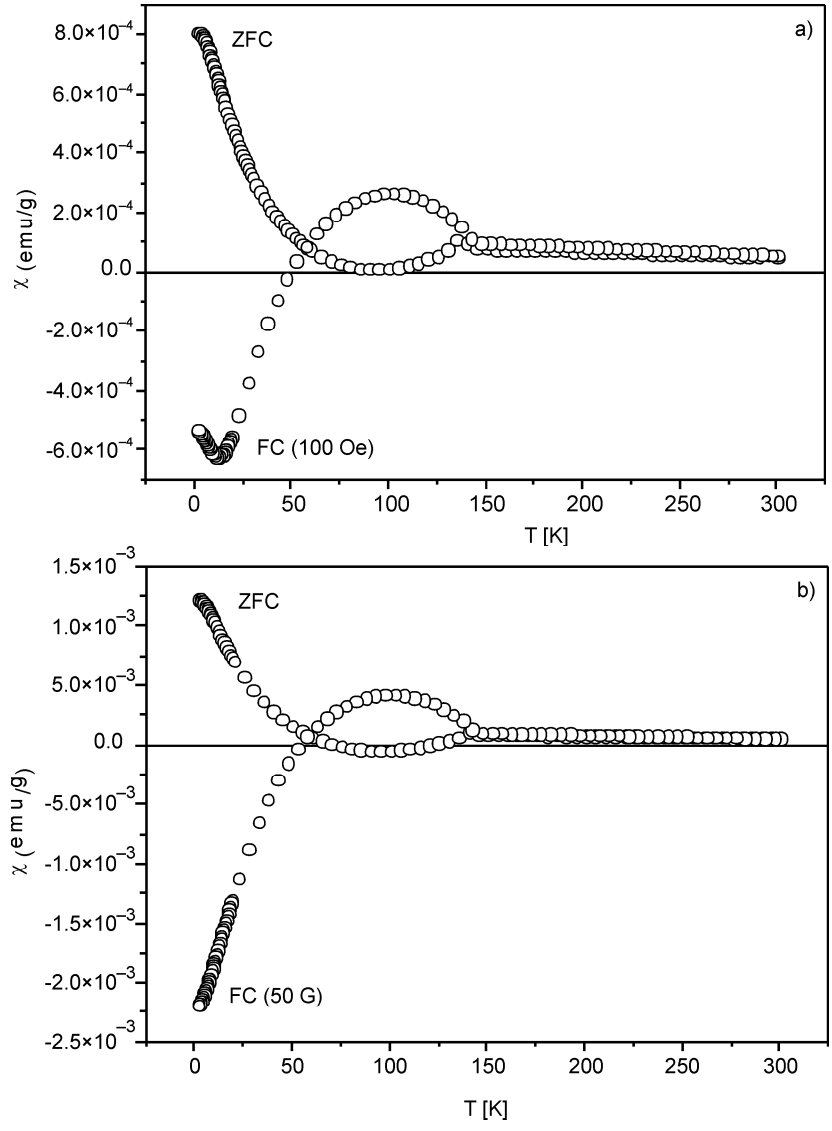

Fig. 3. ZFC and FC magnetic susceptibilities vs. temperature
for polycrystalline $YbFe_4Al_8$ [1] in the magnetic fields of 100 Oe (a) and 50 Oe (b)

In Figure 4, the $\chi(T)$ dependence is shown for an imperfect single crystal sample. One can see that the negative magnetic susceptibility is absent, however, a clear difference between ZFC and FC runs is observed. The maximum in ZFC and anomaly in FC runs are seen at 24 K [8].

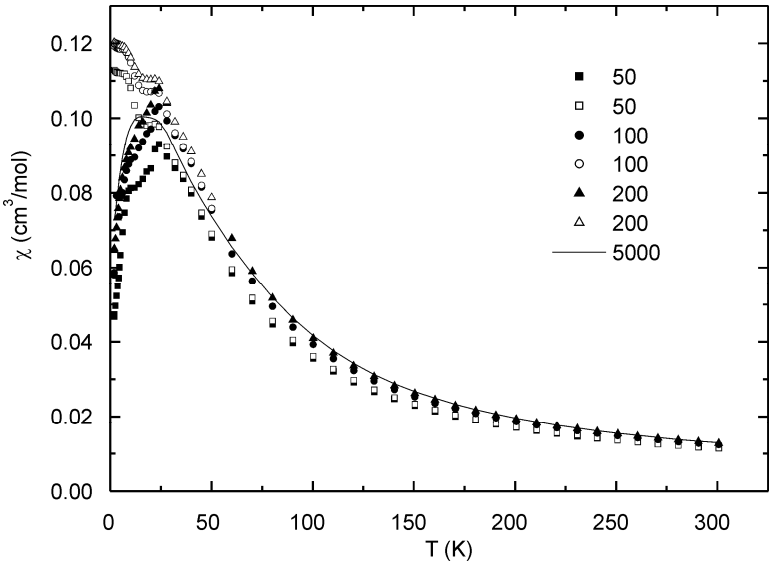

Fig. 4. Magnetic susceptibility vs. temperature for imperfect single crystal $YbFe_4Al_8$ [8]. Full symbols – ZFC, open symbols – FC

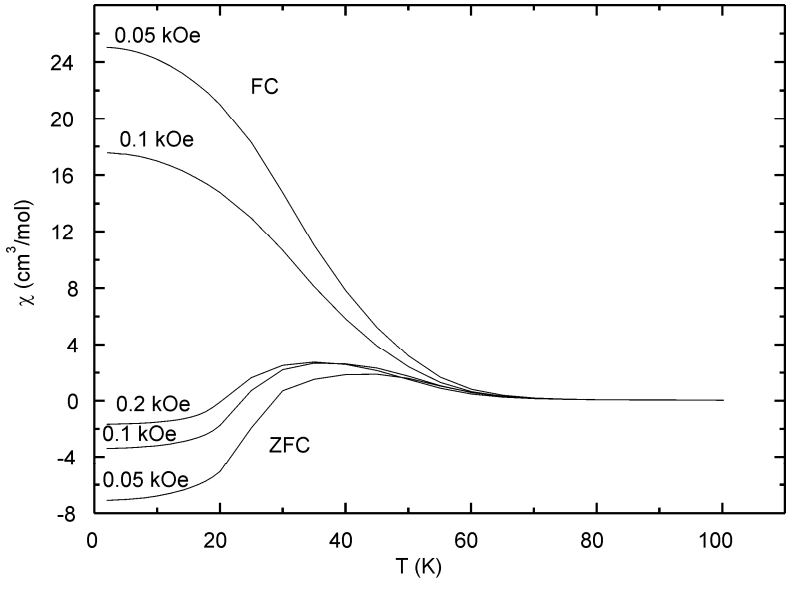

Fig. 5. Magnetic susceptibility vs. temperature for $UCu_{3.5}Fe_{1.5}Al_7$ [5]

Totally different behaviour is observed in the uranium pseudoternary alloy $UCu_{3.5}Fe_{1.5}Al_7$ [5]. This compound is supposed to be ferrimagnetic below 32 K [5], however, the transition was neither confirmed in the temperature dependences of the electrical resistivity [5] nor of the specific heat [9]. The temperature dependence of the magnetic susceptibility presented in Fig. 5 for the FC sample corresponds to

a "normal" ferri- or ferromagnet but for the ZFC sample, the magnetic susceptibility is negative below about 20 K, its absolute value decreasing with an increase of magnetic field. Although an approximate evaluation of the effective magnetic moment suggests that both U and Fe atoms carry magnetic moment, it does not mean that the magnetic ordering is established in both sublattices. The absence of two anomalies in the $\chi(T)$ dependence is not a serious argument for the absence of two magnetic sublattices because the spatial extent of the 5f shell can prevent creation of two separate magnetic transitions.

The next example of the negative magnetization is rhombohedral $Tb_{2.1}Co_{14.9}Si_3$ [6] which is ferro(ferri)magnetic below 623 K. At low temperatures, the temperature dependence of magnetization, $M(T)$, measured in magnetic field of 50 Oe (Fig. 6), exhibits the thermal hysteresis for all ternaries $Tb_{2.1}(Co,Si)_{17}$ but additionally a negative magnetization is seen below ~170 K in ZFC run and below ~90 K in FC run for $Tb_{2.1}Co_{14.9}Si_3$ alloy. However, in the latter case, the M(1.9K) value is apparently lower than the former one. It is worthwhile to note that such a behaviour was not observed in analogous Fe compounds [10–12]. Also the compounds of light rare earths and Co do not show negative magnetization [13]. Moreover, this behaviour seems to be connected with deeper crystallographic disorder growing with the increase of substitution of Si for Co. The contribution of the magnetically active atoms to magnetic ordering is not determined on the basis of the present preliminary investigations. The $M(T)$ plots exhibit an increase at low temperature upon heating but this can be related to the domain structure or a spin-glass state.

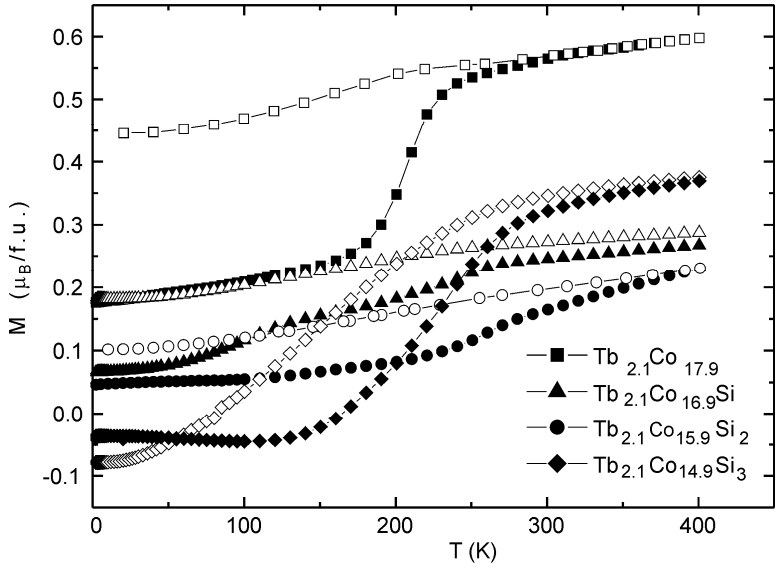

Fig. 6. Magnetization vs. temperature for $Tb_{2.1}Co_{14}Si_3$ [6].
Full symbols – ZFC, open symbols – FC

All above discussed materials crystallize in quite complicated crystal structures. Figure 7 shows the $ThMn_{12}$ type tetragonal structure (space group *I*/4*mmm*). Only exceptionally binary compounds exhibit this type of structure and as a rule ternaries are stabilized by alloying with other p or d electron elements. Forming of the ternaries is easy because there are 4 crystallographic sites available. In principle, for the RT_4Al_8 composition (superstructure) the 2(a) sites are occupied by the R (rare earth or actinide metal) atoms, the transition metal (Fe) is predominantly located in the 8(f) position and the Al atoms reside in the 8(i) and 8(j) sites. It is the picture which is assumed for the Yb compound, however for the compounds with the stoichiometry other than 4:8, 8(f) and 8(i) positions are occupied by the transition and Al atoms, respectively, while the remaining transition elements and Al atoms are distributed at random in 8(j) sites.

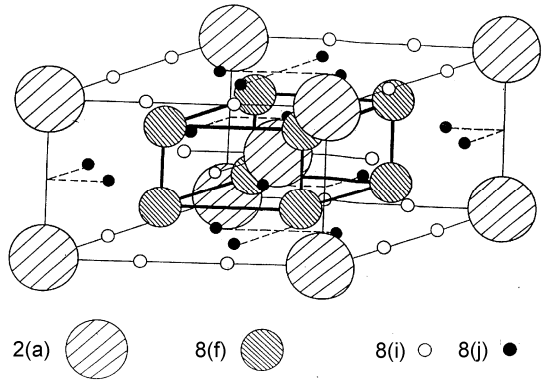

Fig. 7. The $ThMn_{12}$ type structure

The rhombohedral Th_2Zn_{17} type structure presented in Fig. 8 is even more complicated with a variety of available crystallographic positions. Different separation of the individual positions is a reason for the possibility of different types of magnetic interactions. At this point, it is worth mentioning that the type of magnetocrystalline anisotropy for the iron magnetic sublattice is axial whereas for the cobalt sublattice it is planar in the frequent cases. Therefore, such complicated crystal structures can be a reason for forming more than one magnetic sublattices which can be distinguished by different types and directions of magnetocrystalline anisotropy and by their various temperature dependences. The competition of these factors can create negative magnetization or magnetic susceptibility under favourable conditions.

Recently, negative magnetization for ZFC sample of UPdSb (hexagonal, $CaIn_2$ type, space group $P6_3/mmc$), ferromagnetic below 77 K has been reported [14]. In this case there is only one magnetic sublattice and therefore the reasoning presented above about the negative magnetization is not valid.

Summarizing, we can claim that the negative magnetization is observed in at least three groups of compounds. The first one is of ferrimagnetic ground state ($SmFe_5Al_7$, $TbFe_5Al_7$, $UCu_{3.5}Fe_{1.5}Al_7$ and $Tb_{2.1}(Co,Si)_{17.9}$), the other is of ferromagnetic one with

a strong magnetocrystalline anisotropy (UPdSb) and the last class includes $YbFe_4Al_8$, for which the magnetic ground state seems to be antiferromagnetic [1–3]. However, considering the presence of two magnetic sublattices (M1 and M2) in compounds belonging to the first group, one can find some ground for understanding their negative magnetization in the Néel theory [15].

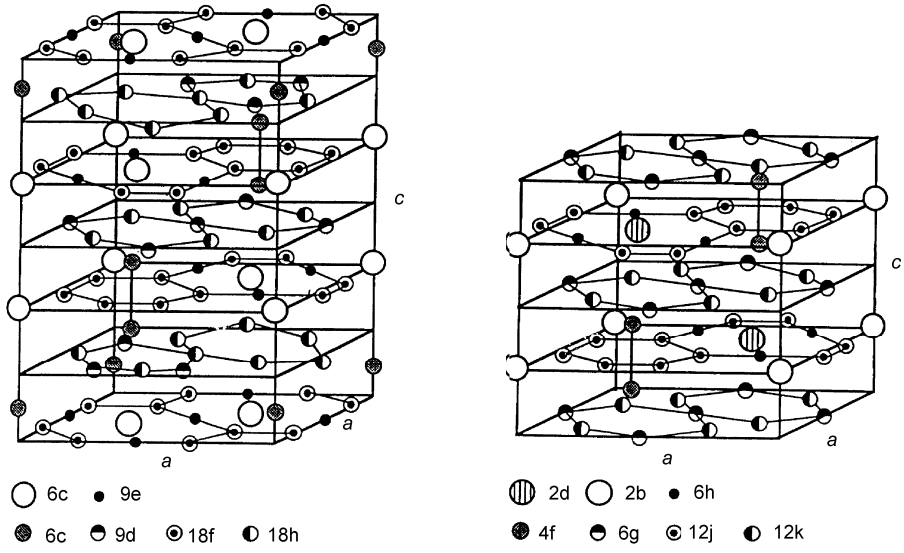

Fig. 8. The Th_2Zn_{17} type structure (left) and the Th_2Ni_{17} type structure (right)

Because M1 and M2 may have different temperature dependences, the total magnetization $M = [M1 - M2]$ is not ascribed to a Brillouin type shape, but strongly depends on history and measurement conditions. For the second group, the temperature dependence of magnetization can be explained in a similar manner as for ferrimagnets. The existing domain structure and/or anisotropy may act as the second magnetic sublattice. The behaviour of the Yb compound is less clear. Its magnetic susceptibility is strongly field dependent, even at temperatures clearly above T_N. This feature suggests that there exists a ferromagnetic correlation of unknown origin. Thus, one can suspect that Fe impurities may form ferromagnetic clusters being "imitation" of the second magnetic sublattice in ferrimagnets, and consequently they may contribute to the negative magnetization. However, the arguments presented above have speculative character and final conclusion can be formulated after further, more sophisticated experiments carried out on more perfect samples.

3. Conclusions

Summarizing, we can claim that the phenomenon of negative magnetization is not limited to one compound only, $YbFe_4Al_8$, but can be observed in other alloys, pre-

dominantly with $ThMn_{12}$ type structure. However, their stoichiometry is different from 4:8, this being a favourable condition for the creation of more than one magnetic sublattice. This observation allows one to point to the importance of stoichiometry and crystallographic excellence for physical properties.

References

[1] DRULIS H., GACZYŃSKI P., IWASIECZKO W., SUSKI W., KOTUR B.YA., Solid State Commun., 123 (2002), 391.
[2] ANDRZEJEWSKI B., KOWALCZYK A., FRĄCKOWIAK J.E., TOLIŃSKI T., SZLAFEREK A., PAL S., SIMON CH., phys. stat. sol. (b), 243 (2006), 295.
[3] TOLIŃSKI T., ANDRZEJEWSKI B., KOWALCZYK A., CHEŁKOWSKA G., SZLAFEREK A., FRACKOWIAK J., J. Phys. Chem. Solids, 67 (2006), 751.
[4] NOWIK I., FELNER I., [in:] Intern. Conf. Magnetism of Rare-Earths and Actinides, Central Institute of Physics, Bucharest, 1983, p. 24.
[5] SUSKI W., WOCHOWSKI K., GILEWSKI A., MYDLARZ T., BADURSKI D., [in:] Recent Advances in Actinide Science, I. May, R. Alvares, N. Bryan (Eds.), Royal Society of Chemistry Publ., Cambridge, 2006, pp. 797–799.
[6] SUSKI W., BIELAN B., GLADYSHEVSKII R., BODAK O.I., GILEWSKI A., MYDLARZ T., WOCHOWSKI K., J. Magn. Magn. Mater., 300 (2006), 221.
[7] FELNER I., NOWIK I., J. Magn. Magn. Mater., 74 (1988), 31.
[8] SUSKI W., STĘPIEŃ-DAMM J., MISIOREK H., TALIK E., WOCHOWSKI K., private communication.
[9] SUSKI W., GOFRYK K., HACKEMER A., WOCHOWSKI K., J. Alloys Comp., 423 (2006), 37.
[10] BRENNAN S., QI QINIAN, COEY J.M.D., J. Magn. Magn. Mater. 140–144 (1995), 977.
[11] SUSKI W., BELAN B., GILEWSKI A., MYDLARZ T., WOCHOWSKI K., Physica B, 346–347 (2004), 174.
[12] SUSKI W., BELAN B., BODAK O.I., GILEWSKI A., MYDLARZ T., WOCHOWSKI K., Fiz. Metal. Metall., 99 (suppl. 1),(2005), 38.
[13] SUSKI W., GLADYSHEVSKII R., VITYK N., GILEWSKI A., MYDLARZ T., WOCHOWSKI K., J. Alloys Comp., in press.
[14] GOFRYK K., KACZOROWSKI D., J. Phys.: Condens. Matter, 18 (2006), 3887.
[15] NÉEL L., Ann. Phys. 3 (1948), 137.

Received 7 May 2006
Revised 1 September 2006

Materials Science-Poland, Vol. 25, No. 2, 2007

Observation of non-Fermi liquid behaviour in new Yb-based alloys

V.H. TRAN*

W. Trzebiatowski Institute of Low Temperature and Structure Research,
Polish Academy of Sciences, P.O. Box 1410, 50-950 Wrocław 2, Poland

In this contribution, after presenting the existing theoretical models, we discuss the evidence for non-Fermi liquid behaviour in $Yb(Cu_{1-x}Si_x)_{2-y}$ that have been investigated for the last years in our Institute. The alloys crystallize in the hexagonal AlB_2 type structure and exhibit a dramatic change in the electronic properties upon change of the electron concentration. Undoped $YbSi_{2-y}$ is an intermediate valent system, whereas the doping with 10% Cu ensures $\chi(T) \propto T^n$, $\rho(T) \propto T$ and $C_p \propto T^{-1/2}$ dependences. Comparison of the data with the Griffiths phase model shows that this model can describe some of the observed results. We present also a study of the Hall effect. The Hall coefficient at 7 T is found to follow a ln$T$ dependence below 10 K, thus showing the behaviour opposite to that in Fermi-liquid heavy-fermion systems.

Key words: *non Fermi liquid; Yb-based intermetallic; Hall effect*

1. Introduction

For over half a century, the Landau Fermi liquid (LFL) theory has been successfully applied to describe the low-temperature properties of metals and intermetallic compounds [1]. In particular, this theory is useful in understanding the behaviour of strongly correlated electron systems (SCES) in which the particle–particle interaction is significant [2]. For instance, the application of LFL theory helps us to explain the enormous enhancement of effective electron masses m^* and other coefficients of physical quantities, observed in heavy fermion (HF) compounds. Other predictions of the theory (quadratic temperature dependence of the electrical resistivity, linear temperature dependence of the electronic specific heat and temperature independence of the magnetic susceptibility) are also valid in a number of SCES. There is, however, a growing number of systems showing an anomalous behaviour which distinctly deviates from the behaviour of the Landau theory. These non-Fermi liquid (NFL) systems

*E-mail: V.H.Tran@int.pan.wroc.pl

are mainly Ce-, U- and Yb-based intermetallics, that are identified as systems closely related to magnetic instability, superconductivity state and quantum critical point. Some macroscopic properties characteristic of the NFL behaviour are as follows [3]: (i) weak power law and logarithmic divergences in temperature of the specific heat, $C(T)/T \propto \gamma_0 \ln(T_0/T)$ or $\propto T^{-1+\lambda}$, $\lambda < 1$, (ii) diverging magnetic susceptibility, $\chi^{-1}(T) \propto T^{\beta}$, $\beta < 1$, $\propto -\ln(T/T_0)$, (iii) quasi-linear temperature dependence in the electrical resistivity, $\rho(T) \propto T^n$, $n < 2$, (iv) frequency scaling of the dynamic spin susceptibility, $\chi(\varpi, T) \propto \varpi^{-\alpha} Z(\omega, T)$, $\alpha < 1$.

At present, there exist no theoretical models giving a universal description of the NFL behaviour. Several researches consider fluctuations around quantum critical point as a suitable mechanism leading to the NFL behaviour [4], [5]. This point of view can be supported by the recognition that the NFL properties emerge at either the magnetic instability in a typical Doniach phase diagram for HF compounds or near to a quantum critical point (QCP) where superconducting phase transition may occur. Within the Doniach lattice model [6], magnetic order vanishes when the energy of the single-ion Kondo scattering, $k_B T_K$ becomes larger than that of the Ruderman –Kasuya–Kittel–Yosida (RKKY) interaction, $k_B T_{RKKY}$. Therefore, a suitable substitution (chemical pressure) or application of hydrostatic pressure may force the system to pass through the critical value at $T_K \sim T_{RKKY}$. This may be the case for very small doping $CeCu_{6-x}Au_x$ with $x = 0.1$, where the exact quantum critical point seems to exist [7]. Other examples are undoped NFL systems like as U_2Pt_2In [8] and $CeNi_2Ge_2$ [9]. The most pronounced QCP–NFL examples are superconductors under pressure $CePd_2Si_2$ [10] and UGe_2 [11].

However, there are other NFL systems, those with large contents of substituted elements. It seems that these alloys are not related to QCP at all. Instead, the role of crystallographic disorder becomes crucial. Here, two examples: $UCu_{5-x}Pd_x$ with $x = 0.7$ [12] and $U_2Cu_{17-x}Al_x$ with $x = 5$ [13] one may mention. In this class of NFL materials, it is not possible to define exact Kondo temperature, since the existing disorder creates a very wide distribution of Kondo temperatures. According to Bernal et al. [14], Kondo temperatures depend exponentially on the Kondo coupling parameter λ via $T_K \propto \exp(-1/\lambda)$ and are distributed by the probability $P(T_K) = |d\lambda/dT_K|P(\lambda)$. Furthermore, Miranda et al. [15] have considered the correlations between unquenched magnetic moments and conduction electrons. As the main result, the authors predicted a linear temperature dependence of electrical resistivity of such NFL systems. Neto et al. [16] discussed how disorder and the competition between RKKY and Kondo interactions lead to the formation of the Griffiths phase. The latter authors have shown that due to a crystallographic disorder, magnetic clusters appear in the paramagnetic phase close to a QCP, and this is the reason why NFL properties have been observed.

The NFL features have also been observed in alloys with a large dilution, like $Y_{0.8}U_{0.2}Pd_3$ [17] and $U_{0.2}Y_{0.8}Pd_2Al_3$ [18]. Owing to the fact that the amounts of magnetic ions in these materials are small, one may regard the magnetic ions as single Kondo ions. To explain the NFL behaviour of these systems, theoretical models have

included the multichannel Kondo effect of either magnetic or electric nature [19], [20]. Both an underscreening and overscreening of the impurity spin by the conduction electrons cannot ensure a singlet ground state. As a consequence, power laws emerge for the spin contribution to the resistivity $\rho(T) \propto T^{1/2}$ and to susceptibility $\chi(T) \propto T^{1/2}$, whereas a logarithmic upturn to the specific heat appears: $C(T)/T \propto \ln(T)$ [21]–[23].

The aim of the short description of the NFL phenomenon above is to show that a great deal of the interest in NFL systems simply results from the unusual temperature, magnetic field and pressure dependences of the physical quantities of NFL materials, for which one needs a new physics. Besides, due to a close relationship between NFL materials and unconventional superconductors, it will also be desirable to investigate in more detail the NFL behaviour. Such a study certainly will not only serve the interpretation of the behaviour of excited electrons in the strongly correlated electron systems but will also contribute to understanding of the nature of these superconductors. Recently, we discovered two new NFL systems, $Yb(Cu_{1-x}Si_x)_{2-y}$ [24] and $URh_{1-x}Ru_xGe$ [25]. In the present contribution, we attempt to summarize the low-temperature NFL characteristics of the former system. We report also the results of the Hall effect measurement. Selected data of the latter system are given in the paper by Miiller and Tran [26]. In short, the substitution of Rh by Ru in the ferromagnetic URhGe (T_C = 9.5 K) suppresses ferromagnetic order in the alloy $URh_{1-x}Ru_xGe$ at x = 0.30. The vanishing of ferromagnetism accompanies short-range magnetic correlations for x = 0.3–0.35, preceding the formation of a NFL phase around x = 0.4. It was also observed that the NFL behaviour in the investigated system ($\chi(T) \propto T^n$, $\rho(T) \propto T$) is easily depressed by the application of a magnetic field. The results of magnetization, electrical resistivity and magnetoresistance measurements strongly imply that the NFL $URh_{1-x}Ru_xGe$ alloys locate nearby a magnetic instability.

2. Non-Fermi liquid behaviour in Cu-doped alloy $Yb(Cu_{0.151}Si_{0.849})_{1.883}$

Among NFL materials, there are as few as two Yb-based alloy systems such as $YbRh_2(Si_{1-x}Ge_x)_2$ [27] and $Yb(Cu,Al)_5$ [28] so far well studied. Thus, a discovery of a new Yb-based NFL material is highly requested. In recent years, our investigation has been focused on the Yb-based intermetallics. Amongst them, the binary compound $YbSi_{2-x}$ seems to be of interest for scientists searching for new NFL materials. This compound crystallizes in the hexagonal AlB_2 type structure with a great deficit in the Si sites, even with x up to 0.3 [29]. The system was also reported to show an intermediate valence behaviour [30]. We thought it would be worth to investigate the effect of electron doping on the behaviour of the Yb ions. We put the Cu atoms in the vacancies, thus increasing electron content in the system. It turned out that as many as 10% of the Cu atoms can be doped into the binary $Yb(Cu/Si)_{2-x}$ compounds. Keeping

the hexagonal AlB_2 type structure, the doping increases the unit-cell volume V from 50.82 Å^3 in $YbSi_{2-x}$ to 53.25 Å^3 in $Yb(Cu_{0.151}Si_{0.849})_{1.883}$, and simultaneously decreases the concentration of vacancies. This change apparently reduces the exchange constant J, equivalent to a weakening in the hybridization between the 4f and conduction electrons. In the framework of the Doniach lattice diagram [6], such a doping may bring the alloy about the critical regime with $T_K \sim T_{RKKY}$.

The procedure of synthesis and sample characterization was described in details in [24]. The investigated sample adopted the AlB_2 type crystal structure with the lattice parameters a = 0.3981 nm and c = 1.3720 nm. In Figure 1, we show low-temperature data of $Yb(Cu_{0.151}Si_{0.849})_{1.883}$, which demonstrate the NFL characteristics of the compound.

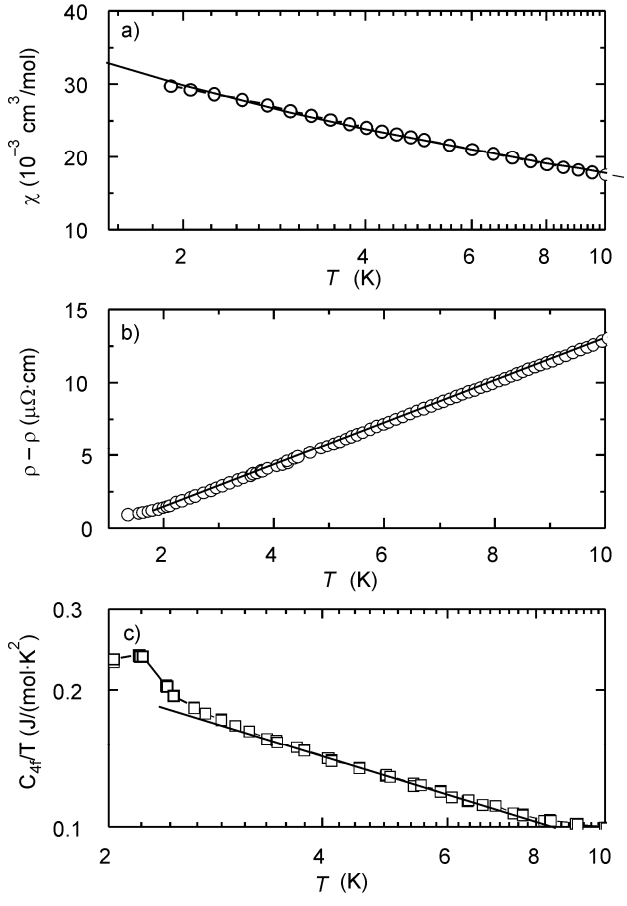

Fig. 1. The temperature dependences of: a) magnetic susceptibility obtained at 0.5 T, b) electrical resistivity, c) Yb contribution to the specific heat of $Yb(Cu_{0.151}Si_{0.849})_{1.883}$

The susceptibility data below 10 K, displayed in Fig. 1a, have been fitted by the power dependence $\chi(T) = 37.2T^{-1+\lambda}$ with $\lambda = 0.68$ (solid line). The non-Curie behav-

iour of the susceptibility indicates a contribution of electron correlations to the NFL phenomenon. It should be noted that a similar power exponent was found in other NFL materials like several solid solutions $UCu_{5-x}Pd_x$ with x = 0.7–1.5 [12]. In the context of the Griffiths phase model [16], the exponent λ describes the power-law decay of the cluster magnetization.

The resistivity data shown in Fig. 1b can be described by the linear dependence $\rho(T) - \rho_0 \propto AT$ in the temperature range 2–10 K. Such a behaviour represents the temperature dependence of resistivity based on the Kondo disorder model [14] but an alternative explanation for the linear resistivity may be the scattering due to spin fluctuations [31]–[33]. Therefore, such a dependence of resistivity may occur in number of NFL materials with different physical origins ($YbRh_2Si_2$, $CeCu_{5.9}Au_{0.1}$, $U_{0.9}Th_{0.1}Ni_2Al_3$, $U_{0.2}Y_{0.8}Pd_2Al_3$ [3]).

The low-temperature data of specific heat of the Yb ions (Fig. 1 c) exhibit a power-law behaviour, $C_{4f}/T \propto T^{-1/2}$. Neto et al. [16] in the framework of the Griffiths model predicted power-law behaviour for the specific heat $C/T \propto T^{-1+\lambda}$. Though there are some Yb_2O_3 impurities present in the sample that manifest themselves as a small anomaly at 2.2 K, we believe that the upturn in the specific heat data below 10 K is intrinsic, since in the specific heat measured at 0.5 T no peak structure can be detected.

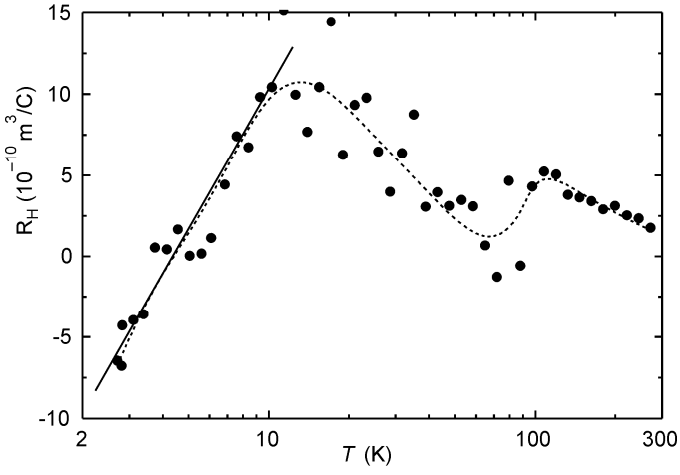

Fig. 2. Temperature dependence of the Hall coefficient at 7 T for $Yb(Cu_{0.151}Si_{0.849})_{1.883}$. The dashed and solid lines are guides for the eye

Figure 2 shows the temperature dependence of the Hall coefficient at 7 T for $Yb(Cu_{0.151}Si_{0.849})_{1.883}$. At room temperature, the Hall coefficient is positive and weakly varies with decreasing temperature. At about 12 K we observe a clear maximum, below which R_H follows a ln$T$ dependence. Accordingly to the theory developed by Fert and Levy [34] for the Hall effect of heavy fermion systems, one expects a maximum on the $R_H(T)$ curve at the coherence temperature T_0, and below which R_H levels off

due to a reduction of the skew scattering and formation of the coherent ground state. The lack of any stabilization in the Hall coefficient of $Yb(Cu_{0.151}Si_{0.849})_{1.883}$ suggests a strong correlation between magnetic ions and conduction electrons. Thus the Hall effect in $Yb(Cu_{0.151}Si_{0.849})_{1.883}$ in the studied temperature range distinctly deviates from that expected in conventional heavy-fermion systems.

3. Conclusions

We have shown selected data of the magnetic, thermodynamic and electron transport properties of $Yb(Cu_{0.151}Si_{0.849})_{1.883}$. The observed power-law dependences in the susceptibility and specific heat, as well as the linear dependence of resistivity strongly indicate the NFL behaviour of the investigated system. The remarkable finding is the $\ln T$ dependence of the Hall coefficient. Since, to our knowledge, no theoretical studies of the Hall effect for the NFL ground state have been reported yet, the R_H behaviour of $Yb(Cu_{0.151}Si_{0.849})_{1.883}$ will be useful in the development of a universal model which would be able to describe anomalous physical properties observed in NFL materials.

Aknowledgements

This work was supported by the Ministry of Science and Higher Education in Poland under Grant No. N202 082 31/0449.

References

[1] LANDAU L.D., Sov. Phys-JETP, 3 (1956), 920; 5 (1957), 101; 8 (1958), 70.
[2] STEGLICH F., SÜLLOW S., [in:] *Encyclopedia of Materials: Science and Technology*, Elsevier Science Ltd., (2001), p. 3747.
[3] STEWART G.S., Rev. Mod. Phys., 73 (2001), 797.
[4] CONTINENTINO M.A., Z. Phys. B, 101 (1996), 197.
[5] COLEMAN P., Physica B, 259–291 (1999), 353.
[6] DONIACH S., Physica B, 91 (1977), 231; LACROIX C., CYROT M., Phys. Rev. B, 20 (1979), 1969.
[7] SCHROEDER A., AEPPLI G., COLDEA R., ADAMS M., STOCKERT O., LÖHNEYSEN H.V., BUCHER E., RAMAZASHVILI R., COLEMAN P., Nature, 407 (2000), 351.
[8] ESTRELLA P., DE VISSER A., NAKA T., DE BOER F.R., NIEUWENHUYS G.J., PEREICA L.C.J., ALMEIDA M., Physica B, 259–261 (1999), 409.
[9] STEGLICH F., BUSCHINGER B., GEGENWART P., LOHMANN M., HELFRICH R., LANGHAMMER C., HELLMANN P., DONNVERT L., THOMAS S., LINK A., GEIBEL C., LANG M., SPARN S., ASSMUS W., J. Phys.: Condens. Matter, 8 (1996), 9909.
[10] GROSCHE F.M., AGARWAL P., JULIAN S.R., WILSON N.J., HASELWIMMER R.K.W., LISTER S.J.S., MATHUR N.D., CARTER F.V., SAXENA S.S., LONZARICH G.G., J. Phys.: Condens. Matter, 12 (2000), 533.
[11] SAXENA S.S., AGARWAL P., AHILAN K., GROSCHE F.M., HASELWIMMER R.K.W., STEINER M.J., PUGH E., WALKER I.R., JULIAN S.R., MONTHOUX P., LONZARICH G.G., HUXLEY A., SHEIKIN I., BRAITHWAITE D., FLOUQUET J., Nature, 406 (2000), 587.
[12] CHAU R., ARONSON M.C., FREEMAN E.J., MAPLE M.B., J. Phys.: Condens. Matter, 12 (2000), 4495.
[13] PIETRI R., RAKA B., TROĆ R., TRAN V.H., Phys. Rev. B, 56 (1997), 14505.

[14] BERNAL O.O., MACLAUGHLIN D.E., LUKEFAHR H.G., ANDRAKA B., Phys. Rev. Lett., 75 (1995), 2023.
[15] MIRANDA E., DOBROSAVLJEVIC V., KOTLIAR G., Phys. Rev. Lett., 78 (1997), 290.
[16] NETO A.H.C., CASTILLA G., JONES B.A., Phys. Rev. Lett., 81 (1998), 3531.
[17] MAPLE M.B., DICKEY R.P., HERRMANN J., DE ANDRADE M.C., FREEMAN E.J., GAJEWSKI D.A., CHAU R., J. Phys.: Condens. Matter, 8 (1996), 9773.
[18] ZAPF V.S., FREEMAN E.J., DICKEY R.P., HO P.C., MAPLE M.B., Physica B, 312–313 (2002), 448.
[19] NOZIERES P., BLANDIN A., J. Phys. (Paris), 41 (1980), 193.
[20] COX D.L., ZAWADOWSKI A., Adv. Phys., 47 (1988), 599.
[21] TSVELIK A.M., J. Phys. C, 18 (1985), 159.
[22] SACRAMENTO P.D., SCHLOTTMANN P., Phys. Lett. A, 142 (1989), 245.
[23] COX D.L., MAKIVIC M., Physica B, 199–200 (1994), 391.
[24] TRAN V.H., KACZOROWSKI D., GRYTSIV A., ROGL P., Phys. Rev. B, 72 (2005), 115116.
[25] MIILLER W., TRAN V.H., [in:] Proc. of 36. J. Actinides, Oxford, England, 1–4 April, 2006; TRAN V.H., MIILLER W., BAENITZ M., STEGLICH F., Quantum Complexities in Condensed Matter, Cambridge, UK, 4–7 July 2006.
[26] MIILLER W., TRAN V.H., KONDRAT A., Mater. Sci.-Poland, 25 (389), 2007.
[27] TROVARELLI O., GEIBEL C., MEDERLE S., LANGHAMMER C., GROSCHE F.M., GEGENWART P., LANG M., SPARN G., STEGLICH F., Phys. Rev. Lett., 85 (2000), 626.
[28] BAUER E., HAUSER R., GALATANU A., MICHOR H., HILSCHER G., SERENI J., BERISSO M.G., PEDRAZZINI P., GALLI M., MARABELLI F., BONVILLE P., Phys. Rev. B, 60, 1238 (1999).
[29] GRYSIV A., KACZOROWSKI D., LEITHE-JASPER A., TRAN V.H., PIKUL A., ROGL P., POTEL M., NOËL H., BOHN M., VELIKANOVA T., J. Solid State Chem., 163 (2002), 178.
[30] IANDELLI A., PALENZONA P., OLCESE G.L., J. Less-Common Met., 64 (1979), 213.
[31] MORIYA T., TAKIMOTO T., J. Phys. Soc. Jpn., 64, (1995), 960.
[32] MILLIS A.J., Phys. Rev. B, 48, (1993), 7183.
[33] HERTZ J.A., Phys. Rev. B, 14, (1976), 1165.
[34] FERT A., LEVY P.M., Phys. Rev. B, 36 (1987), 1907.

Received 7 May 2006
Revised 1 September 2006

Materials Science-Poland, Vol. 25, No. 2, 2007

Domain-wall contribution to magnetoresistance in ferromagnetic (Ga,Mn)As film

T. WOSIŃSKI*, O. PELYA, T. FIGIELSKI, A. MĄKOSA, A. MORAWSKI, J. SADOWSKI, W. DOBROWOLSKI, R. SZYMCZAK, J. WRÓBEL

Institute of Physics, Polish Academy of Sciences, al. Lotników 32/46, 02-668 Warsaw, Poland

Simple magnetoresistive nanodevices formed by narrow constrictions of submicron width in the epitaxial film of a ferromagnetic (Ga,Mn)As semiconductor have been fabricated employing the electron-beam-lithography patterning and low-energy low-dose oxygen ion implantation. Low-temperature charge-carrier transport through the constrictions has been investigated and correlated with magnetic properties of the film. The constricted devices revealed abrupt jumps of a reduced resistance that appeared when the sweeping magnetic field crossed the regions of the coercive field of the film magnetization. In contrast, the non-constricted reference device displayed abrupt jumps of an enhanced resistance at the same values of magnetic field. We interpret the both features, whose positions on the magnetic-field scale reflect the hysteresis loop of magnetization, as manifestation of domain wall contribution to the (Ga,Mn)As film resistance. Presumably, the suppression of the weak localization effects by a domain wall located at the constriction results in a negative contribution of a domain wall to the resistance, while the spin-orbit interaction can be responsible for its positive contribution to the resistance.

Key words: *ferromagnetic semiconductor; nanostructure; domain wall; magnetoresistance*

1. Introduction

Electron transport through domain walls (DWs) in ferromagnetic nanowires and constrictions became the subject of great current interest stimulated by possible applications of the magnetoresistance associated with DWs in magnetoelectronic devices. On the other hand, recent advance in the growth of ferromagnetic semiconductors based on III–V compounds gives rise to a possible integration of electronic and magnetoelectronic devices providing a basis for future spin electronics. In particular, homogeneous films of $Ga_{1-x}Mn_xAs$ containing up to 8% of Mn atoms can be grown by a low-temperature molecular-beam epitaxy (LT-MBE) [1]. When intentionally undoped, the films are of p-type where Mn atoms, substituting the Ga lattice atoms, sup-

*Corresponding author, e-mail: wosin@ifpan.edu.pl

ply both mobile holes and magnetic moments. Below the Curie temperature, T_C, the films become ferromagnetic due to the hole-mediated ordering of Mn spins ($S_{Mn} = 5/2$ for Mn^{2+} charge state) [2]. Although the highest T_C in the as-grown (Ga,Mn)As films remains so far at 110 K, it has been increased up to 173 K till now [3] by means of post-growth low-temperature (180–250 °C) annealing treatments [4–6]. The main effect of annealing, leading to the efficient increase in both the hole density and T_C, is outdiffusion from the (Ga,Mn)As films of Mn interstitials that act as double donors in GaAs. It is expected that further optimization of the MBE-growth conditions and the post-growth annealing will succeed in obtaining (Ga,Mn)As films of about 10% Mn content showing room-temperature ferromagnetism [7].

In the present study, we fabricated and investigated simple magnetoresistive nano-devices formed by narrow constrictions in the epitaxial film of a ferromagnetic (Ga,Mn)As semiconductor with the aim to explore the impact of a domain wall pinned at the constriction on the charge-carrier transport across it.

2. Experimental

Ferromagnetic $Ga_{0.99}Mn_{0.01}As$ film has been grown on a semi-insulating (001) GaAs substrate by means of LT-MBE in a dedicated III–Mn–V MBE system located at MAX-Lab, Lund University, Sweden; see Ref. [8] for more details. The film 50 nm thick was covered with a 10 nm thick GaAs cap layer. Magnetization of the film, which exhibits an in-plane easy axis of magnetization and the Curie temperature of 50 K, was measured using a superconducting quantum interference device (SQUID) magnetometer with a magnetic field applied parallel to the film plane, along the

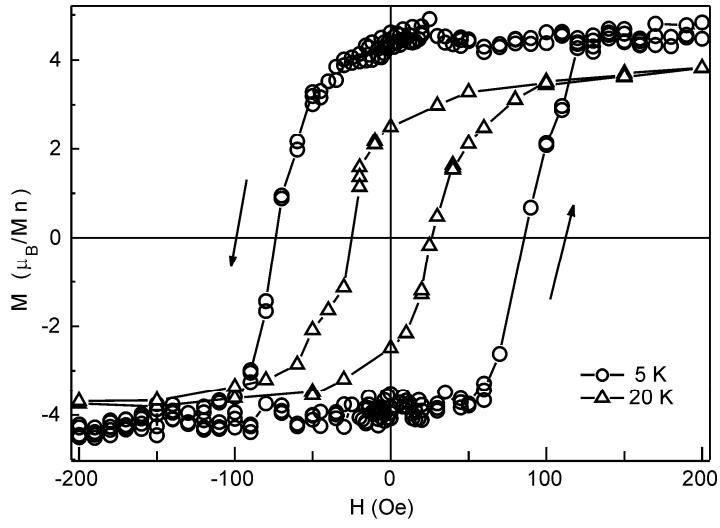

Fig. 1. Magnetization hysteresis loops for $Ga_{0.99}Mn_{0.01}As$ film recorded with SQUID magnetometer at 5 K and 20 K after subtraction of diamagnetic contribution from the GaAs substrate

cleavage edge, i.e. the ⟨110⟩ crystallographic axis. Figure 1 presents the magnetization hysteresis curves recorded at 5 and 20 K, showing a strong dependence of the hysteresis loop width on temperature. A large value of the low-temperature saturation magnetization of the film, of $4.5\mu_B$ per Mn atom, and a relatively high Curie temperature evidence a high quality of the investigated ferromagnetic film.

We fabricated constrictions of submicron width in the (Ga,Mn)As film by the method of low-energy (25 keV) low-dose (5×10^{13} ions/cm^2) oxygen ion implantation through a mask consisting of a thick resist deposited on the top of the film and containing windows patterned by the electron-beam lithography. Previously, we have found that such an implantation destroys both the conductivity and ferromagnetism in the layer [9]. The lithographic widths of the constrictions were in the range of 200–1000 nm. Individual devices, of an outline 2.5×1 mm^2 and the shape shown in the inset of Fig. 2, were defined in the film and their distant terminals were supplied with Ohmic contacts. All the results presented in this paper refer to the constriction with lithographic width of 400 nm, whose microscopic image is shown in the inset in Fig. 4, and, additionally, to a reference (non-constricted) device of a bar (1.5×0.5 mm^2) shape. The contribution of the constricted part of the device to its total resistance is comparable to that carried in by the wide leads.

3. Results

We measured the sample resistance, *R*, as a function of a magnetic field, *H*, using the pseudo-four-probe method and lock-in technique with a sensing voltage of a few mV

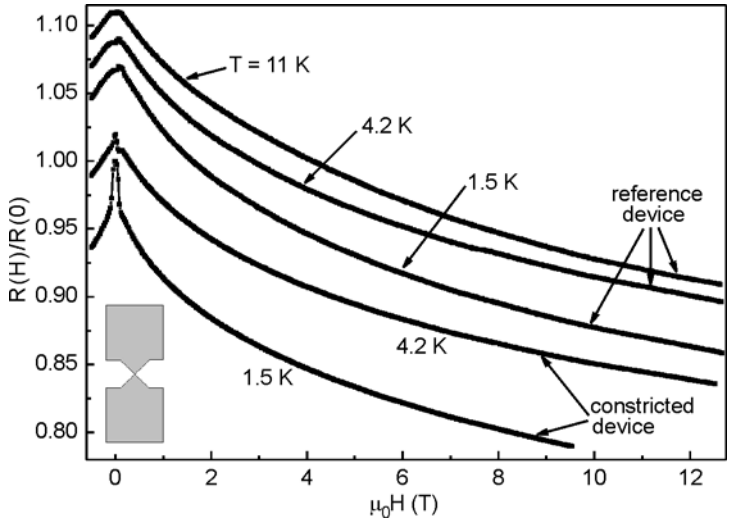

Fig. 2. Relative magnetoresistance vs. in-plane (perpendicular to the current) magnetic field for the reference and constricted devices measured at various temperatures. The curves are vertically offset for clarity. Inset: constricted device design

at 770 Hz. Relative magnetoresistance, $R(H)/R(0)$, plotted as a function of magnetic field applied parallel to the film plane (perpendicular to the current) is shown in Fig. 2. Both the reference and constricted devices investigated by us exhibit a large negative magnetoresistance (MR) at low temperatures, extending far outside the field of ferromagnetic hysteresis loop. Such a behaviour of MR, which has been also observed by us for the perpendicular orientation of magnetic field with respect to the film plane [10, 11], is typical of (Ga,Mn)As films. It has been commonly attributed to the reduction of spin-disorder scattering of charge carriers caused by the ordering of localized Mn spins in an external magnetic field – a mechanism well known in ferromagnetic metals. Another mechanism, which possibly dominates at the lowest temperatures, is the suppression of carrier quantum localization by an external magnetic field [10–14]. In fact, we have recently shown [11] that the low-temperature MR of our (Ga,Mn)As film under perpendicular magnetic field can be successfully described within the weak localization theory for two-dimensional ferromagnetic systems developed by Dugaev et al. [15]. The inelastic scattering length derived from the fitting of our MR results to this theory was about 90 nm [11], while the hole mean free path in the (Ga,Mn)As film is of the order of 1 nm.

A striking difference has been revealed between MR measured in the reference and constricted devices in a narrow range of a magnetic field around $H = 0$ (Figs. 3 and 4). At the magnetic field corresponding to the coercive fields of the film magnetization, MR of the reference device exhibits abrupt jumps followed by regions of an enhanced resistance (Fig. 3). With increasing temperature, the spacing between the jumps corresponding to the field swept in opposite directions narrows similarly as does the width of the magnetization hysteresis loop.

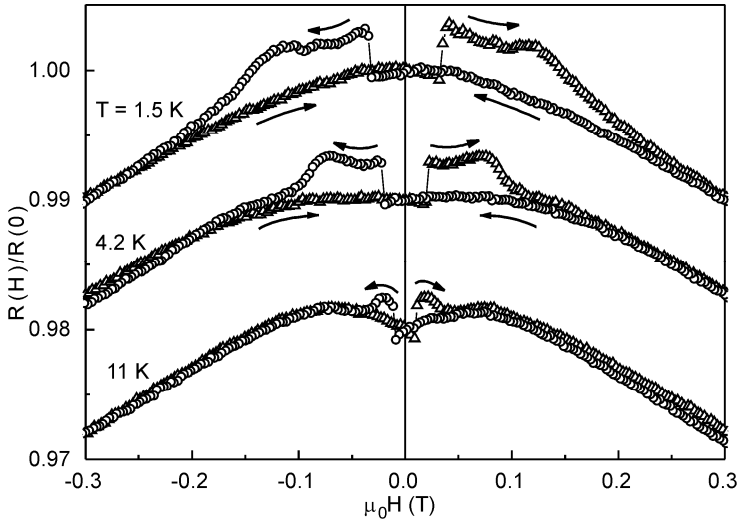

Fig. 3. Relative magnetoresistance for the reference device vs. in-plane (perpendicular to the current) magnetic field swept in opposite directions measured at 1.5, 4.2 and 11 K. The sweep directions are indicated by the arrows. The data for the two latter temperatures have been vertically offset for clarity

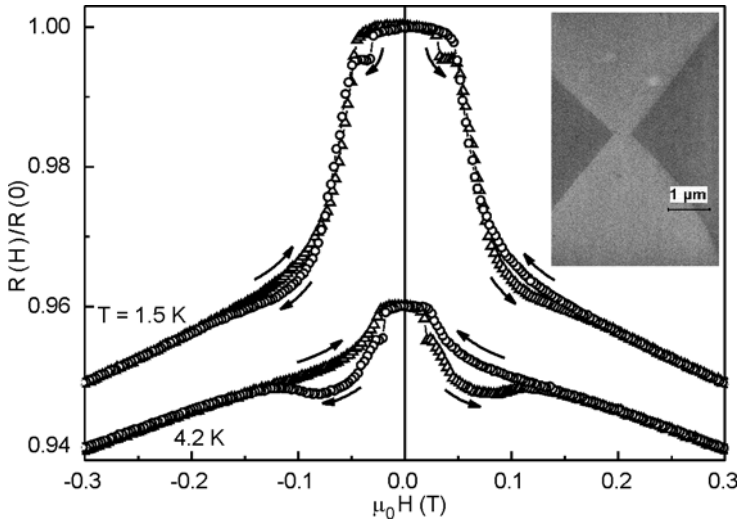

Fig. 4. Relative magnetoresistance for the constricted device vs. in-plane (perpendicular to the current) magnetic field swept in opposite directions measured at 1.5 and 4.2 K. The sweep directions are indicated by the arrows. The data for the latter temperature have been vertically offset for clarity. Inset: secondary electron image in a scanning electron microscope of the constriction patterned by oxygen ion implantation; the darker contrast corresponds to the implanted areas

The extension and magnitude of the regions of enhanced resistance decrease with increasing temperature and they practically disappear at 15 K. MR of the constricted device shown in Fig. 4 displays an essentially different behaviour. In a narrow range of a magnetic field around $H = 0$, its resistance considerably increases forming a high bump while sweeping a magnetic field through the zero value. The height of this bump and its width, which extends from –50 to 50 mT at 1.5 K, decrease rapidly with increasing temperature. On a background of this increased resistance, abrupt jumps followed by regions of a lowered resistance appear. Positions of these jumps reflect, as for the reference device, the hysteresis loop of magnetization. Similar jumps of a lowered resistance have been revealed by us also for two other constricted devices measured under magnetic field perpendicular to the film plane and interpreted as resulting from a contribution of a magnetic DW, pinned at the constriction, to the resistance [10, 11].

4. Discussion and conclusions

Both positive [16, 17] and negative [10, 11, 18] contributions of DWs to the resistance have been recently revealed experimentally in microstructures fabricated from (Ga,Mn)As films. Several authors studied theoretically the effect of electron scattering at DWs on resistivity of ferromagnetic metals and semiconductors (cf. [19] and

references therein). Theoretical calculations predict generally a positive contribution of DW to the resistivity, which can be efficiently increased in the case of thin DWs (on the scale of the Fermi wavelength of conducting charges) in ferromagnetic semiconductors owing to the presence of spin-orbit interaction, as shown in [19]. In turn, (Ga,Mn)As epitaxial films demonstrate extremely simple domain structure with large domains of the size of hundreds of micrometers, and thin and well-defined DWs [20]. The DW thickness in (Ga,Mn)As films has been determined to be about 15 nm both for the Bloch [21] and Néel wall [22], and almost independent of both the temperature and Mn content. This value is by a factor of two larger than the estimated value of Fermi wavelength in our (Ga,Mn)As film. In view of the above results, we believe that the jumps of enhanced resistance appearing in our reference device at the magnetic field corresponding to the coercive fields, i.e. when DWs are just nucleated, result from a DW contribution to the (Ga,Mn)As film resistance.

On the other hand, Tatara and Fukuyama [23] first predicted that a DW can destroy the charge-carrier phase coherence necessary for the quantum weak localization (WL), what leads to a negative contribution of DW to the resistivity. WL can coexist with ferromagnetism in our (Ga,Mn)As film. The maximum value of an internal magnetic induction, $B_{\mathrm{int}} \approx \mu_0 M_{\mathrm{s}} = 11$ mT, estimated from the magnitude of saturation magnetization, M_{s}, obtained from our SQUID measurements (Fig. 1), is small enough to be generally neglected in a WL correction to resistivity. An external magnetic field suppresses WL as it introduces a phase difference between the time-reversed paths, proportional to the enclosed magnetic flux, thus giving rise to an apparent negative MR. Consequently, we propose that the high bump of increased resistance occurring for the constricted device around $H = 0$ results from a contribution of WL in the constriction to the resistance.

In the constricted devices DWs tend to localize themselves in the constriction in order to minimize their energy, cf. [24], and their width, which is essentially determined by the constriction size, is of the order of the constriction width. Thus, the appearance of the jumps of reduced resistance imposed on a background of the bump of increased resistance in the constricted device can be understood as due to erasure of the quantum localization by a DW located at the constriction. Each region of a reduced resistance would extend over the field range, in which the DW remains pinned at the constriction.

In conclusion, we have argued that both the jumps of an enhanced resistance in the reference device and those of a reduced resistance in the constricted devices, which appear when the sweeping magnetic field crosses the regions of the coercive field of the film, represent a DW contribution to the (Ga,Mn)As film resistance. The opposite sign of this contribution revealed in the reference and constricted devices results from different properties of DWs formed in the two types of structures. Thin DWs formed in the non-constricted (Ga,Mn)As film give rise to the positive contribution to the film resistance. On the other hand, the diffusive charge transport through a thick DW pinned at the constriction results in the erasure of quantum localization effects, thus

giving rise to the negative contribution of DW to the resistance in the constricted device.

Acknowledgement

This work has been partly supported by the Polish Ministry of Science under Grant No. 1 P03B 052 26.

References

[1] MATSUKURA F., OHNO H., SHEN A., SUGAWARA Y., Phys. Rev. B, 57 (1998), R2037.
[2] DIETL T., OHNO H., MATSUKURA F., Phys. Rev. B, 63 (2001), 195205.
[3] WANG K.Y., CAMPION R.P., EDMONDS K.W., SAWICKI M., DIETL T., FOXON C.T., GALLAGHER B.L., AIP Conf. Proc. 772 (2005), 333.
[4] KU K.C., POTASHNIK S.J., WANG R.F., SEONG M.J., JOHNSTON-HALPERIN E., MEYERS R.C., CHUN S.H., MASCARENHAS A., GOSSARD A.C., AWSCHALOM D.D., SCHIFFER P., SAMARTH N., Appl. Phys. Lett., 82 (2003), 2302.
[5] EDMONDS K.W., BOGUSŁAWSKI P., WANG K.Y., CAMPION R.P., NOVIKOV S.V., FARLEY N.R.S., GALLAGHER B.L., FOXON C.T., SAWICKI M., DIETL T., BUONGIORNO NARDELLI M., BERNHOLC J., Phys. Rev. Lett., 92 (2004), 037201.
[6] ADELL M., ILVER L., KANSKI J., STANCIU V., SVEDLINDH P., SADOWSKI J., DOMAGALA J. Z., TERKI F., HERNANDEZ C., CHARAR S., Appl. Phys. Lett., 86 (2005), 112501.
[7] JUNGWIRTH T., WANG K.Y., MAŠEK J., EDMONDS K.W., KÖNIG J., SINOVA J., POLINI M., GONCHARUK N.A., MACDONALD A.H., SAWICKI M., RUSHFORTH A.W., CAMPION R.P., ZHAO L.X., FOXON C.T., GALLAGHER B.L., Phys. Rev. B, 72 (2005), 165204.
[8] SADOWSKI J., DOMAGAŁA J.Z., Phys. Rev. B, 69 (2004), 075206.
[9] FIGIELSKI T., WOSIŃSKI T., MORAWSKI A., PELYA O., SADOWSKI J., TÓTH A.L., JAGIELSKI J., Phys. Stat. Sol. (a), 195 (2003), 228.
[10] FIGIELSKI T., WOSIŃSKI T., PELYA O., SADOWSKI J., MORAWSKI A., MĄKOSA A., DOBROWOLSKI W., JAGIELSKI J., WRÓBEL J., Acta Phys. Pol. A, 103 (2003), 525.
[11] FIGIELSKI T., WOSIŃSKI T., PELYA O., SADOWSKI J., MORAWSKI A., MĄKOSA A., DOBROWOLSKI W., SZYMCZAK R., WRÓBEL J., [in:] *Physics, Chemistry and Applications of Nanostructures*, V.E. Borisenko, S.V. Gaponenko, V.S. Gurin (Eds.), World Scientific, Singapore, 2005, pp. 289–292.
[12] DIETL T., MATSUKURA F., OHNO H., CIBERT J., FERRAND D., *Recent Trends in Theory of Physical Phenomena in High Magnetic Fields*, [in:] I.D. Vagner et al. (Eds.), Kluver Academic Publishers, Dordrecht, 2003, pp. 197–210.
[13] EDMONDS K.W., CAMPION R.P., WANG K.-Y., NEUMANN A.C., GALLAGHER B.L., FOXON C.T., MAIN P.C., J. Appl. Phys., 93 (2003), 6787.
[14] MATSUKURA F., SAWICKI M., DIETL T., CHIBA D., OHNO H., Physica E, 21 (2004), 1032.
[15] DUGAEV V.K., BRUNO P., BARNAŚ J., Phys. Rev. B, 64 (2001), 144423.
[16] RÜSTER C., BORZENKO T., GOULD C., SCHMIDT G., MOLENKAMP L.W., LIU X., WOJTOWICZ T.J., FURDYNA J.K., YU Z.G., FLATTÉ M.E., Phys. Rev. Lett., 91 (2003), 216602.
[17] CHIBA D., YAMANOUCHI M., MATSUKURA F., DIETL T., OHNO H., Phys. Rev. Lett., 96 (2006), 096602.
[18] TANG H.X., MASMANIDIS S., KAWAKAMI R.K., AWSCHALOM D.D., ROUKES M.L., Nature, 431 (2004), 52.
[19] DUGAEV V.K., BARNAŚ J., BERAKDAR J., IVANOV V.I., DOBROWOLSKI W., MITIN V.F., Phys. Rev. B, 71 (2005), 024430.
[20] WELP U., VLASKO-VLASOV V.K., LIU X., FURDYNA J.K., WOJTOWICZ T., Phys. Rev. Lett., 90 (2003), 167206.
[21] DIETL T., KÖNIG J., MACDONALD A.H., Phys. Rev. B 64 (2001), 241201(R).

[22] POTASHNIK S.J., KU K.C., MAHENDIRAN R., CHUN S.H., WANG R.F., SAMARTH N., SCHIFFER P., Phys. Rev. B, 66 (2002), 012408.
[23] TATARA G., FUKUYAMA H., Phys. Rev. Lett., 78 (1997), 3773.
[24] HONOLKA J., MASMANIDIS S., TANG H.X., ROUKES M.L., AWSCHALOM D.D., J Appl Phys., 97 (2005), 063903.

Received 7 May 2006
Revised 1 September 2006

Materials Science-Poland, Vol. 25, No. 2, 2007

Electronic structure of Fe_2VGa

J. GORAUS, A. ŚLEBARSKI*

Institute of Physics, University of Silesia, 40-007 Katowice, Poland

We present the band structure calculations on the Heusler alloy Fe_2VGa which shows a pseudogap at the Fermi level. The compound is found to be nonmagnetic. We observed, however, that an atomic disorder which has been experimentally observed can lead to the behaviour characteristic of the heavy-Fermion compounds. The antisite Fe defects locate the d states forming a narrow d-band at the Fermi level.

Key words: *electronic structure; strong electron correlations*

1. Introduction

The physics of d-electron intermetallic compounds with electronic gaps or pseudogaps at the Fermi level continues to attract attention. This gap (pseudogap) in materials containing localized magnetic orbitals may be due to hybridization or Kondo -type singlet formalism (e.g., [1]).

Recently, the Heusler-type Fe_2VAl [2] and Fe_2TiSn [3] compounds have been discussed as possible d-Kondo insulators of the FeSi-type [4] due to their unusual electric transport and thermodynamic properties. Namely, the electrical resistivity of both compounds exhibits semiconducting behaviour and the low-T specific-heat data revealed an unusual upturn in C/T, commonly observed in most heavy fermion systems. From the band-structure calculations and infrared studies it follows, however, that Fe_2VAl [5] and Fe_2TiSn [6] are semimetals with a pseudogap at the Fermi level. In our recent work [7], we discussed the low-T properties of these compounds based on the Kimball–Falicov model [8] well describing the temperature characteristics attributed to the narrow d-antisite band, strongly correlated and located at the Fermi level.

Similarly, Fe_2VGa is predicted from the band structure calculations to be semimetallic [9, 10] and nonmagnetic. However, in some Fe_2VGa samples characteristic features of superparamagnetic glass due to the presence magnetic defects are reported (e.g., in [11]). It has been suggested that the wrong-site Fe atoms on V sites (Fe_{AS}

*Corresponding author, e-mail: slebar@us.edu.pl

antisite) are magnetic and can play a significant role in the magnetism of this compound. We therefore present our LAPW calculations on the ordered Fe_2VGa, and on the disordered one, in which an atomic disorder results from the Fe/V site exchange. Our calculations show that the antisite defects locate the d-states at the Fermi level, resulting in formation of a narrow d-band, but the system is nonmagnetic. However, magnetic Fe-defects are expected for stronger atomic disorder.

2. Results and discussion

In our investigations, we used FP-LAPW (Wien2k) code, with GGA96 type gradient corrections [12]. We performed calculations for base Fe_2VGa compound, and also for a 2×1×1 supercell, where two Fe atoms were replaced by two V atoms and vice versa. Atomic radii were chosen 2.32 Å for Fe and V and 2.2 Å for Ga. We used 816 *k*-points in reduced Brillouin zone for the calculations of base compound and 162 *k*-points for the supercell calculations.

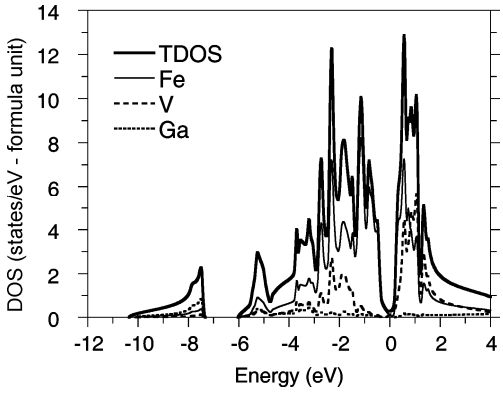

Fig. 1. Total density of states calculated for Fe_2VGa. Also, the partial total DOSs for Fe, V and Ga components are shown

In Figure 1, we present numerical calculations of the electronic densities of states (DOS) of the ordered Fe_2VGa compound. Also shown in the figure are the total DOSs of Fe, V and Ga. The electronic bands exhibit a pseudogap at the Fermi level with a small value of the total DOS of about 0.25 states/eV-formula unit. In our calculations, Fe_2VGa is nonmagnetic. To better understand the properties of real Fe_2VGa crystals, exhibiting strong atomic disorder, we also investigated the electronic structure of the Fe_2VGa alloy with one Fe atom occupying the V site. The results of our calculations are presented in Figs. 2a–d. The total DOS has a pseudogap located ~0.2 eV above the Fermi level and a sharp and narrow peak in the DOS just at ε_F. The DOS of this peak is composed mainly of the Fe_{AS} d-states of iron defects occupying the V sites (the inset in Fig. 2b). V defects have similar sharp and narrow d-electron peaks in the DOS (Fig. 2c). However, Fe_2VGa in our calculations is again nonmagnetic. Our recent calculations have shown that this narrow d-band originating from the impurity Fe atoms is responsible for the unusual temperature dependence of

heavy Fermi-like behaviours observed either in Fe_2VAl [2] or in Fe_2TiSn [3]. The nature of the physics in the both Heusler alloys seems to be similar to that in Ce and U compounds, analyzed [7] in a many-body investigation along the line described by Liu [8]. Another explanation of the unusual low-temperature dependences of the specific heat can be discussed on the base of the spin fluctuation theory.

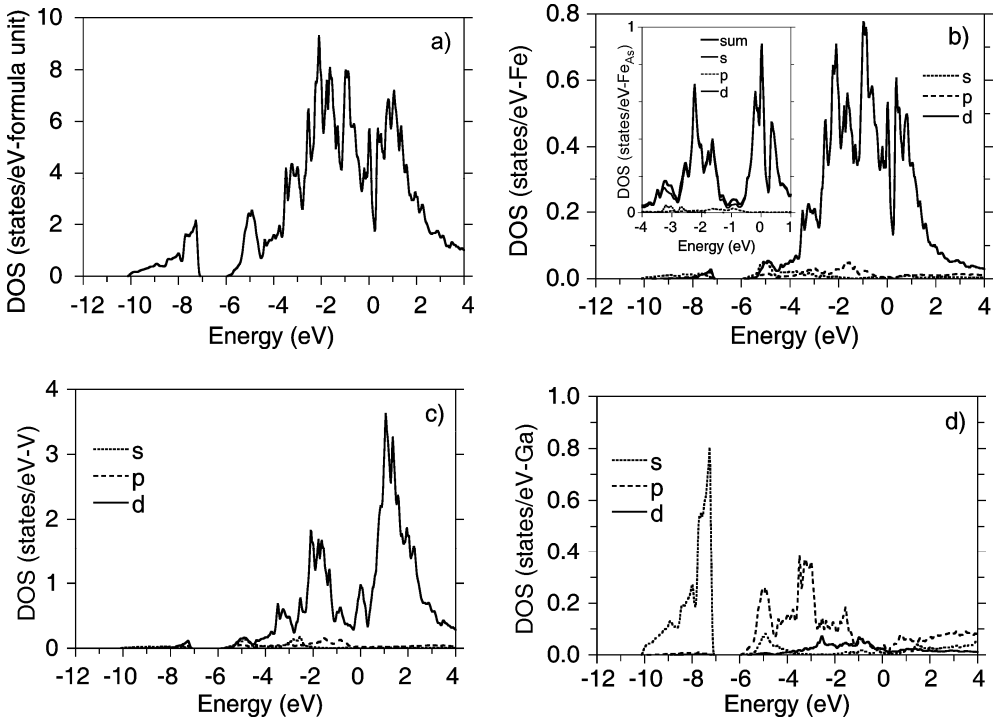

Fig. 2. The total DOS calculated for the disorder Fe_2VGa alloy, where one Fe atom occupies the V atomic position (a) and partial DOSs for s, p and d states of Fe in the disordered Fe_2VGa; the inset shows the DOSs of the Fe_{AS} defects, occupying the V sites (b); partial DOSs in Fe_2VGa (c), partial Ga DOSs in Fe_2VGa (d)

The heavy Fermi-like behaviour has not been, however, observed in the Fe_2VGa alloy probably because of strong atomic disordering, which can lead to weak super-paramagnetism, recently observed in the magnetic susceptibility experimental data [11]. The problem of magnetic/nonmagnetic ground state properties of the Fe_2VGa alloy is expected to be investigated experimentally soon.

Acknowledgements

The authors thank the Ministry of Science and Higher Education for financial support from Projects Nos. 1 P03B 052 28 and 1 P03B 094 30. We also acknowledge the Grant No. 1 PO3B 094 30 of the Ministry of Science and Information Technology.

References

[1] DEGIORGI L., Rev. Mod. Phys. 71 (1999), 687.
[2] NISHINO Y., KATO M., ASANO S., SODA K., HAYASAKI M., MIZUTANI U., Phys. Rev. Lett., 79 (1997), 1909.
[3] ŚLEBARSKI A., MAPLE M.B., FREEMAN E.J., SIRVENT C., TWORUSZKA D., ORZECHOWSKA M., WRONA A., JEZIERSKI A., CHIUZBAIAN S., NEUMANN M., Phys. Rev. B, 62 (2000), 3296.
[4] SCHLESINGER Z., FISK Z., ZHANG H-T., MAPLE M.B., DITUSA J.F., AEPPLI G., Phys. Rev. Lett., 71 (1993), 1748.
[5] OKUMARA H., KAWAHARA J., NANBA T., KIMURA S., SODA K., MIZUTANI U., NISHINO Y., KATO M., SHIMOYAMA I., MIURA H., FUKUI K., NAKAGAWA K., KINOSHITA T., Phys. Rev. Lett., 84 (2000), 3674.
[6] DORDEVIC S.V., BASOV D.N., ŚLEBARSKI A., MAPLE M.B., Phys. Rev. B, 66 (2002), 75122.
[7] ŚLEBARSKI A., DENISZCZYK J., BORGIEŁ W., JEZIERSKI A., SWATEK M., WINIARSKA A., MAPLE M.B., YUHASZ W.M., Phys. Rev. B, 69 (2004), 155118.
[8] LIU S.H., Physica B, 240 (1997), 49.
[9] WEHT R., PICKETT W.E., Phys. Rev. B, 58 (1998), 6855.
[10] BANSIL A., KAPRZYK S., MIJNARENDS P.E., TOBOŁA J., Phys. Rev. B, 60 (1999), 13396.
[11] LUE C.S., ROSS JR J.H., RATHNAYAKA K.D.D., NAUGLE D.G., WU S.Y., LI W-H, J. Phys.: Cond. Matter, 13 (2001), 1585.
[12] BLAHA P., SCHWARZ K., MADSEN G. K. H., KVASNICKA D., LUITZ J., WIEN2k, *An Augmented Plane Wave + Local Orbitals Program for Calculation Crystal Properties* (Karlheinz Schwarz, Techn. Universität Wien, Austria), 2001; PERDEW J.P., BURKE K., ERNZERHOF M., Phys. Rev. Lett. 77 (1996), 3865.

Received 7 May 2006
Revised 1 September 2006

Materials Science-Poland, Vol. 25, No. 2, 2007

Mössbauer investigations of the magnetic structure of γ-Fe–Mn

K. SZYMAŃSKI[1*], W. OLSZEWSKI[1], D. SATUŁA[1], L. DOBRZYŃSKI[1, 2]

[1]Institute of Experimental Physics, University of Białystok, 15-424 Białystok, Poland

[2]The Sołtan Institute for Nuclear Studies, 05-400 Otwock-Świerk, Poland

Mössbauer polarimetry was used for investigations of orientations of Fe magnetic moments in a γ-Fe–Mn system. External magnetic field was applied to single crystal samples. Since the hyperfine field is a vector quantity, it forms a vector sum with the external magnetic field, and this quantity obviously depends on the magnetic structure of a system under study. Investigations with various orientations of external magnetic field with respect to the crystalline directions were performed. There is a clear experimental evidence that the distribution of Fe moments is present, which explains the already reported disagreement between simulated and measured results. Shapes of the spectra are best explained under the assumption of a coexistence of Q_2 and Q_3 structures. Influence of plastic deformation on the distribution of hyperfine fields is reported.

Key words: *γ-Mn-Fe alloy; manganese alloy; iron alloy; plastic deformation; Mössbauer spectroscopy*

1. Introduction

Magnetic structure of chemically disordered alloys in which atoms occupy *fcc* lattice positions has been a subject of intensive investigations. The symmetry of cubic structure allows at least three various antiferromagnetic structures with wave vectors $Q_1 = (1,0,0)$, $Q_2 = (1,1,0)$ and $Q_3 = (1,1,1)$, respectively. Because of formation of antiferromagnetic domains, all the magnetic structures result in the same neutron diffraction pattern. This makes experimental discrimination between the structures very difficult.

Mössbauer spectroscopy is sensitive to the direction of hyperfine magnetic field. Hyperfine magnetic field is a vector sum of external magnetic field and the local field. Thus the distribution of hyperfine fields observed in Mössbauer experiments depends on the magnetic structure (Q_1, Q_2 or Q_3) and the external magnetic field. The first measurements of single crystal γ-$Mn_{44.2}Fe_{55.8}$ by Kennedy and Hicks [1] disproved the

*Corresponding author, e-mail: kszym@alpha.uwb.edu.pl

Q_1 structure. Neither was the agreement of the spectra measured in the fields up to 9 T with simplest predictions for Q_2 or Q_3 structures satisfactory.

Other experiments were performed on $Mn_{60}Fe_{37}Cu_3$single crystals in which an external magnetic field of 1.3 T was applied along different crystalline directions [2]. In the spectra analysis, hyperfine fields were modelled by a binomial distribution (resulting from assumed random arrangements of atoms in the *fcc* lattice). The experiment was sensitive enough to detect the dependence of the orientation of hyperfine field on the applied external field. However, within the binomial approximation used in [2], the observed anisotropy could not be fully explained.

To check whether the distribution of atoms in Fe–Mn alloy is really random, we performed experiments in which crystal was plastically deformed. One expects that plastic deformation induces a change of the short range order, which should result in a change of the distribution of hyperfine fields. The spatial arrangement of spins in plastically deformed crystal was investigated with the use of circularly polarized radiation in Mössbauer measurements. This technique is sensitive to the sign of the hyperfine field, e.g. it can distinguish between parallel and antiparallel orientation of the magnetic moments with respect to the photon **k** vector.

2. Experimental

A single crystal γ-$Mn_{60}Fe_{37}Cu_3$ alloy was grown by the Bridgman method. Small amount of Cu was added to stabilize the *fcc* structure. Three flat samples of the thickness of about 0.5 mm were cut with their surfaces parallel to (100), (110) and (111) crystal planes, respectively. The samples were thinned by grinding to about 50–60 μm. In the next step, the samples were thinned by electrochemical methods to the thickness suitable for the Mössbauer transmission experiment [2]. Part of the crystal with linear dimensions 0.9 mm was cold rolled to a foil 6 μm thick.

Mössbauer measurements were performed in constant acceleration mode with unpolarized radiation. When no external field is applied to the absorber, the shape of the Mössbauer spectrum does not depend on the orientation of the **k** vector with respect to the crystalline direction [2], and the spectrum averaged over all measurements is shown in Fig. 1a. For the measurements in the magnetic field, the samples were placed in the hole of the permanent rare earth magnet producing an axial field of 1.3 T. The field was parallel to the **k** vector of the radiation and perpendicular to the sample surface. An example of the spectrum for **k** and $\mathbf{B}_{ext}$ perpendicular to the (100) and (111) planes is shown in Figs. 1b, c. The difference spectrum is shown in Fig. 2.

Measurement on the plastically deformed foil was performed in a texture free mode [3] with unpolarized radiation. The result is shown in Fig. 3a and is equivalent to the measurements averaged over random orientations of the absorber. Results of the Mössbauer polarimetric measurements with the use of circularly polarized radiation obtained by resonant filter technique [4], carried out on the deformed crystals in an

external field of 1.1 T, are shown in Figs. 3b, c. All Mössbauer measurements were performed at room temperature.

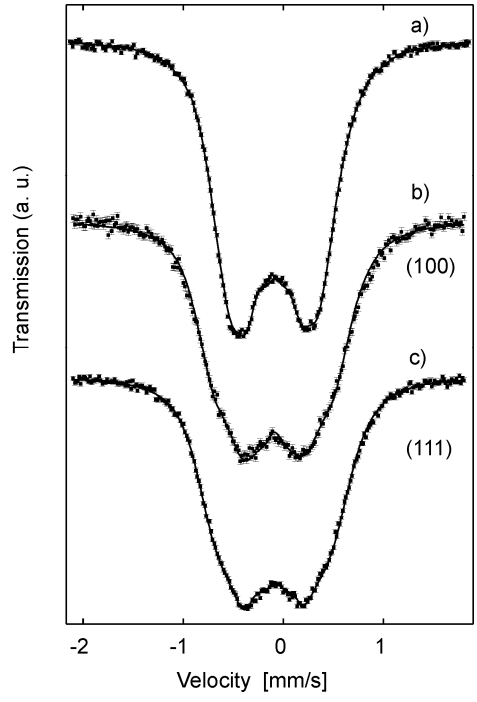

Fig. 1. Mössbauer spectra of a single crystal recorded with no applied external field (a), with external field of 1.3 T perpendicular to the (100) (b) and (111) (c) crystal planes

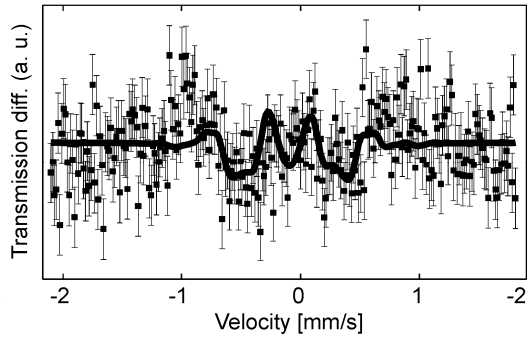

Fig. 2. Difference between the data shown in Fig 1b and c ((111) – (100)). The solid line shows the result of the simulation when Q_2 and Q_3 structures are present in the proportion 3:1

The principles of the Mössbauer polarimetric methods in the presence of a distribution of hyperfine fields are given elsewhere [5, 6]. We assume that the local hyperfine magnetic field $\mathbf{B}_{hf}$ is antiparallel to the Fe magnetic moments in the Q_i (i = 1, 2, 3) structure. The observed local field is a vector sum of the external magnetic field $\mathbf{B}_{\text{ext}}$ and the local hyperfine field $\mathbf{B}_{hf}$. Line intensities a_i in the Zeeman sextet are proportional to

$$\begin{aligned} a_1 : a_2 : a_3 : a_4 : a_5 : a_6 &= 3\left(1 \mp \cos\theta\right)^2 : 4\sin^2\theta : \left(1 \pm \cos\theta\right)^2 \\ &: \left(1 \mp \cos\theta\right)^2 : 4\sin^2\theta : 3\left(1 \pm \cos\theta\right)^2 \end{aligned} \tag{1}$$

where θ is an angle between the hyperfine magnetic field $\mathbf{B}_{ext} + \mathbf{B}_{hf}$ and the photon wave vector **k**.

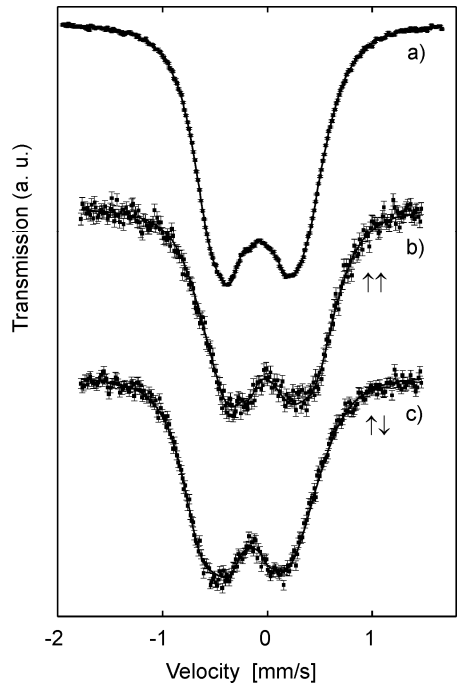

Fig. 3. Plastically deformed single crystal measured with: a) unpolarized radiation, b), c) circularly polarized radiation under an applied axial external magnetic field of 1.1 T. The arrows indicate two circular polarization states of the radiation. The solid lines, which show the best fits, are almost covered by the experimental points

Upper and lower signs correspond to the two opposite circular polarizations. In the case of unpolarized radiation, the expression is reduced to:

$$a_1 : a_2 : a_3 : a_4 : a_5 : a_6 = 3\left(1+\cos^2\theta\right) : 4\sin^2\theta : \left(1+\cos^2\theta\right) : \left(1+\cos^2\theta\right) : 4\sin^2\theta : 3\left(1+\cos^2\theta\right), \tag{2}$$

Next, we assume a certain distribution of the hyperfine magnetic field $P(|\mathbf{B}_{hf}|)$ and perform a simultaneous fit to all the spectra measured on single crystals. $P(|\mathbf{B}_{hf}|)$ distribution was approximated by the discrete set of $|\mathbf{B}_{hf,\mathbf{i}}|$ values and probabilities P_i. A nonlinear correlation between *IS* and $|\mathbf{B}_{hf}|$ was allowed, see Fig. 4. Zero quadrupole splitting was assumed according to previous investigations [1, 2]. Similar fit was performed to all the spectra measured on the deformed sample.

3. Results

For a given Q_i structure, the simultaneous fit procedure ("Mathematica" package used, for details of simultaneous fit and thickness correction see [5]) allows us to find $P(|\mathbf{B}_{hf}|)$ distribution for which agreement between measured and simulated spectra was

the best. We have found that for Q_1 structure, the agreement was definitely worse than for Q_2 and Q_3 structures. It was difficult to decide which of the two structures fits better. Moreover, we found that the best agreement is attained when the presence of both structures, Q_2 and Q_3 is assumed. This case is illustrated with typical examples in Fig 1, where ratio of volumes of the Q_2 and Q_3 phases was 3:1. To show clearly the anisotropy induced by an external field applied to a single crystal, difference of the spectra together with the difference of simulated curves are presented in Fig. 2. Some slight systematic deviation can be observed on the difference (Fig. 2), the origin of this behaviour being obscure. Nevertheless, the overall agreement shown in Fig. 1 is much better than in the already reported works [1, 2]. The distribution $P(|\mathbf{B}_{hf}|)$ found in the simultaneous fit to all measured spectra of single crystals is shown in Fig. 4 (note the areas of the circles).

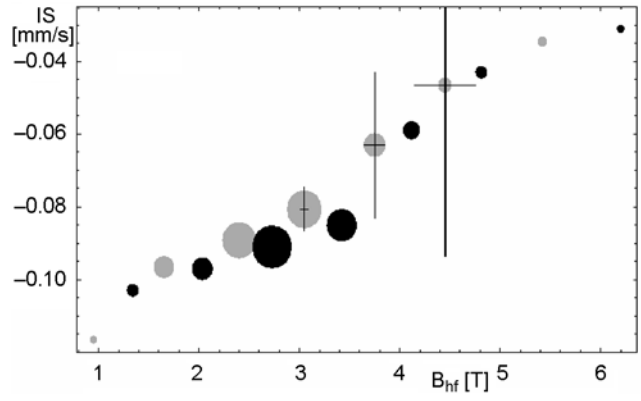

Fig. 4. Correlation between hyperfine magnetic field B_{hf} and isomer shift *IS*. The black circles correspond to single crystals, gray ones – to the plastically deformed samples. The area of the circle is proportional to the probability $P(|\mathbf{B}_{hf}|)$ and $P(IS)$

The plastically deformed sample is no longer a single crystal and was measured in the texture free mode in order to extract its distribution of the hyperfine field. As described in the previous section, all the experiments performed on the plastically deformed sample were simultaneously fitted under the assumption that the local field is equal to $\mathbf{B}_{ext}+\mathbf{B}_{hf}$, where and $\mathbf{B}_{hf}$ are arranged in random directions. The extracted hyperfine field distribution is shown in Fig. 4 by gray symbols and typical examples of the simulated spectra are shown in Fig. 3 by solid lines.

4. Discussion

In the interpretation of the results of the pioneering experiment of Kennedy and Hicks [1], the authors considered the movement of the domain walls. However, although the occupation of the domains was a free parameter, the shape of the simulated

spectra did not agree with the measured ones [1]. The presented results demonstrate clearly that the most important factor deciding on the agreement of simulated spectra with the measured ones is the shape of the distribution of hyperfine fields. A proper choice of the $P(|\mathbf{B}_{hf}|)$ function, achieved by fitting, results in the overall agreement of the measured spectra in zero field and in an applied external field. The method of determination of the $P(|\mathbf{B}_{hf}|)$ is so precise that it is possible to detect changes in short range order induced by plastic deformation. The differences, shown schematically in Fig. 4, can be presented clearly on the histograms (Fig. 5). It is clear from Fig. 5 that in the case of single crystals, both $P(|\mathbf{B}_{hf}|)$ and $P(IS)$ distributions, are narrower. Plastic deformation causes a slip of atomic planes resulting in the mixing of atoms and a more random distribution.

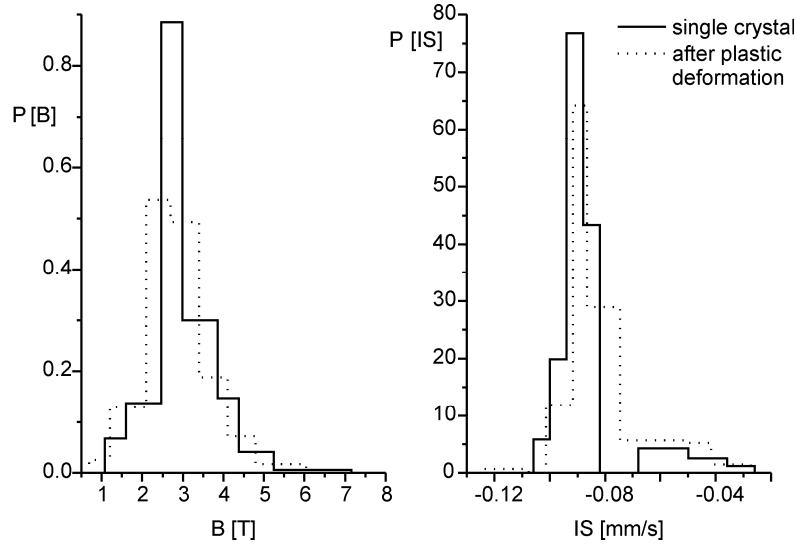

Fig. 5. Histograms related to $P(|\mathbf{B}_{hf}|)$ and $P(IS)$ distributions

The measurements with polarized radiation show that the spatial arrangement of magnetic moments remains unchanged, i.e. the recorded spectra can be explained by rigid arrangements of local hyperfine field vectors plus the external applied field. This picture is consistent with recent self-consistent tight binding linearized muffin-tin orbital approach allowing a noncollinear spin structure. It was shown that the ground spin states in a fully ordered and fully disordered gamma Fe–Mn alloys are different and their spin ordering is driven by the random substitutional disorder, a phenomenon known as ordering due to disorder [7]. In the measurements with circularly polarized radiation, only the Fe system is detected as a nuclear ^{57}Fe probe. Thus, the presented results show that in the system under investigation we do not observe, within an experimental accuracy, an antiparallel ordering of two systems: Fe and Mn. This important point was considered in electronic band structure calculations [8].

As presented in the previous section, the assumption regarding the presence of Q_2 or Q_3 state in a single crystal leads to a similar quality of the simultaneous fit, while the best agreement of simulations and measurements being obtained when the presence of both structures was assumed. This observation is in agreement with the first principles electronic structure calculations of noncollinear magnetic structures [8]. The Korringa–Kohn–Rostocker multiple-scattering approach, in conjunction with an extension of the single site coherent potential approximation, show that the Q_3 and Q_2 structures are both stable solutions. The energy difference between the two noncollinear states is relatively small with the Q_3 being more favorable. It was mentioned [8] that the difference, which corresponds to 60 K, is so small that the systems may occupy both states.

5. Conclusions

We have shown that in order to understand the magnetism of the alloy under study, a precise determination of the shape of the hyperfine magnetic field (h.m.f) distribution is required. Plastic deformation changes the short range order of atoms in a measurable way resulting in a change of the h.m.f. distribution. Among the two possible reasons influencing the shape of the spectra under the applied external field, i.e. the movement of domain walls and the presence of h.m.f. distribution, the latter one is more important.

Adjusting properly the shape of the distribution, we performed fits which indicate that Q_1 structure cannot be accepted, Q_2 and Q_3 structures result in a similar quality of the fits, while the assumption regarding the presence of both Q_2 and Q_3 structures gives the best fits. This can be expected from the results of the theoretical band structure calculations which indicate a small energy difference between Q_2 and Q_3.

References

[1] KENNEDY S.J., HICKS T.J., J. Phys. F: Met. Phys., 17 (1987), 1599.
[2] SZYMANSKI K., OLSZEWSKI W., DOBRZYNSKI L., SATULA D., JANKOWSKA-KISIELINSKA J., Nukleonika, 49 (2004), S75.
[3] GRENECHE M.J., VARRET F., J. Phys.-Lett., 43 (1982), L-233.
[4] SZYMAŃSKI K., DOBRZYŃSKI L., PRUS B., COOPER M.J., Nucl. Instr. Meth., B119 (1996), 438.
[5] SZYMANSKI K., SATULA D., DOBRZYNSKI L., VORONINA E.V., YELSUKOV E.P., MIYANAGA T., Phys. Rev. B 72 (2005), 104409.
[6] SZYMANSKI K., Phys. Rep. 423 (2006), 295.
[7] SPISAK D., HAFNER J., Phys. Rev. B, 61(2000), 11569.
[8] SCHULTHESS T.C., BUTLER W.H., MAAT S., MANKEY G.J., STOCKS G.M., J. Appl. Phys. 85(1999), 4842.

Received 7 May 2006
Revised 1 September 2006

Materials Science-Poland, Vol. 25, No. 2, 2007

The influence of substrate and cap layer on magnetic characteristics of some multilayers

I. STANIUCHA*, A. URBANIAK-KUCHARCZYK

Department of Solid States Physics, University of Łódź, ul. Pomorska 149/153, 90-236 Łódź, Poland

The influence of non-symmetrical boundary conditions, caused by different materials of the substrate and covering, on some properties of the systems consisting of magnetic layers separated by nonmagnetic spacer have been considered. Magnetic properties like spin wave patterns, FMR spectra, Curie temperature, magnetization and spin wave parameter B have been investigated for symmetrical and non-symmetrical structures like: Cu(111)/$(Fe/Cu)_n$/Fe/Cu/Si(111), vacuum/$(Fe/Cu(111))_n$/Fe/vacuum, vacuum/$(Fe/Cu)_n$/Si(111) and Cu/$(Fe/Cu)_n$/Fe/GaAs, vacuum/$(Fe/Cu)_n$/Fe/GaAs, where n is equal 1 or 2. Influence of roughness on selected characteristics of magnetic systems with non-symmetrical conditions on external surfaces has been also investigated.

Key words: *multilayers; FMR; Curie temperature; magnetisation; spin wave parameter*

1. Introduction

The structures consisting of magnetic layers separated by nonmagnetic spacer are interesting objects of research due to the their possible applications. Investigation of multilayers is always connected with the existence of a substrate determining crystal structure and anisotropy on the boundary surfaces. The other external surface should be protected by the cap layer. The process of preparation is the source of some roughness on the surfaces and interfaces of the structure; it modifies both interlayer exchange coupling and anisotropy parameters. Numerous papers have been devoted to the investigation of in what way cap layer thickness changes the Curie temperature [1–4] but only a few [5, 6] to the influence of external layers on the properties of multilayers. In the present paper, we consider the influence of substrate as well as cap of layers and their roughness on the basic magnetic properties of exchange coupled multilayers.

We assume the model according to which the interaction between magnetic layers separated by nonmagnetic metallic spacer can be described by the Heisenberg-type Hamiltonian:

*E-mail: staniuch@uni.lodz.pl

$$H = -\frac{1}{2}\sum_{\nu j,\nu' j'} J_{\nu j,\nu' j'} S_{\nu j} S_{\nu' j'} - g\mu_B H_{\text{eff}} \sum_{\nu j} S_{\nu j}^z - \frac{1}{2}\sum_{\nu j,\nu' j'} A_{\nu j,\nu' j'} S_{\nu j}^z S_{\nu' j'}^z \tag{1}$$

where ν denotes the number of monatomic planes and j the position of a lattice point in the plane, respectively.

The first sum in Eq. (1) is an exchange part of the Hamiltonian with the parameter $J_{\nu j,\nu' j'}$ equal to J inside magnetic layers and J_{12} standing for the interlayer exchange coupling parameter between the layers neighbouring the spacer. $A_{\nu j,\nu' j'}$ is the anisotropy parameter, being the sum of uniaxial volume anisotropy, and surface as well as interface anisotropy parameters, which are determined by the material of substrate and cap layer. H_{eff} denotes the sum of the external field oriented perpendicularly to the surface and the demagnetising field. The interlayer exchange coupling J_{12} in our paper has been derived based on the model proposed by Bruno and Chappert [7, 8], and can be modified similarly as in [9] by roughness described by solid-on-solid and discrete Gaussian models [10–12]. According to the relation proposed by Bruno [13] we took into account decreasing of anisotropy parameters for rough surfaces and interfaces in comparison to the ideal ones.

2. Results

In this section, we discuss numerical results for the Curie temperature, magnetisation, and spin waves parameter obtained for several systems using the Green function formalism [14]. First, we consider the influence of the substrate and cap layer materials (via surface anisotropy parameters) on the spin wave patterns and FMR spectra of magnetic trilayers. Figure 1a presents characteristics obtained for structures with the same material taken for the substrate, cap layer and spacer. We observe only one-peak FMR spectra. Changing the material and anisotropy parameters on both surfaces (Fig. 1b) causes a shift of the most intensive peak and appearance of an additional line in the FMR spectra. "Non-symmetrical" boundary conditions, related to different materials on external surfaces presented in Fig. 1c, give a small shift of the first mode line and a change of intensities of the others. In the presented example, only the latter configuration leads to a visible modification of spin wave patterns.

We have also examined the dependence of the Curie temperature of bi- and trilayers as a function of the spacer thickness. The results obtained are presented in Fig. 2. One can see from Fig. 2a that different materials on the surfaces of the multilayer are the source of reduction of the Curie temperature in comparison to the systems with the same materials on both external surfaces. Our results were obtained for a selected system, thus one should be very careful with generalizing them because shift of T_c depends on the number of magnetic layers, their thickness and anisotropy parameters on the surfaces and interfaces.

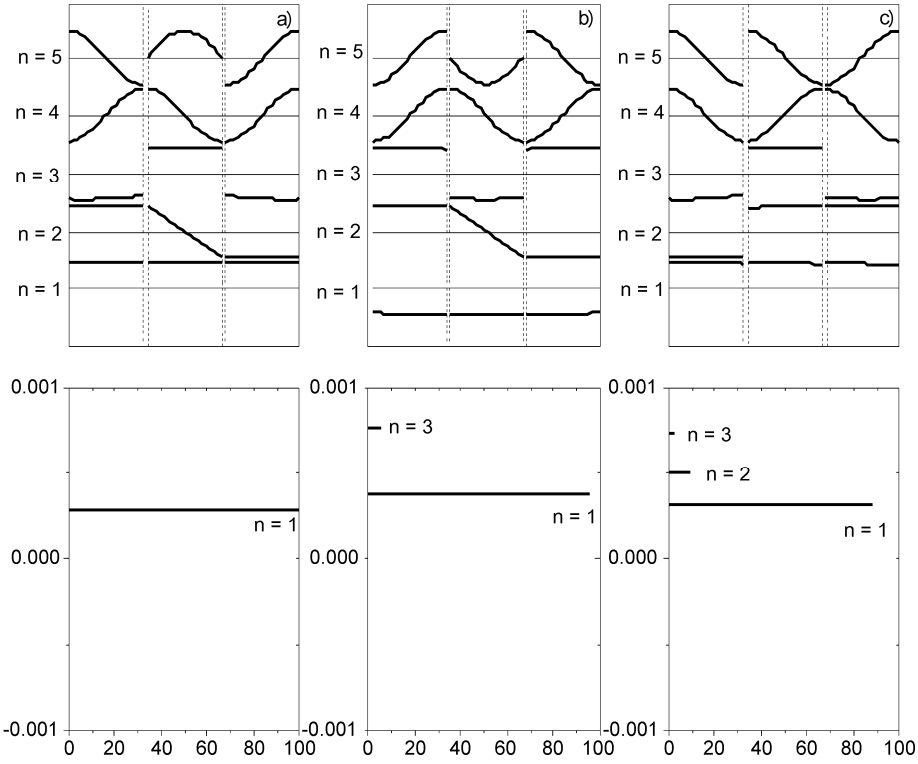

Fig. 1. Spin wave patterns (upper plots) and FMR spectra (bottom) for the systems: a) Cu(111)/Fe/Cu/Fe/Cu/Fe/Cu/Si(111) [15, 16], b) vacuum/Fe/Cu/Fe/Cu/Fe/vacuum [17], c) vacuum/Fe/Cu/Fe/Cu/Fe/Cu/Si(111). The layers of Si do not give any contribution to the anisotropy parameters. The thickness of each magnetic layer is equal to 20 ML's (labelling of horizontal axis of upper plots is omitted). The thickness of each spacer equal to 3ML's; *n* corresponds to the successive number of the spin wave mode. The energy axis in FMR spectra is given in arbitrary units

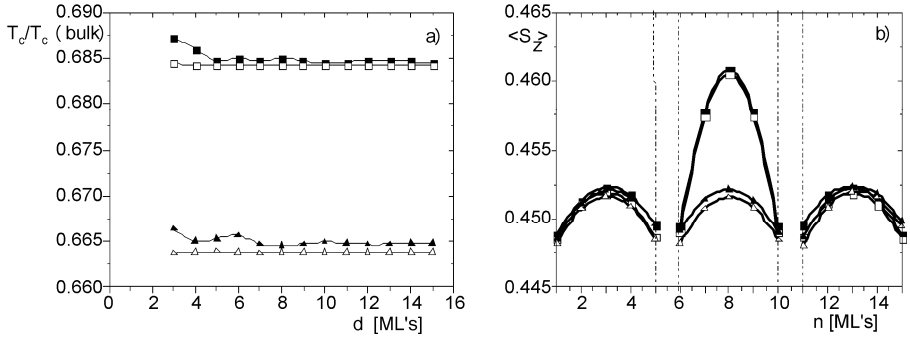

Fig. 2. The Curie temperature as a function of spacer thickness (a) and magnetisation profiles (b) for ■ – Cu/…./Cu/Si(111) (flat), □ – Cu/…./Cu/Si(111) (rough), ▲ – vacuum/…./Cu/Si(111) (flat) and △ – vacuum/…./Cu/Si(111) (rough), where rough or flat in brackets denotes degrees of surface roughness. Thickness of each magnetic layer is equal to 5 MLs and the spacer – 3 ML's. The structure between the slashes /…/ is Fe/Cu/Fe/Cu/Fe. The width of the "gap" is not related to the spacer thickness

Figure 2b shows magnetisation profiles for the same systems as in Fig. 2a. In this case, modification of magnetisation in an *n*-th monolayer of magnetic layers by changing the boundary surface anisotropies is especially visible in the middle of the structure. For the system with "non-symmetric" boundary condition, the magnetisation is significantly smaller in comparison to the system with the same material on both surfaces. The magnetisation inside the external magnetic layers is only slightly modified, a similar behaviour is observed in magnetic bilayers. The results presented in Fig. 2b indicate that changes in magnetisation distribution caused by the change of boundary conditions are too small to expect their experimental verification.

This behaviour of the Curie temperature and magnetisation is observed for both flat and rough surfaces and interfaces as we can see from the comparison of the characteristics with open symbols in Fig. 2 to those with filled symbols. The shift of respective curves is more significant for different systems than for the same ones but with different degrees of roughness.

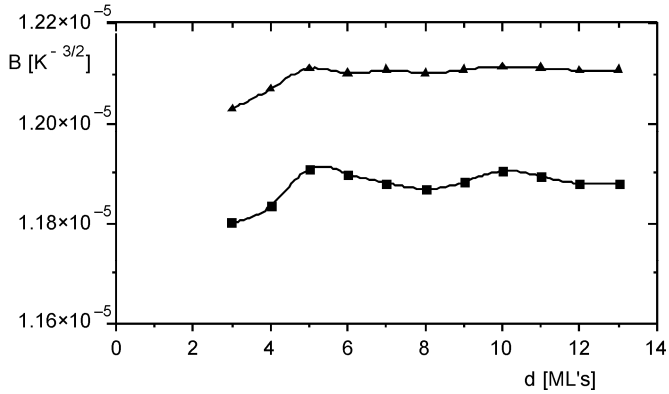

Fig. 3. The influence of spacer thickness on spin wave stiffness parameter for: ■ – Cu(111)/Fe/Cu/Fe/Cu/Fe/Cu/Si(111) and ▲ – vacuum/Fe/Cu/Fe/Cu/Fe/Cu/Si(111). The thickness of each spacer is equal to 3 ML's and of magnetic layers to 5 ML's

We obtained numerical results for the spin wave parameter B appearing in the Bloch law for two chosen structures: Cu(111)/Fe/Cu/Fe/Cu/Fe/Cu/Si(111) and vacuum/Fe/Cu/Fe/Cu/Fe/Cu/Si(111). Although the difference between the values of this parameter for the considered structures is not significant, both characteristics in Fig. 3 can be easily distinguished. As we expected, the B parameter is an oscillating and decreasing function of the spacer thickness similarly as the interlayer exchange parameter J_{12} [18].

3. Conclusions and final remarks

Results presented in this paper can be approximately compared to the experimental results for the Curie temperature [19] and for spin wave parameter [20, 21],

respectively. The order of magnitude for both cases is the same but a more exact comparison requires experimental investigation of the considerd systems. As we have shown, the influence of the roughness of surfaces and interfaces on the considered characteristics is less pronounced than the influence of anisotropy parameters in the border layers. We expect that it is possible to observe a visible experimental effect of the influence of diversity of substrate and cap layers on the properties of multilayered magnetic structures.

Acknowledgements

This work has been partially sponsored by the Grant of Uniwersity of Łódź, No 505/692.

References

[1] BRUNO P., KUDRNOVSKÝ J., PAJDA M., DRCHAL V., TUREK I., J. Magn. Magn. Mater., 240 (2002), 346.
[2] VOLLMER R., VAN DIJKEN S., SCHLEBERGER M., KIRSCHNER J., Phys. Rev. B, 61 (2000), 1303.
[3] WILHELM F., BOVENSIEPEN U., SCHERZ A., POULOPOULOS P., NEY A., WENDE H., CEBALLOS G., BABERSCHKE K., J. Magn. Magn. Mater., 222 (2000), 163.
[4] RÜDT C., SCHERZ A., BABERSCHKE K., J. Magn. Magn. Mater., 285 (2005), 95.
[5] MADAMI M., TACCHI S., CARLOTTI G., GUBBIOTTI G., STAMPS R.L., Phys. Rev. B, 69 (2004), 144408.
[6] ENDERS A., MONCHESKY T.L., MYRTLE K., URBAN R., HEINRICH B., KIRSCHNER J., ZHANG X.-G., BUTLER W.H., J. Appl. Phys., 89 (2001), 7110.
[7] BRUNO P., CHAPPERT C., Phys. Rev. B, 46 (1992), 261.
[8] BRUNO P., CHAPPERT C., Phys. Rev. Lett., 67 (1991), 1602.
[9] WANG Y., LEVY P.M., FRY J.L., Phys. Rev. Lett., 65 (1990), 2732.
[10] WEEKS J., [in:] *Ordering in Strongly Fluctuating Condensed Matter System*, T. Riste (Ed.), Plenum Press, New York (1980), p. 293.
[11] SAITO Y., [in:] *Ordering in Strongly-Fluctuating Condensed Matter Systems*, T. Riste (Ed.), Plenum Press, New York (1980) p. 319.
[12] SAITO Y., Z. Physik B, 32 (1978), 75.
[13] BRUNO P., J. Appl. Phys., 64 (1988), 3153.
[14] URBANIAK-KUCHARCZYK A., phys. stat. sol. (b), 203 (1997) 195.
[15] GUBBIOTTI G., CARLOTTI G., MADAMI M., TACCHI S., VERDINI L., phys. stat. sol. (a), 189 (2002), 403.
[16] GUBBIOTTI G., CARLOTTI G., MONTECCHIARI A., DE CRESCENZI M., ZIVIERI R., GIOVANNINI L., NIZZOLI F., Phys. Rev. B, 62 (2000), 16 109.
[17] MONCHESKY T.L., HEINRICH B., URBAN R., MYRTLE K., KLAUA M., KIRSCHNER J., Phys. Rev. B, 60 (1999), 10242.
[18] BAYREUTHER G., BENSCH F., KOTTLER V., J. Appl. Phys., 79 (1996), 4509.
[19] VOLLMER R., VAN DIJKEN S., SCHLEBERGER M., KIRSCHNER J., Phys. Rev. B, 61 (2000), 1303.
[20] KUPRIN A.P., CHENG L., ALTOUNIAN Z., RYAN D.H., J. Appl. Phys., 87 (2000), 6591.
[21] PECHAN M.J., FULLERTON E.E., SCHULLER I.K., J. Magn. Magn. Mater., 183 (1998), 19.

Received 7 May 2006
Revised 1 September 2006

Materials Science-Poland, Vol. 25, No. 2, 2007

Photoemission study of Eu 2+/3+ ions in ferromagnetic (Eu,Gd)Te semiconductor layers

P. DZIAWA[1*], B. A. ORŁOWSKI[1], V. OSINNIY[1], M. PIETRZYK[1]
B. TALIASHVILI[1], T. STORY[1], R.L. JOHNSON[2]

[1]Institute of Physics, Polish Academy of Sciences, al. Lotników 32/46, 02-668 Warsaw, Poland

[2]Hamburger Synchrotronstrahlungslabor HASYLAB am Deutschen Elektronen-Synchrotron DESY, Notkestr. 85, D-22603 Hamburg, Germany

(Eu,Gd)Te ferromagnetic semiconductor layers grown by molecular beam epitaxy technique on BaF_2 (111) monocrystalline substrates were investigated by resonant photoemission spectroscopy using synchrotron radiation. In n-(Eu,Gd)Te layers, a ferromagnetic transition induced by electron concentration is observed. Magnetic as well as electrical properties of this material depend strongly on the charge state (2+ vs. 3+) of Eu and Gd ions known to be sensitive to crystal stoichiometry and formation of oxide complexes. The relative concentration of Eu^{2+} and Eu^{3+} ions was determined from the analysis of the resonant photoemission energy distribution curves (EDC), measured at photon energies close to 4d–4f resonance. After various in-situ annealing and Ar sputtering procedures, a clear improvement of crystal stoichiometry of (Eu,Gd)Te layers was observed as manifested by the increase of Eu^{2+} intensity in the spectra. Contribution of Eu 4f shell to the total density of states was also analyzed and found at the valence band edge for Eu^{2+} ions and about 6 eV lower for Eu^{3+} ions.

Key words: *spintronics; ferromagnetic semiconductor; rare earth compound; photoemission*

1. Introduction

Due to a strong ionic bonding in EuX (X = O, S, Se, Te), Eu ions are expected to be divalent in all members of the group of europium monochalcogenides resulting in a half-filled $4f^7$ shell of Eu. It yields spin only magnetic moment $S = 7/2$ localized on Eu ions in the rock-salt crystal lattice of EuX. This feature makes these materials an excellent example of a model Heisenberg magnet. In the EuX family, there are two ferromagnets (EuO and EuS) and one antiferromagnetic material (EuTe), whereas EuSe exhibits a more complicated phase diagram due to the compensation of ferro-

*Corresponding author, e-mail: dziawa@ifpan.edu.pl

magnetic (nearest neighbour) and antiferromagnetic (next nearest neighbour) exchange interactions [1–4]. Doping EuX with an electrically active element brings an additional indirect exchange interaction between magnetic moments of Eu via spin polarization of quasi-free carriers (the Ruderman–Kittel–Kasuya–Yosida, RKKY mechanism). EuX doped with gadolinium is particularly interesting. Gd ions substituted in (Eu,Gd)X are expected to be in 3+ charge state having the same electronic ($4f^7$) configuration. This substitution does not affect the magnetic subsystem but supplies the material with quasi-free electrons in the conduction band. Assuming that each Gd ion gives one extra electron, one can obtain very high concentration of electrons ($n \approx 1.4\times10^{20}$ cm^{-3} corresponds to 1 at. % of Gd in EuTe). For bulk (Eu,Gd)X increase of critical temperature with increasing Gd concentration and, in particular, transformation type of the magnetic transition from antiferro- to ferromagnetic in the case of (Eu,Gd)Te at Gd content about 5 at. % was reported in [1]. Hence the latter makes it possible to change simultaneously both electrical properties, from insulator for EuTe to n-type metallic conductivity for (Eu,Gd)Te, and magnetic ordering from antiferromagnetic to ferromagnetic, respectively.

Eu (as well as Gd) is known to form not only monochalcogenides (EuX) with Eu ions in 2+ charge state but also other compounds like Eu_2X_3 with Eu ions in 3+ state. Detailed experimental information on Eu charge state in (Eu,Gd)Te is very important for both magnetic and electrical properties of this material. It was reported that an excess of Te in (Eu,Gd)Te can result in a strong decrease of very high concentration of electrons, even leading to a total compensation of charge carriers and dramatic changes in magnetic properties [5]. There was also observed a behaviour qualitatively different from a typical response of ferromagnetic material on applied external magnetic field for n-(Eu,Gd)Te which can be attributed to creation of complexes other than Eu–Te or Gd–Te [6]. In this work, we use resonant photoemission spectroscopy technique to verify the Eu charge state in (Eu,Gd)Te layers grown by molecular beam epitaxy on BaF_2 (111) substrates. We analyze the influence of various annealing and sputtering procedures on the Eu^{2+}/Eu^{3+} concentration ratio. We also determine the binding energy of Eu ion states derived from magnetic 4f orbitals with respect to valence band edge of (Eu,Gd)Te. This experiment is based on the Fano effect when the energy of excitation photons is adjusted to 4d–4f transition which is manifested in an asymmetrical shape of photoemission spectra observed as maximum and minimum at the energies corresponding to resonance and anti-resonance [7].

2. Experimental results

The (Eu,Gd)Te epitaxial layers were grown using a home-built MBE system equipped with effusion cells for Eu, Gd and Te solid sources. Freshly cleaved, (111)-oriented BaF_2 monocrystals were used as substrates. First, an EuTe buffer layer, up to 0.1 μm thick, was grown, and next, 0.25 μm thick (Eu,Gd)Te layer was depos-

ited. The substrate temperature during the growth of both layers was about 270 ºC. *In-situ* growth control using reflection high-energy electron diffraction (RHEED) revealed well defined streaky pattern indicating a two-dimensional mode of layer growth. Intensity oscillations of the RHEED specular spot allowed us to determine quite low rate of growth of 0.1 ML/s (ML – monolayer). X-ray diffraction (XRD) measurements proved good monocrystallinity of the epilayers with full width at half maximum (FWHM) X-ray rocking-curve parameter in the range of 200–400 arcsec. From energy dispersive X-ray fluorescence (EDXRF) analysis, the Gd content was determined to be typically close to 1 at. %.

The photoemission experiments were performed at the FLIPPER II beam line at the HASYLAB synchrotron radiation laboratory in Hamburg. Angle-integrated photoemission spectra were recorded using a cylindrical-mirror energy analyzer (CMA -type, PHI 25-260) with energy resolution of 250 meV. (Eu,Gd)Te was exposed to a beam of photons with energy in the range from 120 eV to 160 eV. The experiment was carried out sequentially. Four annealing processes (each for 3 h) were performed at the following temperatures: 240 °C, 270 °C, 300 °C and 350 °C. After each annealing process, the set of energy distribution curves (EDC) was taken. Finally, sputtering with Ar ions with an energy of 600 eV was applied for 1 h to remove the thin top layer, which may contain excess Te diffused during the annealing processes.

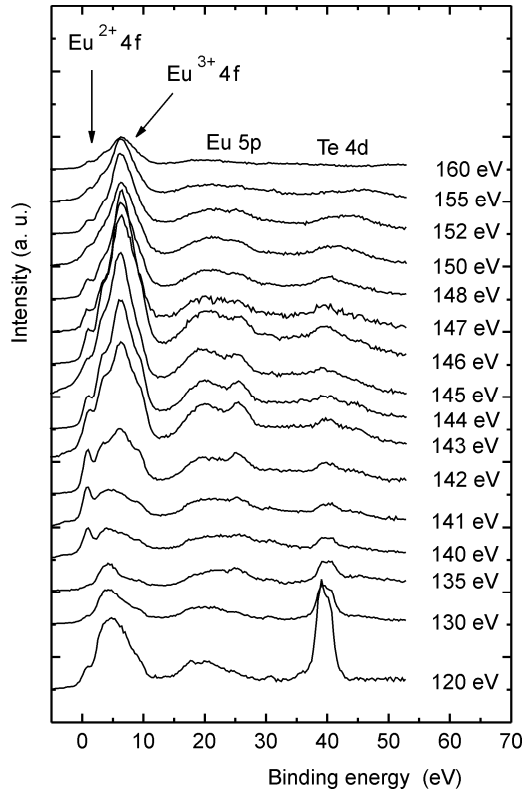

Fig. 1. The set of energy distribution curves for (Eu,Gd)Te epilayer taken after annealing of as introduced sample at 240 °C. The energy of excitation of photons equal to 141 eV corresponds to the resonance for Eu^{2+} ions. Energy position of Eu^{2+} was found to be at the edge of the valence band, while Eu^{3+} is located at approximately 6 eV below it. The spectra show major contribution of Eu^{3+} connected to an excess of Te as well as oxidation in the sample volume

Figure 1 presents a set of the energy distribution curves of photoemission spectra collected after the first annealing process at 240 °C. The graph shows peaks originated from the 4f-shell of Eu in both charge states 2+ and 3+ located at the edge of the valence band and about 6 eV below it, respectively. The 5p shell of Eu was established to be at binding energy position of about 20 eV. The Te 4d core shell with binding energy about 40 eV was also observed. In the set of EDCs, there was observed both a strong enhancement and extinction of intensity at energy position of Eu^{2+} and Eu^{3+} related to intra-ion transitions in Eu known as Fano resonance. Namely, apart from classical photoemission process (direct excitation of electron from $4f^7$ shell to vacuum) there was also observed an additional emission process as follows:

$$[\mathrm{Xe}]\ 4d^{10}4f^7 + h\nu \rightarrow ([\mathrm{Xe}]\ 4d^9 4f^8)^* = [\mathrm{Xe}]\ 4d^{10}4f^6 + e \quad (1)$$

$$[\mathrm{Xe}]\ 4d^{10}4f^6 + h\nu \rightarrow ([\mathrm{Xe}]\ 4d^9 4f^7)^* = [\mathrm{Xe}]\ 4d^{10}4f^5 + e \quad (2)$$

where * denotes excited state. Based on these results, the Fano profile shown in Fig. 2 was obtained. The resonant energies were found to be equal 141.5 and 145.2 eV for Eu^{2+} and Eu^{3+}, respectively.

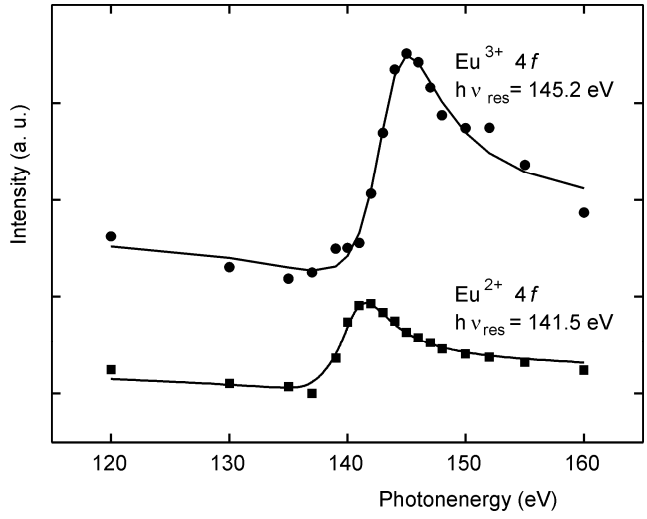

Fig. 2. Fano resonance for Eu^{2+} and Eu^{3+} ions of (Eu,Gd)Te layers obtained based on the EDC spectra measured after the first annealing process. Resonant (4d–4f transition) energies for Eu^{2+} and Eu^{3+} are marked in the figure

To verify the influence of thermal treatment on (Eu,Gd)Te epilayers, the EDC spectra at resonant energy of 141 eV were taken at sequential stages of preparation. To enhance the changes, the plots were normalized to intensity at energy position of Eu^{3+}. At the first step, for the as introduced layer, it was observed that the contribution of Eu^{3+} ions is comparable to Eu^{2+} ions. This fact can result from the excess of Te in the layer, but more likely it is related to surface oxidation. Further annealing processes

show the increase of the Eu^{2+} peak intensity against the Eu^{3+} one. Despite an improvement of the stoichiometry in the sample volume due to diffusion of Te, a substantial increase of Te in thin film close to the surface was expected. This supposition was confirmed by observation of a high intensity peak originated from Eu^{3+}. To check this assumption, sputtering with Ar ions was carried out and the top layer of about 50–100 nm was removed. As shown in Fig. 3, this procedure results in a further increase of the Eu^{2+}/Eu^{3+} ratio of photoemission intensities revealing considerable decrease of Eu^{3+} ions concentration (although still observed). It seems that this is connected to the creation of oxides (Eu_2O_3). Very recent secondary ions mass spectrometry (SIMS) investigations performed on a (Eu,Gd)Te sample grown two years ago showed the incorporation of oxygen in the whole volume of the sample on a significant level. Such results point out the necessity of protecting the surface of (Eu,Gd)Te layer with Te or PbTe thin capping layer.

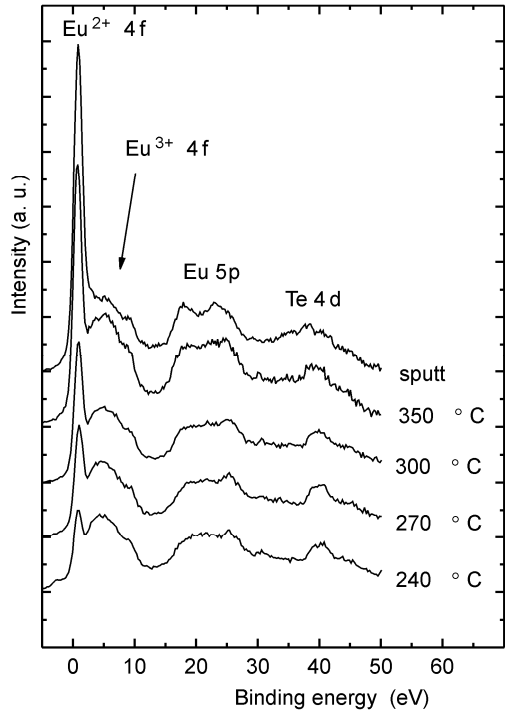

Fig. 3. EDC spectra of (Eu,Gd)Te layer after sequential surface preparation procedures (see the experimental section). All presented curves were normalized to their intensities at energy position of Eu^{3+}

3. Conclusions

In this work, the (Eu,Gd)Te epitaxial layers were investigated by resonant photoemission spectroscopy using synchrotron radiation. From the analysis of the energy distribution curves, Fano resonances were determined for both Eu^{2+} and Eu^{3+} ions at the energies of 141.5 and 145.2 eV, respectively. Contribution of Eu 4f-shell to the total density of states was found to be located at the valence band edge for Eu^{2+} ions

while it was about 6 eV lower for Eu^{3+}ions. From EDC spectra measured after different annealing procedures (varying the annealing temperature) at a photon energy close to 4d–4f resonance transition for Eu in 2+ charge state, we found the improvement of crystal stoichiometry of (Eu,Gd) Te layers manifested by the increase of Eu^{2+} intensity in the photoemission spectra. The complete disappearance of Eu^{3+} contribution to the photoemission spectra could not be achieved, what we attribute to the formation of Eu oxide complexes in the layer.

Acknowledgements

This work was supported by MEiN research project.

References

[1] HOLTZBERG F., MCGUIRE T.R., METHFESSEL S., J. Appl. Phys., 37 (1966), 976.
[2] WATCHER P., *Handbook on the Physics and Chemistry of the Rare Earth*, North Holland, Amsterdam, 1979.
[3] MAUGER A., GODART C., Phys. Rep., 141 (1986), 51.
[4] MOLNAR VON S., J. Supercond., 16 (2003), 1.
[5] DZIAWA P., TALIASHVILI B., DOMUCHOWSKI W., ŁUSAKOWSKA E., ARCISZEWSKA M., DEMCHENKO I., DOBROWOLSKI W., DYBKO K., FEDORYCH O.M., NADOLNY A.J., OSINNIY V., PETROUCHYK A., STORY T., Acta Phys. Pol. A, 106 (2004), 215.
[6] DZIAWA P., OSINNIY V., TALIASHVILI B., DOMUKHOVSKI V., ŁUSAKOWSKA E., DYBKO K., DOBROWOLSKI W., KOWALCZYK L., STORY T., GOIRAN M., Proc. 12th Int. Conf. on Narrow Gap Semiconductors, Toulouse 2005, IOP Conf. Ser., 187 (2006), 21.
[7] KOWALSKI B.J., GOŁACKI Z., GUZIEWICZ E., KOZANECKI A., ORŁOWSKI B.A., GHIJSEN J., JOHNSON R.L., J. Alloys Comp., 286 (1999), 121.

Received 7 May 2006
Revised 1 September 2006

Materials Science-Poland, Vol. 25, No. 2, 2007

Optical and magneto-optical study of Fe/Si multilayers

L. UBA[1*], S. UBA[1], A. POLEWKO-KLIM[1], E. MINIUK[1], T. LUCIŃSKI[2], P. WANDZIUK[2], A.N. YARESKO[3], V.N. ANTONOV[4]

[1]Institute of Physics, University of Białystok, 15-424 Białystok, Poland

[2]Institute of Molecular Physics, Polish Academy of Sciences, 60-179 Poznań, Poland

[3]Max-Planck Institut for the Physics of Complex Systems, Dresden D-01187, Germany

[4]Institute of Metal Physics, Kiev 252142, Ukraine

Experimental and theoretical investigations of the optical and magneto-optical (MO) properties of sputter deposited Fe/Si_xFe_{1-x} multilayers (MLS) are presented. The diagonal and off-diagonal components of the optical conductivity tensor of the MLS have been determined in the photon energy range 0.8–5.8 eV from the measurements of the magneto-optical complex Kerr angles and the optical data measured by the spectroscopic ellipsometry and compared with the theoretical ones calculated from first principles in density functional theory by the LMTO method within the supercell approach. The calculations have been performed for different models of iron silicide structures. In particular, various spacer layer structures: metallic FeSi and semiconducting $FeSi_2$ iron-silicide phases, as well as pure Si and Fe were investigated. The comparison of the recorded and calculated spectra confirm the conclusion inferred from other studies that the spacer layer structures represent semiconducting ε-FeSi and β-$FeSi_2$ phases rather than the metallic FeSi phase.

Key words: *magnetic multilayer; interface; magneto-optical spectrum; ab-intio calculations*

1. Introduction

Multilayered films consisting of transition metals and semiconductors have attracted a lot of interest because of their unique properties and possible application in the semiconductor industry. The basic phenomenon of the Fe/Si multilayer systems that will decide about the future application of the structure in the area of spintronics is the strong antiferromagnetic (AF) coupling between Fe sublayers within a wide

[*]Corresponding author, e-mail: uba@alpha.uwb.edu.pl

range of nonmagnetic spacer layer thicknesses [1]. Many studies have been done to understand the mechanism of interlayer coupling in the system and its relation to the transformation of Si spacer layer into iron silicides [1–3]. Fe and Si form a rich variety of stable bulk binary alloys and several iron silicides have been identified. The nonmagnetic $FeSi_2$ compound exists in a stable orthorhombic semiconducting phase known as β-$FeSi_2$ and an unstable tetragonal metallic α-$FeSi_2$ phase. FeSi silicides exist in two phases: a stable semimetallic nonmagnetic ε-FeSi with cubic *B*20 type of structure and a metastable metallic with *B*2 (CsCl) structure. Moreover, there are few ferromagnetic phases that include Fe_5Si_3 alloy with the Mn_5Si_3 structure, Fe_3Si with the DO_3 structure, and metallic hexagonal Fe_2Si phase.

The nature of iron-silicides spontaneously formed during MLS growth responsible for the observed Fe/Si MLS magnetic and electrical properties was the subject of many studies [1–7]. A strong AF coupling in the Fe/Si MLS is mediated by Fe–Si silicides which may arise from the interdiffusion during the growth. There is an experimental evidence that Fe-Si silicides responsible for the AF coupling between Fe layers can exhibit semiconducting highly resistive character [2–4] or (depending on sublayer thicknesses and preparation technique) metallic properties [1, 5–7].

It is clear that the composition of the spacer layer formed during deposition of films is nonuniform [1, 3]. There is still some controversy about the structure and stoichiometry of the Fe/Si MLS interface region and the goal of the present work was to provide additional information about the chemical composition of the interface by applying experimental optical and magneto-optical spectroscopy methods, phenomenological multireflection calculations and *ab-initio* calculations of some model structures [8]. Effective optical and magneto-optical response of the layered structures is directly related to the thickness and properties of constituent sublayers that, in turn, depend on the nominal thickness of Fe and Si, interfacial mixing and roughness. The structure of Fe/Si MLSs can be verified by comparing the results of model calculations with the experiment.

2. Experimental

The set of Fe/Si_xFe_{1-x} MLS films was prepared in UHV chamber by magnetron-sputtering method on oxidized, (001)-oriented Si substrate. Various spacer layer compositions (x = 100, 66, 50) were intentionally deposited and the spacer layer thickness d was varied within the range from 0.5 nm to 3.0 nm. Each film was composed of 15 (Fe/Si) bilayer periods, the nominal Fe sublayer thickness being fixed at 3 nm. Crystal structures of the samples and their periodicity were examined by the high- and low angle X-ray diffraction. The analysis of the X-ray data indicates that the resulting film structure is close to amorphous. The films after deposition were characterized by many techniques [2, 3]. In this work, the optical and magneto-optical spectroscopy and magneto-optical magnetometry studies were carried out to study the composition of Fe/Si_xFe_{1-x} MLS spacer layers.

The films were studied experimentally by means of the Kerr effect in polar and longitudinal geometry as a function of magnetic field up to 2.4 T and photon energy in the range of 0.74–5.8 eV. The diagonal and off-diagonal components of the optical conductivity tensor of the MLS were determined from the measured Kerr rotation and ellipticity and the optical data were recorded by spectroscopic ellipsometry. The theoretical spectra were calculated from first principles in the density functional theory by the LMTO method with the use of the supercell approach. Details of the experimental and theoretical procedures have been published elsewhere [9].

3. Results and discussion

Magnetic, optical and magneto-optical properties were studied at room temperature for Fe/Si_xFe_{1-x} MLS with nominal thicknesses $d_{Fe} = 3$ nm and $d_{Si} = 0.9$, 1.35, 2.55 nm. Figure 1 shows the dependence of the Kerr rotation on the magnetic field applied parallel and perpendicular to the film surface for three various spacer layer compositions. The measured polar and longitudinal Kerr hysteresis loops for the Fe/Si_xFe_{1-x} MLS films exhibit behaviour typical of the AF coupled sublayers. The strength of the interlayer coupling depends strongly on thickness and composition of the spacer layer and agrees with the results obtained from magnetometry measurements [2]. The in-plane saturation field determines the strength of the AF interlayer exchange coupling. The strongest AF coupling has been found for Fe/Si MLS with nominal Si thickness equal to 1.35 nm. The Kerr rotation dependence on the magnetic field applied perpendicular to the films shows that the Fe/Si sample with the strongest AF has no saturation in the field of up to 2.4 T, suggesting the presence of an important paramagnetic fraction with high susceptibility or strong in-plane anisotropy. As is seen from Fig. 1, the magnetization is in the sample plane. It has been verified experimentally that no easy axis exists in the MLS film planes.

To answer the question which Fe–Si phase promotes the MLS interlayer exchange coupling, the optical properties of the spacer layer prepared by the same technique were investigated at first step. In Figure 2, the measured optical conductivity components are shown for Fe, $Fe_{50}Si_{50}$ and $Fe_{33}Si_{66}$ alloy films, and for Si(100) substrate. The results of the energy dependence of optical conductivity show for both the $Fe_{50}Si_{50}$ and $Fe_{33}Si_{66}$ alloys large and positive dispersive parts, and strongly decreasing absorptive parts with the decrease of photon energy in the IR region of spectra, characteristic of a semiconducting-like behavior. These alloys represent semiconducting ε-FeSi and β-$FeSi_2$ phases rather than metallic α-FeSi and c-FeSi with CsCl structure.

To support the observation, optical conductivity spectra were calculated from first principles for ε-FeSi, β-$FeSi_2$, c-FeSi, and *bcc* Fe. The results are presented in Fig. 3 together with the calculated spectra of the crystalline and amorphous silicon. From the comparison of the recorded and calculated spectra it can be seen that the results confirm the above stated conclusion, despite the existing differences in the amplitudes, widths and energy positions of the spectral peaks. In particular, the optical conductivi-

ty spectra of the metallic c-FeSi system exhibit different behaviour in the UV-spectral range as compared to semiconducting ε-FeSi alloy.

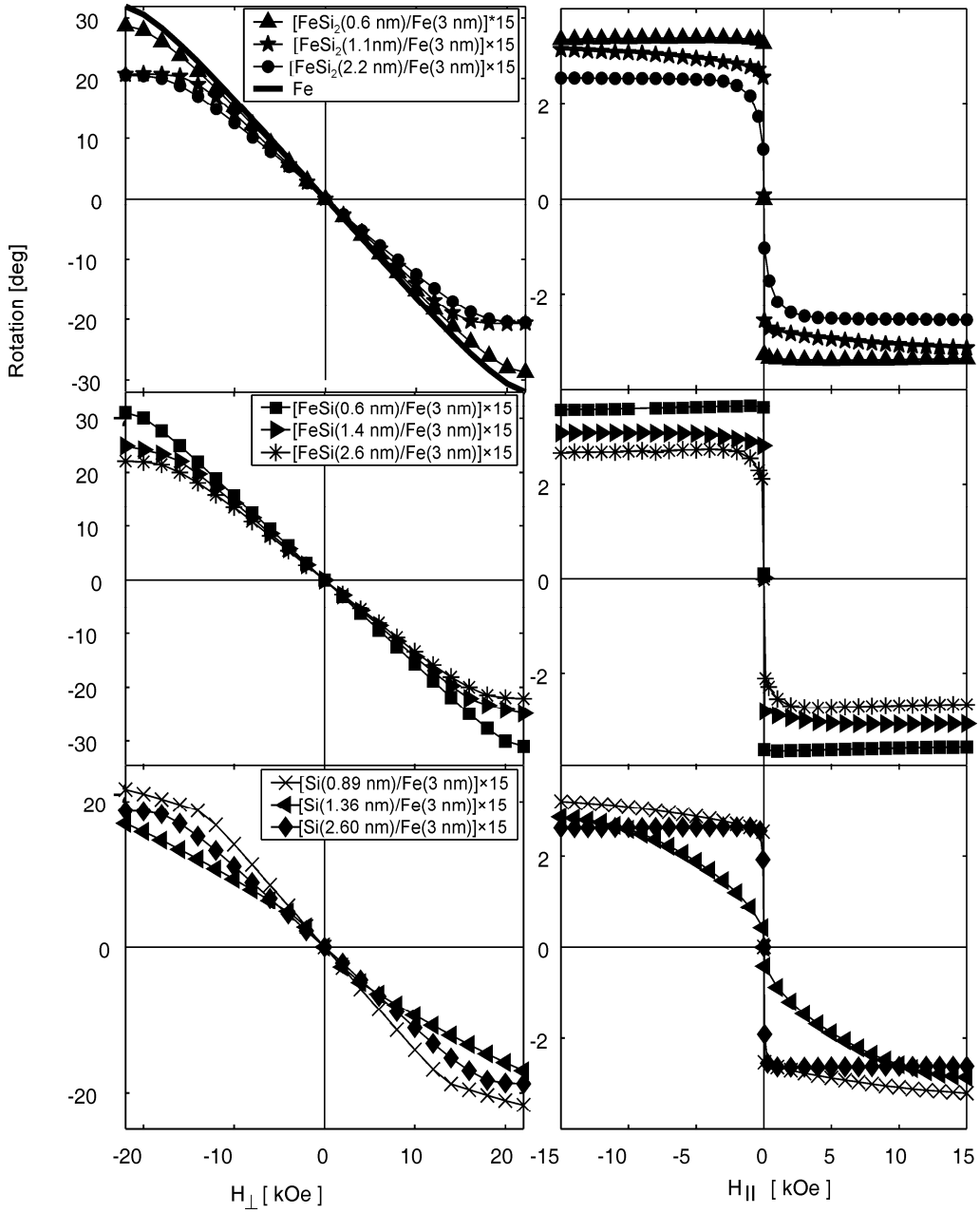

Fig. 1. The Kerr rotation dependence on the magnetic field applied perpendicular (left panel) and parallel (right panel) to the sample surface for the series of Fe/Si_xFe_{1-x} MLS

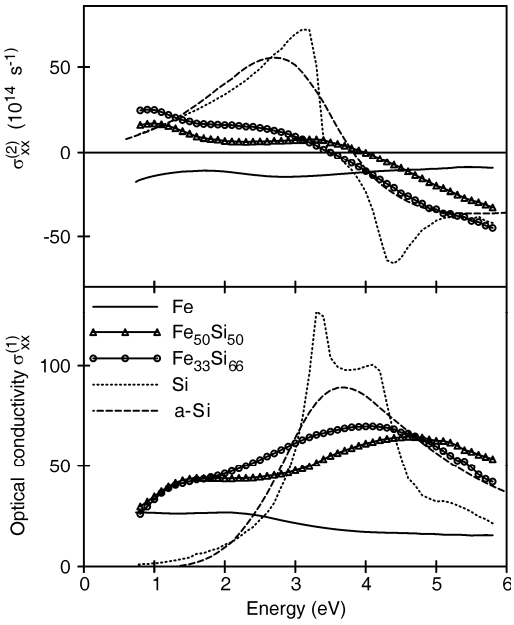

Fig. 2. Recorded spectra of the optical conductivity tensor components for sputter deposited Fe, $Fe_{50}Si_{50}$ and $Fe_{33}Si_{66}$ alloy films, and Si(100) substrate. Data for a-Si (amorphous) were taken from literature

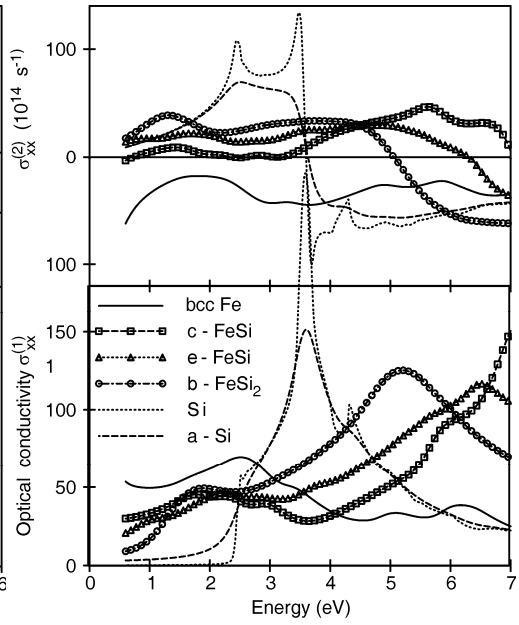

Fig. 3. Calculated spectra of the optical conductivity for Fe, metallic c-FeSi, semiconducting β-$FeSi_2$, ε-FeSi, Si crystal and amorphous a-Si

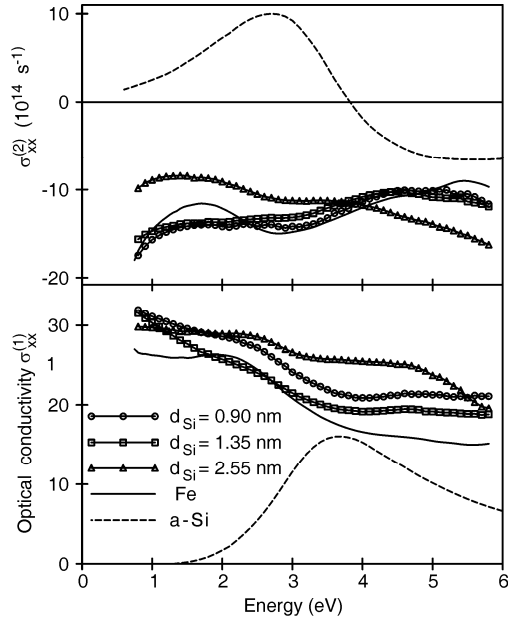

Fig. 4. Measured optical conductivity tensor components for as-deposited Fe/Si multilayers with fixed d_{Fe}= 3 nm and varied d_{Si}. The spectra of the Fe films and bulk amorphous a-Si (multiplied by the factor of 0.18) are included for comparison

The above conclusion obtained from the analysis of the optical conductivity spectra is in line with the results of CEMS study. The CEMS spectra [3] indicate that AF coupling can be mediated by formation of nonmagnetic Fe–Si compounds at the interfaces and/or in spacer layers, e.g., semiconducting ε-FeSi, non-stoichiometric metallic c-Si_xFe_{1-x} and intermixed crystalline or amorphous Fe–Si.

These alloy systems constitute spacer sublayers in the MLS structures. The situation is more difficult to analyze and to determine the exact structure of the interfacial phase because the formed interface region is inhomogeneous. In Figure 4, the exemplary optical conductivity spectra are presented for three Fe/Si MLS with increasing spacer layer thickness. The spectra carry information on the effective optical conductivity of the MLS. As can be seen in Figure 4, this effective optical response, even for the thickest Si spacer, is closer to the Fe spectral dependence. Overall evolution of the conductivity is in agreement with the prediction of effective medium approximation theory [10]. It is clear that, on average, the MLS structures exhibit metallic-like behaviour. This conclusion was verified by multireflection calculation results, not presented in the paper. The optical conductivity spectra of the MLS films prepared with intentionally chosen alloy spacer layers of the $Fe_{50}Si_{50}$ and $Fe_{33}Si_{66}$ compositions have similar to that energy dependences seen in the case of the Si spacer.

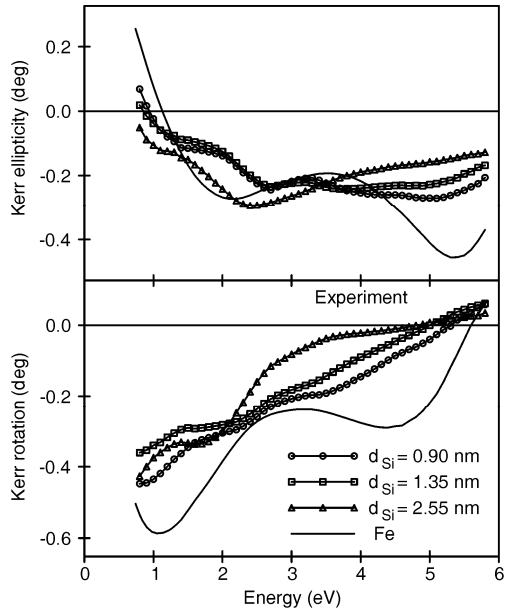

Fig. 5. Recorded complex Kerr rotation spectra for pure iron thick film and Fe/Si MLS with fixed d_{Fe} = 3 nm and varied d_{Si}

The measured magneto-optical response of the Fe/Si MLS is presented in Fig. 5, together with the spectrum of Fe that is the source of magnetism in the system. It is clearly seen from the Kerr rotation that the peaks at ~1.1 eV and ~3.5 eV characteristic of *bcc* Fe disappear and the amplitude of the spectra diminishes, although generally it is not scaled with the Fe content in the whole spectral range. It can be concluded

that the main contribution to the magneto-optical response comes from the intrinsic part of Fe sublayers, and iron silicides formed at Fe-Si interface contribute significantly to the spectra. To elucidate the magneto-optical nature of the interface, the first principles calculations are necessary. Such calculations are difficult to perform owing to the large Fe sublayer thickness.

In conclusion, the comparison of the measured and *ab initio* calculated optical conductivity spectra of the alloys shows that the alloys represent semiconducting ε-FeSi and β-$FeSi_2$ phases rather than a metallic FeSi phase, which confirms the conclusions inferred from other methods. The measured magneto-optical response of the MLS studied comes mainly from the intrinsic part of Fe sublayers that mask the contribution of iron silicides formed at the Fe-Si interface. The detailed *ab initio* modeling of the magneto-optical response of complex multilayer structures is in progress.

References

[1] FULLERTON E.F., MATTSON J.E., LEE S.R., SOWERS C.H., HUANG Y.Y., FELCHER G., BADER S.D., J. Appl. Phys., 73 (1993), 6335.
[2] WANDZIUK P., KOPCEWICZ M., SZYMAŃSKI B., LUCINSKI T., Mol. Phys. Rep., 40 (2004), 182.
[3] KOPCEWICZ M., LUCINSKI T., WANDZIUK P., J. Magn. Magn. Mater., 286 (2005), 488.
[4] ENDO Y., KITAKAMI O., SHIMADA Y., Phys. Rev. B, 59, 4279 (1999); J. Appl. Phys. 87 (2000), 6836.
[5] DE VRIES J.J., KOHLHEPP J., DEN BROEDER F.J.A., COEHOORN R., JUNGBLUT R., REINDERS A., DE JONGE W.J.M., Phys. Rev. Lett., 78 (1997), 3023.
[6] STRIJKERS G.J., KOHLHEPP J.T., SWAGTEN H.J.M., DE JONGE W.J.M., Phys. Rev. B, 60 (1999), 9583.
[7] KUDRYAVTSEV Y.V., NEMOSHKALENKO V.V., LEE Y.P., KIM K.W., RHEE J.Y., DUBOWIK J., J. Appl. Phys., 90 (2001), 2903.
[8] CLARK S.J., AL-ALLAK H.M., BRAND S., ABRAM R.A., Phys. Rev. B, 58 (1998), 103089.
[9] UBA L., UBA S., ANTONOV V.N., YARESKO A.N., ŚLĘZAK T., KORECKI J., Phys. Rev. B, 62 (2000), 13731.
[10] ABE M., GOMI M., Jap. J. Appl. Phys. 23 (1984), 1580.

Received 7 May 2006
Revised 1 September 2006

Materials Science-Poland, Vol. 25, No. 2, 2007

Magnetic phase diagram of the $URh_{1-x}Ru_xGe$ system

W. MIILLER*, V.H. TRAN, A. KONDRAT

W. Trzebiatowski Institute of Low Temperarure and Structure Research,
Polish Academy of Sciences, 50-950 Wrocław 2, Poland

Magnetic phase diagram of the $URh_xRu_{1-x}Ge$ solid solutions has been reinvestigated by means of dc-magnetization, ac-susceptibility and electrical resistivity. We confirm ferromagnetic order only in alloys with $x \leq 0.2$. For a limited range of concentrations x between 0.3 and 0.35, we found features characteristic of short-range magnetic interactions. For compositions close to $x = 0.4$, non-Fermi liquid signature is observed in the low temperature resistivity. Thus, we report on the evolution of non Fermi-liquid behaviour at a magnetic–nonmagnetic border, neighbouring with the region of the short-range interactions.

Key words: *non-Fermi liquid; uranium ternary compounds, $URh_{1-x}Ru_xGe$; dc-magnetization, ac-susceptibility; electrical resistivity*

1. Introduction

The uranium intermetallic ternaries UT(Si, Ge) with the orthorhombic TiNiSi-type structure form one of the largest isostructural series of the uranium compounds [1]. The physical properties of these intermetallics have been extensively investigated for more than twenty years [2]. It turns out that within this series of compounds, a variety of magnetic properties can be observed by changing T – 3d, 4d or 5d electron transition metals involved. It is widely accepted that the development of magnetic behaviour is intimately associated with the strength of the 5f-ligand hybridization. Bearing in mind this mechanism, one can understand, for instance, the nonmagnetic ground state in URuGe and magnetic order in URhGe (T_C = 9.5 K) [2]. Since Ru possesses the electron configuration of $4d^75s^1$ whereas the configuration in Rh is $4d^85s^1$, the increasing number of conduction electrons in the sequence URuGe–URhGe weakens the 5f–4d hybridization. In consequence, it gives rise to formation of U 5f magnetic moments in the latter compound. Recent study of solid solutions $URh_{1-x}Ru_xGe$ made

*Corresponding author, e-mail: w.miiller@int.pan.wroc.pl

by Sakarya et al. [3] indicated a significant role of the 5f–4d hybridization. Moreover, the authors have shown an interesting magnetic phase diagram. The substitution of Rh by Ru first increases the Curie temperature up to about 11 K at $x = 0.1$, but with more Ru substitution T_C decreases and the ferromagnetic ordering disappears at $x \sim 0.38$. Because of possible experimental realization of a non-Fermi liquid ground state in a strongly correlated electron system at the magnetic-nonmagnetic border [4], we undertook to reinvestigate the magnetic phase diagram of $URh_{1-x}Ru_xGe$ [5]. We have carried out a detailed investigation of the low-temperature ac-magnetic susceptibility, dc-magnetization and electrical resistivity of samples between $0 \le x \le 1$. In this contribution, we present these new results, which partly confirm the reported diagram. One of the most remarkable findings to emerge from our study is that the non-Fermi liquid behaviour appears around the critical concentration $x_{cr} = 0.4$. We will also argue that the magnetic order vanishes actually near $x = 0.3$ and short-range correlations take place in alloys with x between 0.3 and 0.35.

2. Experimental details

The alloys with nominal compositions of the $URh_{1-x}Ru_xGe$ system, namely with x equal to 0, 0.1, 0.2, 0.3, 0.35, 0.375, 0.38, 0.4, 0.6, 1.0, were synthesized by arc melting in a Ti-gettered pure argon atmosphere. The samples were then wrapped in a Ta foil and annealed at 800 °C in evacuated silica tube for 60 h. The powder X-ray diffraction diffractometry (DRON and STOE, $Cu_{K\alpha}$ radiation) and EDAX microprobe analysis were used to examine the crystal structure, homogeneity and purity of the prepared materials. The Rietveld refinements were performed using the FULLPROF software. dc-Magnetization of powdered samples was measured using a Quantum Design SQUID magnetometer in the temperature range from 2 to 400 K and in magnetic fields up to 5.5 T. The measurements of ac susceptibility were performed using an Oxford Instrument susceptometer; ac field with the amplitude of 10 Oe and frequency 1 kHz were applied. Electrical resistivity measurements were performed on bar-shaped samples using the standard four-probe DC technique in the temperature range 2–290 K.

3. Results and analysis

3.1. Crystallographic data

The crystallographic data of URuGe and URhGe have been investigated by several groups [1]. These compounds were reported to crystallize in the orthorhombic TiNiSi -type structure and are characterized by the ratios $b/a = 0.651$ and $a/c = 0.885$, and 0.630 and 0.916, respectively. Based on the X-ray powder diffraction patterns, we conclude that all the investigated solid solutions of the $URh_{1-x}Ru_xGe$ system crystal-

lize in the same crystal structure as their parent compounds do. The respective lattice parameter ratios are presented in Fig. 1. An Inspection of the lattice parameters reveals that the *a* and *c* parameters change systematically with the concentration, while the *b* parameter remains almost constant. As a result, the unit cell volume seems to deviate from the linear behaviour at = 0.1, though a linear dependence of the *b*/*a* and *a*/*c* ratios with increasing *x* is found (see Fig. 1).

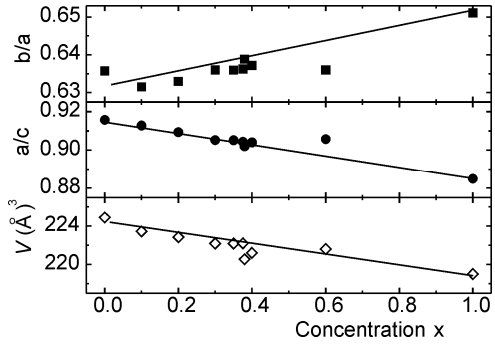

Fig.1. The ratio *a*/*c*, *b*/*a* and unit cell volume of $URh_{1-x}Ru_xGe$ as a function of concentration *x*

3.2. DC magnetization and ac-magnetic susceptibility

Figure 2 shows the temperature dependence of the reciprocal magnetic susceptibility $\chi^{-1}(T)$ for selected $URh_{1-x}Ru_xGe$ samples. Owing to a curvature of the $\chi^{-1}(T)$ curves, an analysis of the data was done with the use of a modified Curie–Weiss law:

$$\chi(T) = \frac{C}{T - \theta_p} + \chi_0$$

where $C = \dfrac{N_A \mu_{\text{eff}}^2 \mu_B^2}{3k_B}$ and θ_p is the paramagnetic Curie temperature, and χ_0 is a constant term, associated certainly with the Pauli paramagnetic contribution.

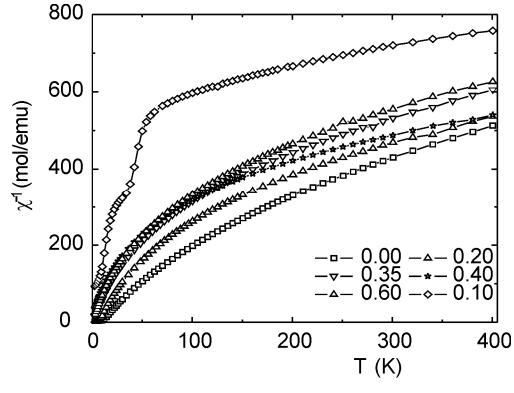

Fig. 2. Reciprocal susceptibility of selected $URh_{1-x}Ru_xGe$ solid solutions as a function of temperature. $\mu_0 H = 0.5$T

The fitted parameters for the data in the temperature range 100–400 K are given in Table 1. One recognizes that the θ_p values are found to be negative for all x. This fact implies the existence of antiferromagnetic interactions in all the studied alloys. A small magnitude of the effective moments hints rather an itinerant electron magnetism of the system.

The dc magnetization of compositions with $x < 0.3$ exhibits an anomaly associated with magnetic order of the U magnetic moments at low temperatures (not shown here). A gradual loss of magnetic order due to Ru substitution is illustrated in Fig. 3, where magnetization collected at 2 K is plotted versus the magnetic field.

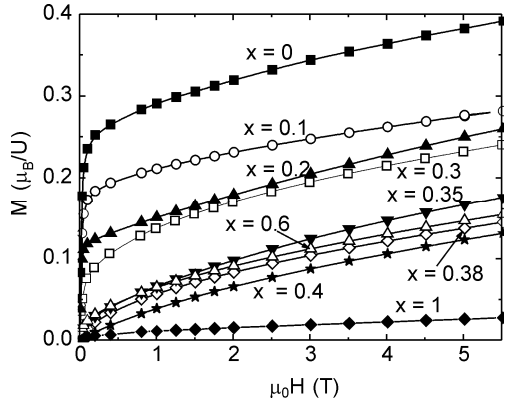

Fig. 3. Magnetization as a function of applied field for selected $URh_{1-x}Ru_xGe$ alloys. $T = 2$ K

Clearly, at 5.5 T the uranium magnetic moment steadily decreases with increasing concentration x. Further, for $x = 0$, 0.1 and 0.2 there is a spontaneous magnetization, that evidences the magnetic order in these alloys. On the other hand, the magnetization of alloys with $0.4 \geq x \geq 0.35$ resembles the behaviour of paramagnets. However, an attempt to fit these data to the expression

$$M = \chi_1 + \frac{\chi_3 H^3}{3!} + \ldots$$

up to the eleventh order failed (not shown here). Furthermore, the magnetic behaviour of $x = 0.3$ bears a resemblance to that of ferromagnets, however, as we show later, this composition does not show any long-range magnetic order at all.

An analysis of the Arrott plots may help us to determinate correctly the values of the Curie temperature for $x = 0$, 0.1 and 0.2. As an illustration, we display such an analysis in Fig. 4a for $x = 0.1$. As can be seen in Fig. 4b, there is no spontaneous magnetization in the sample $x = 0.3$. Therefore, we have no support for a long-range magnetic order in this alloy.

Complementary information on the magnetism of the $URh_{1-x}Ru_xGe$ alloys is provided via the ac-susceptibility measurements (Fig. 4). The maximum at T_{max} found in a real $\chi'(T)$ and imaginary parts $\chi''(T)$ of the ac-susceptibility of $x = 0$, 0.1 and 0.2 confirms the magnetic order in these alloys, but it not the case for $x = 0.3$.

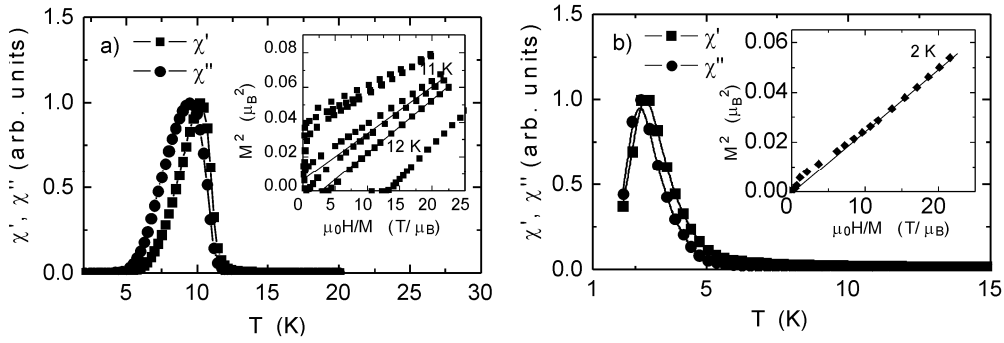

Fig. 4. Temperature dependence of ac-susceptibility for: a) $x = 0.1$ and b) $x = 0.3$. The Arrott plots for these samples are shown in the respective inset.

In particular, a slow decrease in the susceptibility (tail behaviour) in the sample of this composition for $T > T_{max}$ can evidence for some magnetic short-range interactions.

3.3. Electrical resistivity

The temperature dependences of the electrical resistivity of several $URh_{1-x}Ru_xGe$ compositions are depicted in Fig. 5. A characteristic feature of the $\rho(T)$ curves is the appearance of a broad maximum around 130 K. Further investigations are needed to clarify the nature of the observed phenomenon. At present, we tentatively attribute it to a Kondo-like effect. The magnetic order in compositions with $x \leq 0.2$ is supported by a drop in the resistivity at their T_C. No anomaly at low temperatures is visible in compositions with $x = 0.3$, 0.35, 0.38, 0.4, corroborating their nonmagnetic ground state.

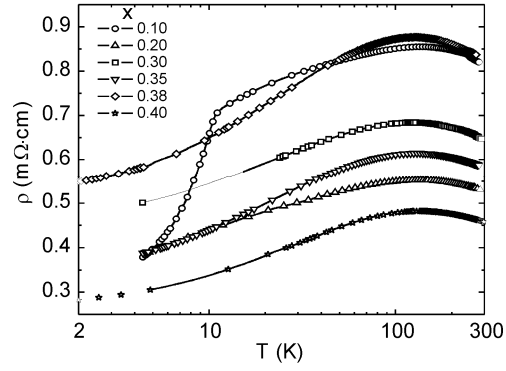

Fig. 5. Electrical resistivities of several $URh_{1-x}Ru_xGe$ solid solutions as a function of temperature

The resistivity data in the low temperature range, shown in Fig. 6, can be fitted well to a power law:

$$\rho(T) = \rho_0 + AT^n$$

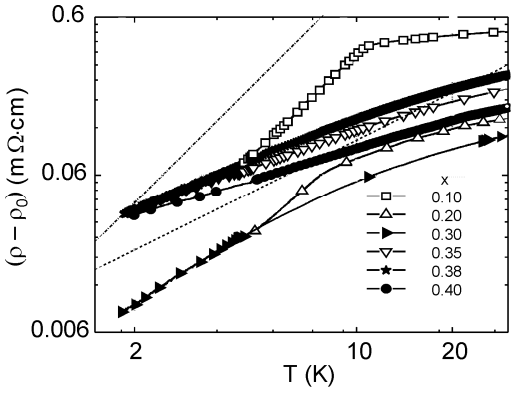

Fig. 6. Low temperature resistivity of selected $URh_{1-x}Ru_xGe$ samples. Dotted lines denote power T^n functions with $n = 2$ and 1, respectively

The change in the coefficient A and exponent n with x (Table 1) reflects changes in the magnetic properties of the alloys. For ferromagnetic alloys, the exponent n attains the value close to 2, characteristic of an electron–electron scattering. On the other hand, for nonmagnetic alloys $x = 0.35$–0.38, we found n close to 1. Such a value of the exponent implies a breakdown of the Fermi liquid behaviour [4]. The composition $x = 0.3$ is characterized by $n = 1.32$, very close to that of spin glasses ($n = 1.5$) [6].

Table 1. Physical properties of selected $URh_{1-x}Ru_xGe$ solid solutions*

x	μ_{eff} (μ_B/U)	θ (K)	T_C (K)			A (mΩ·cm·K^{-n})	n
			Arrott	AC sus.	$d\rho/dT$		
0.00	1.84	–3	9	–	9	0.011	2
0.10	1.51	–10	11–12	10.2	10.7	0.004	1.95
0.20	1.47	–6	7–8	7.5	8	0.002	1.75
0.30	1.60	–31	–	T_{max} =3	–	0.002	1.32
0.35	1.64	–55	–	–	–	0.022	0.99
0.38	1.59	–55	–	–	–	0.019	0.89
0.40	1.54	–59	–	–	–	0.023	0.7
1.00	1.27	–190	–	–	–	–	–

*The values of T_C were determined with various measurement techniques, such as the analysis of the Arrott plots, as well as the ac-susceptibility and electrical resistivity measurements.

4. Concluding remarks

Several samples of the pseudoternary $URh_{1-x}Ru_xGe$ system were synthesized and characterized by X-ray diffraction and EDX analysis. The crystallographic data indicate that the system adopts an orthorhombic TiNiSi-type structure. The lattice parameters seem to deviate from a simple Vegard law around $x = 0.1$. We found that the substitution of Rh by Ru causes vanishing of ferromagnetic order at $x = 0.25$ where the system undergoes a crossover onto a nonmagnetic ground state with short-range

magnetic interactions (x between 0.3 and 0.35). The latter feature differs from that reported by Sakarya et al. [3], who claimed magnetic order even up to $x = 0.325$ (see Fig. 7). As the main result of our study, we found the characteristic features of the non-Fermi liquid state. In summary, we propose a magnetic phase diagram of the $URh_{1-x}Ru_xGe$ system (Fig. 7).

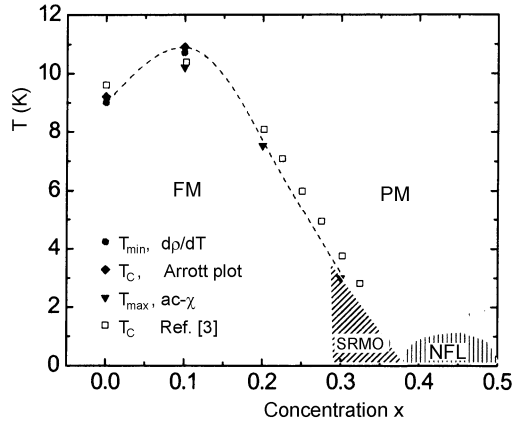

Fig. 7. Tentative magnetic phase diagram of the $URh_{1-x}Ru_xGe$ system. Three different magnetic ground states are shown: FM – ferromagnetic, SRMO – short range magnetic order, and NFL non-Fermi liquid ground state

Acknowledgement

This work was supported by the Ministry of Science and Higher Education in Poland under Grant No. N202 082 31/0449. The authors are grateful to Prof. A. J. Zaleski for help with some ac-susceptibility measurements.

References

[1] SECHOVSKY V., HAVELA L., *Intermetallic Compounds of Actinides*, [in:] *Ferromagnetic Materials*, E.P. Wohlfarth, K.H.J. Buschow (Eds.), Vol. 4, Amsterdam, North-Holland (1998), p. 309 and the references therein.

[2] TROĆ R., TRAN V.H., J. Magn. Magn. Mater., 73 (1988), 389.

[3] SAKARYA S., VAN DIJK N.H., HUY N.T., DE VISSER A., [in:] Proc. of Intern. Conf. on SCES, Vienna, July 26–30, 2005.

[4] VON LÖHNEYSEN H., *Encyclopedia of Materials: Science and Technology*, 2001 Elsevier, p. 6185.

[5] MIILLER W., TRAN V. H., [in:] Proc. of 36emees Journées des Actinides, Oxford, England, 1–4 April, 2006.

[6] MYDOSH J. A., Spin Glasses, Taylor and Francis, London (1995).

Received 7 May 2006
Revised 1 September 2006

Materials Science-Poland, Vol. 25, No. 2, 2007

Magnetic properties of cementite (Fe_3C) nanoparticle agglomerates in a carbon matrix

K. LIPERT[1*], J. KAŹMIERCZAK[1], I. PEŁECH[2], U. NARKIEWICZ[2], A. ŚLAWSKA-WANIEWSKA[1], H.K. LACHOWICZ[1]

[1]Institute of Physics, Polish Academy of Sciences, Al. Lotników 32/46, 02-668, Warsaw

[2]Institute of Chemical and Environment Engineering, Technical University of Szczecin, al. Piastów 19, 70-322 Szczecin

Magnetic properties of two FeC samples with different amounts of carbon have been studied. In both cases, the amount of carbon was well above the mass sufficient to transform nanocrystalline iron into iron carbide (cementite). Through the dc magnetic and transmission electron microscopy (TEM) measurements it was shown that cementite nanoparticles formed agglomerates; the size distribution of these nanoparticles was very wide, and superparamagnetic-like behaviour was not observed even at room temperature.

Key words: *superparamagnetism; coercivity; iron carbide; Stoner–Wohlfarth model*

1. Introduction

First theoretical considerations and calculations of the critical size of magnetic particle (typically few nanometers), that is the size below which the most energetically favourable magnetic state is a single domain state, were carried out by Charles Kittel in 1946 [1]. Superparamagnetism is the phenomenon by which the system containing single domain magnetic nanoparticles, dispersed in a nonmagnetic matrix, may exhibit at temperatures above the so-called blocking temperature T_B, a behaviour similar to that of a paramagnetic material. At a temperature higher than the blocking temperature, a stable bulk magnetization cannot be established because of thermal fluctuations acting on each particle in a system, and so the bulk material exhibits superparamagnetism (SPM). At temperatures below T_B, thermal fluctuations cannot overcome the energy barrier connected with the magneto-crystalline anisotropy en-

*Corresponding author, e-mail: lipert@ifpan.edu.pl

ergy, and then magnetic moments of particles are confined in random directions, lying along easy axis of magnetization and cannot change their directions spontaneously from one easy direction to the other. The first model of monodispersed, non-interacting, single domain magnetic particles with uniaxial anisotropy, embedded in a nonmagnetic matrix was proposed by Stoner and Wolhfarth [2].

The thermal relaxation of magnetic nanoparticles is excellently described by the Arrhenius–Néel formula [3]:

$$t_{\mathrm{rel}} = t_0 \exp\left(\frac{E_A}{k_B T}\right) \tag{1}$$

where t_{rel} is the relaxation time of the particle magnetic moment, E_A is the anisotropy energy barrier, t_0 is the characteristic relaxation time, ranging typically from 10^{-11} to 10^{-9} s. In the absence of external magnetic field, the anisotropy barrier E_A is proportional to the particle volume, V, and can be expressed as $E_A = KV\sin^2\alpha$, where K is the effective magnetic anisotropy constant and α is the angle between magnetic moment of the particle and its easy magnetization direction.

In the recent decade, great attention has been focused on magnetic nanoparticles [4, 5] because of their unique physical properties and also because of the possibility of their practical application in medicine and biotechnology (e.g., hyperthermia [6], targeted drug delivery [7], contrast agents in MRI [8]) as well as in catalysis, magnetic separation, gas sensors and many others. The aim of the present work was to investigate structural characteristics and magnetic properties of nanoparticle agglomerates of iron carbide (Fe_3C) embedded in a carbon matrix.

2. Preparation of samples and shape characterization

Samples were prepared in the process of carburisation of nanocrystalline iron with ethylene [9]. The nanocrystalline iron was doped with a small amount of two promoter oxides (Al_2O_3 and CaO). The samples were obtained by the fusion of magnetite with the promoter oxides. The alloy obtained was crushed after cooling and then sieved to separate the fraction of 1.2–1.5 mm. To obtain metallic iron, polythermal reduction with hydrogen was used. The pyrophoric specimens obtained after reduction were passivated using nitrogen with a 0.5% addition of oxygen. The chemical composition after passivation was determined using inductively coupled plasma atomic emission spectroscopy (AES-ICP). Besides iron, the samples contained 2.9 wt. % of Al_2O_3, 3.0 wt. % of CaO, 0.3 wt. % of SiO_2, and 1 wt. % of other metal oxides (Mg, Ni, Cr, Ti, V).

The carburisation process was carried out in a spring thermobalance. A single layer of grains of the sample was placed in a platinum basket and hung in the thermobalance. Changes in the mass of samples were recorded with a cathetometer. Before carburisation, the samples were reduced under hydrogen at a temperature rising from

293 to 773 K. After reduction (when a constant mass of the sample was reached), the carburisation process was started using ethylene (40 dm^3/h). The carburisation was

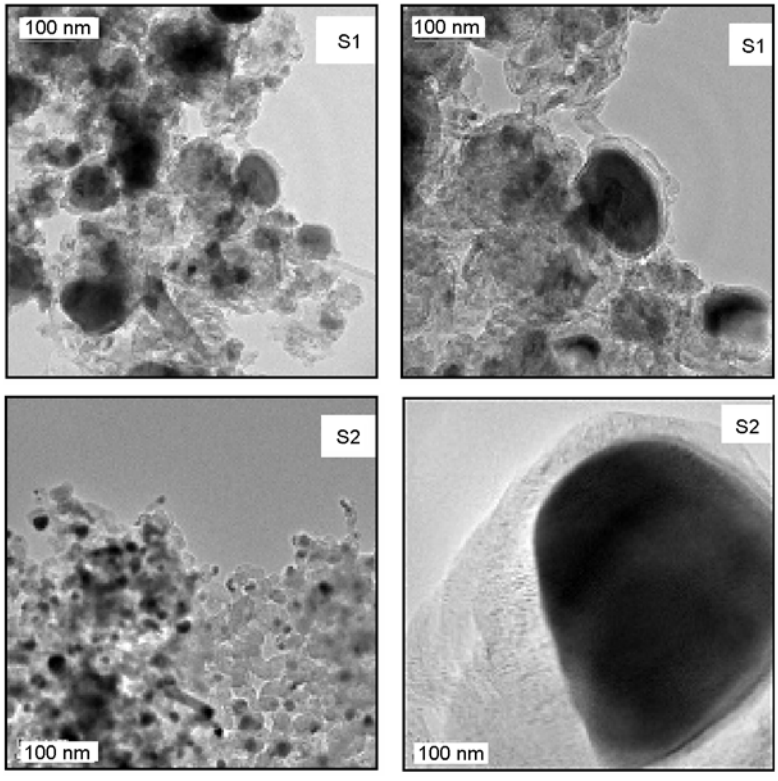

Fig. 1. Transmission electron microscope (TEM) pictures
with various enlargements for samples 1 (upper) and 2 (bottom)

carried out isothermally, at the temperature of 773 K. The products of the carburisation of nanocrystalline iron with ethylene are iron carbide and carbon deposits. Iron carbide is formed only as cementite, which crystallizes in an orthorhombic structure. Its particles form relatively large agglomerates (see Fig. 1, left). Individual particles are also large (right). Such a shape of nanoparticles has large impact on magnetic properties of the samples, as will be shown in Sec. 3.

3. Measurements of magnetic parameters

Magnetic parameters were measured using vibrating sample magnetometer VSM. Thermo-remanence magnetization (not shown here), hysteresis loops, zero field- and field-cooled measurements (M_{ZFC} and M_{FC}) were carried out in the temperature range from 5 to 300 K. Figure 2 shows the hysteresis loops for both samples at 5 K and 300 K. It is clear that both samples did not exhibit superparamagnetic-like behaviour

within this temperature range, since even at room temperature their coercivity is far from zero.

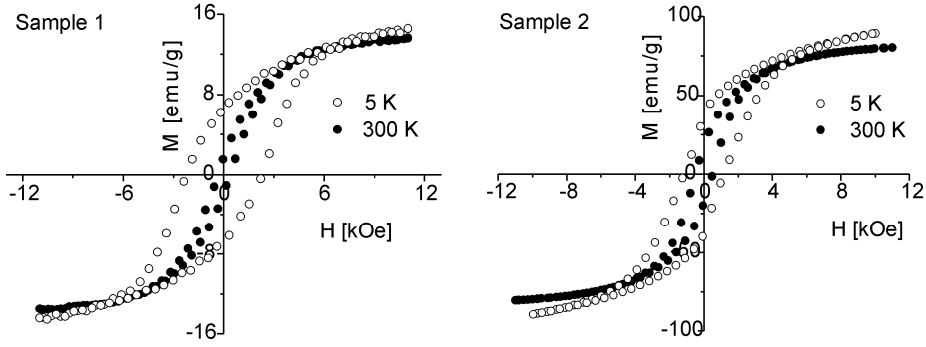

Fig. 2. Hysteresis loops at 5 K and 300 K for samples 1 and 2

Figure 3 shows the so called zero field- (ZFC) and field-cooled (FC) magnetization curves recorded in the presence of external magnetic field of 100 Gs. Using the dependences presented in Fig. 3, one can find the distribution of the blocking temperature in the studied system. As shown in [10], the derivative of the difference of these two magnetizations by temperature $d(M_{ZFC} - M_{FC})/dT$, represents the number of particles whose blocking temperature falls into the range of a given temperature. The calculated temperature dependence of the described relationship is shown in Fig. 3 for sample 1. As can be seen, the distribution of the blocking temperatures is very wide, showing, similarly as the hysteresis loops, that even at room temperature not all particles are superparamagnetic.

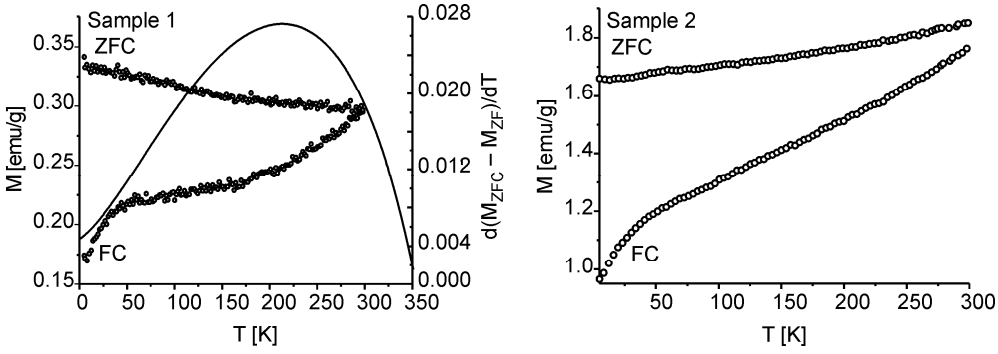

Fig. 3. Zero field- (ZFC) and field-cooled (FC) curves recorded at the field of 100 Gs for the samples S1 and S2; corresponding distribution of blocking temperatures for the sample S1 is also shown

At low temperature, where all the magnetic moments of a system of randomly oriented and non-interacting particles are blocked, the coercivity is equal to the value for monodomains, H_{C0}. At a sufficiently high temperature, when all moments fluctuate with

the relaxation time shorter than the measuring time, coercivity equals zero. For intermediate temperatures, the coercivity H_C can be evaluated from the formula [11]:

$$H_C(T) = H_{C0}\left[1-\left(\frac{T}{T_B}\right)^{1/2}\right] \tag{2}$$

where H_{C0} is the coercivity at $T = 0$ K and T_B is the blocking temperature of the largest particle in the system.

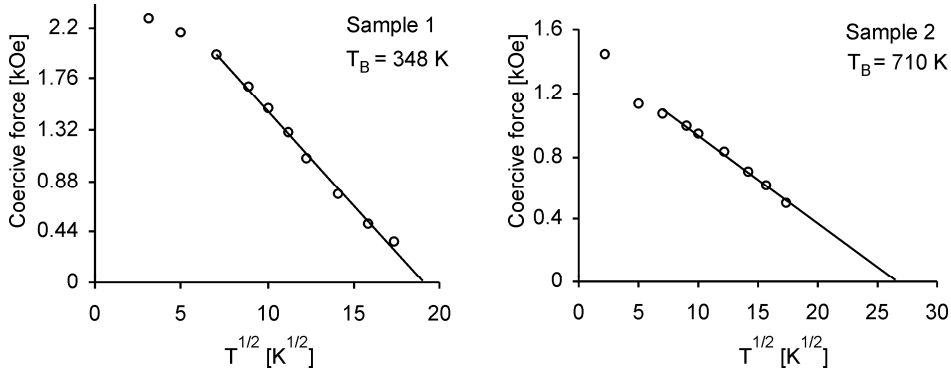

Fig. 4. Coercivity vs. square root temperature for the samples S1 and S2

Figure 4 shows the coercivity derived from the hysteresis loops measured for both samples, plotted as a function of the square root of temperature. As can be seen, both dependences are linear in the range of higher temperatures. The extrapolated values of the maximum blocking temperature T_B (i.e., blocking temperature of the largest particles) calculated according to the above equation are equal to 348 K and 710 K for the samples S1 and S2, respectively. It is worth to note, that the value of the remanence magnetization at low temperatures is very close to half of the value of saturation magnetization, being equal to 0.46 and 0.41 for the S1 and S2 sample, respectively. This seems to be in a good agreement with the Stoner–Wohlfarth model.

Table 1. Summary of certain properties of studied samples

Sample	Carbon mass increase m_C/m_{Fe}	Mass ratio m_{Fe_3C}/m_C	Coercive force* [kOe]	M_{REM}/M_{SAT}	T_B [K]
S1	1.687	0.662	0.365	0.46	348
S2	0.715	1.659	0.504	0.41	710

*At room temperature.

4. Conclusions

As can be seen in the TEM pictures, the particles form agglomerates which can behave like a large single particle because of the exchange interactions acting between particles forming individual agglomerates. The investigated particles display relatively wide distribution of their sizes resulting, in accordance with Eq. (1), in a wide distribution of the blocking temperatures. Since size of the particles is relatively large, larger than the critical size, they may exhibit a multi-domain magnetic structures. Both the studied samples do not display superparamagnetic like behaviour even at room temperature. Similarly, their blocking temperatures are well above the room temperature.

References

[1] KITTEL C., Phys. Rev., 70 (1946), 965.
[2] STONER E.C., WOHLFARTH E.P., IEEE Trans. Magn., 27 (1991), 3475.
[3] NÉEL L., Compt Rend. (Paris), 228 (1949), 604.
[4] ŚLAWSKA-WANIEWSKA A., GUTOWSKI M., LACHOWICZ H.K., KULIK T., MATYJA H., Phys. Rev. B, 46 (1992), 14594.
[5] DIDUKH P., NEDELKO O., ŚLAWSKA-WANIEWSKA A., J. Magn. Magn. Mater., 242 (2002), 1077.
[6] YOSHIDA J., KOBAYASHI T., J. Magn. Magn. Mater., 194 (1999), 176.
[7] PANATAROTTO D., PRTIDOS C.D., HOEBEKE J., BROWN F., KRAMER E., BRIAND J.P., MULLER S., PRATO M., BIANCO A., Chem. Biol., 10 (2003), 961.
[8] WEISSLEDER R., ELIZONDO G., WITTENBURG J., RABITO C.A., BENGELE H.H., JOSEPHSON L., Radiol., 175 (1990), 489.
[9] NARKIEWICZ U., KUCHAREWICZ I., ARABCZYK W., LENART S., Mater. Sci.-Poland, 23 (2005), 939.
[10] JIN LU LU, HONG YUAN DENG, HUEI LI HUAN, J. Magn. Magn. Mater., 209 (2000), 37.
[11] CANDELA G.A., HAINES R.A., Appl. Phys. Lett., 34 (1979), 868.

Received 7 May 2006
Revised 1 September 2006

Materials Science-Poland, Vol. 25, No. 2, 2007

Image processing study of ultrathin cobalt domain structure evolution induced by overlayer structure

W. DOBROGOWSKI[1], Z. KURANT[1, 2], A. NEDZVED[1, 3], W. STEFANOWICZ[1*], M. TEKIELAK[1], L.T. BACZEWSKI[2], A. WAWRO[2], A. MAZIEWSKI[1]

[1]Institute of Experimental Physics, University of Białystok, Lipowa 41, 15-424 Białystok, Poland

[2]Institute of Physics, Polish Academy of Sciences, al. Lotników 32/46, 02-668 Warsaw, Poland

[3]United Institute of Informatics Problems, National Academy of Sciences BY-220012 Minsk, Belarus

Evolution of the domain structure (DS) in ultrathin cobalt films, deposited on sapphire substrate with the following structure: X\Au\Co(d_{Co} nm thick layer or wedge)\X (d_X nm thick layer or wedge perpendicular to Co wedge axis)\Au (where X is V or Mo) with perpendicular magnetization was investigated as a function of thickness d_X. The study was performed using an optical polarizing microscope with CCD camera. Images of DS were recorded during various stages of magnetization reversal. A special software based on LabView® was employed for acquisition and processing of domain images. To analyze the observed domain structures, topology properties of magnetic images were determined. Preferential orientation of domain walls was found in ultrathin Co covered by Mo but not by V.

Key words: *magnetic domains; ultrathin film; cobalt*

1. Introduction

Magnetic ordering of ultrathin films is one of the intensively studied phenomena. Magnetic reorientation phase transition (RPT) in sandwich structures containing ultrathin Co films between vertical and in-plane magnetization states attracts particular attention of scientists all over the world. RPT can be induced by changing: (i) thickness d of the magnetic layer or (ii) overlayer and/or underlayer structures [1, 2]. Changes of magnetic domain structure (DS) in ultrathin Co, approaching RPT have been studied *in-situ* by the SEMPA technique [3] which showed a decrease of DS size, and *ex-situ* by magnetooptical microscopy [4, 5] during which an increase of the density of magnetization reversal nucleation centres and an appearance of dendrite

*Corresponding author e-mail: vstef@uwb.edu.pl

type DSs were observed. In the present work, the influence of V and Mo overlayers on DS geometry near RPT is investigated in detail. An image processing technique was developed for this purpose.

The results were obtained on two selected MBE-grown epitaxial samples, deposited on monocrystalline (11–20) Al_2O_3 substrate, with the following structures: (i) V (20 nm)\Au(111) (20 nm)\Co (6 mm long wedge; 1 nm < d <1.5 nm)\V(6 mm long wedge; 0 < d_V < 0.3 nm perpendicular to the Co one)\Au (8 nm) and (ii) Mo(110) (20 nm)\Au(111) (20 nm)\Co (d =1.2 nm)\Mo (d_{Mo}= 0.15 nm)\Au(8 nm).

All measurements, based on the polar Kerr effect, were performed at room temperature using a classical optical polarizing microscope with a CCD camera. Perpendicular to the sample plane, magnetic field pulses or alternating field H_{AC} with decreasing amplitude was applied after saturation to induce the domain structure. A DS image was recorded after different magnetic histories (Fig. 1). To improve the image contrast, the following normalization numerical procedure was used:

$$P(i, j) = (I_+(i, j) - I_-(i, j))/(I_+(i, j)+I_-(i, j)) \tag{1}$$

where I_- denotes the level in the grey scale of an individual image pixel positioned at (i, j) of the reference image recorded in remnant state after sample saturation at $H_S < 0$ and I_+ describes the pixel value after application of the pulse of magnetic static field with the amplitude H_+ or H_{DS} in the opposite direction (I_+ or I_D) or AC field with decreasing amplitude. The gray level of the pixels is proportional to the local values of both the normalized remnant magnetization m_R and maximal Kerr rotation φ_{max}.

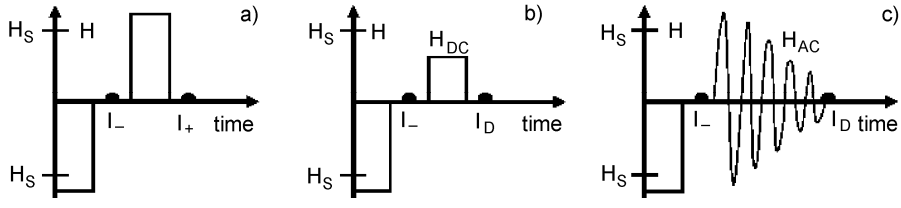

Fig. 1. Various procedures of domain structure imaging

We assume that each image sample element P (i, j) consists of two components: a constant nonmagnetic component presented in all images and a magnetooptical component detected in images with multidomain structure. Considering a constant component as a background of the image, the standard operation of background correction of image improvement [6, 7] is applied:

$$C_{i,j} = \frac{\left(P_{i,j} - B_{i,j}\right)\left(W_{\max} - B_{i,j}\right)}{\left(W_{i,j} - B_{i,j}\right)} \tag{2}$$

where Pi, j is the value of the pixel brightness in the image with magnetooptical component, $B_{i,j}$ – the value of the pixel in an image without a magnetooptical component,

$W_{i,j}$ – the value of the pixel of the image at full CCD saturation of the chamber (light overflow), $W_{\max}$ is the maximum value of brightness of the image at saturation of chamber and $C_{i,j}$ is a new value of the pixel brightness in the corrected image.

We reduced shot noise by applying the median filter. The median filter is a nonlinear lowpass filter which replaces the gray scale value of each pixel by the median grayscale value of the pixel and of its 24 neighbours. This procedure effectively removes shot noise but leaves dendrites, which typically have an effective width covering many pixels.

Let us first describe properties of a double wedge sample with vanadium coverage. Figure 2 illustrates the remnant magnetic state of the sample. Domain structure images recorded in A and B regions marked in Fig. 2, are shown in the first and second row in Fig. 3, respectively. Domain structures were obtained using two following procedures: (i) ac demagnetization (see the scheme in Fig. 1c) after applying alternating field with decreasing amplitude; exemplary images are shown in the first column in Fig. 3; (ii) direct magnetization reversal process [8] (scheme of the procedure in Fig. 1b); images are shown in the second column in Fig. 3. For detection of geometrical characteristics it is necessary to take a binary image. Image binarisation is executed by thresholding using Otsu method [9].

Next we measure such parameters of the domain structure as the area, perimeter, the linear sizes, and shape factor. Because of the digital character of the image there are two ways of calculation of geometrical characteristics: traditional and planimetric. In both of these methods every pixel has a linear size, and calculation of geometrical characteristics is carried out on a selected point. In the traditional method, this point is in the centre of the pixel and the size is equal to the area of pixel. The planimetric calculations operate with the linear distances between points placed in the corners of the pixel. Thus, in planimetric calculations the vertical and horizontal distances between points are equal to the linear sizes of a pixel, but diagonal distances are defined by Pythagorean theorem. The perimeter is calculated in similar terms as a contour of object.

For determination of topological parameters of the image, the binarisation of images was done as in the previous case. Topological characteristics are allocated by means of the Boolean logic operations for images and mathematical morphology smoothing. We defined three topological regions in dendrite images: body of dendrites, fiords and holes (Fig. 3 AIII, BIII). Fiords and holes are the regions between dendrites. Fiords are connected with free space. Holes are enclosed only by white body of dendrites. For the description of these topology features, we propose the following characteristics: total area, fiord ratio, hole ratio, dendrite ratio. The total area is defined as a sum of all topological region areas. Other characteristics corresponding to space filling are defined by relations between areas of particular regions and total area. For description of other topological properties of dendrites, it is necessary to extract the dendrite skeleton from a binary image. This operation is realized by the binary thinning operation (Zang–Suen algorithm [10]). The basic objects used for the calculations are body, skeleton, nodes and tails (Fig. 4), where body corresponds to

the region of white domain; skeleton is the mean line of dendrites; nodes are the points of dendrite branching, segments are the branches between two nodes and tails are the "last branches" of dendrites. To describe the topology features of a dendrite, we define the following characteristics: dendrite length, mean dendrite width, tailness, tail curliness, tails ratio. The dendrite length corresponds to the length of the skeleton. The tailness and tails curliness are defined as count of tails per skeleton length unit and the ratio between the count of tails and the count of segments and the last parameter – tails ratio is the ratio between length of tails and length of skeleton.

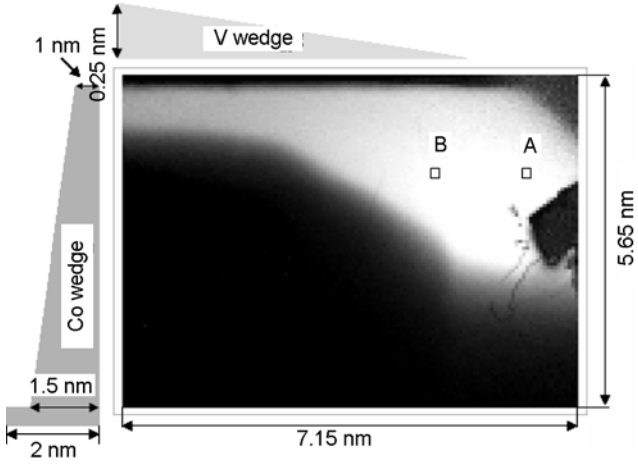

Fig. 2. Remnant magnetization state of the sample with vanadium overlayer

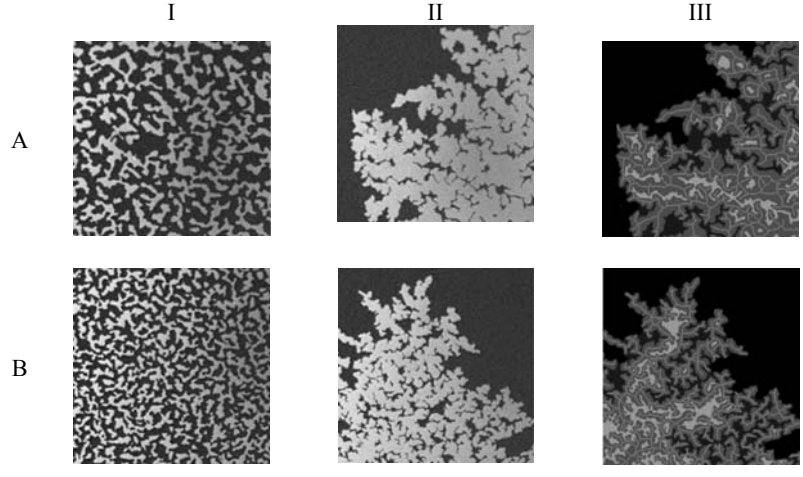

Fig. 3. Domain structures in V-covered sample. The images from the first and the second row were recorded in the A and B areas marked with squares in Fig. 2. Images in the columns were obtained by: (i) ac procedure after applying alternating field (first column); (ii) direct magnetization reversal process (see Fig. 1b) applying DC field pulse to initially saturated sample (second column); (iii) processing of images from the second column (third column). Images size is $100 \times 100\ \mu m^2$

Dendrite width is a more complicated characteristic because it changes from point to point. Moreover, it is impossible to define skeleton width in points corresponding to the nodes and dendrite crossings. Points of skeleton ends distinguish from noise points in a very complex way. To solve these problems, we approximate the mean dendrite width by a relation between the area of dendrites and the length of a skeleton.

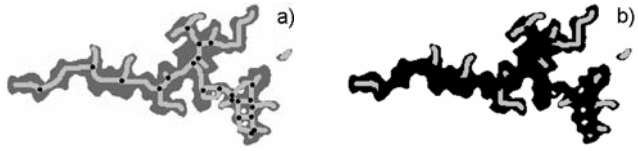

Fig. 4. Topological parameters of dendrites: a) gray – dendrite body, light gray – skeleton, black – nodes; b) black – dendrite body, gray – tails

The last characteristic of the domain structure that is necessary to introduce is the dendrite orientation. The orientation diagram (see insets in Fig. 5) illustrates the dependence of segment length on direction (the angle between line containing segment and horizontal line in the image). The preference of DS direction may be connected with in-plane anisotropy introduced by the molybdenum overlayer.

Table 1. Topological parameters of DS images

Image	Total area [μm^2]	Fiord ratio	Hole ratio	Dendrite ratio	Dendrite length [μm]	Mean dendrite width [μm]	Tailness [μm^{-1}]	Tail curliness	Tail ratio
A	6970	0.16	0.09	0.75	1405	4.96	0.11	0.37	0.33
B	5970	0.18	0.12	0.70	1484	4.02	0.15	0.50	0.39

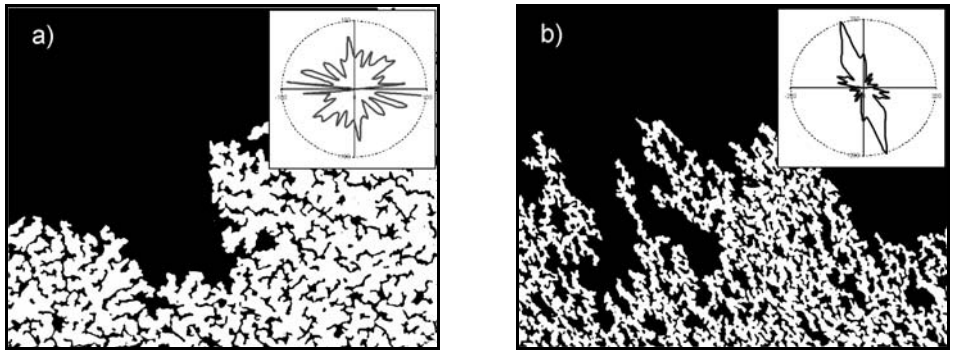

Fig. 5. Domain structure images of sample with: a) vanadium (effective d_V = 0.03 nm), b) molybdenum overlayer. Insets illustrate orientation of dendrites

The values of the parameters described above are given in Table 1. Comparing images in Fig. 3 one can mention that the size of domains decreases with approaching RPT, the mean width of dendrites also decreases, and such parameters as tailness, tail

curliness etc. also change. Mo induced domain orientation is shown in Fig. 5. The observed preference of DS in Fig. 5 could be related to in-plane magnetic anisotropy which is connected with pseudomorphic growth of Mo overlayer.

References

[1] HEINRICH B., BLAND J.A.C., *Ultrathin Magnetic Structures*, Springer, Berlin, 1994 and references therein.
[2] KISIELEWSKI M., MAZIEWSKI A., TEKIELAK M., WAWRO A., BACZEWSKI L.T., Phys. Rev. Lett., 89 (2002), 87203 and references therein.
[3] HOPSTER H., OEPEN H.P., *Magnetic microscopy of nanostructures, NanoScience and Technology*, Springer, Berlin, 2005.
[4] KISIELEWSKI M., KURANT Z., TEKIELAK M., DOBROGOWSKI W., MAZIEWSKI A., WAWRO A., BACZEWSKI L.T., Phys. Status Sol. (a), 196 (2003), 129.
[5] STEFANOWICZ W., TEKIELAK M., BUCHA W., MAZIEWSKI A., ZABLOTSKII V., BACZEWSKI L.T., WAWRO A., Mater. Sci.-Poland, 24 (2006), 783.
[6] RITTER G.X., WILSON J.N., *Handbook of Computer Vision Algorithms in Image Algebra*, CRC Press, Boca Raton, Fl, USA, 1996.
[7] PATURI P., HVOLBEK LARSEN B., JACOBSEN B.A., ANDERSEN N.H., Rev. Sci. Instr., 74 (2003), 2999.
[8] FERRE J., GROLIER V., MEYER P., MAZIEWSKI A., STEFANOWICZ E., TARASENKO S.V., TARASENKO V.V., KISIELEWSKI M., RENARD D., Phys. Rev. B, 55 (1997), 15092.
[9] SAHOO P.K., SOLTANI S., WONG A.K.C., CHEN Y.C. Comp. Vision Graph. Image Proc., 41 (1988), 233.
[10] ZHANG T.Y., SUEN C.Y., Comm. ACM, 27 (1984), 236.

Received 7 May 2006
Revised 1 September 2006

Materials Science-Poland, Vol. 25, No. 2, 2007

Electronic structure and electric properties of $Gd(In_{1-x}Sn_x)_3$ compounds

M. KWIECIEŃ, G. CHEŁKOWSKA*, A. BETLIŃSKA

A. Chełkowski Institute of Physics, Silesian University, Uniwersytecka 4, 40-007 Katowice, Poland

Results of measurements of the electrical resistivity, crystal and electronic structure of $Gd(In_{1-x}Sn_x)_3$ compounds are reported. All these compounds crystallize in the cubic $AuCu_3$ type structure. The effect of partial substitution of In by Sn atoms is reflected in a linear increase of the unit cell volume. The temperature dependence of the electrical resistivity ρ strongly depends on the composition. For compounds with $x \geq 0.1$, the $\rho(T)$ behavior, observed at low temperatures, is untypical of metals. The electronic structure of all systems was studied by using X-ray photoelectron spectroscopy. The chemical shift of the 4f Gd peak to higher binding energy with the increase of Sn concentration was detected. The valence band near the Fermi level is dominated by hybridized 5d Gd and 5p In/Sn states.

Key words: *intermetallics; photoelectron spectroscopy; electrical resistivity*

1. Introduction

Intermetallic compounds RSn_3 and RIn_3 and their pseudobinary alloys show many interesting properties such as the presence of various magnetic structures, valence fluctuations and magnetic moment formation. Some of these features are not fully understood, hence the study of a system with R = Gd, which has a half-filled shell, seems to be well-founded. Both $GdIn_3$ and $GdSn_3$ are antiferromagnets with the transition temperatures (T_N) of 45 K and 31 K, respectively, and crystallize in the cubic $AuCu_3$-type of structure (space group *Pmcm*) [1, 2]. The measurements of the magnetic susceptibility for the $Gd(Sn_{1-x}In_x)_3$ performed by Lin, Yuen et al. [3] exhibited an oscillatory variation of the antiferromagnetic transition temperature T_{N1} across the whole series, as well the appearance of the second magnetic transition T_{N2} at lower temperatures for some In-doped samples. The Mössbauer results [4] have shown that magnetic structure of the system changes from type I antiferromagnetic ordering on the Sn-rich side to type II antiferromagnetic ordering on the very rich In side. For the

* Corresponding author, e-mail: gchelkow@us.edu.pl

range of intermediate In concentrations, the type I antiferromagnetic or the canted antifferomagnetic ordering state was proposed. The oscillatory behaviour in T_{N1} has been attributed to a band-structure effect arising from the mixing of 5d electrons from the rare-earth ions and the s and p bands of Sn and In.

The aim of this work was to investigate the effect of a partial substitution of In by Sn atoms on the electronic structure, examined with the use of X-ray photoelectron spectroscopy (XPS), as well as the electrical resistivity of the $Gd(In_{1-x}Sn_x)_3$ system.

2. Experimental

Polycrystalline samples of the $Gd(In_{1-x}Sn_x)_3$ system with x = 0.0, 0.05, 0.10, 0.20, 0.50, 0.80 and 1.00 were prepared from stoichiometric amounts of the constituent metals by arc melting under argon atmosphere. After melting, the samples were annealed in quartz tubes at 650 °C for 5 days. Phase identification of the alloys was performed by powder X-ray diffraction technique using Siemens D5000 diffractometer at room temperature. All samples had a cubic $AuCu_3$ type of structure. The temperature dependence of the electrical resistivity $\rho(T)$ was measured by means of the standard four-probe technique in the temperature range from 4.2 K to 300 K. The samples were cut with a wire saw to a size of $1 \times 1 \times 5$ mm^3.

The electronic structure was studied by means of X-ray photoelectron spectroscopy. The XPS spectra were obtained with monochromatized AlK_α radiation ($h\omega$ = 1486.6 eV) at room temperature using a PHI 700/660 Physical Electronics Spectrometer. The spectra were measured immediately after scraping the surface with diamond file in vacuum of 10^{-10} Torr. The scraping in high vacuum produced clean surfaces, free of oxygen and carbon contamination.

3. Results and discussion

The substitution of In by Sn in the $Gd(In_{1-x}Sn_x)_3$ system caused a linear increase of the lattice parameter a with concentration x in agreement with Vegard's law (Fig. 1). The character of the temperature variation of the electrical resistivity $\rho(T)$ below the Néel temperature (T_N) indicated a strong dependence on x (Fig. 2). For indium rich compounds (with x = 0.0 and 0.05), pronounced changes in the slope of the $\rho(T)$ curves at T_N = 45 K and 44 K (respectively) were observed, which is typical of metallic systems. The substitution of 10% In by Sn atoms in the system caused essential change in the character of $\rho(T)$ in the low temperature range. For this compound, the $\rho(T)$ curve shows two minima, at 43 K and 13 K. A non-typical dependence of $\rho(T)$, reflected in an increase of the resistivity with decreasing temperature below T_N was observed for the sample with x = 0.2. For higher concentrations of Sn, these minima were very weakly visible. According to the Matthiesen rule, the thermal dependence of electrical resistivity is given by the equation:

$$\rho(\mathrm{T}) = \rho_0 + \rho_{\mathrm{ph}}(T) + \rho_{\mathrm{mag}}(T)$$

where the first term represents a residual resistivity, the second the phonon contribution and the third one the spin-disorder contribution which is caused by the scattering of the conduction electrons on 4f moments.

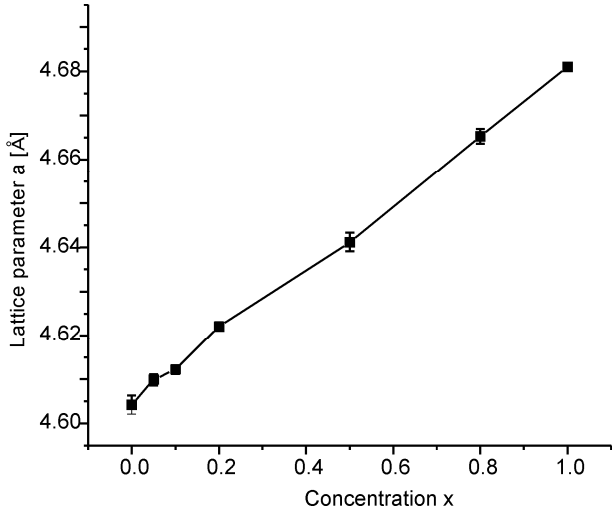

Fig. 1. Lattice parameter *a* versus concentration *x* for the $Gd(In_{1-x}Sn_x)_3$ system

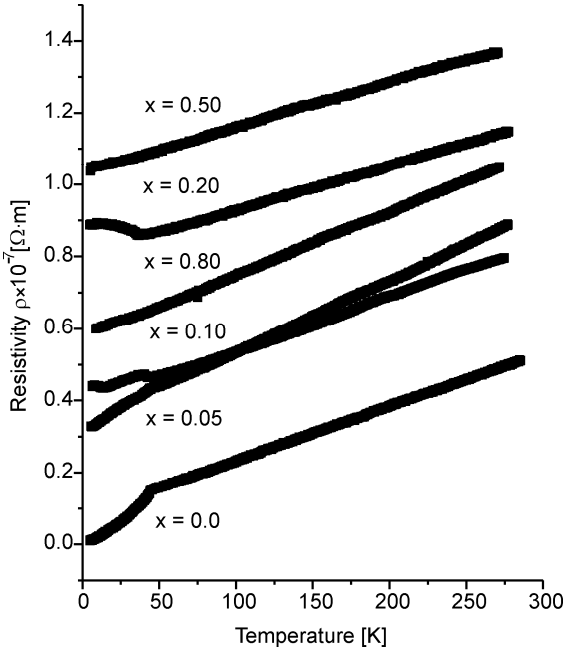

Fig. 2. Temperature dependence of the electrical resistivity of $Gd(In_{1-x}Sn_x)_3$ compounds

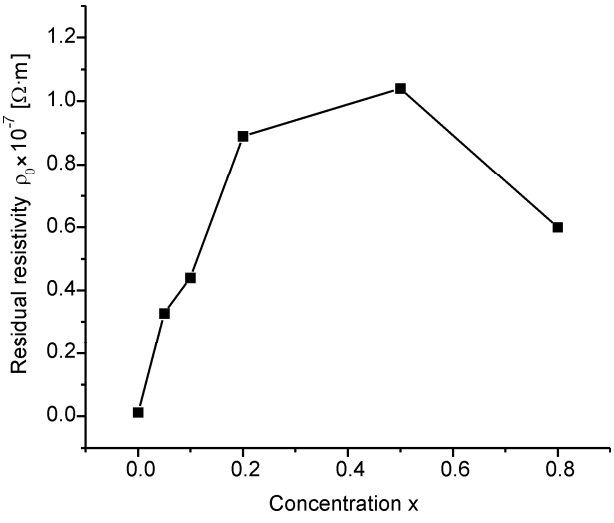

Fig. 3. Residual resistivity $\rho_0(T)$ versus x for the $Gd(In_{1-x}Sn_x)_3$ system

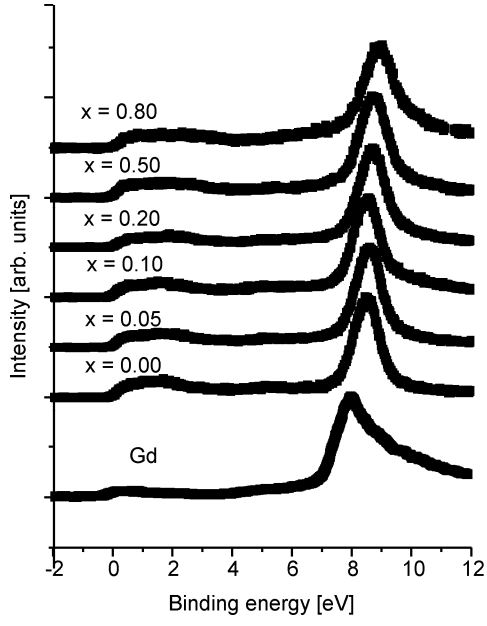

Fig. 4. XPS valence band region of the $Gd(In_{1-x}Sn_x)_3$ system.
The spectrum of pure Gd is included for comparison

In the investigated $Gd(In_{1-x}Sn_x)_3$ system, the residual resistivity ρ_0 increases with x, reaches a maximum around $x = 0.5$ and decreases for Sn-rich compounds (Fig. 3). Such a behaviour of $\rho_0(x)$ can be related to some crystal disorder in the In/Sn sublattice upon the substitution, nevertheless this disorder cannot be the only reason for the non-typical dependence of $\rho(T)$ at low temperatures. The increase of $\rho(T)$ observed

below T_N must be connected with some additional mechanism which increases the scattering of conduction electrons. We attribute this anomaly to the complex magnetic structure of these compounds reported in [3, 4].

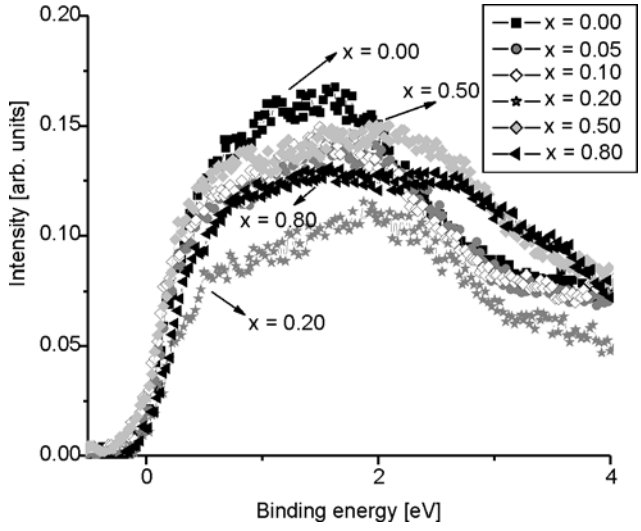

Fig. 5. The XPS spectrum of $Gd(In_{1-x}Sn_x)_3$ compounds near the Fermi level

Table1. Binding energy of 4f Gd and 4d Gd of the $Gd(In_{1-x}Sn_x)_3$ system*

Compound	The position of 4f Gd [eV]	The position of 4d Gd [eV]
$GdIn_3$	8.5	140.6
$Gd(In_{0.9}Sn_{0.1})_3$	8.6	140.7
$Gd(In_{0.8}Sn_{0.2})_3$	8.7	140.8
$Gd(In_{0.5}Sn_{0.5})_3$	8.8	141.0
$Gd(In_{0.2}Sn_{0.8})_3$	9.0	141.1

* For 4d Gd, the first line of the multiplet was taken into account.

The XPS spectra in the valence band region for $Gd(In_{1-x}Sn_x)_3$ (x = 0.0, 0.05, 0.1, 0.2, 0.5 and 0.8) are presented in Figs. 4 and 5. All spectra are normalized to the maximum intensity of the 4f Gd peak. The spectrum for pure Gd is added for comparison. In all compounds, the position of 4f Gd photoemission peak is shifted to higher binding energy in relation to that in the metallic Gd. The value of the shift for $GdIn_3$ is about 0.4 eV and is in agreement with the result obtained by Szade et al. [5]. Upon replacing In by Sn atoms, an additional shift of 4f Gd peak is observed. Similar changes in the energy positions were found for 4d Gd levels (not presented here). For analyzing the shift of the 4d Gd level, the first line of the multiplet was taken into account. The values of binding energies of 4f Gd and 4d Gd peaks in all investigated

compounds are collected in Table 1. The observed shifts are probably caused by the increase of the environmental potential, resulting from charge transfer from Gd to neighbouring atoms. Gadolinium has lower electronegativity than In and Sn and has a tendency to transfer electrons to other metal sites. The region of binding energy close to the Fermi level E_F (Fig. 5) is characterized by a contribution coming from the 5d Gd, 5p In and 5p Sn states. The observed change in the photoemission intensity, as well as a change of the shape of peaks near E_F with increasing Sn concentration, are caused by the hybridization effect in this energy range, which seems to be consistent with earlier investigations.

Acknowledgements

The research was supported by the Polish MEiN, Grant No. 1 PO3B 107 30.

References

[1] BUSCHOW K.H.J., DE WIJN H.W., VAN DIEPEN A.M., J. Chem. Phys., 50 (1969), 137.
[2] DELONG L.E., GUERTIN R.P., FONER S., Solid State Commun., 32 (1979), 833.
[3] LIN C.L., YUEN T., MIHALISIN T., Phys. Rev. B, 54 (1996), 9254.
[4] YUEN T., LIN C.L., MIHALISIN T., BYKOVETZ N., J. Appl. Phys., 70 (1991), 5995.
[5] SZADE J., NEUMANN M., J. Phys., Condens. Matter, 11 (1999), 3887.

Received 7 May 2006
Revised 1 September 2006

Materials Science-Poland, Vol. 25, No. 2, 2007

Magnetic properties of Au/Co/$Ni_{80}Fe_{20}$/Co/Au layered structures

K. ZAŁĘSKI[1, 2], M. URBANIAK[1], B. SZYMAŃSKI[1], M. SCHMIDT[1], J. ALEKSIEJEW[1], F. STOBIECKI[1*]

[1]Institute of Molecular Physics, Polish Academy of Sciences, M. Smoluchowskiego 17, 60-179 Poznań, Poland

[2]Institute of Physics, Adam Mickiewicz University of Poznań, Umultowska 85, 61-614 Poznań, Poland

The influence of an ultrathin cobalt layer at permalloy/gold interfaces in Au/$Ni_{80}Fe_{20}$/Au sandwiches and spin-valve $(Ni_{80}Fe_{20}/Au/Co/Au)_N$ multilayers on their magnetic and magnetotransport properties is investigated. We show that an effective magnetic anisotropy of Co/$Ni_{80}Fe_{20}$/Co hybrid structures sandwiched between Au layers can be easily varied by the thickness adjustment of Co and $Ni_{80}Fe_{20}$ layers. We also show that changes of the anisotropy are mainly determined by the Co layer deposited on Au. On the other hand, the influence of Co layer deposited on $Ni_{80}Fe_{20}$ is relatively small. The use of hybrid layers in the spin valve MLs with alternating easy plane and perpendicular anisotropy in consecutive ferromagnetic layers leads to significant changes of their magnetoresistance effect.

1. Introduction

Magnetic thin film layered structures with new magnetic properties are potentially applicable in spintronic devices. This paper presents a study of the magnetic properties of Co/$Ni_{80}Fe_{20}$/Co trilayers sandwiched between gold layers. The main goal was to develop hybrid layers in which the effective anisotropy field H_K^{eff} (the saturation field for the perpendicular configuration) can be varied over a wide range. This can be realized in systems with strong perpendicular surface anisotropy such as Au/Co/Au [1, 2]. In the Au/Co/Au system, H_K^{eff} monotonically increases with increasing Co thickness for $t_{\text{Co}} > t_{\text{crit}}$ (t_{crit} – critical cobalt thickness corresponding to the spin reorientation transition) due to the competition between the shape and surface anisotropy.

*Corresponding author: stfeliks@ifmpan.poznan.pl

It is to be expected that replacing a single Co layer in the Au/Co/Au system with Co/$Ni_{80}Fe_{20}$/Co trilayer could significantly influence H_K^{eff}. The Co thickness range corresponding to the creation of continuous Co layer in which the surface anisotropy contribution increases gradually, seems to be especially interesting.

The giant magnetoresistance effect and magnetization reversal in spin valve (SV) type $(F_{\|}/S/F_{\perp}S)_N$ ($F_{\|}$, $F_{\perp}$ – ferromagnetic layers with in-plane and out-of-plane anisotropy, respectively, S – spacer, N – repetition number) multilayers with the [Au/$Ni_{80}Fe_{20}$/Au/$Co_{\perp}$/Au] structure where permalloy layer was replaced with the Co/$Ni_{80}Fe_{20}$/Co trilayer was discussed in detail in our previous paper [3]. The paper presented correlations between resistance and magnetization dependences and explained how to determine H_K^{eff} of Co/$Ni_{80}Fe_{20}$/Co layer ($F_{\|}$). We explained there how the changes of the H_K^{eff} of $F_{\|}$ layer influence effects associated with the presence of a domain structure. The present paper describes supplementary investigations of structures with different $F_{\|}$. The main purpose was to determine the differences between H_K^{eff} (t_{Co}) dependences of the structures having a Co layer at both interfaces (Co/$Ni_{80}Fe_{20}$/Co) or at only one interface (Co/$Ni_{80}Fe_{20}$ or $Ni_{80}Fe_{20}$/Co). It should be noted that investigated bi- and trilayers, because of their total thickness much lower than the domain wall thickness, can be treated as magnetically homogeneous [4], i.e. with magnetization vector constant along the normal to the film surface.

2. Experimental

The multilayers were prepared by magnetron sputtering. Preparation details are given in the previous paper [5]. The value of H_K^{eff} as a function of thickness of $Ni_{80}Fe_{20}$ and Co layers was determined from $M(H)$ dependences measured using magnetooptical Kerr effect in polar configuration (MOKE, 1mm spot size). MOKE measurements were performed on the sandwich structure: substrate/buffer/Co-wedge/$Ni_{80}Fe_{20}$-steps/Co-wedge/Au. Si(100) substrate (15×20 mm^2 in size) was covered with a buffer ($Ni_{80}Fe_{20}$-2nm/Au-3 nm)$_{10}$ multilayer. The multilayered buffer ensured the topmost Au layer with large crystal grain size (20 nm lateral dimensions determined by STM) and (111) texture. The Co thickness in the wedges was varied from 0 to 1 nm and the thickness gradient was parallel to the long edge of the sample. The permalloy layer was introduced in a form of three steps (5 mm wide, running perpendicularly to the Co wedge gradient) with thickness t_{NiFe} = 0, 0.25, 0.5 nm. Three series of the SV structures were also deposited. In SV samples with the $(F_{\|}/S/F_{\perp}/S)_N$ structure, 2.2 nm thick Au spacer ensured a negligibly weak interaction between $F_{\|}$ and $F_{\perp}$ [5]. 0.8 nm thick Co layer was used as $F_{\perp}$, later denoted as $Co_{\perp}$ (for $0.3 \le t_{\text{Co}} \le 1.2$ nm perpendicular anisotropy is observed in this type of multilayers). The ferromagnetic $F_{\|}$ layers with in-plane anisotropy were prepared as tri- or bilayers: Co/$Ni_{80}Fe_{20}$/Co (series (SV-a)), Co/$Ni_{80}Fe_{20}$ (series (SV-b)) and $Ni_{80}Fe_{20}$/Co (series

(SV-c)). The total thickness of the $F_{||}$ layers was kept constant at 3.2 nm and t_{Co} thickness was varied. The t_{Co} values were 0, 0.2, 0.4, 0.6 for all series and additionally t_{Co} = 1.6 nm for series (SV-a) (in this case $F_{||}$ was a single 3.2 nm thick Co layer). H_K^{eff} value of SV multilayers with a number of repetitions N = 10 was determined from hysteresis loops (M(H) dependences) measured with a vibrating sample magnetometer (VSM) and from magnetoresistance measurements (R(H) dependences). All measurements were carried out at room temperature with magnetic field perpendicular to the sample surface.

3. Results and discussion

Figure 1a shows a typical M(H) dependence measured using MOKE for sandwich samples. Its shape indicates clearly that it is a superposition of two hysteresis loops. One loop comes from the reversal of $Ni_{80}Fe_{20}$ (buffer) layer which saturates at about 0.6 T. This corresponds to the shape anisotropy of that layer ($4\pi M_S^{NiFe}$). The other one originates from the reversal of the investigated (Co/NiFe/Co) trilayer, with much smaller H_K^{eff} value. The contribution from the trilayer is clearly visible due to a significant difference between effective anisotropy field of the buffer and the trilayer, and a weak coupling between the two across the Au spacer [5]. It allowed us to determine H_K^{eff} of Co/$Ni_{80}Fe_{20}$/Co trilayer and Co film sandwiched between Au layers.

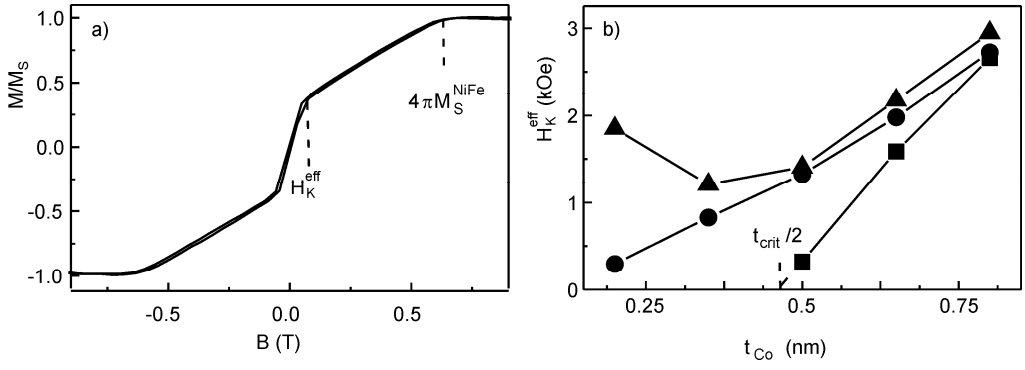

Fig. 1. Exemplary hysteresis loop (a) and the dependence of effective anisotropy field H_K^{eff} on cobalt layer thickness t_{Co} in [($Ni_{80}Fe_{20}$/Au)$_{10}$/Co/$Ni_{80}Fe_{20}$-t_{NiFe}/Co/Au] layered films for t_{NiFe} = 0 nm (■); 0.25 nm (●); 0.5 nm (▲) (b)

Figure 1b shows the effective anisotropy field H_K^{eff} of the trilayer as a function of Co thickness ($0.2 \le t_{Co} \le 0.8$ nm) for three various permalloy sublayer thicknesses t_{NiFe} = 0, 0.25 and 0.5 nm (for t_{NiFe} = 0, the total thickness of Co layer is $2t_{Co}$). The H_K^{eff} (t_{Co}) dependence of a single Co layer is typical of a system with a significant contribution of surface anisotropy. The critical Co thickness (determined from

$H_K^{\text{eff}}(t_{\text{Co}})$ dependence for $t_{\text{NiFe}} = 0$, Fig. 1b) corresponding to magnetization reorientation from out-of-plane to in-plane is about 0.9 nm. $H_K^{\text{eff}}(t_{\text{Co}})$ monotonically increases for $t_{\text{Co}} > t_{\text{crit}}$ indicating a diminishing contribution of surface anisotropy to the effective anisotropy described by the well-known equation $K_{\text{eff}} = K_{\text{V}} + 2K_{\text{S}}/t$, ($K_{\text{V}}$ and K_{S} – volume and surface anisotropy constants, respectively). For permalloy thickness $t_{\text{NiFe}} = 0.5$ nm, the function $H_K^{\text{eff}}(t_{\text{Co}})$ exhibits a minimum at $t_{\text{Co}} \approx 0.4$ nm. The observed dependence probably reflects a weak contribution of the Au/Ni-Fe interface to K_{S} and the fact that the contribution of Au/Co interface to K_{eff} is the largest when Co layer becomes continuous. It should be noted that Co layer grown on Au(111) becomes continuous for the thickness greater than two atomic layers [6].

For small t_{Co}, the trilayer with an intermediate permalloy thickness $t_{\text{NiFe}} = 0.25$ nm exhibits a linear increase of $H_K^{\text{eff}}(t_{\text{Co}})$ with the slope considerably smaller comparing to the sample without permalloy. The comparison of the $H_K^{\text{eff}}(t_{\text{Co}})$ dependences for Au/Co/Au and Au/Co/$Ni_{80}Fe_{20}$/Co/Au structures indicates that the introduction of an ultrathin NiFe layer in the middle of the Co layer results in a strong decrease of t_{crit}.

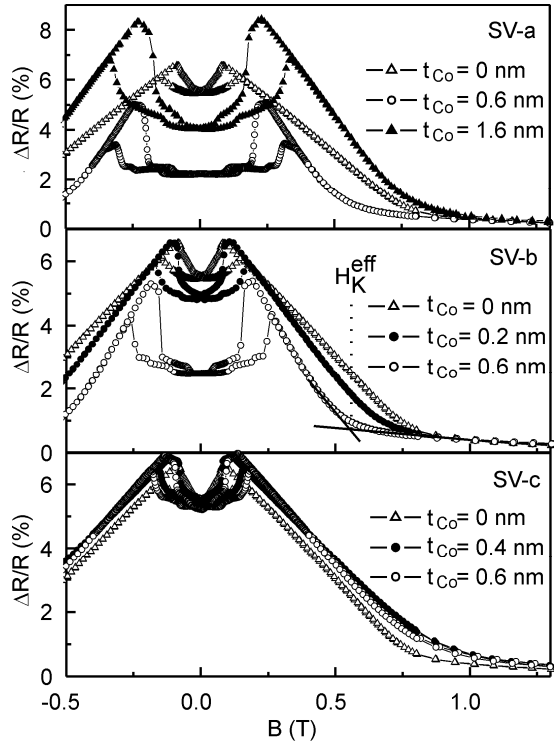

Fig. 2. Magnetoresistance effect of three sets of $(F_{\|}/S/F_{\perp}/S)_{10}$ spin valve multilayers (see also description in Experimental) with S = Au 2 nm, $F_{\perp}$ = $Co_{\perp}$ 0.8 nm and $F_{\|}$ = Co/NiFe/Co (SV-a), $F_{\|}$ = Co/NiFe (SV-b), $F_{\|}$ = NiFe/Co (SV-c) with $t_{F\|} = 3.2$ nm, the thicknesses of Co layers are given in the figure; $\Delta R/R$ dependences are shown in a limited field range for clarity

Figure 2 shows $\Delta R/R(H)$ dependences as a function of Co thickness for all three types of SV structures. It can be seen that placing an ultrathin Co layer at both interfaces or at the bottom interface only leads to similar changes in magnetoresistance dependences. The changes in magnetoresistance indicate the decrease of H_K^{eff} value for $t_{\text{Co}} \leq 0.6$ nm (Figs. 2a, b). Simultaneously, the effects associated with the presence of the domain structure, i.e. a sudden resistance decrease in small fields, are stronger. On the contrary, in structures with a Co layer at the upper interface only, the changes of $R(H)$ dependence indicate slight increase of H_K^{eff} with t_{Co} and small changes in magnetic fields corresponding to the presence of the domain structure.

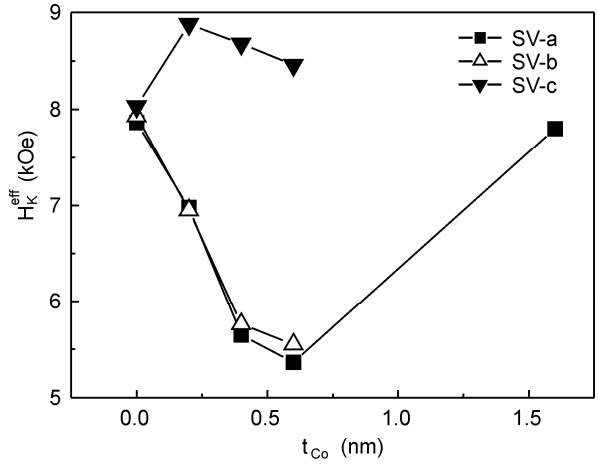

Fig. 3. Effective anisotropy field H_K^{eff} as a function of cobalt layer thickness determined from $\Delta R/R(H)$ dependences measured for three series of spin valve multilayers

Figure 3 shows the effective anisotropy field for all three series of spin valves as a function of cobalt thickness. A comparison of the dependences shown in Fig. 1 for $t_{\text{NiFe}} = 0.5$ nm and those shown in Fig. 3 reveal that $H_K^{\text{eff}}(t_{\text{Co}})$ dependences for structures with Co layer at both interfaces and at the bottom interface only are similar. For both cases described above, $H_K^{\text{eff}}(t_{\text{Co}})$ shows a local minimum which, in our opinion, is due to the growth of a continuous Co layer on gold. The differences in H_K^{eff} values for the Co/$Ni_{80}Fe_{20}$/Co structures shown in Figs. 1 and 3 originate from different permalloy layer thicknesses. The presence of a weak maximum in $H_K^{\text{eff}}(t_{\text{Co}})$ dependence for structures with Co layer at the upper interface only indicates that the effective perpendicular anisotropy of Co layers is lower (compare the discussion of Fig. 1). The initial increase of H_K^{eff} with t_{Co} is thus the result of the increase of the effective magnetization of NiFe/Co bilayer. At higher Co coverage, the perpendicular anisotropy leads to a slow decrease of H_K^{eff}.

4. Conclusions

Hybrid thin film samples consisting of Co and $Ni_{80}Fe_{20}$ layers sandwiched between Au were investigated. It was shown that the insertion of thin cobalt layer at the lower interface of the Au/$Ni_{80}Fe_{20}$/Au structure, resulting in Au/Co/$Ni_{80}Fe_{20}$/Au structure, significantly decreases the easy-plane type anisotropy field. The anisotropy field of hybrid layers can be controlled in a wide range by permalloy and cobalt layers thickness. It was also shown that this property of hybrid layers can be applied to a significant modification of magnetoresistance dependences of spin valves with alternating easy plane and perpendicular magnetic anisotropy in consecutive ferromagnetic layers.

Acknowledgements

Supported by the Polish State Committee for Scientific Research with Grant 3 T08A 03127 and from the science resources as a joint research program within the scientific network "New materials and sensors for optoelectronics, informatics, energetic and medicine".

References

[1] CHAPPERT C., LE DANG K., BEAUVILLAIN P., HURDEQUINT H., RENARD D., Phys. Rev. B, 34 (1986), 3192.
[2] BLAND J.A.C., HEINRICH B., *Utrathin Magnetic Structures I*, Springer, Berlin, 1994.
[3] STOBIECKI F., URBANIAK M., SZYMAŃSKI B., SCHMIDT M., LUCIŃSKI T., phys. stat. sol. B, 243 (2006), 210.
[4] ASTI G., SOLZI M., GHIDINI M., NERI F.M., Phys. Rev. B, 69 (2004), 174401.
[5] STOBIECKI F., SZYMAŃSKI B., LUCIŃSKI T., DUBOWIK J., URBANIAK M., K. RÖLL K., J. Magn. Magn. Mater., 282 (2004), 32.
[6] VOIGTLÄNDER B., MEYER G., AMER N.M., Phys. Rev. B, 44 (1991), 10354.

Received 7 May 2006
Revised 1 September 2006

Materials Science-Poland, Vol. 25, No. 2, 2007

Surface segregation effect in nanocrystalline Mg–Ni alloys and composites

K. SMARDZ[1], L. SMARDZ[2*], I. OKOŃSKA[1] , M. JURCZYK[1]

[1]Institute of Materials Science and Engineering, Poznań University of Technology, M. Skłodowskiej-Curie 5, 60-965 Poznań, Poland

[2]Institute of Molecular Physics, Polish Academy of Sciences, Smoluchowskiego 17, 60-179 Poznań, Poland

X-ray photoelectron spectroscopy studies showed that the surface segregation of Mg atoms and width of the valence band in the nanocrystalline Mg_2Ni alloy are greater compared to those observed in polycrystalline Mg_2Ni thin films. Especially, a strong surface segregation of Mg atoms was observed for the Mg_2Ni/Pd composites. In this case, Mg atoms strongly segregate to the surface and form an Mg-based oxide layer under atmospheric conditions. The lower lying Ni and Pd atoms form a metallic subsurface layer and could be responsible for the observed, relatively high hydrogenation rate. Furthermore, the valence band broadening observed in the nanocrystalline Mg_2Ni alloys and Mg_2Ni/Pd composites could also significantly influence their hydrogenation properties.

Key words: *Ni–Mg alloy; nanocrystalline alloy; electronic structure*

1. Introduction

A large number of experimental investigation on $LaNi_5$, TiFe, ZrV_2-type compounds have been performed up to now in relation to their exceptional hydrogenation properties [1]. Magnesium-based hydrogen storage alloys have also been considered to be possible candidates for electrodes in Ni-MH batteries [2].

An important process on the surface of the hydrogenated material is the splitting of hydrogen molecules into atoms. Many clean transition metal surfaces have the capability of dissociating hydrogen but lose this property upon oxidation. It is well known that the oxidation process causes the sealing of the surface to H_2 in metals and compounds such as Nb, V, Ta, FeTi, and others [3]. On the other hand, in a surface layer of $LaNi_5$, La segregates and Ni form ferromagnetic precipitations [3, 4]. Lantha-

*Corresponding author, e-mail: smardz@ifmpan.poznan.pl

num atoms bind the impurities as oxide or hydroxide and keep the Ni metallic, which is then able to split the hydrogen molecule [3]. Therefore, the surface segregation process of lanthanum in the presence of O_2 or H_2O explained the excellent hydrogenation properties of $LaNi_5$ [3–5].

In this paper, we study the surface segregation effect in polycrystalline and nanocrystalline Mg_2Ni alloys and Mg_2Ni/Pd composites using X-ray photoelectron spectroscopy (XPS) with depth profile analysis. The structure of the samples has been studied by X-ray diffraction (XRD) with CoK_α radiation, and with an atomic force microscope (AFM). Their bulk chemical compositions were measured using the X-ray fluorescence (XRF) method. These studies may supply useful indirect information about the influence of the surface segregation effect in Mg–Ni-based alloys and composites on their hydrogenation properties.

2. Experimental procedure

Polycrystalline Mg–Ni alloy thin films were deposited onto glass substrates using a computer-controlled ultra high vacuum (UHV) magnetron co-sputtering. The chemical compositions and the cleanness of all layers were checked *in-situ*, immediately after deposition, transferring the samples to an UHV (4×10^{-11} mbar) analysis chamber equipped with XPS. All emission spectra were measured immediately after transferring of the sample in a vacuum of 8×10^{-11} mbar. The thicknesses and compositions of the deposited films were determined using XRF.

The nanocrystalline Mg_2Ni-type alloys were prepared using mechanical alloying (MA), followed by annealing. MA was performed under argon atmosphere using a SPEX 8000 Mixer Mill. The purities of the starting metallic elements Mg and Ni were 99.9 and 99.95 wt.%, respectively. The mill was run up to 90 h for every powder preparation. The as-milled powders were heat treated at 723 K for 1 h under high purity argon to form an ordered phase. Furthermore, we have also prepared Mg_2Ni/Pd composites with Pd content up to 10 wt. %. The MA and annealed Mg_2Ni powder were mixed with 10 wt. % Pd powder (74 μm, purity 99.95 %) and milled for 1 h in a SPEX Mixer Mill. The weight ratio of hard steel balls to mixed powder was 30:1.

The surface chemical compositions and the cleanness of the samples were measured in UHV using XPS and repeated 3 keV argon ion beam sputtering. Before loading to the UHV preparation chamber, a sample of the studied material with a well -polished surface was rinsed with twice-distilled water and dried in air. In the preparation chamber (10^{-9} mbar) the sample was mounted on the holder equipped with a heater using a special transfer system. The sample was first heated in the preparation chamber at 525 K for 3 h and then *in-situ* transferred to the analysis chamber for the XPS measurements. The above UHV heating procedure at relatively low temperature does not change the microstructure of the studied samples. The XPS spectra were recorded at room temperature using a SPECS EA 10 PLUS energy spectrometer with

AlK_α radiation of 1486.6 eV. The energy spectra of the electrons were analysed by a hemispherical analyser ($FWHM_{Mg\ K\alpha}$ = 0.8 eV for Ag $3d_{5/2}$).

3. Results and discussion

The MA process has been studied by XRD and microstructural investigations, using Mg_2Ni as a representative alloy example. Figures 1a and 1b show XRD patterns of

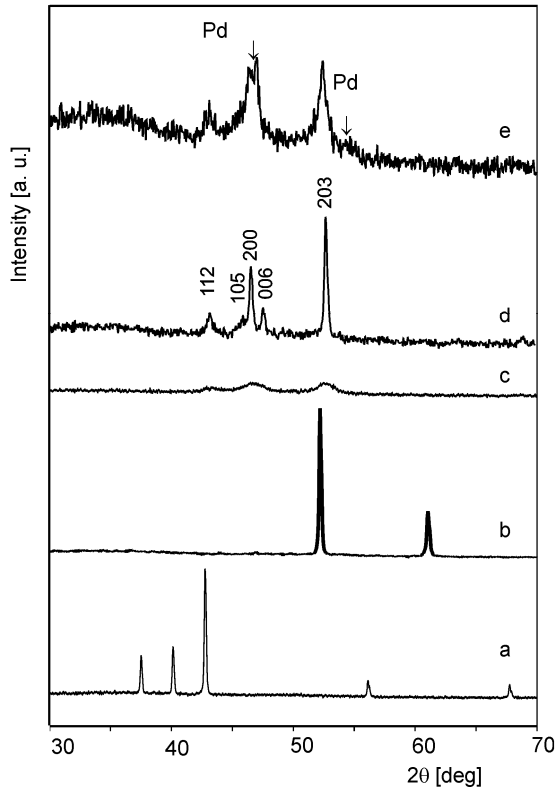

Fig. 1. X-ray diffraction patterns ($CoK_{\alpha 1}$) of pure powders of magnesium (a) and nickel (b), and a mixture of 2Mg and Ni powders after MA for 45 h (c) followed by annealing at 723 K for 1 h (d). Curve (e) represents XRD spectrum of Mg_2Ni/Pd composite

the initial state (elemental powder mixture) of Mg and Ni powders, respectively. The originally sharp diffraction lines of Mg and Ni gradually become broader and their intensity decreases with milling time. Features due to nanostructured Mg_2Ni with broad diffraction peaks are already found after 5 h of MA process. XRD pattern of 2Mg and Ni powders (0.453 wt. % Mg + 0.547 wt. % Ni) after MA for 45 h is shown in Fig. 1c. The powder mixture milled for more than 45 h transform completely to the amorphous phase, without formation of another phase. Formation of the nanocrystalline alloy was achieved by annealing the amorphous material in high purity argon atmosphere at 723 K for 1 h (Fig. 1d). All diffraction peaks were assigned to those of the hexagonal crystal structure with cell parameters a = 5.216 Å, c = 13.246 Å. The

average size of nanocrystalline grains, according to AFM studies, was of the order of 30 nm. Curve e) in Fig. 1 represents XRD spectrum of the Mg_2Ni/Pd composite.

At room temperature, the original nanocrystalline alloy, Mg_2Ni, absorbs hydrogen but almost does not desorb it. At temperatures above 523 K, the kinetics of the absorption-desorption process improves considerably and for nanocrystalline Mg_2Ni alloy the reaction with hydrogen is reversible [6]. The hydrogen content in this material at 573 K is 3.25 wt. %. Upon hydrogenation, Mg_2Ni transforms into the hydride Mg_2Ni-H phase. It is important to note that between 483 and 528 K the hydride Mg_2Ni-H phase transforms from a high temperature cubic structure to a low temperature monoclinic phase [7]. When hydrogen is absorbed by Mg_2Ni beyond 0.3H per formula unit, the system undergoes a structural rearrangement to the stoichiometric complex Mg_2Ni-H hydride, with an accompanying 32% increase in volume.

The Mg_2Ni electrode, mechanically alloyed and annealed, displayed the maximum discharge capacity (100 $mA \cdot h \cdot g^{-1}$) at the first cycle but degraded strongly with cycling. The poor cyclic behaviour of Mg_2Ni electrodes is attributed to the formation of $Mg(OH)_2$ on the electrodes, which has been considered to arise from the charge -discharge cycles [8]. To avoid the surface oxidation, we have examined the effect of magnesium substitution by Mn and Al in Mg_2Ni-type material. This alloying greatly improved the discharge capacities. In the nanocrystalline $Mg_{1.5}Mn_{0.5}Ni$ alloy, discharge capacities up to 241 $mA \cdot h \cdot g^{-1}$ were measured [9].

The experimental XPS valence band measured for the MA nanocrystalline Mg_2Ni-type alloy and Mg_2Ni/Pd composite showed a significant broadening compared to that obtained for the polycrystalline thin film. The substitution of Ni by Mn in the nanocrystalline Mg_2Ni alloy causes a further band broadening [9]. The reasons for the band broadening of the nanocrystalline Mg_2Ni- type alloys and composites are probably associated with a strong deformation of the nanocrystals in the MA samples [10 -12]. The strong modifications of the electronic structure of the nanocrystalline Mg_2Ni-type alloy and composites could significantly influence its hydrogenation properties [13, 14], similarly to the behaviour observed earlier for the nanocrystalline FeTi- [11] and $LaNi_5$-type [12] alloys.

Results on XRF measurements revealed the assumed bulk chemical composition of the polycrystalline and nanocrystalline Mg_2Ni-type alloys. On the other hand, core -level XPS showed that the surface segregation of Mg atoms in the MA nanocrystalline samples is stronger compared to that of polycrystalline thin films. In particular, a strong surface segregation of Mg atoms was observed for the Mg_2Ni/Pd composites. Figure 2 shows normalised integral intensities of Mg, O, Ni, and Pd XPS peaks versus sputtering time as converted to the depth for Mg_2Ni/Pd composite. The XPS Mg 1s, Ni $2p_{3/2}$, and Pd $3d_{5/2}$ peaks were normalised to the intensities of in-situ prepared pure Mg, Ni, and Pd thin films, respectively. The oxygen 1s peak was normalised to the O 1s intensity in the MgO single crystal. Results presented in Fig. 2 show that Ni and Pd atoms are practically absent on the composite surface. On the other hand, Mg atoms strongly segregate to the surface and form a Mg based oxide layer under atmospheric conditions. The oxidation process is depth-limited so that an oxide-covering layer

with a well-defined thickness is formed by which the lower lying metal is prevented from a further oxidation.

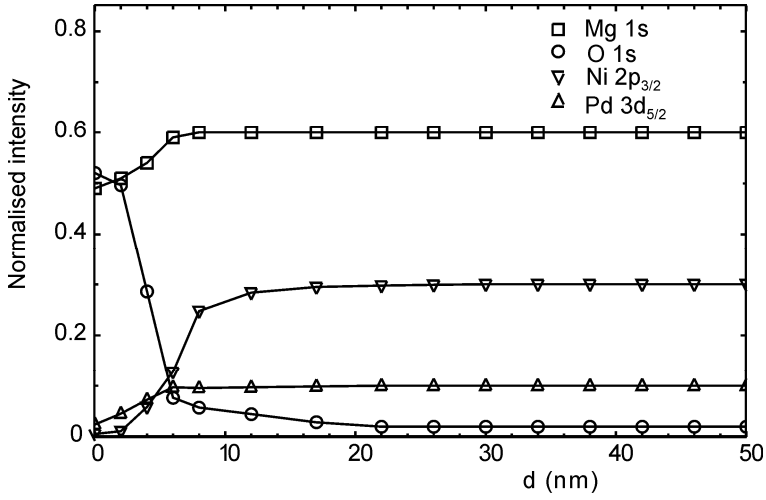

Fig. 2. Normalised integral intensities of Mg, O, Ni, and Pd XPS peaks versus sputtering time as converted to the depth for Mg_2Ni/Pd composite. The XPS Mg 1s, Ni $2p_{3/2}$, and Pd $3d_{5/2}$ peaks were normalised to the intensities of in-situ prepared pure Mg, Ni, and Pd thin films, respectively. The oxygen 1s peak was normalised to the O 1s intensity in the MgO single crystal. The XPS measurements were performed immediately after heating in UHV conditions (see text) which allowed us to remove the adsorbed impurities (mainly carbonates) excluding a stabile oxide top layer

In this way, one can obtain a self-stabilised oxide-metal structure. The lower lying Ni and Pd atoms form a metallic subsurface layer and are responsible for the observed relatively high hydrogenation rate [3, 4]. The surface segregation process of Mg atoms in Mg_2Ni/Pd composite is stronger compared to that observed for the Mg_2Ni nanocrystalline alloy. Furthermore, we have observed no segregation effect for the in-situ prepared polycrystalline Mg_2Ni thin films. On the other hand, the Mg_2Ni thin films naturally oxidised in air for 24 h show a small segregation effect of the Mg atoms to the surface.

4. Conclusions

The surface segregation process of Mg atoms in Mg_2Ni/Pd composite is stronger compared to that observed for the MA nanocrystalline Mg_2Ni alloy. Furthermore, the XPS valence bands measured in MA nanocrystalline alloys and composites showed a significant broadening compared to that obtained for polycrystalline thin film. Strong modifications of the electronic structure and surface segregation effect in the MA nanocrystalline alloys and composites could significantly influence their hydrogenation properties, similar to the behaviour observed earlier for the nanocrystalline FeTi-

[11] and $LaNi_5$-type [12] alloys. The mechanical alloying is a suitable procedure for obtaining Mg–Ni based alloy electrodes for Ni-MH batteries.

Acknowledgements

This work was financially supported by the Polish Committee for Scientific Research under grant No. 3 T10A 033 29.

References

[1] ZALUSKI L., ZALUSKA A., STRÖM-OLSEN J.O., J. Alloys Comp., 217 (1995), 245.
[2] LEI Y.Q., WU Y.M., YANG Q.M., WU J., WANG Q.D., Z. Phys. Chem., 183 (1994), 379.
[3] SIEGMANN H.C., SCHLAPBACH L., BRUNDLE C.R., Phys. Rev. Lett., 40 (1978), 972.
[4] SCHLAPBACH L., *Hydrogen in Intermetallic Compounds*, II, Springer, Berlin, 1992, p. 165.
[5] SCHLAPBACH L., SEILER A., STUCKI F., SIEGMANN H.C., J. Less Common Met., 73 (1980), 145.
[6] ORIMO S., FUJII H., Intermetallics, 6 (1998), 185.
[7] GUPTA M., BERLIN E., SCHALPBACH L., J. Less Common Met., 103 (1984), 389.
[8] MU D., HATANO Y., ABE T., WATANABE K., J. Alloys Comp., 334 (2002), 232.
[9] SMARDZ K., SZAJEK A., SMARDZ L., JURCZYK M., Mol. Phys. Rep., 40 (2004), 131.
[10] FITZSIMMONS M.R., ESTMAN J.A., ROBINSON R.A., LAWSON A.C., THOMPSON J.D., MORSHOVICH R., Phys. Rev., B48 (1993), 8245.
[11] SMARDZ K., SMARDZ L., JURCZYK M., JANKOWSKA E., phys. stat. sol. a, 196 (2003), 263.
[12] SMARDZ L., SMARDZ K., NOWAK M., JURCZYK M., Crys. Res. Technol., 36 (2001), 1385.
[13] BOUTEN P.C., MIEDEMA A.R., J. Less Common Met., 71 (1980), 147.
[14] GRIESSEN R., PHYS. Rev., B38 (1988) , 3690.

Received 7 May 2006
Revised 1 September 2006

Materials Science-Poland, Vol. 25, No. 2, 2007

In-plane magnetic anisotropy symmetry in ultrathin Co films grown on sapphire substrates

A. STUPAKIEWICZ[1*], A. MAZIEWSKI[1], P. TRZCIŃSKI[1],
L.T. BACZEWSKI[2], A. WAWRO[2], R. KALINOWSKI[2]

[1]Institute of Experimental Physics, University of Białystok, Lipowa 41, 15-424 Białystok, Poland

[2]Institute of Physics, Polish Academy of Sciences, al. Lotników 32/46, 02-668 Warsaw, Poland

We report on the study of in-plane magnetic anisotropy and magnetization reversal in MBE grown ultrathin epitaxial Mo/Au/Co/Au magnetic films. We used a magneto-optical polar Kerr effect-based magnetometer and real-time data analysis using LabView software. A two-fold in-plane magnetic anisotropy symmetry was deduced from the shape analysis of the magnetization curves measured for various directions of in-plane applied magnetic field. The direction of easy magnetization axis in the sample plane is a result of a small, unintentional miscut of the sapphire substrate found by in-situ STM and X-ray diffraction measurements.

Key words: *magnetic anisotropy; ultrathin film; cobalt*

1. Introduction

In multilayered ultrathin magnetic films, phenomena associated with magnetic ordering, spin-reorientation transition, self-assembling etc., have been intensively studied. In order to understand these phenomena, the knowledge of magnetic anisotropy, strongly depending on the substrate surface morphology, is essential [1, 2]. In this work, we have studied the in-plane magnetic anisotropy and magnetization reversal in ultrathin Au/Co/Au magnetic films.

2. Experimental

The nanostructures deposited on sapphire single crystal (11–20) wafers had the following composition: (i) first buffer layer of 20 nm Mo(110) deposited at 1000 °C

*Corresponding author: and@uwb.edu.pl

(ii) second buffer layer of 10 nm Au(111) deposited at room temperature and annealed at 200 °C for 15 min (iii) 3 nm Co layer; (iv) 8 nm thick Au cover layer. The structure of the samples was monitored in-situ by RHEED and Auger spectroscopy. The azimuthal directions and angle of about 0.9° of the substrate miscut were determined by X-ray diffraction.

The study of magnetization reversal was performed at room temperature using the magneto-optical Kerr-effect (MOKE)-based magnetometer with laser light: wavelength of 640 nm and spot diameter of 0.5 mm. Three magnetization components were measured as a function of adjustable magnetic fields. Polar (P) magnetization component was measured using the P-MOKE with the laser light close to normal incidence. The longitudinal (L) and transversal (T) MOKE hysteresis loops measurements were performed in the magnetic field applied in different azimuthal directions in the plane of the samples with the angle of light incidence equal to 49°. The longitudinal and transversal in-plane components were measured using the L-MOKE configuration [3]. The LabView program controlled the measurements of both the P-MOKE hysteresis loops and in-plane hysteresis loops and visualized the loop parameters (saturation, remanence, coercive field) in real-time, as a function of the angle between the field direction and the fixed axis.

3. Results and discussion

P-MOKE hysteresis loop for the perpendicular magnetic field $\theta_H = 0$ is shown in Fig. 1. This curve corresponds to the hard magnetization axis normal to the plane of a sample. A similar effect was observed in Au/Co/Au films with Co thickness > 2 nm [4].

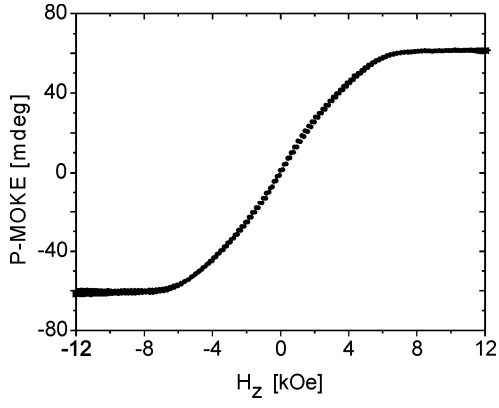

Fig. 1. Hysteresis loops measured as the polar Kerr ellipticity with magnetic field perpendicular to the plane of the sample. The perpendicular magnetic anisotropy constant $K_{u1} = 10.2 \times 10^6$ erg/cm^3

The L-MOKE and T-MOKE hysteresis loops were measured in the applied magnetic fields oriented at various φ_H angles with respect to the direction perpendicular to the substrate miscut. The curves shown in Fig. 2 illustrate magnetization reversal when magnetic field is applied along hard ($\varphi_H = 90°$) and easy ($\varphi_H = 0°$) directions, respectively.

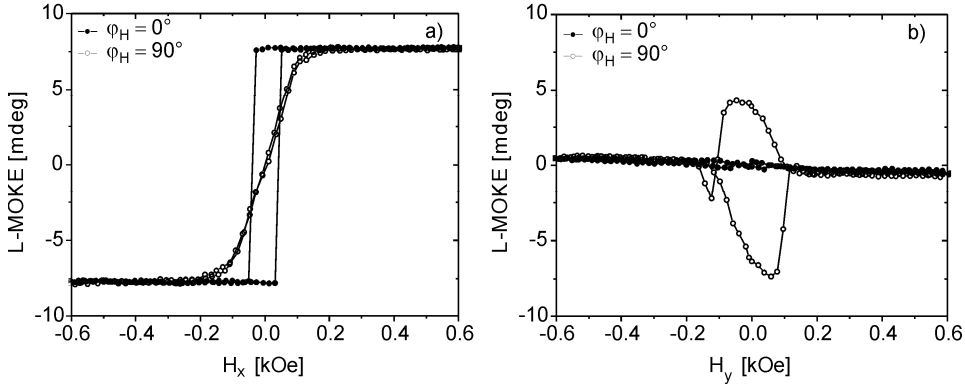

Fig. 2. Hysteresis loops measured as longitudinal (a) and transversal (b) Kerr ellipticity for the in-plane magnetic field applied in $\varphi_H = 0°$ and $\varphi_H = 90°$ directions. The in-plane anisotropy constant $K_{step}^{(2)} = -0.33 \times 10^6$ erg/cm^3

Figure 3 shows the angular dependence of the longitudinal and transversal remanence as a proof of the existence of anisotropy. The observed angular dependence is characteristic of magnetic anisotropy in the sample plane with two-fold symmetry. The maxima of azimuthal L-MOKE dependence and minima of T-MOKE correspond to the easy axis magnetization in the plane of the sample.

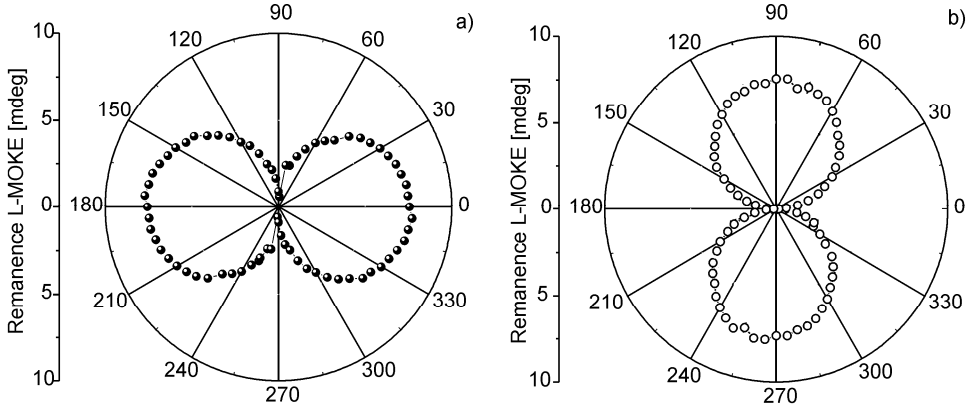

Fig. 3. Azimuthal dependence of the ellipticity remanence for longitudinal (a) and transversal (b) magnetization components. The orientation of easy axis magnetization corresponds to maximum of L-MOKE ellipticity remanence (or minimum from T-MOKE)

The experimental data are discussed taking into account the following energy contributions to the simplified model [5]: (i) perpendicular uniaxial anisotropy; (ii) demagnetization term; (iii) and step-induced uniaxial anisotropy:

$$E_A(\theta,\varphi) = K_{u1}\sin^2\theta - 2\pi M_S^2 \sin^2\theta + K_{\text{step}}^{(2)} \sin^2\theta \sin^2\varphi \qquad (1)$$

where K_{u1} – the uniaxial perpendicular anisotropy constant, $K_{\text{step}}^{(2)}$ – uniaxial in-plane step-induced anisotropy constants, M_S – the value of saturation magnetization equal to 1420 G, θ is the angle between magnetization direction and the sample plane normal, φ is the angle of in-plane magnetization orientation from perpendicular to miscut direction. Magnetic anisotropy constants $K_{u1} = 10.2\times10^6$ erg/cm^3 and $K_{\text{step}}^{(2)} = -0.33\times10^6$ erg/cm^3 were obtained as fitting parameters of the theoretical curves to the experimental data.

The results could be explained assuming that the easy magnetization axis in the sample plane is induced by a small (<1°) unintentional miscut of the sapphire substrates. Similar results were observed in Au/Co/Au ultrathin films grown on vicinal substrate with miscut equal to 1.2° [5].

Moreover, the in-situ STM measurements carried out earlier in another UHV system on the same type of sapphire substrate covered with Mo buffer show a surface morphology typical of low-angle miscut (Fig. 4). Our previous investigations showed Au grows smoothly on Mo [6] and due to the epitaxy, it reproduces on its surface vicinal character of the substrate covered with Mo buffer. The presence of parallel monatomic steps on Mo buffer surface related with the substrate miscut has an influence on the growth of Co magnetic layer and, in consequence, induces the magnetic anisotropy in the plane of the samples, observed in our experiment.

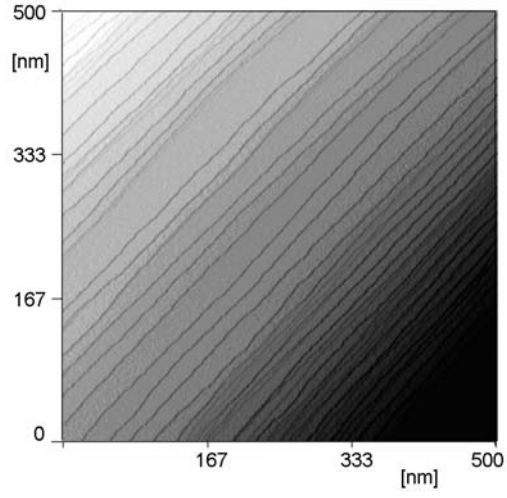

Fig. 4. The in-situ STM image of surface Mo/Al_2O_3 sample

In summary, we have shown that magneto-optical magnetometry is a powerful technique for high sensitivity anisotropy analysis. The two-fold symmetry of the in-plane anisotropy was observed for sample with 3 nm Co layer thickness. The unintentional miscut of the substrate may induce an additional magnetic anisotropy in the plane of the Au/Co/Au ultrathin system.

Acknowledgement

The authors are very grateful to prof. dr Roland Wiesendanger from University of Hamburg for giving us the opportunity to obtain the in-situ STM image of the Mo buffer. This work was supported by the Polish State Committee for Scientific Research (Grant No. 4 T11B 006 24) and Marie Curie Fellowships for "Transfer of Knowledge" ('NANOMAG-LAB" N 2004-003177).

References

[1] JUBERT P.-O., FRUCHART O., MEYER C., Phys. Rev. B, 64 (2001), 115419.
[2] QIU Z.Q., PEARSON J., BADER S.D., Phys. Rev. Lett., 70 (1993), 1006.
[3] DING H.F., PUTTER S., OEPEN H.P., KIRSCHNER J., J. Magn. Magn. Mat., 212 (2000), L5.
[4] KISIELEWSKI M., MAZIEWSKI A., TEKIELAK M., WAWRO A., BACZEWSKI T., Phys. Rev. Let., 89 (2002), 087203.
[5] STUPAKIEWICZ A., GIENIUSZ R., MAZIEWSKI A., POSTAVA K., WAWRO A., BACZEWSKI L.T., phys. stat. sol. (b), 243 (2006), 202.
[6] WAWRO A., BACZEWSKI L.T., PANKOWSKI P., KISIELEWSKI M., SVEKLO I., MAZIEWSKI A., Thin Solid Films, 412 (2002), 34.

Received 7 May 2006
Revised 1 September 2006

Materials Science-Poland, Vol. 25, No. 2, 2007

Aharonov–Bohm interferometry with the T-shaped capacitively coupled quantum dots in the orbital Kondo regime

D. KRYCHOWSKI, S. LIPIŃSKI*

Institute of Molecular Physics, Polish Academy of Sciences,
M. Smoluchowskiego 17, 60-179 Poznań, Poland

The magnetic field dependence of coherent transport through a pair of wires attached to two Aharonov–Bohm rings with embedded double dots is considered. The double dots are electrostatically coupled. The many-body problem is studied within the mean field slave boson approach and complementarily by the method of equation of motion in the limit of infinite intra and finite or infinite interdot Coulomb interactions.

Key words: *quantum dot; Aharonov–Bohm ring; Kondo effect; Fano effect*

1. Introduction

There is currently a great interest in phase coherence effects in nanoscopic systems due to their potential applications in quantum computers [1]. At present, various Aharonov–Bohm (AB) rings with embedded quantum dots in the arms have been fabricated, and quantum interference effects have been examined [2]. In these systems, the interplay of strong correlations and interference [3–5] attracts special attention. In the present paper, we discuss capacitively coupled AB interferometers containing double quantum dots (DQDs). This system enables us to manipulate each of the interferometers separately and to examine Coulomb-induced transfer of AB oscillations between the rings. The Kondo effect in strongly electrostatically coupled dots has two possible sources: the spin and orbital degeneracies. For vanishing Zeeman splitting at the dots, the transmission is a periodic function of the enclosed magnetic fluxes. For the broken spin degeneracy, the ideal periodicity is perturbed and the spin polarization of conductance is observed.

*Corresponding author, e-mail: lipinski@ifmpan.poznan.pl

2. Model

We study a pair of capacitively coupled double dots embedded in AB rings and side-attached to quantum wires. Each of the DQDs consists of an open dot (OQD) contacted by the leads and the "interacting" dot (IQD) (see the diagram in the inset to Fig. 1). The corresponding Hamiltonian reads:

$$H = \sum_{k\alpha j\sigma} \varepsilon_{k\alpha j\sigma} c^{+}_{k\alpha j\sigma} c_{k\alpha j\sigma} + \sum_{j\sigma} \varepsilon_0 c^{+}_{j\sigma} c_{j\sigma} + \sum_{j\sigma} \varepsilon_{j\sigma} d^{+}_{j\sigma} d_{j\sigma} + \sum_{j} U_0 n_{j\uparrow} n_{j\downarrow} + \sum_{\sigma\sigma'} U n_{1\sigma} n_{2\sigma'} + \sum_{k\alpha j\sigma} t\left(c^{+}_{k\alpha j\sigma} c_{j\sigma} + c.c.\right) + \sum_{k\alpha j\sigma} t'\left(e^{i\varphi_j/2} c^{+}_{j\sigma} d_{j\sigma} + e^{-i\varphi_j/2} c^{+}_{j\sigma} d_{j\sigma} + c.c.\right) \tag{1}$$

where $\varepsilon_{j\sigma} = \varepsilon_d + g\mu_B \sigma h_j$ and h_j denotes local magnetic field at the dot j (we set $|e|=\mu_B=1$). The first term of Eq. (1) describes electrons in the electrodes, the second and third represent the OQDs and IQDs, the next two terms account for intra- (U_0) and intercoulomb (U) interactions ($n_{j\sigma} = d_{j\sigma} + d_{j\sigma}$), and the last two terms describe tunneling to the leads and interdot IQD-OQD tunneling. The effect of the magnetic flux Φ is included by introducing the Peierls phase factors $e^{\pm i\varphi/2}$ ($\varphi = 2\pi\Phi/\Phi_0$, where Φ_0 is the magnetic flux quantum hc/e). The intradot charging energy is assumed to be strong ($U_0 \to \infty$) and we discuss the two opposite limits of weak ($U \sim \Gamma$) and strong ($U \to \infty$) interdot interaction. Γ denotes the level broadening

$$\Gamma = \pi t_0^2 \Sigma_{k\alpha\sigma} \delta\left(\varepsilon - \varepsilon_{k\alpha\sigma}\right)$$

hereafter taken as a unit of energy. The currents flowing through the wires can be expressed in terns of the transmissions through the open dots [6]:

$$I_{j\sigma} = \frac{e^2}{\hbar} \frac{\Gamma}{2} \int_{-\infty}^{\infty} \frac{d\omega}{2\pi} \left(f_{jL}(\omega) - f_{jR}(\omega) \right) \mathrm{Im}\left[G^{OQD}_{j\sigma, j\sigma}(\omega) \right] \tag{2}$$

where $G^{OQD}_{j\sigma, j\sigma}$ denotes the Green function of the open dot and f_{jr} are the Fermi distribution functions of the electrodes. The Green functions are determined by the mean field slave boson approach (SBMFA) [7]. The corresponding functions for the open and interacting dots are:

$$G^{OQD}_{j\sigma, j\sigma}(\omega) = \frac{1}{\omega - \varepsilon_0 + i\Gamma} \left(1 + \frac{|t'|^2 \left(2 + 2\cos\left[\varphi_j\right]\right) b_j^2 G^{IQD}_{j\sigma, j\sigma}(\omega)}{\omega - \varepsilon_0 + i\Gamma} \right) \tag{3}$$

$$G^{IQD}_{j\sigma, j\sigma}(\omega) = \frac{1}{\omega - \varepsilon_{j\sigma} - \dfrac{|t'|^2 \left(2 + 2\cos\left[\varphi_j\right]\right) b_j^2}{\omega - \varepsilon_0 + i\Gamma}} \tag{4}$$

where b_j denote mean values of the auxiliary boson fields. In the following, we use SBMFA to discuss only the limit of the vanishing Zeeman splitting at the dots, in

which case the use of two auxiliary fields is sufficient. To get an insight into the mixed valence range and the case of lifting of the spin degeneracy at the dots, we complement the calculations by the equation of motion treatment (EOM) using the decoupling procedure proposed by Lacroix [8].

3. Numerical results and discussion

Strong dot–dot interaction ($U \to \infty$). In this case, only one electron is accommodated in the system of coupled dots, i.e. $\langle n_1 + n_2 \rangle \approx 1$. The transmission is strongly affected by the interference between the ballistic channels of the wires and the Kondo resonant channels from IQDs.

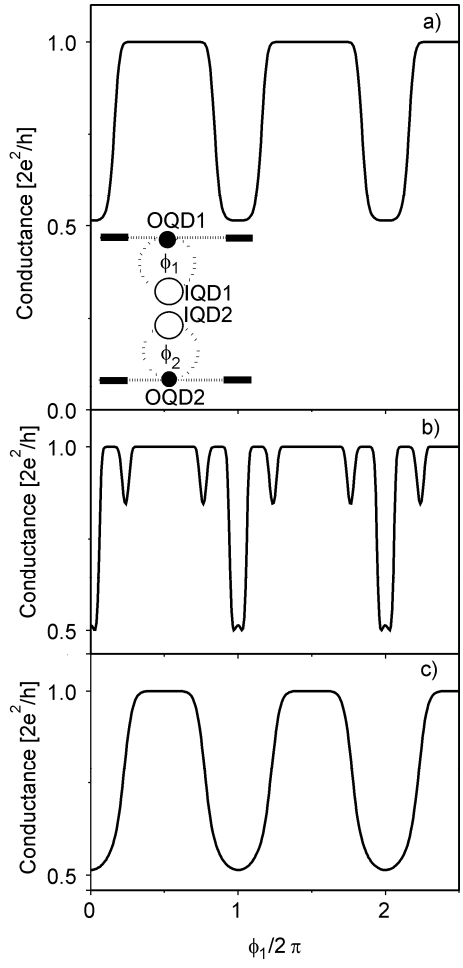

Fig. 1. AB oscillations of the upper circuit in the limit $U \to \infty$ for the cases of: a) equal magnetic fluxes $\varphi_1 = \varphi_2$, b) different fluxes $\varphi_1/\varphi_2 = 1/4$, c) the flux is applied to only one ring $\varphi_2 = 0$, in this case conductance of the lower circuit is presented. The calculations were performed within SBMFA for $\varepsilon_0 = 0$, $\varepsilon_d = -3$ and half the bandwith $D = 50$. The system is depicted in the inset

For the symmetrically coupled identical DQDs near the 0 flux [$\varphi \approx 0$ (mod 2π)], the spin and charge degrees of freedom are totally entangled and the Fermi liquid

ground state with $SU(4)$ symmetry is realized (phase shift $\delta_{j\sigma} = \pi/4$). In consequence of a destructive interference, a half-reflection is observed (anti-Kondo resonance). Figure 1 presents the influence of the applied magnetic fluxes. We discuss first the spin degenerate case ($h_j = 0$). Figure 1a shows the conductance oscillations for equal phases $\varphi_1 = \varphi_2$. Although $SU(4)$ symmetry is preserved, the flux strongly influences both the interference and the Kondo resonance leading to a modification of transmission probability through the system near the Fermi level. While increasing the flux, the destructive interference is replaced by a constructive one and the conductance reaches the unitary limit and then drops again for $\varphi \approx 2\pi$.

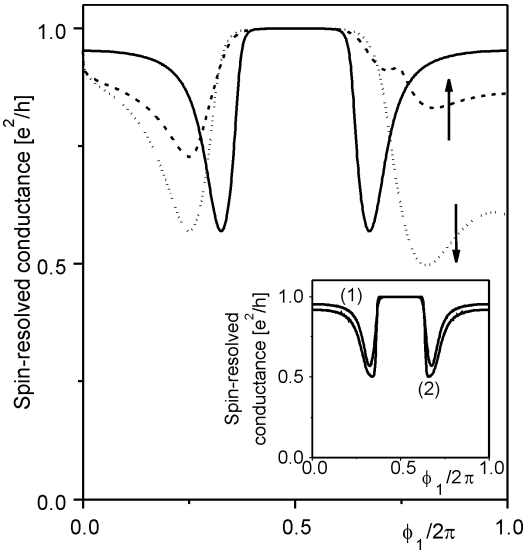

Fig. 2. Spin dependent AB oscillations for equal fluxes $\varphi_1 = \varphi_2$ and equal local magnetic fields at the IQDs $h_1 = h_2 = \alpha\varphi_1$, $\alpha = 0.125$ (dashed and dotted lines) compared with the case $\alpha = 0$ (solid lines). $\varepsilon_d = -0.9$ and the rest of parameters as in. Calculations were performed by the EOM method. The inset represents a comparison of the EOM results (line (1)) with SBMFA (line (2)) calculations

For different fluxes $\varphi_1 \neq \varphi_2$, the orbital degeneracy is broken. Figure 1b ($\varphi_1/\varphi_2 = 1/4$) presents an example of the two-period oscillations of conductance and Fig. 1c illustrates the Coulomb induced AB oscillations (oscillations observed also in the ring, where no magnetic flux is applied, $\varphi_2 = 0$). Figure 2 shows how the flux dependence of conductance changes in the mixed valence (MV) range and what are the consequences of lifting the spin degeneracy ($h_j \neq 0$). Concerning the former aspect, the conductance for $\varphi \approx 0$ is strongly enhanced compared to the Kondo regime and it is due to a much smaller effect of the destructive interference with a Kondo-like resonant channel. In this intermediate range, the resonance is deformed, broadened, lowered and shifted towards higher energies. The initial decrease of conductance is clearly observed in a wide range of the flux. It reflects the fact that the resonance is not centred at the Fermi level. Breaking of the spin degeneracy results in perturbing the periodicity of AB oscillations and conductance becomes spin dependent (Fig. 2). For some values of the flux, the spin polarization of conductance is significant, which can be used for spin filtering. The results for the nonvanishing Zeeman splitting are presented for the case when the local fields are equal to the homogenous field

$h = \Phi/(\pi r^2)$. For the radii of the rings $r_1 = r_2 = 20$ nm, the first quasi-period of AB oscillations ($\varphi = 1$) is reached for $h_0 = 0.125$, which for typical values of $\Gamma \approx 0.1$–0.5 meV [9] gives h_0 lying in the range (0.03–0.15) T.

Weak dot–dot interaction. The two IQDs are both singly occupied in this case $\langle n_1 \rangle = \langle n_2 \rangle \approx 1$ and behave as separate Kondo impurities. Fano-like suppression of the Kondo-mediated conductance for vanishing fluxes results in an almost perfect reflection, which is a consequence of a $\pi/2$ phase shift characteristic for $SU(2)$ symmetry of the ground state. In Figure 3, we present the evolution of the Coulomb induced AB oscillations with the increase of interdot interaction.

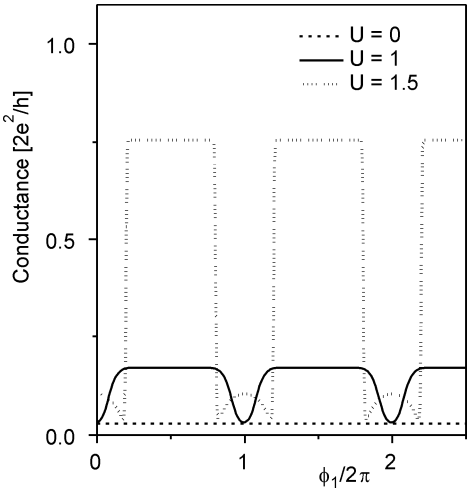

Fig. 3. AB oscillations in the limit of weak interdot interaction for the circuit with no directly applied magnetic flux ($\varphi_2 = 0$) (SBMFA)

Summarizing, the present paper provides a picture of combined influence of interference, the Kondo effect and interdot interactions on transport through a system of coupled quantum dots in the presence of applied magnetic fluxes.

References

[1] DI VINCENZO D.P., Science, 270 (1995), 255.
[2] KOBAYASHI K., AIKAWA H., KASUMOTO S., IYE Y., Phys. Rev. Lett., 85 (2002), 256806.
[3] BUŁKA B.R., STEFAŃSKI P., Phys. Rev. Lett., 86 (2001), 5128.
[4] LOPEZ R., SANCHEZ D., LEE M., CHOI M.S., SIMON P., LE HUR K., Phys. Rev., B, 71 (2005), 115312.
[5] TANAKA Y., KAWAKAMI N., J. Phys. Soc. Jpn., 75 (2006) 015004.
[6] MEIER Y., WINGREEN N.S., LEE P.A., Phys. Rev. Lett., 70 (1993), 2601.
[7] COLEMANN P., Phys. Rev. B, 29 (1984), 3035.
[8] LACROIX C., J. Phys. F, Met. Phys., 11 (1981), 2389.
[9] GERLAND U., VON DELFT J., COSTI T.A., OREG Y., Phys. Rev. Lett., 84 (2000), 3710.

Received 7 May 2006
Revised 1 September 2006

Materials Science-Poland, Vol. 25, No. 2, 2007

Magnetic domains studies in strongly and weakly exchange coupled Co/NiO bilayers

L. SMARDZ[1*], H. NIEDOBA[2], K. SMARDZ[3]

[1]Institute of Molecular Physics, Polish Academy of Sciences,
Smoluchowskiego 17, 60-179 Poznań, Poland

[2]GEMaC de l´Université de Versailles, 45, av. Des Etats-Unis, 78035 Versailles, France

[3]Institute of Materials Science and Engineering, Poznań University of Technology,
M. Skłodowska-Curie 5 Sq., 60-965 Poznań, Poland

Results of the Auger electron spectroscopy measurements with depth profiling showed that at the Co–NiO interface only oxygen is present, making it very likely that only NiO is formed and no other nickel or cobalt compounds, which grow apparently with smaller probability. It has been also found that the average exchange coupling energy for the Co–NiO interface strongly depends on the preparation conditions. For the Co layers with strong interface exchange coupling, we have observed large uniform domains and 180° walls. On the other hand, the Co layers with the weak interface coupling showed large domains with a strong ripple structure and non-uniform 180° walls.

Key words: exchange biasing; unidirectional anisotropy

1. Introduction

Magnetic bilayers containing antiferromagnetic (AFM) transition metal oxides have received considerable interest in recent years due to the exchange biasing effect [1–7]. From the technological point of view, this phenomenon plays an important role in advanced devices such as magnetic read heads [2] and magnetic memory cells [3]. Despite extensive studies, however, the exchange bias is still poorly understood, largely due to the lack of techniques capable of providing detailed information about the arrangement of magnetic moments near interfaces.

The exchange biasing is attributed to the interfacial exchange interactions between spins of the ferromagnetic (FM) layer and spins of the AFM domains in the AFM layer. Originally, it was thought that the AFM spins order in single domains with all

*Corresponding author, e-mail: smardz@ifmpan.poznan.pl

interfacial AFM spins perfectly aligned in a single direction parallel to the FM spins, resulting in a net moment due to the uncompensated antiferromagnetic spins at the interface. However, measurements show that the biasing fields are typically one or two order of magnitude smaller than expected [5]. Theoretical work supported by neutron diffraction suggests domain formation resulting from a 90° coupling between AFM and FM moments [3]. On the other hand, direct measurements of the uncompensated spins at the surface of CoO layers in CoO/MgO and CoO/$Ni_{81}Fe_{19}$ superlattices [4] were carried out. It was found that approximately 1% of one monolayer of Co surface spins was uncompensated leading to the exchange biasing when CoO is used in FM/AFM bilayers. Experimental results also showed that the alignment of the ferromagnetic spins is determined, domain by domain, by the spin directions in the underlying antiferromagnetic layer [8]. In this paper, we report on the magnetic domains studies in Co layers strongly and weakly exchange-coupled to the AFM NiO layer.

2. Experimental procedure

Co/NiO bilayers were deposited onto glass and SiO_2(101)/Si(111) substrates in the temperature range 293–350 K using UHV (5×10^{-10} mbar) RF/DC magnetron sputtering. The Co layers were deposited using a DC source in an Ar atmosphere. The NiO-layer was prepared using a RF source in Ar + O_2 atmosphere. The chemical composition and the cleanness of all layers was checked *in-situ*, immediately after deposition, by transferring the samples to an UHV (4×10^{-11} mbar) analysis chamber equipped with X-ray photoelectron spectroscopy (XPS). Typical deposition rates for the Co and NiO layers were equal to 0.1 and 0.05 nm/s, respectively. After preparation of Si(111) substrate with native SiO_2(101) surface layer [7], we first deposited NiO layers. The Co layers were then grown immediately onto NiO. The top Co layers had a step-like wedge form. Wedge-shaped layers were grown by steeply moving a shutter in front of the substrate during deposition. Finally, 5 nm Cu cap layer was deposited to prevent the oxidation of the Co layer. Selected samples were also analysed by the Auger electron spectroscopy (AES) with depth-profile analysis in order to confirm with a chemical method the actual composition of the NiO–Co interfaces.

The structure of the samples was examined *ex-situ* by standard θ–2θ X-ray diffraction with CoK_α radiation. The magnetic characterisation of the bilayers was carried out at room temperature using the magnetooptical Kerr effect and a vibrating sample magnetometer (VSM). The observation of magnetic domains and walls was carried out at room temperature using the high-resolution longitudinal Kerr effect with digital image processing.

3. Results and discussion

For the Co/NiO bilayers with $d_{Co} > 20$ nm, the high-angle X-ray diffraction patterns show an appreciable (111) texture of *fcc* Co and NiO. The average cobalt grain

size in the direction perpendicular to the substrates, as determined from the Scherrer equation, are comparable to their respective sublayer thicknesses. From the exponential variation of the XPS Co-2p and Ni-2p integral intensities with increasing layer thickness, we conclude that the Co and NiO layers grow homogeneously.

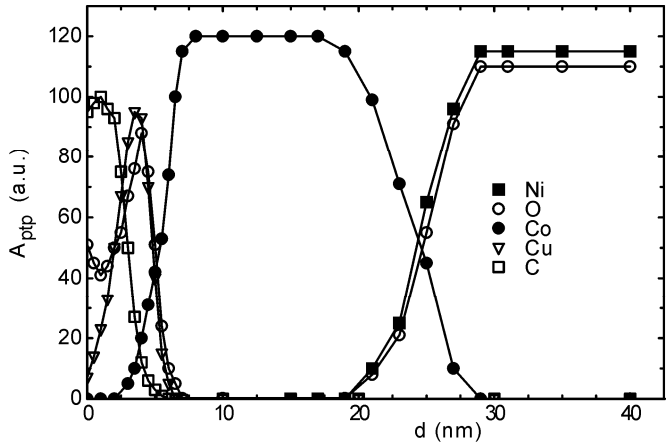

Fig. 1. AES spectrum vs. sputtering time, as converted to depth. The figure shows the peak-to-peak intensities of Co, Ni, O, and C. The surface of the sample is on the left-hand side, the substrate is on the right-hand side (not seen here)

Figure 1 shows the element-specific Auger intensities as a function of the sputtering time, converted to depth. On the left-hand side is the top of the sample and on the right-hand side is the NiO film followed finally by the substrate. Only relative intensities of five most abundant elements (carbon, oxygen, copper, cobalt, and nickel) are displayed. As can be seen, there is a relatively high concentration of carbon and oxygen on the surface of the sample. The reason of this behaviour could be due to carbonates or adsorbed atmospheric CO_2. Carbon concentration decreases towards the Cu–Co interface. At the Co–NiO interface only oxygen is present, making it very likely that only NiO is formed and no other nickel or cobalt compounds, which apparently grow with a lower probability.

Furthermore, the NiO layer has been studied *in-situ*, immediately after preparation, using X-ray photoelectron spectroscopy. In our case, the spectrum of the most intensive Ni-2p line was recorded immediately after preparation of the 40 nm NiO layer. The peak positions and the shape of the spectrum revealed formation of the single phase NiO layer during the reactive RF sputtering. The above result is very important in interpretation of magnetic properties of the NiO/Co bilayers because the exchange coupling at the interface is effective only for nickel monoxide, which is antiferromagnetic.

Results of magnetic measurements showed that the exchange-biasing and coercivity fields are inversely proportional to the Co layer thickness down to 2 nm [9]. On the other hand, an average exchange coupling energy for the Co–NiO interface

strongly depends on the preparation conditions. Figures 2a and 3a show typical in-plane hysteresis loops (measured at room temperature in easy and hard direction) for the Co/NiO bilayer (d_{Co} = 4.5 nm) prepared at 350 K onto glass and at 293 K onto SiO_2(101)/Si(111) substrates.

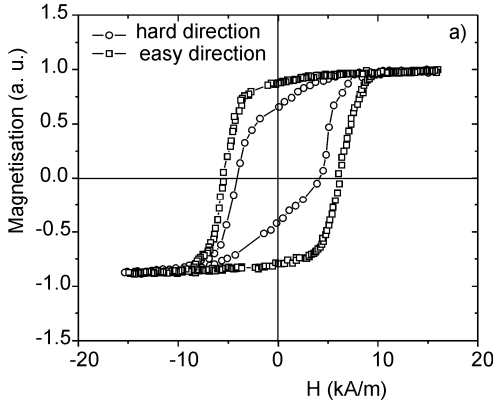

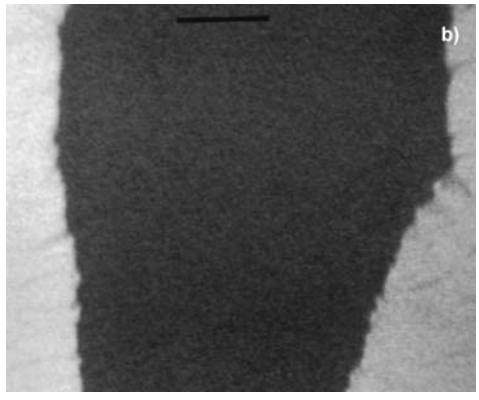

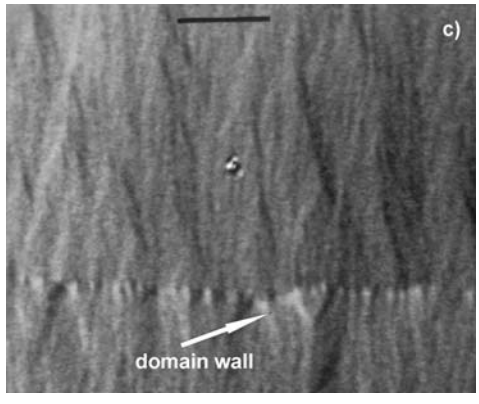

Fig. 2. Typical in-plane hysteresis loops (a) of the 4.5 nm Co/40 nm NiO bilayer measured in the easy and hard direction of the uniaxial anisotropy of the top Co layer. The sample was deposited at 350 K onto glass substrate and exhibits a weak (0.005 mJ/m^2) exchange coupling at the Co–NiO interface. Typical magnetic domain (b) and wall (c) images observed near coercive field for the same bilayer. The lengths of the black lines in Figs. 1b and 1c correspond to 10 μm

The Co layer exhibits weakly (Fig. 2a) or strongly (Fig. 3a) displaced from the origin and broadened hysteresis loops compared to those measured for the Co layer of the same thickness but without the antiferromagnetic NiO layer. The value of this displacement (H_{EB}) defines directly the exchange-biasing field. The hysteresis loop experiences a field offset that opposes the field direction in which the system has been cooled through the Neél temperature of NiO. In our case, the bilayer was cooled in a magnetic field of about 400 kA/m. As the origin of these effects, the exchange coupling between the spins of the ferromagnetic Co atoms and the spins of the Co ions in the antiferromagnetic NiO is invoked.

The coupling energy determined for the samples deposited at 350 K onto glass substrates was very small and equal to about 0.005 mJ/m^2. On the other hand, the bilayers prepared at 293 K onto SiO_2(101)/Si(111) substrates showed the average interface coupling energy as large as 0.04 mJ/m^2 [9]. Therefore, samples with strong

(0.04 mJ/m^2) and weak (0.005 mJ/m^2) coupling energy were studied by the Kerr microscopy to determine the domains and walls structures of the top Co layers during the magnetisation reversal process [10].

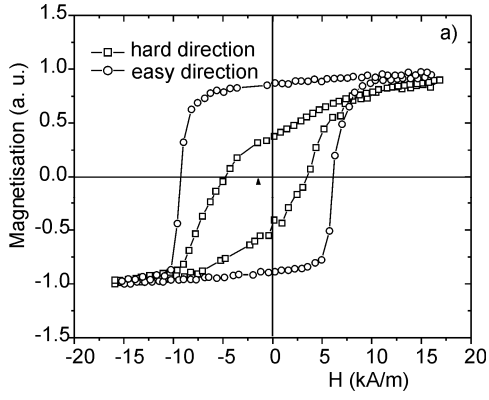

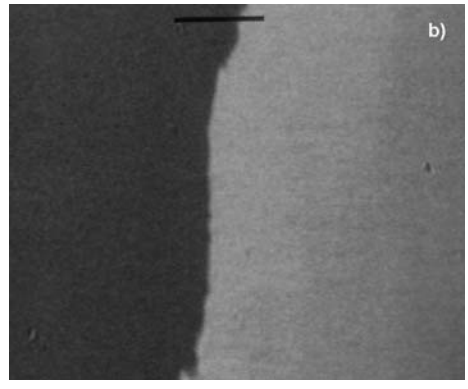

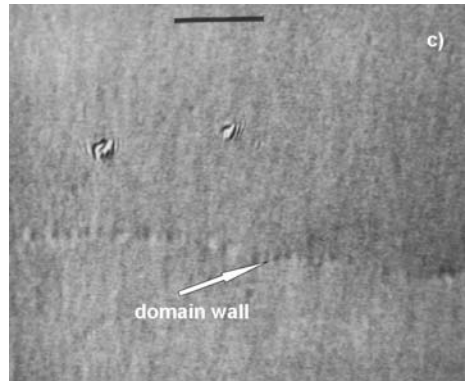

Fig. 3. Typical in-plane hysteresis loops (a) of the 4.5 nm Co/40 nm NiO bilayer measured in the easy and hard direction of the uniaxial anisotropy of the top Co layer. The sample was prepared at 293 K onto SiO_2(101)/Si(111) substrate and exhibits a strong (0.04 mJ/m^2) exchange coupling at the Co–NiO interface. Typical magnetic domain (b) and wall (c) images observed near coercive field for the same bilayer. The length of the black line in Figs. 1b and c corresponds to 10 μm

For the Co layers with a strong interface exchange coupling we have observed large uniform domains (Fig. 3b) and 180° walls (Fig. 3c). On the other hand, the Co layers with the weak interface coupling showed large domains (Fig. 2b) with a strong ripple structure and non-uniform 180° walls (Fig. 2c).

4. Conclusions

Basing on the *in-situ* XPS and AES measurements with depth profiling, we can rule out chemical impurities at the Co–NiO interface as a factor reducing the exchange energy. The Co layers with the strong interface exchange coupling showed large uniform domains and 180° walls. On the other hand, for the Co layers with the weak interface coupling we have observed large domains with a strong ripple structure and non-uniform 180° walls.

References

[1] MILTÉNYI P., GIERLINGS M., KELLER J., BESCHOTEN B., GÜNTHERODT G., NOWAK U., USADEL K.D., Phys. Rev. Lett., 84 (2000), 4224.
[2] HEIM D.E., FONTANA R.E. Jr., TSANG C., SPERIOSU V.S., GURNEY B.A., WILLIAMS M.L., IEEE Trans. Mag., 30 (1994), 316.
[3] PARKIN S.S.P., ROCHE K.P., SAMANT M.G., RICE P.M., BEVERS R.B., SCHEUERLEIN R.E., O'SULIVAN E.J., BROWN S.L., BUCCHIGANO J., ABRAHAM D.W., LU Y., ROOKS M., TROUILLOUD P.L., WANNER R.A., GALLAGHER W.J, J. Appl. Phys., 85 (1999), 5828.
[4] TAKANO K., KODAMA R.H., BERKOWITZ A.E., CAO W., THOMAS G., Phys. Rev. Lett., 79 (1997), 1130.
[5] NOGUÉS J., SCHULLER I.K., J. Magn. Magn. Mater., 192 (1999), 203.
[6] SMARDZ L., KÖBLER U., ZINN W., Vacuum, 42 (1991), 283.
[7] SMARDZ L., KÖBLER U., ZINN W., J. Appl. Phys., 71 (1992), 5199.
[8] NOLTING F., SCHOLL A., STÖHR J., SEO J.W., FOMPEYRINE J., SIEGWART H., LOCQUET J.-P., ANDERS S., LÜNING J.,.FULLERTON E.E, TONEY M.F., SCHEINFEINK M.R., PADMORE H.A., Nature, 405 (2000), 767.
[9] SMARDZ L., J. Magn. Magn. Mater., 240 (2002), 273.
[10] SMARDZ L., SMARDZ K., NIEDOBA H., J. Magn. Magn. Mater., 220 (2000), 175.

Received 7 May 2006
Revised 1 September 2006

Materials Science-Poland, Vol. 25, No. 2, 2007

Field-induced magnetization of a free-electron gas in thin films

T. BALCERZAK[1*]

[1]Department of Solid State Physics, University of Łódź, Pomorska 149/153, 90-236 Łódź, Poland

A free-electron model in thin film embeded in an external magnetic field is considered. Based on the paramagnetic susceptibility, a formula for magnetization of the electron gas in the uniform magnetic field is derived. Selected results are presented for the films with the thickness of several atomic planes, and with the electron density corresponding to copper.

Key words: *thin film; free-electron gas; paramagnetic susceptibility; magnetization*

1. Introduction

Studies of combined electronic and magnetic properties of thin films are important from the point of view of modern technology [1]. As far as the theoretical description is concerned, the model of free electrons placed in a quantum well turned out to be very useful for the discussion of various physical properties of thin films [1, 2]. In the present paper, this model will be further analyzed in order to study the magnetization of the electronic gas in thin films when the magnetization is induced by the external field.

Thin film is understood here as a set of n monoatomic layers perpendicular to the z-axis, with each layer having its own thickness d. As a result, the total thickness of the film is given by $L_z = nd$, and the total volume is $V = L_z S$, where S is the film surface area ($\sqrt{S} >> L_z$). Apart from the thickness, the important parameter is a dimensionless electron density ρ, defined by the formula: $\rho = (N_e/V)d^3$, where N_e is the total number of electrons in the sample, and the volume is expressed in d^3 units.

The considerations of single-particle electronic states in such a model system lead to the discretization of the Fermi surface, as discussed in detail in [3]. In particular, the formulas for the Fermi wave vector k_F in thin film and the parameter τ_F have been

[*]Corresponding author, e-mail: t_balcerzak@uni.lodz.pl

derived, where τ_F is the highest number of the standing-wave mode in the ground state. In order to avoid a redundant repetition of the formalism, for the method of determination of k_F and τ_F adopted in this paper the reader is referred to Ref. [3].

2. Theory

The magnetization of the electron gas (i.e., the magnetic moment per unit volume) induced by the external field at a point $(z,\vec{r})$ of the thin film is given by the expression:

$$\sigma(z,\vec{r}) = \frac{1}{V}\sum_{p}\sum_{\vec{q}} \chi_{p,\vec{q}}\, H_{p,\vec{q}} \exp\left[-i\left(\frac{2\pi}{L_z}\right)pz\right]\exp\left[-i\vec{q}\vec{r}\right] \tag{1}$$

where $\vec{r}$ denotes the position of a given point in the film plane, whereas z denotes the coordinate perpendicular to the film ($0 \le z \le L_z$). $H_{p,\vec{q}}$ is the Fourier component of the external field and $\chi_{p,\vec{q}}$ stands for the paramagnetic susceptibility. In Eq. (1), a quasi-continuous summation over $\vec{q}$ is performed in the film plane, and the discrete summation over p ($p = 0, \pm1, \pm2, ...$) concerns the perpendicular modes.

The paramagnetic electronic susceptibility in a thin film is given by the formula [4]:

$$\chi_{p,\vec{q}} = \frac{m}{\hbar^2} g_e \mu_B \frac{1}{2}\sum_{\tau=1}^{\tau_F}\left[\, f_{\tau,|\tau+2p|}(q) + f_{\tau,|\tau-2p|}(q)\right] \tag{2}$$

where $f_{\tau,\tau'}(q)$ is a generalized Lindhard function:

$$f_{\tau,\tau'}(q) = \frac{S}{4\pi}\left(1+\frac{a_{\tau,\tau'}}{q^2}\right)\left[1-\sqrt{1-b_{\tau,\tau'}(q)}\,\theta\left(1-b_{\tau,\tau'}(q)\right)\right] \tag{3}$$

where

$$a_{\tau,\tau'} = \left(\frac{\pi}{L_z}\right)^2\left(\tau'^2-\tau^2\right) \tag{4}$$

$$b_{\tau,\tau'}(q) = \left(\frac{2k_{F\tau}}{q}\,\frac{1}{1+\dfrac{a_{\tau,\tau'}}{q^2}}\right)^2 \tag{5}$$

and

$$k_{F\tau}^2 = k_F^2 - \frac{\pi^2\tau^2}{L_z^2} \tag{6}$$

It has been shown in Ref. [4] that Eq. (3) presents a generalization of the ordinary Lindhard function as being discussed in [5] for a two-dimensional system.

Assuming in Eq. (1) that the external field is spatially uniform, we have:

$$H_{p,\vec{q}} = H\delta_{p,0}\delta_{\vec{q},0} \tag{7}$$

With the help of Eqs. (7) and (2)–(6) we can then obtain from Eq. (1) the magnetization induced by this field in the form:

$$\sigma\left(z,\vec{r}\right) = \frac{1}{V}\chi_{0,0}H = \frac{1}{4\pi}\frac{m}{\hbar^2}\,g_e^2\,\mu_{\mathrm{B}}^2\frac{\tau_{\mathrm{F}}}{L_z}H \equiv \sigma \tag{8}$$

For such a case it is seen from Eq. (8) that the magnetization of electron gas in the film is also uniform (we denote it by σ).

As a system with the reference magnetization, we shall assume the bulk material in which the magnetization of the electron gas induced by the same external field is given by the formula:

$$\sigma_0 = \frac{1}{V}\chi_{\mathrm{P}}^b H = \frac{1}{4\pi^2}\frac{m}{\hbar^2}g_e^2\mu_{\mathrm{B}}^2 k_{\mathrm{F}}^b H \tag{9}$$

In Eq. (9) χ_{P}^b is the Pauli paramagnetic susceptibility [6] and k_{F}^b is the Fermi wave vector of the bulk material. By dividing Eqs. (8) and (9) by sides, we finally obtain the relative field-induced magnetization in the form:

$$\frac{\sigma}{\sigma_0} = \pi\frac{\tau_{\mathrm{F}}}{n}\frac{1}{dk_{\mathrm{F}}^b} \tag{10}$$

The above magnetization depends on the film thickness L_z and the electron density ρ (via dependence of τ_{F} and k_{F}^b upon ρ). In the limiting case (when $n\to\infty$) we have $\pi\tau_{\mathrm{F}}/nd \to k_{\mathrm{F}}^b$ (see [3]) and thus $\sigma\to\sigma_0$.

3. Numerical results and discussion

The numerical results are obtained based on Eq. (10). The value of d = 1.805 Å is assumed to correspond to the interplanar distance of the (100) planes in copper. In Fig. 1, the relative magnetization σ/σ_0 is shown for several film thicknesses n, when the dimensionless density ρ is freely changed from 0 to 1. The value of ρ = 0.5 corresponds exactly to copper. It can be seen that for the monolayer (with n = 1), magnetization is a monotonously decreasing function of ρ (whereas $\sigma > \sigma_0$). It is connected with the fact that for n = 1 we have the only value τ_{F} = 1 in this range of ρ. However, for n = 2 and n = 3 the curves are no longer monotonic. For instance, for n = 2, a jump

of magnetization can be observed at $\rho = 0.589$, which is connected with the change from $\tau_F = 1$ to $\tau_F = 2$, whereas ρ increases. In the same way, two jumps are apparent for $n = 2$; the first at $\rho = 0.175$ is connected with the change from $\tau_F = 1$ to $\tau_F = 2$, and the second at $\rho = 0.756$ is the change from $\tau_F = 2$ to $\tau_F = 3$. In particular, it can be seen in Fig. 1 that for $\rho = 0.5$ the magnetization of the trilayer system (with $n = 3$) is between those of $n = 1$ and $n = 2$.

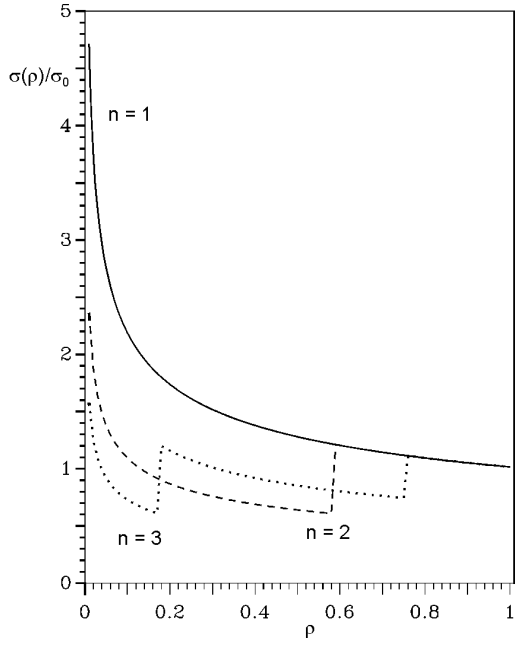

Fig. 1. Dependence of the field-induced relative magnetization σ/σ_0 of the electron gas upon the dimensionless density ρ. The three curves labelled by $n = 1$ (solid), $n = 2$ (dashed) and $n = 3$ (dotted) correspond to various film thicknesses

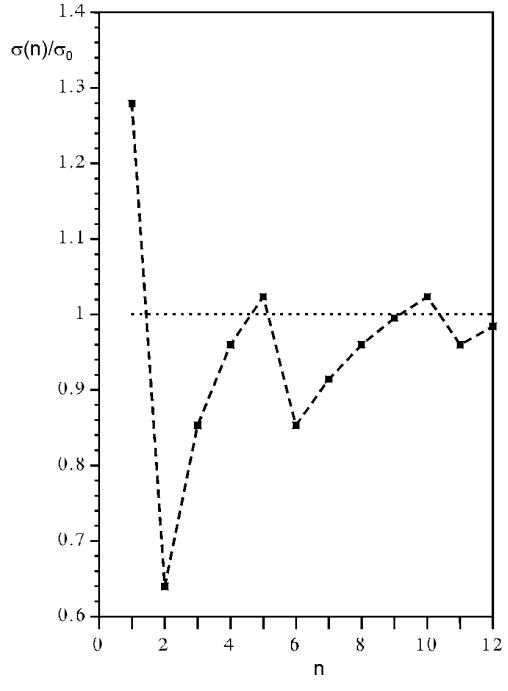

Fig. 2. Dependence of the field-induced relative magnetization σ/σ_0 of the electron gas upon the film thickness n, when $\rho = 0.5$. The interplanar distance is $d = 1.805$Å (the same as in Fig. 1), which corresponds to the (100) film of copper

Figure 2 corresponds to the case when $\rho = 0.5$ is constant but the thickness n changes. One can see that the magnetization is an oscillating, saw-toothed function of the film thickness. The amplitude of the oscillations decreases as n increases. A detailed analysis shows that this behaviour is the same as the oscillations of the density of states at the Fermi surface, as found for this model in [3]. It is worth noting that the oscillating behaviour of the density of states has been found experimentally ([2] and references therein). Thus, we see that the behaviour of the field-induced magnetization in thin films is directly correlated with the density of states at the Fermi level. Such a correlation could be expected to some extent because an analogous relationship is well established in bulk materials. However, in the bulk material there are no size-dependent oscillations. The final conclusion which can be drawn from the paper

is of a general character: despite of the relatively simple model considered here, the predicted results seem to be interesting and non-trivial.

Acknowledgements

The author is indebted to Mrs. Teresa Rychtelska for her valuable help in the preparation of the figures.

References

[1] DAVIES J.H., *The Physics of Low-Dimensional Systems*, Cambridge Univ. Press, Cambridge, 2000.
[2] HIMPSEL F.J., J. Phys.: Cond. Matter, 11 (1999), 9483.
[3] BALCERZAK T., Thin Solid Films, 500 (2006), 341.
[4] BALCERZAK T., Thin Solid Films, 515 (2006), 2814.
[5] BEAL-MONOD M.T., Phys. Rev. B, 36 (1987), 8835.
[6] YOSIDA K., *Theory of Magnetism*, Springer, Berlin, 1998.

Received 7 May 2006
Revised 1 September 2006

Materials Science-Poland, Vol. 25, No. 2, 2007

Current-induced torque in ferromagnetic single-electron devices in the limits of the fast and slow spin relaxation

M. KOWALIK[1*], I. WEYMANN[1], J. BARNAŚ[1, 2]

[1]Department of Physics, Adam Mickiewicz University, Umułtowska 85, Poznań 61-614, Poland

[2]Institute of Molecular Physics, Polish Academy of Sciences, Smoluchowskiego 17, Poznań 60-179, Poland

Theoretical analysis of the spin-transfer torque acting on the magnetic moment of the central electrode (island) in a single-electron ferromagnetic transistor has been performed for the spin relaxation time in the island ranging from fast to slow spin relaxation limits. The magnetic configuration of the system can be generally arbitrary. Spin accumulation on the island, due to the spin asymmetry of tunnelling processes, is taken into account. Electric current flowing through the device is calculated in the regime of sequential transport, and the master equation is used to calculate probabilities of different charge and spin states in the island. The torque acting on the central electrode is then calculated from the spin current absorbed by magnetic moment of the island.

Key words: *ferromagnetic single-electron transistor, spin-polarized current, spin-transfer torque*

1. Introduction

Despite preliminary theoretical predictions that spin transfer in tunnel junctions could be imperceptible [1], mainly due to the much smaller current density than in the case of metallic devices, current-driven magnetic switching in tunnel junctions has been found [2, 3]. Motivated by recent theoretical and experimental findings, we present calculations of the spin-transfer torque in ferromagnetic double-barrier junctions with Coulomb blockade effects. Spin accumulation in the central electrode due to the spin asymmetry of tunnelling processes is taken into account. The electric current flowing through the system is calculated in the regime of sequential transport. The master equation is set up to determine the relevant occupation probabilities of differ-

[*]Corresponding author, e-mail: kowalik@amu.edu.pl

ent charge and spin states in the island. The torque acting on the central electrode is then calculated from the spin current absorbed by the magnetic moment of the island.

2. Model and method

The system considered in this paper is presented in Fig. 1. It consists of three ferromagnetic electrodes – the left (*l*), right (*r*) and the middle one (*i*) referred to as an island. The magnetic configuration of the system can be generally non-collinear. The vectors $\vec{S}_l$ ($\vec{S}_r$) and $\vec{S}_i$ indicate the net spin moments of the left (right) electrode and of the island, respectively. As indicated in the figure, the net spin of each electrode can form an angle with the net spin of the island. There is also a bias voltage applied to the system, $V = V_l - V_r$, where V_l and V_r are electrostatic potentials of the left and right electrodes. Apart from this, the island is capacitively coupled to a gate with the corresponding voltage V_g.

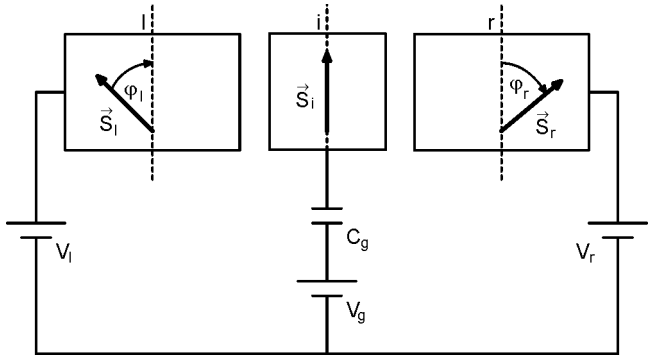

Fig. 1. A schematic diagram of the ferromagnetic single-electron transistor with all the electrodes being ferromagnetic. The vectors $\vec{S}_l$, $\vec{S}_r$ and $\vec{S}_i$ indicate the net spin moments of the external electrodes and of the island, respectively. The angle between the net spin of the left (right) electrode and the net spin of the island is denoted by φ_r and φ_l. There is a bias voltage applied to the left and right electrodes, while the island is capacitively coupled to a gate voltage V_g

We assume that the island is large enough so that the level quantization can be neglected but, on the other hand, sufficiently small to have the charging energy $e^2/2C$ significantly larger than the thermal energy k_BT, where C is the total island capacitance, e is the electronic charge, k_B denotes the Boltzmann constant, while T stands for temperature. If this condition is fulfilled, the electrons tunnel through the system one by one, giving rise to a flowing current. Furthermore, the system exhibits the so-called single-electron charging effects, such as, for example, blockade of the current below a certain threshold voltage (Coulomb blockade), the step-like I–V characteristics (Coulomb staircase), etc. [4] In addition, if the electrodes are ferromagnetic, further interesting effects arise due to the interplay of single-charge tunnelling and ferromag-

netism. They include the oscillations of tunnel magnetoresistance when sweeping the bias voltage, spin accumulation, etc. [5, 6].

In order to calculate transport properties, the two-channel model is applied; the current flows through the system due to consecutive tunnelling events in the spin-majority and spin-minority channels. Each tunnel junction is characterized by its resistance for the spin-majority and spin-minority electrons, and by its capacitance. In this analysis, we assume that the total resistance of each tunnel barrier R_k ($k = l, r$) is much larger than the quantum resistance $R_q = h/e^2$. This condition implies that the charge on the island is localized well and the orthodox theory [4] is applicable. Within this theory, only the sequential tunnelling processes are taken into account, while the corresponding rates are given by the Fermi golden rule. Having determined all the possible tunnelling rates, one can set up a master equation to calculate the probabilities that there is a given number of extra electrons on the island. The current flowing through the system can be then calculated from the appropriate equations, as described for example by Amman et al. [7].

Moreover, in this analysis we assume that the energy relaxation time is much shorter than the time between two successive tunnelling events, while the spin relaxation time in the island, τ_{sf}, may be arbitrary. If the spin relaxation time is longer than the time between two tunnelling processes, there is a nonequilibrium spin accumulation induced in the island. Because the island is ferromagnetic, the shifts of the Fermi level for the spin-majority and spin-minority bands due to spin accumulation are not equal. The ratio of the Fermi level shifts for the corresponding subbands is determined by the ratio of the density of states for a given electron subband. Therefore, to calculate the shift of the Fermi level for an arbitrary spin relaxation time τ_{sf}, the following balance equation [5, 6, 8] should be solved self-consistently:

$$\left(I_r^\sigma - I_l^\sigma\right) - \frac{D_i \Omega_i}{\tau_{sf}} \Delta E^\sigma = 0$$

Here, I_r^σ and I_l^σ are the currents flowing through the right and left junctions, respectively, in the spin-majority ($\sigma = \uparrow$) or spin-minority ($\sigma = \downarrow$) channels, D_i indicates the density of states of the island, while Ω_i is the island volume. The shifts of the Fermi level for the spin-majority or spin-minority electrons are denoted by ΔE^σ, where $\sigma = \uparrow\downarrow$.

Due to the spin asymmetry of ferromagnetic electrodes, the currents flowing in the spin-majority and spin-minority channels are different. Furthermore, if there is a certain angle between the net spin of the island and each of the electrodes, a single electron when tunnelling from one electrode to the island adjusts its spin orientation in an interfacial layer of atomic thickness. As a consequence, some angular momentum is transmitted to the local magnetization of the island and the electrode, producing spin torque. The torque acting on the magnetic moment of the island can be calculated from the difference between the spin current flowing into the island and the spin current leaving the island, in a similar way as presented in the papers by Slonczewski

[9, 10]. In the case of our system, the total torque τ_i acting on the net spin moment of the central electrode can be determined from the following equation:

$$\tau_i = \sum_{k=l,r} \left(\Delta I_k - \Delta I_{i(k)} \cos\varphi_k \right) \frac{1}{\sin\varphi_k}$$

where $\Delta I_k = I_k^+ - I_k^-$ and $\Delta I_{i(k)} = I_{i(k)}^{\uparrow} - I_{i(k)}^{\downarrow}$ for $k = l, r$. I_k^+, I_k^- denote the currents in the spin-majority and spin-minority channels taken at the atomic distance from the barrier for a given electrode k, whereas $I_{i(k)}^+$, $I_{i(k)}^-$ are the currents in the spin-majority and spin-minority channels in the island close to the barrier between the island and the k-th electrode.

3. Numerical results and discussion

In this section, we present numerical results for ferromagnetic single-electron transistors calculated for an arbitrary magnetic configuration of the system and for arbitrary spin relaxation time in the island. The angular dependences of the Fermi level shifts for the spin-majority and spin-minority electrons for several values of the spin relaxation time is presented in Fig. 2.

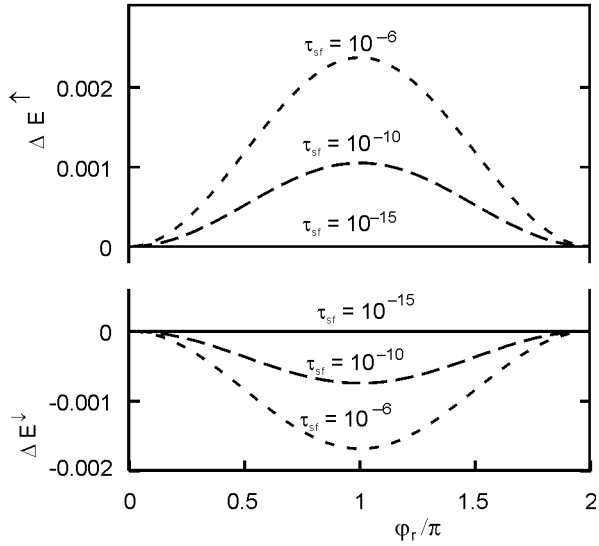

Fig. 2. The shift of the Fermi energy for spin-majority ($\Delta E^{\uparrow}$) (upper part) and spin-minority (($\Delta E^{\downarrow}$) (lower part) electrons due to spin accumulation for various spin relaxation times τ_{sf} as a function of φ_r, where φ_l =0. The other parameters are: $R_l^{\uparrow p} = 0.3$ MΩ, $R_l^{\downarrow p} = 0.15$ MΩ, $R_r^{\uparrow p} = 5$ MΩ, $R_l^{\downarrow p} = 2.5$ MΩ, where for $k = l, r$ $R_k^{\uparrow ap} = R_k^{\downarrow ap} = (R_k^{\uparrow p} R_k^{\downarrow p})^{1/2}$, $C_l = C_r = C_g = 1$ aF, $V_l = 0.5$ V, $V_r = 0$ V, $V_g = 0$ V, $D_i\Omega_i = 1000$ (eV)$^{-1}$ and $T = 4{,}2$ K

The time between two successive tunnelling events can be estimated to be of the order of 10^{-12}–10^{-10} s. Consequently, in the case of $\tau_{sf} = 10^{-15}$ s (solid line in Fig. 2) there is no spin accumulation. This is because the spin relaxation time is much shorter than the time between consecutive tunnelling events and the electron spin relaxes before the next tunnelling events occur. However, if $\tau_{sf} = 10^{-10}$ s, the spin relaxation time becomes of the order of the time between successive tunnelling events and there appears a non-zero shift of the Fermi level (see the dashed line in Fig. 2). On the other hand, the third case when $\tau_{sf} = 10^{-6}$ s corresponds to the limit of long spin relaxation and spin accumulation is much enhanced as compared to the two previous cases, see the dotted line in Fig. 2. The upper (lower) part of Fig. 2 shows the shift of the Fermi level for the spin-majority (spin-minority) electrons. It is also worth noting that generally $\Delta E^{\uparrow} > \Delta E^{\downarrow}$, due to the asymmetry in the densities of states of the respective electron bands. Furthermore, as shown in Fig. 2, the maximum spin accumulation occurs for $\varphi_r = \pi$, which corresponds to the antiparallel configuration.

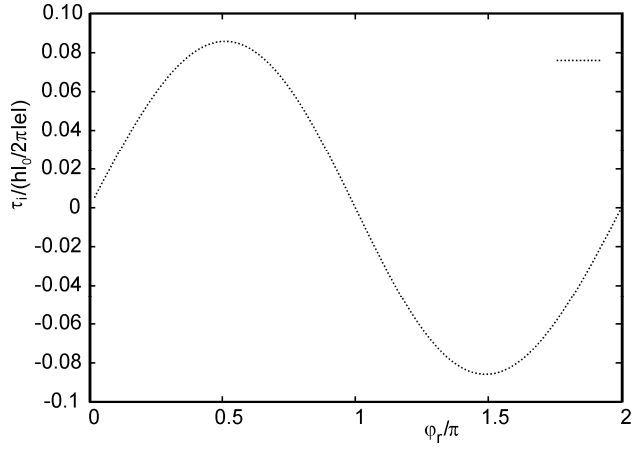

Fig. 3. The normalized torque acting on the island due to the spin-polarized current as a function of φ_r calculated for $\varphi_l = 0$ and for different spin relaxation times. The other parameters are the same as in Fig. 1

In Figure 3, we present the normalized torque acting on the central electrode due to the spin polarized current as a function of φ_r (while $\varphi_l = 0$) for three different spin relaxation times. As previously, the three values of the spin relaxation time correspond to the limits of fast and slow spin relaxation, and the crossover between those two limits, correspondingly. The normalized torque is defined as $\tau/\hbar I_0/|e|$, where I_0 is the current flowing through the system at a constant bias voltage. First of all, one can see that the dependence of the normalized torque on the angle between the right electrode and the island resembles the sine function. Thus, by changing φ_r, it is possible to produce either positive or negative torque acting on the island. Furthermore, the maximum torque occurs for $\varphi_r = \pi/2$. The normalized torque is independent of the spin relaxation time. This fact can be understood by realizing that both the current and

torque apparently depend on τ_{sf}, the normalized torque, however, given by the ratio of the torque and the current, does not.

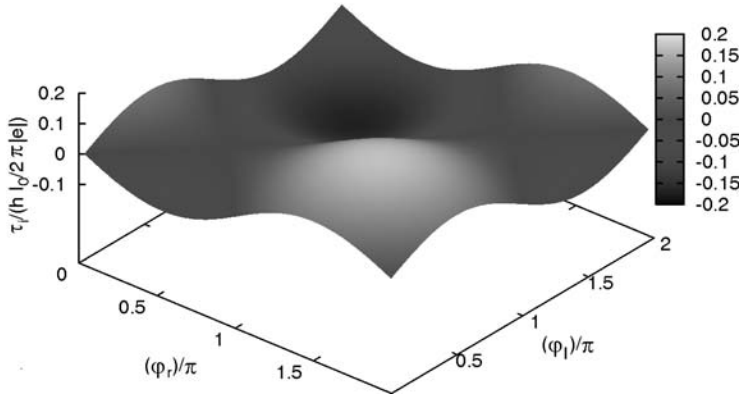

Fig. 4. The normalized torque acting on the island due to the spin-polarized current as a function of φ_r and φ_l for spin relaxation time $\tau_{sf} = 10^{-6}$ s. The other parameters are the same as in Fig. 1

The dependence of the normalized torque on both angles φ_r and φ_l is presented in Fig. 4. This figure was calculated for the spin relaxation time corresponding to the limit of slow spin relaxation. However, because the normalized torque only slightly depends on spin relaxation, see Fig. 3, the numerical results presented in this figure can be considered as the dependence of normalized torque on arbitrary values of spin relaxation time. From Fig. 4 one can easily identify the regions where the normalized torque is negative and positive, as well as the regions where the maximum torque occurs.

References

[1] SLONCZEWSKI J.C., J. Magn. Mater., L1 (1996), 159.
[2] HUAI Y., ALBERT F., NGUYEN P., PAKALA M., VALET T., Appl. Phys. Lett., 84 (2004), 3118.
[3] FYCHS G.D., EMLEY N.C., KRIVOROTOV I.N., BRAGANCA P.M., RYAN E.M., KISELEV S.I., SANKEY J.C., RALPH D.C., BUHRMAN R.A., KATINE J.A., Appl. Phys. Lett., 85 (2004), 1205.
[4] *Single Charge Tunnelling*, H. Grabert, M.H. Devoret (Eds.), NATO Advanced Study Institute, Series B, Vol. 294, Plenum Press, New York, 1992.
[5] WEYMANN I., BARNAŚ J., Phys. Status Sol. B, 236 (2003), 651.
[6] BARNAŚ J., FERT A., J. Magn. Mater., 192 (1999), 391.
[7] AMMAN M., WILKINS R., BEN-JACOB E., MAKER P.D., JAKLEVIC R.C., Phys. Rev. B, 43 (1991), 1146.
[8] KOROTKOV A.N., SAFAROV V.I., Phys. Rev. B, 59 (1999), 89.
[9] SLONCZEWSKI J.C., J. Magn. Magn. Mat., 195 (1999), L261.
[10] SLONCZEWSKI J.C., Phys. Rev. B, 71 (2005), 024411.

Received 7 May 2006
Revised 1 September 2006

Materials Science-Poland, Vol. 25, No. 2, 2007

Transport in nanostructures. Recent developments

K. I. WYSOKIŃSKI*

Institute of Physics and Nanotechnology Centre, M. Curie-Skłodowska University,
ul. Radziszewskiego 10, 20-031 Lublin, Poland

The recent work on the transport through nanostructures is discussed. It turns out that such structures very often directly serve as monitoring and/or controlling devices. They enable us to study transport properties and many body effects in highly controlled conditions. The simplest configuration discussed in the paper consists of a quantum dot (QD) connected to two external electrodes *via* tunnel barriers. Another important goal of the recent studies is to use the electron spin instead of charge in modern electronic devices. For the realization of electronics with spins (called spintronics), a precise control and efficient monitoring of spins is necessary. One way of achieving the goal that is briefly discussed in the paper is by means of the electric field in the presence of spin-orbit coupling *via* the so-called spin Hall effect (SHE).

Key words: *quantum transport; nanostructure; spin Hall effect*

1. Introduction

In this paper, I will concentrate on two aspects related to the general subject of transport in nanostructures. These are: (i) the Kondo effect as an example of many body interaction effects in transport through quantum dot based devices and (ii) the spin Hall effect. The properties discussed are in one way or another related to the spin of electrons and are or may be of importance for the development of spin-based electronics (spintronics) [1].

Theoretical and experimental studies of nanostructures, i.e. systems of a few nanometres dimensions face some common problems such as: (a) discreetness of the spectrum, (b) large charging energies and (c) geometrical and other asymmetries of the structure.

*E-mail: karol@tytan.umcs.lublin.pl

Due to a small size of the structure, its energy spectrum is discrete with typical distances between energy levels ΔE ranging from a fraction of to few millielectronvolts and can be observed even at room temperatures. The small size of the devices also means small capacitance C and large charging energy $E_C = e^2/2C$, where e is the electron charge. Contacts between various parts of the devices are realised *via* tunnelling with controlled tunnel resistance. This allows study of various regimes of electron transport with the Coulomb blockade phenomenon being an important example.

As an example of the many body effects induced by large charging energy, which in the language of interacting systems means large on-site Coulomb repulsion usually known in the solid state community as Hubbard U, the Kondo effect is presented [2] and its influence on some thermoelectric phenomena including conductivity and thermoelectric power of a quantum dot connected to non-magnetic and ferromagnetic leads. It is important to realise that many body effects may have quite an unexpected influence on the behaviour and properties of nanostructures. For example, it has been recently proposed theoretically [3] that the charges detected in the noise of backscattered currents in the system showing Kondo effect should possess values e^* differing from electron charge e. Fractional values of charge of quasi-particles is a property of elementary excitations of two-dimensional electron gas placed in strong perpendicular magnetic field. They have been observed in tunnelling studies of fractional quantum Hall effect [4] with $e^* = e/3$ and in superconductors where $e^* = 2e$. Unlike quantum Hall effect or superconductors, where e^* has a meaning of quasiparticle charge, in the Kondo regime the effective charge is a result of inelastic processes connected with interactions. This observation is potentially important in view of recent proposals to use devices measuring electron charge and based on quantum dots in nano-metrology applications [5].

One of the most important ideas of the recent years is to use quantum mechanical principles for information storage and processing. One of the proposals is to make use of the spin degrees of freedom in quantum dots. This requires coherent control and manipulation of spins. There exist a huge activity, both theoretical and experimental, connected with various proposals to control spins via electrical means. As one example of the technique of spin control and manipulation, we discuss the spin Hall effect.

2. The Kondo effect in transport via a quantum dot

Quantum dots (QD) are small islands containing finite number of charges. If connected to external electrodes, they have been proposed as building blocks of single electron transistors [6], quantum bits or registers of future computers [7] working according to quantum logic, as efficient factories of entangled states [8], precise ampere (current) meters [5] or potentially efficient energy conversion instruments [9]. Because of their small size, the charging energy in the considered structures is large and gives rise to many interesting phenomena. The Kondo effect [10] appearing in quantum dots weakly coupled to external electrodes at low temperatures is one of them. In quantum dots, it has been studied in various geometries. The dots attached to

normal (N-QD-N structure), superconducting (S-QD-N or S-QD-S' structures) or (ferro-) magnetic leads (FM-QD-FM structure) were considered. The effect of Kondo correlations on the conductance of the system with normal, magnetic or superconducting leads has been extensively studied [11–13].

Consider the ultrasmall quantum dot (with very large charging energy and sparse, discrete spectrum), weakly coupled to external electrodes via tunnel barriers. Even for non-magnetic leads, the spin of an electron manifests itself in the appearance of the Kondo effect. If one allows magnetic electrodes, there appear additional interesting effects. The Kondo scale itself depends on the polarisation P of the ferromagnetic leads. The Kondo temperature T_K has been found to be [14]

$$T_K(P) \approx D \exp\left\{-\frac{1}{N(0)J_0}\frac{\operatorname{arctanh} P}{P}\right\} \tag{1}$$

where $N(0)$ is the total density of states at the Fermi energy, D the effective scale, J_0 the Kondo coupling and $P = (N_\uparrow - N_\downarrow)/(N_\uparrow + N_\downarrow)$ the polarisation.

Quantum-dot-based devices also allow us the study of strongly nonlinear transport. The presence of the signatures of the equilibrium and non-equilibrium Kondo effect in transport through quantum dots has first been predicted theoretically [15, 16] and later confirmed [17] in measurements of the differential conductance $G(V) = dI/dV$. In metals containing magnetic impurities, the Kondo effect manifests itself as an increase of resistance at temperatures $T < T_K$, while in transport through quantum dots one gets enhancement of zero bias conductance $G(0)$ which eventually reaches the unitary limit $2e^2/h$.

The nanostructure consisting of a quantum dot and external electrodes (normal or otherwise) can be modelled by the Anderson Hamiltonian

$$H = \sum_{\mathbf{k},\beta,\sigma} \xi_{\mathbf{k},\beta} c^+_{\mathbf{k},\beta\sigma} c_{\mathbf{k},\beta\sigma} + \sum_\sigma \varepsilon_d d^+_\sigma d_\sigma + U n_{d\uparrow} n_{d\downarrow} + \sum_{\mathbf{k},,\beta,\sigma} (V_{\mathbf{k},,\beta} c_{\mathbf{k},\beta\sigma} d^+_\sigma + V^*_{\mathbf{k},\beta} d_\sigma c^+_{\mathbf{k},\beta\sigma}) \tag{2}$$

Here the operators $c_{\mathrm{k}\beta\sigma}, c^+_{\mathrm{k}\beta\sigma}$ correspond to annihilation and creation of the conduction electrons in the (normal) leads, the energies $\xi_{\mathbf{k}\beta\sigma} - \mu_\beta$ in the left ($\beta = L$) or right h.s. ($\beta = R$) electrodes are measured with respect to the chemical potentials μ_L and μ_R. Operators d_σ, d^+_σ refer to the localised electrons on the dot which is characterised by a single energy level ε_d and the charging energy U. The last term in Eq. (2) describes hybridisation between the electrons on the dot and external leads.

A proper technique to study the non-equilibrium transport is the Keldysh non-equilibrium Green's function method [18] and non-crossing approximation to treat many body interactions.

In Figures (1) and (2) we show the temperature dependence of the conductance G and thermopower S of the quantum dot connected to non-magnetic leads. The Green functions have been calculated in the non-crossing approximation and the limit of

infinitely large charging energy $U = \infty$ has been assumed. Note the increase of G at low temperatures and its saturation at $T = 0$, where $G = 2e^2/h$ – the unitary limit. The important point is that S changes the sign at temperatures close to the Kondo temperature. It is the appearance of the Kondo resonance which changes the slope of the spectrum of electrons at the Fermi level and this leads to the change of sign of the thermopower.

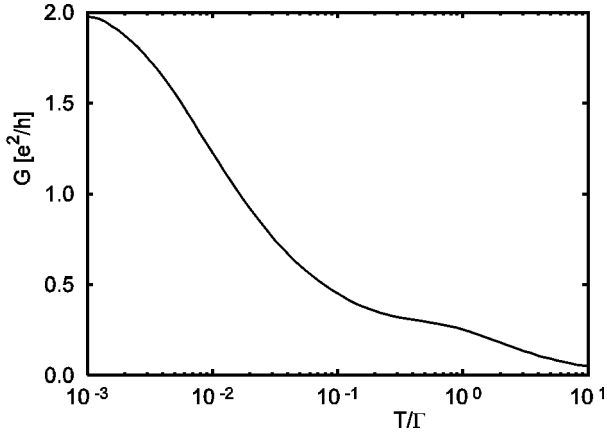

Fig. 1. Temperature dependence of the conductance G of a quantum dot calculated in the non-crossing approximation. Note the increase of G at low temperatures and its saturation at $T = 0$, where $G = 2e^2/h$ – the unitary limit

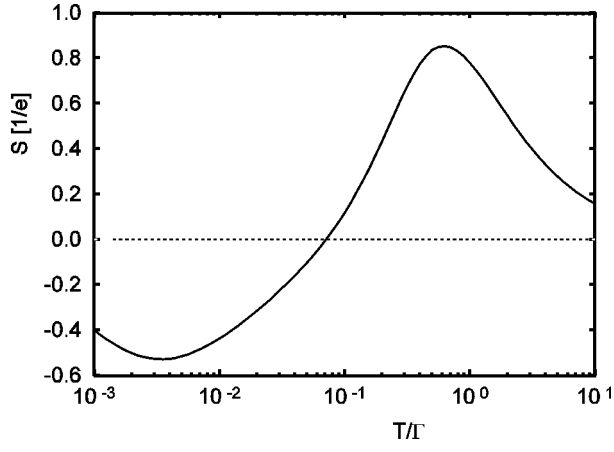

Fig. 2. Temperature dependence of the thermopower S of a quantum dot calculated in the non-crossing approximation. The change of sign of S marks the appearance of the Kondo effect

To understand the change of sign of the thermopower with decreasing temperature one has to note that the Kondo resonance forms slightly above the Fermi energy. It

changes the slope of the density of states. The thermopower which depends on the asymmetry (slope) of the density of states at the Fermi level thus changes sign.

Recently, we studied the thermoelectric phenomena of a quantum dot attached to two magnetically polarised [19], as well as nonmagnetic [20] leads. The Kondo effect becomes less pronounced with increasing magnetic polarisation of the leads and this influences all the transport coefficients. It is an interesting observation that the Fermi liquid behaviour is recovered at temperatures $T < T_K$ both for normal as well as magnetic electrodes.

3. The spin Hall effect

The driving force behind the studies of spintronics is the desire to use the electron spin in information storage and processing devices. Spin control, injection and detection require clever tricks. Methods enabling fast generation and manipulation of spin currents by applying electric field are of particular interest. It is the spin Hall effect which has become of great interest. The effect has been analysed in a number of theoretical papers.

The spin Hall effect (SHE) is closely related to the well-known anomalous Hall effect (AHE), frequently observed in ferromagnetic materials. In ferromagnets, the anomalous Hall effect is connected *inter alia* with spin-orbit interaction. The spin up (down) carriers moving under the influence of external voltage in the presence of spin -orbit interaction preferably scatter to the left (right) with respect to original trajectory causing the transverse spin current. This is the essence of the spin Hall effect. Such scattering does not produce an extra charge imbalance and vice versa the spin current, i.e. the movement of spin up electrons in the direction opposite to spin down electrons under the influence of spin-orbit scattering induces an extra perpendicular voltage, which contributes to the anomalous Hall effect.

The SHE has been theoretically predicted in the early seventies [21] and rediscovered a few years ago [22]. Since then, in view of possible applications in spintronic devices it has been very intensively studied theoretically and experimentally [23]. The effects are very subtle. One distinguishes the intrinsic and extrinsic SHE. For the purpose of this paper, it is enough to say that the extrinsic effect requires spin dependent scattering on impurities, while the intrinsic SHE is due to spin-orbit coupling (SOC) terms in single particle Hamiltonian of a clean system. These can be of two types, commonly known as Dresselhaus and Rashba couplings. The Dresselhaus SOC results from the bulk band structure, and is connected with the absence of bulk inversion symmetry (the lattice without an inversion centre) and depends on the material studied. On the other hand, the Rashba SOC develops because of structure inversion asymmetry (no centre of inversion in nanostructure confining potential) and may thus be controlled by electric field applied to, e.g., quantum wells. It has been found that in narrow 2D quantum well of GaSb, the Dresselhaus spin-orbit coupling takes on the form:

$$H_D = \alpha_D(\sigma_x \hat{k}_x - \sigma_y \hat{k}_y) \tag{3}$$

where σ_x, σ_y are the Pauli matrices, $\hat{k}_i$ is the unit vector in the direction i, α_D – the coupling constant $(2–20)\times10^{-10}$ eV·cm) and diminishes with increasing the width of the well. The Rashba term has a similar structure

$$H_R = \alpha_R(\sigma_x \hat{k}_y - \sigma_y \hat{k}_x) \tag{4}$$

The coupling constant α_R in InAs based quantum well can be as large as (1–6) $\times10^{-9}$ eV·cm. It is important to realise that in semiconductors the effective spin-orbit coupling may exceed that calculated for an electron in vacuum by 6 orders of magnitude.

In narrow samples, the spin Hall effect leads to spin accumulation at the opposite edges of the sample. Recently, the effect has been observed experimentally *via* optical techniques [24] and more recently by direct measurement [25]. The comparison of experiment with theory, however, is not satisfactory and calls for better understanding of the effect.

Acknowledgements

It is my great pleasure to thank Mariusz Krawiec, Agnieszka Donabidowicz and Tadeusz Domański for collaboration and useful discussions, Dr. M. Krawiec for performing numerical calculations presented in Figs. 1 and 2, and prof. St. Lipiński for his help. The work has been partially supported by the grant PBZ-MIN-008P032003.

References

[1] DIETL T., Nature Mat., 2 (2003), 643; DIETL T., *Spintronics and ferromagnetism in wide bandgap semiconductors*, 27th International Conference on the Physics of Semiconductors, Flagstaff, AR, USA, July 2004, J. Mendez (Ed.) (AIP Proceedings).

[2] HEWSON A.C., *The Kondo problem*, *to Heavy Fermions*, Cambridge Univ. Press, Cambridge, 1999.

[3] SELA E., OREG Y., VON OPPEN F. AND J KOCH J., Phys. Rev. Lett., 97 (2006), 086601.

[4] DE-PICCIOTTO R., REZNIKOV R., HEIBLUM M., UMANSKY M., BUNIN V., MAHALU G., BRAUN D., Nature, **(**1997), 162; SAMINADAYA L., GLATTLI D.C., JUN C.Y., ETIENNE B., Phys. Rev. Lett., 79 (1997), 2526.

[5] FLENSBERG K., ODINTSOV A.A., LIEFRINK F., TEUNISSEN P., Int. J. Mod. Phys. B, 13 (1999), 2651.

[6] AVERIN D.V., LIKHAREV K.K., [in:] *Mesoscopic Phenomena in Solids*, B.L. Altshuler, P.A. Lee, R.A. Webb, North Holland, Amsterdam, 1991.

[7] NIELSEN M.A., CHUANG I.L., *Quantum*, *Computation and Quantum Information*, Cambridge Univ. Press, Cambridge, 2000.

[8] FABIAN J.J., HOHENESTER U., Phys. Rev. B, 72 (2005), 201304 and references therein.

[9] HEREMANS J.P., THRUSH C.M., MORELLI D.T., Phys. Rev. B, 70 (2004), 115334 and references therein.

[10] KOUWENHOVEN L.P., GLAZMAN L., Phys. World, January 2001, p. 33.

[11] KRAWIEC M., DOMAŃSKI T., WYSOKIŃSKI K.I., Acta Phys. Polon., A94 (1998) 411; KRAWIEC M., WYSOKIŃSKI K.I., Mol. Phys. Rep., 28 (2000), 64; Sol. State Commun. 115

(2000), 141; Acta Phys. Polon. A, 97 **(**2000), 197; Phys. Rev. B, 66 (20002), 165408; KRAWIEC M., WYSOKIŃSKI K.I., Supercond. Sci. Technol., 17 (2004), 103; DOMAŃSKI T., KRAWIEC M.. MICHALIK M., WYSOKIŃSKI K.I., Cond. Matter Phys., 7 (2004), 331.

[12] BUŁKA B.R., LIPIŃSKI S., Phys. Rev. B, 67 (2003), 024404.

[13] MARTINEK J., SINDEL M., BORDA L., BARNAŚ J., KÖNIG J., SCHÖN G., VON DELFT J., Phys. Rev. Lett., 91 (2003), 247202; KÖNIG J., MARTINEK, J., BARNAŚ J., SCHÖN G., *GFN Lectures on Functional Nanostructures*, K. Busch, A. Powell, C. Röthig, G. Schön, J. Weismüller (Eds.), *Lecture Notes in Physics*, 658 (2005), 145; MARTINEK J,, SINDEL M., BORDA, L., BARNAŚ J., BULLA R., KÖNIG J., SCHÖN G., MAEKAWA S., VON DELFT J., Phys. Rev. B 72 (2005), 121302(R); ŚWIRKOWICZ R., BARNAŚ J., WILCZYŃSKI M., Phys. Rev. B, 68 (2003), 195318.

[14] MARTINEK J., UTSUMI Y., IMAMURA H., BARNAŚ J., MAEKAWA S., KÖNIG, J., SCHÖN G., Phys. Rev. Lett., 91 (2003), 127203.

[15] NG T.K., LEE P.A., Phys. Rev. Lett., 61 (1998), 1768.

[16] GLAZMAN L.I., RAIKH M.E., JETP Lett., 47 (1998), 452.

[17] GOLDHABER-GORDON D., SHTRIKMAN H., MAHALU D., ABUSCH-MAGDER D., MAIRAV U., KASTNER M.A., Nature, 391 (1998), 156; CRONENWETT S.M., OOSTERKAMP T.H., KOUWENHOVEN L.P., Science 281 (1998), 540; VAN DER WEIL W.G., DE FRANCESCHI, FUJISAWA S.T., ELZERMAN J.M., TARUCHA S., KOUWENHOVEN L.P., Science 289 (2000), 2105; SCHMID J., WEIS J., EBERL K., VON KLITZING K., Physica B, 256–258, (1998), 182; SIMMEL F., BLICK R.H., KOT-THAUS J.P., WEGSCHEIDER W., BICHLER M., Phys. Rev. Lett., 83 (1999), 804; SCHMID J., WEIS J., EBERL K., VON KLITZING K., Phys. Rev. Lett., 84 (2000), 5824.

[18] HAUG H., YAUHO A.P., *Quantum*, *Kinetics in Transport and Optics of Semiconductors*, Springer -Verlag, Berlin, 1996; KELDYSH L.V., Sov. Phys. JETP, 20, 10 (1965), 108.

[19] KRAWIEC M., WYSOKIŃSKI K.I., Phys. Rev. B 73 (2006), 075307; SCHEIBNER R., BUCHMANN H., REUTER D., KISELEV N.N., MOLENKAMP L.W., Phys. Rev. Lett., 95 (2005), 176602.

[20] DONABIDOWICZ A., DOMAŃSKI T., WYSOKIŃSKI K.I., in preparation.

[21] DYAKONOV M.I., PEREL V.I., Zh. Eksp. Teor. Fiz., 13 (1971), 657 (English transl. JETP Lett., 13 (1971) 467); Phys. Lett., 35A (1971), 59.

[22] HIRSCH J., Phys. Rev. Lett., 83 (1999), 1834.

[23] SCHLIEMANN J., Int. J. Mod. Phys. B, 20 (2006), 1015; ENGEL H.A., RASHBA E.I., HALPERIN B.I., http://arxiv.org/PS_cache/cond-mat/pdf/0603/0603306v3.pdf and references therein.

[24] KATO Y.K., MYERS, R.C., GOSSARD A.C, AWSCHALOM D.D., Science, 306 (2004)**,** 1910; WUNDERLICH J., KAESTNER B., SINOVA J., JUNGWIRTH T., Phys. Rev. Lett., 94 (20005), 047204; SIH V., MYER R.C., KATO Y.K, LAU W.H., GOSSARD A.C., AWSCHALOM D.D., Nature Phys., 1 (2005), 31.

[25] VALENZUELA S.O., TINKHAM M., Nature 442 (2006), 176.

Received 7 May 2006
Revised 1 September 2006

Materials Science-Poland, Vol. 25, No. 2, 2007

Electronic transport in a ferromagnetic single-electron transistor with non-collinear magnetizations in the co-tunnelling regime

J. WIŚNIEWSKA[1*], J. BARNAŚ[1, 2]

[1] Department of Physics, Adam Mickiewicz University, Umultowska 85, 61-614 Poznań, Poland

[2]Institute of Molecular Physics, Polish Academy of Sciences,
M. Smoluchowskiego 17, 60-179 Poznań, Poland

Spin-dependent electronic transport in a ferromagnetic single-electron transistor (FM SET) is studied theoretically in the Coulomb blockade regime [1]. Two external electrodes and the central part (island) of the device are assumed to be ferromagnetic, with the corresponding magnetizations being non-collinear in a general case. First order (sequential) transport is suppressed in the Coulomb blockade regime, so the second order (co-tunnelling) processes give the dominant contribution to the current. The co-tunnelling processes take place *via* four intermediate (virtual) states of the island: two of them are with one extra electron on the central electrode of the device (in the spin-majority or spin-minority subbands), whereas the other two virtual states are with a hole (in the spin-majority or spin-minority subbands) in the central electrode. The co-tunnelling processes create electron-hole excitations of the central electrode, and in a general case they also can create spin excitations. However, we assume relatively fast spin relaxation in the island, hence the spin accumulation is neglected. Basic transport characteristics, like tunnelling current and tunnel magnetoresistance are calculated for an arbitrary magnetic configuration of the system.

Key words: *ferromagnetic single-electron transistor; spin-polarized transport; co-tunnelling*

1. Introduction

Electronic transport through magnetic nanometer-size devices has been extensively studied due to expected future application. In such nanoscale systems, one can manipulate not only a single electron charge, but also a single electron spin. In real double-barrier tunnel junctions, magnetic moments of the electrodes can form a non-collinear magnetic configuration and can have strong influence on the transport characteristics. In our recent paper [2], we have shown that transport characteristics in the sequential tun-

[*]Corresponding author, e-mail: justyw@amu.edu.pl

nelling regime strongly depend on the magnetic configuration of ferromagnetic single-electron transistor (FM SETs).

In this paper, we present the results of our theoretical analysis of spin-dependent co-tunnelling transport in a FM SET whose all three electrodes are ferromagnetic and made of the same material. The corresponding magnetizations are generally non-collinear and oriented in a common plane. In a general case, an external gate voltage can be applied to the island. The gate, however, is neglected in this paper, where we analyze the dependence of electric current and tunnel magnetoresistance (TMR) on the transport voltage and on the angles between magnetizations. Since the analysis is restricted to co-tunnelling processes only, the results are applicable for bias voltage significantly below the resonance (threshold voltage, at which the first Coulomb step appears).

The numerical analysis of the transport characteristics is restricted to the zero temperature limit, with the corresponding transition rates determined from the Fermi golden rule for the second-order transitions. It is also assumed that spin relaxation on the island is sufficiently fast to neglect spin accumulation. The electric current flowing through the device and the resulting tunnel magnetoresistance are calculated for different magnetic configurations of the device.

2. Model and theoretical description

The considered FM SET consists of three electrodes made of the same ferromagnetic material – a small metallic central electrode (called an island) connected by tunnel barriers to two external ferromagnetic electrodes, to which a transport voltage V is applied. Magnetic moments of the electrodes are oriented arbitrary within a common plane.

In our considerations, we take into account only co-tunnelling processes at zero temperature. If the barrier resistances exceed significantly the quantum resistance, $R_j >> R_q = h/e^2$ (j = 1, 2), the sequential tunnelling in the Coulomb blockade regime for $T \to 0$ K is exponentially suppressed ($I \propto \exp(\Delta E/kT)$, with ΔE being the increase in the energy), and the dominant contribution to current is due to co-tunnelling processes. The co-tunnelling processes go *via* intermediate (virtual) states of the island. In the case considered, we have four virtual states of the island; two of them are with one extra electron (spin-majority or spin-minority) on the central electrode of the device, whereas the other two virtual states are with a hole (in the spin-majority or spin-minority subbands) in the central electrode. An important property of the co-tunnelling is that the electrons involved in the co-tunnelling processes not only transfer charge, but also create electron-hole excitations of the central electrode (inelastic co-tunnelling). The calculations in this paper are carried out in the limit of fast spin relaxation processes (no spin accumulation on the island). Apart from this, the island is assumed to be large enough to neglect the quantization effects in the island (the relevant energy spectrum can be treated as a continuous one).

The second-order electron tunnelling rate from the spin majority/minority (+/–) subband of the left (L) electrode to the spin majority/minority (+/–) electron channel of the right (R) electrode is given by [3]:

$$\Gamma_{L\to R}^{\pm\to\pm}=\frac{2\pi}{\hbar}\sum_{i,f}\left|\sum_{v}\frac{\langle i|H_T|v\rangle\langle v|H_T|f\rangle}{\varepsilon_v-\varepsilon_i}\right|^2\delta\left(\varepsilon_i-\varepsilon_f\right) \tag{1}$$

where ε_i and ε_f are the energies of initial $|i\rangle$ and final $|f\rangle$ states of the system, ε_v is the energy of the virtual state $|v\rangle$, and $H_T|\rangle$ is the tunnelling Hamiltonian.

Taking into account the local quantization axes in all three electrodes (two external and the central one), and assuming constant (independent of energy) density of states in the leads and constant transfer matrix elements, one can write the tunnelling rate from the spin majority/minority (+/–) subband of the left electrode to the spin majority/minority (+/–) electron channel of the right electrode in the form,

$$\Gamma_{L\to R}^{+\to+}=\frac{\cos^2\frac{\beta}{2}\cos^2\frac{\alpha}{2}}{R_{1,+}^{P}R_{2,+}^{P}}\gamma+\frac{\sin^2\frac{\beta}{2}\sin^2\frac{\alpha}{2}}{R_{1,+}^{AP}R_{2,+}^{AP}}\gamma \tag{2a}$$

$$\Gamma_{L\to R}^{+\to-}=\frac{\cos^2\frac{\beta}{2}\sin^2\frac{\alpha}{2}}{R_{1,+}^{P}R_{2,-}^{AP}}\gamma+\frac{\sin^2\frac{\beta}{2}\cos^2\frac{\alpha}{2}}{R_{1,+}^{AP}R_{2,-}^{P}}\gamma \tag{2b}$$

$$\Gamma_{L\to R}^{-\to+}=\frac{\sin^2\frac{\beta}{2}\cos^2\frac{\alpha}{2}}{R_{1,-}^{AP}R_{2,+}^{P}}\gamma+\frac{\cos^2\frac{\beta}{2}\sin^2\frac{\alpha}{2}}{R_{1,-}^{P}R_{2,+}^{AP}}\gamma \tag{2c}$$

$$\Gamma_{L\to R}^{-\to-}=\frac{\sin^2\frac{\beta}{2}\sin^2\frac{\alpha}{2}}{R_{1,-}^{AP}R_{2,-}^{AP}}\gamma+\frac{\cos^2\frac{\beta}{2}\cos^2\frac{\alpha}{2}}{R_{1,-}^{P}R_{2,-}^{P}}\gamma \tag{2d}$$

where $\beta\,(\alpha)$ are the angles between magnetic moments of the left (right) electrode and the island, $R_{1,\pm}^{P}$ ($R_{2,\pm}^{P}$) denotes the spin-dependent resistance of the left (right) barrier in the parallel magnetic configuration, and $R_{1,\pm}^{AP}$ ($R_{2,\pm}^{AP}$) have similar meaning for the antiparallel configuration.

In Eqs. (2a)–(2d) the parameter γ is defined as

$$\begin{aligned}\gamma=&\frac{\hbar}{2\pi e^4}\int d\varepsilon_1 d\varepsilon_2 d\varepsilon_3 d\varepsilon_4 f\left(\varepsilon_1\right)\left[1-f\left(\varepsilon_2\right)\right]f\left(\varepsilon_3\right)\left[1-f\left(\varepsilon_4\right)\right]\\&\times\left(\frac{1}{\varepsilon_2-\varepsilon_1+E_1}+\frac{1}{\varepsilon_4-\varepsilon_3+E_2}\right)^2\delta\left(eV+\varepsilon_1-\varepsilon_2+\varepsilon_3-\varepsilon_4\right)\end{aligned} \tag{3}$$

where $f(\varepsilon)$ is the Fermi distribution function, ε_1 and ε_4 are the energies measured from the Fermi level of the left and right electrodes, whereas ε_2 and ε_3 are measured from the Fermi level of the island. Apart from this, E_1 and E_2 are the changes in the electrostatic energies associated with the two different virtual states:

$$E_1 = e\left(\frac{\frac{e}{2} - VC_2}{C_\Sigma}\right) \quad \text{and} \quad E_2 = e\left(\frac{\frac{e}{2} - VC_1}{C_\Sigma}\right)$$

where C_1 and C_2 are the capacitances of the left and right junctions, and $C_\Sigma = C_1 + C_2$. In the zero temperature approximation and for small voltages ($eV << E_1, E_2$), the above integral can be calculated analytically and one gets

$$\gamma \approx \frac{\hbar}{12\pi e}\left(\frac{1}{E_1} + \frac{1}{E_2}\right)^2 V^3 \tag{4}$$

In the co-tunnelling regime, the electric current flowing through the system can be then calculated as

$$I_{L\to R}(V) = e\sum_{\sigma=+,-}\sum_{\sigma'=+,-}\left[\Gamma_{L\to R}^{\sigma'\to\sigma} - \Gamma_{R\to L}^{\sigma\to\sigma'}\right] \tag{5}$$

where $\Gamma_{R\to L}^{\sigma\to\sigma'}$ is the spin-dependent tunnelling rate for backward processes.

Let us now present some numerical results on electric current and tunnel magnetoresistance, obtained with the formulas derived above.

3. Numerical results and discussion

Using Equation (5), we can calculate co-tunnelling current for any magnetic configuration of the device, and hence also the tunnel magnetoresistance effect defined by the ratio [4]

$$TMR = \frac{I(\beta = 0, \alpha = 0)}{I(\beta, \alpha)} - 1 \tag{6}$$

where $I(\beta,\alpha)$ is the current flowing in the non-collinear magnetic configuration (in the parallel configuration we have $\beta = 0$ and $\alpha = 0$).

In Figure 1, we show the results of numerical calculations of electric current flowing through the system as a function of the bias voltage for selected values of the angles. The upper part corresponds to $\beta = 0$, whereas the lower one to $\beta = \alpha$. The electric current in the Coulomb blockade regime varies as the third power of the voltage, $I \propto V^3$.

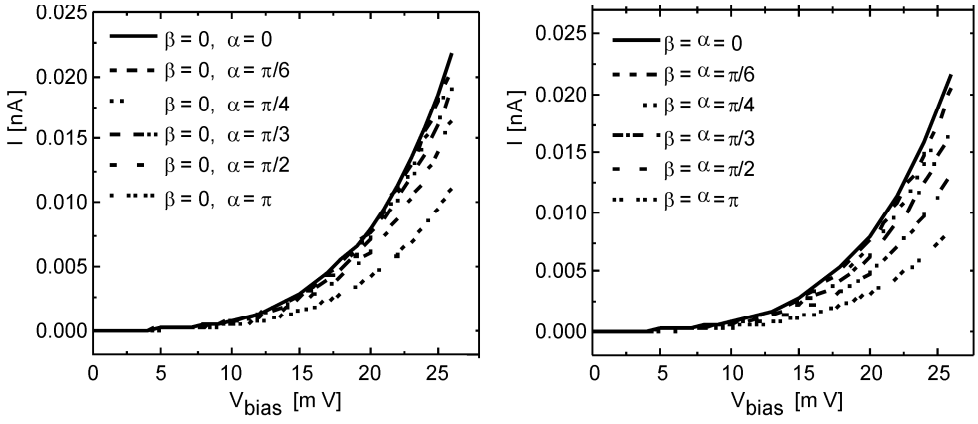

Fig. 1. The electric current as a function of the bias voltage in a FM SET with non-collinear magnetizations for different angles between magnetic moments. The parameters taken in numerical calculations are: $C_1 = C_2 = 1$ aF, $R_1^{p,+} = 0.5\ \mathrm{M\Omega}$, $R_1^{p,-} = 0.1\ \mathrm{M\Omega}$, $R_2^{p,+} = 25\ \mathrm{M\Omega}$, $R_2^{p,-} = 5\ \mathrm{M\Omega}$, whereas $R_i^{ap} = \sqrt{R_i^{p,+} R_i^{p,-}}$ for $i = 1, 2$. The bias voltage was applied symmetrically: $V_2 = -V_1 = -V/2$.

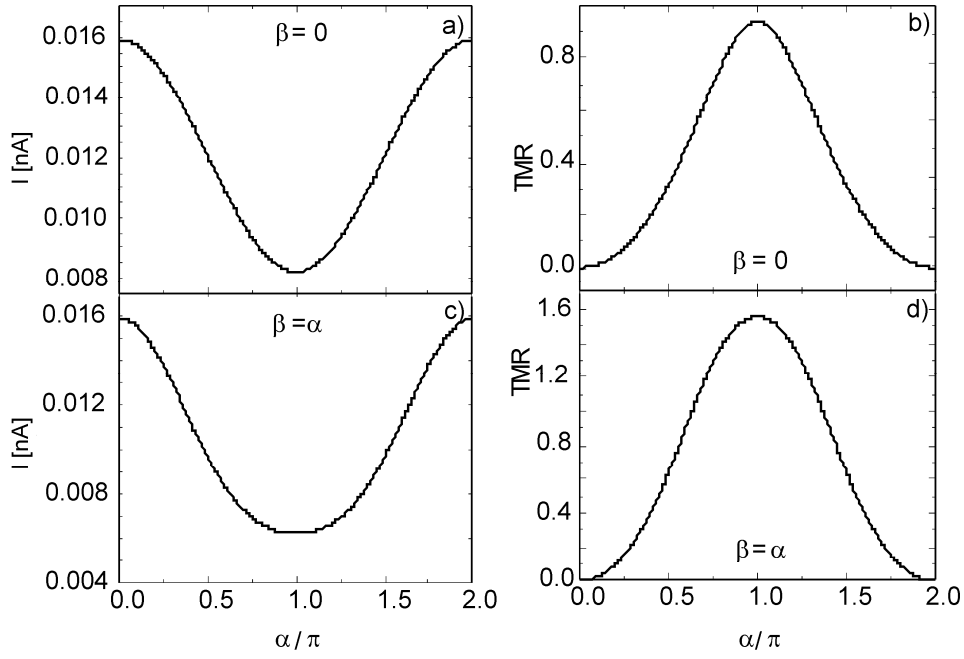

Fig. 2. The dependences of electric current (a), (c) and TMR (b), (d) on the angles between magnetizations, calculated for the bias voltage $V = 24$ mV. The other parameters are the same as in Fig.1.

The currents flowing in the system depend on its magnetic configuration, and this difference gives rise to a nonzero TMR which, however, is constant over the whole bias range (this may change in systems where the assumptions made in this paper are

not obeyed). The angular dependence of current and the associated TMR is shown in Fig. 2 which clearly shows that electric current has a minimum in the antiparallel magnetic configuration, which corresponds to a maximum in TMR.

4. Conclusions

In this paper, we have studied transport characteristics of a single-electron transistor in the co-tunnelling regime. The analyzed device consists of a ferromagnetic particle (island) and two ferromagnetic external electrodes (made of the same material), whose magnetizations are oriented arbitrary. We have calculated electric current flowing through such a device and the corresponding TMR. Bias dependence of electric current reveals its variation with the bias as $I \propto V^3$, while the TMR effect is independent of the bias voltage. Furthermore, the current flowing through the system, as well as the TMR, strongly depend on the angles between magnetizations.

References

[1] GRABERT H., DEVORET M.H., *Single Charge Tunnelling*, NATO ASI Series B, Vol. 294, Plenum Press, New York, 1992.
[2] WIŚNIEWSKA J., WEYMANN I., BARNAŚ J., Mater. Sci.-Poland, 22 (2004), 461.
[3] FEYMANN R.P., HIBBS A.R., *Quantum Mechanics and Path Integrals*, McGraw-Hill, New York, 1965.
[4] JULLIERE M., Phys. Lett. A, 54 (1975), 225.

Received 7 May 2006
Revised 1 September 2006

Materials Science-Poland, Vol. 25, No. 2, 2007

The study of silver nanoparticles by scanning electron microscopy, energy dispersive X-ray analysis and scanning tunnelling microscopy

M. PUCHALSKI*, P. DĄBROWSKI, W. OLEJNICZAK,
P. KRUKOWSKI, P. KOWALCZYK, K. POLAŃSKI

Department of Solid State Physics, University of Łódź, Pomorska 149/153, 90-236 Łódź, Poland

The authors present results of studies on commercially available silver nanoparticles fabricated by Amepox Microelectronics and delivered in the form of silver powder. The studies were carried out by scanning electron microscopy (SEM), energy dispersive X-ray analysis (EDX) and scanning tunnelling microscopy (STM). Chemical analysis performed with the use of EDX revealed that the powder contains about 74% of silver. Further studies of the silver granulate by use of SEM explicitly indicated the presence of micromete-size conglomerates composed of much smaller particles. Silver powder was dissolved in *n*-hexane, and colloid solution was obtained, in which the particles were subjected to the process of segregation. The colloid, obtained with this method, in which one expected to find particles of smaller sizes, was deposited on the Au(111) surface. The results of the studies of the sample prepared by means of STM enabled us to estimate the distribution of silver nanoparticles size, which appeared to be normal with a relatively small standard deviation.

Key words: *silver nanoparticle; STM; SEM; EDX*

1. Introduction

Over the past few years, studies on nanosilver have remained of interests to many scientific groups because of its potential technological application in many spheres of life. The properties of silver nanoparticles investigated so far allow their use among others in medicine [1, 2], optics [3, 4], or in electronics [5, 6]. From the nanotechnological point of view, the application of nanosilver in the form of colloidal ink for forming conducting tracks with micrometrical width [7, 8] is of potential interest.

The technique of producing silver particles of nanometrical size is well known and widely used. It is based on thermal decomposition of silver salt of a fatty acid in the atmosphere of neutral gas (Argon) [9]. As a result of that process, powder consisting of silver particles surrounded by stabilising substances in the form of alkyl chain is

*Corresponding author, e-mail: mpuchalski@std2.fic.uni.lodz.pl

obtained. Such particles demonstrate strong tendency for aggregation and formation compact micrometrical structures [10] only possible to segregate in organic solvents such as toluene, hexane, benzene [11].

In this paper, we describe results of nanosilver studies carried out by means of the following techniques: scanning electron microscopy (SEM), energy dispersive X-ray analysis (EDX) and scanning tunnelling microscopy (STM). Studies carried out by SEM and EDX, global techniques, enabled not only a detailed examination of silver powder morphology, but also its chemical composition analysis. However, they appeared insufficient for distribution analysis of single particle sizes. For this purpose, the STM high resolution technique was used. In the conducted experiment we managed to separate particles from the silver powder by means of hexane and then deposit them on the Au(111) surface. It allowed us to observe single particles with the use of STM and carry out a detailed distribution analysis of their size. The results we obtained proved a narrow particle size distribution which is well described by normal distribution.

2. Experimental

We used nanosilver in the form of silver powder supplied by Amepox Microelectronics. The studies of silver powder were carried out by means of a scanning electron microscope Vega 5135 MM from Tescan company (SE Detector, 30 kV, high vacuum 5×10^{-3} Pa) working with EDX Link 300 ISIS from Oxford Instruments (Detector Si(Li), 30 kV, low vacuum 10 Pa, resolution 60 eV). The samples were prepared by fixing the powder particles to microscope holder, using a conducting carbon strip.

For single nanoparticle studies, we used a home-built STM [12] working in air at room temperature. Preparing the sample required separating single silver particles from the powder delivered for studies. For this purpose, we dissolved 1 mg of silver powder in 5 ml of hexane (Aldrich, Chromasolvz, 97%). The solution prepared in this way was subjected to the process of particles selection. Particles of sizes larger than nanometrical, deposited on the test tube bottom formed sediment but the smallest ones formed a homogeneous colloid solution. After 24 hours, 20 μl of the obtained colloid was additionally dissolved in 5 ml hexane, which allowed obtaining a transparent solution which was deposited on the Au(111) surface (Georg Albert PVD – Beschichtungen). After the evaporation of the solvent (two hours), the sample was examined with the STM microscopy. The studies were carried out under constant current mode I_t =1 nA, at tip sample voltage U_t = 0.2 V. For the experiment, we used a mechanically sharpened, platinum-iridium tip (Pt 90%, Ir 10%).

3. Results and discussion

Figure 1 shows typical results of the studies of silver powder deposited on a carbon strip by means of SEM. Part (a) of the figure represents the view of the sample

at 300× magnification which stands for examining the area of 800×800 μm^2 surface. Around the examined area, one can notice the presence of objects of sizes within 200 μm to 300 μm. Those objects consist of tiny particles, as can be proved by SEM studies results gathered on one of the particles.

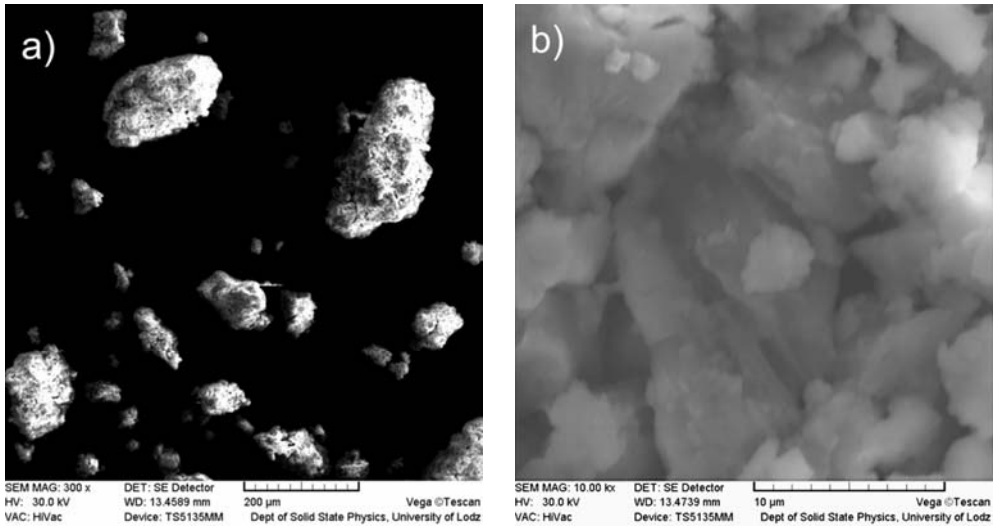

Fig. 1. SEM pictures of silver powder granulate deposited on a carbon strip: a) 300× magnification, b) 10 000× magnification. An example of strong aggregation of particles in the granulate, lack of visible nanoparticles

The above results are shown in Fig. 1b (25×25 μm^2 area, magnification 10 000×). It is easy to notice that the examined particles consist of a number of smaller objects of 0.5 μm to few micrometers in size. However, we did not manage to examine the structure of the observed nanoparticles because of difficulties connected with getting higher magnification. The problem was caused by washing out the details on SEM picture which appeared as a result of sample charging. The charging evidences low electric conductivity of the medium. It should be mentioned that the examined silver nanoparticles are surrounded by a nonconducting carbon stabilizer. In our opinion, the stabilizer is responsible for sample loading effects during the attempts of receiving a higher magnification. Another factor responsible for difficulties connected with getting higher magnification was high susceptibility of nanoparticles to aggregate into larger conglomerates. We should point here that, except for nanoparticle conglomerates, in silver powder there may appear stable grain of size ranging even to single micrometers. It is not unlikely that a part of the examined objects belongs to such categories.

In Figure 2, a standard EDX spectrum recorded on the examined sample is shown. In the middle part of the presented spectrum one can clearly see five peaks located between 2 kV and 4 kV. Those maxima are directly related to the silver characteristic lines K and L. The maximum located on the left part of the spectrum at 0.2 kV clearly

comes from carbon. The hardly visible maximum located at 0.5 keV is connected with the oxygen characteristic line. The carbon and oxygen spots in the examined samples confirm the presence of stabilizers composed of alkyl chains. The spectra obtained during EDX studies were used for carrying out the quantitative analysis. For that purpose, SEMQuant software and the ZAF procedure were applied. Quantitative analysis proved high silver contents (74%) in the examined samples. Except for silver, we also show the presence of coal and oxygen, the contents of which amounted to 21% and 5%, respectively.

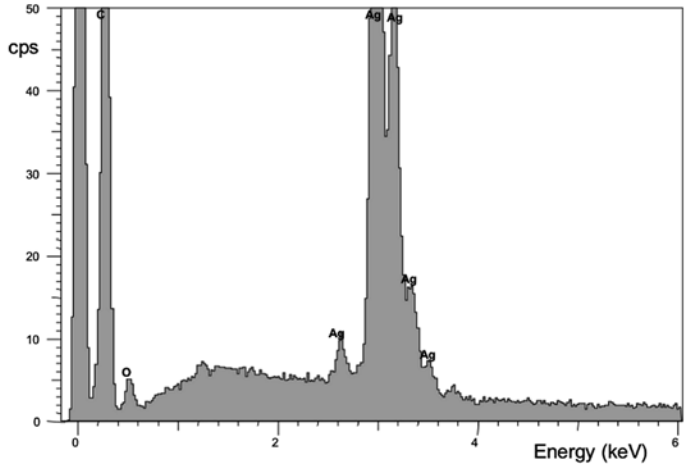

Fig. 2. EDX characteristic spectrum obtained for silver powder. Visible peaks confirm the presence of carbon and oxygen substances in the sample

Because of the failure of examining particles at high magnification with SEM, we decided to use microscope allowing picturing conducting surfaces with single nanometer resolution – STM. However, low conductivity of particles seemed to be an obstacle, which was indicated by SEM studies. But we should remember that STM can picture the areas and objects having relatively high resistances because of a high resistance of the tunnel junction. An additional argument for using STM was the relatively high silver contents in the examined samples, as well as their grained structure. In order to carry out STM studies, we had to use an additional preparing procedure by dissolving the powder in hexane.

The particles of nanometer size were separated and deposited on Au(111) surfaces, which was chosen as a surface for STM studies. In Figure 3a, a topographical 150×150 nm^2 STM picture of pure Au(111) just before deposition of particles is shown. In this picture, one can see large monoatomic flat area surfaces and a monoatomic 0.24 nm high step. Additionally, the height profile recorded along white arrow depicted in the figure is shown in the inset. Such topographic pictures are characteristic of pure gold and were recorded in various parts of Au(111) surfaces. After deposition of particles, we could also observe monoatomic flat terraces and 0.24 nm high

steps. But we also notice additional objects, not observed on pure gold. A typical topographical picture, obtained after deposition is shown in Fig. 3b. One can see that although thiol was not used as substance for binding nanopartilces to the gold surface [3], we managed to deposit firmly the sample.

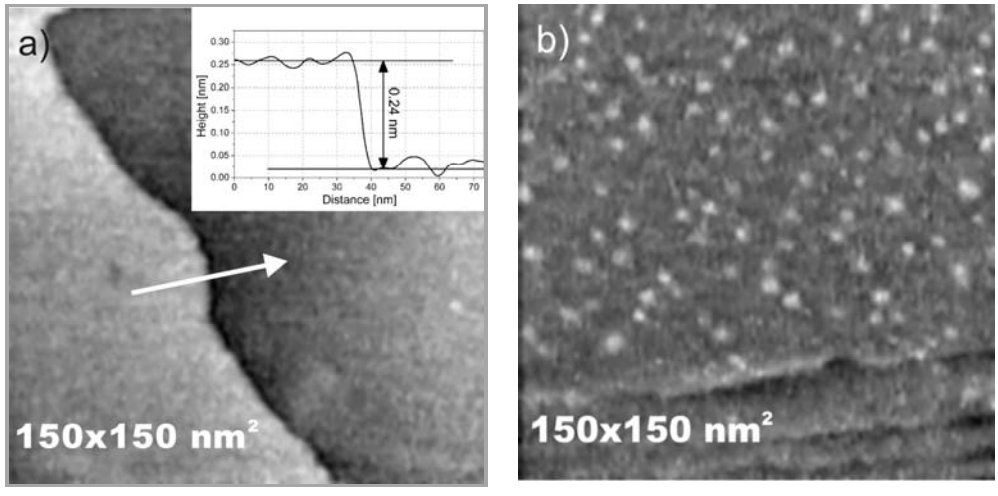

Fig. 3. The STM picture of Au(111) surface before (a) and (b) after silver nanoparticle deposition, the area of scanning –150×150 nm^2. Inset in Fig. 3a shows the height profile taken along an arrow depicted in the figure

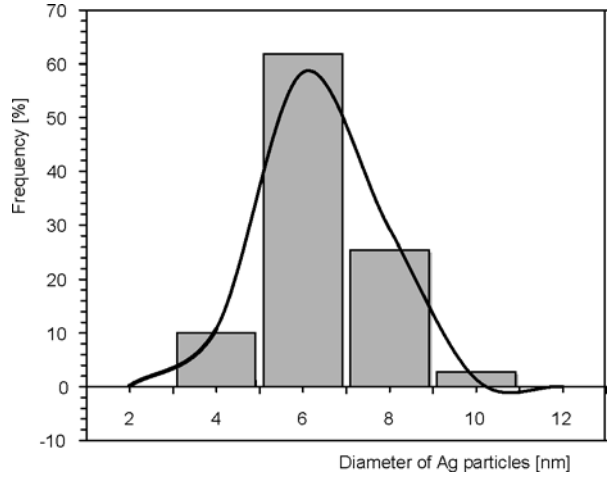

Fig. 4. The histogram of silver nanoparticles sizes obtained by means of the STM results

A sample prepared in this way exhibited stability during the studies in air and lack of coagulation processes. Observation of immobile single nanoparticles enabled the analyses of their size distributions. The obtained histogram (Fig. 4) confirms the fact

that for 100 observed nanoparticles – distribution of their sizes is a narrow normal one with a 6.4 nm average value and a 1.4 nm standard deviation. The theoretical curve of standard distribution fitted to the results of our studies (Fig. 4) was calculated by means of MS Excel program. The nanoparticle sizes calculated by us are comparable with the results of similar studies conducted with other measurement techniques [14, 15].

4. Conclusions

The obtained results of SEM and EDX studies confirm the fact that silver powder consists of micrometrical conglomerates which contain large amounts of silver (about 74%). During the studies, we have managed to separate single nanoparticles from the powder and deposit them on Au(111) surface without using thiol molecules. The results of STM studies demonstrated that the colloid created specially for these studies contained nanometrical particles and the nanoparticle silver analysis has shown that spread of sizes is a subject of normal distribution with a 6.4 nm average value and a 1.4 nm standard deviation

References

[1] ELECHIGUERRA J.L., BURT J.L., MORONES J.R., CAMACHO-BRAGADO A., GAO X., LARA H.H., YACAMAN M.J., J. Bionanotechnol., 3 (2005), 6.
[2] JAIN P., PRADEEP T., Biotechnol. Bioeng., 90 (2005), 59.
[3] STEPANOV A.L., POPOK V.N., KHAIBULLIN I.B., KREIBIG U., Nucl. Instr. Meth. B. 191 (2002), 473.
[4] MURPHY C.J., SAU T.K., GOLE A.M., ORENDORFF C.J., GAO J., GOU L., HUNYADI S.E., LI T., J. Phys. Chem. B., 109 (2005), 13857.
[5] LI Y., WU Y., ONG B.S., J. Am. Chem. Soc., 127 (2005), 3266.
[6] TENG K.F., VEST R.W., IEEE Trans. Comp. Hybrids Manu. Tech., 11 (1988), 291.
[7] Metal Powder Rep., 59 (2004), 14.
[8] DEARDEN A.L., SMITH P.J., SHIN D.Y., REIS N., DERBY B., O'BRIEN P., Macromol. Chem. Rapid Commun., 26 (2005), 315.
[9] NAGASAWA H., MARUYAMA M., KOMATSU T., ISODA S., KOBAYASHI T., Phys. Stat. Sol. (a), 191 (2002), 67.
[10] ALT V., BECHERT T., STEINRÜCKE P., WAGENER M., SEIDEL P., DINGELDEIN E., DOMANN E., SCHNETTLER R., Biomater., 25 (2004), 4383.
[11] ABE K., HANADA T., YOSHIDA Y., TANIGAKI N., TAKIGUCHI H., NAGASAWA H., NAKAMOTO M., YAMAGUCHI T., YASE K., Thin Solid Films, 327–329 (1998), 524.
[12] KLUSEK Z., OLEJNICZAK W., PAWLOWSKI S., KOBIERSKI P., Electron Technol., 31 (1998), 508.
[13] TALEB A., GUSEV A.O., SILLY F., CHARRA F., PILENI M.P., Appl. Surf. Sci., 162–163 (2000), 553.
[14] XU J., HAN X., LIU H., HU Y., Colloids and Surfaces A: Physicochem. Eng. Aspects, 273 (2006), 179.
[15] RONG M., ZHANG M., LIU H., ZENG H., Polymer, 40 (1999), 6169.

Received 7 May 2006
Revised 1 September 2006

Materials Science-Poland, Vol. 25, No. 2, 2007

Phase diagrams and properties of the ground state of the anisotropic Kondo lattice model

M. SIDOWSKI*, S. ROBASZKIEWICZ

Division of Electronic States of Solids, Institute of Physics Adam Mickiewicz University, ul. Umultowska 85, 61-614 Poznań

The properties of the half-filled Kondo lattice model with anisotropic intersubsystem exchange interaction J_{XY} and J_Z are discussed. The phase diagram and ground state characteristics of the system are determined within a variational mean-field approximation for the case of rectangular density of states (DOS) for itinerant electrons. The ground state phase diagram is found to exhibit five different phases: Kondo singlet state, two planar antiferromagnetic phases, and two Ising antiferromagnetic (Néel) phases.

Key words: *Kondo lattice; exchange interaction; phase diagram*

1. Introduction

The Kondo lattice model (KLM) is one of the most common models for heavy fermion materials, Kondo insulators and also for manganites (in its ferromagnetic version). In the model, charge fluctuations for localized electrons are suppressed, which leads to a coupled electron–spin system. Crucial for physics of this system is a strong competition between demagnetization resulting from the Kondo effect and magnetism, which tends to yield magnetic orderings. Up to now, most of the studies of this model focused on the case of isotropic exchange interaction [1–6].

In this paper, we present some of our results concerning the case of the Kondo lattice model (KLM) with anisotropic exchange couplings J_{XY} and J_Z. The model is defined by the following Hamiltonian:

$$H = \sum_{\langle ij\rangle\sigma} t_{ij} c_{i\sigma}^{+} c_{j\sigma} + \sum_i J_Z S_i^z \sigma_i^z + \frac{1}{2} J_{XY} \left(S_i^+ \sigma_i^- + S_i^- \sigma_i^+ \right) \tag{1}$$

*Corresponding author, e-mail: masi@amu.edu.pl

where S_i^α and σ_i^α are the spin operators for localized *d* electrons at *i*th site and those for itinerant *c* electrons, respectively:

$$S_i^\mu = \frac{1}{2}\sum_{\sigma\sigma'} d_{i\sigma}^+ \tau_{\sigma\sigma'}^\mu d_{i\sigma'}, \qquad \sigma_i^\mu = \frac{1}{2}\sum_{\sigma\sigma'} c_{i\sigma}^+ \tau_{\sigma\sigma'}^\mu c_{i\sigma'}$$

with the Pauli matrices $\tau_{\sigma\sigma'}^\mu$, and with a local constraint $d_{i\uparrow}^+ d_{i\uparrow} + d_{i\downarrow}^+ d_{i\downarrow} = 1$, such that every d orbital is always occupied by just one electron. The bandwidth parameter *D* of c electron band is defined by $2D = 2zt$, where *z* is the number of nearest neighbours (nn).

We performed a detailed analysis of the phase diagrams and thermodynamic properties of model (1) for *d*-dimensional hypercubic lattices and arbitrary, positive and negative J_{XY} and J_Z [7]. In the analysis, we used an extended mean-field approximation (MFA-HFA), analogous to that used in the treatment of the isotropic Kondo lattice model [2, 4]. Below, we only quote the main results of this investigation, concentrating on the case of a half-filled electron band. We restrict our analysis to the pure phases and assume rectangular density of states (DOS) for c electron band.

Considered phases are characterised by the following order parameters:

- planar antiferromagnetic (AF_{XY})

$$\sigma_Q^{XY} \neq 0, \qquad S_Q^{XY} \neq 0$$

where

$$\sigma_Q^{XY} = \frac{1}{2N}\sum_i \left\langle \sigma_{ic}^+ \right\rangle e^{-iQR_i}, \qquad S_Q^{XY} = \frac{1}{2N}\sum_i \left\langle S_{id}^+ \right\rangle e^{-iQR_i}$$

$$\sigma_{ic}^+ = c_{i\uparrow}^+ c_{i\downarrow}, \qquad S_{id}^+ = d_{i\uparrow}^+ d_{i\downarrow}, \qquad \vec{Q} = \left(\frac{\pi}{a}, \frac{\pi}{a}, \frac{\pi}{a}\right)$$

- uniaxial AF state (AF_Z)

$$\sigma_Q^z \neq 0, \qquad S_Q^z \neq 0$$

where

$$\sigma_Q^z = \frac{1}{N}\sum_i \left\langle 2\sigma_{ic}^z \right\rangle e^{-iQR_i}, \qquad S_Q^z = \frac{1}{N}\sum_i \left\langle 2S_{id}^z \right\rangle e^{-iQR_i}$$

- Kondo state (K)

$$\lambda = \frac{1}{2N}\sum_i \left(\left\langle d_{i\sigma}^+ c_{i\sigma} \right\rangle + hc \right) = \frac{1}{2N}\sum_k \left(\left\langle d_{k\sigma}^+ c_{k\sigma} \right\rangle + hc \right)$$

2. Results and discussion

The ground state phase diagram of the considered model calculated for rectangular density of states (DOS) is shown in Fig. 1. In the next two figures, the plots of the order parameters and the quasi-particle gaps in the excitation spectrum as a function of increasing interactions are presented: in Fig. 2 as a function of $J_{XY}/2D$ for $J_Z = 0$, whereas Fig. 3 as a function of $J_Z/2D$ for $J_{XY}/2D = 0.14$.

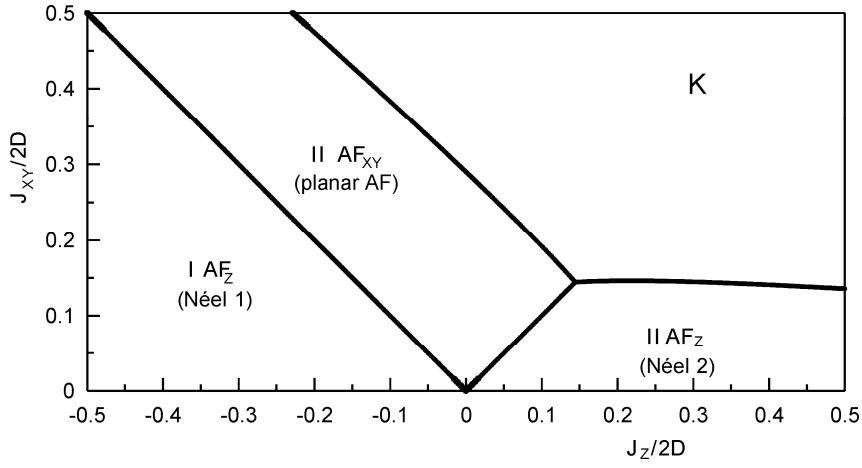

Fig. 1. Ground state phase diagram of the anisotropic Kondo lattice model at half-filling, plotted as a function of $J_{XY}/2D$ and $J_Z/2D$, for rectangular DOS

The diagram in Fig. 1 has been derived for $J_{XY} \geq 0$ and consists of four phases: K Kondo singlet state, I AF_Z Néel 1 (Ising AF with parallel sublattice uniaxial magnetizations of spins and electrons), II AF_Z Néel 2 (Ising AF with antiparallel sublattice magnetizations) and II AF_{XY} (planar AF with antiparallel sublattice *XY* magnetization).

For $J_{XY} \leq 0$ the diagram has the same form with the replacement of II AF_{XY} by I AF_{XY} (planar antiferromagnet with parallel sublattice *XY* magnetizations of spins and electrons).

Let us shortly point out the main conclusions:

- For small values of JXY/2D and JZ/2D the ground states are AFXY, if |JXY|>|JZ| and AFZ if |JXY|<|JZ|, for both signs of JXY and JZ.
- For |JXY|>|JZ| with increasing |JXY|/2D the system exhibits a transition from AFXY to Kondo state at (|JXY|/2D)c. The value (|JXY|/2D)c depends on the strength of JZ: JZ > 0 reduces this critical value, whereas JZ < 0 enhances it (cf. Fig. 1).
- For 0 < |JXY|<|JZ|, the system remains in the I AFZ state for any |JZ|/2D, if JZ < 0, whereas for JZ > 0 the increase of |JZ|/2D yields a transition II AFZ → K, at the critical value (|JXY|/2D)c which slowly decreases with increasing JZ/2D (cf. Fig. 1).

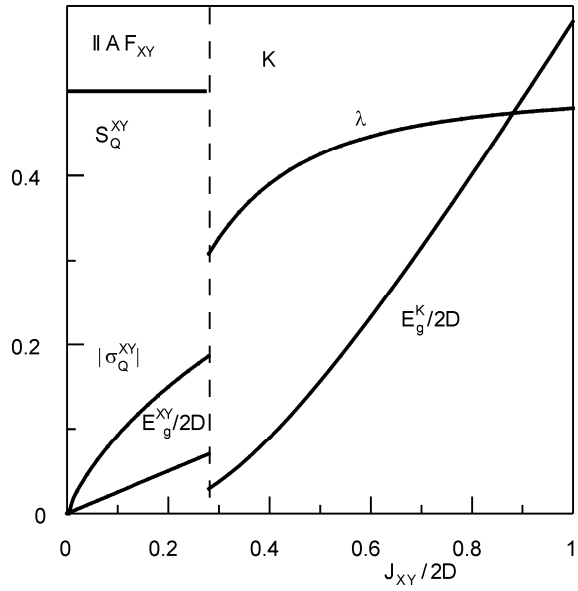

Fig. 2. Variation of the II AF_{XY} and Kondo (K) order parameters and the quasiparticle gap at $T = 0$ as a function of $J_{XY}/2D$ for $J_Z = 0$

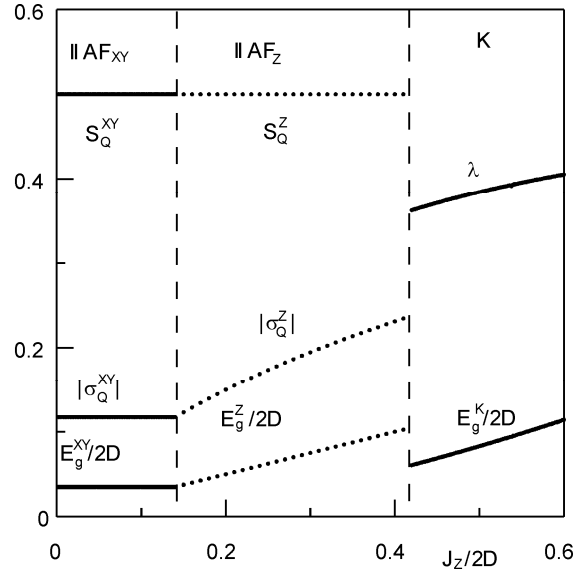

Fig. 3. Variation of the II AF_{XY}, II AF_Z and Kondo (K) order parameters and the quasiparticle gap at $T = 0$ as a function of $J_Z/2D$ for $J_{XY}/2D = 0.14$

• In the considered case of half filled electron band at $T = 0$ all phases are nonmetallic, with the quasi-particle gaps: $E_g = |J_Z S_Q^z|$, for AF_Z states, $E_g = |J_{XY} S_Q^{XY}|$, for

AF_{XY} states and $E_g = \sqrt{D^2 + X^2} - D$, where $X = (2J_{XY} + J_Z)\lambda$, for K state. Notice a sharp decrease of the gap at the transitions from AF_{XY} and AF_Z to Kondo state (cf. Figs. 2 and 3).

• With increasing $J_Z/2D$ ($-\infty < J_Z/2D < \infty$) for fixed $J_{XY}/2D > 0$ one can observe the following sequences of transitions (cf. Figs. 1, 3):

$$\text{I } AF_Z \to AF_{XY} \to \text{II } AF_Z \to \text{K}, \quad \text{if} \quad |J_{XY}|2D < (J_{XY}/2D)_0$$

$$\text{I } AF_Z \to AF_{XY} \to \text{K}, \quad \text{if} \quad |J_{XY}|/2D > (J_{XY}/2D)_0,$$

where $(J_{XY}/2D)_0 \approx 0.145$ for a rectangular DOS.

Our present studies of model (1) concentrate on the effects of external magnetic field and take into consideration mixed ordered phases.

Acknowledgements

We thank R. Micnas for helpful discussion. This work was supported in part by the Polish State Committee for Scientific Research (KBN), Grant No. 1 P03B 084 26.

References

[1] ZHENG W., OITMAA J., Phys. Rev. B 67, 214406 (2003).
[2] RUPPENTHAL A.R., IGLESIAS J.R., , GUSMÃO M.A., Phys. Rev. B 60, 7321 (1999).
[3] GULÁCSI M., Advances in Physics 53, 769 (2004).
[4] BEACH K.S.D., LEE P.A., , MONTHOUX P., Phys. Rev. Lett. 92, 026401 (2004).
[5] ASSAAD F.F., Phys. Rev. B 70, 020402 (2004).
[6] DAGOTTO E. YUNOKI S., MALVEZZI A.L., MOREO A., HU J., CAPPONI S., POLIBLANC D., FURUKAWA N., Phys. Rev. B 58, 6414 (1998).
[7] SIDOWSKI M., ROBASZKIEWICZ S., in preparation.

Received 7 May 2006
Revised 1 September 2006

Materials Science-Poland, Vol. 25, No. 2, 2007

Properties of extended Hubbard models with anisotropic spin-exchange interaction

W. R. CZART*, S. ROBASZKIEWICZ

Division of Electronic States of Solids, Institute of Physics, Adam Mickiewicz University, ul. Umultowska 85, 61-614 Poznań, Poland

The phase diagrams and electron orderings of the half-filled extended Hubbard models with anisotropic spin-exchange interactions ($J_\perp$, $J_{||}$) are studied. The cases of ferromagnetic ($J_\alpha < 0$) and antiferromagnetic ($J_\alpha > 0$) exchange couplings are considered for repulsive on-site interaction ($U \geq 0$). The analysis of these t–U–$J_{||}$–$J_\perp$ models is performed for d-dimensional hypercubic lattices including $d = 1$ and $d = \infty$ by means of the (broken symmetry) HFA supplemented, for $d = \infty$, by the slave-boson mean-field method. The basic features of the derived phase diagrams are discussed.

Key words: *phase diagram; Hubbard model; anisotropic spin exchange*

1. Introduction

The extended Hubbard model with anisotropic spin exchange interactions is a conceptually simple phenomenological model for studying correlations and for description of magnetism and other types of electron orderings in narrow band systems with easy-plane or easy-axis magnetic anisotropy.

The model Hamiltonian is of the form:

$$H = -\sum_{i,j,\sigma} t_{ij} c_{i\sigma}^{+} c_{j\sigma} + U \sum_{i,j,\sigma} n_{i\uparrow} n_{i\downarrow} + (1/2) {\sum_{i,j}}' J_\perp \left(\sigma_i^{+} \sigma_j^{-} + hc \right) + \sum_{i,j}{}' J_\parallel \sigma_i^z \sigma_j^z \qquad (1)$$

where t is the single electron hopping integral, U is the on-site density interaction, $J_\perp$ and $J_\parallel$ are XY and Z components of intersite magnetic exchange interaction, respectively, μ is the chemical potential, and Σ' restricts the summation to nearest neighbours (nn). The spin operators $\{\vec{\sigma}_i\}$ are defined by $\sigma_i^z = (1/2)(n_{i\uparrow} - n_{i\downarrow})$, $\sigma_i^{+} = c_{i\uparrow}^{+} c_{i\downarrow} = (\sigma_i^{-})^{+}$.

*Corresponding author, e-mail: czart@amu.edu.pl

For strong on-site repulsion and isotropic antiferromagnetic exchange ($J_{||} = J_{\perp} = J > 0$) the model (1) was extensively studied in the context of high T_c superconductivity (HTS). Recently, such a model with transverse (*XY*-type) anisotropic exchange has been proposed by Japaridze et al. [1] as a suitable approach for description of narrow band systems with easy-plane magnetic anisotropy. In particular, the authors studied the weak-coupling ground-state phase diagram of the one-dimensional t–U–$J_{\perp}$ model at half filling ($n = 1$) using the continuum-limit (infinite band) field theory approach [1] as well as (for $U > 0$) the density-matrix renormalization group (DMRG) method [2].

The purpose of our research is an extension of those studies and discussion of the properties of the t–U–$J_{\perp}$–$J_{||}$ model in arbitrary dimension ($1 \le d \le \infty$), both at $T = 0$ and $T > 0$.We performed a detailed analysis of the phase diagrams and thermodynamic properties of this model for d-dimensional hypercubic lattices [3]. Preliminary results for the case $J_{\|} = 0$, and $2 \le d \le \infty$ have been given in [4].

In the analysis, we have used the (broken symmetry) HFA supplemented for $d = \infty$ by the spin and charge rotationally invariant slave boson mean-field approach (SBMFA), analogous to that applied previously for the attractive Hubbard model [5] and the Penson–Kolb–Hubbard model [6]. In the following, we shortly summarize the results of our investigation of the model (1) obtained for $1 \le d \le \infty$ lattices in the case of exchange interactions $J_{\|}$, $J_{\perp}$ of either sign and $U \ge 0$, and discuss basic features of the derived phase diagrams.

2. Summary of the results

In Figures 1–3 we show representative ground state diagrams of the model (1) at half-filling and $U \ge 0$ derived for lattice structures of various dimensions, including $d = 1$, $d = 2$ and $d = \infty$. Figures 1 are plotted for $J_{\perp} \neq 0$, $J_{\|} = 0$, Figs. 2 – for $J_{\|} \neq 0$, $J_{\perp} = 0$ and Fig. 3 for $J_{||} = J_{\perp} = J$.

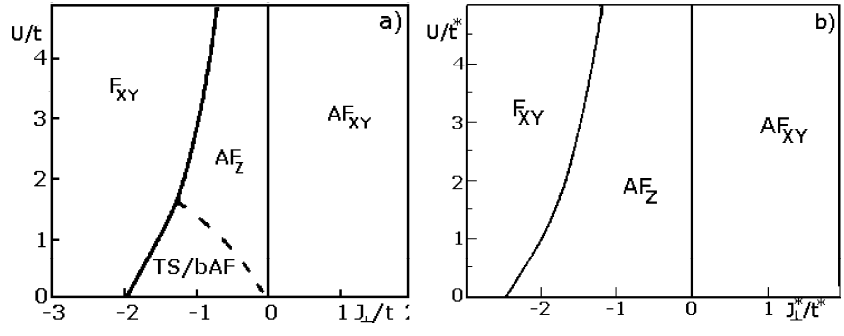

Fig. 1. Ground state phase diagrams of the half-filled t–U–$J_{\perp}$ ($J_{\|} = 0$) model: a) for the 1 D chain, b) for $d = \infty$ hypercubic lattice, determined within the broken symmetry HFA. The SBMFA phase diagram for $d = \infty$ is almost identical to (b). In 1Fig. b: $t^* = td^{1/2}$, $J_{\perp}^* = J_{\perp}d$

For $d = \infty$ the diagrams involve exclusively site-located magnetic orderings (cf. Fig. 1b): uniaxial ferromagnetic (F_Z) phase, with $x_{F_Z} = (1/N)\sum_i \langle \sigma_i^Z \rangle \neq 0$, and antiferromagnetic (AF_Z) one, with $x_{AF_Z} = (1/N)\sum_i \langle \sigma_i^Z \rangle e^{i\vec{Q}\cdot\vec{R}_i} \neq 0$, as well as the planar ferromagnetic (F_{XY}) phase, with $x_{F_{XY}} = (1/N)\sum_i \langle \sigma_i^+ \rangle \neq 0$, and antiferromagnetic (AF_{XY}) one, with $x_{AF_{XY}} = (1/N)\sum_i \langle \sigma_i^+ \rangle e^{i\vec{Q}\cdot\vec{R}_i} \neq 0$. It is shown in Fig. 1b plotted for the case of $J_\perp \neq 0$, $J_\parallel = 0$.The diagram for $J_\parallel \neq 0$, $J_\perp = 0$ has exactly the same form as Fig. 1b if one makes the replacements: $J_\perp \rightarrow J_{||}$, $F_{XY} \rightarrow F_Z$, $AF_Z \rightarrow AF_{XY}$ and $AF_{XY} \rightarrow AF_Z$. The phase diagrams for $d = \infty$ determined within SBMFA are almost identical to those obtained in HFA, although the values of the order parameters and the energy gaps in various phases can be substantially reduced by the correlation effects.

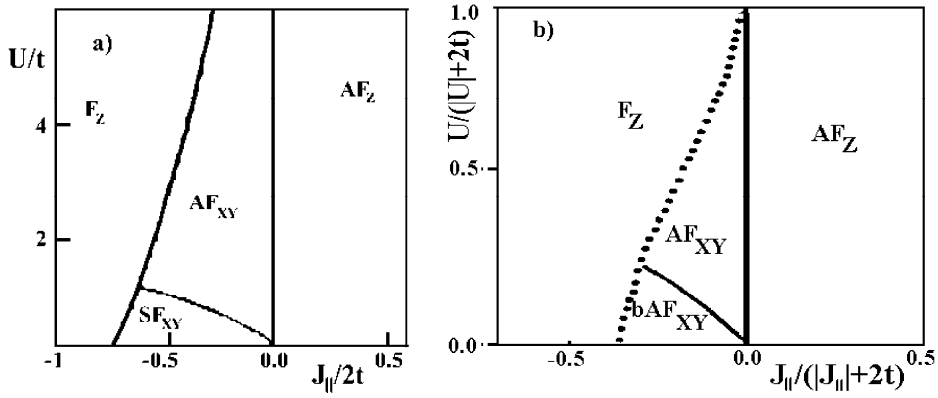

Fig. 2. Ground state phase diagrams of the half-filled t–U–$J_{||}$ ($J_\perp = 0$) model (a) for the d = 2SQ lattice determined within the (broken symmetry) HFA, and (b) for the 1D chain, obtained numerically, using level-crossing approach for finite-size clusters (L = 12)

For $d \leq 3$, the model can also exhibit various bond-located orderings. In the considered case of repulsive U, they are realized for ferromagnetic exchange interactions ($J_\alpha < 0$) in the weak/intermediate coupling regimes: in the case of t–U–$J_\perp$ model ($J_\parallel = 0$) this is the triplet superconductivity (TS) order for $d = 1$ (Fig. 1a), whereas for the t–U–$J_{||}$ model ($J_\perp = 0$) the bond AF_{XY} order (bAF_{XY}) for $d = 1$ (Fig. 2b) and the spin-flux (spin nematic) order (SF_{XY}) for $d = 2$ (Fig. 2a). The phase diagram of t–U–$J_{||}$ model for $d = 1$ shown in Fig. 2b has been obtained numerically using the level crossing approach for finite-size clusters, analogous to that applied previously for the Hubbard model with intersite Coulomb interaction by Nakamura [7]. The corresponding HFA diagram has a very similar form, except that close to the boundary line separating the AF_{XY} and bAF_{XY} states one finds a narrow regime of the mixed ordered phase: AF_{XY}+bAF_{XY}.

In any dimension, for anisotropic exchange interactions the transition at $T = 0$ to the ferromagnetic phases (F_{XY} and F_Z) is of the first order (except of $U = 0$ for $d = \infty$) and occurs only above some critical values of $|J_\alpha|/D$ ($J_\alpha < 0$, $\alpha = \perp, \|$) which for large U decrease with increasing U (Figs. 1–3). This is in obvious contrast with the properties of the antiferromagnetic phases (AF_{XY} and AF_Z), which at $T = 0$ and $U \geq 0$ are stable for any $J_\alpha > 0$ and exhibit smooth crossovers from the weak coupling limit to the local magnetic moment regime with increasing $J_\alpha > 0$.

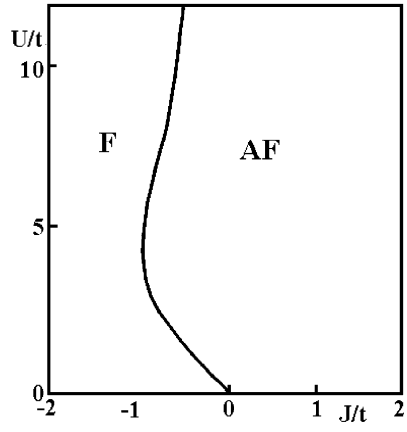

Fig. 3. Ground state diagram of the t–U–J model ($J = J_\perp = J_\|$) at half filling for $d = 2$ SQ lattice calculated within (broken symmetry) HFA. The line denotes first-order phase boundary

In Figure 4, we present the plots of order parameters with increasing $|J_\||$ at $T = 0$ for F_Z and AF_Z phases of the t–$J_\|$ model ($U = 0$) in $d = \infty$.

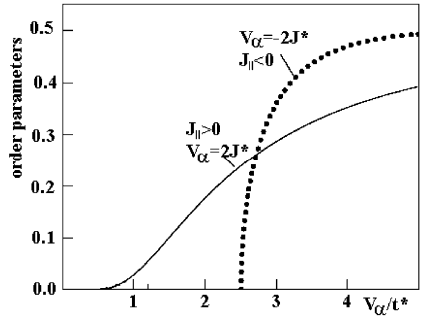

Fig. 4. The order parameters x_α at $T = 0$ as a function of the coupling parameters V_α for AF_Z phase of the t–$J_\| > 0$ model (solid curve, $V_\alpha = 2J^*$) as well as for the F_Z phase of the t–$J_\| < 0$ model (dotted curve, $V_\alpha = -2J^*$), calculated for the $d = \infty$ lattice ($J^* = J_\| d$, $t^* = td^{1/2}$, $J_\perp = 0$, $U = 0$)

Let us shortly summarize our findings concerning possible effects of anisotropic spin exchange interactions at half-filling.

(i) The XY spin exchange ($J_\perp$) can stabilize planar ferro- (antiferro) magnetic orderings with $x_{F_{XY}} \neq 0$ (for $J_\perp < 0$) and $x_{AF_{XY}} \neq 0$ (for $J_\perp > 0$), as well as the triplet superconductivity (TS), for $d = 1$ lattices in the weak/intermediate coupling regime and $J_\perp < 0$ (Fig. 1a), and the charge-flux (orbital AF) order for $d = 2$ lattices [3].

(ii) The longitudinal exchange ($J_{\|}$) favorize uniaxial ferro- (antiferro) magnetic orderings with $x_{F_Z} \neq 0$ (for $J_{\|} < 0$), x_{AF_Z} (for $J_{\|} > 0$), as well as the bond AF_{XY} order in the weak/intermediate coupling limit and $J_{\|} < 0$ for $d = 1$, and the spin-flux (spin nematic) order for $d = 2$ lattice (Figs. 2a, b and Fig. 4).

(iii) In the case of isotropic spin exchange ($J_{||} = J_{\perp} = J$) and $U = 0$ the stable phase at $T = 0$ is the isotropic AF (F) state, for any $J > 0$ ($J < 0$), whereas $U > 0$ favourizes the AF phase and makes this state stable also in a definite range of $J < 0$ (cf. Fig. 3).

The problems studied are of relevance for various classes of narrow band magnetic materials including the transition metal and rare earth compounds, where the effects of exchange anisotropy can be important. Possible applications of the model considered include also unconventional superconductors showing close proximity of magnetic and superconducting orderings (see [1, 2] and references therein), e.g. (i) $(TMTSF)_2$ X family of organic materials (the Bechgaard salts), (ii) UGe_2, URhGe and $ZrZn_2$ (coexistence of TS with magnetic orderings), (iii) the ruthenate compounds: Sr_2RuO_4 (TS), $SrRuO_3$ (F), $SrRuYO_6$ (AF). Let us also mention the experimentally observed easy plane anisotropy of the spin exchange in Sr_2RuO_4.

Acknowledgements

We thank R. Micnas for helpful discussion. This work was supported in part by the Polish State Committee for Scientific Research (KBN), Grant No: 1 P03B 084 26; 2004-2006, and by the Foundation for Polish Science.

References

[1] JAPARIDZE G.I., MULLER-HARTMANN E., Phys. Rev. B, 61 (2000), 9019.
[2] DZIURZIK C., JAPARIDZE G.I., SCHADSCHNEIDER A., ZITTARTZ J., Eur. Phys. J. B, 37 (2004), 453.
[3] CZART W., ROBASZKIEWICZ S., in preparation.
[4] CZART W., ROBASZKIEWICZ S., Phys. Stat. Sol. (b), 243 (2006), 151.
[5] BUŁKA B., ROBASZKIEWICZ S., Phys. Rev. B, 54 (1996), 13138.
[6] ROBASZKIEWICZ S., BUŁKA B., Phys. Rev. B, 59 (1999), 6430.
[7] NAKAMURA M., Phys. Rev. B, 61 (2000), 16377; J. Phys. Soc. Jpn., 68 (1999), 3123.

Received 7 May 2006
Revised 1 September 2006

Materials Science-Poland, *Vol. 25, No. 2, 2007*

Fracton oscillations in the net fractals

Z. BĄK*

Institute of Physics, Jan Długosz University of Częstochowa,
al. Armii Krajowej 13/15, 42-201 Częstochowa, Poland

Assuming that the force constants scale as $\sigma(\lambda x) = \lambda^{-\alpha}\sigma(x)$, we construct the model of elastic (linear) excitations on a fractal (fractons). We show that the fractons, a specific class of fractals, "net fractals", can be assumed as the log-scale phonons. Further, we discuss propagation of elastic medium perturbation in terms of fractional dynamics. Within this approach we find two different modes of vibrations, both expressed with the help of generalized Mittag–Leffler functions.

Key words: *fractals; fractons; fractional dynamics*

1. Introduction

The concept of fractal has become a powerful tool in analysis of common aspects of many complex processes observed in physics, biology, chemistry or earth sciences. Brownian motion, turbulence, colloid aggregation or biological pattern formation can be fully understood only when the idea of self-similarity of fractal structures is applied [1]. The hallmark of fractality is a hierarchical organization of its elements, described by discrete scaling laws, which makes the fractal, regardless of the magnification or contraction scale, look the same. This property of fractals is called self-similarity, self-affinity or self-replicability. Although physical systems modelled by fractals are non-translation invariant, it is a well known fact that the self-similar fractals, as well as the physical quantities on fractal systems, show log-periodicities [1]. This opens the possibility to describe the symmetries of self-similar fractals in the way that is reminiscent of conventional formalism developed for crystalline systems. Motivated by this fact, we present a study of fractal excitations (fractons), which is similar in spirit to the phonon approach in the solid state theory.

A self-similar symmetry of a fractal is a transformation that leaves the system invariant, in the sense that taken as a whole it looks the same after transformation as it

*E-mail: z.bak@ajd.czest.pl

did before, although individual points of the pattern may be moved by the transformation. We say that $\mathbf{K} \subset \mathbf{R}^n$ satisfies the scaling law **S**, or is a self-similar fractal, if $\mathbf{S}:\mathbf{K} = \mathbf{K}$. Let us limit our considerations to fractals in which the self-similarity can be realized only via linear maps, i.e., transformations which point $\mathbf{r} = (x_1, x_2, x_3) \in \mathbf{K} \subset \mathbf{R}^3$ transform into point $\mathbf{r}' = (x_1' x_2', x_3')$ according to the formula $x_i' = S_{i1} x_1 + S_{i2} x_2 + S_{i3} x_3$; where $i = 1, 2, 3$. The vector form of the linear self-similar transformation can be written as $\mathbf{r}' = \mathbf{S}:\mathbf{r}$, where **S** is the matrix of the linear self-similar transformation. If we orient coordinate axes along the eigenvectors of the matrix **S** (i.e., $\mathbf{x} = (x_1, x_2, x_3) \rightarrow (\varepsilon, \eta, \rho)$), then the linear self-similar mapping reduces to the transformation $\mathbf{S}$: $(\varepsilon, \eta, \rho) \rightarrow (\lambda_1\varepsilon, \lambda_2\eta, \lambda_3\rho)$. In the case of infinite-size fractals, also the inverse $\mathbf{S}^{-1}$ mapping fulfils the self-similarity conditions $\mathbf{S}^{-1}:\mathbf{K} = \mathbf{K}$ and for any $\mathbf{x} \in \mathbf{K}$, we have

$$\mathbf{S}^{-1} : \mathbf{x} = \mathbf{S}_1^{-1} \cdot \mathbf{S}_2^{-1} \cdot \mathbf{S}_3^{-1} : \mathbf{x} = \left(\lambda_1^{-1}\varepsilon, \lambda_2^{-1}\eta, \lambda_3^{-1}\rho \right) \tag{1}$$

Consider a more general transformation of the type $S^{(m,n,l)} = (S_1)^n \cdot (S_2)^m \cdot (S_3)^l$, where $(S_i)^n$ denotes n-tuple superposition of transformation S_i and define a class of infinite "net fractals" G_{nf}, for which the relation $S^{(m,n,l)}:G_{nf} = G_{nf}$ is valid. Action of $S^{(m,n,l)}$ transforms any point $x \in \mathbf{R}^3$ according to the formula $S^{(m,n,l)}:x = (\lambda_1^{-1}\varepsilon, \lambda_2^{-1}\eta, \lambda_3^{-1}\rho)$, where m, n, l are arbitrary (negative or positive) integers. In view of this relation, we have that $S^{(m,n,l)}:G_{nf} \subset G_{nf}$, i.e. $S^{(m,n,l)}$ are the injective scaling mappings. For any linear S_1 and $F_1 \subset \mathbf{R}$ by definition we have $S_1:F_1 = F_1$ and for any $x_0 \in F_1$ we have $S_1: x_0 = \lambda_1 x_0$, consequently $(S_1)^m: x_0 = \lambda_1{}^m: x_0$. Using the logarithmic scale we have $\log(x_m/x_0) = m\ln\lambda_1 (m = \pm 1, \pm 2\ldots)$. This is nothing but a 1 D crystal lattice with the lattice spacing given by $a_1 = \ln\lambda_1$. Using the multi-logarithmic scale, we can see that the family of mappings $S^{(m,n,l)}$ is isomorphic with a 3D crystal lattice. This means that the isomorphism $S^{(m,n,l)} \leftrightarrow (ma_1, na_2, la_3)$ holds, the same refers to the placement of its characteristic building blocks. The purpose of this paper is to study the vibrations in a system deformable over fractal subset.

2. Fractons

Most theoretical studies of the vibrations of a fractal limit to considerations at universal level without referring the specific physical model. In our study, we focus on a specific model which, we believe, describes behaviour of some real systems. Consider a "net fractal" cluster as defined above, consisting of N atoms with unit mass and linear springs connecting nearest-neighbour sites. The equations of motion of the atoms are [2]:

$$\ddot{u}_n(t) + \sum_m k_{n,m} u_n(t) = 0 \tag{2}$$

where the sum goes over all nearest neighbour sites of the fractal site n. When trying to work with Eq. (2), one meets two problems: first, elastic constants $k_{m,n}$ and mass

distribution depend on coordinates, and secondly, it is associated with the ambiguities in the definitions of the local displacements u_n. The local strain **e** ($\mathbf{e} \propto \nabla \mathbf{u}(r,t)$) and local displacements on the fractal system can be defined in two ways. One of the definitions refers to the internal geometry and microscopic interactions, while the other defines the strain directly in terms of the effect of deformations on the (suitably averaged) mass distribution. Since we are interested in the study of fractal acoustics, we should use the latter definition which is directly relevant to the experiment. As was pointed out by Alexander [2], in this case the vibrational displacements are the vectors in the embedding space and are not restricted by the internal geometry of the fractal. Let us now discuss the non-homogeneities of mass and force constants. Since, due to rapid fluctuations, on a short length scales the strains and density can be defined only as the scale dependent local averages [2], we can assume that fractal of the size r has, on the average a mass $m(r) = m_0(r/a)^d$, where d is the fractal mass dimension. It is natural to assume that the self-similarity of the fractal is reflected also in the dilation symmetry. Assuming that ω is the eigenfrequency of the fracton oscillations, we can find that the force constants k_i scale as $k_i = m_k\omega_k^2 \propto (r/a)^d \omega_\kappa^2$. In view of the latter relation, from here on, we assume that the forces which tend to restore the equilibrium positions of species, are linear (as regards to the coordinates of the excited fractal system). However, contrary to the conventional solid elastic constants, they are not homogenous and depend on coordinates.

Let us assume that elastic forces follow the common power law scaling with the separation [2]. As we have shown above, when presented in the logarithmic coordinates, the mass density of such a fractal becomes uniform, the same refers to the elastic constants. Suppose the fractal is perturbed locally (e.g., in the vicinity of the equilibrium position x_0, with the energy ε_0 and consider the amplitude of this excitation. In real space, the amplitude of local fluctuation has the form $u_n = |x_{0n} - \mathrm{x}_n|$, while in the log coordinates we have $\zeta_n = |\xi_n^0 - \xi_n|$, where $\zeta_n = \ln x_n$. Consider first a somewhat unrealistic case when there are no broken bonds in the log-scale picture. In this case (in the log scale) we have a homogeneous system with uniform mass and elastic constant distribution. Under above conditions, application of the continuous medium approximation is justified. Thus, when perturbed the log coordinates ζ_n and the local displacement $\zeta_n(x,t)$ should satisfy the classical wave equation $\nabla^2\zeta - (1/c^2)(\partial^2\zeta/\partial t^2) = 0$ with the plane wave solution $\zeta_i = \zeta_i^0 \exp(ik_i\zeta_i - i\omega t) = \zeta_i^0(x_i)^{ik}{}_i \exp i\omega t$, when the relation $\zeta_n = \ln x_n$ is taken into account. As we can see from above, the fracton appears to be the log-scale phonon. When transformed to the physical space, the log-scale phonon solution displays power law scaling with purely imaginary scaling exponent. The extensive discussion of the systems with complex scaling factors was given by Sornette [3], who proved that this type of scaling results in log-periodic oscillations of physical quantities. In classical physics, the Huygens principle says that any point of an isotropic medium reached by a travelling wave is the source of an outcoming spherical wave. By analogy to the Huygens principle, we assume that the fractal excitation can excite neighbouring fractal cluster provided that there is some contact between them.

This means that wave propagation in a fractal, granular medium is associated with chaotic trajectories, which travel over chaotically distributed fractal clusters. There is no straight lanes which characterize sound propagation in conventional physics. The dead ends with no connection to the neighbouring fractal clusters play the role of temporary traps which slow down the propagation. This is nothing but the picture of continuous random walks (CTRW). Such scenario indicates that the model of space-time fractional diffusion can be applied in description of wave propagation [5] . Within this approach, the generalized wave equation for the amplitude of local oscillation $u(x,t)$ can be formally written as [6]

$$ {}_{|x|}D^{2\beta}u(x,t) - \frac{1}{c^{2\alpha}}\,{}_{t}D_{*}^{2\alpha}u(x,t) = 0 \tag{3} $$

The fractional time derivative reflects the CTRW effect while fractional space derivatives describe the reduced dimensionality of the system. Let us write down the fractal counterpart of the wave-equation. Since there are many definitions of fractional derivatives in any approach which involves the fractional calculus techniques one should define which definition of fractional pseudo-differential are used. Following the approaches of [4, 5] we assume that the fractional time derivatives ${}_{t}D^{\alpha}{}_{*}$ are that of Caputo, while the space ${}_{|x|}D^{\beta}$ ones are these of Riesz [5, 6]. To avoid many cumbersome aspects of these operators it is enough to work with the Fourier transforms $F\{u\}$ of the oscillation amplitude $u(x,t)$ [5]:

$$ F\{{}_{|x|}D^{2\beta}u(x,t)\} = -|k|^{2\beta}\,F\{u(x,t)\} \tag{4} $$

where k is the transform variable. A similar relation holds for the time derivative. Finding the solution of Eq. (3) for arbitrary values α and β in its most general form is impossible, however, under additional assumptions we can find some specific solutions. Indeed, suppose we can separate the variables x and t. This means we assume that $u(x,t) = u_1(x)u_2(t)$. Provided that our solutions fulfill such an assumption, we can rewrite Eq. (3) as:

$$ \frac{1}{u_1(x)}\,{}_{|x|}D^{2\beta}u_1(x) - \frac{1}{c^{2\alpha}u_2(t)}\,{}_{t}D_{*}^{2\alpha}u_2(t) = 0 \tag{5} $$

Equation (4) is equivalent to two independent differential equations of single variable x or t which solved give us the oscillation amplitude in the form

$$ u(x,t) = u_o|x|^{\beta-1}t^{\alpha-1}E_{\beta,\beta}(iK|x|)E_{\alpha,\alpha}(iKct) \tag{6} $$

where $E_{\alpha,\alpha}(x)$ is the generalized Mittag–Leffler function given by:

$$ E_{\alpha,\beta}(x) = \sum_{j=0}^{\infty}\frac{x^j}{\Gamma(j\alpha+\beta)} $$

3. Discussion and summary

The Mittag–Leffler function $E_{\alpha,\alpha}(x)$ behaves like a stretched-exponential $\exp(-|x|^{\alpha})$, at short times [4, 5] and like x^{α} as $x \to \infty$. As we know, the generalized Mittag–Leffler function can be assumed as the counterparts of exponential function defined on a space of fractional dimension. This means that for $\alpha \to 1$ solution of Eq. (6) reduces to conventional plane-wave $u \propto \exp(kx - i\omega t)$. Suppose that our finite system is extended over a continuous manifold M limited by the boundary ∂M. Let us set the typical, Cauchy type, boundary conditions in the form $u(x,t)|_{\partial M} = 0$. It can be easily seen that in the case of symmetrical M (e.g., $x \in [-L, L]$) solution of Eq. (6) can satisfy these boundary conditions. Indeed, our boundary conditions are equivalent to $E_{\alpha,\alpha}(iK|L|) = 0$. This means that the number of allowed vibrational eigenmodes is equal to the number of zeroes x_n, i.e. $E_{\alpha,\alpha}(x_n) = 0$ of the generalized Mittag–Leffler functions. Thus, the allowed values of K (K is the counterpart of the wave vector k in the conventional, bulk systems) becomes quantized, $K_n = x_n/L$. As we know, Mittag–Leffler functions have a finite and odd number of zeroes thus the conditions $u(x,t)|_{\partial M} = 0$ makes that only a finite number of vibrational eigenmodes within finite fractal system is possible.

In summary, we have shown that the fracton excitations on the "net fractals", when presented in the log-scale, resemble phonons in conventional 3 D solids. The results obtained above refer to the "net fractals" which are ideal generalizations of some real fractals. Most real fractals consist of backbone and sidebranches (dead ends) attached to it. Thus, real fractals differ from the discussed above "net fractals" since they show the log-periodicity, at least along the backbone. It was suggested [2] that during vibration only the fractal backbone is stressed, while these parts of the mass which are located on the sidebranches are moved along rigidly without being strained. The arguments given above suggest that in a real dendritic fractal at most one vibrational eigenmode should display the log-scale features. We should point here that the fractal systems can be formed by an assembly of mobile particles (e.g. excitons or electrons confined within quantum well [7]). Their mobility and vibrations described by fractional spectral dimension are the source of unusual physical phenomena in these systems [8]. We believe that the presented model of fractal excitations provides a guideline for analysis of other phenomena on mesoscopic fractal systems like spin waves, resonant transmission/absorption through fractal slits, fractal plasmons or fractal antennas (fractal electrodynamics).

References

[1] VICSEK T., SHLESINGER M., MATSUSHITA M., *Fractals in Natural Sciences*, World Scientific, Singapore, 1994.

[2] ALEXANDER S., Phys. Rev. B, 40 (1989), 7953.

[3] SORNETTE D., Phys. Rep., 297 (1998), 239.

[4] SAMKO S.G., KILBAS A.A., MARICHEV O.I., *Integrals and Derivatives of Nonintegral Order with Some Applications* (in Russian), Nauka i Tekhnika, Minsk, 1987.
[5] MAINARDI F., LUCHKO Y., PAGNANI G., Fract. Calc. Appl. Anal., 4 (2001), 153.
[6] HANYGA A., Proc. Roy. Soc. (London), A, 457 (2001), 2993.
[7] POVSTENKO Y.Z., Int. J. Eng. Sci., 43 (2005), 977.
[8] MIKHAILOV I.D., BETANCUR F.J., ESCORCIA R.A., SIERRA-ORTEGA J., Phys. Rev. B, 67 (2003), 115317.
[9] BAK Z., Phys. Rev. B, 68 (2003), 064511.

Received 7 May 2006
Revised 1 September 2006

Materials Science-Poland, *Vol. 25, No. 2, 2007*

The effect of electron–electron interactions on the conditions of existence of a surface state

J. KŁOS*

Surface Physics Division, Faculty of Physics, Adam Mickiewicz University,
ul. Umultowska 85, 61-614 Poznań, Poland

Electronic surface states in one-dimensional two-band tight-binding approximation model are studied using the Green function method. The local density of states at successive atoms in a semi-infinite chain, even in the case of atoms distant from the surface, is found to be clearly different from that observed in an unperturbed (infinite) chain. The surface atom occupancy is calculated self-consistently, with the effect of electron–electron interactions taken into account. The electron–electron interactions are shown to have a significant impact on the conditions of existence of surface states.

Key words: *electron–electron interactions; surface state; Green function*

1. Introduction

The presence of electronic surface states has a substantial effect on the properties of solids. Many apparently surprising features of mesoscopic and nanoscopic systems in which surface effects are particularly conspicuous, the surface representing a significant part of the whole, can be elucidated by the conditions of existence of surface states.

One of the basic models used for description of electronic properties of solids is the tight binding approximation (TBA) model. The pioneering studies on the conditions of existence of an electronic surface state, based on a single-band model of a finite crystal, were reported by Goodwin [1]. The single-band model was then generalized by Artman [2], who introduced a double-band model to investigate the existence of two types of surface states: Shockley states which are induced only by breaking the translational symmetry of a crystal, and Tamm states, generated as a result of introducing an additional perturbation [3]. A breakthrough was marked by the paper by Kalkstein and Soven [4], in which Green's function formalism was used for the

*E-mail: klos@amu.edu.pl

determination of properties of surface and bulk states in a semi-infinite crystal with a perturbed surface.

The problem of multi-electron effects and their impact on conditions of existence of a surface state has not yet been exhaustively discussed. Papers on chemisorption which is a related issue, are available, though [5, 6]. As in the case of chemisorption, the simplest way of including the impact of the multi-electron effects on the conditions of surface state existence consists in incorporating interaction of electron with charge density into the Coulomb model. Introducing the Hartree potential into the TBA model of a semi-infinite crystal amounts (in the simplest case) to surface atom site energy renormalization.

This study is focused on surface states in a 1 D semi-infinite atom chain being a model of an ionic crystal with two atoms in the unit cell [7, 8]. Multi-electron effects are taken into account only in the Hartree approximation. The surface atom occupancy and site energy values are found through self-consistent calculations using Green's function formalism [4].

2. Model

The model assumes non-zero resonance integral values only for neighbouring sites. Orbitals s and p are alternately attributed to successive chain sites. Hence, resonance integrals for successive site pairs alternate in sign, taking values site energies associated with s or p orbitals denoted α_e or α_0, respectively (Fig. 1).

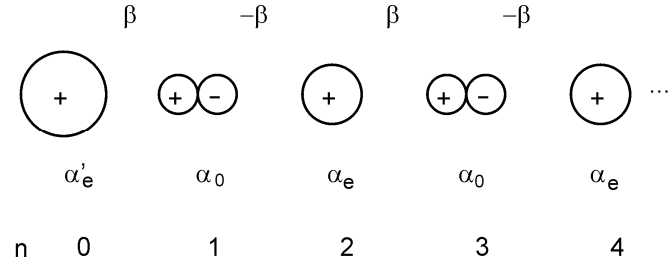

Fig. 1. The model of a semi-infinite 1 D crystal with two-atom unit cell. The surface site ($n = 0$) is occupied by an adatom with the site energy α'_e. The alternating resonance integral sign is a consequence of interaction between s and p orbitals

The wave function in the TBA model is assumed to be a linear combination of atomic functions:

$$|k\rangle = \sum_{n}^{N} \left(c_{2n} |2n\rangle + c_{2n+1} |2n+1\rangle \right) \tag{1}$$

the sum involving all the two-atom unit cells. Expressed in the atomic function basis, the Hamiltonian of an infinite (unperturbed) chain has the following form:

$$\hat{H}_0 = \sum_n \left(\alpha_e |2n\rangle\langle 2n| + \alpha_0 |2n+1\rangle\langle 2n+1| + \beta |2n\rangle\langle 2n+1| - \beta |2n+1\rangle\langle 2n| \right) \tag{2}$$

A surface introduced into the system is regarded as a perturbation breaking the infinite chain into two separate semi-infinite ones [6]:

$$\hat{H} = \hat{H}_0 + \hat{V} \tag{3}$$

$$\hat{V} = (\alpha'_e - \alpha_e)\left(|-1\rangle\langle -1| + |0\rangle\langle 0| \right) + \beta\left(|-1\rangle\langle 0| + |0\rangle\langle -1| \right) \tag{4}$$

The non-zero values of elements $V(0,0)$ and $V(1,1)$ allow adsorption of atoms of various types.

Derived from the secular equation for Hamiltonian $\hat{H}_0$, the expansion coefficients c_n and the dispersion relation read as follows:

$$\begin{cases} c_{2m} = Ae^{im\theta/2} \\ c_{2m+1} = ABe^{im\theta/2} \end{cases} \tag{5}$$

$$X = \pm\sqrt{\tau^2 + 2 - 2\cos\theta} \tag{6}$$

where

$$A = \sqrt{\frac{X+\tau}{2N\xi}}, \quad B = \frac{2i\sin(\theta/2)}{X+\tau} \tag{7}$$

and

$$\xi = \begin{cases} X, & |X| > \tau \\ \tau, & |X| < \tau \end{cases} \tag{8}$$

Parameters X and θ represent the dimensionless energy and wave vector, respectively:

$$X = \frac{E - \bar{\alpha}}{\beta}, \qquad \theta = \frac{2\pi k}{N} \tag{9}$$

$\bar{\alpha}$ and τ are defined as follows:

$$\bar{\alpha} = \frac{\alpha_e + \alpha_o}{2}, \qquad \tau = \frac{\alpha_e - \alpha_o}{2\beta} \tag{10}$$

The Greenian matrix elements:

$$\hat{G}_0(k) = \sum_k \frac{|k\rangle\langle k|}{E - E(k)} \tag{11}$$

expressed in the atomic function basis, read within the energy bands:

$$G_0\left(2m,2n\right)=-\frac{X+\tau}{\beta}\frac{t_<^{n-m}}{t_<-t_>} \tag{12}$$

$$G_0\left(2m+1,2n+1\right)=-\frac{X-\tau}{\beta}\frac{t_<^{n-m}}{t_<-t_>} \tag{13}$$

$$G_0\left(2m,2n+1\right)=\frac{1-t_<}{\beta}\frac{t_<^{n-m}}{t_<-t_>} \tag{14}$$

$$G_0\left(2m+1,2n\right)=\frac{1-t_<^{-1}}{\beta}\frac{t_<^{n-m}}{t_<-t_>} \tag{15}$$

where

$$t_>=Z+\operatorname{sign}\left(X\right)i\sqrt{Z^2-1},\qquad t_<=Z-\operatorname{sign}\left(X\right)i\sqrt{Z^2-1} \tag{16}$$

and

$$Z=\frac{\tau^2+2-X^2}{2}=\cos\theta \tag{17}$$

Selected Greenian matrix elements for perturbed (semi-infinite) crystal can be found from the Dyson equation:

$$\hat{G}=\hat{G}_0+\hat{G}_0\hat{V}\hat{G} \tag{18}$$

The diagonal elements read:

$$G\left(m,m\right)=G_0\left(m,m\right)+\frac{G_0\left(0,m\right)\left(G_0\left(m,0\right)V\left(0,0\right)+G_0\left(m,-1\right)V\left(-1,0\right)\right)}{1-G_0\left(0,0\right)V\left(0,0\right)-G_0\left(0,-1\right)V\left(-1,0\right)} \tag{19}$$

This allows the determination of the local density of states (LDOS):

$$\rho\left(X,m\right)=-\pi\operatorname{Im}\left[\beta G\left(m,m\right)\right] \tag{20}$$

and the surface state occupancy in successive chain sites:

$$\left\langle n\left(m\right)\right\rangle=\operatorname{Res}\left[G\left(m,m\right),X_s\right] \tag{21}$$

where X_s is the surface state energy determined from the condition of $G(m,m)$ zeroing.

Self-consistent renormalization of the site energy at successive sites is necessary for electron–electron interactions to be taken into account. By defining

$$\tau_m = \frac{\alpha_m - \bar{\alpha}}{\beta}, \quad \alpha_m = \alpha'_e, \alpha_o, \alpha_e, \alpha_o, \alpha_e, \ldots \tag{22}$$

we get:

$$\tau'_m = \tau_m + U\left\langle n(m)\right\rangle \tag{23}$$

where U is a parameter defining interaction of electron with charge density. Surface state localization is equivalent to state occupancy fading inward the crystal. Therefore, the highest site energy gradient is expected at the surface. In the first approximation, site energy modification can concern only the surface atom.

The surface perturbation parameter can be expressed as follows:

$$\Delta_e = \frac{\alpha'_e - \alpha_e}{\beta} = \tau_0 - \tau_{2m}, \quad m = 1, 2, 3, \ldots \tag{24}$$

When interaction of electron with charge density is taken into account:

$$\Delta'_e = \tau'_0 - \tau_{2m}, \quad m = 1, 2, 3, \ldots \tag{25}$$

In the case considered here ($\tau = 1$), the surface state energy is expressed by the following formula:

$$X_{s\pm} = \frac{1 + \Delta'_e \pm \sqrt{1 - 4\Delta'_e + 6\Delta'^2_e + 4\Delta'^3_e + \Delta'^6_e}}{2\Delta'^2_e} \tag{26}$$

X_{s+} and X_{s-} being the solutions valid for $\left|\Delta'_e + 1/2\right| > \sqrt{5}/2$ and $\Delta'_e < 0$ respectively.

3. Results

Computations were performed at $\tau = 1$ ($\alpha_e - \alpha_0 = 2\beta$). Figure 2 shows the surface state energy, X_s, plotted versus the surface perturbation. No Shockley states are found to exist in the model discussed [5], as no surface states are found in the absence of perturbation. Tamm states, induced through modifying the surface atom site energy, are found to emerge from the upper energy band (associated with α_e).

The surface states emerging from the bottom edge of the band are induced by an arbitrarily small perturbation value. For surface states to be induced above the upper band, however, the perturbation value must be positive and fulfil the condition $\Delta'_e > 1/2(\sqrt{5} - 1)$. Perturbation values from the interval $0 < \Delta'_e < 1/2(\sqrt{5} - 1)$ correspond to the non-existence of surface states. The solid and dotted lines in Fig. 2 represent

surface state levels found with or without the electron–electron interactions taken into account, respectively. Clearly, the multi-electron effects (in the Hartree approximation) boost the surface state energy levels, resulting in weakened or strengthened localization of surface states below or above the upper band, respectively. However, the electron–electron interactions have no effect on the interval of surface perturbation parameter values at which surface states are found to exist.

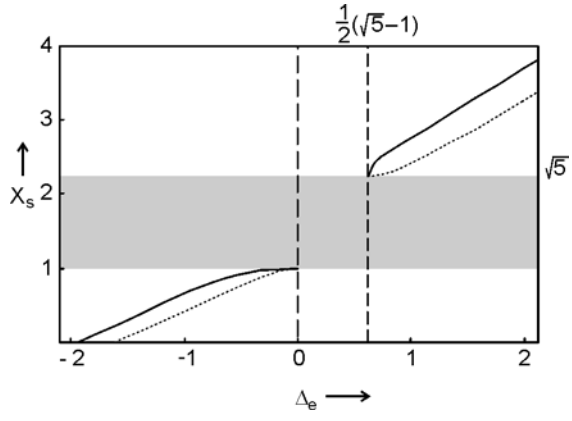

Fig. 2. Surface state levels around the upper band (gray area).
The solid and dotted lines represent the state levels found with and without the electron–electron interactions taken into account, respectively.
The dashed lines delimit the region in which no surface states exist

The effect of the surface on the electronic states in the considered chain is the most evident in the LDOS spectrum. Figure 3 shows the LDOS plots obtained for the four sites closest to the surface: $n = 0, 1, 2, 3$. Three different perturbation values are assumed, corresponding to surface state appearing below the upper band ($\Delta_e = -0.75$), not induced at all ($\Delta_e = 0.5$), and induced above the upper band ($\Delta_e = 1$). The solid and dotted lines represent the LDOS calculated with multi-electron effects taken into account or neglected, respectively. As a result of including the multi-electron effects, the LDOS in the upper band is increased; at the same time, the occupancy of the surface state below the band decreases, and the state moves towards the band edge. An opposite effect is found to occur for the surface state above the upper band: the LDOS in the band is found to decrease, while the surface state occupancy increases and the state moves inwards the gap. Comparing relative occupancy changes at successive sites, one notes a stronger localization in states closer to the band edge. Because of band asymmetry, the surface state occupancy should be compared between either even or odd sites. With multi-electron effects taken into account, the occupancy ratio of site ($n = 0$) (the surface atom) to site $n = 2$ is found to increase or decrease for states above or below the upper band, respectively. Note that even in the absence of surface states, the presence of the surface still affects the LDOS spectrum. The van Hove singularities at the band edges are eliminated, and LDOS minima appear inside the bands.

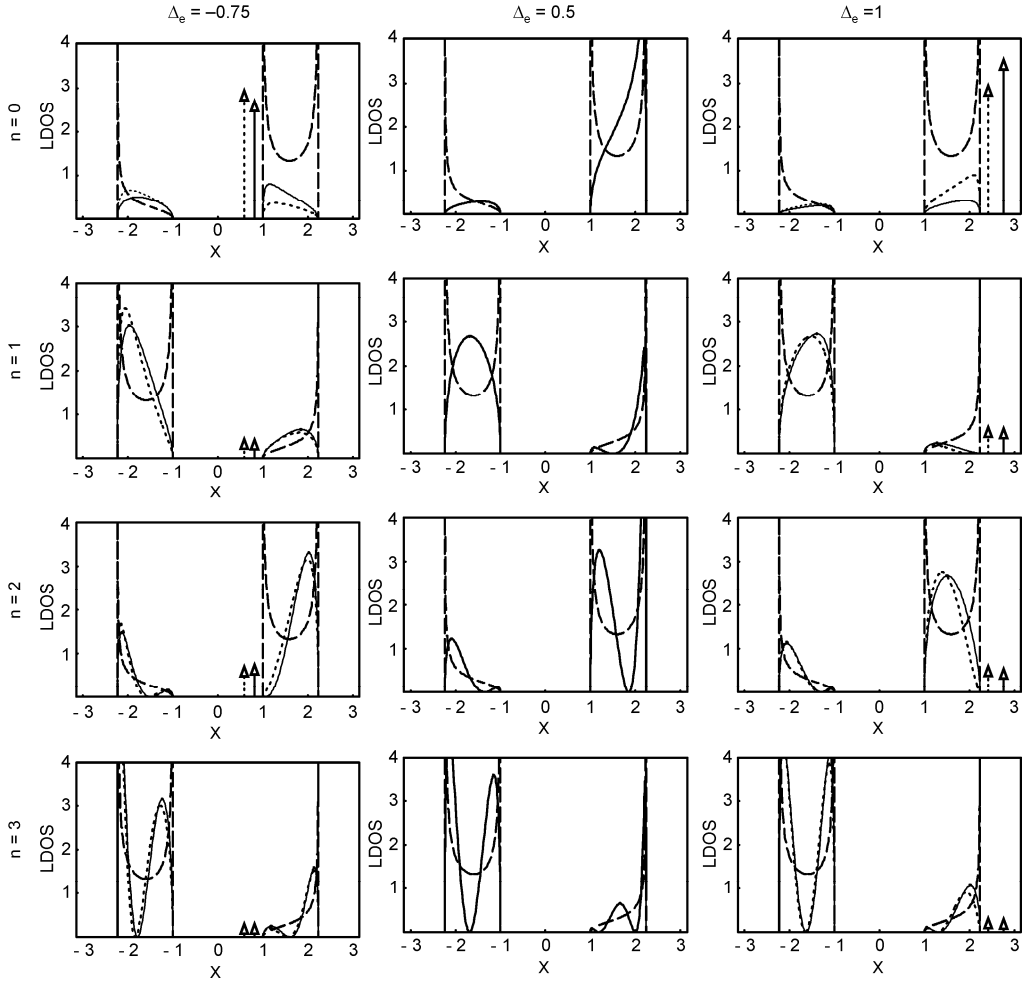

Fig. 3. The local densities of states, ($\pi\rho(X)$) at successive chain sites starting from the surface (n = 0, 1, 2, 3). Results obtained at three different perturbation values, Δ_e, are grouped into columns. The dashed line represents the LDOS for infinite chain. The dotted and solid lines represent the LDOS found for semi-infinite chain with electron–electron interactions neglected or taken into account, respectively. The arrows indicate the surface state occupancy

4. Conclusions

Focused on the effect of electron–electron interactions on the conditions of surface state existence (in the Hartree approximation), the study presented above shows that the localization of surface states generated above or below the upper energy band can be increased or decreased, respectively, by the electron–electron interactions in the considered model. However, the interval of perturbation of the values of surface

parameters corresponding to surface state existence is found to remain unaffected by taking these interactions into account in the calculations.

References

[1] GOODWIN E.T., Proc. Cambridge Philos. Soc., 35 (1939), 221; 35 (1939), 232.
[2] ARTMAN K., Z. Phys., 131 (1952), 244.
[3] ZAK J., Phys. Rev. B, 32 (1985), 2218.
[4] KALKSTEIN D., SOVEN P., Surf. Sci., 26 (1970), 85.
[6] NEWNS D.S., Phys. Rev., 178 (1968), 1123.
[7] SCHRANZ D.W., DAVISON S.G., Int. J. Quant. Chem., 67 (1998), 377.
[8] BOSE S.M., FOO E-NI, Phys. Rev B, 10 (1974), 3534.
[9] LEVINE J.D., DAVISON S.G., Phys. Rev., 174 (1968), 911.

Received 7 May 2006
Revised 1 September 2006

Materials Science-Poland, Vol. 25, No. 2, 2007

Spin reversal processes in a single molecular magnet between two ferromagnetic leads

M. MISIORNY[1*], J. BARNAŚ[1, 2]

[1]Adam Mickiewicz University, Department of Physics, ul. Umultowska 85, 61-614 Poznań, Poland

[2] Polish Academy of Sciences, Institute of Molecular Physics,
Smoluchowskiego 17, 60-179 Poznań, Poland

The effect of spin polarized transport between ferromagnetic metallic electrodes on the relaxation process of a single molecular magnet (SMM) is considered theoretically. The relaxation times are calculated in the second order approximation (Fermi golden rule). The main objective of the work is to analyze the possible mechanisms responsible for the reversal of a SMM's spin. We investigate the regime in which the spin reversal is driven by an external magnetic field. In such a case, the magnetic switching of a SMM is essentially induced by the quantum tunneling of magnetization. The total charge flowing between the electrodes during the reversal process is calculated, and the analysis shows that such a system under consideration can serve as an electronic pump.

Key words: *single molecular magnet; quantum tunneling of magnetization; transport through magnetic structures*

1. Introduction

In recent years, with the advent of new experimental techniques allowing to attach electrodes to individual molecules, transport properties of single molecules have attracted much attention [1–4]. Among many distinctive classes of molecules, the ones with permanent magnetic moment (single molecular magnets, SMMs) are of particular interest. Their uniqueness follows from their special behaviour in the presence of magnetic field [5, 6]. Due to their large spins and high anisotropy barriers, these molecules exhibit magnetic hysteresis loops with characteristic steps caused by the quantum tunneling of magnetization (QTM). Both their properties and their nanoscale size put SMMs forward as a potential candidate for future applications in information storage and information processing, as well as in spintronics devices.

*Corresponding author, e-mail: maciej_misiorny@epf.pl

The main objective of this work is to investigate the influence of exchange interaction between tunneling electrons and a SMM on the relaxation processes which accompany QTM driven by an external magnetic field. Coupling of the SMM to external leads (via tunneling electrons) is the main source of spin relaxation in the case under consideration. Moreover, the relaxation processes are associated with a transfer of charge from one lead to the other (at zero bias voltage). Consequently, the system may be considered an electronic pump, in which the charge flow between electrodes is driven by an external magnetic field due to the effect of QTM.

2. Model

The system under consideration consists of a SMM sandwiched between two ferromagnetic leads: left (L) and right (R). Magnetic moments of the leads are collinear and either parallel or antiparallel to an external magnetic field along the z axis. The leads are characterized by parabolic conduction bands with the energy dispersion $\varepsilon_{k\sigma}^{p}$, for $p = L, R$. Interaction between the electrons in the leads and the SMM is described by the Appelbaum Hamiltonian [7, 8]:

$$H_T^{\mathrm{int}} = \sum_{kk'\alpha\beta} \left\{ \frac{J}{\sqrt{N_L N_R}} \boldsymbol{\sigma}_{\alpha\beta} \cdot \mathbf{S} \left(a_{k\alpha}^{L+} a_{k'\beta}^{R} + a_{k\alpha}^{R+} a_{k'\beta}^{L} \right) \right\} \tag{1}$$

where $\boldsymbol{\sigma} = (\sigma_x, \sigma_y, \sigma_z)$ is the Pauli spin operator, $\mathbf{S}$ stands for the SMM spin operator, $a_{k\sigma}^{p+}$ ($a_{k\sigma}^{p}$) is the creation (annihilation) operator of an electron in the lead p ($p = L, R$), and J is the exchange interaction constant (assumed independent of energy and polarizations of both leads). Furthermore, J is normalized in such a way that it is independent of the size of the electrodes, and N_L, (N_R) denotes the number of elementary cells in the left (right) lead. Using the Hamiltonian (1), we restrict our considerations only to the case of all electrons scattered off the SMM to the opposite electrode (electrons interact with the SMM during the tunneling processes).

The effective Hamiltonian for the ground state spin multiplet of an independent SMM can be written in the form [5, 6],

$$H_{SMM} = -DS_z^2 + E\left(S_x^2 + S_y^2\right) + g\mu_B \left(H_z S_z + H_x S_x\right) \tag{2}$$

where D and E are the second-order anisotropy constants, and the last term stands for the Zeeman energy. The transverse terms (the terms proportional to E and H_x) account for the occurrence of QTM at resonant fields during the magnetic field sweeping. In the absence of transverse terms and assuming that $H_Z = -H$, the energy of the state corresponding to $S_z = m$ is

$$E_m = -Dm^2 - g\mu_B Hm \tag{3}$$

3. Theory and method

The Fermi golden rule was applied to derive characteristic transition times between the neighbouring molecular states. The times for transitions from $S_z = m$ to $S_z = m + 1$, i.e., to the state with larger S_z component, are given by the following formulae:

$$\frac{1}{\tau_m^{>}} = \frac{1}{\tau_m^{LR>}} + \frac{1}{\tau_m^{RL>}} \tag{4}$$

$$\begin{cases} \dfrac{1}{\tau_m^{LR>}} = \dfrac{2\pi}{\hbar} |J|^2 \, \nu_{ec}^L D_\uparrow^L \, \nu_{ec}^R D_\downarrow^R \, [A_+(m)]^2 \, \zeta\left[D(2m+1) + g\mu_B H \right] \\ \dfrac{1}{\tau_m^{RL>}} = \dfrac{2\pi}{\hbar} |J|^2 \, \nu_{ec}^L D_\downarrow^L \, \nu_{ec}^R D_\uparrow^R \, [A_+(m)]^2 \, \zeta\left[D(2m+1) + g\mu_B H \right] \end{cases} \tag{5}$$

where the indices LR and RL distinguish between electrons tunneling from left to right and from right to left, respectively. Apart from this, D_σ^p is the density of states at the Fermi level in the lead p, ν_{ec}^p is its primitive cell volume, $A_\pm(m) = \sqrt{S(S+1) - m(m \pm 1)}$, and $\zeta(\varepsilon) = \varepsilon/[1 - \exp(-\varepsilon\beta)]$ with $\beta = (k_B T)^{-1}$. Analogously, for the transitions from $S_z = m$ to $S_z = m - 1$ we find

$$\frac{1}{\tau_m^{<}} = \frac{1}{\tau_m^{LR<}} + \frac{1}{\tau_m^{RL<}} \tag{6}$$

$$\begin{cases} \dfrac{1}{\tau_m^{LR<}} = \dfrac{2\pi}{\hbar} |J|^2 \, \nu_{ec}^L D_\uparrow^L \, \nu_{ec}^R D_\downarrow^R \, [A_-(m)]^2 \, \zeta\left[-D(2m-1) - g\mu_B H \right] \\ \dfrac{1}{\tau_m^{RL<}} = \dfrac{2\pi}{\hbar} |J|^2 \, \nu_{ec}^L D_\downarrow^L \, \nu_{ec}^R D_\uparrow^R \, [A_-(m)]^2 \, \zeta\left[-D(2m-1) - g\mu_B H \right] \end{cases} \tag{7}$$

Now, we calculate the mean value of the SMM's spin as a function of magnetic field H taking into account the effect of QTM in the molecule:

$$\langle S_z \rangle = -S\left(1 - \sum_{n=0}^{M} P_{S-n}(H) \right) + \sum_{n=0}^{M} (S-n) P_{S-n}(H) \tag{8}$$

with the system assumed to occupy initially the state $S_z = -S$. Furthermore, the state $S_z = S - M$ is the state with the lowest S_z component, to which the system can tunnel before the complete depletion of the state $S_z = -S$.

The probabilities of a given spin state of the SMM were found by solving numerically the set of master equations, separately for all field ranges between the successive resonant fields. For Mth resonant field the equations are:

$$\begin{cases} c\dot{P}_S = \dfrac{1}{\tau^{>}_{S-1}} P_{S-1} \\ c\dot{P}_m = \dfrac{1}{\tau^{>}_{m-1}} P_{m-1} - \dfrac{1}{\tau^{>}_{m}} P_m, \qquad S-M+1 \le m \le S-1 \\ c\dot{P}_{S-M} = -\dfrac{1}{\tau^{>}_{S-M}} P_{S-M} \end{cases} \tag{9}$$

where $\dot{\circ} \equiv d\circ/dH$ and $c \equiv dH/dt$ is the field sweeping rate. In Eqs. (9) we neglected the relaxation to the lower states, for transition times $\tau^{<}_m \to 0$ when $m \ge 1$ for the relevant magnetic fields. Additionally, relaxation times $\tau^{>}_m$ are considerably smaller than the time scale set by the rate at which the field is varied. Consequently, we assumed that the SMM relaxes to the state $S_z = S$ before each subsequent tunneling act. Therefore the boundary conditions for resonant field $H^{(M)}$ are:

$$\begin{cases} P_S\left(H = H^{(M)}\right) = \sum\limits_{j=0}^{M-1} \tilde{P}_{S-j} \\ P_m\left(H = H^{(M)}\right) = 0, \qquad S-M+1 \le m \le S-1 \\ P_{S-M}\left(H = H^{(M)}\right) = \tilde{P}_{S-M} \end{cases} \tag{10}$$

where $\tilde{P}_{S-j}$ is the probability for SMM to tunnel from the state $S_z = -S$ to the state $S_z = S - j$. The latter can be obtained analytically with the use of the two-level Landau–Zener model [1, 9, 10],

$$\tilde{P}_{S-j} = \left(1 - F_j\right) \prod_{n=0}^{j-1} F_n \qquad \text{and} \qquad F_n = \exp\left[-\frac{\pi \Delta_n^2}{2\left(2S-n\right)\hbar g \mu_B c} \right] \tag{11}$$

Each relaxation process is associated with a single electron charge transfer from one electrode to the other. The total average number of electrons flowing between the electrodes due to relaxation processes during the reversal of the SMM's spin driven by an external magnetic field owing to QTM is

$$Q_{LR} = \frac{1}{c} \sum_{j=1}^{M} \int_{H^{(j)}}^{H^{(j+1)}} dH \;\; P_{S-j}\left(H\right) \left[\frac{1}{\tau^{LR>}_{S-j}\left(H\right)} - \frac{1}{\tau^{RL>}_{S-j}\left(H\right)} \right] \tag{12}$$

where M is determined from the condition $\tilde{P}_{S-(M+1)} \approx 0$, which essentially means that QTM is no longer observed in the system. Since relaxation processes due to the interaction of electrons tunneling between the leads with the SMM take place extremely

fast, we assumed that transition times $\tau_{S-j}^{LR>}$ and $\tau_{S-j}^{RL>}$ do not depend on the field. Consequently, we were able to solve analytically Eqs. (9) and (12):

$$Q_{LR} = \Gamma \sum_{j=1}^{M} j \, \tilde{P}_{S-j} \tag{13}$$

where Γ is the coefficient whose value depends on whether we consider the parallel or anitiparallel configuration of magnetic moments of the electrodes. It can be expressed in terms of polarizations of the electrodes, P^p for $p = L, R$, defined as

$$P^p = \frac{D_+^p - D_-^p}{D_+^p + D_-^p}$$

where + and – denote majority and minority electrons in the electrodes, respectively:

$$\Gamma_{\text{parallel}} = \frac{P^L - P^R}{1 - P^L P^R} \qquad \text{and } \Gamma_{\text{antiparallel}} = \frac{P^L + P^R}{1 + P^L P^R} \tag{14}$$

4. Numerical results and discussion

Consider now the numerical results obtained with the formulae derived above. The average spin of a SMM (see Fig. 1) and the number of electrons pumped between the electrodes during the reversal of the SMM's spin driven by an external magnetic field (Fig. 2), have been calculated for Fe_8, using the parameters from Refs. [5] and [10]. Since the blocking temperature for Fe_8 is 0.36 K, the numerical calculations have been done for $T = 0.01$ K, when no thermal excitations are allowed. For the electrodes we assumed: $v_{ec}^L = v_{ec}^R = 10^{-28}$ m^3, and free electron density $n \approx 10^{29}$ m^3. Apart from this, we assumed $J = 1$ meV.

It is apparent that the average charge, Q_{LR}, transferred between the electrodes during the reversal process of SMM's spin depends on M, i.e. the number of states to which the system can tunnel from its initial state $S_z = -S$ (Eq. (13)). Moreover, Q_{LR} depends on the field sweeping rate c through the probabilities $\tilde{P}_{S-j}$ (Eq. (11)). It follows from the analysis of their behaviour as functions of c that we can restrict considerations to the range $0.1 \le c \le 1$ T/s, in which up to 5 levels are engaged in the reversal process.

The mean value of the SMM's spin is shown in Fig. 1 as a function of magnetic field. It exhibits characteristic steps which occur owing to the QTM for certain values of the field. The height of steps depends on the field sweeping rate through the Landau–Zener probabilities (11). The higher the rate, the more levels take part in the reversal process.

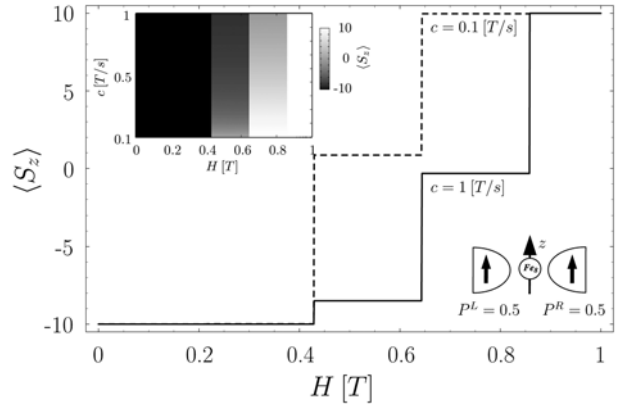

Fig. 1. The mean value of the SMM's spin as a function of magnetic field for $P^L = P^R = 0.5$ in the parallel configuration. The inset presents the continuous change of the field sweeping rate in the range $0.1 \le c \le 1$ T/s

The average charge pumped between the leads depends on the field sweeping rate, magnetic configuration of the electrodes, and the spin polarization of the leads. In Figure 2, we show the average charge pumped between the electrodes in the parallel configuration. One may notice that the sign of the average charge pumped between the leads (direction of average electron flow) is determined by the electrode polarizations. The direction of electron flow can be described by an auxiliary parameter $\alpha = P^R/P^L$. Let us assume that P^L is kept constant, while P^R is varied. In the case shown in Fig. 2, the electrons flow from left to right for $0 \le \alpha < 1$, whereas for $1 < \alpha \le 1/P^L$ they flow in the opposite direction. For $\alpha = 1$ there is no resultant flow of charge.

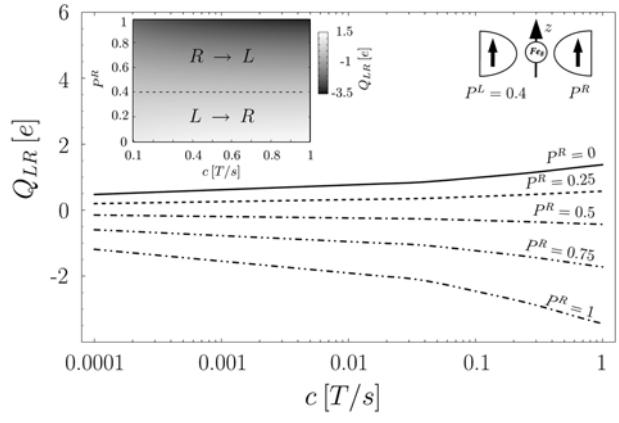

Fig. 2. The average charge pumped between the electrodes in the spin reversal process as a function of the field sweeping rate for various polarizations of the right lead. The leads are kept in the parallel configuration

In conclusion, we have shown that the exchange interaction of electrons tunneling between two electrodes and a SMM leads to charge pumping during the spin reversal process due to QTM driven by an external magnetic field. The effect can be accounted for by taking into account spin relaxation processes involving electron transitions between different electrodes.

References

[1] KIM G.-H., KIM T.-S., Phys. Rev. B, 92 (2004), 137203.
[2] TIMM C., ELSTE F., Phys. Rev. B, 73 (2006), 235304.
[3] TIMM C., ELSTE F., Phys. Rev. B, 73 (2006), 235305.
[4] HEERSCHE H.B., DE GROOT Z., FOLK J.A., VAN DER ZANT H.S.J., ROMEIKE C., WEGEWIJS M.R., ZOBBI L., BARRECA D., TONDELLO E., CORNIA A., Phys. Rev. Lett., 96 (2006), 206801.
[5] WERNSDORFER W., SESSOLI R., Science, 284 (1999), 133.
[6] GATTESCHI D., SESSOLI R., Angew. Chem. Int. Ed., 42 (2003), 268.
[7] APPELBAUM J., Phys. Rev., 17 (1966), 91.
[8] APPELBAUM J.,Phys. Rev., 154 (1967), 633.
[9] ZENER C., Proc. Roy. Soc. London Ser. A, 137 (1932), 696.
[10] RASTELLI E., TASSI A., Phys. Rev. B, 64 (2001), 64410.

Received 7 May 2006
Revised 1 September 2006

Materials Science-Poland, *Vol. 25, No. 2, 2007*

Electronic structure of U_5Ge_4

A. SZAJEK*

Institute of Molecular Physics, Polish Academy of Sciences,
ul. Smoluchowskiego 17, 60-179 Poznań, Poland

U_5Ge_4 crystallizes in a hexagonal Ti_5Ga_4 type structure with two inequivalent crystallographic sites occupied by uranium atoms. The band structure calculations were performed by the method of tight binding version of the linear muffin-tin orbital in the atomic sphere approximation (TB-LMTO ASA). The calculations showed that both types of uranium atoms can be magnetically ordered and then their spin magnetic moments are equal to 0.5 and –1.2 μ_B/atom, respectively.

Key words: *uranium compound; electronic structure; magnetic moment*

1. Introduction

Uranium germanides have been widely investigated both experimentally and theoretically because of their interesting anomalous physical properties. The recent thorough reinvestigation of the U–Ge system has finally established the existence of six compounds with the chemical formulae U_5Ge_4, UGe, U_3Ge_5, UGe_2, UGe_3 and UGe_{2-x}, where $0.30 < x < 0.35$ [1]. U_5Ge_4 crystallizes in a hexagonal Ti_5Ga_4 type structure with *P*63/*mcm* space group [2]. The unit cell has a complex structure and contains 18 atoms: uranium atoms occupy two inequivalent sites, 4d and 6g, and germanium atoms also two sites: 6g and 2b. Magnetic susceptibility investigations showed a nearly temperature independent paramagnetic behaviour down to 2 K [1, 2]. Lack of magnetic order was explained by a direct overlap between 5f shells of uranium U(4d) along the *c* axis, according to a short distance between each U(4d) atom, and delocalization of 5f electrons of U(6g) atoms probably occurring via hybridization effects with the sp shells of the surrounding germanium atoms. The interatomic distances between uranium atoms are as follows [2]: U(4d)–U(4d) 2.931 Å, U(4d)–U(6g) 3.484 Å and U(6g)–U(6g) 3.832 Å. This means that the distances are below and above so-called Hill limit [3] equal to ca. 3.4 Å, and one can expect magnetic moments lo-

*E-mail: szajek@ifmpan.poznan.pl

cated on U(6g) atoms. A similar situation was observed in UGe [4], where for one of three types of uranium atoms, the inter-uranium distances were below the Hill limit, and for remaining ones – above the Hill limit, which strongly influenced their magnetic moments.

The aim of this paper is to present the electronic structure of U_5Ge_4 for both nonmagnetic and a hypothetical magnetic case.

2. The method of calculations and results

The electronic structures for nonmagnetic and magnetic cases were calculated using the spin-polarized tight-binding linear muffin-tin orbital (TB LMTO) method in the atomic sphere approximation (ASA) [5, 6].

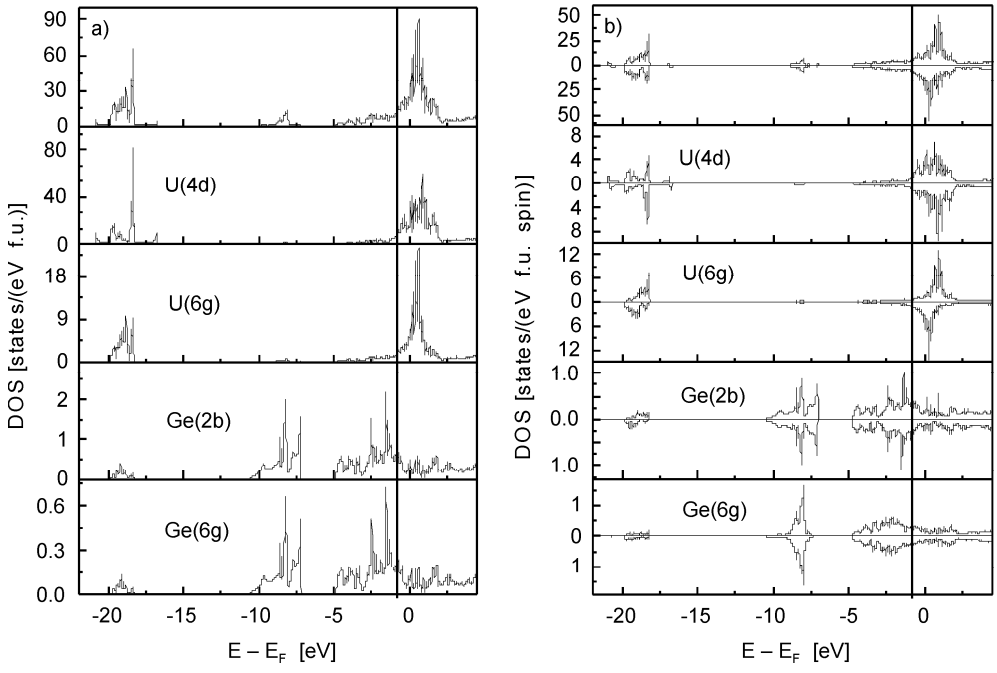

Fig. 1. The total (per f.u.) and site projected (per atom) densities of electronic states (DOS) for U_5Ge_4 in the paramagnetic state (a) and a hypothetical magnetic state (b)

The overlap volume of the muffin-tin spheres is about 9%. The standard combined corrections [5] for overlapping were used to compensate errors due to the ASA. The experimental values of the lattice constants [2] were used in the calculations. Spin -orbit interactions were taken into account in the form proposed by Min and Jang [7]. The exchange correlation potential was assumed in the form proposed by von Barth and Hedin [8]. Self-consistent calculations were carried out for 396 *k*-points in the

irreducible wedge (1/24) of the Brillouin zone. For integration over the Brillouin zone the tetrahedron method was used [9]. The iterations were repeated until the total energies of the consecutive iteration steps were the same within the error of 0.01 mRy.

The X-ray photoemission spectroscopy (XPS) is a very useful tool to confirm the band structure calculations. To the best of our knowledge, up to now, spectra of U_5Ge_4 have not been recorded. We present computed photoemission spectra. The method used here consists in weighting the density of states (DOS) with appropriate atomic cross sections for photon scattering [10] and applying a convolution with a Gaussian function which accounts for a finite experimental resolution δ. In our case, the photon energy is equal to 1486.6 eV (AlK_α source) and the parameter δ is equal to 0.3 eV.

The densities of electronic states (DOS) are presented in Fig. 1 for nonmagnetic and magnetic cases. In both cases, the valence bands can be divided into three parts:

- around 18–20 eV below the Fermi level (E_F) formed mainly by 6p electrons of the uranium atoms;
- around 7–10 eV below E_F formed mainly by Ge(4s) electrons;
- between 5 and 0 eV below E_F, formed by Ge(4p) and U(6d+5f) electrons.

Table 1. Spin projected (↑,↓) densities of electronic states (DOS [states/(eV spin (f.u. or atom))]) at the Fermi level for U_5Ge_4 in a nonmagnetic state (PM) and a magnetic one (FM)

Type of DOS	Spin direction	Total and l-decomposed DOS (per f.u.)		Atom (position)	Spin direction	Site-projected DOS (per atom)	
		PM	FM			PM	FM
Total	↑	–	10.65	U(4d)	↑	–	2.91
	↓	–	12.12		↓	–	1.07
	↑+↓	23.32	22.77		↑+↓	3.67	3.98
Total for s electrons	↑	–	0.14	U(6g)	↑	–	1.37
	↓	–	0.06		↓	–	3.15
	↑+↓	0.21	0.20		↑+↓	5.01	4.52
Total for p electrons	↑	–	0.61	Ge(6g)	↑	–	0.19
	↓	–	0.36		↓	–	0.11
	↑+↓	0.85	0.97		↑+↓	0.22	0.30
Total for d electrons	↑	–	1.91	Ge(2b)	↑	–	0.15
	↓	–	1.00		↓	–	0.14
	↑+↓	2.56	2.91		↑+↓	0.27	0.29
Total for f electrons	↑	–	7.98				
	↓	–	10.72				
	↑+↓	19.69	28.72				

The main contribution to the total DOS at the Fermi level is provided by U(5f) electrons. The values of DOS ($E = E_F$) are collected in Table 1. Total energy calculations showed that the magnetically ordered state of the U_5Ge_4 is more stable than the nonmagnetic one. The isostructural antimonide U_5Sb_4 [11] and stannide U_5Sn_4 [2], having slightly larger interatomic distances than U_5Ge_4, exhibit ferromagnetic order-

ing. In the case of U_5Ge_4, the calculated spin magnetic moments are equal to: 0.50, –1.21, 0.01, and 0.03 μ_B/atom for U(4d), U(6g), Ge(6g), and Ge(2b), respectively. We see that the U(4d) atom, with the shortest inter-uranium distances, has significantly reduced moment comparing with the moment of the U(6g) atom. For U(4d) atoms, the hybridization effects reduce the heights of 5f and 6p DOS plots, and the appropriate bands are more broadened than for U(6g) atoms.

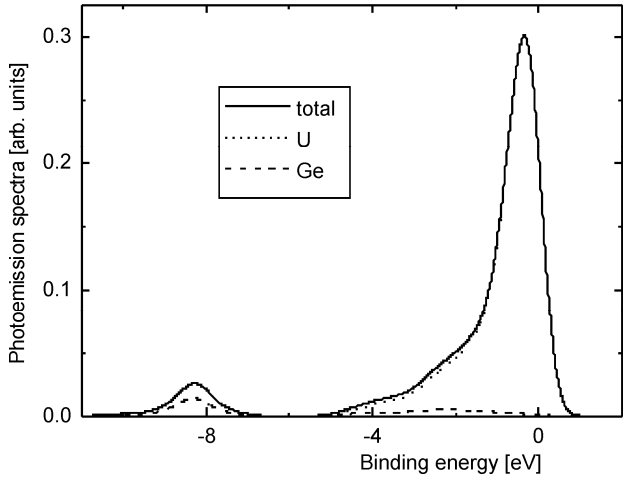

Fig. 2. X-ray photoemission spectra of U_5Ge_4

The calculated photoemission spectra are presented in Fig.2. The spectra were calculated based on the paramagnetic DOS functions since the system is nonmagnetic down to 2 K. The total spectrum is dominated by one main peak located close to the Fermi level. Ge atoms provide only small contribution to the total spectrum. The significant uranium contribution comes from considerable contribution of DOS function and large value of cross sections for 5f electrons.

3. Conclusions

In this paper, the electronic structure of U_5Ge_4 has been calculated by the TB-LMTO method. The calculations were performed with and without spin polarization. The main results are summarized as follows:

The results of calculations of the band structure show that the magnetically ordered state of U_5Ge_4 is more stable than the nonmagnetic one.

The U(5f) bands dominate the densities of states near the Fermi level on calculated X-ray photoemission spectrum.

The values of spin magnetic moments on uranium atoms are strongly dependent on the local environments and are equal to 0.50 and –1.21 μ_B/atom for U(4d) and U(6g) atoms, respectively.

Acknowledgements

Financed from the science resources as a joint research program within scientific network "New materials and sensors for optoelectronics, informatics, power industry and medicine".

References

[1] TROĆ R., NOËL H., BOULET P., Phil. Mag. B, 82 (2002), 805.
[2] BOULET P., POTEL M., LEVET J.C., NOËL H., J. Alloys Compd., 262–263 (1997), 229.
[3] HILL H.H., [in:] *Plutonium and Other Actinides*, W.N. Miner (Ed.), Vol. 1, 1970, Metal. Soc. AIME, New York, 1971, p. 2.
[4] SZAJEK A., J. Magn. Magn. Mater., 272–276 (2004), e347.
[5] ANDERSEN O.K., JEPSEN O., ŠOB M., [in:] *Electronic Structure and Its Applications*, M.S. Yussouff (Ed.), Springer, Berlin, 1987, p. 2.
[6] KRIER G., JEPSEN O., BURKHARDT A., ANDERSEN O.K., The TB-LMTO-ASA program (source code, version 4.7, available upon request from the program authors).
[7] MIN B.I., JANG Y.-R., J. Phys. Cond. Matter, 3 (1991), 5131.
[8] VON BARTH U., HEDIN L., J. Phys. C, 5 (1972), 1629.
[9] BLÖCHL P., JEPSEN O., ANDERSEN O.K., Phys. Rev. B, 49 (1994), 16223.
[10] YEH J.J., LINDAU I., At. Data Nucl. Data Tables, 32 (1985), 1.
[11] PAXIAO J.A., REBIZANT J., BLAISE A., DELAPALME A., SANCHEZ J.P., LANDER G.H., NAKOTTE H., BURLET P., BONNET M., Physica B, 203 (1994), 137.

Received 7 May 2006
Revised 1 September 2006

Materials Science-Poland, *Vol. 25, No. 2, 2007*

Polaronic transport through molecular quantum dots. Charging-induced NDR and rectification

K. WALCZAK*

Institute of Physics, Adam Mickiewicz University, ul. Umultowska 85, 61-614 Poznań, Poland

The polaronic transport through molecules weakly connected to metallic electrodes in the nonlinear response regime has been studied. Molecule itself is treated as a quantum dot with discrete energy levels, its connection to the electrodes is described within the wide-band approximation, while the charging is incorporated by means of the self-consistent potential. Non-perturbative computational scheme, used in this work, is based on the Green's function theory within the framework of polaron transformation. This method transforms the many-body electron-phonon interaction problem into a one-body multi-channel single-electron scattering problem with occupation of polaron levels calculated in a self-consistent way. In particular, three different phenomena are discussed in detail resulting from charging in polaronic transport via discrete quantum states: the suppression of the current at higher voltages, negative differential resistance (NDR effect), and rectification.

Key words: *polaronic transport; decoherence; molecular quantum dot; negative differential resistance (NDR); rectification*

1. Introduction

Electronic conduction through molecular junctions composed of molecules sandwiched between electrodes is of great importance because of their potential to become future electronic devices [1]. The current–voltage characteristics (*I–V* spectra) of such nanojunctions were measured experimentally and negative differential resistance (NDR effect) [2–4] as well as rectifying behaviour [5–8] were reported. Suggested possible mechanisms for NDR involve charging and/or conformational changes [9–13], while the dominant factors in inducing rectification are some geometric asymmetry in the molecular junction and in the electrostatic potential spatial profile [14–17]. Anyway, transport characteristics are usually discussed in the context of simple tunnelling through existing energy levels (molecular orbitals).

*E-mail: walczak@amu.edu.pl

Since molecules involved in the conduction process can be thermally activated to vibrations (phonon modes are excited), their transport properties should be strongly affected by electron-phonon interactions in the case when an electron spends enough time on the molecule. The contact time τ_c of the conduction electron with the molecule can be estimated by a straightforward generalization of the uncertainty principle: $\tau_c \approx \hbar\beta L/\Delta E_G$ ($\beta \approx 1$ Å^{-1}) is the structure-dependent decay length of the electron transfer process, L is the length of the molecular bridge, while ΔE_G is the excitation gap between the injection energy and the isolated bridge frontier orbital energy. The above dependence has important physical implications. For short bridges with large gaps (σ-bonded systems), the contact time τ_c ~ fs is far too short for significant vibronic coupling. For longer bridges with smaller gaps (π-type systems), the contact time τ_c ~ ps is of order of magnitude comparable to vibrational period. In the latter case, the vibronic coupling can be strong enough to lead to polaronic transport through molecular bridge, where the electronic virtual excitations of polaron states create conduction channels.

This paper is devoted to the question of polaronic transport through molecules weakly connected to the electrodes in the nonlinear response regime. The molecule itself is treated as a quantum dot with discrete energy levels, the molecule–metal couplings are described within the wide-band model, while the charging is incorporated by means of the mean-field approximation. Here we show that NDR and rectification can occur also in the case of polaronic transport due to the charging effects.

2. Model and method

Let us consider the simplest possible situation in which the molecular quantum dot is represented by one spin-degenerate electronic level coupled to a single vibrational mode (primary mode) while being also connected to two reservoirs of non-interacting electrons. The Hamiltonian of the whole system can be written in the form:

$$H = \sum_{k\in\alpha} \varepsilon_k c_k^+ c_k + \sum_{k\in\alpha} \left(\gamma_k c_k^+ c_j + h.c.\right) + \varepsilon_j c_j^+ c_j + \Omega d^+ d - \lambda\left(d + d^+\right) c_j^+ c_j \qquad (1)$$

where: ε_j and ε_k are the energies of electronic states on the molecular bridge and in the reservoirs (with momentum k), γ_k is the strength of the molecule-reservoir coupling, G is the phonon energy, λ is the electron-phonon interaction parameter, $\alpha = L, R$ stands for the left and right reservoir. c_k, c_j, d and their adjoints are annihilation and creation operators for electrons in the bridge level and in the reservoirs, and for the primary phonon mode, respectively.

We apply the so-called polaron transformation [18–21] where the electron states are expanded into the direct product states composed of single-electron states and m-phonon Fock states: $|j,m\rangle = c_j^+ (d^+)^m |0\rangle/\sqrt{m!}$, $|k,m\rangle = c_k^+ (d^+)^m |0\rangle/\sqrt{m!}$ ($|0\rangle$ denotes the vacuum state). This method maps exactly the many-body hole-phonon inter-

action problem into a one-body multi-channel scattering problem. After eliminating the reservoir degrees of freedom, we can present the effective Hamiltonian of the reduced molecular system as:

$$H_{\text{eff}} = \sum_{m,\alpha} \left(\varepsilon_j^m + \Sigma_\alpha^m \right) | j,m \rangle \langle j,m | - \sum_m \lambda^m \left(| j,m \rangle \langle j,m+1 | + | j,m+1 \rangle \langle j,m | \right) \qquad (2)$$

where: $\varepsilon_j^m = \varepsilon_j + U_{SCF} + m\Omega$, $\lambda^m = \lambda\sqrt{m+1}$, $\Sigma_\alpha^m = -i\Gamma_\alpha^m/2$ is the self-energy in the wide-band approximation, while $\Gamma_\alpha^m = 2\pi |\gamma_\alpha^m|^2 \rho_\alpha$ is the so-called linewidth function with $\gamma_\alpha^m (\equiv \gamma_k)$ as the strength of the coupling between the mth conduction level and the α electrode described by density of states ρ_α. Particular energy levels are redefined with the help of the self-consistent potential $U_{SCF} = UQ_j^m$, in order to take into account the charging effects, where the U parameter represents the on-level Hubbard -type interaction constant, while the occupation of particular channels (polaron levels) can be computed as:

$$Q_j^m = \frac{2}{\pi} \int_{-\infty}^{+\infty} d\varepsilon \frac{f_L^m(\varepsilon)\Gamma_L + f_R^m(\varepsilon)\Gamma_R}{4\left(\varepsilon - \varepsilon_j^m\right)^2 + \left(\Gamma_L + \Gamma_R\right)^2} \qquad (3)$$

where $f_\alpha^m(\varepsilon) = \left(1 + \exp\left(\beta(\varepsilon + m\Omega - \mu_\alpha\right)\right)^{-1}$ is the Fermi function. Here the electrochemical potentials are given as: $\mu_L = \varepsilon_F + \eta eV$, $\mu_R = \varepsilon_F - (1 - \eta)eV$, ε_F denotes the Fermi energy, V is applied bias, while the voltage division factor is $\eta = 1/2$. Since the potential U_{SCF} is determined by the occupation Q_j^m, while Q_j^m depends on U_{SCF} – both quantities are recalculated in the self-consistent procedure. Index m numbers the particular channels and their accessibility before scattering is determined by an appropriate weight factor:

$$P_m = \left[1 - \exp(-\beta\Omega)\right] \exp(-m\beta\Omega)$$

where $\beta = 1/k_B\theta$, with θ being the device working temperature. In practice, the maximum amount of phonon quanta excited on each site is restricted to a finite number $m = m_{\max}$ because of the numerical efficiency.

Choosing an appropriate matrix element of the molecular Green function defined as: $F(\varepsilon) = (J\varepsilon - H_{\text{eff}})^{-1}$, where J is the unit matrix, we can define the transmission probability of each possible transition, where an electron incoming from the left reservoir (channel m) can suffer inelastic collisions by absorbing or emitting phonons before outgoing to the right reservoir (channel n):

$$T_{m,n}(\varepsilon) = \Gamma_L \Gamma_R |F_{m+1,n+1}(\varepsilon)|^2$$

The electrical current flowing through the system is given by:

$$I = \frac{e}{\pi\hbar}\int_{-\infty}^{+\infty} d\varepsilon \sum_{m,n} T_{m,n}(\varepsilon)\left(P_m f_L^m(\varepsilon)\left(1 - f_R^n(\varepsilon)\right) - P_n f_R^n(\varepsilon)\left(1 - f_L^m(\varepsilon)\right)\right) \tag{4}$$

3. Results and discussion

Figure 1 presents the current–voltage dependences obtained for the symmetric anchoring case, i.e. the strength of the molecule–electrode connections is the same at both ends. We have chosen the following parameters of the model (given in eV): $\varepsilon_j = 0$ (the reference energy of the LUMO level), $\varepsilon_F = -1$, $\Omega = 1$, $\lambda = 0.5$, $\rho_L^{-1} = \rho_R^{-1} = 20$ (both electrodes are made of the same material), while the temperature of the system is set at $\theta = 300$ K ($\beta = 40$ eV^{-1}). Maximum number of allowed phonons $m_{\max} = 4$ is used to obtain the results with accuracy better than 2% for all the chosen parameters.

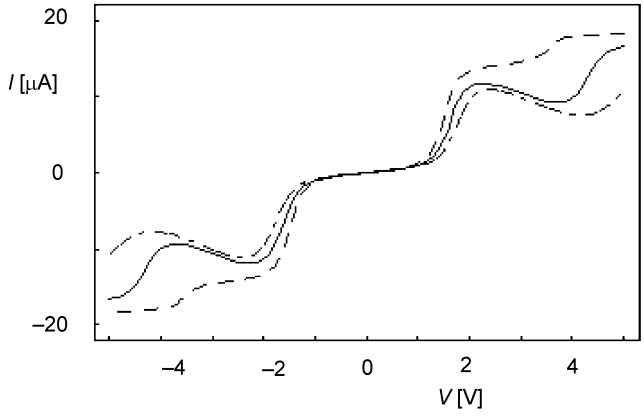

Fig. 1. Current–voltage characteristics for a molecular quantum dot symmetrically connected with two reservoirs ($\gamma_L = \gamma_R = 0.5$ V) for three different charging parameters: $U = 0$ (dashed line), $U = 2$ eV (solid line) and $U = 4$ eV (dashed-dotted line)

The *I*–*V* function reveals the well-known staircase-like structure. When we neglect the vibronic coupling, only one current step positioned at $V_0 = 2|\varepsilon_j - \varepsilon_F|/e$ (= 2 V) is expected. However, in the presence of a strong electron-phonon coupling, two current steps in the *I*–*V* dependence are observed due to the polaron formation. Using the formula for polaron energies it is possible to deduce the positions of the main conductance peak $V \approx V_0 - 2\lambda^2/(e\Omega)$ (= 1.5 V) and a one phonon side peak $V \approx V_0 - 2\Omega/e - 2\lambda^2/(e\Omega)$ (= 3.5 V). The height of the latter peak as associated with the first excited state of a polaron is much smaller than that of the former peak which corresponds to the polaron ground state.

In the case of a non-zero charging parameter, we also observe two current steps but their positions are shifted towards higher biases. Moreover, inclusion of extremely large values for *U* results in suppression of the current at higher voltages. Surpris-

ingly, the charging-induced smoothing of the *I–V* curves (or equivalently the charging-induced broadening of the *G–V* function) is negligibly small. This conclusion stands in contradiction to the results obtained in the absence of phonons (see the paper by Walczak in [17]). Besides, after the first current step the NDR effect is documented (the differential conductance reaches negative values). Here we can formulate the following general conclusion: the higher is the value of the *U* parameter, the stronger NDR effect is observed. It is important to note that NDR cannot be generated by only one of the two considered interactions being combined effect of both polaron formation and charging.

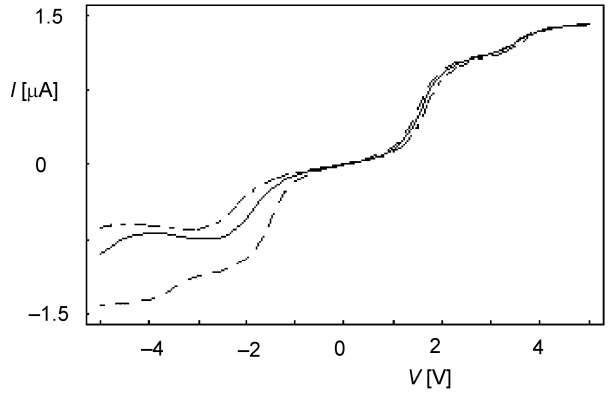

Fig. 2. Current–voltage characteristics for a molecular quantum dot asymmetrically connected with two reservoirs ($10\gamma_L = \gamma_R = 1$ eV) for three different charging parameters: $U = 0$ (dashed line), $U = 2$ eV (solid line) and $U = 4$ eV (dashed-dotted line)

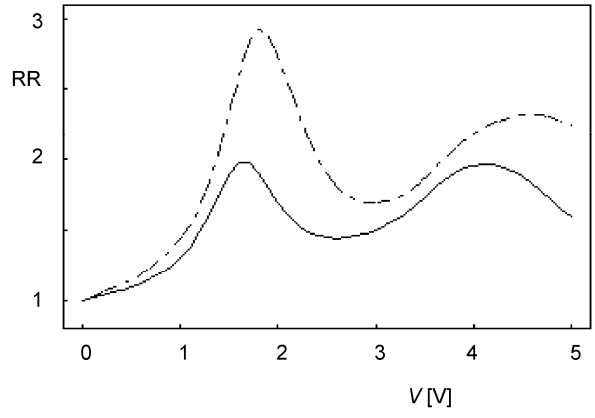

Fig. 3. Rectification ratios (RR) as functions of bias voltages for molecular quantum dot asymmetrically connected with two reservoirs ($10\gamma_L = \gamma_R = 1$ eV) for two different charging parameters: $U = 2$ eV (solid line) and $U = 4$ eV (dashed-dotted line)

In Figure 2, we plot transport characteristics for the asymmetric anchoring case, i.e. for the strength of the molecule–electrode connections being different at both ends. This situation can be realized experimentally by adjusting the molecule–electrode bond length or by linking the molecule with two electrodes with the help of different anchoring groups. Since the magnitude of the current flowing through the system is approximately proportional to the square of the smaller coupling γ parameter, the current in this case is lower.

Our calculations indicate that the *I–V* dependence is symmetric in the absence of charging (for $U = 0$). The rectification effect, in which the magnitude of the junction current depends on the bias polarity, is observed for the case of non-zero charging energy parameter (for $U > 0$). Within our model, this rectifying behaviour for higher voltages is due to a combined effect of asymmetric connections with the electrodes and charging itself. It is easy to draw the following general conclusion: asymmetry in transport characteristics increases with increasing the value of the U parameter.

To quantify the asymmetry of the *I–V* curve, we plot the rectification ratio $RR(V) = |I(V)/I(-V)|$ in Fig. 3. Here we show that for the chosen set of model parameters, the junction rectifies with factor $1 < RR < 2$ for $U = 2$ eV and $1 < RR < 3$ for $U = 4$ eV. The oscillatory character of the RR quantity as a function of bias voltage is a direct consequence of the staircase-like structures of the *I–V* dependences.

4. A concluding remark

In summary, it should be mentioned that recently Galperin et al. presented a "pure" polaron model where all the charging effects are omitted [22]. They have suggested that polaronic mechanism can be responsible for NDR and hysteretic/switching behaviour in molecular junctions. In their model, the self-consistency is associated with the energy of the resonant level shifted by polaron formation that in turn depends on the electronic occupation in that level. Here, in contrast, we describe a slightly different approach to polaronic transport, where the self-consistency is related to the energy of polaron level shifted by charging energy that in turn depends on the electronic occupation in that level.

References

[1] WADA Y., TSUKADA M., FUJIHIRA M., MATSUSHIGE K., OGAWA T., HAGA M., TANAKA S., Jpn. J. Appl. Phys., 39 (2000), 3835.
[2] CHEN J., REED M.A., RAWLETT A.M., TOUR J.M., Science, 286 (1999), 1550.
[3] AMLANI I., RAWLETT A.M., NAGAHARA L.A., TSUI R.K., Appl. Phys. Lett., 80 (2002), 2761.
[4] KIEHL R.A., LE J.D., CANDRA P., HOYE R.C., HOYE T.R., Appl. Phys. Lett., 88 (2006), 172102.
[5] GEDDES N.J., SAMBLES J.R., JARVIS D.J., PARKER W.G., SANDMAN D.J., Appl. Phys. Lett., 56 (1990), 1916.
[6] ZHOU C., DESHPANDE M.R., REED M.A., JONES II L., TOUR J.M., Appl. Phys. Lett., 71 (1997), 611.

[7] ASHWELL G.J., GANDOLFO D.S., J. Mater. Chem., 11 (2001), 246.
[8] METZGER R.M., Chem. Rev., 103 (2003), 3803.
[9] XUE Y., DATTA S., HONG S., REIFENBERGER R., HENDERSON J.I., KUBIAK C.P., Phys. Rev. B, 59 (1999), R7852.
[10] SEMINARIO J.M., ZACARIAS A.G., TOUR J.M., J. Amer. Chem. Soc., 122 (2000), 3015.
[11] EMBERLY E.G., KIRCZENOW G., Phys. Rev. B, 64 (2001), 125318.
[12] KARZAZI Y., CORNIL J., BRÉDAS J.L., Nanotechnology, 14 (2003), 165.
[13] TAYLOR J., BRANDBYGE M., STOKBRO K., Phys. Rev. B, 68 (2003), R121101.
[14] AVIRAM A., RATNER M.A., Chem. Phys. Lett., 29 (1974), 277.
[15] ELLENBOGEN J.C., LOVE J.C., Proc. IEEE, 88 (2000), 386.
[16] KORNILOVITCH P.E., BRATKOVSKY A.M., WILLIAMS R.S., Phys. Rev. B, 66 (2002), 165436.
[17] WALCZAK K., Physica E, 25 (2005), 530.
[18] HAULE K., BONČA J., Phys. Rev. B, 59 (1999), 13087.
[19] NESS H., FISHER A.J., Chem. Phys., 281 (2002), 279.
[20] ČIŽEK M., THOSS M., DOMCKE W., Phys. Rev. B, 70 (2004), 125406.
[21] WALCZAK K., Physica E, 33 (2006), 110.
[22] GALPERIN M., RATNER M.A., NITZAN A., Nano Lett., 5 (2005), 125.

Received 7 May 2006
Revised 1 September 2006

Materials Science-Poland, Vol. 25, No. 2, 2007

First principle calculations of zinc blende superlattice surfaces and multilayers with ferromagnetic dopants

A. WRONKA*

Department of Solid State Physics, University of Łódź, ul. Pomorska 149/153, 90-236 Łódź, Poland

In order to understand conditions for appearance of half-metallicity in MnAs/AsGa(001) digital alloy superlattices, we calculated the electronic and magnetic structure of zinc blende multilayers in various ab initio supercell geometries for ferromagnetic dopants (Fe, Cr). The bulk atomic structure model is extended allowing consideration of the surface ferromagnetic metal monolayer (Fe, Cr) in the slab approximation. The calculations were performed using the density functional theory (DFT) method within the full-potential and linearized augmented plane-wave (LAPW) approach. This work presents detailed information about total and atom projected density of states (DOS) functions in the surface region of the investigated systems. Our interest was to look for common trends and differences in the electronic structures for different locations of ferromagnetic adatoms and surface monolayer (Fe, Cr) in the zinc blende digital alloy surfaces and multilayers.

Key words: *digital ferromagnetic heterostructure; density functional theory; half-metal*

1. Introduction

Use of the molecular beam epitaxy (MBE) for microfabrication of magnetic semiconductor heterostructures allowed fabricating magnetic semiconductor multilayer structures, i.e., producing controlled magnetism via changes in the number of magnetic layers and the direction of spin momentum.

Investigating and synthesizing new spintronic materials has a great practical importance due to their application in future information technology and electronic devices. Among all proposed materials, semiconductors made by doping with magnetic ions (V, Cr, Mn, Fe, Co, and Ni) or preparing a hybrid structure of magnetic element with a semiconductor [1] exhibit the most promising properties. The (Ga,Mn)As heterostructures have opened a completely new method to combine magnetism with charge transport in well known semiconductor device structures.

*E-mail: awronka@uni.lodz.pl

Half-metallic (HM) random (diluted) and digital ferromagnetic dopants attract much interest as they have only one occupied set of spin density of states at the Fermi level, and thus should in principle be capable of 100% polarized spin current injection. They have been examined as the source of spin polarized electrons for innovative spintronic devices and sophisticated experiments [2]. Digital ferromagnetic heterostructures (i.e., digital alloys) have been fabricated by alternately depositing semiconductors such as GaAs and one submonolayer MnAs using low temperature molecular beam epitaxy, because only 0.5 ML of Mn can be deposited with this technique.

Theoretical calculations focused on conventional alloys containing randomly distributed Mn in the semiconductor host, predict T_C on the basis of Zenner mode [3] and prove that an increase of the Mn concentration increases the Curie temperature of the random alloy $Ga_{1-x}Mn_xAs$ systems. The highest critical temperatures observed so far in (Ga,Mn)As have been in the range 50–110 K but the theory predicts that even at room temperature magnetism could be achievable. One approach to increasing T_C is to replace random heterostructures with digital ferromagnetic heterostructures (DFH). The density functional theory (DFT) calculations for zinc blende (ZB) superlatices and their surfaces have been performed by few authors [4–6]. It has been reported that the half-metallicity of MnAs/AsGa digital alloys can be destroyed by Fe monolayers (0.5 ML) embedded in these zinc blende superlattice materials [7].

2. Method of calculation and results

The half-metallic properties of a M/MnAs/GaAs(001) (M = Fe, Cr) digital alloy superlattice surfaces have been investigated within the density functional theory, using the highly precise all-electron full-potential linearized augmented plane-wave (FP LAPW) method within the generalized gradient approximation (GGA Perdew –Burke–Ernzerhof 96) for the exchange and correlation functionals, implemented in WIEN2k program package [8].

Surfaces have been modelled using a supercell-slab model with periodic boundary conditions containing a set of 12 or 15 atoms (Fig. 1). Calculations have been performed for zinc blende (ZB) tetragonal unit cell geometry with $a_0/\sqrt{2}$ in the **a** and **b** directions for different spin channels with optimized lattice constant. Different spin channels self consistent slab calculations have been performed for a **k**-point set equivalent to one **k** point, until obtaining convergence and to four **k** points for DOS convergent calculations. All DOS surface (multilayer) calculations were performed after the surface relaxation calculations.

Each DFH slab (Fig. 1) was constructed by considering three GaAs tetragonal unit cells (four atoms in the cell), surface metallic 1 ML and a vacuum of 8–10 MLs, aligned along the *x* direction. Further details of the method have been published in Ref. [1]. One Ga atomic monocrystal plane in the first and third AsGa unit is substituted with the atomic Mn plane. The atomic structure of $M/Ga_{0.5}Mn_{0.5}As/\ Ga_{0.5}X_{0.5}As\ /Ga_{0.5}Mn_{0.5}As(001)$ (X = As, Cr, Fe and M = Fe, Cr) digital alloy multilayer consists of 14 atomic layers with one Fe

(Cr) layer on Ga-terminated surface. The first metallic plane is located on surface Ga positions and the second one in bcc geometry Fe (Cr) positions.

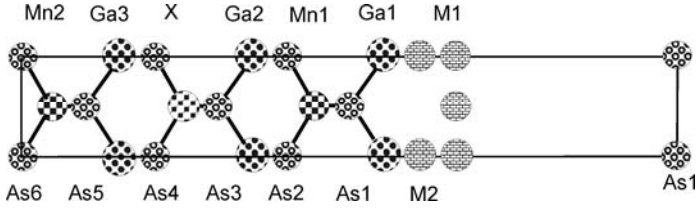

Fig. 1. The geometry of a supercell containing zinc blende 11 atomic ML, 1 ML surface metal and 8 ML vacuum, arranged along the *x*-axis

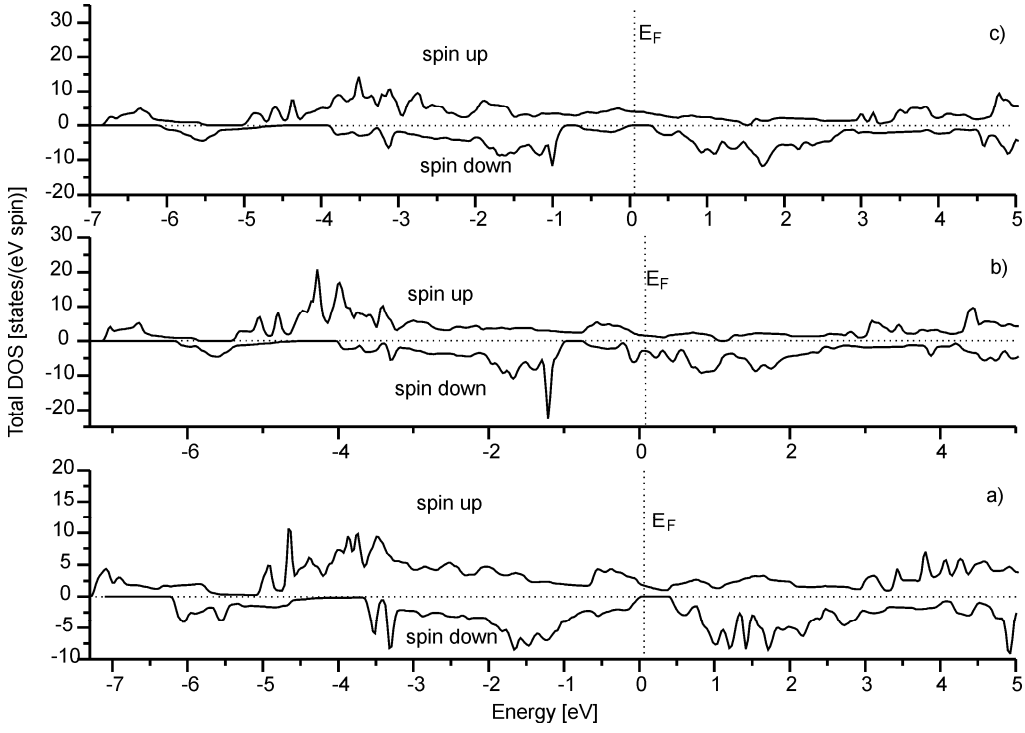

Fig. 2. The DOS functions of zinc blende $Ga_{0.5}Mn_{0.5}As/Ga_{0.5}X_{0.5}As/Ga_{0.5}Mn_{0.5}As(001)$, where atom of X dopant is: a) Ga, b) Cr, c) Fe atom

The total DOS calculations presented in Fig. 2 were performed for the $Ga_{0.5}Mn_{0.5}As$ /$Ga_{0.5}X_{0.5}As$ /$Ga_{0.5}Mn_{0.5}As(001)$ (X = Ga, Fe, Cr) multilayers which simulate DOS function (001) surface calculations. The atomic slab construction from Fig. 1 has no surface metallic monolayer. The specific semiconductor gap of ~ 0.5 eV which is characteristic of half metallic compounds is evident in Fig. 2a (X = Ga) and Fig. 2c (X = Cr) for the minority spin DOS at the Fermi energy level. The half-metallicity is destroyed with 0.5 ML of Fe on the X plane position (Fig. 1) which is evident in

Fig. 2b and the DOS for that a multilayer has a sharp semiconductor character. It was found in experiment that bilayers CrAs and GaAs can be grown in zinc blende structure by molecular epitaxy [9].

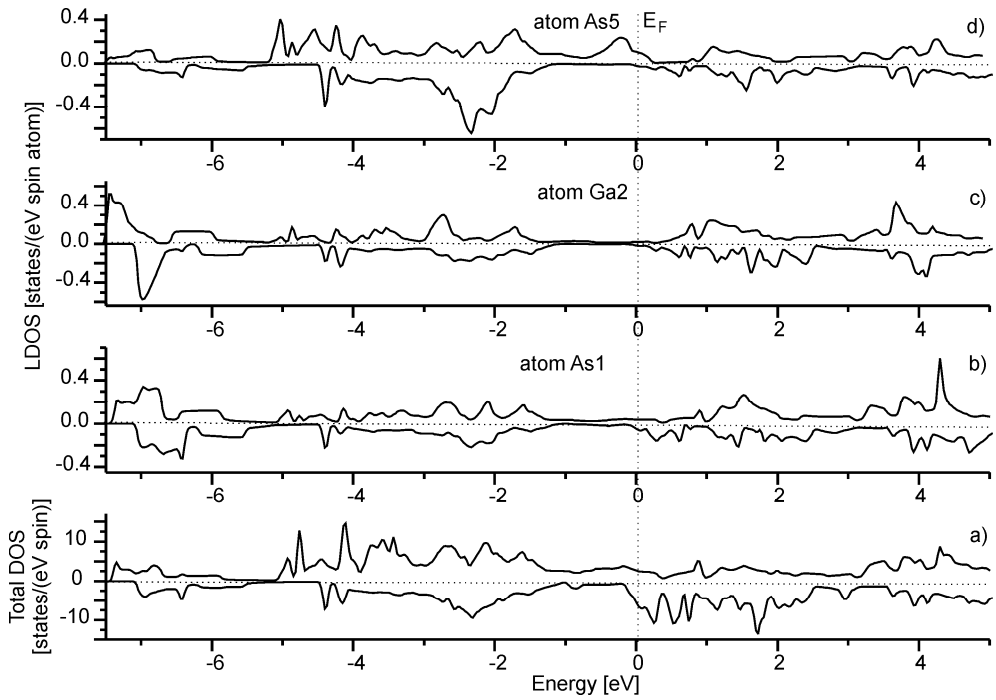

Fig. 3. The DOS functions of ZB Fe/$Ga_{0.5}Mn_{0.5}As$/GaAs/$Ga_{0.5}Mn_{0.5}As$(001):
a) total DOS, b) local DOS for As1 atom, c) the Ga2 atom LDOS, and d) the As5 atom LDOS

Figures 3a–c and 3d show total DOS and local DOS functions for the magnetic states of 1 ML Fe on the Ga-terminated surface. The LDOS are calculated in planes of As1, Ga2 and As5 atoms, and the slab construction for this atomic configuration is explained in Fig. 1. The value of lattice mismatch of α-Fe (*bcc*) which is grown epitaxially on the (001) GaAs is only 1.4% [10] and is preferable for forming heterostructures to that of δ-Fe and γ-Fe, thus we use one of Fe interface atomic plane on Ga surface positions, and one atomic plane of *bcc* Fe geometry.

A similar slab construction is used for Cr/$Ga_{0.5}Mn_{0.5}As$/ GaAs /$Ga_{0.5}Mn_{0.5}As$(001) surface DOS calculation but LDOSs are calculated for Mn1, X = Ga and Mn2 atomic planes and presented in Fig. 4.

The results of calculations of DOS functions in Fig. 3 confirm that 1 ML Fe surface layer deposited on Ga-terminated half metallic zinc blende superlattice destroys the half-metallicity of the entire multilayer. The local DOS function in As1, Ga2 and As5 planes have an evident semiconductor character. Although the minority spin total DOS function in Fig. 4 shows very small semiconductor gap at the E_F level, visibly the LDOS for ferromagnetic dopants Mn1 and Mn2 have a half-metallic character.

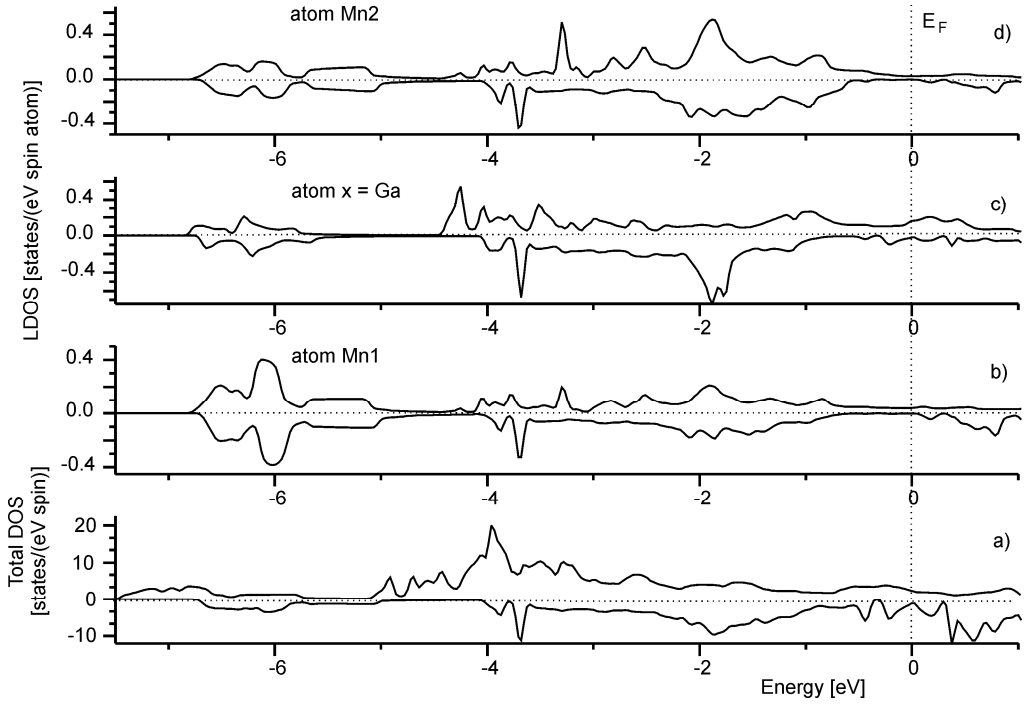

Fig. 4. The DOS functions of ZB Cr/$Ga_{0.5}Mn_{0.5}As$/GaAs/$Ga_{0.5}Mn_{0.5}As$(001):
a) total DOS, b) local DOS for Mn1 atom, c) LDOS for atom X = Ga, and d) the Mn2 atom LDOS

The calculated magnetic moments have the values in the range of (3.9–4.0)μ_B for Mn, (2.9–3.0)μ_B for Fe, and (2.8–3.1)μ_B for Cr atomic spheres in different superlattice geometries.

3. Conclusions

We investigated relaxed surfaces of zinc blende superlattices with ferromagnetic dopants (X = Fe, Cr) and M/$Ga_{0.5}Mn_{0.5}As$/ GaAs /$Ga_{0.5}Mn_{0.5}As$(001) (M = Fe, Cr) multilayers using the self-consistent FLAPW method based on the spin polarized GGA approach for total and local DOS calculations. The main results of the calculations are as follows:

- Zinc blende $Ga_{0.5}Mn_{0.5}As$/ $Ga_{0.5}X_{0.5}As$ /$Ga_{0.5}Mn_{0.5}As$(001) (X = Ga, Cr, Fe) superlattice surfaces simulated by 11 ML atomic system show half-metallic total DOS character for X = Ga and Cr, and a loss of half-metallicity for 0.5 ML of Fe in X atom position.
- The ZB heterostrucrure surface M/$Ga_{0.5}Mn_{0.5}As$/ GaAs /$Ga_{0.5}Mn_{0.5}As$(001) (M = Fe, Cr) with 1 ML metal M deposited on Ga-terminated surface loses of half-metallicity.
- Investigated ZB digital alloys demonstrate ferromagnetic arrangement of their metallic dopants (Mn, Fe, Cr).

References

[1] PEARTON S.J., ABERNATHY C.R., NORTON D.P., HEBART A.F., PARK Y.D., BOATNER L.A., BUDAI J.D., Mat. Sci. Eng. R, 40 (2003), 137.
[2] DIETL T., Europhysics News, 34 (2003), 216.
[3] OHNO H., CHIBA D., MATSUKURA F., OMIYA T., ABE E., DIETL T., OHNO Y., OHTANI K., Nature, 408 (2000), 944.
[4] SANVITO S., HILL N.A., Phys. Rev. Lett., 87 (2001), 267202-1.
[5] QIAN M.C., FONG C.Y., PICKETT W.E., PASK J.E., YANG L.H., DAG S., Phys. Rev. B, 71 (2005), 012414-1.
[6] KANG B.-S., CHUANG J.-S., KANG H.-J., OH S.-K., Phys. Stat. Sol. (b), 242 (2005), 2447.
[7] WRONKA A., Mater. Sci.-Poland, 24 (2006), 725.
[8] BLAHA P., SCHWARZ K., MADSEN G., KVASNICKA D., LUITZ J., *WIEN2k, An Augmented Plane Wave + Local Orbitals Program for Calculating Crystal Properties*, Karlheinz Schwarz, Techn. Universität Wien, Austria, 2001. ISBN 3-9501031-1-2.
[9] MIZUGUCHI M., AKINAGA H., MANAGO T., ONO K., OSHIMA M., SHIRAI M., YURI M., J.LIN H., HSIEH H.H., HEN C.T., J. Appl. Phys., 91 (2002), 7917.
[10] HANEDA S., YAMURA M., HARA K., MUNEKATA H., J. Vac. Sci. Technol. B, 18 (2000), 1.

Received 7 May 2006
Revised 1 September 2006

Materials Science-Poland, *Vol. 25, No. 2, 2007*

Prospect for research on spintronics of U_3As_4 ferromagnet and its semiconducting Th derivatives

P. WIŚNIEWSKI, Z. HENKIE*

Institute of Low Temperature and Structure Research, Polish Academy of Sciences,
P. O. Box 1410, 50-950 Wrocław 2, Poland

Low magnetic field magnetisation along easy magnetic axis [111], Hall resistivity and the effect of magnetic field of different directions on U_3As_4 resistivity along the easy axis as well as along the hard one ([100]) have been examined. The Hall resistivity reaches the highest value $\rho_{H=}$ 1.75 μΩ·m at T = 113 K where it yields the giant anomalous Hall coefficient R_S = 6.25 μΩ·m·T^{-1} and the tangent of the Hall angle of 0.42. Magnetic field exceeding the demagnetisation field H_{demag} < 0.28 T changes the resistivity by up to 36 % at T = 77 K.

Key words: *ferromagnet; electronic transport; uranium compound, magnetic domain effect*

1. Introduction

Studies of magnetic and semiconducting properties in solid-state systems have served as an important test for understanding basic physics and discovering new applications in spintronics [1, 2]. During the last several decades, the anomalous Hall resistivity (AHR) and ferromagnetic anisotropy of resistivity FAR for sd electron systems have been experimentally investigated, to great extent motivated by the technological importance of both effects. On the other hand, these effects originate from anisotropy of the density of states and spin-orbit interaction [3], which can be fairly high in f-electron systems, thus we chose U_3As_4 and its thorium derivatives for AHR and FAR examinations in f-electron systems.

Uranium pnictides with U_3X_4 (X = P, As, Sb, and Bi) crystallise in a cubic structure and show ferromagnetic ordering with strongly anisotropic magnetisation and complex magnetic structures [4]. Two first compounds of the series show noncollinear magnetic structure with effective moment along the [111] axis (easy magnetic axis). The sublattice of U ions is split into 3 further sublattices with magnetic mo-

*Corresponding author, e-mail: Z.Henkie@int.pan.wroc.pl

ments of each tilted by a small angle α from the easy axis to [100], [010] and [001] axes, respectively. The two remaining pnictides show collinear magnetic ordering with the easy magnetic axis [100] and one third of uranium moments higher than the others. In this group of compounds, U_3As_4 has the highest Curie temperature T_C = 198 K, while its α = 3.1°. Magnetic field of 2 T applied along the hard axis at 77 K does not tilt noticeably the magnetic moments from the easy axis but 20 T at 4.2 K causes a spin-reorientation transition [5, 6]. These features favoured a long-standing interest in high-field magnetic properties of the U_3X_4 series. In this paper, we turn to examination of low magnetic field effect on electron transport properties of U_3As_4 because of its strong spin-orbit interaction and high anisotropy of density of states [7] that can be related to the spintronics. First Hall effect [8] and resistivity [9] examinations of U_3As_4 single crystals came before any study of their magnetic structure and should have been re-examined in reference to a previous short report on low-magnetic-field effect on resistivity [10].

2. Experimental

Crystals of U_3As_4 and Th_3As_4 were grown by the method of chemical vapour transport [11, 12]. Their crystal axes were determined with an optical goniometer. Next they were shaped into plates of dimensions 2.5×1.4×0.45 mm^3 along the <110>, <112> and <111> directions, respectively, by cutting with a wire saw and polishing. Magnetisation (M) was measured along <111>, Hall resistivity along <112>, with electrical current along <110>. Two specimens of a pillar shape of about 1 mm^2 cross-sections and 3 mm length along [111] and [100], respectively, were used for determination of resistivity in magnetic fields of various directions. Measurements of $M(T,H)$ were performed using a Quantum Design Magnetic Properties Measurement System, while resistivity and the Hall resistivity were determined using the conventional 4-point DC technique and an electromagnet.

3. Spontaneous Hall effect and ferromagnetic anisotropy of resistivity

The magnetisation was determined for the magnetic field H applied along [111] easy axis perpendicular to the plate of U_3As_4. Data presented in Fig. 1 allowed us to determine (by the shown linear extrapolation) the demagnetization field $H_{demag.}$ = 0.286 T and magnetic moment of U ion μ_U = 1.85 μ_B at 4 K, that can be compared to μ_U = 1.82 μ_B determined by means of neutron diffraction [4].

The Hall resistivity data $\rho_H = (V_H d)/I$ for the plate with the previously established magnetisation are presented in Fig. 2 for magnetic field H = 0.78 T (V_H is the Hall

voltage, *d* is the plate thickness and *I* is the electric current through the plate). Following Ref. 13 we have calculated the anomalous Hall coefficient using formulae (1):

$$\rho_H = R_0 B + R_S 4\pi M \quad \text{for } T < T_C \quad \text{and} \quad \rho_H/H = R_0 + R_S 4\pi\chi(1 + 4\pi\chi N) \quad \text{for} \quad T_C < T \tag{1}$$

The demagnetising field determines the demagnetising factor *N*, i.e., $H_{demag} = 4\pi NM$. R_0 and R_S denote the normal and anomalous Hall coefficients, and χ is the magnetic susceptibility. Previous high temperature studies (up to 450 K) showed that R_0 is by about 4 orders lower than R_S. ρ_H reaches the highest value at 113 K, where it amounts to $R_S = 6.25\ \mu\Omega\cdot m\cdot T^{-1}$. The tangent of the Hall angle at this temperature is of about 0.42.

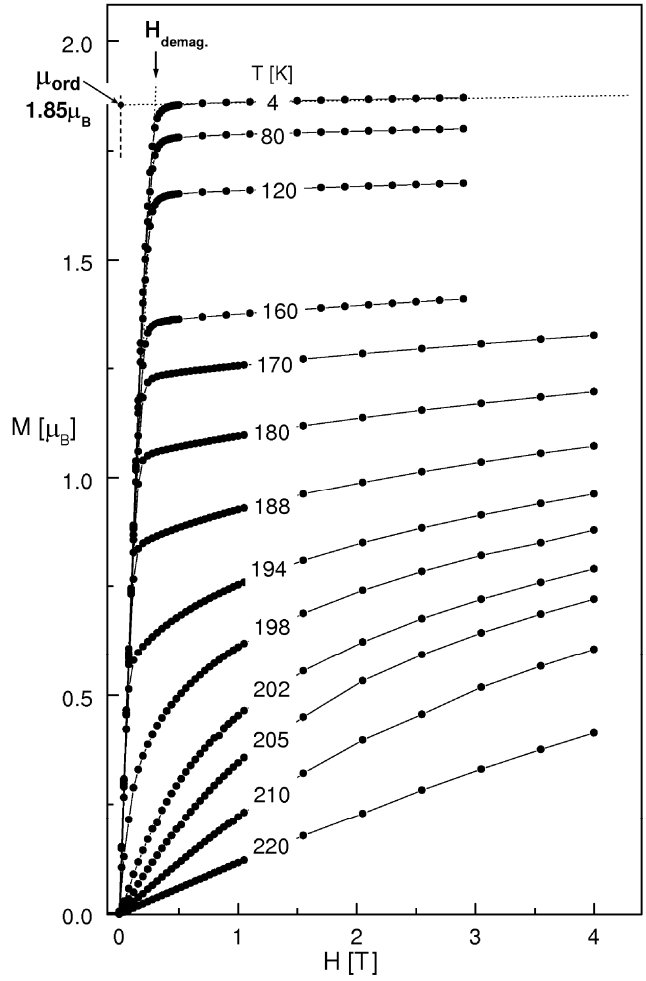

Fig. 1. Magnetisation vs. magnetic field applied along the easy magnetic axis perpendicular to the U_3As_4 plate

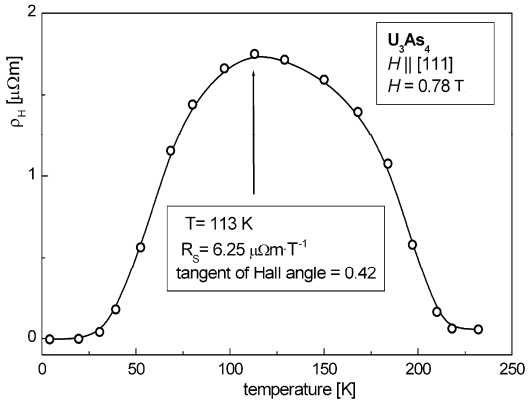

Fig. 2. Temperature dependence of the Hall resistivity for the same plate sample as in Fig. 1

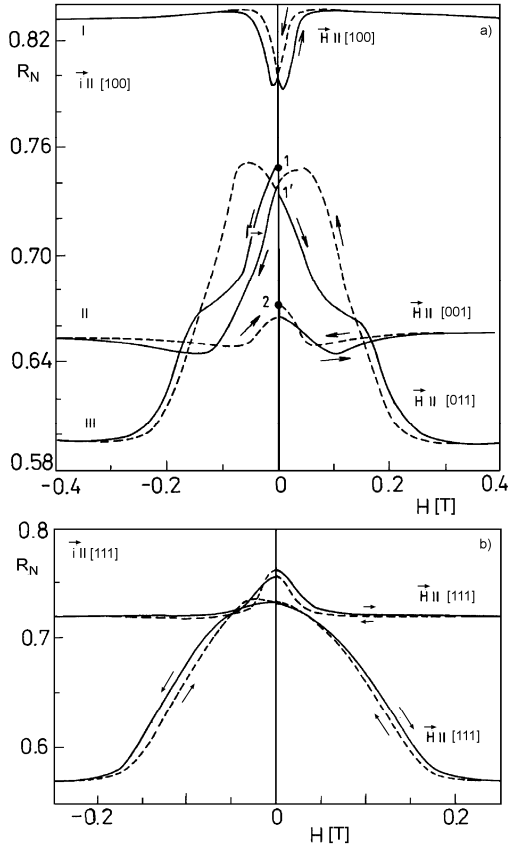

Fig. 3. The dependence of U_3As_4 resistivity measured along: a) [100] axis, b) [111] axis, with the magnetic field along several crystal axes indicated on the plots

Figure 3 shows the dependence of U_3As_4 resistivity along the [100] axis (a) and along [111] axis (b) on the magnetic field in various crystallographic directions at 77 K. The resistivity is normalized to that at T_C i.e. $R_N = \rho(H,T)/\rho(0,T_C)$. In the case of Fig. 3a the direction of magnetic field is in the middle between two ($H \parallel [011]$) or four ($H \parallel [100]$ or $H \parallel [001]$) easy directions. As such a low field cannot tilt the magnetic moment from the easy axis, we assume that in all these cases the saturation of magnetic domain is reached and that three different polydomain states of the sample are attained. We note that the resistivity of the specimen cut along [100] axis saturates in transverse field exceeding the value of $H_{demag.}$ determined, as shown above, from the $M(H)$ dependence (for H along the easy magnetic axis perpendicular to the plate). In the case of Fig. 3b presenting the resistivity of U_3As_4 along the [111] axis, the direction of the field is parallel to the easy axis being either parallel to the pillar specimen axis ($H \parallel [111]$) or at the 70.5º angle with the specimen axis ($H \parallel [11\bar{1}]$). As the magnetisation examination shows, this corresponds to the case of the monodomain state of specimen.

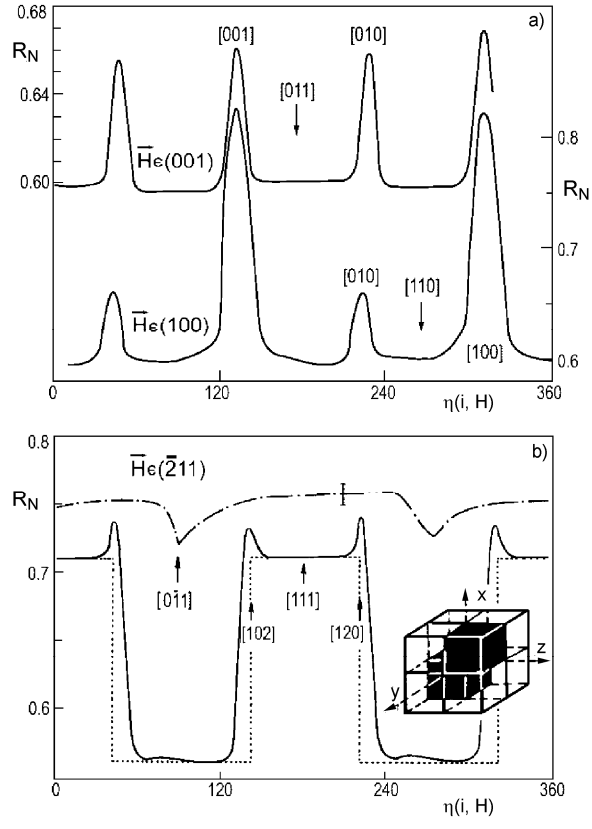

Fig. 4. Resistivity of U_3As_4 measured at T = 77 K along: a) [111] axis, b) [100] axis, magnetic field H = 0.65 T, rotating: a) in (100) or (001) plane for upper and lower curve of (a), respectively, b) in $(\bar{2}11)$ plane

The solid line in Fig. 4b represents the resistivity of U_3As_4 along the [111] axis at 77 K in the field of 0.65 T rotating in the $(\bar{2}11)$ plane, thus missing the $H \,||\, [11\bar{1}]$ direction. The dotted curve represents the resistivity expressed by the formula:

$$R_N(\alpha_i, \beta_i) = a_0 + a_1\left(\sum_{i=1,2,3} \alpha_i\beta_i\right)^2 + 2(a_2 - a_1)\sum_{i\neq j} \alpha_i\beta_i\alpha_j\beta_j \qquad (2)$$

where α_1, α_2 and α_3 are the directional cosines of the spontaneous magnetisation with respect to the crystal axes [14]. The resistivity is measured in the direction determined by β_1, β_2 and β_3 cosines, while a_0, a_1 and a_2 are electrical anisotropy constants. Their values obtained by fitting Eq. (2) to resistivity measured at 77 K are: $a_0 + a_1/3 = 0.600$ and $a_2 = 0.166$. The step behaviour of the dotted curve is due to passing the magnetic field directions from black to white octant in the cube in Fig. 4b, causing the change of the α_i cosines. The dashed curve presents the resistivity after switching off the magnetic field in the given direction. One can see that there is an additional resistivity over the dotted curve in the cases when the polydomain structure is expected, i.e. at zero field or the peaks at the steps of the solid lines.

From the solutions of Eq. (2) for the resistivity of U_3As_4 along [100] axis at 77 K, we find $R_N = a_0 + a_1/3$ for each magnetic domain and we may expect angle-independent resistivity in the field of 0.65 T, which only switches the spotaneous magnetisation from one easy axis to another. As a matter of fact, we observe peaks of R_N on the field rotating by an angle η. We attribute this effect to polydomain structure and giant Hall resistivity, as proposed ealier [15]. The current passing the magnetic domains is bent to different directions in various domains due to different directions of the spontaneous magnetisation. This extends the current path and hence increases the resistivity

4. Remarks and conclusions

Examination of diluted n-type ($m^*/m_o \sim 0.2$) solid solutions of U_3As_4 [16] in semiconducting Th_3As_4 ($\Delta E = 0.43$ eV) showed a location of the $5f$ states well below the conduction band. The recent report on obtaining p-type Th_3As_4 with an effective mass of the carrier higher by one order of magnitude seems to open a new ferromagnetic semiconductor field of research.

U_3As_4 exhibits a giant anomalous Hall effect. AHR reaches the highest value $\rho_H = 1.75$ μΩm at temperature $T = 113$ K, where it yields giant spontaneous Hall coefficient $R_S = 6.25$ μΩ·m·T^{-1}. The tangent of the Hall angle at this temperature is about 0.42. On the other hand, the magnetic field of 0.3 T at 77 K is sufficient to switch the magnetisation of any domain to an easy magnetic axis closest to the field direction. This changes the resistivity due to FAR by up to 30 %. Additional components of

variation of the resistivity of the same order as the FAR contribute to the AHR. This offers various possibilities to modify the resistivity of U_3As_4.

References

[1] DIETL T., [in:] *Advances in Solid State Physics*, B. Kramer (Ed.), Springer, Berlin, 2003, p. 413
[2] ZUTIC I., FABIAN J., SARMA S.D., Rev. Mod. Phys., 76 (2004), 323.
[3] BANHART J., EBERT H., Europhys. Lett., 32 (1995), 517.
[4] WIŚNIEWSKI P., GUKASOW A., HENKIE Z., Phys. Rev. B 60 (1999), 6242.
[5] BELOV K.P., HENKIE Z., DMITRIEVSKY A.S., LEVITIN R.Z., TRZEBIATOWSKI W., Zh. eksper. teor. fiz., 64 (1973), 1351.
[6] TROC R., SZNAJD J., NOVOTNY P., MYDLARZ T., J. Magn. Magn. Mater. 23 (1981), 129.
[7] SANDRATSKII L.M., KÜBLER J., Phys. Rev. B, 55 (1997), 11395.
[8] HENKIE Z., Bull. Acad. Polon. Sci., ser. sci. chim., 20 (1972), 531.
[9] HENKIE Z., BAZAN C., phys. stat. sol. (a), 5 (1971), 259.
[10] HENKIE Z., Physica B, 102 (1980), 329.
[11] HENKIE Z., Roczn. Chem., 42 (1968), 363.
[12] HENKIE Z., MARKOWSKI P.J., J. Crystal Growth, 41 (1977), 303.
[13] RHYNE J.J., Phys. Rev., 172 (1968), 523.
[14] JAN J.-P., [in:] *Solid State Physics*, F. Seitz and D. Turnbull (Eds.), 5 (1957), 1.
[15] BERGER L., J. Appl. Phys., 49 (1978), 2156.
[16] MARKOWSKI P.J., HENKIE Z., WOJAKOWSKI A., Solid State Commun., 32 (1979), 1119.

Received 7 May 2006
Revised 1 September 2006

Materials Science-Poland, *Vol. 25, No. 2, 2007*

Poisson's ratio of a soft sphere system

K. V. TRETIAKOV, K. W. WOJCIECHOWSKI*

Institute of Molecular Physics, Polish Academy of Sciences,
ul. Smoluchowskiego 17, 60-179 Poznań, Poland

Monte Carlo simulations of soft spheres interacting through inverse power potentials, $u(r) \propto r^{-n}$, have been performed. Poisson's ratio of the soft sphere face-centred cubic crystals were determined using the constant pressure ensemble with variable box shape. It was shown that at high densities, particle motions decrease Poisson's ratio with respect to the static case which corresponds to zero temperature. It was also shown that increasing the exponent n in the potential, one can decrease Poisson's ratio.

Key words: *soft sphere; inverse power potential; elastic constant; Poisson's ratio*

1. Introduction

In recent years, quickly growing interest in the systems interacting through the inverse power potential has been observed in the colloid and interface science communities. One of the reasons is that particles of different softness can be used for various applications. In the present work, we study Poisson's ratio of three-dimensional soft spheres in the face-centred cubic phase (fcc). The studied system interacts by the inverse power potential [1–7]:

$$u(r) = \varepsilon \left(\frac{\sigma}{r} \right)^n \tag{1}$$

where r is the separation between two particles, σ is the particle diameter, ε sets the energy scale and $n > 0$ is a parameter determining the potential hardness (the softness is proportional to $1/n$).

This work is a part of a project concentrating on the investigation of Poisson's ratio in various model systems. We expect that studies of simple and well defined models constitute a way to a better understanding and description of a new class of mate-

*Corresponding author, e-mail: kww@ifmpan.poznan.pl

rials [8–14] which exhibit anomalous (negative) Poisson's ratio [15]. Such unusual materials are of interest both for the fundamental research and for applications. Searching for mechanisms which can decrease Poisson's ratio of model systems can help in designing new materials with negative Poisson's ratios.

The aim of the paper is to investigate the influence of the exponent n on Poisson's ratio of the fcc soft sphere crystalline phase as well as to determine explicitly the influence of temperature on Poisson's ratio of the hard sphere system.

2. Details of simulation

The Monte Carlo (MC) simulations were performed in the variable box shape (NpT) ensemble by a method following the Parrinello-Rahman idea of averaging strain fluctuations [16] which was further developed in Refs. [17, 18]. The version of this method applied here is based on Refs. [19–21].

The MC simulation was carried out for particles interacting through the inverse power potential (1) for several values of n: 12, 16, 24, 48, 96, 192, 384, 768. In all the simulations reduced units of the energy $E^*=E/\varepsilon$, the dimensionless pressure $p^*=p\sigma^3/\varepsilon$ and the dimensionless temperature $T^*=k_BT/\varepsilon$ were used. A standard interaction cut off of 2.5 for $n \leq 48$, and 2.0 for $n > 48$ was applied.

Two kinds of trial motions were used. The first concerned changes of the sphere positions, and its acceptance ratio was kept close to 30%. The second kind of the motions corresponded to changes of the components of the symmetric box matrix and was tried about $N^{1/2}$ times less frequently than the sphere motions. The box motions determined the size and the shape of the box and their acceptance ratio was close to 20%.

We simulated systems of 256 particles with periodic boundary condition whose $T = 0$ ground state configuration is the fcc. lattice occupying a cubic box of the side $4\sqrt{2}a_0$ (a_0 is the nearest-neighbour distance). It has been shown [22] that simulations of systems as small as $N = 256$ give the elastic constants and Poisson's ratios differing by only a few percent from the results obtained by extrapolation to the $N \to \infty$ limit.

Typical lengths of the runs were equal 5×10^6 trial steps per particle (Monte Carlo cycles), after equilibration of 10^6 MC cycles.

3. Results and discussion

The question concerning the influence of particle motions (i.e. positive temperature) on the elastic properties of the soft sphere system can be answered by considering a static, i.e. zero temperature fcc lattice whose nearest-neighbouring sites (distanced by a) interact by the potential (1). The expressions for pressure, bulk modulus, elastic constants, and Poisson's ratio of such a lattice can be found in Ref. [22]. Here, we only recollect Poisson's ratio of the static model:

$$\nu = \frac{n+6}{3n+6} \tag{2}$$

It is worth noting that Poisson's ratio of a static model equals 1/3 in the limit $n \to \infty$.

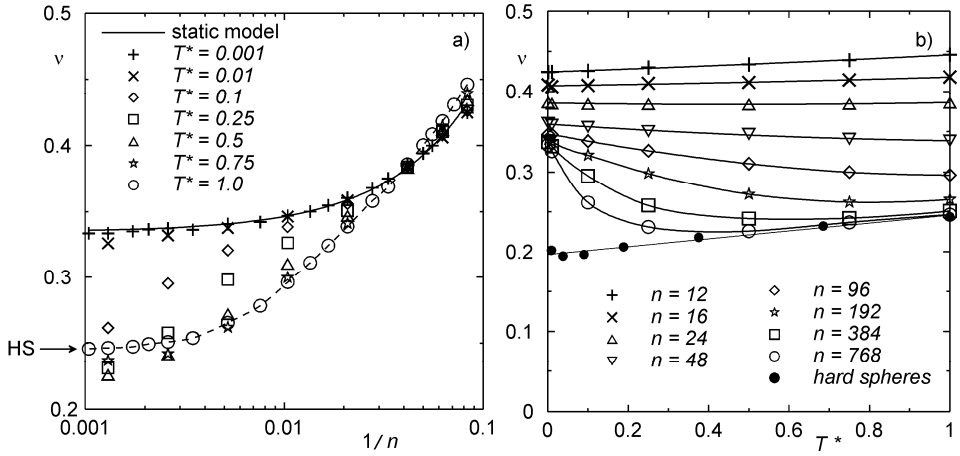

Fig. 1. Poisson's ratio vs. softness (a) and temperature (b) at $p^* = 37.69$; HS – hard spheres

In Figure 1a, Poisson's ratio of the soft sphere systems at the same pressure is plotted versus the softness parameter $1/n$. One can see that when $T^* \to 0$, the limiting values of Poisson's ratio for $n \to \infty$ tend towards the values of the static model. When $T^* \to 1$, Poisson's ratio tends to its value obtained for the hard sphere system at the same pressure. An interesting conclusion which follows from this observation (see also Fig. 1b) is that when $n \to \infty$ there is a discontinuity ("jump") of Poisson's ratio between its value 1/3 obtained for $T = 0$ for any finite n and the value $\nu \approx 0.2$ obtained for $T > 0$ for hard spheres [22]. A detailed analysis of this surprising effect will be made in a separate work. For large n ($n > 384$) and for temperatures in the range $0.25 \le T^* \le 0.75$, the values of Poisson's ratio are lower then those obtained in the hard sphere limit ($n \to \infty$). In the latter case, Poisson's ratio is lower than that for the static system. A similar effect has been observed for the soft disk system in two dimensions [23].

The temperature dependence of Poisson's ratio is shown in Fig. 1b. An increase of the power n in the interaction potential leads to a decrease of Poisson's ratio for soft spheres in the whole temperature range considered. It can be also seen that by increasing the temperature in the range $0 \le T \le 0.2$, one can decrease Poisson's ratio of soft spheres with respect to the static case (i.e. to the zero temperature limit) for $n \ge 25$.

4. Summary and conclusions

Poisson's ratios were determined for a wide range of the softness parameter ($1/n$) of the soft sphere potential and for a wide range of temperatures. These data can be used to construct temperature-softness dependence of this property.

Simulations of the soft spheres indicate that at $T^* = 0.001$, the difference between Poisson's ratio for that model and for the static model is less than 2% when $n \geq 12$. On the other hand, simulations of the soft spheres at $T^* = 1$ show that Poisson's ratio of hard spheres differs by less than 2% from that of the soft sphere system when $n \geq 384$.

We have shown that by introducing particle motions (i.e. by rising the temperature from $T = 0$ to small positive values, $T > 0$), one can decrease Poisson's ratio of the soft sphere system with respect to the static case (i.e. to the zero temperature case) for finite $n \geq 25$. We have also found that by increasing the exponent n in the interaction potential, one can decrease Poisson's ratio at high pressures/low temperatures.

Acknowledgements

This work was partially supported by the grant 4T11F01023 of the Polish Committee for Scientific Research (KBN). Part of the calculations was performed at the Poznań Supercomputing and Networking Center (PCSS).

References

[1] HOOVER W.G., ROSS M., JOHNSON K.W., HENDERSON D., BARKER J.A., BROWN B.C., J. Chem. Phys., 52 (1970), 4931.
[2] CAPE J.N., WOODCOCK L.V., Chem. Phys. Lett., 59 (1978), 271.
[3] HEYES D.M., J. Chem. Phys., 107 (1997), 1963.
[4] BRAŃKA A.C., HEYES D.M., Phys. Rev. E, 69 (2004), 021202.
[5] CARDENAS M., TOSI M.P., Phys. Lett. A, 336 (2005), 423.
[6] HYNNINEN A.-P., DIJKSTRA M., Phys. Rev. Lett., 94 (2005), 138303.
[7] DAVIDCHACH R.L., LAIRD B.B., Phys. Rev. Lett., 94 (2005), 086102.
[8] LAKES R., Adv. Mater., 5 (1993), 293.
[9] BAUGHMAN R.H., SHACKLETTE J.M., ZAKHIDOV A.A., STAFSTROM S., Nature, 392 (1998), 362.
[10] EVANS K.E., ALDERSON A., Adv. Mater., 12 (2000), 617.
[11] EVANS K.E., ALDERSON K.L., Eng. Sci. Educ. J., 4 (2000), 148.
[12] WOJCIECHOWSKI K.W., [in:] *Properties and Applications of Nanocrystalline Alloys from Amorphous Precursors*, B. Idzikowski, P. Švec, M. Miglierini (Eds.), Kluwer, Dordrecht, 2005, pp. 241–252.
[13] KONYOK D.A., WOJCIECHOWSKI K.W., PLESKACHEVSKII Y.M., SHILKO S.V., Mekh. Kompoz. Mater. Konstr., 10 (2004), 35 (in Russian).
[14] See, e.g., http://www.ifmpan.poznan.pl/zp10/auxet/ main.html.
[15] LANDAU L.D., LIFSHITS E.M., KOSEVICH A.M., PITAEVSKII I.P., *Theory of Elasticity*, Pergamon Press, London, 1986.
[16] PARRINELLO M., RAHMAN A., J. Chem. Phys., 76 (1982), 2662.
[17] RAY J.R., RAHMAN A., J. Chem. Phys., 80 (1984), 4423.
[18] RAY J.R., RAHMAN A., J. Chem. Phys., 82 (1985), 4243.
[19] WOJCIECHOWSKI K.W., TRETIAKOV K.V., Comput. Phys. Commun., 121–122 (1999), 528.
[20] WOJCIECHOWSKI K.W., Comp. Meth. Sci. Technol., 8 (2002), 77.
[21] WOJCIECHOWSKI K.W., TRETIAKOV K.V., BRAŃKA A.C., KOWALIK M., J. Chem. Phys., 119 (2003), 939.
[22] TRETIAKOV K.V., WOJCIECHOWSKI K.W., J. Chem. Phys., 123 (2005), 074509.
[23] TRETIAKOV K.V., WOJCIECHOWSKI K.W., unpublished results.

Received 7 May 2006
Revised 1 September 2006

Materials Science-Poland, *Vol. 25, No. 2, 2007*

Interference and Coulomb correlation effects in spin-polarized transport through coupled quantum dots

P. TROCHA[1*], J. BARNAŚ[1,2]

[1]Department of Physics, Adam Mickiewicz University, ul. Umultowska 85, 61-614 Poznań, Poland

[2]Institute of Molecular Physics, Polish Academy of Sciences,
ul. Smoluchowskiego 17, 60-179 Poznań, Poland

Spin-dependent transport through two coupled single-level quantum dots attached to ferromagnetic leads with collinear (parallel and antiparallel) magnetizations is analyzed theoretically. The intra-dot Coulomb correlation is taken into account, whereas the inter-dot Coulomb repulsion is neglected. Transport characteristics, including conductance and tunnel magnetoresistance associated with the magnetization rotation from parallel to antiparallel configurations, are calculated by the noneqiulibrium Green function technique. The relevant Green functions are derived by the equation of motion method in the Hartree–Fock approximation. We have found a splitting of the Fano peak, induced by the intra-dot Coulomb interaction. Apart from this, the intra-dot electron correlations are shown to lead to an enhancement of the tunnel magnetoresistance effect.

Key words: *quantum dot; tunnel magnetoresistance; Fano effect*

1. Introduction

The Fano effect originates from quantum interference between resonant and non-resonant transmission processes [1]. The effect appears in experiments as an asymmetric line shape of the transmission spectra. Owing to a tunability of the parameters describing quantum dots (QDs), experimental investigation of the Fano effect in systems including QDs offers new possibilities, not accessible in traditional situations.

The Fano effect in electrical conductance occurs when the phase of electron wave in the non-resonant channel changes insignificantly within the energy Γ centred at the resonance level, where Γ stands for the discrete level width. The Fano line shape in various QD systems has been recently observed experimentally, and the experiments initiated extensive theoretical works on the coherent transport through coupled QDs

*Corresponding author, e-mail: piotrtroch@o2.pl

[2–4]. However, in most theoretical works, the electron–electron interaction was neglected. Moreover, the considered situations were limited to transport through two quantum dots coupled either in series or in parallel to nonmagnetic electron reservoirs. The electron correlations in two QDs coupled in series to nonmagnetic leads have been taken into account in a recent paper [5]. As concerns transport through double quantum dots (DQDs) attached to magnetic leads, only a few papers have addressed this issue up to now [6–8].

In this paper we consider electronic transport through two QDs which are coupled to two ferromagnetic leads. The tunnel barrier between the dots is assumed to be magnetic, hence the inter-dot hopping parameter is spin dependent. The considerations are limited to QDs with vanishing inter-dot Coulomb interaction, while the intra-dot electron correlation is taken into account. Transport characteristics in the linear response regime are calculated using the Green function formalism [9–13]. Since the systems with Coulomb interaction usually cannot be treated exactly, we applied the Hartree–Fock approximation scheme to calculate the Green functions from the relevant equations of motion. The average values of the occupation numbers (which enter the expressions for the Green functions) have been calculated self-consistently.

2. Model and analytical solution

We consider two single-level quantum dots attached to ferromagnetic leads, and for simplicity we restrict our considerations to the case where magnetic moments of the leads are either parallel or antiparallel. The system is then described by Hamiltonian of the general form $H = H_{\text{leads}} + H_{\text{DQD}} + H_{\text{tunnel}}$. The term H_{leads} describes the left (L) and right (R) electrodes in the non-interacting quasi-particle approximation, $H_{\text{leads}} = H_L + H_R$, with $H_\alpha = \sum_{k\sigma} \varepsilon_{k\alpha\sigma} c^+_{k\alpha\sigma} c_{k\alpha\sigma}$ (for $\alpha = L, R$). Here, $c^+_{k\alpha\sigma}$ ($c_{k\alpha\sigma}$) is the creation (annihilation) operator of an electron with the wave number k and spin σ in the lead α, whereas $\varepsilon_{k\alpha\sigma}$ denotes the corresponding single-particle energy.

The second term of the Hamiltonian describes the two coupled quantum dots:

$$H_{DQD} = \sum_{i\sigma} \varepsilon_{i\sigma} d^+_{i\sigma} d_{i\sigma} + \sum_{\sigma} (t_\sigma d^+_{1\sigma} d_{2\sigma} + h.c.) + \sum_i U_i n_{i\sigma} n_{i\bar{\sigma}} \tag{1}$$

where $\varepsilon_{i\sigma}$ is the energy of an ith dot level, t_σ is the inter-dot hopping parameter, and $n_{i\sigma} \equiv d^+_{i\sigma} d_{i\sigma}$ is the particle number operator. Both t_σ and $\varepsilon_{i\sigma}$ are assumed to be spin-dependent in a general case. The last term in Eq. (1) describes the intra-dot Coulomb interactions, with U_i ($i = 1, 2$) denoting the corresponding Coulomb integrals.

The last term of the Hamiltonian, H_{tunnel}, describes electron tunneling from the leads to dots (and *vice versa*), and takes the form:

$$H_{\text{tunnel}} = \sum_{k\alpha} \sum_{i\sigma} \left(V^\alpha_{ik\sigma} c^+_{k\alpha\sigma} d_{i\sigma} + h.c. \right) \tag{2}$$

where $V^{\alpha}_{ik\sigma}$ is the relevant matrix element. Coupling of the dots to external leads can be parameterized in terms of $\Gamma^{\alpha}_{ij\sigma}(\varepsilon) = 2\pi \sum_k V^{\alpha}_{ik\sigma} V^{\alpha *}_{jk\sigma} \delta(\varepsilon - \varepsilon_{k\alpha\sigma})$. We assume that $\Gamma^{\alpha}_{ij\sigma}(\varepsilon)$ is constant within the energy band, $\Gamma^{\alpha}_{ij\sigma}(\varepsilon) = \Gamma^{\alpha}_{ij\sigma}$ = const for $\varepsilon \in \langle -D, D \rangle$, and $\Gamma^{\alpha}_{ij\sigma}(\varepsilon) = 0$ otherwise. Here, 2D denotes the electron band width in the electrodes.

Electric current J flowing through the system can be determined from the following standard formula [12, 13]:

$$J = \sum_{\sigma} J_{\sigma} = \frac{ie}{2\hbar} \sum_{\sigma} \int \frac{d\varepsilon}{2\pi} \mathrm{Tr} \Big\{ \Big[\mathbf{\Gamma}^{L}_{\sigma} - \mathbf{\Gamma}^{R}_{\sigma} \Big] \mathbf{G}^{<}_{\sigma}(\varepsilon) + \Big[f_L(\varepsilon) \mathbf{\Gamma}^{L}_{\sigma} - f_R(\varepsilon) \mathbf{\Gamma}^{R}_{\sigma} \Big] \Big[\mathbf{G}^{r}_{\sigma}(\varepsilon) - \mathbf{G}^{a}_{\sigma}(\varepsilon) \Big] \Big\} \tag{3}$$

where $f_{\alpha}(\varepsilon) = \Big[\exp\big\{ (\varepsilon - \mu_{\alpha})/k_B T \big\} + 1 \Big]^{-1}$ is the Fermi–Dirac distribution function in the lead α, $\mathbf{G}^{<}_{\sigma}(\varepsilon)$ and $\mathbf{G}^{r(a)}_{\sigma}(\varepsilon)$ are the Fourier transforms of the lesser and retarded (advanced) Green functions of the dots, and Γ^{α}_{σ} describes coupling of the dots to the lead α ($\alpha = L,R$),

$$\mathbf{\Gamma}^{\alpha}_{\sigma} = \begin{pmatrix} \Gamma^{\alpha}_{11\sigma} & \sqrt{\Gamma^{\alpha}_{11\sigma} \Gamma^{\alpha}_{22\sigma}} \\ \sqrt{\Gamma^{\alpha}_{11\sigma} \Gamma^{\alpha}_{22\sigma}} & \Gamma^{\alpha}_{22\sigma} \end{pmatrix} \tag{4}$$

In the parallel magnetic configuration one can write:

$$\Gamma^{L}_{11\sigma} = \Gamma_0 (1 \pm p_L), \qquad \Gamma^{L}_{22\sigma} = \beta \Gamma_0 (1 \pm p_L)$$

$$\Gamma^{L}_{12\sigma} = \Gamma^{L}_{21\sigma} = \Gamma_0 \sqrt{\beta} (1 \pm p_L), \qquad \Gamma^{R}_{11\sigma} = \gamma\beta \Gamma_0 (1 \pm p_R)$$

$$\Gamma^{R}_{12\sigma} = \Gamma^{R}_{21\sigma} = \gamma \sqrt{\beta} \Gamma_0 \sqrt{\beta} (1 \pm p_R), \qquad \Gamma^{R}_{22\sigma} = \gamma \Gamma_0 (1 \pm p_R)$$

for $\sigma = \uparrow$ (upper sign) and $\sigma = \downarrow$ (lower sign). Here, p_{α} is the polarization strength of the αth lead, Γ_0 is a constant, the parameter β takes into account the difference in the coupling strengths of a given electrode to the two dots, whereas γ describes asymmetry in the coupling of the dots to the left and right leads. For $\beta = 0$ one finds DQDs connected in series.

To calculate the Green functions $\mathbf{G}^{r(a)}_{\sigma}(\varepsilon)$, we apply the method of equation of motion. First we write the equation of motion for the casual Green function

$$G_{ij\sigma}(\varepsilon) \equiv \langle\langle d_{i\sigma} \mid d^{+}_{j\sigma} \rangle\rangle$$

$$\varepsilon \langle\langle d_{i\sigma} \mid d^{+}_{j\sigma} \rangle\rangle = \langle \{ d_{i\sigma}, d^{+}_{j\sigma} \} \rangle + \langle\langle [d_{i\sigma}, H] \mid d^{+}_{j\sigma} \rangle\rangle \tag{5}$$

where H denotes the full Hamiltonian of the system. Taking into account the explicit form of H, one arrives at the equation

$$\begin{aligned}(\varepsilon-\varepsilon_{i\sigma})\langle\langle d_{i\sigma}\mid d_{j\sigma}^{+}\rangle\rangle=\delta_{ij}+\delta_{i1}t_{\sigma}\langle\langle d_{2\sigma}\mid d_{j\sigma}^{+}\rangle\rangle+\delta_{i2}t_{\sigma}^{*}\langle\langle d_{1\sigma}\mid d_{j\sigma}^{+}\rangle\rangle\\ +\sum_{k\alpha}V_{ik\sigma}^{\alpha*}\langle\langle c_{k\alpha\sigma}\mid d_{j\sigma}^{+}\rangle\rangle+U_{i}\langle\langle n_{i\bar{\sigma}}d_{i\sigma}\mid d_{j\sigma}^{+}\rangle\rangle.\end{aligned}\tag{6}$$

Applying equation of motion to the Green function $\langle\langle c_{k\alpha\sigma}\mid d_{j\sigma}^{+}\rangle\rangle$ one finds

$$\langle\langle c_{k\alpha\sigma}\mid d_{j\sigma}^{+}\rangle\rangle=\frac{1}{\varepsilon-\varepsilon_{k\alpha\sigma}}\sum_{i'}V_{i'k\sigma}^{\alpha}\langle\langle d_{i'\sigma}\mid d_{j\sigma}^{+}\rangle\rangle\tag{7}$$

Now, the Hartree–Fock approximation is applied to the higher-order Green function generated on the right hand side of Eq. (6):

$$\langle\langle n_{i\bar{\sigma}}d_{i\sigma}\mid d_{j\sigma}^{+}\rangle\rangle\approx\langle n_{i\bar{\sigma}}\rangle\langle\langle d_{i\sigma}\mid d_{j\sigma}^{+}\rangle\rangle\tag{8}$$

Applying the above decoupling procedure and introducing:

$$\Sigma_{ij\sigma}=\Sigma_{ij\sigma}^{L}+\Sigma_{ij\sigma}^{R}\tag{9}$$

where

$$\Sigma_{ij\sigma}^{\alpha}=\sum_{k}\frac{V_{ik\sigma}^{\alpha}V_{jk\sigma}^{\alpha*}}{\varepsilon-\varepsilon_{k\alpha\sigma}}\tag{10}$$

one can rewrite Eq.(6) in the form,

$$\begin{aligned}(\varepsilon-\varepsilon_{i\sigma}-U_{i}\langle n_{i\bar{\sigma}}\rangle)\langle\langle d_{i\sigma}\mid d_{j\sigma}^{+}\rangle\rangle=\delta_{ij}+\delta_{i1}t_{\sigma}\langle\langle d_{2\sigma}\mid d_{j\sigma}^{+}\rangle\rangle\\ +\delta_{i2}t_{\sigma}^{*}\langle\langle d_{1\sigma}\mid d_{j\sigma}^{+}\rangle\rangle+\sum_{i'}\Sigma_{i'i\sigma}\langle\langle d_{i'\sigma}\mid d_{j\sigma}^{+}\rangle\rangle\end{aligned}\tag{11}$$

Now, the set of equations is closed and the casual Green function can be calculated. Having found the casual Green function, one can calculate the retarded and advanced Green functions $G_{ij\sigma}^{r(a)}(\varepsilon)$ as $G_{ij\sigma}^{r(a)}(\varepsilon)=G_{ij\sigma}(\varepsilon\pm i0^{+})$. Writing the Green functions in the matrix form one arrives at the following formula:

$$\mathbf{G}_{\sigma}^{r(a)}(\varepsilon)=\frac{1}{\Omega_{r(a)\sigma}^{2}(\varepsilon)}\begin{pmatrix}\varepsilon-\varepsilon_{2\sigma}-\Sigma_{22\sigma}^{r(a)}(\varepsilon)-U_{2}\langle n_{2\bar{\sigma}}\rangle & t_{\sigma}+\Sigma_{21\sigma}^{r(a)}(\varepsilon)\\ t_{\sigma}^{*}+\Sigma_{12\sigma}^{r(a)}(\varepsilon) & \varepsilon-\varepsilon_{1\sigma}-\Sigma_{11\sigma}^{r(a)}(\varepsilon)-U_{1}\langle n_{1\bar{\sigma}}\rangle\end{pmatrix}\tag{12}$$

where $\Omega_{r(a)\sigma}$ is defined as

$$\Omega^2_{r(a)\sigma}(\varepsilon) = (\varepsilon - \varepsilon_{1\sigma} - \Sigma^{r(a)}_{11\sigma} - U_1\langle n_{1\bar{\sigma}}\rangle)(\varepsilon - \varepsilon_{2\sigma} - \Sigma^{r(a)}_{22\sigma} - U_2\langle n_{2\bar{\sigma}}\rangle) - (t_\sigma + \Sigma^{r(a)}_{21\sigma})(t^*_\sigma + \Sigma^{r(a)}_{12\sigma}) \tag{13}$$

In Equation (13), the energy dependence of the self energies $\Sigma^{r(a)}_{ij\sigma}$ is not indicated explicitly for clarity reasons. The self-energies have the form:

$$\Sigma^{r(a)}_{ij\sigma}(\varepsilon) = \Lambda_{ij\sigma}(\varepsilon) \mp \frac{i}{2}\Gamma_{ij\sigma} \tag{14}$$

with

$$\Gamma_{ij\sigma} = \Gamma^L_{ij\sigma} + \Gamma^R_{ij\sigma} \tag{15}$$

and

$$\Lambda_{ij\sigma}(\varepsilon) = \frac{1}{2\pi}\Gamma_{ij\sigma}\ln\left(\frac{D-\varepsilon}{D+\varepsilon}\right) \tag{16}$$

The lesser Green function $\mathbf{G}^<_\sigma(\varepsilon)$ can be derived from the Keldysh equation:

$$\mathbf{G}^<_\sigma(\varepsilon) = \mathbf{G}^r_\sigma(\varepsilon)\mathbf{\Sigma}^<_\sigma(\varepsilon)\mathbf{G}^a_\sigma(\varepsilon) \tag{17}$$

In the zero bias (equilibrium) limit, the lesser self-energy $\mathbf{\Sigma}^<_\sigma(\varepsilon)$ is given by the expression:

$$\mathbf{\Sigma}^<_\sigma(\varepsilon) = i[\, f_L(\varepsilon)\mathbf{\Gamma}^L_\sigma + f_R(\varepsilon)\mathbf{\Gamma}^R_\sigma]$$

Finally, the average values of the occupation numbers, $\langle n_{i\sigma}\rangle$, have to be calculated self-consistently using the formula

$$\langle n_{i\sigma}\rangle = -i\int\frac{d\varepsilon}{2\pi}G^<_{ii\sigma}(\varepsilon) \tag{18}$$

3. Numerical results

Using the formulas derived above, one can calculate numerically basic transport characteristics, like conductance and tunnel magnetoresistance. The latter quantity describes the change in the system resistance when magnetic configuration of the system varies from parallel to antiparallel, and is described quantitatively by the ratio $(R_{AP}-R_P)/R_P$, where R_{AP} and R_P are the resistances in the antiparallel and parallel magnetic configurations, respectively. For the following discussion, we assume that the dot levels are spin-degenerate and equal, $\varepsilon_{i\sigma} = \varepsilon_0$ (for i = 1, 2 and $\sigma = \uparrow, \downarrow$). The inter-

dot hopping parameter is assumed to be real and independent of the spin orientation, $t_\sigma = t = t^*$ (for $\sigma = \uparrow, \downarrow$), and for numerical calculations we take $t = 0.6$ (the energy in this paper is measured in the units of Γ_0). We note that for positive t, the symmetric (anti-symmetric) state becomes anti-bonding (bonding) – the situation is reversed for negative t. Apart of this, we assume the same spin polarizations of the leads ($p_L = p_R = p = 0.4$), different coupling of a given electrode to the two dots (described by the parameter $\beta = 1/3$), and left-right symmetry of the coupling ($\gamma = 1$). Finally, we assume the same intra-dot Coulomb parameters for both dots: $U_1 = U_2 = U$. We point that the numerical results shown in this paper are valid for temperatures above the corresponding Kondo temperature T_K.

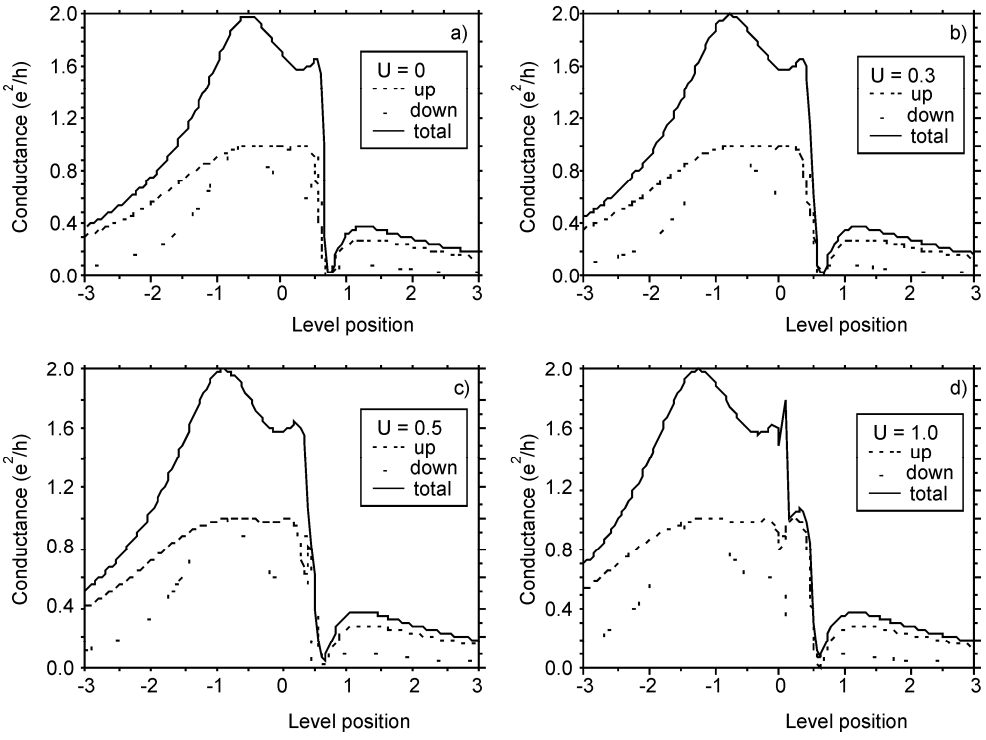

Fig. 1. Linear conductance in the parallel configuration as a function of the position of the dot levels (ε_0), calculated for indicated values of the intra-dot Coulomb repulsion parameter U and for $p = 0.4$, $t = 0.6$, and $k_B T = 0.01161$. The energy is measured in the units of Γ

Let us consider first a noninteracting ($U = 0$) case (see Fig. 1a). The inter-dot coupling lifts the level degeneracy. Consequently, the peak in the density of states becomes split into two components: a broad peak centred at the anti-bonding state and a narrow one corresponding to the bonding state [2, 8]. The conductance associated with the bonding state reveals the antiresonance behaviour with the characteristic Fano line shape clearly seen in Fig. 1a. In turn, the peak associated with the anti-

bonding state is relatively broad. As the asymmetry of the dot coupling to a given electrode is reduced, the width of the anti-bonding (bonding) resonance increases (decreases). Numerical results for $\beta = 1$ (not presented in this paper) show that the resonance corresponding to the bonding state becomes δ-like, while the resonance due to the anti-bonding state acquires the width $\sim 4\Gamma_0$. Since coupling of the dots to external leads is spin-dependent, the corresponding level widths depend on the spin orientation, too. This is the reason why the splitting for the down spin orientation is clearly seen, whereas the one for the spin-up orientation is not well resolved (there is rather an abrupt drop in the conductance for $\varepsilon_0 \sim t$).

Let us discuss now the influence of intra-dot Coulomb repulsion on the picture described above (Fig. 1) for $U > 0$. One can note a splitting of the Fano resonance in the total conductance, which occurs for a sufficiently large Coulomb integral U (of the order or larger than the Fano-line width) and increases with increasing U. On the other hand, no such splitting can be seen for the anti-bonding peak. This is because the line width of the anti-bonding level (strongly coupled to the leads) is much larger than U assumed in Fig. 1. It is also worth noting that no splitting of the Fano peak occurs for a sufficiently small value of U (smaller than the Fano-line width).

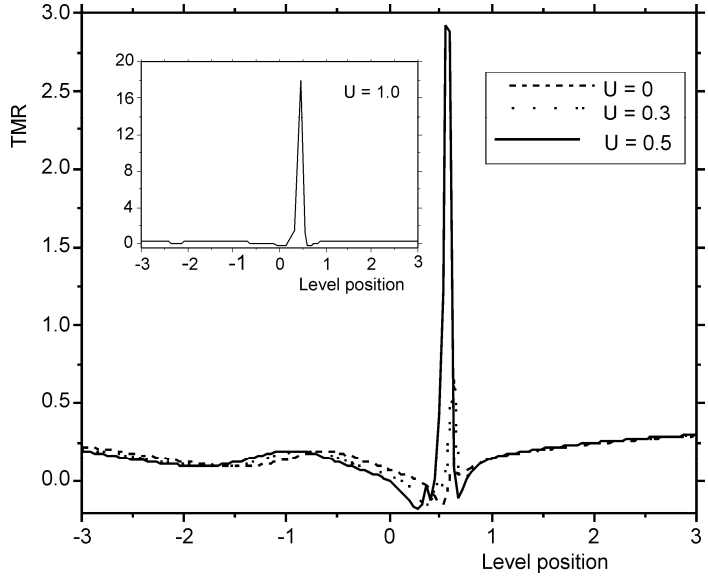

Fig. 2. TMR in the linear response regime as a function of the level position (ε_0) calculated for indicated values of the intra-dot Coulomb parameter U, leads polarization $p = 0.4$, inter-dot coupling $t = 0.6$, and $k_B T = 0.01161$

The splitting of the Fano antiresonance line, induced by the Coulomb correlation in the dots, is also visible in each spin contribution of the conductance, as clearly visible in Fig. 1 for $U = 1$. However, the conductance vanishes only for one component of the split Fano line, while the second component corresponds to a finite and

positive conductance. This behaviour gives rise to the splitting of the Fano line in the total conductance, observed in Fig. 1. The two components of the Fano resonance are well separated, and the separation is of the order of U. Positions of the two Fano resonances are approximately at $\varepsilon_0 \sim t$ and $\varepsilon_0 \sim (t-U)$, as one could expect.

In Figure 2, we show TMR for indicated values of the Coulomb repulsion U. When the dot levels are well above or well below the Fermi level of the leads, TMR tends to the Julliere value, $2p^2/(1-p^2)$, observed in planar magnetic junctions with the same ferromagnetic electrodes. When the dot levels approach the Fermi energy, the situation becomes more complex and TMR displays new features, as for instance some enhancement for $\varepsilon_0 \sim t$.

4. Summary and conclusions

In this paper, we considered transport through two coupled quantum dots attached to ferromagnetic leads. We have found the Lorenzian line shape resonance associated with the anti-bonding state, and the Fano line shape resonance associated with the bonding state. The influence of the resonances on the tunnel magnetoresistance was also analyzed and we found some enhancement of the magnetoresistance due to the intra-dot Coulomb correlations. These results have been obtained in the Hartree-Fock approximation. However, we have also performed calculations using higher order decoupling schemes, in particular we have analyzed transport in the Kondo regime. The details will be presented elsewhere.

Acknowledgements

One of us (P. T.) acknowledges support from the MAGELMAT network. The authors also thank Wojciech Rudziński for help in numerical calculations.

References

[1] FANO U., Phys. Rev. 124 (1961),1866.
[2] LANDRÒN DE GUEVARA M. L., CLARO F., ORELLANA P. A., Phys. Rev. B 67 (2003), 195335.
[3] LU H., LÜ R., ZHU B.-F., J. Phys.: Condens. Matter 18 (2006), 8961.
[4] DING G.-H., KIM C. K., NAHM K., Phys. Rev. B 71 (2005), 205313.
[5] BUŁKA B. R., KOSTYRKO T., Phys. Rev. B 70 (2004), 205333.
[6] TROCHA P., BARNAŚ J., phys. stat. sol. (c), 3 (2006), 113.
[7] TANAKA Y., KAWAKAMI N., Phys. Rev. B 72 (2005), 085304.
[8] WYSOCKI A., BARNAŚ J., Acta Phys. Superfic., 9 (2006), 177.
[9] ŚWIRKOWICZ R., WILCZYŃSKI M., BARNAŚ J., J. Phys. Condens. Matter 18 (2006), 2291.
[10] WEYMANN I., BARNAŚ J., KÖNIG J., MARTINEK J., SCHÖN G., Phys. Rev. B 72 (2005), 113301.
[11] RUDZIŃSKI W., BARNAŚ J., ŚWIRKOWICZ R., WILCZYŃSKI M., Phys. Rev. B 71 (2005), 205307.
[12] MEIR Y., WINGREEN N. S., Phys. Rev. Lett. 68, (1992) 2512.
[13] JAUHO A. -P., WINGREEN N. S., MEIR Y., Phys. Rev. B 50 (1994), 5528.

Received 7 May 2006
Revised 1 September 2006

Materials Science-Poland, *Vol. 25, No. 2, 2007*

Role of the magnetic impurities in $Ni_2Ti_{1-x}Mn_xSn$ Heusler type alloys. Ab-initio calculations

A. JEZIERSKI[1*], P. KOWALEWSKI[2], J. DUBOWIK[1]

[1]Institute of Molecular Physics, Polish Academy of Sciences, 60-179 Poznań, Poland

[2]Faculty of Technical Physics, Poznań University of Technology, 60-965 Poznań, Poland

We have studied electronic and magnetic properties of $Ni_2Ti_{1-x}Mn_xSn$ Heusler type alloys. The calculations were carried out within the density functional theory using ab-initio TB LMTO-ASA method. We found that $Ni_2Ti_{1-x}Mn_xSn$ becomes magnetic for a small manganese concentration $x = 0.0625$.

Key words: *electronic structure; magnetic moment; Heusler alloy; LMTO*

1. Introduction

The electronic and magnetic properties of Ni_2TiSn and Ni_2MnSn Heusler type alloys have been studied in the last years experimentally and theoretically [1–8]. An interesting physical problem is the dependence of the magnetic moment on the distribution of atoms in the unit cell as well as the influence of the impurities on the magnetic and electronic properties. Ni_2TiSn is a Pauli paramagnet, however, in Ni_2MnSn the total magnetic moment is close to 4.0 μ_B [8]. We have analyzed the role of the magnetic impurities on the electronic structure and magnetic properties of the of $Ni_2Ti_{1-x}Mn_xSn$ Heusler type alloys by ab-initio TB LMTO-ASA [9, 10] method. The recent ab-initio calculations [1–3, 5–6] have shown that chemical and atomic disorder strongly modify the electronic and magnetic properties of Heusler-type alloys. In this work, we present the electronic and magnetic properties of $Ni_2Ti_{1-x}Mn_xSn$ as a function of Mn concentration.

2. The model and method of calculations

The electronic and magnetic properties were calculated using the spin polarized tight binding linearised muffin tin orbital (TB LMTO) method [9, 10] within the

*Corresponding author, e-mail: andrzej.jezierski@ifmpan.poznan.pl

atomic sphere approximation (ASA). The band calculations were performed for the theoretical lattice parameters estimated from the minimum of the total energy (Table 1).

Table 1. Lattice parameters for $Ni_2Ti_{1-x}Mn_xSn$ alloys

Parameter	Mn concentration x				
	0.00	0.25	0.50	0.75	1.00
Exp. lattice parameter [a.u.] [4]	11.47	11.45	11.44	11.43	11.42
Lattice parameter para [a.u.]	11.46	11.44	11.42	11.32	11.24
Lattice parameter ferro [a.u.]	11.55	11.32	10.88	10.76	10.39

In the TB LMTO-ASA method, the atomic spheres were chosen in such a way that the sum of the volumes of all the atomic spheres of the unit cell and the overlapping of the atomic spheres was less then 10%. The exchange correlation potential was assumed in the form proposed by von Barth and Hedin [11] and we included in the calculations also the non-local corrections [12]. In the LMTO method, the scalar relativistic approximation for the band electrons and the fully relativistic treatment of the frozen core electrons were assumed during the self-consistent band calculations. The band calculations were performed for 256 k points in the irreducible wedge of the Brillouin zone. Ni_2TiSn and Ni_2MnSn crystallize into $L2_1$ type structure consisting of four interpenetrating *fcc* sublattices. Each *fcc* sublattice can be divided into four simple cubic lattices and hence the $L2_1$ type structure can be considered as a 16-atom unit cell. In the case of the spin polarized system, we have performed the band calculations for 32- and 64-atom unit cells in order to get a smaller value of Mn concentration $x = 0.125$ and $x = 0.0625$, respectively. The titanium and manganese atoms are distributed randomly in Ti–Mn sublattices.

3. Results

Ab-initio band calculations were performed for paramagnetic and ferromagnetic $Ni_2Ti_{1-x}Mn_xSn$ alloys. The theoretical lattice parameters were estimated from the minimum of the total energy and the values are listed in Table 1 for paramagnetic and ferromagnetic systems. The theoretical values of the lattice parameters for the paramagnetic alloy are very close to the experimental results, however, the values obtained for the ferromagnetic systems are lower than the experimental ones. In the supercell model, Ti and Mn atoms were distributed in different sites of Ti–Mn sublattice. The density of states was calculated for the distribution of atoms for which the total energy had a minimum. In Figure 1, we present the total density of states for paramagnetic $Ni_2(Ti_{1-x}Mn_x)Sn$ alloys for $x = 0.0$, 0.25, 0.50, 0.75 and 1.0. The density of states at the Fermi energy $N(E_F)$ increases with the increasing Mn concentration.

We have also performed the spin-polarized calculations for the theoretical lattice parameters (Table 1) from which we estimated the magnetic moment.

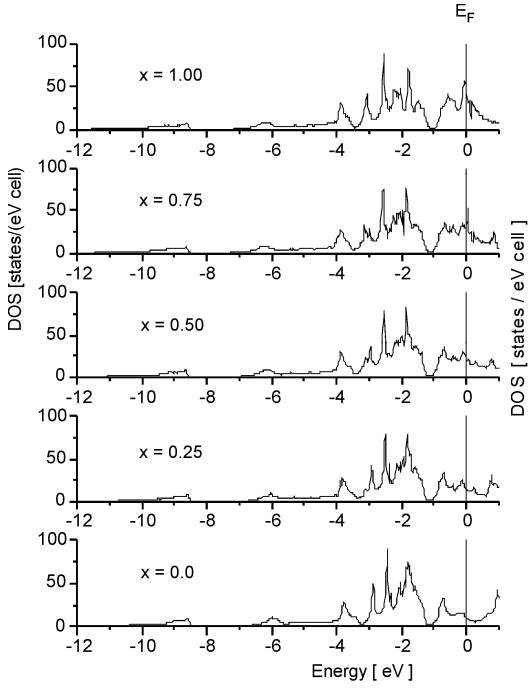

Fig. 1. The total density of states for paramagnetic $Ni_2Ti_{1-x}Mn_xSn$ alloys. The Fermi level is located at $E = 0$

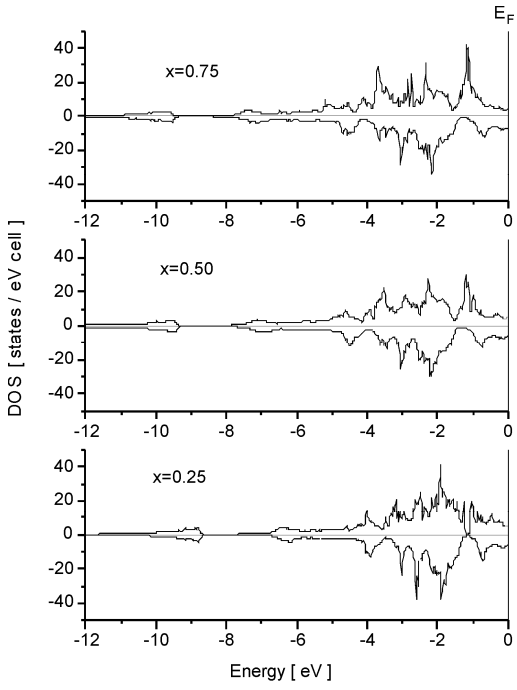

Fig. 2. The total density of states for ferromagnetic $Ni_2Ti_{1-x}Mn_xSn$ alloys. The Fermi level is located at $E = 0$

The total density of states for the ferromagnetic $Ni_2(Ti_{1-x}Mn_x)Sn$ is presented in Fig. 2 for $x = 0.25$, 0.5 and 0.75. We observe the variation of positions of the peaks in the majority spin band. The change of the density of states at the Fermi level for the ferromagnetic alloys is listed in Table 2.

Table 2. Total $N(E_F)$ and partial $N_T(E_F)$ (T = Mn, Ni, Ti, Sn) density of states at the Fermi level (states/eV) for the ferromagnetic $Ni_2Ti_{1-x}Mn_xSn$ alloys

x	$N(E_F)$	Mn	Ni	Ti	Sn
0.00	9.7	0.0	5.75	3.20	0.75
0.25	9.88	0.79	5.79	2.46	0.83
0.50	10.15	1.94	5.69	1.64	0.87
0.75	11.54	2.94	5.78	0.92	0.90
1.00	10.85	3.31	5.78	0.0	0.73

The maximum of $N(E_F)$ is observed for $x = 0.75$. The contribution from Ni and Sn to the total $N(E_F)$ is almost constant, however the contributions from Mn and Ti de-

pend on the concentration x. The total magnetic moment increases with the increase of the Mn concentration (Fig. 3).

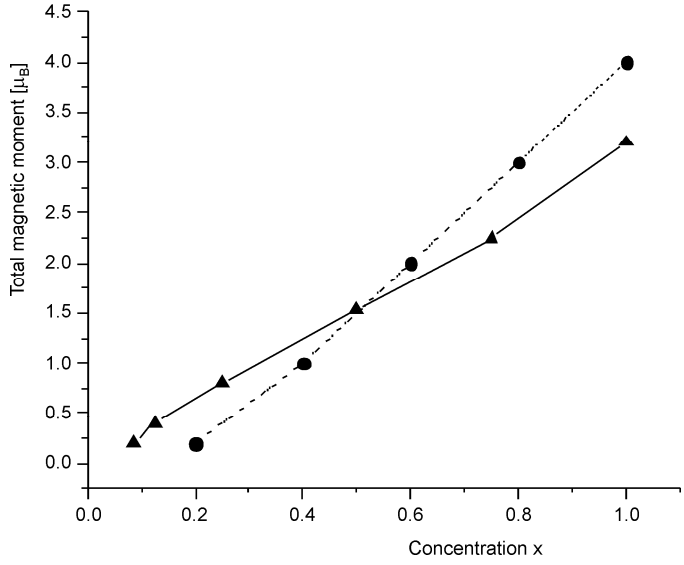

Fig. 3. The dependence of the total magnetic moment on manganese concentration in $Ni_2Ti_{1-x}Mn_xSn$ alloys. The dots denote the experimental data [4], and triangles denote the theoretical values obtained for the theoretical lattice parameters

The triangles denote the theoretical values and the dots represent the experimental data [4]. We observe that $Ni_2(Ti_{1-x}Mn_x)Sn$ becomes magnetic for $x > 0.0625$. The theoretical dependence of the magnetic moments is in a good agreement with the dependence $M_t = (Z_t - 24)\ \mu_B$ for the full-Heusler alloys, where Z_t is the total number of valence electrons per unit cell. Worse agreement between experimental and theoretical values of the total magnetic moments may be connected to the lower values of the theoretical lattice parameter (Table 1).

4. Conclusions

The electronic and magnetic properties of $Ni_2Ti_{1-x}Mn_xSn$ change with the increase of manganese concentration. The spin-polarized ab-initio calculations indicate that a small concentration of manganese ($x = 0.0625$) leads to ferromagnetic ground states of the $Ni_2Ti_{0.94}Mn_{0.06}Sn$ alloy. The theoretical values of the total magnetic moment change linearly with the increase of manganese concentration.

Acknowledgements

We acknowledge the support from the Polish Committee for Scientific Research, Project KBN 4T08C04525. The work is financed from the science resources as a joint program within the scientific network *New materials and sensors for optoelectronics, informatics, energetics and medicine.*

References

[1] JEZIERSKI A., ŚLEBARSKI A., J. Mag. Mag. Mater., 223 (2001), 33.
[2] JEZIERSKI A., J. Phys. Condens. Matter, 12 (2000), 8127.
[3] JEZIERSKI A., phys. stat. sol. b, 196 (1976), 357.
[4] CAMPBELL C.C.M., STAGEN C.V., Can. J. Phys., 54 (1976), 2179.
[5] KUEBLER J., Phys. Rev. B, 67 (2003), 220403.
[6] TOBOLA J., PIERRE J., KOUACOU M.A., KAPRZYK S., SKOLOZDRA R.V., J. Magn. Magn. Mater., 159 (1996), 192.
[7] KRENKE T., ACET M.,WASSERMANN E.F., MOYA X., MANOSA L., PLANES A., Phys. Rev. B, 72 (2005), 014412.
[8] SASIOGLU E., SANDRATSKII L.M., BRUNO P., Phys. Rev. B, 70 (2004), 024427.
[9] ANDERSEN O.K., JEPSEN O., Phys. Rev. Lett., 53, (1984), 2572.
[10] ANDERSEN O.K., JEPSEN O., SOB M., [in:] *Electronic Structure, Its Applications*, M. Yussouff (Ed.), Lecture Notes in Physics, Springer, Berlin, 1987, Vol. 283 p. 2.
[11] VON BARTH U., HEDIN L., J. Phys., C5 (1972), 1629.
[12] HU D., LANGRETH D.C., Phys. Scripta, 32 (1985), 391.

Received 7 May 2006
Revised 1 September 2006

Materials Science-Poland, Vol. 25, No. 2, 2007

Modelling of thermomagnetic curves obtained with Mössbauer spectrometry for two-phase nanocrystalline alloys

T. SZUMIATA*, M. GZIK-SZUMIATA, K. BRZÓZKA

Department of Physics, Technical University of Radom, ul. Krasickiego 54, 26-600 Radom, Poland

Thermomagnetic curves obtained with Mössbauer spectrometry for two-phase nanocrystalline alloys have been analyzed theoretically. The main goal was to understand a slope jump in the temperature dependence of the hyperfine field for crystalline phase of higher Curie temperature at the Curie point of the amorphous phase. We propose a simple model introducing an effective exchange integral for one phase depending on mean spin value in the other phase. We also consider a strong spin polarization of the amorphous phase by penetrating field originating from nanocrystallites. Results of numerical calculations within the mean field approximation (MFA) reproduce qualitatively the experimental curves for nanocrystalline FINEMET and Fe–Nb–B alloys.

Key words: *nanocrystalline alloy; thermomagnetic curve; two-phase coupled system; MFA approximation; Mössbauer spectrometry*

1. Introduction

Nanocrystalline magnetic alloys of two-phase structure have recently been the object of intensive investigations due to their great application potential as soft magnets. The interactions between grains determine the thermomagnetic properties of nanocrystalline alloys which cannot be explained just as a combination of the magnetism of the independent crystalline and amorphous constituents. The main goal of this work is to analyse peculiarities in the thermomagnetic curves of the nanocrystalline phase when exceeding the Curie temperature of the amorphous matrix which is significantly lower than Curie temperature of the crystalline phase. The experimental data [1–5] obtained with Mössbauer spectrometry are interpreted within a simple thermodynamical model with effective exchange interactions considering both spin relaxation effects and spin polarization of the amorphous matrix induced by nanocrystallites.

*Corresponding author, e-mail: t.szumiata@pr.radom.pl

2. Theoretical model

Thermomagnetic behaviour of a ferromagnetic grain immersed in a weakly ferromagnetic matrix has been systematically investigated by Monte Carlo simulations [6]. However, this analysis was limited to the case of low temperature spin ordering. Moreover, a single-grain approximation provided a good description for the matrix only, whereas it did not properly consider possible spin relaxation effects (like superparamagnetism and superferromagnetism), important for nanocrystalline grains. Thus in our work we have implemented a simple phenomenological model which takes into account changes of inter-grain coupling caused by the weakening magnetism of the amorphous matrix at higher temperatures.

We assume that in the system composed of two magnetically coupled phases of distinctly different Curie points, an effective exchange integral (say, for the second phase) takes the form:

$$J_2^{\mathrm{eff}} = J_2(1 + q_2 < S_1^z > /S_1)/(1 + q_2) \tag{1}$$

where J_2 denotes the exchange integral for the second phase (a crystalline one) in a bulk form, $< S_1^z >$ and S_1 signifies the mean value of spin projection and spin number of the first phase (i.e., amorphous matrix), respectively, and q_2 is the dimensionless coupling coefficient which depends on the magnitude of possible spin relaxation and surface effects. At low temperatures $< S_1^z > /S_1 \to 1$ and $J_2^{\mathrm{eff}} \to J_2$, because the entirely ordered magnetic system of the matrix suppresses spin relaxation of the strongly coupled grains. On the other hand, at temperatures above the Curie point T_{C1} of the matrix, $< S_1^z > /S_1 = 0$ and $J_2^{\mathrm{eff}} \to J_2/(1+q_2)$, which means that due to spin relaxation effects the effective exchange integral value drops by the factor $1+q_2$.

The analytical calculations of the mean spin values $< S_1^z >$ and $< S_2^z >$ within the mean field approximation (MFA) applied to Ising spin system lead to the following equations:

$$\begin{aligned} < S_1^z > &= B_{S_1}\left(\frac{z_1 S_1 J_1 \cdot < S_1^z > \cdot (1 + q_1 \cdot < S_2^z > / S_2)/(1 + q_1)}{kT}\right) \\ < S_2^z > &= B_{S_2}\left(\frac{2 z_2 S_2 J_2 \cdot < S_2^z > \cdot (1 + q_2 \cdot < S_1^z > / S_1)/(1 + q_2)}{kT}\right) \end{aligned} \tag{2}$$

where B_{S1} and B_{S2} are the Brillouin functions, z_1 and z_2 are the numbers of the nearest neighbours of the spins in the first and the second magnetic subsystem, respectively, T denotes absolute temperature and k is the Boltzman constant.

In some nanocrystalline alloys the magnetization of the amorphous matrix has been observed not to vanish up to the Curie point of the grains [2–4, 6]. This phenomenon can be explained in terms of magnetic polarization of amorphous residual ma-

trix by penetrating exchange fields (of exponential decay) arising from nanocrystalline grains [6–8]. In our model, we consider these phenomena assuming that effective mean spin field felt by spins in the amorphous matrix is given by:

$$< S_1^z >^{\text{eff}} = < S_1^z > + q_1 < S_2^z > \tag{3}$$

in which q_1 (dimensionless quantity) describes the strength of the penetrating exchange field. Equation (3) has been introduced to the first dependence of Eqs. (2).

3. Model fitting to experimental data

The Mössbauer spectrometry (MS) provides information about magnetization state for various phases of the magnetic system, as well as for different magnetic sublattices within a given phase. Thus, this experimental technique is a very effective tool in the investigation of magnetically coupled systems such as nanocrystalline alloys. We have analyzed the MS thermomagnetic data available in literature for selected nanocrystalline materials and interpreted them in terms of our theoretical model. We have applied a simultaneous fitting procedure of theoretical curves with complete set of parameters for amorphous and nanocrystalline phases. Curves are the result of the numerical solution of the equations system (2) with fixed point method. For simplicity, we set spin numbers for both phases as $S_1 = S_2 = 1$ and coordination numbers as $z_1 = z_2 = 8$.

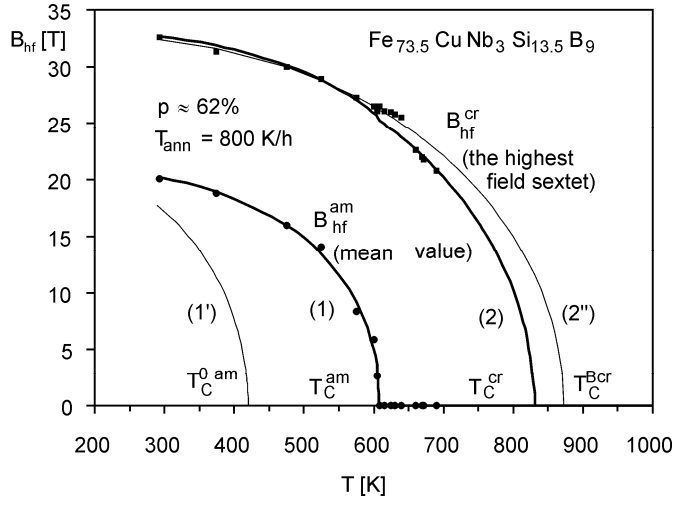

Fig. 1. Mössbauer experimental data [1] (points) and theoretical fits (thick solid lines) of thermal dependence of hyperfine magnetic fields for amorphous (1) and nanocrystalline phases (2) in FINEMET alloy. Additional thin solid line (1′) corresponds to the case of unpolarised amorphous matrix and line (2″) is for the bulk crystalline phase

First, we examined a typical nanocrystalline FINEMET alloy of nominal composition $Fe_{73.5}Cu_1Nb_3Si_{13.5}B_9$. The sample was obtained by the controlled isothermal annealing of metallic glass ribbons rapidly quenched at 803 K during one hour [1]. The crystalline volume fraction was estimated with Mössbauer spectrometry as p = 62%. Temperature dependences of hyperfine fields are shown in Fig. 1. For the amorphous matrix, mean values of broad hyperfine field distributions were calculated from MS spectra. Fe–Si nanocrystalline grains of the disordered DO_3 structure are represented in the MS spectra by several sharp sextets. In Figure 1, only the sextet of the maximum hyperfine field is considered (which corresponds to the Mössbauer nuclei surrounded by 8 iron atoms as their nearest neighbours). Since magnetic phase transition of the amorphous matrix occurs at well defined Curie point ($T_C^{am} \approx 609$ K), a model with an effective exchange interaction of the form (1) for both phases was applied in the fitting procedure. The estimated value of coupling parameter for the amorphous matrix is very high ($q^{am} \approx 0.6$), which means that without the ferromagnetic crystalline phase a Curie temperature of the amorphous matrix would be much lower ($T_C^{0am} \sim 420$ K – see Fig. 1). The experimental temperature dependence of hyperfine field for nanocrystallites shows a peculiar behavior in the vicinity of T_C^{am} of the amorphous matrix. The theoretical curve reproduces the main feature, i.e. a change of decay rate of hyperfine field with increasing temperature in the region above T_C^{am}, which can be interpreted as a signature of the spin relaxation effects in the grains. Though the estimated value $q^{cr} \approx 0.051$ seems to be relatively small, it results in a noticeable reduction of "bulk" value of the Curie temperature extrapolated from the region $T < T_C^{am}$ (i.e. $T_C^{Bcr} \approx 873$ K) to the value $T_C^{cr} \approx 831$ K extrapolated from high temperature part of experimental data set (see Fig. 1). The former value corresponds to the Curie temperature of the bulk Fe–Si alloy of about 22% silicon content, which coincides with Si content in the grains determined on the basis of relative absorption areas of Mössbauer subspectra [1]. However, the theoretical model does not explain the question why the observed drop of the hyperfine field occurs not exactly at T_C^{am} (the hyperfine field almost does not change at all up to the temperature higher by about 30 K with respect to T_C^{am}). We suppose that the crucial role in this phenomenon could be played by the interface region between the grains and the amorphous remainder and it should be considered a third phase in the magnetically coupled system. However, in the case of FINEMET it is very difficult to separate the contribution of the interface layers because of the complexity of the Mössbauer spectra [1, 3, 10].

Another material analyzed in terms of thermomagnetic properties was the nanocrystalline $Fe_{80.5}Nb_7B_{12.5}$ alloy obtained by annealing of as cast amorphous ribbons for 1 hour at 783 K [4]. In the considered material, the grains are simple α-Fe phase of *bcc* structure. Thus they contribute to the Mössbauer spectra as a single Zeeman sextet, whereas the amorphous matrix is represented by very broad hyperfine field distribution (HFD). The volumetric fraction of crystalline phase was determined

as $p \approx 26\%$. High-temperature part of the hyperfine field evolution is presented in Fig. 2, for both the amorphous matrix (mean value of HFD) and nanocrystalline grains.

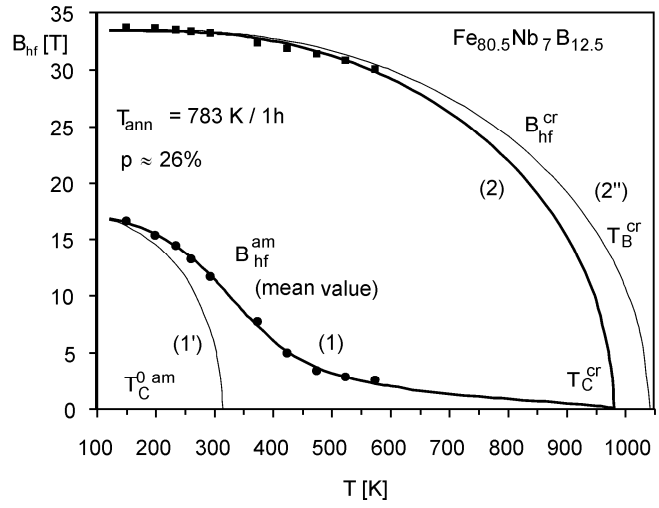

Fig. 2. Mössbauer experimental data [4] (points) and theoretical fits (thick solid lines) of thermal dependence of hyperfine magnetic fields for amorphous (1) and nanocrystalline (2) phases in Fe–Nb–B alloy. Additional thin line (1′) corresponds to the case of unpolarised amorphous matrix and line (2′′) is for the bulk crystalline phase

A very distinct feature is that hyperfine field (and magnetization) of the amorphous matrix does not fall to zero in the temperature range covered in the experiment. This suggests that spin polarization of the matrix by penetrating exchange field resulting from grains is very strong and deep. Thus we applied a model which assumes that an effective mean spin field in the amorphous matrix takes the form of Eq. (3). This model fits very well the experimental points corresponding to the amorphous matrix for $q^{am} \approx 0.13$. Within our model the Curie temperature for amorphous matrix $T_C^{0\,am}$ without inter-phase magnetic coupling would be only about 313 K (Fig. 2), whereas predicted hyperfine magnetic field of amorphous matrix polarized by grains completely vanishes only at the Curie temperature of the crystalline phase. The theoretically estimated $T_C^{0\,am}$ well corresponds to the point above which an experimental thermomagnetic curve for nanocrystallites changes the rate of decay. However, this phenomenon is not as pronounced as in FINEMET because of muddy magnetic phase transition in the amorphous phase. The theoretical curve for grains generally reproduces this feature, the quality of the fit, however, is not perfect. Introducing into the model an experimental value of the Curie temperature for a bulk α-Fe phase ($T_C^{B\,cr}$ = 1041 K) we have estimated the value of the Curie temperature of the grain as $T_C^{cr} \approx 980$ K and the value of parameter $q^{cr} \approx 0.063$.

4. Conclusions

Our simple MFA model describes main features of thermomagnetic behaviour of nanocrystalline alloys considered as a magnetically coupled two-phase system in which both spin polarization of the amorphous matrix by the grains and spin relaxation effects in nanocrystallites are important. We obtained satisfactory fits of the theoretical model to the experimental data provided by the Mössbauer spectrometry for FINEMET and Fe–Nb–B alloys. The model qualitatively predicts the experimentally observed change of the slope of thermomagnetic curve for nanocrystallites above Curie temperature of the amorphous matrix, however it does not reproduce all details in the vicinity of this point (in particular, in the case of FINEMET). It also describes not vanishing magnetism of the amorphous matrix in Fe–Nb–B nanocrystalline material up to the Curie temperature of the strongly ferromagnetic grains. It is worth noticing that in Fe–Zr–B (NANOPERM) nanocrystalline materials magnetization of the amorphous material falls down even slower then in Fe–Nb–B [2] which cannot be explained in terms of the developed model. We intend to improve the model by considering the interface region as a third component of magnetically coupled nanocrystalline system as well as some inhomogeneity of the amorphous remainder. Both these factors are recognized as very important in the description of the magnetic properties of nanocrystalline alloys [2–6, 9, 10].

References

[1] BRZÓZKA K., ŚLAWSKA-WANIEWSKA A., JEZUITA K., GAWROŃSKI M., LACHOWICZ H.K., Proc. All-Polish Seminar on Mössbauer Spectroscopy OSSM ′96, Lublin, 1996, 13.
[2] BRZÓZKA K., ŚLAWSKA-WANIEWSKA A., JEZUITA K., GAWROŃSKI M., GRENÈCHE J.M., Mol. Phys. Rep., 22 (1998) 27.
[3] GRENÈCHE J.M., MIGLIERINI M., *Mössbauer Spectroscopy in Material Science*, M. Miglierini, D. Petridis (Eds.), NATO Advanced Science Institute Series, Subseries 3. High Technology, Vol. 66, Kluwer, Dordrecht, 1998, p. 243.
[4] ŠKORVÁNEK I., KOVÁČ J., GRENÈCHE J.M., J. Phys. Cond. Matt., 12 (2000), 9085.
[5] SZUMIATA T., GÓRKA B., ZORKOVSKÁ A., SOVÁK P., J. Magn. Magn. Mater., 288 (2005), 37.
[6] CRISAN O., GRENÈCHE J.M., LE BRETON J.M., CRISAN A.D., LABAYE Y., BERGER L., FILOTI G., Eur. Phys. J. B, 34 (2003), 155.
[7] NAVARRO I., ORTUÑO M., HERNANDO A., Phys. Rev. B, 53 (1996), 11656.
[8] GARITAONANDIA J.S., SCHMOOL D.S., BARANDIARÁN J.M., Phys. Rev. B, 58 (1998), 12147.
[9] ŚLAWSKA-WANIEWSKA A., ROIG A., MOLINS E., GRENÈCHE J.M., ŻUBEREK R., J. Appl. Phys., 81 (1997), 4652.
[10] MIGLIERINI M., GRENÈCHE J.M., *Mössbauer Spectroscopy in Material Science*, M. Miglierini, D. Petridis (Eds.), NATO Advanced Science Institute Series, Subseries 3. High Technology, Vol. 66, Kluwer, Dordrecht, 1998, p. 257.

Received 7 May 2006
Revised 1 September 2006

Materials Science-Poland, *Vol. 25, No. 2, 2007*

Quantum spin system with on-site exchange in a magnetic field

G. PAWŁOWSKI*

Institute of Physics, Adam Mickiewicz University, 61-614 Poznań, ul. Umultowska 85, Poland

We present the results of a full diagonalisation applied to a 1 D quantum spin system with on-site exchange anisotropy. The model considered is a quantum generalization of the 1 D classical Blume–Capel model. Thermodynamic properties of the system in the presence of magnetic field are examined taking into account a quantum spin ladder with a periodic boundary condition, where each rung of the ladder contains two interacting spins –1/2. This effective spin –1 system exhibits very rich thermodynamic behaviour. We present the ground state results, showing many various types of magnetic configurations and compare it with the classical case. The calculations are performed in the unified simulation environment ALPS, which offers the fulldiag application.

Key words: *quantized spin model; spin ladder*

1. Introduction

We have studued the magnetic orderings in the frustrated quantum spin –1/2 ladder with the interaction anisotropy (the AF Heisenberg generalized ladder with $J_{II} = J_{diag} = J$, $J_{\perp} = \Delta$ [1]). The scheme of the considered structure is shown in Fig. 1.

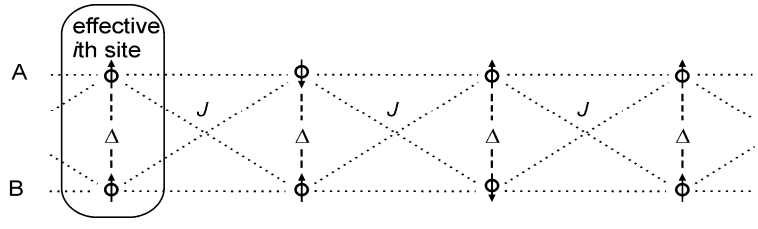

Fig. 1. The scheme of the frustrated quantum spin –1/2 ladder with the interaction anisotropy

*E-mail: gpawlo@amu.edu.pl

The exchange interactions between spins on the rung and along the main direction of the ladder are different. We examine the thermodynamic properties of the system as a function of Δ/J. The Hamiltonian of the system considered takes the form:

$$\hat{H} = J \sum_{i,\alpha,\beta} \hat{\sigma}_{i\alpha}\hat{\sigma}_{i+1\beta} + \Delta \sum_{i} \hat{\sigma}_{iA}\hat{\sigma}_{iB} \tag{1}$$

where $\hat{\sigma}_{i\alpha}$ is the quantum spin –1/2 operator on the ith rung and α-leg of the ladder. We take into account the influence of external magnetic field h on the z component of the spin and we add the Zeeman term

$$\hat{H}(h) = \hat{H} - h \sum_{i} (\hat{\sigma}^{z}_{iA} + \hat{\sigma}^{z}_{iB}) \tag{2}$$

Such a model can be treated as the effective interacting (J) chain of spin –1 on the ith site with the on-site exchange (Δ) [2] in the presence of a magnetic field (h).

We can show that the Hamiltonian (1) has a similar form as the well known Blume–Capel (BC) model [3] (we use the "classical" sign convention)

$$H_{BC} = -J \sum_{i,j} S_i S_j + D \sum_{i} S_i^2 \tag{3}$$

where S_i is the classical spin –1 Ising operator which takes the values $\{-1,0,1\}$, J is the exchange interaction and D is the single-ion anisotropy. Formally, the Hamiltonian (3) can be rewritten into the equivalent form in terms of spin –1/2. Let us express each spin S_i over the sum $\tilde{S}_i = \sigma_{iA} + \sigma_{iB}$ of two classical spins $\sigma_{i\alpha} = \pm 1/2$ on the ith site. This transformation is non-one-to-one and changes the number of eigenstates of effective spin $\tilde{S}_i = \{-1,0,0,1\}$. In our recent paper [4], we show that such a spin model with "zero"-state degeneracy can be transformed into the BC model with a temperature-dependent single ion anisotropy (at T=0 the models are identical). We rewrite the Hamiltonian (3) for $\tilde{S}_i$ in the new variable $\sigma_{i\alpha}$

$$\tilde{H} = -\tilde{J} \sum_{i,j,\alpha,\beta} \sigma_{i\alpha}\sigma_{j\beta} + 2\tilde{D} \sum_{i} \sigma_{iA}\sigma_{iB} + C \tag{4}$$

where $\alpha, \beta = \{A,B\}$, $\tilde{J} = J$, $\tilde{D} = D - k_B T \ln 2$ and $C = ND/2$, which yields a similar form as in Eq. (1).

In the analysis of the system, we have implemented the unified simulation environment ALPS [5], which offers the fulldiag application [6]. Using the XML language, we have first defined a new "diagonally connected ladder" graph structure, where i = 1..., x (Fig. 2) where x is the number of rungs, $2x$ – number of vertices, 1A, 1B, $x\alpha$, $x\beta$, … – are the proper symbols of the vertex number.

dd-graph.xml

```
<LATTICES>
 <GRAPH name="generalized ladder" vertices="2x">
  <VERTEX id="1α" type="0"/>
  ...
  <VERTEX id="xα" type="0"/>
  <EDGE type="0" source="1A" target="1B"/>
  ...
  <EDGE type="0" source="xA" target="xB"/>
  <EDGE type="1" source="1α" target="2β"/>
  ...
  <EDGE type="1" source="(x-1)α" target="xβ"/>
  <EDGE type="1" source="xα" target="1β"/>
 </GRAPH>
</LATTICES>
```

Fig. 2. "Diagonally connected ladder" graph structure

On the last defined 'EDGE' we impose periodic boundary conditions. In the diagonalization procedure we use also the model-dspin.xml file in which the quantum interactions between local spins –1/2 are defined. After preparing the parameter.xml file, where we specify the type of the system, temperature, the value of the interactions etc., we start with the fulldiag procedure to get the eigenvalues of the system. Then we use the fulldiag-evaluate program to obtain thermodynamic properties of the system.

2. Results

We present the exact results of 12 quantum spins on the ladder with antiferromagnetic (AF) exchange interaction ($\Delta > 0$, $J = 1$). For the family of Δ/J values we obtained the following thermodynamic characteristics: magnetization, specific heat, susceptibility, entropy and energy as functions of the magnetic field. In Figure 4, exemplary results for $\Delta = 1.8$ are presented. The diagrams are symmetrical due to the spin degeneracy in the absence of magnetic field. Figure 4 presents possible magnetic orderings in the ground state in the plane $h\Delta$ for the quantum case (Fig. 4a) and in hD for the classical case (Fig. 4b) (the results have been extrapolated from very low temperatures). In the quantum case, we observe some states with magnetization analogous as in the classical case. The classical disordered phase ($M = 0$) corresponds to the dimer phase D2 of singlets along the rungs, while the Ising spin –1 AF1 phase (–1,1) is replaced by the dimer phase D1 (equivalent to the Haldane phase of the $S = 1$ chain) [3, 7]. For $|M| = 0.5$ we observe equivalent magnetic order in the classical, as well as in the quantum case. For $|h| > h_c$ there is paramagnetic state (the saturated ferromagnetic) in both situations.

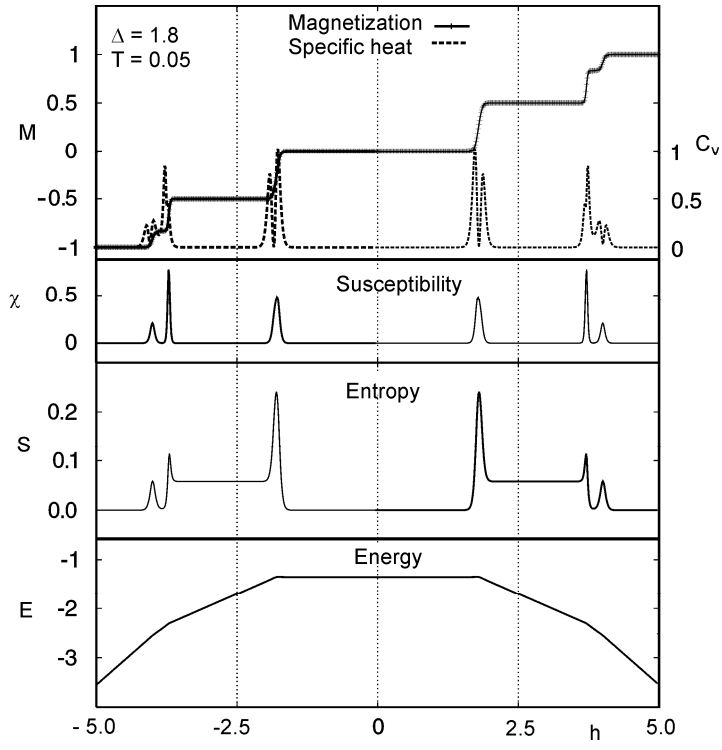

Fig. 3. The thermodynamic characteristics of the system as a function of external magnetic field h for $\Delta = 1.8$ and $T = 0.05$

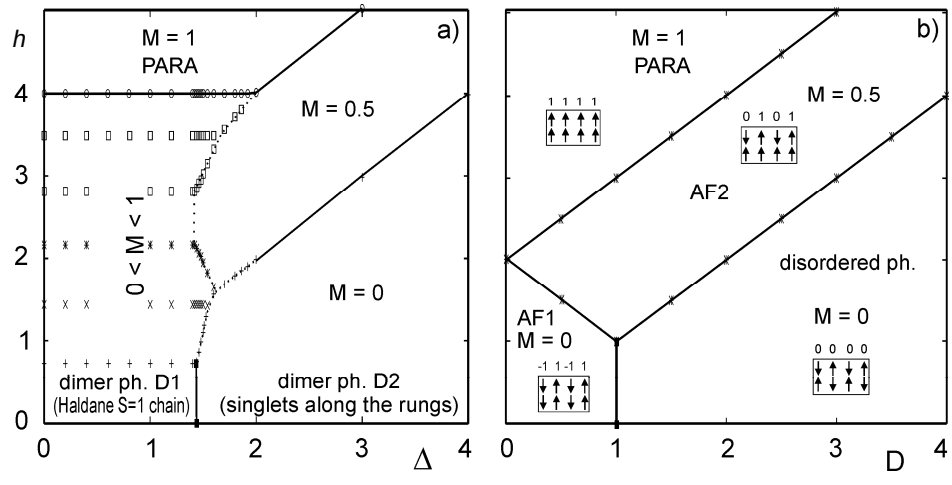

Fig. 4. The magnetic orderings in the ground state in the presence of magnetic field for the antiferromagnetic ladder described by the quantum model (a) and by the classical one (b)

Though the detailed structure of phase diagrams of the classical BC model (Fig. 4b) must be different from that presented for the quantum system (Fig. 4a), the mulitiphase composition for large Δ and h of both models is similar.

Acknowledgement

The author would like to thank S. Robaszkiewicz for useful discussions. This work was supported in part by the Polish State Committee for Scientific Research, Grant No. 1 P03B 08426.

References

[1] CHATTOPADHYAY E., BOSE I., Physica A, 318 (2003), 14.
[2] WHITE S., Phys. Rev. B, 53 (1996), 52; HIDA K., Phys. Rev. B, 45 (1992), 2207.
[3] BLUME M., Phys. Rev., 141 (1966), 517; Capel H.W., Physica (Amsterdam), 32 (1966), 966.
[4] PAWŁOWSKI G., Eur. Phys. J. B, 53 (2006), 471.
[5] ALBUQUERQUE A.F., ALET F., CORBOZ P., DAYAL P., FEIGUIN A., FUCHS S., GAMPER L., GULL E., GÜRTLER S., HONECKER A., IGARASHI R., KÖRNER M., KOZHENIKOV A., LÄUCHLI A., MANMANA S.R., MATSUMOTO M., MCCULLOCH I.P., MICHEL F., NOACK R.M., PAWŁOWSKI G., POLLET L., PRUSCHKE T. SCHOLLWÖCK U., TODO S., TREBST S., TROYER M., WERNER P., WESSEL S., J. Magn. Magn. Mater., 310 (2007), 1187; http://alps.comp-phys.org.
[6] TROYER M., Lect. Notes Comp. Sci., 1732 (1999), 164.
[7] XIAN Y., Phys. Rev. B, 52 (1995), 12485.

Received 7 May 2006
Revised 1 September 2006

Do Autora: proszę uaktualnić Ref. 4.

Materials Science-Poland, *Vol. 25, No. 2, 2007*

Precessional modes due to spin-transfer in spin-valve nanopillars

M. GMITRA[1, 3*], J. BARNAŚ[2], D. HORVÁTH[3]

[1]Department of Physics, Adam Mickiewicz University, UL. Umultowska 85, 61-614 Poznań, Poland

[2]Institute of Molecular Physics, Polish Academy of Sciences,
M. Smoluchowskiego 17, 60-179 Poznań, Poland

[3]Department of Theoretical Physics and Astrophysics, P. J. Šafárik University,
Park Angelinum 9, 040 01 Košice, Slovak Republic

Current-driven magnetic switching and magnetic dynamics in spin-valve nanopillars are considered in the framework of the macrospin model. The corresponding spin transfer torque is calculated in terms of the macroscopic model based on spin diffusion equations. Critical currents for switching from parallel to antiparallel magnetic configurations and to precessional regime are derived. Frequencies of the precessional modes are also calculated as a function of external magnetic field and electric current.

Key words: *spin-transfer; switching; spintronics*

1. Introduction

The quantum-mechanical phenomenon of spin transfer between polarized conduction electrons and localized magnetic moments of a thin magnetic film can induce switching and/or precession of the film magnetization [1]. The current-driven magnetization manipulation has been observed in experiments carried out on multilayers, nanowires, small particles, tunnel junctions, and nanopillar spin valves. The latter ones provide the most convincing experimental data [2, 3]. A typical nanopillar spin valve consists of thick and thin magnetic layers separated by a non-magnetic spacer layer, the thick layer acting as a source of spin current. Several theoretical models have also been developed to describe physical mechanisms of the spin-transfer and magnetic switching phenomena [4–7].

*Corresponding author, e-mail: martin.gmitra@upjs.sk

It has also been found that at some conditions electric current can cause transition to steady precessional modes where the energy is pumped from conduction electrons to localized magnetic moments [8, 9]. This phenomenon is of high importance due to possible applications in microwave generation. In typical Co/Cu/Co spin-valve systems, the precessional modes were found in a non-zero external magnetic field and for current exceeding certain critical value [10–13]. The critical current depends on the applied external magnetic field and intrinsic parameters of the nanopillar, like interfacial resistances, bulk resistivities, demagnetization field, anisotropy field or damping parameter of a thin film. In Co/Cu/Co spin valves, the current-induced steady precessions exist for external magnetic fields larger than the anisotropy field of the thin layer [10, 11]. For lower values of external field, the current drives switching to antiparallel (AP) or parallel (P) states, depending on the initial state of the system [12].

In this paper, we present the effects of spin-transfer torque on steady magnetization precessions, whose frequency can be manipulated by the external magnetic field and current density flowing through the system. We also discuss current-driven transition between two kinds of steady precessions.

2. Macrospin model

We consider a tri-layer system which is attached to two external nonmagnetic leads. A qualitative behaviour of a thin (free or sensing) layer can be described within the single-domain approximation (macrospin model) [10, 13]. Magnetic dynamics of the sensing layer is then described by the generalized Landau–Lifshitz–Gilbert equation:

$$\frac{\mathrm{d}\hat{\mathbf{s}}}{\mathrm{d}t} = -|\gamma_g|\,\mu_0\,\hat{\mathbf{s}}\times\boldsymbol{H}_{\mathrm{eff}} - \alpha\hat{\mathbf{s}}\,\frac{\mathrm{d}\hat{\mathbf{s}}}{\mathrm{d}t} + \frac{|\gamma_g|}{M_s d}\boldsymbol{\tau} \tag{1}$$

where $\hat{\mathbf{s}}$ is the unit vector along the spin moment of the sensing layer, γ_g is the gyromagnetic ratio, μ_0 is the magnetic vacuum permeability, $\mathbf{H}_{\mathrm{eff}}$ is an effective magnetic field acting on the sensing layer, α is the damping parameter, M_s stands for the saturation magnetization, and d is the layer thickness. The effective field includes an external magnetic field H_{ext}, the uniaxial magnetic anisotropy field H_a, and the anisotropy due to the demagnetization field H_d;

$$H_{\mathrm{eff}} = -H_{\mathrm{ext}}\hat{\mathbf{e}}_z - H_a(\hat{\mathbf{s}}\cdot\hat{\mathbf{e}}_z)\hat{\mathbf{e}}_z + H_d(\hat{\mathbf{s}}\cdot\hat{\mathbf{e}}_x)\hat{\mathbf{e}}_x$$

where $\hat{\mathbf{e}}_x$ and $\hat{\mathbf{e}}_z$ are the unit vectors along the axes x (normal to the layers) and z (in-plane), respectively. The last term in Eq. (1) stands for the torque due to spin transfer,

$$\boldsymbol{\tau} = aI\hat{\mathbf{s}}\times(\hat{\mathbf{s}}\times\hat{\mathbf{S}}) + bI\hat{\mathbf{s}}\times\hat{\mathbf{S}}$$

Here, $\hat{\mathbf{S}}$ is the unit vector along the spin moment of the thick (fixed) magnetic layer ($\hat{\boldsymbol{S}} = \hat{\boldsymbol{e}}_z$), a and b are the parameters that generally depend on the intrinsic nanopillar parameters and on magnetic configuration of the system [7]. The current I is defined as positive when it flows from the thick magnetic layer towards the thin one. On linearizing Eq. (1) and performing standard stability analysis, one finds the critical current that destabilizes the P ($\hat{\mathbf{s}} = \hat{\mathbf{S}}$) configuration in the form [14]

$$I_c = \frac{\alpha \mu_0 M_s d}{a - b\alpha}\left(H_a + H_{\text{ext}} + \frac{H_d}{2} \right) \tag{2}$$

where the parameters a and b are to be calculated for the P configuration. For $I > I_c$, the system is driven to AP state for $H_{\text{ext}} < H_a$ and to steady precessional regime for $H_{\text{ext}} > H_a$ [10, 15].

3. Numerical results

The numerical analysis is focused on the current-driven oscillatory magnetoresistance behaviour of the nanopillar Cu/Co(30)/Cu(10)/Co(4)/Cu (the numbers are layer thicknesses in nanometers). For the sensing layer, we assume saturation magnetization M_s = 17.8 kOe, anisotropy field H_a= 986 Oe, demagnetization field $H_d = 0.65M_s$, and the Gilbert damping parameter α = 0.003. The current induced torque, actually the parameters a and b, have been calculated in terms of a macroscopic model in the diffusive transport regime [7], assuming that the spin current component perpendicular to the spin moment of the sensing layer is entirely absorbed in the interfacial region [4, 5]. The calculations have been performed for typical parameters obtained from CPP GMR experiments [16]. For the Co layers we assumed the bulk resistivity ρ^* = 5.1 μΩ·cm, spin asymmetry factor β = 0.51, and spin-flip length l_{sf} = 60 nm, and for Cu layers ρ^* = 0.5 μΩ·cm, l_{sf} = 1000 nm. In turn, for Co/Cu interfaces we assume the interfacial resistance $R^* = 0.52\times10^{-15}$ Ω·m^2, the interface spin asymmetry factor γ= 0.76, and the mixing conductances $\text{Re}\{G_{\uparrow\downarrow}\} = 0.542\times10^{15}$ Ω^{-1}·m^{-2} and $\text{Im}\{G_{\uparrow\downarrow}\} = 0.016\times10^{15}$ Ω^{-1}·m^{-2}.

The simulations were started with a nearly P configuration and for $I > I_c$ (the initial in-plane spin bias shift of the order of one degree was assumed). The inset in Fig. 1a shows the current dependence of the switching time t_0 from the P configuration to steady precessional regime for the magnetic fields as indicated. The switching time t_0 is defined as the point where $\hat{\mathbf{s}}$ crosses zero for the first time. The current dependence of t_0 reveals a simple rational behaviour. However, the slope of the inverse plot does not depend on the applied magnetic field but we found its significant dependence on the initial bias (not shown). From the latter it follows that duration of the transient regime can be significantly affected by the initial bias, dependent, for example, on the thermal noise.

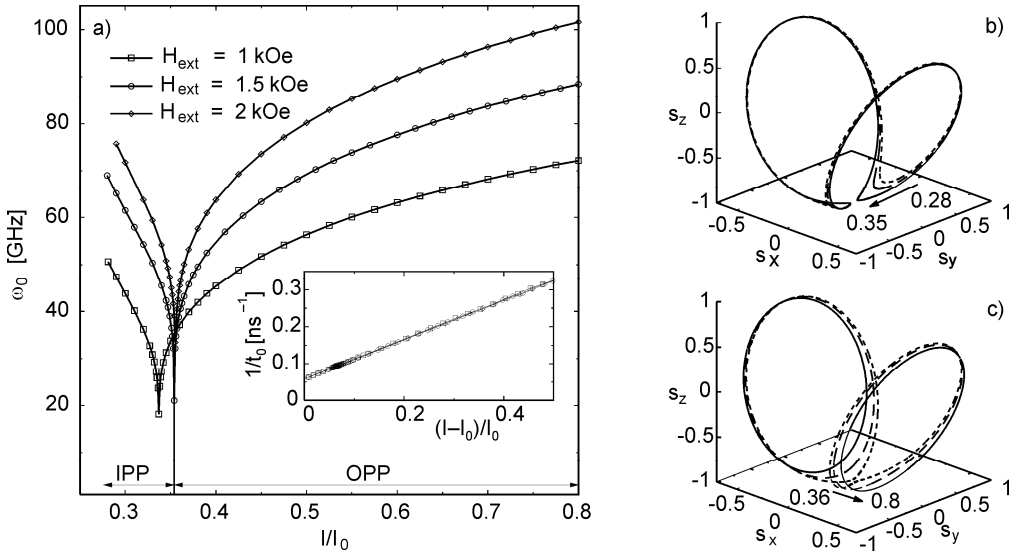

Fig. 1. Fundamental frequency of the magnetoresistance oscillations in Cu/Co(30)/Cu(10)/Co(4)/Cu (a), calculated as a function of the reduced current density, where $I_0 = 10^8$ A/cm^2, and for magnetic fields as indicated. The inset shows the corresponding current dependence of the switching times (see text) for $H_{ext} = 1.5$ kOe; steady in-plane orbits for $I/I_0 = 0.28$, 0.3, 0.35 (b), and out-of-plane orbits for $I/I_0 = 0.36$, 0.50, 0.80 for $H_{ext} = 1.5$ kOe (c). The arrows indicate the change in orbits as the current increases

The fundamental frequency ω_0 (first harmonics) of the magnetoresistance oscillations is shown in Fig. 1a as a function of the current density and for different magnetic fields. The frequency first decreases with increasing current, and then increases showing a profound minimum. To understand the current dependence of the frequency, it is instructive to analyze steady spin orbits of the sensing layer. Figure 1b shows saddle-shaped in-plane precession (IPP) orbits. The arrow indicates the change in orbits as the current increases. Along the segments where $\hat{\mathbf{s}}$ moves almost in the layer plane, the spin precesses mainly around H_a and H_{ext}, with the angular velocity proportional to $|\gamma_g|(H_a + H_{ext})$. Along the remaining part ($\hat{\mathbf{s}}$ moves almost perpendicularly to the layer plane), the angular velocity is higher and proportional to $|\gamma_g|(H_a + H_{ext} + H_d)$. With increasing I, the average orbital speed decreases while the arc length of the orbit increases. Consequently, ω_0 decreases with increasing I.

At a certain value of the current, at which the segments touch each other near the –z axis, the IPP orbit bifurcates into two so-called out-of-plane (OOP) orbits (Fig. 1c). The orbits are interchangeable with respect to the $x \to -x$ and $y \to -y$ reflections. The mirror symmetry with respect to the x axis has been reported in Ref. [13]. In our case, the additional mirror symmetry with respect to the y axis is due to a non-zero value of b. A further increase in current increases spin torque and tends to push the orbit away from the layer plane. The arc length decreases and orbital speed increases due to larger demagnetization field. Consequently, ω_0 increases with increasing I.

The frequency ω_0 increases with the increased external magnetic field in both, IPP and OPP cases. We compared the field dependence of the recorded ω_0 for selected current densities to the Kittel formula for small-angle elliptical precession of a thin film ferromagnet. For OPP we have found an increase in effective demagnetization term with increased current. Although, the formula fits very well to the $\omega_0(H_{ext})$ dependence, the effective demagnetization term differs from that considered in simulation. Similar discrepancies have been observed in experiments [10, 11]. The discrepancy can be associated with an additional effective field induced due to spin-transfer which pumps energy to the system and enables such precessions. In turn, for IPP the $\omega_0(H_{ext})$ reveals a dependence that cannot be fitted to the Kittel formula.

4. Conclusions

Spin polarized current is shown to drive magnetic switching and steady oscillations of the magnetic moment of the sensing layer. Frequency of the oscillations has been calculated as a function of the magnetic field and electric current. Two kinds of steady orbits have been revealed: in-plane and out-of-plane. The main features of these steady precessions have been also discussed.

Acknowledgements

This work has been partly supported by the Slovak Ministry of Education as a research project MVTS POL/SR/UPJS07, Slovak Grant Agency VEGA 1/2009/05, and by EU through RTN Spintronics (contract HPRN-CT-2000-000302).

References

[1] SLONCZEWSKI J.C., J. Magn. Magn. Mater., 159 (1996), L1; 195 (1999), L261; BERGER L., Phys. Rev. B, 54 (1996), 9353.
[2] KATINE J.A., ALBERT F.J., BUHRMAN R.A., MYERS E.B., RALPH D.C., Phys. Rev. Lett., 84 (2000), 3149.
[3] GROLLIER J., CROS V., HAMZIC A., GEORGE J.M., JAFFRES H., FERT A., FAINI G., YOUSSEF J.B., LEGALL H., Appl. Phys. Lett., 78 (2001), 3663.
[4] STILES M.D., ZANGWILL A., Phys. Rev. B, 66 (2002), 014407.
[5] BRATAAS A., NAZAROV YU.V., BAUER G.E.W., Eur. Phys. J. B, 22 (2001), 99.
[6] ZHANG S., LEVY P.M., FERT A., Phys. Rev. Lett., 88 (2002), 236601 (2002); SHPIRO A., LEVY P.M., ZHANG S., Phys. Rev. B, 67 (2003), 104430.
[7] BARNAS J., FERT A., GMITRA M., WEYMANN I., DUGAEV V.K., Phys. Rev. B, 72 (2005), 024426.
[8] SUN J.Z., Phys. Rev. B, 62 (2000), 570; LI Z., ZHANG S., Phys. Rev. B, 68 (2003), 024404.
[9] SLAVIN A.N., TIBERKEVICH V.S., Phys. Rev. B, 72 (2005), 094428.
[10] KISELEV S.I., SANKEY J.C., KRIVOROTOV I.N., EMLEY N.C., SCHOELKOPF R.J., BUHRMAN R.A., RALPH D.C., Nature (London), 425 (2003), 380; KISELEV S.I., SANKEY J.C., KRIVOROTOV I.N., EMLEY N.C., GARCIA A.G.F., BUHRMAN R.A., RALPH D.C., Phys. Rev. B, 72 (2005), 064430.
[11] RIPPARD W.H., PUFALL M.R., KAKA S., RUSSEK S.E., SILVA T.J., Phys. Rev. Lett., 92 (2004), 027201.
[12] XI H., LIN Z., Phys. Rev. B, 70 (2004), 092403.

[13] XIAO J., ZANGWILL A., STILES M.D., Phys. Rev. B, 72 (2005), 014446.
[14] GMITRA.M., BARNAS J., Phys. Rev. Lett., 96 (2006), 207205.
[15] RUSSEK S.E., KAKA S., RIPPARD W.H., PUFALL M.R., SILVA T.J., Phys. Rev. B, 71 (2005), 104425; GMITRA M., BARNAS J., HORVATH D., J. Alloys. Comp., 423 (2006), 194.
[16] BASS J., PRATT JR. W.P., J. Magn. Magn. Mater., 200 (1999), 274.

Received 7 May 2006
Revised 1 September 2006

Materials Science-Poland, Vol. 25, No. 2, 2007

Polaronic transport through DNA molecules

M. SIDOWSKI*, K. WALCZAK

Institute of Physics, Adam Mickiewicz University, ul. Umultowska 85, 61-614 Poznań, Poland

We present results of theoretical studies on polaronic and incoherent transport through a DNA-based junction. Decoherence itself is modelled through the use of an imaginary dephasing potential. Non-perturbative computational scheme, used in this work, is based on Green's functions within the framework of the so-called polaron transformation (GFT-PT). This method maps exactly the many-body hole –phonon interaction problem into a one-body multi-channel scattering problem, where the availability of particular conduction channels is determined by an appropriate weight factor. The results obtained for poly(dG)-poly(dC) DNA molecule reveal saturation effect of the current at high voltages, where for short chains we establish an exponential DNA length dependence. Besides, we document strong coupling and exponential dephasing dependences of the maximum current.

Key words: *polaronic transport; DNA-based device; DNA electronics; decoherence*

1. Introduction

Recent advances in nanofabrication allow us to fabricate devices composed of individual DNA molecules connected to metallic electrodes and to measure current-voltage (*I–V*) characteristics of such junctions [1–4]. The actual magnitude of DNA conductivity and its physical mechanism is still under debate [5, 6]. In particular, long DNA oligomers are expected to be true insulators, while short biomolecules are rather semiconductors with a relatively large HOMO-LUMO gap. Since the residence time of the charge carrier on guanine G (nucleobase with lower oxidation potential) is long in comparison with characteristic time associated with molecular vibrations, the hole-type (positive ion) conduction is treated as incoherent. This means that the charge carrier is temporarily localized on guanine, losing its phase and exchanging energy with the biomolecule.

Since nucleobases involved in the conduction process are thermally activated to vibrations (phonon modes are excited) and vibrational coupling parameter is suffi-

*Corresponding author: masi@amu.edu.pl

ciently strong, charge carriers are locally coupled to phonons, leading to polaron formation. The main purpose of this work is to study the polaronic and incoherent transport through short poly(dG)-poly(dC) DNA treated as a linear chain of quantum dots, where only one HOMO level on each guanine is taken into consideration, as shown in Fig. 1.

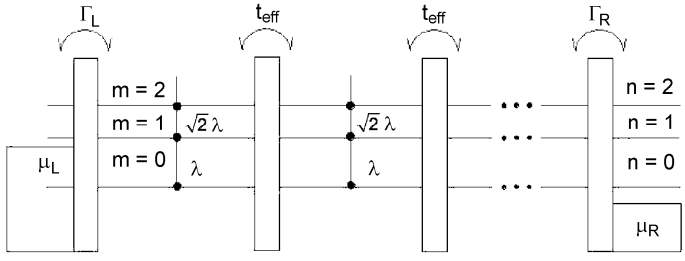

Fig. 1. A schematic representation of the inelastic scattering problem for the device composed of a series of molecular quantum dots connected to metals

Decoherence itself is modelled trough the use of an imaginary (optical) dephasing potential, where all the phase-breaking processes are included [7, 8]. This potential has the sense of the coupling with external environment. It should be also noted that recently polaron hopping was suggested as a possible mechanism to explain the transport found on DNA stacks [9–12].

2. The model and method

In modelling the process of charge transfer through DNA, we consider the nucleotide sequence as a system of N sites, in which each site corresponds to a GC base pair. In this chain, a hole travels along energetically appropriate HOMO levels of guanine bases, since their oxidation potential is lower than that of cytosine nucleotides. Let us write down a simplified Hamiltonian of the whole system in the form:

$$\begin{aligned} H = &\sum_j \left[(\varepsilon_j - i\phi_j) - \lambda(d_j + d_j^+) \right] c_j^+ c_j - \sum_j \left[t_{eff} c_j^+ c_{j+1} + \text{h.c.} \right] \\ &+ \sum_j \Omega d_j^+ d_j + \sum_{k\in\alpha} \varepsilon_k c_k^+ c_k + \sum_{k\in\alpha, j} \left[\gamma_k c_k^+ c_j + h.c. \right] \end{aligned} \tag{1}$$

where: ε_j and ε_k are the energies of holes on the jth site of the molecule and in the reservoirs with momentum k, ϕ_j is the on-site dephasing potential, λ is the electron –phonon interaction parameter, t_{eff} denotes the hopping integral between two neighbouring sites (guanines), Ω is the phonon energy, γ_k is the strength of the molecule–reservoir coupling. Furthermore, c_k, c_j, d_j and their adjoints are annihilation and

creation operators for holes in the reservoirs, at the molecular sites, and for the primary on-site phonons, respectively.

To proceed, we apply the so-called polaron transformation [13–16], where the electron states are expanded into the direct product states composed of single-electron states and *m*-phonon Fock states:

$$\left|j,m\right\rangle = c_j^+ (d_j^+)^m \left|0\right\rangle / \sqrt{m!}\,, \qquad \left|k,m\right\rangle = c_k^+ (d_j^+)^m \left|0\right\rangle / \sqrt{m!}$$

where $\left|0\right\rangle$ denotes the vacuum state. This method maps exactly the many-body hole –phonon interaction problem into a one-body multi-channel scattering problem. After eliminating the reservoir degrees of freedom, we can present the effective Hamiltonian of the reduced molecular system as:

$$\begin{aligned} H_{\text{eff}} = & \sum_{j,m,\alpha} \left(\varepsilon_j - i\phi_j^m + m\Omega + \Sigma_\alpha^m\right) \left|j,m\right\rangle\left\langle j,m\right| \\ & -\sum_{j,m} t_{eff}^m \left(\left|j,m\right\rangle\left\langle j+1,m\right| + \left|j+1,m\right\rangle\left\langle j,m\right|\right) \\ & -\sum_{j,m} \lambda\sqrt{m+1}\left(\left|j,m\right\rangle\left\langle j,m+1\right| + \left|j,m+1\right\rangle\left\langle j,m\right|\right) \end{aligned} \tag{2}$$

where: $\Sigma_\alpha^m = -i\Gamma_\alpha^m/2$ is the self-energy in the wide-band approximation, while $\Gamma_\alpha^m = 2\pi\,|\,\gamma_k^m\,|^2\,\rho_\alpha$ is the so-called linewidth function with ρ_α as the density of states related to the α electrode. Index *m* numbers the particular channels and their accessibility before scattering is determined by an appropriate weight factor: $P_m = \left[1-\exp(-\beta\Omega)\right]\exp(-m\beta\Omega)$, where $\beta = 1/k_B\theta$, while θ is the device working temperature. In practice, the maximum amount of phonon quanta excited on each site is restricted to a finite number $m = m_{\max}$ because of the numerical efficiency.

Choosing an appropriate matrix element of the molecular Green function defined as: $F(\varepsilon) = (J\varepsilon - H_{\text{eff}})^{-1}$, where *J* is the unit matrix, we can define the transmission probability of each possible transition, where hole incoming from channel *m* is scattered on the DNA molecule, and then outgoing to channel *n*:

$$T_{m,n}(\varepsilon) = \Gamma_L^m \Gamma_R^n \,|\, F_{m+1,\bar{n}+1}(\varepsilon)\,|^2$$

where $\bar{n} = n + (N-1)m_{\max}$. The electrical current flowing through the system is given by the following relation:

$$I = \frac{e}{\pi\hbar}\int_{-\infty}^{+\infty} d\varepsilon \sum_{m,n} T_{m,n}(\varepsilon)\left[P_m f_L^m(\varepsilon)\left(1-f_R^n(\varepsilon)\right) - P_n f_R^n(\varepsilon)\left(1-f_L^m(\varepsilon)\right)\right] \tag{3}$$

where:

$$f_\alpha^m(\varepsilon) = \frac{1}{1+\exp\left[\beta(\varepsilon + m\Omega - \mu_\alpha)\right]}$$

is the Fermi function, while the electrochemical potentials are defined as: $\mu_L = \varepsilon_F + eV/2$, $\mu_R = \varepsilon_F - eV/2$, ε_F denoting the Fermi energy and V being the applied bias.

3. Numerical results and discussion

A difficult part of the calculations of polaron properties is associated with choosing parameters for DNA. Here, we take the following energy parameters (given in eV): $\Gamma_L^m = \Gamma_R^m = 0.2$ (the case of weak molecule-metal contacts), $\varepsilon_j = 0$ (the reference energy of the HOMO level of guanine), $\varepsilon_F = -1.73$ (as deduced from the experimentally obtained conductivity gap), $\lambda = 0.3$ (as estimated from the reorganization energy), $\phi_j^m = 0.185$ (the fitting parameter), $\Omega = 0.13$, $t_{\text{eff}}^m = 0.6$ (as obtained from ab initio calculations of the two energy levels for a pair of overlapped guanine bases). Temperature θ is set at 300 K ($\beta = 0.025$/eV), while maximum amount of phonon quanta $m_{\max} = 10$ is chosen to give fully converged results with the accuracy better than 1%.

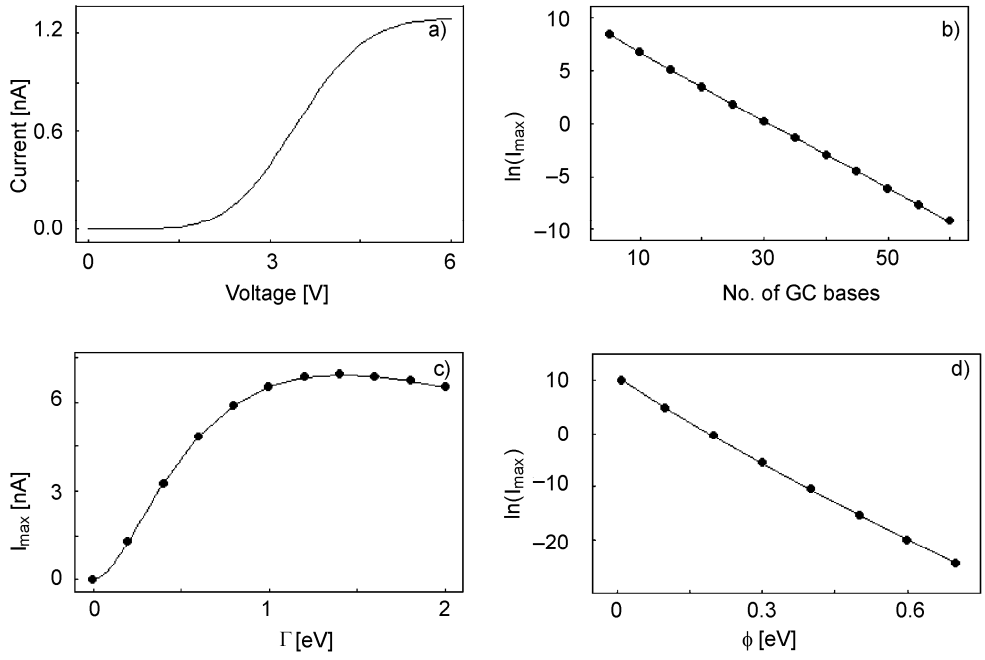

Fig. 2. Current-voltage dependence for $N = 30$ pair poly(dG)-poly(dC) DNA (a); maximum value of the current as a function of the number of GC bases in the logarithmic scale (b); maximum current as a function of the coupling strength parameter for $N = 30$ (c); maximum value of the current as a function of dephasing potential in the logarithmic scale for $N = 30$ (d)

The calculated I–V characteristics for a double-stranded 30-base pair poly(dG)-poly(dC) DNA molecule connected to two metallic electrodes is demonstrated in

Fig. 2a, where all the model parameters were reasonably chosen to quantitatively reproduce the experimental data (cf. Porath et al. [2]). Here, we observe the saturation effect at high voltages after the smoothing increase of the current, where we have $dI/dV = 0$. Our calculations indicate that the magnitude of the current flow exponentially depends on the DNA length: $\ln(I_{\max}) \approx 9.91 - 0.32N$ (as shown in Fig. 2b), the maximal current given in μA can thus be estimated from the following relation: $(I_{\max}) \approx 20.13\exp(-0.32N)$. This conclusion is in contradiction to the previous rate-equation calculations indicating the algebraic length dependence [17, 18]. The shape of the *I–V* curve does not change significantly upon changes in a wide range of model parameters, but the magnitude of the current flow is very different. Figure 2c shows that the maximum current smoothly increases with the increase of the coupling parameter $\Gamma = \Gamma_L^m = \Gamma_R^m$. Interestingly enough, for extremely strong coupling ($\Gamma > 1.4$) we observe the opposite trend. The strength of the DNA-electrode coupling can be controlled by changing the distance between them. Furthermore, the magnitude of the current flow exponentially decreases with the increase of the dephasing potential: $\ln(I_{\max}) \approx 9.7 - 50\phi$, so the maximum current given in μA can be estimated from the following relation: $(I_{\max}) \approx 16.3\exp(-50\phi)$.

4. A brief summary

We have studied the polaronic and incoherent transport through DNA molecule (treated as a linear chain of quantum dots) using non-perturbative computational scheme (based on Green's functions theory within the framework of polaron transformation), where decoherence is modelled through the use of an imaginary dephasing potential. It was shown that, with the model, we can reproduce experimental data by fitting the model parameters. According to our calculations, at high voltages we observe the saturation effect after the smoothing increase of the current. Here we found the exponential dependence of the saturation current vs. the length of the molecular bridge, so the transport through DNA does not have a purely hopping character. It was also shown that the maximum current smoothly increases with the increase of the coupling parameter until some critical point ($\Gamma = 1.4$) and then it starts decreasing. Besides, our predictions indicate the exponential decrease of the current flow with the increase of the dephasing potential.

Acknowledgements

This work was supported by the Polish State Committee for Scientific Research (KBN), Grant No. 1 P03B 084 26.

References

[1] CAI L., TABATA H., KAWAI T., Appl. Phys. Lett., 77 (2000), 3105.
[2] PORATH D., BEZRYADIN A., DE VRIES S., DEKKER C., Nature, 403 (2000), 635.

[3] YOO K.-H., HA D.H., LEE J.-O., PARK J.W., KIM J., KIM J.J., LEE H.-Y., KAWAI T., CHOI H.Y., Phys. Rev. Lett., 87 (2001), 198102.
[4] HWANG J.S., KONG K.J., AHN D., LEE G.S., AHN D.J., HWANG S.W., Appl. Phys. Lett., 81 (2002), 1134.
[5] DEKKER C., RATNER M.A., Phys. World, 14 (2001), 29.
[6] ENDRES R.G., COX D.L., SINGH R.R.P., Rev. Mod. Phys., 76 (2004), 195.
[7] ZOHTA Y., EZAWA H., J. Appl. Phys., 72 (1992), 3584.
[8] BROUWER P.W., BEENAKKER C.W.J., Phys. Rev. B, 55 (1997), 4695.
[9] LY D., SANII L., SCHUSTER G.B., J. Amer. Chem. Soc., 121 (1999), 9400.
[10] HENDERSON P.T., JONES D., HAMPIKIAN G., KAN Y., SCHUSTER G.B., Proc. Nat. Acad. Sci. USA, 96 (1999), 8353.
[11] CONWELL E.M., RAKHMANOVA S.V., Proc. Nat. Acad. Sci. USA, 97 (2000), 4556.
[12] RAKHMANOVA S.V., CONWELL E.M., J. Phys. Chem. B, 105 (2001), 2056.
[13] HAULE K., BONČA J., Phys. Rev. B, 59 (1999), 13087.
[14] ČIŽEK M., THOSS M., DOMCKE W., Phys. Rev. B , 70 (2004), 125406.
[15] DONG B., CUI H.L., LEI X.L., HORING N.J.M., Phys. Rev. B, 71 (2005), 045331.
[16] WALCZAK K., Physica E, 33 (2006), 110.
[17] BIXON M., JORTNER J., Chem. Phys., 319 (2005), 273.
[18] WALCZAK K., Centr. Eur. J. Phys., 4 (2006), 349.

Received 7 May 2006
Revised 1 September 2006

Materials Science-Poland, Vol. 25, No. 2, 2007

Films of Heusler alloys

J. DUBOWIK[1*], I. GOŚCIAŃSKA[2], A. SZLAFEREK[1], Y. V. KUDRYAVTSEV[3]

[1]Institute of Molecular Physic, Polish Academy of Sciences, Poznań 60-179, Poland

[2] Department of Physics, Adam Mickiewicz University, Poznań 61-614, Poland

[3] Institute of Metal Physics, National Academy of Sciences of Ukraine, 252680 Kiev-142, Ukraine

Heusler alloys (HA) are a class of materials which may be metals, semiconductors or semimetals, most of them being ferromagnets. Some new applications of HA in spintronics and micro-electromagnetic actuators require their preparation in the form of thin films. Deposition of a HA film is a challenging task from the point of view of its proper ordering. Local disorder and antisite disorder are the most probable reasons of failure in achieving 100% polarization in nanostructures containing HA layers. We will review some examples of tunnel magnetoresistance structures that include Co_2YZ HA layers (Y = Mn, Cr, Fe, Z = Al, Si, Ga). The influence of structural ordering on the magnetic and transport properties of Co_2MnGa films are given with an emphasis on crystallization process of the films with amorphous structure and a further improvement of its structural ordering. Equally difficult task concerns preparation of HA films with shape memory (SM) effect. Recent achievements in technology of HA with SM will be reviewed. We will focus on non-stoichiometric Ni–Mn–Ga sputtered films. Their SM properties critically depend on composition and post-deposition annealing conditions. By a proper choice of these conditions, the ordered Ni–Mn–Ga films exhibit a well defined SM effect near room temperature.

Key words: *Heusler alloy; thin film; half-metal; ferromagnetic shape memory*

1. Introduction

Heusler alloys (HA) with the chemical formula X_2YZ are a class of materials with a variety of interesting physical properties. Depending on composition, they may be metals, semiconductors or semimetals, and additionally, most of them are ferromagnets. The full Heusler structure consists of four interpenetrating *fcc* sublattices with atoms at A(0,0,0), C(1/2,1/2,1/2), B(1/4,1/4,1/4), and D(3/4,3/4,3/4) positions which results in $L2_1$ crystal structure of the so-called full HA (Fig. 1) in which X_1 and X_2 sublattices are fully occupied. A large number of different elements can be chosen for

*Corresponding author, e-mail: dubowik@ifmpan.poznan.pl

X (Ni, Co, Fe, Pd, …), Y (Mn, Ni, Fe, Co, Ti, …), and Z (Ga, Al, In, Si, …) offering rich possibilities for tuning their magnetic, electrical and mechanical properties.

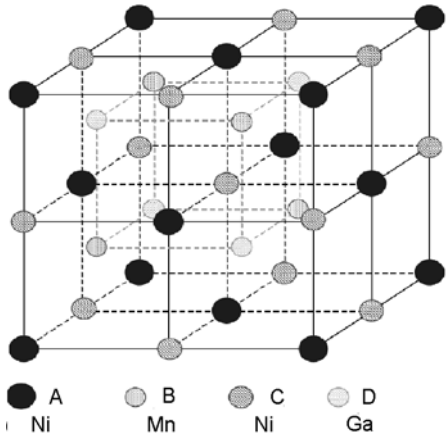

Fig. 1. Crystal structure of X_2YZ full Heusler alloy displaying the $L2_1$ structure consisting of four interpenetrating fcc lattices (A, B, C, D), each occupied by one of the following elements: Ni, Mn, or Ga

In HA there is always some degree of chemical disorder, heavily influencing many of their physical properties. In the fully ordered HA, the four sublattices A, B, C, and D are occupied by X, Y, X, and Z atoms, respectively giving the $L2_1$ type of order as it is shown in Fig. 1. In reality, this fully ordered state is hard to be attained, and there is a variety of possible disorder [1]. When X atoms remain ordered and full disorder occurs between Y and Z sites only, we have a *B*2 (CsCl type) structure, for example. If disorder occurs between one X site and either Y or Z sites, the atomic arrangement may lead to a DO_3 (Fe_3Al) structure. And eventually, an *A*2 structure occurs if there is the atomic arrangement when random order occurs between all X, Y and Z sites.

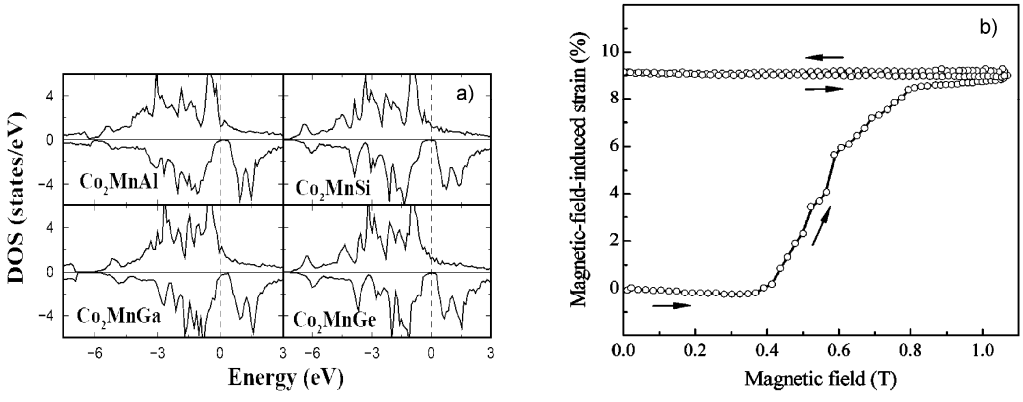

Fig. 2. Spin-resolved DOS for Co_2MnX, X = Al, Si, Ga, Ge (from Ref. [2]) (a) with a spin-split band structure characteristic of insulating behaviour of the spin down electrons; field-induced strain of a single-variant sample of orthorhombic seven-layered phase in the $Ni_{48.8}Mn_{29.7}Ga_{21.5}$ alloy at 300 K (b) measured perpendicular to the magnetic field applied along the (100) direction (from Ref. [7])

Recently, HA has attracted attention since they show great potential for spintronic [2] or for electromechanical [3, 4] applications. The first aspect concerns half-metallic properties of some HA exhibiting 100% spin polarization at the Fermi level. Full spin polarization results from two types of band structures for the majority and minority spin bands: while the majority spin band shows a typical metallic behaviour, the minority spin band exhibits a semiconducting behaviour with a gap in density of states at the Fermi level (Fig. 2a). NiMnSb half Heusler compound was found to reveal a half metallic behaviour as early as in 1983 [5], but full HA such as Co_2MnSi or Co_2MnGe [6] have only recently been found (by electron energy band calculations) to possess full spin polarization.

The second aspect is related to shape memory effect of some HA – a reversible martensitic transformation resulting in a substantial mechanical strain. Ni_2MnGa is the best known HA which exhibits both ferromagnetic behaviour and structural instabilities leading to a low temperature tetragonal distortion of the cubic cell, i.e., a martensitic transformation [3]. Additionally, for off-stoichiometric Ni–Mn–Ga HA, the martensitic transformation temperature may be tuned close to room temperature and various kinds of modulated structures in the martensitic phase may occur. It appeared that in such structurally metastable martensite phase, a rearrangement of martensitic variants can be realized under application of a relatively low magnetic field. As is shown in Fig. 2b, application of the magnetic field of ~1 T results in a huge (~10%) strain [7]. This effect is known as ferromagnetic shape memory effect (FSM). Recently a similar field-induced FSM effect has been found in non-stoichiometric $Ni_{50}Mn_{25+x}Sn_{25-x}$ HA [8].

It is obvious that for any spintronic application one needs HA in the form of thin films. Therefore, a number of papers have been concerned with both theoretical aspects of half-metallic behaviour of the HA thin films as well as with technological aspects aimed at fabrication of HA films with the highest spin polarization under optimum conditions (see, for example Ref. [2]). The formation of a HA film is a challenging task from the point of view of a proper ordering of different elements into the four sublattices. Local disorder and antisite disorder effects are the most probable reasons of failure in achieving 100% polarization in nanostructures containing HA layers.

Equally difficult task concerns preparation of HA films exhibiting ferromagnetic shape memory effect. Single crystals of off-stoichiometric Ni–Mn–Ga alloy exhibit strains of 10% under application of a moderate magnetic field [7] but in the films the effect has been found to be much lower [9]. Recent achievements in the thin film technology of FSM alloys comprise thin Ni–Mn–Ga films deposited by molecular beam epitaxy (MBE) [10], laser ablation [11] and by sputtering [12]. Since their shape memory properties critically depend on composition and post-deposition annealing conditions, and by a constraint from a substrate, by a proper choice of the deposition conditions and post-deposition annealing, the ordered and partially or fully released Ni–Mn–Ga films exhibit a well defined shape memory effect near room temperature.

2. Electronic transport in Heusler alloy films

Spintronics, which uses the spin degrees of freedom, is currently attracting great interest due to a high potential for applications in magnetic sensors and other devices based on tunnel magnetoresistive effect [13]. Hence, the materials with a high degree of spin polarization P at the Fermi level are needed to ensure as high as possible tunnel magnetoresistance ratio (TMR):

$$\mathrm{TMR} = \frac{R_{\uparrow\downarrow} - R_{\uparrow\uparrow}}{R_{\uparrow\uparrow}} = \frac{2P_1P_2}{1 - P_1 P_2} \tag{1}$$

where $R_{\uparrow\downarrow}$ and $R_{\uparrow\uparrow}$ are resistances for antiparallel and parallel magnetization configurations in a magnetic tunnel junction (MTJ), respectively. This definition gives TMR = ∞ (in practice a very high value of $\sim 10^4$) for the full polarization $P_1 = P_2 =$ 100% of the two ferromagnetic electrodes in TMJ.

A systematic search (based on electronic band calculations) for HA has revealed that Co_2MnGe, Co_2MnAl, Co_2MnSi and Co_2MnGa may be regarded as half-metallic ferromagnets with full (or almost full) spin polarization at the Fermi level [2, 6]. Recently, a considerable effort was devoted to HA containing Cr–Co_2CrAl and $Co_2Cr_{1-x}Fe_xAl$ – since they have been also predicted to exhibit a complete spin polarization with both a high magnetization and a high Curie temperature [14, 15]. $Co_2Cr_{1-x}Fe_xAl$ HA showed a high magnetoresistive effect of 60% in pressed powder pallets [14] and since this discovery a number of theoretical papers has confirmed their full polarization [16, 17]. However, in a spin valve MTJ containing $Co_2Cr_{0.6}Fe_{0.4}Al$ electrode only a moderate TMR of ~16% has been found at RT [18].

Despite the predicted half-metallic properties of HA, in HA films much less than 100% spin polarization has been measured so far (see, for example, Ref. [19]). There are few useful methods of determining spin polarizations in ferromagnetic materials. Photoemission [20] and tunnelling spectroscopy [21] have been applied but the most appropriate seems to be point-contact Andreev reflection [22] in which a measurement of the conductance between a superconductor in a point contact with a ferromagnet can determine the spin polarization. Using this method, Clifford et al. [23] found the spin polarization of ~80% in $Co_2Cr_{0.6}Fe_{0.4}Al$ bulk HA. The most extensively applied method, however, for the measurement of the spin polarization in half-metallic thin films is evaluation of P from TMR effect in MTJ devices. Using a CoFe layer ($P \approx 50\%$) as a top electrode and a HA film as a bottom electrode [24] the resulting spin polarization can be simply estimated from the Juliere model described by Eq. (1). Keeping in mind that the magnetoresistance of such an MTJ depends not only on the electronic structure of HA but also on the quality of insulating barrier (AlO_x in most cases), one may regard the resulting spin polarization of HA as a realistic limit determined both by a structural perfection of HA film and a HA/tunnel barrier interface quality on equal foot. On the other hand, such an approach gives some practical

insight on the realization of HA electrodes integrated with other components of an MTJ device.

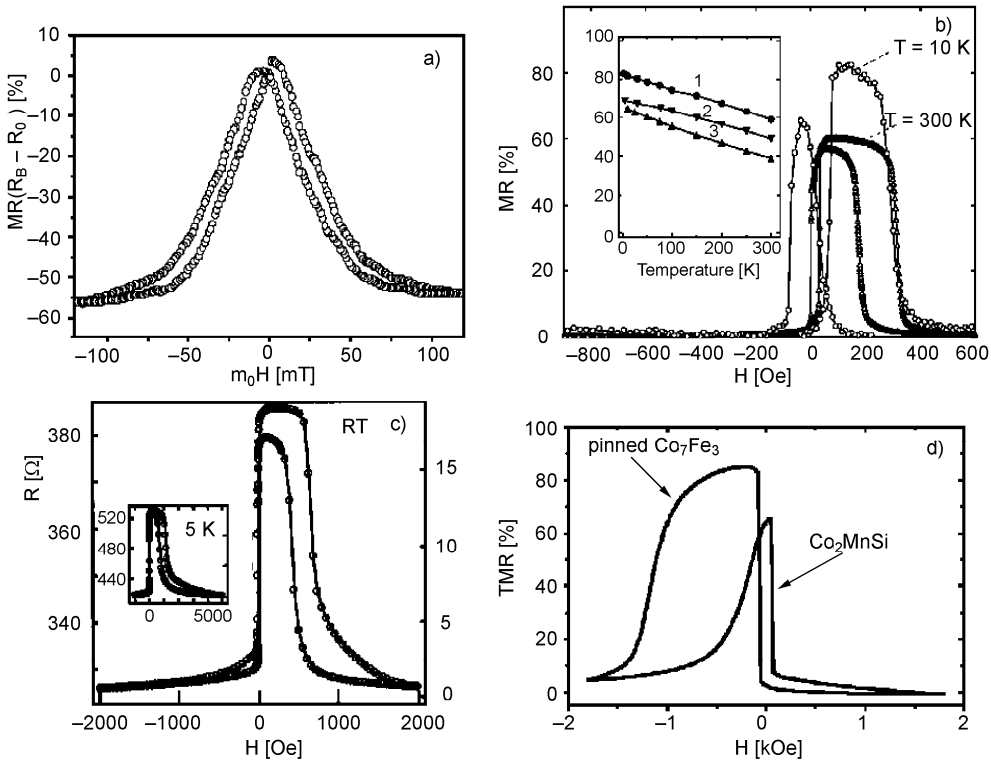

Fig. 3. Magnetoresistance (MR) of a powder pellet of $Co_2Cr_{0.6}Fe_{0.4}Al$ (from Ref. [14]) (a); MR curves of MTJ with the epitaxial Co_2MnAl bottom electrode at 10 K and 300 K (b); the inset shows temperature dependence of MR ratios for MTJ using epitaxial Co_2MnAl (1), polycrystalline Co_2MnAl (2), and $Co_{75}Fe_{25}$ (3) (from Ref. [26]); magnetoresistance curves at RT and 5 K for a spin-valve-type MTJ with a $Co_2Cr_{1-x}Fe_xAl$ electrode (from Ref. [21]) (c); MR loop of MTJ (d) with Co_2MnSi Heusler alloy electrode (from Ref. [28])

Figure 3 juxtaposes some recent results concerning TMR characteristics of MTJ devices which include a HA layer as a bottom electrode. However, the most puzzling result (shown in Fig. 3a) concerns a relatively high TMR effect of ~60% at RT in pressed powder pellets of $Co_2Cr_{0.6}Fe_{0.4}Al/Al_2O_3$ [14]. Such a high value of TMR in the obviously defected samples with nonuniform microstructure resulted in further attempts [18, 25] aimed at fabrication of MTJ containing $Co_2CrFeAl$ HA electrode with structural ordering as good as possible. However, as is seen in Fig. 3b, TMR in a spin valve structure $Co_2Cr_{1-x}Fe_xAl$ (100 nm)/Al_2O_3(1.3 nm)/CoFe(3 nm)/NiFe (5nm)/IrMn (15 nm)/Ta (10 nm) has been found fairly low amounting to ~19% at RT for $x = 0.4$ [25]. It appeared that HA films prepared by magnetron sputtering on thermally oxidized Si substrates do not show the $L2_1$ structure as expected for the bulk, but reveal the $B2$ or

*A*2 structures, depending on Fe concentration. It was pointed out that better TMR characteristics might be obtained for *B*2 structure without Co–Cr type of disorder.

Recently Sakubara et al. [26] fabricated MTJ with epitaxially grown Co_2MnAl bottom electrodes combined with a magnetron sputtered Al–O tunnel barrier. As shown in Fig. 3c, MTJ with a stacking structure of epi-Co_2MnAl/Al–O/CoFe/IrMn exhibits TMR ≈ 65% at RT and 83% at 2 K (see the inset in Fig. 3c). This result suggested that Co_2MnAl with *B*2 order is highly spin polarized, however the estimated spin-polarization of ~59% (Eq. (1)) is still smaller than the expected value of 76% for the *B*2 structure [27]. Besides TMJ containing $Co_2Cr_{1-x}Fe_xAl$ or Co_2MnAl HA electrodes, Co_2MnSi HA integrated in MTJ [28] offers even higher TMR values of ~86% at 10 K which roughly corresponds to P = 60% (Fig. 3d). Recently, Hütten et al. [24] demonstrated TMR value of 108% at 20 K associated with the spin polarization of 72%. All these results clearly show that fabrication of MTJ or other spintronic devices in which HA electrodes would reveal full half-metallic characteristics (i.e. TMR ≈ ∞) is still a challenging task, first of all, due to difficulties in preparation of HA layers with a good ordering, and secondly, due to difficulties with oxidation of HA in the course of the tunnel barrier formation.

Since the problem of ordering of HA films is one of the key issues in the application for spintronic devices, we have investigated kinetics of the ordering in Co_2MnGa HA film. Co_2MnGa has been shown [2] to reveal almost half-metallic behaviour. To obtain the Co_2MnGa alloy films with utmost disorder, they were vapour quenched onto the substrates cooled with liquid nitrogen. The as-deposited Co_2MnGa films were annealed at 293 (RT), 513, 598 and 728 K in high vacuum conditions. The resulting various structural states of Co_2MnGa HA films will be referred to as 1, 2, 3 and 4, respectively, to correspond to the above annealing conditions.

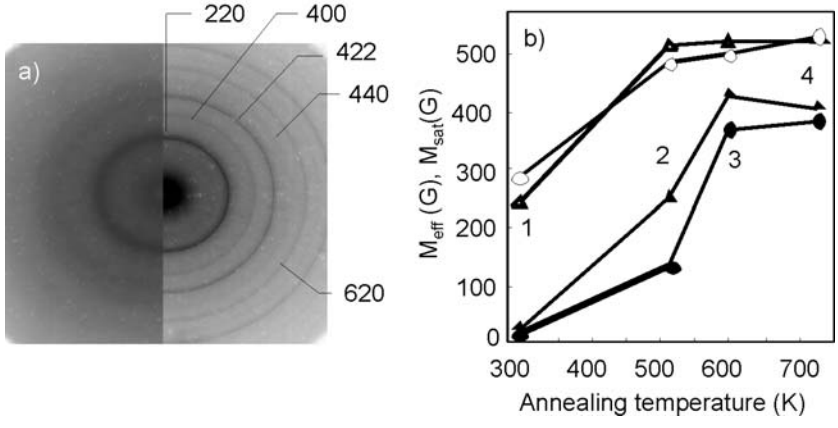

Fig. 4. TEM diffraction patterns of Co_2MnGa alloy films (a) deposited onto a substrate cooled with liquid nitrogen (left panel) and post annealed at 630 K (right panel); the saturation (M_S) and effective (M_{eff}) magnetization of Co_2MnGa films (b) as a function of annealing temperature. The numbers 1–4 denote corresponding films (see text)

Figure 4a (left panel) shows transmission electron microscopy (TEM) diffraction patterns of the Co_2MnGa film deposited onto an NaCl substrate cooled with liquid nitrogen. It is clearly seen that vapour quenching deposition onto cooled substrates leads to formation of an amorphous (nanocrystalline) state. After annealing at 630 K, the amorphous film becomes crystalline with the diffraction lines characteristic of *B*2 HA structure (Fig. 4a, right panel). A thorough X-ray diffraction characterization of the films annealed at $T > 600$ K suggests even the presence of $L2_1$ ordering for film 4. Generally, annealing of the vapour quenched Co_2MnGa films results in the formation of the amorphous, *A*2, *B*2 and $L2_1$ ordering for the films 1, 2, 3 and 4, respectively.

Figure 4b shows the dependence of RT values of M_S (full symbols) and M_{eff} (open symbols) on annealing temperature corresponding to the films 1, 2, 3, and 4, respectively. The amorphous film 1 is only weakly magnetic with $M_S \approx 25$ G. However, M_{eff} of ~200–300 G, estimated from the position of the most intensive ferromagnetic (FMR) absorption, suggests its inhomogeneous magnetic state with local effective fields $4\pi M_{eff}$ as high as ~3000 G. Annealing at elevated temperatures results in a substantial increase in both M_S and M_{eff} up to 400 and 500 G, respectively. Since M_S of the films 3 and 4 is practically the same, we argue that there is practically no difference in the magnetic properties of the Co_2MnGa films with *B*2 and $L2_1$ type of ordering. However, the saturation magnetization M_S ($M_S \approx 450$ G, $2.5\mu_B$ per formula unit) of our films with the highest ordering is still lower than that of the bulk ($4\mu_B$) [2] and Co_2MnGa epitaxial films ($3.5\mu_B$) [29]. Moreover, M_S and M_{eff} differ substantially what may be related to a high easy plane anisotropy of Co_2MnGa films due to magnetostriction [29].

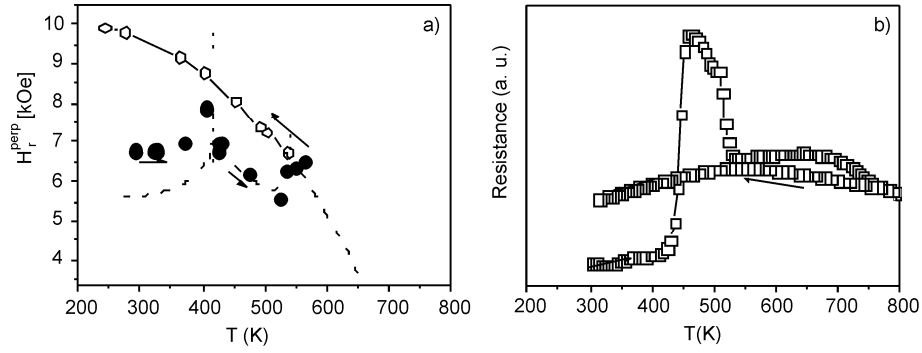

Fig. 5. Changes of FMR resonance field H_r^{perp} in the course of heating (full circles) and cooling (full diamonds) of an initially amorphous Co_2MnGa film (a); resistivity o f the same Co_2MnGa film in the course of heating to ~800 K and cooling to RT (b)

Using high-temperature FMR [30] measurements in the perpendicular configuration, we checked the temperature range in which the amorphous Co_2MnGa films order. Figure 5a shows temperature changes of the resonance field H_r^{perp} in the course of temperature cycling from RT to 570 K and back RT. In the range of ca. 420–430 K, the resonance field increases sharply, then it decreases in a way typical of a ferromagnetic

film with T_C of 600 K and eventually at ~550 K it grows again. In the cooling cycle, the temperature changes of the resonance field H_r^{perp} are typical of a well ordered Co_2MnGa alloy with T_C of ~ 650 K. These anomalies in the behaviour of H_r^{perp} vs. T strongly suggest the presence of two structural transformations in amorphous Co_2MnGa at 430 and 540 K, respectively. Comparing FMR results shown in Fig. 5a with the TEM results, we supposed that these anomalies are related to the "amorphous → A2" and "A2 → B2" transformations, respectively. However, the electric resistivity ρ of the initially amorphous Co_2MnGa film experiences a sharp increase between 450 and 540 K and then at $T \approx 550$ K it decreases again to a considerably higher value than that of the amorphous film, and slightly decreases at T >750 K (Fig. 5b). Our preliminary TEM studies of the structure of the films annealed between 450 K and 540 K suggest formation of a two-phase metastable structure in this temperature region. In the temperature dependence on the cooling cycle, ρ shows a semiconductor-like behaviour at $550 > T > 800$ K with a negative coefficient of resistivity and a metallic behaviour below 600–550 K. Both a high value of the resistivity in $B2$ structural ordering and the change in the temperature dependence of the resistivity may result from half-metallic behaviour of the ordered Co_2MnGa films.

In summary, we have shown, that unlike amorphous Ni_2MnZ (Z = In, Ga, Ge) films, Co_2MnGa films in the amorphous state exhibit some weak ferromagnetic behaviour. According to the FMR and resistivity results, formation of an inhomogeneous metastable structure in the temperature range of 450–550 K has been observed. The structural "$A2(B2) \rightarrow L2_1$" transition causes more significant increase in M_S and M_{eff} than the "amorphous state → $A2$" one. However, the saturation magnetization ($M_S \approx 450$ G, $2.5\mu_B$ per formula unit) of our films with the highest ordering is still lower than that of the bulk ($4\mu_B$) and of Co_2MnGa epitaxial films ($3.5\mu_B$). Resistivity behaviour of the well ordered Co_2MnGa films suggests their half-metallic properties.

3. Ferromagnetic Heusler alloy films with shape memory effect

Ferromagnetic shape memory (FSM) alloys are a class of materials undergoing thermodynamically reversible martensitic transformations in a ferromagnetic state [3]. Such a structural phase transformation of a martensitic type has been reported in ternary intermetallic compounds Co–Ni–Al and Co–Ni–Ge and in iron(cobalt)-based alloys such as Fe–Pd(Pt) and Co–Ni and in Ni–Mn–Al, Co–Ni–Ga HA.

Ni–Mn–Ga HA with various stoichiometries have been the most extensively investigated FSM materials. For bulk stoichiometric Ni_2MnGa, the Curie temperature T_C = 376 K and the martensitic transformation (MT) temperature is $T_M \approx 200$ K [1]. Above T_M, Ni_2MnGa adopts $L2_1$ structure (Fig. 1). In the martensite phase Ni_2MnGa transforms into a twinned structure (as shown schematically in Fig. 6) composed of tetragonal phase with an enhanced anisotropy [3]. Generally, for the nonstoichiometric Ni–Mn–Ga HA there are several different martensite structures of tetragonal or

orthorhombic symmetry. Some of them are modulated with a shuffling of the (110) atomic planes with a period of five (5M) or seven (7M) atomic planes [31, 32], or unmodulated [33, 34]. The lattice constant ratios give the maximum strain which is available from the twin rearrangement. This limit is of 6% in the 5M structure [35], and of 10% in the orthorhombic 7M martensite of $Ni_{1.95}Mn_{1.19}Ga_{0.86}$ [7].

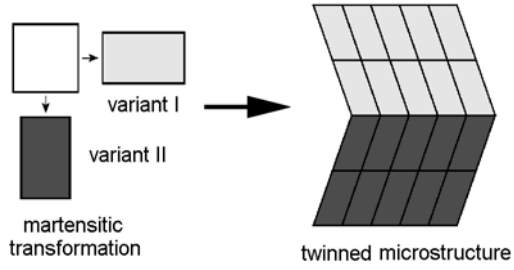

Fig. 6. Schematic illustration of the martensitic transformation and twinning in two dimensions (from Ref. [2])

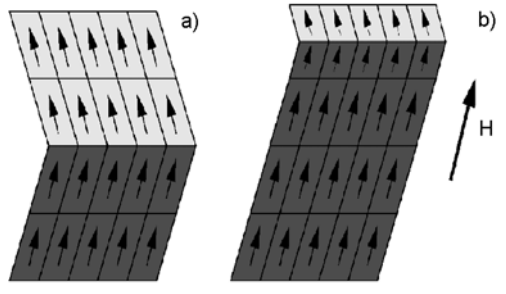

Fig. 7. Schematic representation of the magnetic field-induced redistribution of the martensitic domains (a). Domains benefiting from the applied field dominate (b) in the sample, leading to a macroscopic deformation (from Ref. [2])

As is shown in Fig. 7, magnetic fields or stress can rearrange the volume fraction of martensitic variants by the motion of twin boundaries to minimize the total energy. Such a rearrangement of the martensitic variants with magnetic field results in a large reversible strain. This change of crystallographic domain population by the application of an external magnetic field is the mechanism for the FSM effect (Fig. 7). Depending on a composition, the temperature of the phase transformation can be tuned in a wide range [4]. The large strain and ability to tune the temperature of transformation with the composition make Ni–Mn–Ga alloys a very attractive candidate for magnetic field driven actuators.

Recent efforts have focused on enabling the ferromagnetic shape memory or thermal shape memory effects on micrometer or smaller scales. Figure 8a shows a conceptual design of a microactuator [36]. A film is assumed to be deposited on the substrate in the austenite state, and is unstressed and released from a substrate. At high temperatures the film is in the austenite and is undeformed as shown in Fig. 8a in the left panel. On cooling, the film transforms to the martensite and bulges (Fig. 8a, right panel). Such tiny "machines" have been created [37] in reality (Fig. 8b). To design such "micromachines", free-standing single crystal Ni–Mn–Ga films would be the best candidate since they allow the formation of austenite/single variant interfaces resulting in a specific tent-like deformation in the martensite phase. Recently, single

crystal Ni_2MnGa and $Ni_2Mn_{1.2}Ga_{0.8}$ films (900 Å thick) have been grown by molecular beam epitaxy on (001) GaAs substrates with ScErAs interlayer [10]. The films were ferromagnetic with the Curie temperature of ~340 K. It has been observed that constraint of the substrate inhibited martensitic transformation, but after removal of the substrates to release the films, it enabled a martensitic phase transformation in the free-standing single crystal films to occur. In particular, the $Ni_2Mn_{1.2}Ga_{0.8}$ films transformed into martensite phase at RT and showed the two-way shape memory effect upon thermal cycling. The ferromagnetic shape memory effect was demonstrated in free-standing stoichiometric Ni_2MnGa bridges and cantilevers at 135 K with magnetic field applied perpendicular to the sample surface but with no quantitative measurements of the effect.

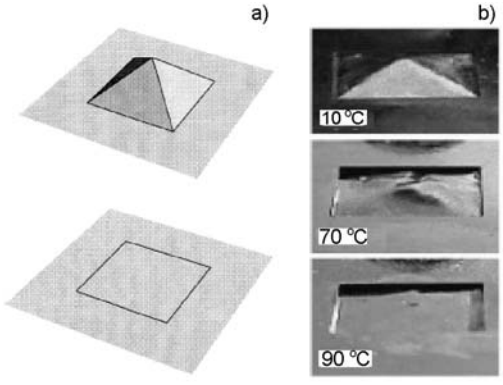

Fig. 8. A tent-like deformation of a film, which is flat in the austenite phase (a) (from Ref. [36]); realization of such a deformation in a CuAlNi foil, released on a 1 cm by 1 cm region, produced by heating and cooling the film (b) (from Ref. [37])

Wuttig et al. [38] reported phase transformations in polycrystalline sputtered 1 μm thick Ni–Mn–Ga films deposited on Si cantilevers. They noticed that the films deposited on substrates held above 385 ºC or annealed at 400 ºC show an austenite/martensite transformation comparable to NiTi shape memory films.

Suzuki et al. [39] and M. Ohtsuka et al. [9] deposited 5 μm thick Ni–Mn–Ga films by sputtering on poly(vinyl alcohol) substrates. After separating from the substrates, the films were annealed at ~1100 K for ordering. They detected the martensitic transformation at ~250 K and ~320 K for the films of nominal composition Ni_2MnGa and $Ni_{2.17}MnGa$, respectively. The two-way shape memory effect for the constraint-aged films was confirmed as well as a small (of 0.08%) FSM effect was detected under application of the external magnetic field of 5 T [9].

Using a new technique of ultra-high vacuum magnetron sputtering from Ni, Mn and Ni_2Ga_3 targets, Takeuchi et al. [12] produced thin film composition spreads onto micromachined arrays of mechanical cantilever libraries. They succeeded in detecting structural transformations and determined crystal structure with a scanning X-ray microdiffractometer, and performed a quantitative magnetization mapping of the spreads. They found that a large previously unexplored region outside the Heusler composition contains reversible martensites that are also ferromagnetic. There were also some attempts to produce Ni–Mn–Ga thin films by laser ablation [11, 40] but the

results obtained did not show any clear signs of MT. We observed some signs of martensitic transformation in the flash-evapourated Ni–Mn–Ga films on mica substrates [41].

The presence of MT in thin films is a prerequisite for any applications in MEMS. However, MT in Ni–Mn–Ga films is much less documented and the results show that the transformation is governed by microstructure [42], constraint from substrates [10] and by structural ordering [9]. Here, we show some new results concerning the influence of MT on the magnetic, electrical and thermal shape memory effect in the sputter deposited Ni–Mn–Ga films.

The films (0.5–1 μm) were deposited by face-to-face sputtering onto rotating glass and mica substrates held at RT. The composition of the films was determined by X-ray fluorescence and was changed in a wide range from $Ni_{60}Mn_{20}Ga_{20}$ to $Ni_{48}Mn_{31}Ga_{21}$ by altering the configuration of Mn and Ni pieces placed on the targets. The $Ni_{49}Mn_{29.6}Ga_{21.4}$ (A) and $Ni_{56.4}Mn_{21.8}Ga_{21.8}$ (B) films were chosen for further characterization since they revealed MT at RT and well above the Curie temperature of ~360 K. The X-ray fluorescence spectroscopy confirmed a very uniform composition profiles of our sputtered samples. The films were annealed in 10^{-4} Pa vacuum at 873 K for 1 h. The structural characterization of the films was carried out by XRD using CuK_α radiation with the sample tilted at an angle of 2^o from the diffraction plane to suppress the reflections from mica substrates The magnetic properties of our Ni–Mn–Ga films were investigated using FMR spectrometer operating at 9.08 GHz at temperatures from 78 K to 400 K in a magnetic field applied perpendicular and parallel to the film plane. The values of $4\pi M_{\text{eff}}$ were determined from the resonance fields H^{perp} taken in the perpendicular configuration at various temperatures; $\omega/\gamma = H^{\text{perp}} - 4\pi M_{\text{eff}}$, where $\omega = 2\pi f$ is a microwave angular frequency and γ is the gyromagnetic ratio corresponding to the g factor of 2 [43].

XRD patterns of our films show typically few broad peaks with (220) as the most prominent reflection (Fig. 9a) due to a high (110) texture. As we will show later, MT in the film A onsets at 310–320 K. Interestingly, the (220) peak of the film A is fairly broad of ~1^o and does not split, a typical feature of our films with MT about RT. This suggests that the (220) reflection is formed by overlapping peaks both from austenite and martensite phases. The position of the (220) peak gives the cubic lattice constant $a = 0.581$ nm, the same as in bulk Ni_2MnGa. Film 9b with a higher MT temperature of ~420 K reveals in XRD the split (202) and (220) peaks characteristic of the tetragonal structure with $a = b = 0.59$, and $c = 0.558$ nm ($c/a = 0.946$).

Figure 10a shows the temperature behaviour of magnetic properties of film 9a; the saturation magnetization $4\pi M_S$, the effective magnetization $4\pi M_{\text{eff}}$ and the FMR linewidth ΔH. Figure 10b shows the temperature dependence of the electric resistance $R(T)$ of the same film. An apparent slope change in $R(T)$ is indicative of the ferromagnetic-paramagnetic transition at the Curie temperature $T_C = 365$ K while an anomalous increase of ~10% in $R(T)$ from 330 to 260 K is due to MT.

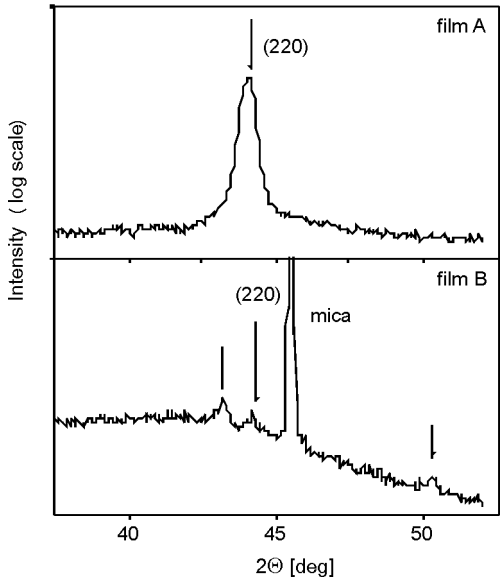

Fig. 9. XRD scans of the $Ni_{49}Mn_{29.6}Ga_{21.4}$ (A) and $Ni_{56.4}Mn_{21.8}Ga_{21.8}$ (B) films deposited on mica substrates. The scans were taken at RT in Θ–2Θ geometry with the substrate tilted slightly from the diffraction plane in order to remove (a) or to suppress (b) the reflections from mica

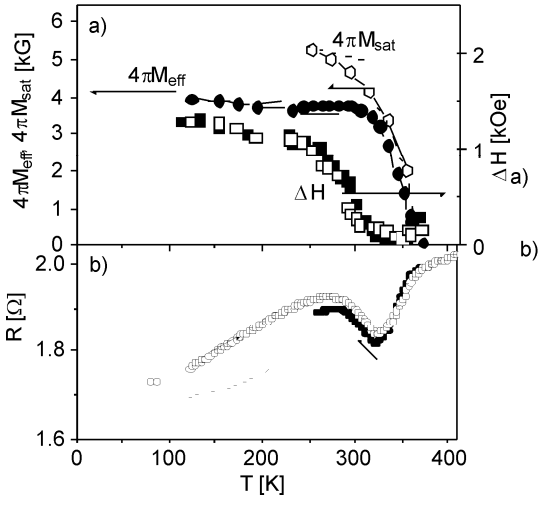

Fig. 10. Temperature dependences of the saturation magnetization $4\pi M_{sat}$, the effective magnetization $4\pi M_{eff}$, the FMR linewidth ΔH (a) and temperature dependence of the electric resistance (b) of an $Ni_{49}Mn_{29.6}Ga_{21.4}$ film (film A)

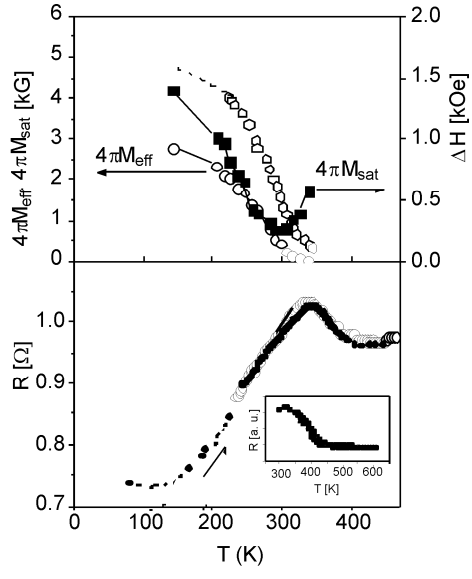

Fig. 11. Temperature dependences of the saturation magnetization $4\pi M_s$, the effective magnetization $4\pi M_{eff}$, the FMR linewidth ΔH (a) and temperature dependence of the electric resistance R (b) of an $Ni_{56.4}Mn_{21.8}Ga_{21.8}$ film (film B); inset in (b) shows $R(T)$ of the film B measured independently at elevated temperatures

An anomalous jumplike feature in $R(T)$ is characteristic of MT in bulk Ni–Mn–Ga alloys [4]. However, in the film A it extends from the martensitic start (M_s) to finish (M_f) temperatures: M_s = 310 K to M_f = 260 K, i.e., the temperature range is much broader than in bulk alloys [44]. Similar extended anomalies due to MT appear in the magnetic behaviour shown in Fig. 10a. While the temperature dependence of $4\pi M_{sat}$ is quite monotonic and saturates at ~6–6.5 kG (i.e., $M_{sat} \approx$ 500 G at 0 K), the growth in $4\pi M_{eff}$ in the martensite phase is strongly diminished and $4\pi M_{eff}$ exhibits a hysteretic behaviour. Simultaneously, the FMR linewidth (measured in the perpendicular configuration) strongly increases from about 100 Oe (at 330 K, i.e., in the austenite phase) to about 1.5 kOe at 100 K (in the martensite phase). Such a behaviour is typical of the martensitic transformation of relatively thick (0.5–1 μm) Ni–Mn–Ga films [44] in which, probably due to a constraint from the substrates (in our case mica), the transformation region is strongly extended. In much thinner Ni–Mn–Ga films the effect of MT is almost completely suppressed [41].

In Figure 11a we show the temperature dependences of $4\pi M_{eff}$ and ΔH in the film B with the martensitic transformation above T_C = 350 K. As follows from the temperature dependence of the electrical resistance (Fig. 11b), MT extends in this film from M_s = 420 K to M_f = 330 K. While the magnetic characteristics ($4\pi M_{eff}$ and ΔH) in the film A (with $M_s < T_C$) clearly show the anomalous behaviour in the martensitic phase (Fig. 10a), in film B (with $M_s > T_C$) they change monotonically. However, $4\pi M_{eff}$ obtained from FMR attains at low temperatures the values of 3– 3.5 kG, that is much lower than $4\pi M_{sat}$ of ~6 kG measured with VSM, and ΔH values near T_C are substantially higher than that in the film A in the austenite phase. Such a behaviour of the magnetic properties is typical of Ni–Mn–Ga films with a columnar microstructure [41] and results from a rather complicated interplay between the shape anisotropy related to the microstructure and a substantial magnetocrystalline anisotropy in the martensite phase [3].

In the film B, we also checked the shape memory effect induced by thermal changes. For this purpose the $Ni_{56.4}Mn_{21.8}Ga_{21.8}$ film was partially released from the mica substrate. Since an Ni–Mn–Ga film deposited by sputtering is always under severe tension, it is curled in the form of a spring after releasing from the substrate as is shown in Fig. 12a, upper panel. The radius of curvature r of the released film B was measured as a function of temperature. The radius reversibly increased on heating (Fig. 12a, bottom panel) and then decreased on cooling in a repeatable manner characteristic of two-way shape memory behaviour [9]. The resulting film strain ε versus T (defined as $\varepsilon = d/2r$, where d = 1 μm is the film thickness) is shown in Fig. 12b. It is seen that the shape recovery arises in the temperature range of 420–330 K in agreement with the results of the electrical resistance measurements but a substantial thermal hysteresis of ~50^o should be rather attributed to some friction between the curled "spring" windings than to the fairly narrow intrinsic hysteretic behaviour of the shape memory effect (see the inset in Fig. 11b). We estimated the magnitude of the strain change accompanied by MT as $\Delta\varepsilon \approx 0.2\%$ resulting from the radii of 0.2 mm and

20 mm of the curled film and that after almost perfect recovery, respectively. It is interesting that the shape memory effect in the film A was much weaker.

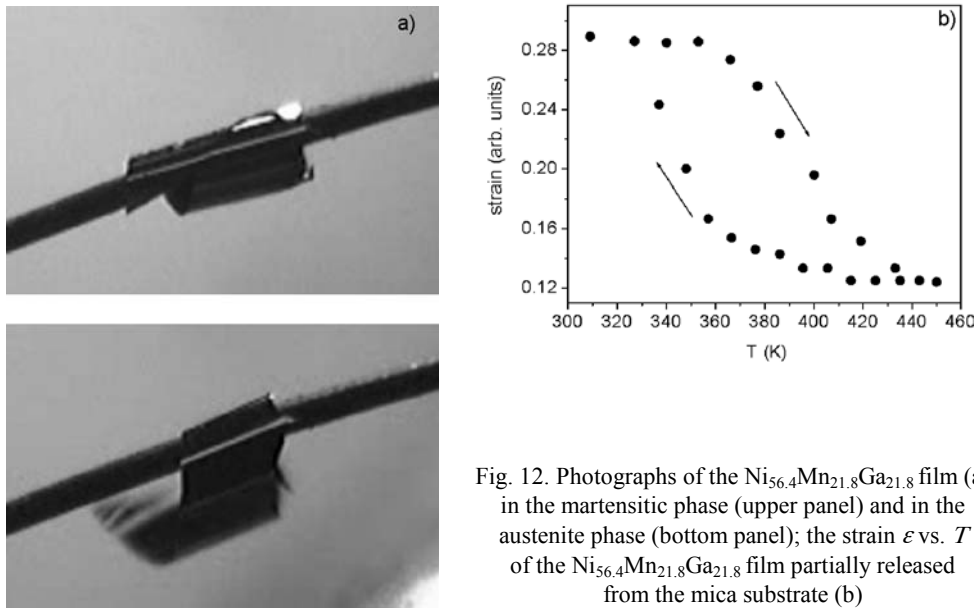

Fig. 12. Photographs of the $Ni_{56.4}Mn_{21.8}Ga_{21.8}$ film (a) in the martensitic phase (upper panel) and in the austenite phase (bottom panel); the strain ε vs. T of the $Ni_{56.4}Mn_{21.8}Ga_{21.8}$ film partially released from the mica substrate (b)

In summary, we have observed the influence of the martensitic transformation on the magnetic and electrical properties in Ni–Mn–Ga films with MT below and above T_C. An anomalous behaviour of the magnetic properties of Ni–Mn–Ga films in the martensite phase has been compared with the electrical resistance vs. T characteristics. The temperature range of MT in our films has been found to be much broader in comparison to that in the bulk Ni–Mn–Ga alloys. The two-way shape memory effect has been confirmed in our films.

4. Conclusions

We reviewed the current status of the technology of the Heusler alloy films with a special emphasis on possible applications of highly sensitive TMR sensors in spintronics as well as in micro-electromechanical systems.

Acknowledgements

Financial support of the Polish Committee for Scientific Research, Grant No. 4 T08C 045 25 is gratefully acknowledged.

References

[1] WEBSTER P.J., Contemp. Phys., 10 (1969), 559.

[2] GALANAKIS I., DEDERICHS P.H., [in:] *Half-metallic Alloys. Fundamentals and Applications*, I. Galanakis, P. H. Dederichs (Eds.), Springer, Berlin, 2005, pp. 1–34.

[3] ENKOVAARA J., AYUELA A., ZAYAK A.T., ENTEL P., NORDSTROM M., DUBE L., JAKALEN J., IMPOLA J., NIEMINEN R.M., Mater. Sci. Eng. A, 376 (2004), 52.

[4] VASIL'EV A.N., BUCHEL'NIKOV V.D., TAKAGI T., KHOVAILO V.V., ESTRIN E.I., Phys. Usp., 46 (2003), 559; http://arxiv.org/abs/cond-mat/0311433.

[5] DE GROOT R.A., MUELLER F.M., VAN ENGEN P.G., BUSCHOW K.H.J., Phys. Rev. Lett., 50 (1983), 2024.

[6] ISHIDA S., AKAZAWA S., FUJII S., KASHIWAGI S., ASANO S., J. Phys. Soc. Jpn., 64 (1995), 2152.

[7] SOZINOV A., LIKHACHEV A.A., LANSKA N., ULLAKO K., Appl. Phys. Lett., 80 (2002), 1746.

[8] KOYAMA K., WATANABE K., KANOMATA T., KAINUMA R., OIKAWA K., ISHIDA K., Appl. Phys. Lett., 88 (2006), 132505.

[9] OHTSUKA M., SANDA M., MATSUMOTO M., ITAGAKI K., Mater. Sci. Eng. A, 378 (2004), 378.

[10] DONG J.W., XIE J.Q., LU J., ADELMANN C., PALMSTROM C.J., SUI J., PAN Q., SHIELD T.W., JAMES R.R.D., MCKERNAN S., J. Appl. Phys., 95 (2004), 2593.

[11] CASTANO F.J., NELSON-CHEESEMAN B., O'HANDLEY R.C., ROSS C.A., REDONDO C., CASTANO F., J. Appl. Phys., 93 (2003), 8492.

[12] TAKEUCHI I., FAMODU O.O., READ J.C., ARONOVA M.A., CHANG K.-S., CRACIUNESCU C., LOFLAND S.E., WUTTIG M., WELLSTOOD F.C., KNAUSS L., OROZCO A., Nature Mat., 2 (2003), 180.

[13] WOLF S.A., AWSCHALOM D.D., BURHMAN R.A., DAUGHTON J.M., VON MOLNAR S., ROUKES M.L., CHTCHEKLKANOVA A.Y., TREGER D.M., Science, 294 (2001), 1488.

[14] BLOCK T., FELSER C., JAKOB G., ENSLING J., MUHLING B., GUTLICH P., CAVA R.J., Sol. St. Chem. 176 (2003), 646.

[15] FELSER C., ELMERS H.-J., FECHER G.H., [in:] *Half-Metallic Alloys. Fundamentals and Applications*, I. Galanakis, P. H. Dederichs (Eds.), Springer-Verlag, Berlin, 2005, pp. 113-149.

[16] GALANAKIS I., J. Phys. Cond. Matter, 16 (2004), 3089.

[17] UMETSU T.Y., KOBAYASHI K., FUJITA A., OIKAWA K., KAINUMA R., ISHIDA K., ENDO N., FUKAMICHI K., SAKUMA A., Phys. Rev. B, 72 (2005), 214412.

[18] INOMATA K., OKAMURA S., GOTO R., YEZUKA N., Jpn. J. Appl. Phys. 42 (2003), L419.

[19] RAPHAEL M., RAVEL B., WILLARD M., CHENG S., DAS B., HARRIS R., BUSSMANN K., CLASSEN J., HARRIS U., Appl. Phys. Lett., 81 (2002), 2812.

[20] *Polarized Electrons in Surface Physics*, R. Feder (Ed.), World Scientific, Singapore, 1985.

[21] TEDROW P.M., MASEVEY R., J. Appl. Phys., 76 (1994), 6101.

[22] SOULEN J., BYERS J.M., OSOFSKY M.S., NADGORNY B., AMBROSE T., CHENG S.F., BROUSSARD P.R., TANAKA C.T., NOWAK J., MOODERA J.S., BARRY A., COEY J.M.D., Science, 282 (1998), 85.

[23] CLIFFORD E., VENKANESAN M., GUNNING R., COEY J.M.D., Sol. State Comm., 131 (2004), 61.

[24] HÜTTEN A., KAMMERER S., SCHMALHORST J., REISS G., [in:] *Half-metallic Alloys. Fundamentals and Applications*, I. Galanakis, P. H. Dederichs (Eds.), Springer-Verlag, Berlin, 2005, pp. 241–264.

[25] INOMATA K., TEZUKA N., OKAMURA S., KUREBAYASHI H., HIROKATA A., J. Appl. Phys., 95 (2004), 7234.

[26] SAKUBARA Y., NAKATA J., OOGANE M., KATO H., SAKUMA A., MYAZAKI T., KUBOTA H., Appl. Phys. Lett., 88 (2006), 022503.

[27] KUBOTA H., NAKATA J., OOGANE M., SUKUMA A., MIYAZAKI T., Jpn. J. Appl. Phys., Part 2, 43 (2004), L984.

[28] SCHMALHORST J., KAMMERER S., SACHER M., REISS G., HUTTEN A., SCHOLL A., Phys. Rev. B, 70 (2004), 024426.

[29] PECHAN M.J., YU C., CARR D., PALMSTRØM C.J., J. Magn. Magn. Mater., 286 (2005), 340.

[30] KUDRYAVTSEV Y.V., OKSENENKO V.A., KULAGIN V.A., DUBOWIK J., LEE Y.P., J. Magn. Magn. Mater, 310 (2007), 2271.
[31] WEBSTER P.J., ZIEBECK K.R.A., TOWN S.L., PEAK M.S., Philos. Mag. B, 49 (1984), 295.
[32] MARTYNOV V.V., KOKORIN V.V., J. Phys., III, 2 (1992), 739.
[33] WANG W.H., WU G.H., CHEN J.L., GAO S.X., ZHAN W., WEN G.H., CHAN X.X., Appl. Phys. Lett., 79 (2001), 1148.
[34] CHERNENKO V.A., SEGUI C., CESARI E., PONS J., KOKORIN V.V., Phys. Rev. B, 57 (1998), 2659.
[35] HECZKO O., SOZINOV A., ULLAKKO K., IEEE Trans. Magn., 36 (2000), 541 3266.
[36] BHATTACHARYA K., JAMES R.D., J. Mech. Phys. Solids, 47 (1999), 531.
[37] BHACHATTARYA K., JAMES R.D., Science, 307 (2005), 53.
[38] WUTTIG M., CRACIUNESCU C., LI J., Mater. Trans. JIM, 41 (2000), 933.
[39] SUZUKI M., OHTSUKA M., SUZUKI T., MATSUMOTO M., MIKI H., Mat Trans. JIM, 40 (1999), 1174.
[40] CHUNG C.Y., CHERNENKO V.A., KHOVAILO V.V., PONS J., CESARI E., TAKAGI T., Mater. Sci. Engn. A, 378 (2004), 444.
[41] DUBOWIK J., KUDRYAVTSEV V.V., LEE Y.P., J. Appl. Phys., 95 (2004), 2912.
[42] DUBOWIK J., GOŚCIAŃSKA I., KUDRYAVTSEV Y.V., LEE Y.P., SOVAK P., KONC M., phys. stat. sol. C, 3 (2006), 143.
[43] PATIL S., TANG D., LOFLAND S.E., BHAGAT S.M., TAKEUCHI I., FAMADU O., READ J.C., CHANG K.-S., CRACIUNESCU C., WUTTIG M., Appl. Phys. Lett., 81 (2002), 1279.
[44] KHOVAILO V.V., TAKAGI T., BOZHKO A.D., MATSUMOTO M., TANI J., SHAVROV V.G., J. Phys. Cond. Matter, 13 (2001), 9655.

Received 7 May 2006
Revised 1 September 2006

Materials Science-Poland, *Vol.* 25, *No. 2, 2007*

Magnetic and transport properties of Fe/Si multilayers with various iron thicknesses

P. WANDZIUK[1*], T. LUCIŃSKI[2], B. ANDRZEJEWSKI[1, 2]

[1]Institute of Molecular Physics, Polish Academy of Sciences,
M. Smoluchowskiego 17, 60-179 Poznań, Poland

[2]Laboratoire CRISMAT, UMR 6508 CNRS-ENSICAEN,
6, Boulevard du Maréchal Juin, 14050 Caen Cedex, France

Resistivity, temperature coefficient of resistance and magnetization as functions of iron thickness have been studied in a series of magnetron sputtered Fe/Si multilayers with constant Si layer thickness. At the Fe/Si interfaces, a significant amount of deposited iron is transformed into nonmagnetic (0.5 nm) and ferromagnetic (up to 2 nm) nonuniform Fe–Si mixture with a gradient of Fe concentration. Finally, for iron thicknesses above 2.5 nm a *bcc*-Fe phase appears.

Key words: *thin films; magnetic multilayers; Hall effect*

1. Introduction

The Fe/Si multilayered system attracts a lot of attention because of the strong antiferromagnetic (AF) interlayer coupling [1–3] and due to potential application in integrated metal-semiconductor devices. Efforts have been made to clarify the origin of the interlayer interaction in the Fe/Si multilayers (Mls)[1–3]. It is well known that intermixing occurs at interfaces and leads to appearance of various structures similar to Fe–Si phases [1, 3] which may be responsible for the AF coupling. Dufour et al. [4] found that at the Fe/Si interface, a 1.8 nm thick mixture consisting of magnetic and nonmagnetic phases is formed. Kläsges et al. [5] found about 2 nm thick amorphous silicide layer with the composition close to Fe_3Si at the interfaces, and they showed that Fe/Si and Si/Fe interfaces are not symmetrical.

In our previous papers, we focused on the Si spacer properties [2, 3], whereas in this paper we follow the evolution of transport and magnetic phenomena as a function

*Corresponding author; e-mail: wandziuk@ifmpan.poznan.pl

of Fe thickness (d_{Fe}). The observed changes of magnetic and transport properties are related to the formation of interfacial Fe–Si structures in Mls with different d_{Fe}.

2. Experimental

A series of [Fe(d_{Fe})/Si(1.1 nm)]$_{15}$ Mls, with constant surface area 3.5×6 mm^2 and iron thickness $0.25 \leq d_{Fe} \leq 4$ nm, have been deposited by magnetron sputtering onto oxidized Si wafers at room temperature (RT). Silicon layer thickness d_{Si} = 1.1 nm has been chosen to assure the maximum of antiferromagnetic coupling between the Fe layers [2]. Additionally, a 30 nm thick pure Fe reference sample has been prepared. Magnetic and transport properties have been investigated by the Hall effect, electrical resistance and magnetic moment measurements carried out in the temperature range 4.2–300 K.

3. Results and discussion

Based on the evolution of the magnetic and electron transport properties of the investigated Mls, shown in Figs. 1 and 2, the dependences can be arbitrarily divided into four regions discussed below.

For d_{Fe} < 0.5 nm (Fig. 1), the absence of magnetic moment is observed. It seems to be due to intermixing at the Fe/Si interfaces resulting in formation of nonmagnetic Fe–Si mixtures. The resultant mixture is Si-rich and characterised by high resistance and negative temperature coefficient of resistance (TCR) (Fig. 2). Its resistivity ρ drops drastically with the increase of Fe thickness within this range.

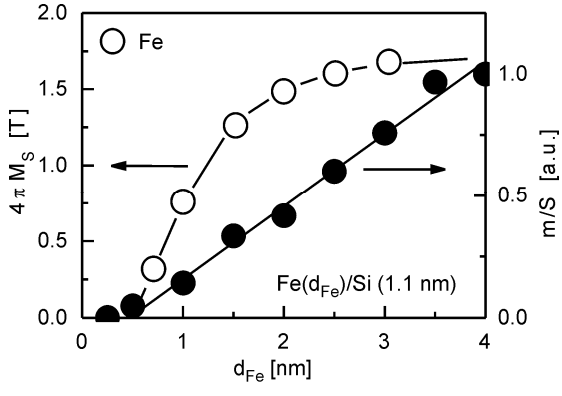

Fig. 1. Magnetic moment per surface area (m/S) and the $4\pi M_S$ values extracted from VSM and anomalous Hall effect, respectively, at room temperature as a function of Fe thickness d_{Fe}. The $4\pi M_S$ value of a Fe single layer sample is also shown

For $0.5 \leq d_{Fe} < 1$ nm, with increasing the amount of deposited Fe, the Fe–Si mixture is enriched with Fe. Therefore, for $d_{Fe} > 0.5$ nm, besides the dominant semiconducting layer consisted of Si-rich mixture, small metallic, ferromagnetic precipitations are formed, hence the magnetic moment appears. Thin metallic grains lower the ρ value but the effective transport properties are dominated by semiconducting matrix with negative TCR. Figure 3a displays temperature dependence of magnetic moment of

the Ml with d_{Fe} = 0.7 nm measured at magnetic field 0.05 T. The magnetic moment, plotted as a function of $T^{3/2}$ (Fig. 3b), can be fitted with two straight lines. This means that for d_{Fe} = 0.7 nm two ferromagnetic phases, with the Curie temperatures T_C = 168 K and 393 K, are present. There exist no crystalline Fe–Si phases with such a low T_C [6]. However, similar T_C values have been observed in the case of amorphous alloys [7], thus the formation of amorphous Fe–Si structures with different Fe concentration at the interfaces cannot be excluded.

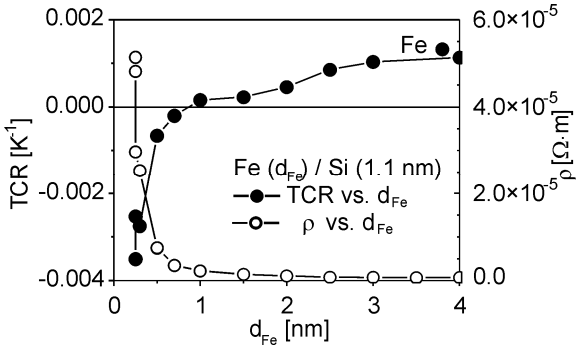

Fig. 2. Temperature coefficient of resistance TCR and resistivity ρ at 250 K as a function of Fe thickness

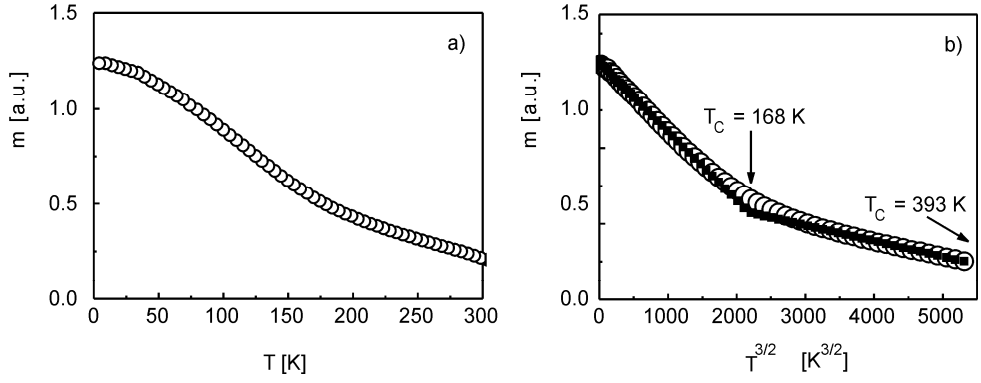

Fig. 3. Magnetic moment of Fe/Si Mls for d_{Fe} = 0.7 nm as a function of: a) T, b) $T^{3/2}$. See text for details

For $1 \leq d_{Fe} < 2.5$ nm, when the continuous metallic layer is formed, a transition from semiconducting to metallic behaviour occurs at about $d_{Fe} \approx 1$ nm. Further increase of the amount of deposited Fe results in an increase of $4\pi M_S$ extracted from anomalous Hall effect (Fig. 1) and positive TCR (Fig. 2) values. The $4\pi M_S$ shown in Fig. 1 is rather the effective magnetization, thus it can be influenced by the magnetic anisotropy (including surface anisotropy) and the AF coupling. The existence of ferromagnetic Fe–Si mixtures was confirmed by the presence of broad sextets in Mössbauer spectra with hyperfine field $H_{hf} \approx 29$ T [3].

Above $d_{Fe} \approx 2.5$ nm both TCR(d_{Fe}) and $4\pi M_S(d_{Fe})$ dependences flatten. Since measured $4\pi M_S$ is the average value of the *bcc*-Fe phase and several different ferromagnetic Fe–Si mixtures with reduced magnetizations (with respect to the *bcc*-Fe phase), the $4\pi M_S$ value of the investigated Mls does not reach the value of bulk Fe. For this d_{Fe} range, the presence of *bcc*-Fe phase (besides the Fe–Si mixtures) was previously indicated by our X-ray scattering and Mössbauer study [3].

Our results clearly show that the interfaces in the Fe/Si Mls are not sharp and a mixture with concentration gradient is formed. Its properties evolve, with the increase of Fe thickness, from nonferromagnetic semiconductor to ferromagnetic metal.

4. Conclusions

A significant amount of interfacial Fe–Si mixture, with nonuniform Fe concentration across the interface profile, has been found in the Fe/Si Mls. For thin iron layer ($d_{Fe} < 0.5$ nm) only nonmagnetic Fe–Si structures are present. Further increase of the iron thickness results in the appearance of ferromagnetic Fe–Si alloys with progressive increase of the $4\pi M_S$ value. The *bcc*-Fe phase appears just above $d_{Fe} \approx 2.5$ nm. Therefore the reduction of $4\pi M_S$ in respect to the bulk *bcc*-Fe value may be due to the averaging of magnetizations of different structures. However, the influence of the anisotropy and the AF coupling cannot be excluded.

Acknowledgements

This work was supported by the funds for science in years 2006/2007 as a research project No. 3 T08E 031 30 and from the science resources as a joint research program within scientific network *New materials and sensors for optoelectronics, informatics, energetic and medicine*. B.A. acknowledges EGIDE for financial support within grant Econet 10188YD.

References

[1] DE VRIES J.J., KOHLHEPP J., DEN BROEDER F.J.A., VERHAEGH P.A., JUNGBLUT R., REINDERS A., DE JONGE W.J.M., J. Magn. Magn. Matter, 165 (1997), 435.

[2] LUCIŃSKI T., WANDZIUK P., BASZYŃSKI J., SZYMAŃSKI B., STOBIECKI F., ZWECK J., Phys. Stat. Sol. (c), 3 (2006), 93.

[3] LUCIŃSKI T., KOPCEWICZ M., HÜTTEN A., BRÜCKL H., HEITMANN S., HEMPEL T., REISS G., J. Appl. Phys., 93 (2003), 6501.

[4] DUFOUR C., BRUSON A., MARCHAL G., GEORGE B., MANGIN PH., J. Magn. Magn. Matter, 93 (1991), 545.

[5] KLÄSGES R., CARBONE C., EBERHARDT., PAMPUCH C., RADER O., KACHEL T., GUDAT W., Phys. Rev. B, 56 (1997), 10801.

[6] KUBASCHEWSKI O., *Iron – Binary Phase Diagrams*, Springer, New York, 1982, pp. 136–139, and references therein.

[7] MARCHAL G., MANGIN PH., PIECUCH M., JANOT C., J. Physique Colloq., 37 (1976), C6-763.

Received 7 May 2006
Revised 1 September 2006